

Controls on axial deep-water channel evolution in compressional basins

Daniel Eray Tek

Submitted in accordance with the requirements for the degree of
Doctor of Philosophy

University of Leeds
School of Earth and Environment
Submitted October 2021

The candidate confirms that the work submitted is their own, except where work which has formed part of jointly authored publications has been included. The contribution of the candidate and the other authors to this work has been explicitly indicated below. The candidate confirms that appropriate credit has been given within the thesis where reference has been made to the work of others.

Chapter 3 – Published

Tek, D.E., Poyatos-Moré, M., Patacci, M., McArthur, A.D., Colombera, L., Cullen, T.M. and McCaffrey, W.D. 2020. Syndepositional tectonics and mass-transport deposits control channelised, bathymetrically complex deep-water systems (Aínsa depocenter, Spain). *Journal of Sedimentary Research*. **90**(7), pp.729–762.

Author contributions:

Tek, D.E. – Main author, organised and led data collection, data analysis, figure and manuscript preparation.

Poyatos-Moré, M. – Fieldwork assistance, conceptualisation and manuscript review.

Patacci, M. – Fieldwork assistance, conceptualisation and manuscript review.

McArthur, A.D. – Fieldwork assistance, conceptualisation and manuscript review.

Colombera, L. – Conceptualisation and manuscript review.

Cullen, T.M. – Fieldwork assistance, conceptualisation and manuscript review.

McCaffrey, W.D. – Fieldwork assistance, conceptualisation and manuscript review.

Submitted: 19 November 2019

Accepted: 26 February 2020

Chapter 4 – Published

Tek, D.E., McArthur, A.D., Poyatos-Moré, M., Colombera, L., Patacci, M., Craven, B. and McCaffrey, W.D. 2021a. Relating seafloor geomorphology to subsurface architecture: How mass-transport deposits and knickpoint-zones build the stratigraphy of the deep-water Hikurangi Channel. *Sedimentology*. doi:10.1111/sed.12890.

Author contributions:

Tek, D.E. – Main author, led data analysis, and figure and manuscript preparation.

McArthur, A.D. – Secured data access, conceptualisation and manuscript review.

Poyatos-Moré, M. – Conceptualisation and manuscript review.

Colombera, L. – Conceptualisation and manuscript review.

Patacci, M. – Conceptualisation and manuscript review.

Craven, B. – Aided methodological development, manuscript review.

McCaffrey, W.D. – Secured data access, conceptualisation and manuscript review.

Submitted: 21 October 2020

Accepted: 20 April 2021

Chapter 5 – Published

Tek, D.E., McArthur, A.D., Poyatos-Moré, M., Colombera, L., Allen, C., Patacci, M. and McCaffrey, W.D. 2021b. Controls on the architectural evolution of deep-water channel overbank wave fields: insights from the Hikurangi Channel, New Zealand. *New Zealand Journal of Geology and Geophysics*. doi.org/10.1080/00288306.2021.1978509.

Author contributions:

Tek, D.E. – Main author, led data analysis, and figure and manuscript preparation.

McArthur, A.D. – Secured data access, conceptualisation and manuscript review.

Poyatos-Moré, M. – Conceptualisation and manuscript review.

Colombera, L. – Conceptualisation and manuscript review.

Allen, C. – Conceptualisation and manuscript review.

Patacci, M. – Conceptualisation and manuscript review.

McCaffrey, W.D. – Secured data access, conceptualisation and manuscript review.

Submitted: 17 July 2021

Accepted: 06 September 2021

Acknowledgements

First of all, I would like to express my sincere gratitude to my supervisors, Bill McCaffrey, Adam McArthur, Luca Colombera, Marco Patacci, and Miquel Poyatos-Moré for their continued support, and for allowing me to follow my interests, and supporting the substantial changes to the direction of the thesis. **Bill**, thank you for being so attentive and supportive, and always being up for a good ol' s***t-shooting session. **Adam** thank you for being a friend, and for always being there to ease my anxieties and to discuss all things Hikurangi. **Luca**, thank you for being so efficient in everything you have done for me, and for your patience and expertise when trying to teach this layman about statistics. **Marco**, thank you for making me realise and understand the importance of data, and of diligent, methodical analysis; I can safely say I wouldn't be half as confident a scientist without you. **Miquel**, thank you for your continued mentorship, and for having stuck by me since our days in Manchester; and, of course, thank you for introducing me to the tastiest fruit of all: paraguayos.

Secondly, I'd like to thank some people who helped shape the path I have taken to this achievement. Thanks to Mark Standfield, who inspired me in my A-Level Geology classes, sparking my interest in all things Earth and Environment. Thanks to Dave Hodgson, for taking a chance on me and allowing me to secure my first academic job, which eventually led to my starting this PhD. And finally, thanks to the many people who transformed fieldwork in Spain into one giant fiesta: Adriana, Adam, Alex, Ashley, Bill, Laura, Marco, Miquel, and Tim.

If I were to compile an exhaustive list of all the friends that have supported me during this PhD, the thesis length would double. The Friday drinks crowd, the BSG-ish crew, the Romeward bounders, the TRG folks, the USA road-trippers, the BSRG peeps, Sed-groupers, and all the other friends I have made along the way; thank you all for the memories! Special thanks go to Tim, Chaz n' Dave, Georgian, Ben and Chloe, for providing a shoulder to cry(/complain) on, and for generally being great people.

Without the continued love and support of my family, I would never have been able to even start a PhD, let alone finish one. Mum, Dad, Katherine, Başak, Buzz and Bozok, thank you so much. Last, but by no means least, thank you Carla, for supporting me through all the stresses of finishing a PhD during a pandemic.

Abstract

Deep-water channels are important agents of sediment, nutrient and pollutant transport; their deposits comprise parts of the largest sedimentary bodies on the earth. However, the initiation and evolution of channels in elongate, compressional basins, remain poorly understood. This shortcoming stems from poor availability of data at the scale required to constrain the development of sedimentary architecture. Here, bathymetry, seismic reflection, and outcrop datasets from two case-studies are used to document the sedimentology and architecture of such channels, constraining models of channel and overbank evolution in different scales of compressional basin.

Analysis of the sedimentology and architecture of the outcropping Arro turbidite system, Ainsa Basin, Spain, revealed that: (1) MTD emplacement into structurally confined basins can both enhance and diminish the ability of subsequent turbidity currents to channelise; (2) the growth of structures with long-axes parallel to flow can encourage channelisation by imposing lateral confinement; (3) nested scales of surfaces that are concave-up in cross-section may have been formed by upstream-migrating bedforms. Two studies of bathymetric, 2D and 3D seismic data imaging a section of the Hikurangi Channel and its overbanks, offshore New Zealand, were used to inform models of large-scale architectural evolution. The first focused on integrating seafloor geomorphology and subsurface architecture, revealing that MTDs derived from channel-wall collapse, together with related upstream migrating knickpoints were responsible for generating channelised stratigraphy. The second focused on the overbanks, revealing that: (1) lateral confinement, here tectonically controlled, may suppress the development of 'wedge-shaped' levees; (2) nine controls influence processes of overbank flow and deposition: flow versus conduit size, overbank gradient, flow tuning, Coriolis forcing, contour current activity, flow reflection, centrifugal forcing, interaction with externally derived flows, and interaction of overspill from different locations; (3) the relative influence of these controls changed throughout the depositional period.

This work advances understanding of how deep-water channels in compressional basins evolve and generate channelised stratigraphy. It has implications for the study of seafloor geohazards, modelling hydrocarbon reservoir heterogeneity, and for evaluating the potential of deep-water sediments to sequester pollutants and organic carbon.

Table of contents

Chapter 1: Introduction	1
1.1 Rationale and research themes	1
1.1.1 <i>Theme 1: Controls on the architecture and evolution of axial channel and overbank deposits in compressional basins</i>	2
1.1.2 <i>Theme 2: Linking seafloor geomorphology to channel and overbank deposit architecture</i>	3
1.1.3 <i>Theme 3: The effect of mass-transport deposits (MTDs) on channel and overbank formation and evolution</i>	4
1.2 Thesis aims and objectives	5
1.2.1 <i>Chapter 3</i>	5
1.2.2 <i>Chapter 4</i>	6
1.2.3 <i>Chapter 5</i>	7
1.3 Thesis Structure	7
1.3.1 <i>Chapter 2 – Literature review</i>	7
1.3.2 <i>Chapter 3 – Syn-depositional tectonics and mass-transport deposits control channelised, bathymetrically complex deep-water systems (Aínsa depocenter, Spain)</i>	8
1.3.3 <i>Chapter 4 – Relating seafloor geomorphology to subsurface architecture: how mass-transport deposits and knickpoint-zones build the stratigraphy of the deep-water Hikurangi Channel</i>	8
1.3.4 <i>Chapter 5 – Controls on the architectural evolution of deep-water channel overbank sediment wave fields: insights from the Hikurangi Channel, New Zealand</i>	8
1.3.5 <i>Chapter 6 – Discussion</i>	9
1.3.6 <i>Chapter 7 – Conclusions and future work</i>	9
Chapter 2 - Literature Review	11
2.1 Subaqueous sediment gravity flows and their deposits.....	11
2.1.1 <i>An introduction to sediment gravity flows and their classification</i> .	11
2.1.2 <i>Turbidity currents and turbidites</i>	16
2.1.3 <i>Mass-transport and Mass-Transport Deposits</i>	17
2.1.4 <i>Facies tract analysis and flow transformation</i>	20
2.1.5 <i>SGF interaction with basin topography</i>	22
2.2 Deep-water sedimentary environments	26
2.2.1 <i>Fan models and architectural element analysis</i>	26
2.2.2 <i>Anatomy of a deep-water depositional system</i>	28
2.2.3 <i>Cyclicity in deep-water deposits</i>	29
2.2.4 <i>External forcing</i>	30
2.2.5 <i>Internal forcing</i>	30

2.2.6	<i>Stratigraphic hierarchy</i>	32
2.2.7	<i>Contour currents and contourites</i>	33
2.3	Deep-water channels	35
2.3.1	<i>Introduction and terminology</i>	35
2.3.2	<i>Deep-water channel equilibrium model</i>	36
2.3.3	<i>Cut-and-fill</i>	37
2.3.4	<i>Overspill</i>	40
2.3.5	<i>Deep-water channel morphologies</i>	41
2.3.6	<i>Channel-fill</i>	43
2.3.7	<i>Internal levee and terrace deposits</i>	45
2.3.8	<i>Channel complex architecture and channel-fill stacking</i>	46
2.3.9	<i>Avulsion</i>	48
2.3.10	<i>MTDs and deep-water channels</i>	49
2.3.11	<i>Deep-water channels and seafloor topography</i>	50
2.3.12	<i>Bedforms in deep-water channels</i>	52
Chapter 3 - Syn-depositional tectonics and mass-transport deposits control channelised, bathymetrically complex deep-water systems (Aínsa depocenter, Spain)		55
3.1	Summary	55
3.2	Introduction	56
3.3	Geological Setting	60
3.4	Data and Methods	62
3.4.1	<i>Large-Scale Trends</i>	62
3.5	Results	71
3.5.1	<i>Facies Analysis</i>	71
3.5.2	<i>Depositional Elements</i>	86
3.6	Discussion	98
3.6.1	<i>Timing of the Structures in the Arro System</i>	98
3.6.2	<i>Controls on Variability in Channel-Deposit Architecture</i>	98
3.6.3	<i>Influence of MTDs on Channelisation and Channel-Deposit Architecture</i>	103
3.6.4	<i>Precursor Deposits and Channel Initiation</i>	106
3.6.5	<i>The Arro System as an Analogue</i>	107
3.7	Conclusions	109
Chapter 4 - Relating seafloor geomorphology to subsurface architecture: How mass-transport deposits and knickpoint-zones build the stratigraphy of the deep-water Hikurangi Channel		111

4.1	Summary	111
4.2	Introduction	112
4.3	Geological Setting	114
4.4	Data	119
4.5	Methods.....	120
4.6	Results	121
4.6.1	<i>Seafloor expression</i>	121
4.6.2	<i>Seismofacies, surfaces and depositional elements</i>	125
4.6.3	<i>Stratigraphic relationships and three-dimensional correlation</i>	140
4.6.4	<i>Architectural variability and integration with seafloor observations</i>	144
4.7	Discussion	147
4.7.1	<i>An alternative model for the stratigraphic evolution of deep-water channels</i>	147
4.7.2	<i>The subsurface expression of knickpoints and knickpoint-zones</i>	155
4.7.3	<i>Comparison with knickpoints and knickpoint-zones in other systems</i>	158
4.7.4	<i>Reconstructing the palaeo-seafloor from seismic data</i>	160
4.8	Conclusions	162
Chapter 5 - Controls on the architectural evolution of deep-water channel overbank sediment wave fields: insights from the Hikurangi Channel, New Zealand		165
5.1	Summary	165
5.2	Introduction	166
5.3	Geological Setting	169
5.4	Data	172
5.5	Methods.....	173
5.5.1	<i>Bathymetry analysis and seismic interpretation</i>	173
5.5.2	<i>Sediment wave orientations and flow analysis</i>	174
5.5.3	<i>Morphological analysis of sediment waves</i>	175
5.6	Results	176
5.6.1	<i>Large-scale seafloor morphology and seismic stratigraphy</i>	176
5.6.2	<i>Outer-bend sediment waves on the seafloor</i>	182
5.6.3	<i>Outer-bend sediment waves in the subsurface</i>	195
5.6.4	<i>Inner-bend overbank waves on landward channel margin</i>	196
5.6.5	<i>Inner-bend waves on oceanward channel margin</i>	202
5.7	Discussion	208
5.7.1	<i>Controls on overspill processes on the overbanks of the Hikurangi Channel</i>	208

5.7.2	<i>Spatio-temporal variability and interaction of controls</i>	212
5.7.3	<i>Inner-bend sediment wave fields</i>	214
5.7.4	<i>Sedimentological implications</i>	215
5.8	Conclusions	217
Chapter 6	- Discussion	219
6.1	Comparison between the Arro turbidite system and the Hikurangi Channel.....	219
6.1.1	<i>Length</i>	220
6.1.2	<i>Basin physiography and width</i>	222
6.1.3	<i>Channel stacking patterns and the absence of avulsion</i>	224
6.1.4	<i>Lateral confinement and aggradation and progradation rates</i>	226
6.1.5	<i>Section summary</i>	227
6.2	Relating seafloor geomorphology to subsurface architecture.....	227
6.2.1	<i>Preservation of cyclic-steps, knickpoints and knickpoint-zones, and their inferred hierarchy</i>	227
6.2.2	<i>Inferring levee deposit geometry from the seafloor expression of levees</i>	230
6.3	The effect of mass-transport deposits on channel evolution and architecture.....	230
6.3.1	<i>Intra-channel MTDs</i>	231
6.3.2	<i>Mass-transport deposits and channelisation</i>	233
Chapter 7	- Conclusions and future work	235
7.1	Conclusions	235
7.1.1	<i>Theme 1: Controls on the architecture and evolution of axial channel and overbank deposits in compressional basins</i>	235
7.1.2	<i>Theme 2: Linking seafloor geomorphology to channel and overbank deposit architecture</i>	236
7.1.3	<i>Theme 3: The effect of mass-transport deposits (MTDs) on channel and overbank formation and evolution</i>	236
7.2	Future work	237
7.2.1	<i>General Recommendations</i>	237
7.2.2	<i>The Arro turbidite system</i>	240
7.2.3	<i>The Hikurangi Channel</i>	241
Chapter 8	- References	245
Chapter 9	- Appendices	307

List of figures

Chapter 2

Figure 2.1 – Environmental diagram illustrating the range of processes that transport and deposit sediment into deep-water (Stow and Mayall, 2000).....12

Figure 2.2 – Conceptual diagrams from Shanmugam (2000), based on original work by Lowe (1982), Bouma (1962) and Stow and Shanmugam (1980), showing: (A) Composite figure combining the facies models and their comparative divisions; (B) Idealised downflow facies transitions based on original diagram of Lowe (1982).....13

Figure 2.3 – (A) Sediment gravity flow classification scheme based on sediment support mechanism (modified after Middleton and Hampton, 1973; ‘flow behaviour’ added from Lowe, 1979); (B) classification diagram of Walker (1978) linking deposits to: flow initiation mechanism, long-distance transport process, late stage modification, and sediment support mechanism (numbered in accordance with those in A).....14

Figure 2.4 – Structure of, and processes acting within: (A) a bi-partite sediment gravity flow (Modified after Postma et al., 1988, Breien et al., 2010 and Manica, 2012), and (B) a cohesive debris flow (inspired by Hampton, 1972, Sohn, 2000, Mohrig and Marr, 2003); (C) Schematic plot showing the velocity and concentration structure of a typical stratified flow following a Roussian stratification profile (after Kneller and Buckee, 2000).....15

Figure 2.5 – (A) Scheme for the classification of mass transport deposits showing how different flow types transition to one another with increasing flow velocity and disaggregation, and their respective flow behaviours (Compiled from Nemeč, 1990; Posamentier and Martinsen, 2011; Ogata et al., 2012); (B) schematic figure (from Bull et al., 2009) showing anatomy of, and kinematic features within a typical MTC: (1) Headwall scarp, (2) Extensional ridges and blocks, (3) Lateral margins, (4) Basal shear surface ramps and flats, (5) Basal shear surface grooves, (6) Basal shear surface striations, (7) Remnant blocks, (8) Translated blocks, (9) Outrunner blocks, (10) Folds, (11) Longitudinal shears / first order flow fabric, (12) Second order flow fabric, (13) Pressure ridges, (14) Fold and thrust system.....19

Figure 2.6 – (A) Turbidite facies classification scheme originally from Mutti et al. (1999) showing 9 commonly observed facies, alongside common erosional features seen

alongside these facies (from Mutti et al., 2009); (B) facies tracts and the effects of flow efficiency on downstream facies segregation (Mutti et al., 1999): (i) a poor efficiency flow; (ii) a high efficiency flow.....20

Figure 2.7 – Schematic diagrams showing the interplay between the height of frontal topography and the internal Froude number (F_{ri}) on the reflection and division of a stratified turbidity current (modified from Kneller and McCaffrey, 1999 with grain-size segregation from Hansen et al., 2015).....23

Figure 2.8 – Early generic fan models: (A) the ‘suprafan model’ based on observations from modern systems (Normark, 1970a); (B) turbidite fan model from Mutti and Ricci Lucchi (1972) based on ancient turbidite deposits; (C) model from Walker (1978) showing a schematic drawing of a fan with the expected facies in each location.....24

Figure 2.9 – (A) Three types of turbidite depositional system observed within the South Pyrenean Foreland Basin in plan-view and longitudinal section (after Mutti, 1985). Type I was attributed to falling sea level, type II to sea level lowstand, and type III to rising sea level. (B) Nine types of deep-water systems (Stow and Mayall, 2000) based on classification by Reading and Richards (1994; original authors identified 12 types). Key controls are input source type and grain-size.....25

Figure 2.10 – Summary figure showing the anatomy of an idealised deep-water depositional system in cross-section (through a mixed erosional and depositional, levee confined channel), plan view, and longitudinal section (modified after Kane et al., 2007). Note that a given deep water system may not contain one or more of the features shown.....28

Figure 2.11 – (A) Figure summarising the process of compensational stacking, whereby avulsion leads to a lateral offset in the maximum thicknesses of two lobes (Prelat et al., 2010); (B) post breach evolution of an avulsion through: (i) the escape of unconfined turbidity currents, through the breach point at the avulsion node into the inter-channel low point depositing HARPs; (ii) progressive flow confinement leads to the accretion of levees and the establishment of a second channel (Flood et al., 1991).....31

Figure 2.12 – (A) Hierarchical classification scheme for deep-water channel deposits used in this review (from Cullis et al., 2018 after Sprague et al., 2005); (B) variety of different types of channel-fill, showing lateral and vertical trends with relatively

symmetrical (i and iii), and asymmetrical (ii) facies distributions (after Hubbard et al., 2014).....32

Figure 2.13 – *Conceptual depositional and process models for the interaction of gravity flows and bottom currents at different temporal scales (Fonnesu et al., 2020).....33*

Figure 2.14 – *Schematic diagram explaining the concept of cut-and-fill and its effects on a whole depositional system (Hodgson et al., 2016).....35*

Figure 2.15 – *(A) Summary diagram of the concept of channel equilibrium profiles with a focus on submarine channels; (B)-(D) show the response of a channel in pursuit of its equilibrium profile relative to its current position (modified after Kneller, 2003 with inspiration from Georgiopoulou and Cartwright, 2013).....36*

Figure 2.16 – *(A) Summary figure explaining the overspill processes responsible for the formation of levees and the effect of flow stratification in controlling their grain-size (after Hansen et al., 2015): (i) continuous overspill, (ii) partial inertial overspill, and (iii) complete inertial overspill; (B) sketch of a fine-grained submarine levee from the Karoo Basin (from Morris et al., 2014a) showing common features, grain-size trends and stratal terminations; denser dot spacing indicates coarser grains.....39*

Figure 2.17 – *(A) Schematic drawing of a sinuous fluvial channel highlighting the parameters of channel length and valley length (modified after Friend and Sinha, 1993); (B) three mechanisms for meander bend expansion and translation (modified from Peakall et al., 2000b); (C) contrasting styles of sinuosity in plan-view: disorganised and organised (after McHargue et al., 2011a).....42*

Figure 2.18 – *(A) Block model showing the three-dimensional architecture of a sinuous channel formed by swing, with channel aggradation being facilitated by overspill (Peakall et al., 2000b); (B) seismic image and (C) interpretation of a cross-section through a sinuous submarine channel in the Benin Major Canyon, western Niger Delta Slope (after Deptuck et al., 2007); Arrows have been added to show the switches in channel migration direction. This channel has experienced multiple stages of cut, widening and aggradation.....47*

Figure 2.19 – *Idealised sequence for the fill of a submarine slope valley (from Mayall and Stewart, 2000) showing (from base to top): lag deposits at the base as remnants of*

the cutting and bypass of the channel; slump or debris flow plugging of the channel; coarse grained sandy channel facies typically with lower sinuosity; a high sinuosity channel belt bound by levees and containing more fine-grained material.....48

Figure 2.20 – *Schematic diagram showing the potential sources of MTDs in a channel system in a structurally confined basin.....50*

Figure 2.21 – *Figure showing the plan-view expression of cyclic-steps in the Monterey Canyon, how they migrate and generate stratigraphy and surfaces (modified after Englert et al., 2021): (A) seafloor map of the Monterey Canyon and its axial channel, displaying the distribution and spacing of the cyclic-steps.; difference map of area in A, between bathymetry data collected in 2013 and 2014, showing areas of erosion and deposition; (C) and (D) seafloor change between two surveys in 2008 (C), and surveys in 2013 and 2014 (D), showing the distribution of deposits shown in E and F; (E) longitudinal profile and (F) cross-section (both located in C and D) showing areas of erosion and deposition between different bathymetry surveys, with the deposits and surfaces generated by migrating cyclic-steps coloured according to their survey interval.....51*

Figure 2.22 – *Figure showing the plan-view expression of knickpoints in Bute Inlet, Canada, how they migrate and generate stratigraphy and surfaces (modified after Heijnen et al., 2021): (A) slope maps generated from bathymetry collected in 2008 (i), and 2016 (ii), and a difference map between them showing how upstream knickpoint / knickpoint-zone migration causes local erosion and deposition; (B) longitudinal profile and (C) cross-section showing areas of erosion and deposition between different bathymetry surveys, with the seafloor position at the time of each survey highlighted by a different colour.....52*

Chapter 3

Figure 3.1 – *Schematic diagrams showing the effect of axial gradient and lateral confinement on flow velocity. Ai) Lateral constriction and release of a flow, or (ii) increasing and decreasing the axial flow gradient can (iii) increase or decrease flow velocity over a longitudinal transect of a flow, or (iv) temporally at the base of a passing flow (modified from Kneller, 1995). B) Velocity response of an unconfined flow (i) as it undergoes progressive lateral confinement (ii).....56*

Figure 3.2 – A) Map showing broad location of the South Pyrenean Foreland Basin in northern Spain. B) Schematic map showing the sediment routing system from Tremp-Graus (east) to Jaca depocenter (west) in the Eocene, modified from Remacha and Fernández (2003) and Caja et al (2010). C) Depositional dip section showing the correlation of fluvio-deltaic units in the distal part of the Tremp-Graus depocenter to their contemporaneous deep-water units in the Aínsa depocenter, with inset showing the chronostratigraphy of the Fosado, Arro and Gerbe systems (modified from Clark et al., 2017).....58

Figure 3.3 – Map of the Arro turbidite system modified from Clark et al. (2017) with data from this study, showing locations and names of major tectonic structures, the top and base of the Arro turbidite system, some summary structural data, and the twenty-two locations used to inform this study with Sierra de Soto Gully, Barranco de la Caxigosa, and Muro de Bellos highlighted. Grid is in degrees, minutes, and seconds, georeferenced in European Datum 1950 UTM zone 30N. Basemap at 1:25,000 scale courtesy of Instituto Geográfico Nacional, available from: http://centrodedescargas.cnig.es/CentroDescargas/locale?request_locale=en.....61

Figure 3.4 – A) Map presenting palaeocurrent data from fourteen of the visited locations illustrating their relationship with the basinal structures. B) Regional palaeocurrent data measured from (i) ripples and cross beds, and (ii) flute casts. C) All strike and dip measurements of bedding, indicating the average structural trend.....63

Figure 3.5 – Photographs of all fifteen facies and sub-facies which constitute the stratigraphy of the Arro system; descriptions are provided in table 1. A) Lf1 - structureless mudstone; B) Lf2 - graded siltstone; C) Lf3 - lenticular siltstone; D) Lf4a - rippled sandstone; E) Lf4b – hummocky-cross-stratified sandstone; F) Lf4c – planar-cross-stratified sandstone; G) Lf5 – parallel-laminated sandstone; H) Lf6a - graded, structureless sandstone; I) Lf6b - ungraded, structureless sandstone; J) Lf6c - sandstone with mudclasts; K) Lf7a - extraclast conglomerate; L) Lf7b - mudclast conglomerate; M) Lf8a - chaotic mudstone; N) Lf8b - deformed heterolithics; O) Lf9 - polymictic, bioclastic sandstone.....68

Figure 3.6 – A – H) Typical nature of facies associations 1 to 8 (FA1 – FA8) respectively. A, Bii-iii, Cii-iii, Dii-iii, Eii, Fii-iii, Gii and Hi) Representative photographs of all eight facies associations; Bi, Ci, Di, Ei, Fi and Gi) representative logs through idealised sections of FA2 – FA7 respectively; Biv) thinning rates and wavelengths of pinching and swelling

beds in FA2; Ci) bed top in FA3 covered by Scolicia; Hi) debritic mass-transport deposit of FA7 forming a steep-walled scour surface into an underlying sandstone bed..... 69-71

Figure 3.7 – Architecture of the Muro de Bellos outcrop. A) Locations of the Muro Sandbody outcrops 1 – 4 and the inferred direction towards their axes, the Muro and Sierra de Araguás thrusts, panels 1 and 2 in part D, and a rose diagram showing all palaeocurrents collected from the outcrop (channelised and non-channelised stratigraphy combined). B) Drone photograph from the east showing the relationship between sandbody outcrops 1 – 4 and their respective elevations; C) Raw (i) and interpreted (ii) photograph of Muro Sandbody outcrop 1. Di) Photomosaic showing the location of panels 1 and 2. Dii) Interpretation of the photopanel shown above (panel numbers and marker horizons are the same as in figure 3.12)..... 73

Figure 3.8 – A) Rose diagram showing local palaeoflow and its relationship with the strike of the outcrop face. B) Drone photograph of the Muro Sandbody outcrop 4. C) Interpretation of photograph in part B, showing bedding planes, facies associations, and log locations. D) Correlation panel built from the logs in part C..... 80

Figure 3.9 – Architecture of the Barranco de la Caxigosa outcrop: A) Summary map showing the locations and orientations of the panels in part C, and the Labuerda and Caxigosa thrusts. B) Rose diagram showing local palaeoflow and its relationship with the strike of panel BCP1. C) Correlation panel built from logs and interpreted photographs, such as in part D, showing bedding planes, facies associations, and channel stories. D) Raw (i) and interpreted (ii) photograph forming the basis for the correlation in the WSW of panel BCP1..... 82

Figure 3.10 – Architecture of the Sierra de Soto Gully outcrop: A) Summary map showing the extent of the panels in parts C and D, and the locations of the pseudo-logs in part E and Sierra de Araguás Thrust. B) Rose diagram showing local palaeoflow and its relationship with the strike of the gully. C) Photomosaic (i) and interpreted line drawing (ii) of the western outcrop panel. D) Photomosaic (i) and interpreted line drawing (ii) of the eastern outcrop panel. E) Correlation panel showing DE1 and DE2, and their constituent vertical and lateral facies association transitions, built from pseudo-logs created using outcrop panel interpretations supported by measured log data..... 86

Figure 3.11 – Schematic diagrams showing the interpreted formation and evolution of depositional elements 1 – 4: A) DE1; B) DE2 and DE4; C) DE3..... 87

Figure 3.12 – A) Map showing the locations of panels 1 and 2, the Sierra de Araguas and Muro thrusts, and local palaeocurrent (rose diagram same as in Fig. 3.7A); B – E) sketch diagrams showing the evolution of the channels in Muro de Bellos through four time steps. Interpreted panels 1 and 2 presented in Fig. 3.7 have been used to inform the interpretation and are displayed herein.....89

Figure 3.13 – Sketch block models showing the evolution of Barranco de la Caxigosa through nine time steps (A – I). Interpretation is informed by panels presented in Fig. 3.9 and displayed herein.....93

Figure 3.14 – Conceptual diagram showing the mechanisms by which MTD emplacement can help (A, C, E, G) or hinder (B, D, F, H, I) channelisation: A, B) interaction with MTD-margin topography; C, D) interaction with MTD-top topography; E, F) syndepositional substrate deformation and/or differential compaction; G, H) megascours excavated by erosive MTDs; I) MTDs filling a fully or partially channelised pathway and resetting basin-floor topography.....102

Figure 3.15 – Conceptual diagrams showing how progressive, structurally derived lateral confinement, and the punctuated emplacement of MTDs can affect channel inception and resultant sedimentary architecture: A) in an unconfined, progradational system experiencing increasing local coarse-grained sediment delivery, a channel will incise through unconfined precursor deposits after a channelisation threshold is crossed (sketches based on Hodgson et al., 2016); B) imposed lateral confinement from growing tectonic structures allows the channelisation threshold to be crossed earlier and at lower rates of delivery of coarse-grained sediment, inhibiting the development of sand-rich unconfined precursor deposits (example from Muro de Bellos); C) regular input of MTDs can interrupt the channelisation process by periodically removing the previously formed lateral confinement, which leads to delayed crossing of the channelisation threshold and the formation of DE3 deposits in replacement of sand-rich unconfined precursor deposits (example from Barranco de la Caxigosa).....105

Chapter 4

Figure 4.1 – Location maps showing: (A) the location of the Hikurangi Margin, and plate-scale features and structures; (B) the most proximal reach of the Hikurangi Channel, showing its relationship with its feeder canyons, slope-traversing trench-perpendicular systems, the Chatham Rise, Hikurangi Trench, and the Hikurangi Subduction Wedge.

Bathymetry were provided by the New Zealand National Institute for Water and Atmosphere (NIWA), and bathymetry is displayed as slope gradient maps with transparent water depth overlays..... 115

Figure 4.2 – (A) Gradient map with bathymetric overlay of the modern Hikurangi Channel within the study area. (B) Interpreted topological line drawing highlighting the location of bends 1 to 6 referenced in the text, main overbank and channel-wall features, and the locations of the profiles and morphometric features shown in Figs 4.3 and 4.4. (C) Detailed longitudinal depth and gradient profile along the thalweg of the channel showing the locations of the two knickpoint-zones, seven knickpoints, and other channel-floor features detailed in Fig. 4.5..... 117

Figure 4.3 – Cross-sectional seafloor profiles 1 to 28 (see Fig. 4.2 for locations), highlighting the features shown in Fig. 4.4..... 118

Figure 4.4 – (A) Summary sketch of the nomenclature used in the text and the parameters presented in parts (B) to (F). (B) Plot of terrace width versus normalised terrace height (its vertical position between the base and top of the host channel-wall), and the kernel density estimations thereof, derived from profiles 1 to 28 (Fig. 4.3). (C) Average and maximum channel-wall gradients against profile (a proxy for along-channel distance, which totals 140 km), and distributions and means thereof. (D) Depth versus distance (profile number) plot of the thalweg, channel-floor edges and tops of the channel-walls, and the distributions thereof. (E) Width versus distance (profile number) plot showing the width of the channel-floor, channel-walls, and total channel width, and distributions thereof. (F) Plot showing the height of the channel-floor edges, channel-wall tops and the height, width and abundance of terraces above the thalweg, and distributions thereof. Note that a section (profiles 6 to 11 inclusive) of the oceanward channel-wall top is outside of the survey extent, measurements in this section are therefore missing in (C) to (F). Data are provided in appendices 1, 2 and 3..... 119

Figure 4.5 – Seafloor gradient maps and profiles from various features in the channel-floor, walls and banks. (A) Map showing the downstream-narrowing channel-floor containing knickpoints 1 to 3 and knickpoint-zone 1, bound by steep channel-walls with terraces of varied widths, adjacent to an area of overbank (to the south) containing scallop-shaped depressions; a seafloor and interpreted seismic profile are provided as insets to aid interpretation of the scallop-shaped features (uninterpreted dip map in appendix 5). (B) Map and longitudinal profile showing thalweg-perpendicular ridges

interpreted as sediment waves and a train of crescentic features on the channel-floor. (C) Map and longitudinal profile through a train of crescentic features upstream of knickpoint 3. (D) Longitudinal profile through section in (A), showing: a low gradient upstream of knickpoint-zone 1; the sizes and gradients of knickpoint-zone 1; knickpoints 1 to 3; and crescentic features. (E) Map of bend 4 showing knickpoint 4 present on the outer bend, a number of small terraces on the inner bank and one larger terrace with dendritic gullies on the outer bank. (F) Map bend 5 showing: the channel-floor narrowing as it passes knickpoint 6 and 7, where it is bound by a newly formed terrace, and widening further downstream; numerous large terraces situated near the top of the inner bend channel-wall.....121

Figure 4.6 – Schematic 3D diagram showing the relationships between the various described seafloor features. The diagram is modelled on the area in Fig. 4.5A but the channel is displayed as straight, rather than sinuous as in reality, and the positions of solitary knickpoints are further upstream than in reality.....123

Figure 4.7 – Seismic sections and z-slices displaying the ten seismofacies and five seismic surfaces observed in the area, containing: (A) RMS amplitude z-slice, from 3000 m depth, and seismic sections showing dominantly SF1, SF2, SF8, HAR-bounding surfaces and channelform surfaces; (B) section showing SF2, SF3, SF8, HAR-bounding surfaces, channelform surfaces, MTD-bases and MTD-tops; (C) section showing SF2, SF8, channelform surfaces, sheet or terrace-bounding surfaces, MTD-bases and -tops; (D) spectral decomposition and interpreted line drawing showing SF3, SF1, HAR-bounding surfaces, channelform surfaces; (E) section showing SF1, SF4, SF5, SF8, HAR-bounding surfaces, channelform surfaces, MTD-bases and MTD-tops; (F) section showing SF1, SF5, SF4, SF5, SF6, SF8, channelform surfaces, sheet or terrace-bounding surfaces, MTD-bases and MTD-tops; (G) section showing SF1, SF5, SF6, SF8, SF9, HAR-bounding surfaces, channelform surfaces, sheet or terrace-bounding surfaces, MTD-bases and MTD-tops; (H) section showing SF7; (I) section showing aerially extensive SF8, SF9 and SF10 deposits, HAR-bounding surfaces, channelform surfaces, MTD-bases and MTD-tops (BSR: Bottom Simulating Reflector); (J) variance attribute z-slice showing aerially extensive SF8 and SF10 deposits and their context with SF5, SF6, MTD-bases, sheet or terrace-bounding surfaces, channelform surfaces; (K) RMS amplitude z-slice showing a aerially non-extensive SF8 deposit and bounding MTD-base, and SF6.....128

Figure 4.8 – Uninterpreted images (left) and interpreted line drawings (right) of seismic sections from: (A) the apex of bend 4; (B) the straight section between bends 4 and 5; (C) upstream of the apex of bend 5; (D) downstream of the apex of bend 5. Note: all sections displayed looking upstream.....139

Figure 4.9 – (A) Minimally interpreted and (B) interpreted sections showing 'sequence-type 1' (described in the text). (C), (D) and (E) Evolutionary block diagrams showing the formation of 'sequence-type 1'.....140

Figure 4.10 – (A) Minimally interpreted and (B) interpreted sections showing 'sequence-type 2' (described in the text). (C), (D) and (E) Evolutionary block diagrams showing the formation of 'sequence-type 2'.....141

Figure 4.11 – Interpretations of sections in Fig. 4.8 showing the relative ages of the different depositional elements, and their longitudinal correlations.....144

Figure 4.12 – Map of the thalwegs and edges of the flat bases of channelform surfaces 1 to 10 that have been traced across the area.....145

Figure 4.13 – (A) Root Mean Square (RMS) amplitude map of the seafloor showing the location of knickpoint-zone 1 (delineated by an area of high RMS amplitude), the flat, wide channel-floor upstream of knickpoint-zone 1, and the narrow channel floor bound by a newly formed terrace downstream of knickpoint-zone 1. (B), (C) and (D) Seismic sections from the shallow subsurface (B) in the area with a wide, flat channel-floor, ca 15 km upstream of knickpoint-zone 1, (C) immediately (ca 300 m) downstream of knickpoint 2 and (D) ca 7.5 km downstream of knickpoint 2.....146

Figure 4.14 – Interpreted seafloor reconstructions detailing the processes by which one palaeo-conduit is infilled and a subsequent one is created through five time-steps: (A) T1 – palaeo-conduit overlying channelform 8 has a wide channel-floor containing regularly spaced knickpoints; (B) T2 – collapse of the channel-wall forms an MTD that partially dams the channel, eliciting a decrease in longitudinal gradient upstream, and an increase downstream; (C) T3 – a knickpoint-zone forms and begins to migrate upstream, incising through, and leaving terrace deposits on top of, the MTD; (D) T4 – the knickpoint-zone migrates further upstream, incising through, and leaving terrace deposits on top of sheet deposits that formed upstream of the blockage but were contemporaneous to initial

knickpoint-zone incision; (E) a new palaeo-conduit is formed in the downstream wake of the knickpoint-zone.....149-151

Figure 4.15 – *Relative change diagrams showing the location of interpreted seafloor aggradation and degradation between the five time steps shown in Fig. 4.14: (A) T1, the initial surface; (B) T1 – T2; (C) T2 – T3; (D) T3 – T4; (E) T4 – T5; (F) cumulative product of T1 – T5.....152*

Figure 4.16 – *Two schematic models of channel evolution, explaining the potential processes responsible for the infill of a composite channelform surface, and the establishment of another. (A) Channel damming by an MTD, then clearance by an upstream-migrating knickpoint-zone causing a localised morphodynamic response. (B) Variations in the nature of the channel-traversing flows causing widespread deposition then incision along the entire channel reach (roughly the same as the studied reach of the Hikurangi Channel). ‘Lower energy channel-fill’ encompasses a range of possible architectures, from weakly confined sheet deposits (this study) to isolated, meandering channels (e.g. Kneller et al., 2020).....153*

Figure 4.17 – *Schematic diagrams showing two contrasting models for the generation of two nested scales of filled, concave-up surface in cross-section. (A) Multiple knickpoints, likely organised into a knickpoint zone, migrate upstream by headward erosion and deposition immediately downstream, leaving a series of concave-up surfaces (equivalent to HARP-bounding surfaces in the Hikurangi Channel), the edges of which constitute a larger-scale, composite surface (equivalent to a channelform surface in the Hikurangi Channel). (B) The formation and infill of multiple small-scale, incisional conduits generate a series of concave-up surfaces (HARP-bounding surface equivalent), the edges of which also constitute a larger, composite surface (channelform surface equivalent). (C) Schematic cross-section showing how both models could generate the same cross-sectional architecture.....157*

Figure 4.18 – *(A) Bathymetry map from the Rhone Delta in Lake Geneva, modified from Corella et al. (2016; original bathymetry from Girardclos et al., 2012), showing a channel with a wide, flat channel-floor upstream of an MTD that is being incised by a knickpoint and a newly-formed conduit; reproduced with permission from Elsevier. (B) Map of seafloor change between AD 2000 and 2012 of the inset shown in (A), again modified from Corella et al. (2016), showing deposition upstream and erosion downstream of knickpoint; reproduced with permission from Elsevier. (C) Map of seafloor change*

between AD 2003 and 2006 on the Fraser River delta, modified from Hill (2012), showing ongoing deposition on the overbanks, and upstream and downstream of a migrating knickpoint, with erosion localised to the knickpoint head; reproduced with permission from the International Association of Sedimentologists (IAS).....159

Figure 4.19 – Schematic cross-sections showing the principles by which uncertainty in seafloor reconstruction may be reduced in the presence of channel-damming MTDs. Sections either: (A) where MTDs are present; or (B) upstream of channel-damming MTDs, can be used to inform seafloor reconstruction.....161

Chapter 5

Figure 5.1 – Schematic diagrams showing how sediment waves migrate via: (A) the lee wave model (from Symons et al., 2016, after Flood, 1988), and (B), the cyclic-step model (from Symons et al., 2016, after Cartigny et al., 2011); flow direction is from right to left on both diagrams.....166

Figure 5.2 – Location maps showing: (A) the location of the Hikurangi Margin; (B) the proximal reach of the Hikurangi Channel, showing its relationship with its feeder canyons, the location of the study area slope-traversing trench-perpendicular systems, the location of the study area (see C) and the extent of the bathymetry and 3D seismic data used herein; (C) seafloor morphology in the study area, highlighting the ten channel bends referenced throughout the text, the sediment wave fields on the channel overbanks, and the channels’ relationships with the Hikurangi subduction wedge, the Chatham Rise, and the Pacific Plate. Bathymetry data were provided by the New Zealand National Institute for Water and Atmosphere (NIWA) and WesternGeco.....168

Figure 5.3 – (A) Interpreted seismic section through the Hikurangi Trench and its fill modified from McArthur and Tek (2021). (B) Annotated part of seismic section in A, showing the key geomorphic and seismic features present in and bounding the trench-fill and the potential sources of trench sedimentation.....170

Figure 5.4 – (A) Uninterpreted seismic section (location on Fig. 5.3B) and (B) interpreted line drawing through the Hikurangi Channel and its landward and oceanward overbanks, highlighting the three subsurface horizons referenced in the text and nine of the ten channel-forms that have been traced across the study area. (C) Map of the thalwegs and

edges of the flat bases of the ten traced channel-forms modified from Tek et al. (2021a).....171

Figure 5.5 – Schematic, fictitious example showing the methodologies applied on the seafloor and subsurface horizons for sediment wave orientations and flow analysis, and morphological analysis of the sediment waves. (A) Shows the segmentation of the wave crests shown in B and C, the distributions of the representative longitudinal profiles used to extract wave measurements in D, and how channel bends are defined. (B) Shows the segmentation of the channel bend and how inferred palaeocurrents are extracted from the segmented wave crests. (C) Rose diagrams illustrating analysis of the orientations of overbank flow directions, of wave crests and of channel trend (data from segments in B). (D) Shows how sediment wave wavelengths and wave heights are calculated in the profiles shown in A.....174

Figure 5.6 – (A) Map (location shown in Fig. 5.2B) showing locations of the trench profiles shown in B and C. (B) – (C) Longitudinal profiles through the trench showing the seafloor morphology of: (B) the tops of the channel walls, highlighting the depth difference between the two channel margins along the channel; (C) trench-perpendicular profiles, each through the apex of successive bends, showing the channel-perpendicular seafloor expression of the channel overbanks on both margins.....176

Figure 5.7 – (A) – (D) Topological maps of the four outer-bend wave fields on the landward channel margin, highlighting their stratigraphic evolution from Overbank Horizon 1 (A), through Overbank Horizons 2 (B) and 3 (C), to the seafloor (D). (E) Dimensions of the wave fields in A - D, showing area, length (measured away from the channel), and width (measured along the channel).....183

Figure 5.8 – Maps showing (A) the seafloor expression of wave field 1a, (B) wave field 2a, (C) wave field 3, and (D) wave field 4. For each wave field, an uninterpreted depth map and an interpreted hillshade map are displayed. On the interpreted map, the wave crests, the trend of the related channel bend, the locations of the longitudinal profiles shown in Fig. 5.10, including the wave field axis, and two inset rose diagrams showing the (bi-directional) orientations of the wave crest segments and the vector directions of the segmented channel bend trend are highlighted.....184

Figure 5.9 – (A) Rose diagrams showing the orientations of interpreted palaeocurrents from wave fields 1a, 2a, 3 and 4 on the seafloor, calculated from the segmented wave

crests. (B) Rose diagrams showing the orientations of interpreted palaeocurrents from wave field 2 / 2a in the 3D seismic survey Overbank Horizon 1, 2, 3 and the seafloor. (C) Graph showing the relationship between the bend curvature, and the bulk curvature of the wave crests in their associated wave fields, calculated using the mean vector lengths of the segmented channel trend and the interpreted palaeocurrents from the segmented wave crests. (D) Plan-view of the trend of bend 4 through the stratigraphy, showing an overall increase in bend curvature from Overbank Horizon 1 to the seafloor. (E) Hemispheric rose diagrams showing the mean vector orientation and length, interpreted palaeocurrents, and orientation of wave field axis through the stratigraphy, showing an overall clockwise rotation from the deep stratigraphy (Overbank Horizons 1 and 2), to the shallow stratigraphy (Overbank Horizon 3) and the seafloor..... 185

Figure 5.10 – Crest-perpendicular seafloor profiles (locations shown in Fig. 5.8) through wave fields 1a (A), wave field 2a (B), wave field 3 (C), and wave field 4 (D). For each wave field, the six profiles used for the extraction of wave dimensions in Fig. 5.12 are shown in depth and flattened to their upstream and downstream ends, and the wave field axis (profile containing the largest overall wavelength and wave heights), which is also shown in depth and flattened..... 186

Figure 5.11 – (A) Seafloor backscatter map imaging part of wave field 2a, showing that higher backscatter values occur on the upstream stoss sides of waves than on their lee sides. (B) Root Mean Squared (RMS) amplitude maps from the seafloor and the subsurface (depth shown in C) showing that, in general, RMS values are higher on the stoss (SW) sides of the waves in wave field 1. (C) Crest-perpendicular seismic section through wave field 1a, showing the locations of the three subsurface horizons and the locations of the horizons in B..... 187

Figure 5.12 – (A) Violin plots showing the distributions of sediment wave wavelengths and wave heights displayed by wave field on the seafloor and by measured Overbank Horizon in the subsurface for waves in wave field 2. (B) Scatterplots showing wavelengths and wave heights extracted from bathymetry data (coloured by wave field), seismic data from wave field 2 (coloured by the horizon they were extracted from), and all data. Separate plots of wave height versus distance from channel wall for each wave field and profile are displayed in Fig. 5.13. (C) Letter-value plots (Hofmann et al., 2017) showing wavelengths and wave heights displayed by profile number (profiles 1 – 6 in Fig. 5.8, 5.10) highlighting up- to down-channel variability in the morphology of waves extracted from bathymetry, seismic, and all data; diamonds represent the minimum

(resolvable) and maximum values, and boxes are scaled proportionally to number of datapoints.....188

Figure 5.13 – Scatter plots showing wave dimensions (wavelengths and heights) versus distance from the channel wall for (A) each wave field on the seafloor, and (B) wave field 2/2a on each subsurface horizon. Best fit lines are coloured by profile (same as in Fig. 5.12; see Fig. 5.9 and Fig. 5.14 for locations). Note that most best fit trends show a general downstream decrease in wavelength and wave height.....189

Figure 5.14 – Maps showing the seafloor expression of wave field 2 / 2a within the extent of the 3D seismic survey on Overbank Horizon 1 (A), Overbank Horizon 2 (B), Overbank Horizon 3 (C), and the seafloor (D). For each horizon, an uninterpreted slope map with depth overlay and an interpreted slope gradient map are displayed. On the interpreted map, the wave crests, the trend of the related channel bend, the locations of the longitudinal profiles shown in Fig. 5.15, including the wave field axis, and two inset rose diagrams showing the (bi-directional) orientations of the wave crest segments and the vector directions of the segmented channel bend trend are highlighted.....193

Figure 5.15 – Crest-perpendicular profiles (locations shown in Fig. 5.14) through wave field 2 / 2a, within the extent of the 3D seismic survey, measured on Overbank Horizon 1 (A), Overbank Horizon 2 (B), Overbank Horizon 3 (C), and the seafloor (D). For each wave field, the six profiles used for the extraction of wave dimensions in Fig. 5.12 are shown in depth and flattened to their upstream and downstream ends, and the wave field axis (profile containing the largest overall wavelength and wave heights), which is also shown in depth and flattened.....194

Figure 5.16 – (A) – (D) Slope maps with depth overlays centred on wave field 2 / 2b showing its relationship with field 2a and field 3, and three ~ crest-perpendicular profiles extracted from: Overbank Horizon 1 (A), Overbank Horizon 2 (B), Overbank Horizon 3 (C), and the seafloor (D).....197

Figure 5.17 – Annotated seismic sections at different angles to the wave crests in wave field 2a and 2b: (A) is orientated oblique (~ 45°) to crests in both fields, (B) is orientated oblique to crests in both fields, but at a higher angle (~ 70°) to crests in field 2b, and a lower angle to those in field 2a, (C) is orientated ~ perpendicular to crests in field 2b and ~ parallel to those in field 2a. Differences in sediment wave height and wavelength are

related to the sections being located at different positions along the channel. Note that these sections do not correspond to the profile locations in Fig. 5.16.....198

Figure 5.18 – (A) Part of Overbank Horizon 3 (same as shown in Fig. 5.16C) displayed in 3D looking down-channel over the inner-overbank of bend 5, annotated with interpreted overbank flow orientations and velocities, and locations of aggradation. (B) Part of the seafloor (same as shown in Fig. 5.16D) displayed and annotated in the same way as A. (C) Interpreted seismic sections through the locations displayed in A and B, showing the thickness of depositional packages between Overbank Horizon 1 and the seafloor, highlighting an overall down-channel decrease in package thickness and that reflector packages associated with wave field 2a are thicker than those of equivalent age in field 2b. (D) Schematic section showing the interpreted nature of overbank flow interaction between wave fields 2a and 2b.....200

Figure 5.19 – (A) – (C) Seafloor maps displayed as slope (A), or hillshade (B and C) maps with depth overlays, showing inner-bend waves on the oceanward margin, on the insides of bends 4, 6 and 10; crest-perpendicular profiles are also included. (D) Slope map with depth overlay showing the waves on the inner-overbank of bend 4 on Overbank Horizon 3; two ~ crest perpendicular profiles included. (E) Annotated seismic section and (F) interpreted line drawing thereof, showing the seismic expression of the waves on the inner-overbank of bend 4 orientated perpendicular to the wave crests.....201

Figure 5.20 – (A) Interpreted part of Overbank Horizon 3 (same as shown in Fig. 5.19D) displayed in 3D looking down-channel over the inner-overbank of bend 4, annotated with interpreted overbank flow orientations and velocities, and locations of aggradation. (B) Interpreted part of the seafloor (same as shown in Fig. 5.19A) displayed and annotated in the same way as A. (C) Interpreted seismic sections through the locations displayed in A and B, showing the thickness of depositional packages between Overbank Horizon 1 and the seafloor, highlighting an overall down-channel decrease in the sediment wave wavelengths and heights.....203

Figure 5.21 – Diagrams showing the formation and evolution of inner-bend waves on the oceanward overbank, specifically on the inside of bend 4. (A) Three-dimensional schematic showing the context of the inner-bend waves detailed in B, and the cause of transverse flow toward the channel and its relationship with trough-axial flow. (B) Detailed schematic diagrams (location on Fig. 5.20A and B; stratigraphic evolution based on upstream section in Fig. 5.20C; note perspective change from Fig. 5.20 to looking up-

channel) demonstrating how the sediment waves evolve from terraces, and how the interaction between axial flow through the wave troughs and transverse flow toward the channel causes sediment wave migration away from the channel. (C) Schematic showing how flow accumulation against the terrace-bounding surface generates a high-velocity component of down-channel flow leading to bypass at the terrace edge and mounding in the centre.....204

Figure 5.22 – Schematic diagrams showing eight of the nine processes interpreted to control overspill from the Hikurangi Channel: (A) flow size relative to conduit size, (B) overbank gradient, (C) flow tuning, (D) the Coriolis force, (E) contour current, (F) centrifugal force, (G) flow reflection, (H) interaction with externally derived flows. The interaction of flows originating from different parts of the channel is demonstrated in Fig. 5.24.....207

Figure 5.23 – Schematic diagrams showing the distribution of sediment waves and interpreted overbank flow in the deep stratigraphy, on Overbank Horizon 1 (A), and on the seafloor (B).....208

Figure 5.24 – Schematic diagram showing how overbank flow originating from different parts of a channel interacts on the overbanks.....211

Chapter 6

Figure 6.1 – Maps displaying the scale difference between the Arro turbidite system and the Hikurangi Channel: (A) map of the Iberian peninsula, showing the location of the Ainsa depocenter; (B) map of the east coast of northern New Zealand at the same scale as the map in A, showing the path of the Hikurangi Channel; (C) ~100 km by ~50 km map showing the reconstructed path of the Arro turbidite system between the outcrops of the Charo Canyon (Millington and Clark, 1995a, b), and the Broto lobes (Mutti, 1983); (D) map at the same scale as the map in C, showing the reach of the Hikurangi Channel imaged by the 3D seismic dataset herein.....219

Figure 6.2 – (A) 3D depositional model of the Arro turbidite system, showing the reconstructed palaeogeography during the late stages of deposition, and the subsurface deposits; (B) zoomed-in insert from part A, showing the interpreted relationships between buried bed or bedset surfaces and channel-story surfaces, with seafloor bedforms such as cyclic-steps, and knickpoints; (C) scale relationships between the surfaces observed

in the deposits of the Arro turbidite system and seafloor bedforms observed in a modern analogue: Bute Inlet, Canada (dimensions taken from Heijnen et al., 2020 and Chen et al., 2021).....220

Figure 6.3 – (A) 3D depositional model of the proximal Hikurangi Trench showing a simplified version of the trench bathymetry and its relationship with the deposits imaged in the 2D and 3D seismic data presented in Chapter 4 and 5; (B) zoomed-in insert from part A, showing the interpreted relationships between HARP-bounding surfaces and channelform surfaces, with knickpoints and knickpoint-zones observed on the seafloor; (C) scale relationships between the surfaces observed in the deposits beneath the Hikurangi Channel, and the observed seafloor features.....222

Figure 6.4 – Schematic showing the plan-view difference between: (A) a laterally confined system where avulsion is inhibited by the lateral confinement, leading the system to prograde quickly, and (B) an unconfined system where frequent avulsion leads to a more even lateral distribution of sediment and impedes progradation.....223

Figure 6.5 – Schematic showing the difference between: (A) an unconfined system where the development of levees that taper gradually away from the channel is permitted, and the channel thalweg is predisposed to become superelevated relative to the surrounding seabed and avulse, and (B) a confined system where overbank flows deposit over the entire basin-floor, leading to elevated vertical aggradation rates and the inhibition of the development of tapering levees, thalweg superelevation, and hence avulsion.....224

Figure 6.6 – Schematic diagrams (modified after Fig. 4.16) showing how, in some locations, similar cross-sectional stratigraphic motifs can be formed by: (A) the localised erosional response to MTD emplacement downstream of the section location, and (B) widespread deposition then erosion along long channel reaches.....230

List of tables

Chapter 3

Table 3.1 – Descriptions of the fifteen facies and sub-facies recognised in the stratigraphy of the Arro system, including their lithologies, typical thicknesses and interpretations of their depositional processes.....64-67

Chapter 4

Table 4.1 – Descriptions and interpretations of the ten seismofacies observed within the studied stratigraphy.....129-132

Table 4.2 – Descriptions and interpretations of the five seismic surfaces observed within the studied stratigraphy.....132-134

Chapter 5

Table 5.1 – Descriptions and interpretations of the seven seismofacies observed within and adjacent to the studied trench-fill.....178-180

Table 5.2 – Descriptions, interpretations, and seismic cross-sections of the three types of overbank geometry observed within the studied trench-fill.....181

Table 5.3 – Minimum (resolvable), maximum and average wavelengths and heights of the sediment waves in each wave field.....190

Table 5.4 – Minimum (resolvable), maximum and average wavelengths and heights of sediment waves across all fields, displayed by profile (shown in Fig. 5.8 and Fig. 5.14); profile 1 is furthest up-channel and profile 6 is furthest down-channel.....191

1 Introduction

1.1 Rationale and research themes

Around one hundred and fifty years ago, Captain Lindenkohl first discovered a large submerged canyon incised into the continental shelf offshore New England, USA (Lindenkohl, 1885). Since this initial discovery, submarine canyons and channels have been identified on the floors of all Earth's seas and oceans, and occur on all continental margins (Harris and Whiteway, 2011). Submarine channels are elongate conduits, concave-up in cross-section, through which turbidity currents and other sediment-laden flows transport sediment to the deep sea (see review in Peakall and Sumner, 2015). They are commonly bound by thick accumulations of relatively fine-grained overbank sediments, deposited from the tops of turbidity currents that are thicker than the depth of the channel they traverse (Piper and Normark, 1983). Alongside very large volumes of sediment (Talling et al., 2007; Mountjoy et al., 2018), submarine channel and overbank deposits can also transport and sequester anthropogenic pollutants (Kane et al., 2020; Zhong and Peng, 2021; Bell et al., 2021), organic carbon (Hage et al., 2020) and nutrients (Heezen et al., 1955). The deposits formed by submarine channels can provide archives of environmental change (Prins and Postma, 2000; Castellort et al., 2017) and catastrophic events such as earthquakes (Goldfinger, 2011; Howarth et al., 2021), and can act as prolific hydrocarbon reservoirs (Mayall and Stewart, 2000; Mayall et al., 2006). Powerful, channel-traversing flows also represent a significant geohazard for seafloor infrastructure, such as submarine telecommunications cables (Carter et al., 2014; Pope et al., 2017). Understanding submarine channel evolution is therefore of great socio-economic and scientific importance.

A myriad of data types can be used to study the morphology of submarine channels and their overbanks on the seafloor, and the architecture of the deposits they generate. However, generally each data type only permits interpretation of channel evolution at a distinct spatio-temporal scale. Analysis of bathymetric data (e.g. Palm et al., 2021) and repeat bathymetric surveying (e.g. Guiastrennec-Faugas et al., 2020, 2021) can provide information on the instantaneous morphology of a channel and its levees, and how this may change over annual to decadal timescales, but provide little insight into the longer-term (hundreds to millions of years) depositional history. Core and outcrop (e.g. Pickering and Corregidor, 2005; Hodgson et al., 2011; Hubbard et al., 2014, 2020; Kneller et al., 2020) data can provide a detailed record of the short- to long-term (annual to millions of years) depositional history, and the small-scale (centimetres to hundreds of metres vertically) depositional architecture, of channel deposits, but these depositional records are typically incomplete and lack three-dimensional constraint.

Seismic data (e.g. Deptuck et al., 2003, 2007; Janocko et al., 2013) typically image the large-scale (tens to thousands of metres vertically) architecture of channel deposits which can provide insight into the long-term, three-dimensional evolution of channels, but lack information on the small-scale architecture and depositional history. Therefore, to understand how channels form and evolve over a range of timescales requires a multifaceted approach. In this thesis, three types of data are integrated: (1) outcrop data from exposed channel and levee deposits of the Arro turbidite system in the structurally-confined Aínsa Depocentre (Spanish Pyrenees); (2) two- and three-dimensional seismic data imaging the subsurface deposits of the Hikurangi Channel (offshore New Zealand) and its overbank areas; (3) seafloor (bathymetric and backscatter) data imaging the seafloor expression of the currently active Hikurangi Channel and its overbank areas. Integration of these datasets allows analysis of the sedimentology, including the two- and three-dimensional depositional architecture, of two channelised depositional systems that run axially in structurally-confined settings, from bed-scale to system scale. This, in turn, allows the interpretation of channel evolution at a range of timescales from that of individual flows, to millions of years.

Due to their economic, societal, and scientific importance, many publications and theses have focused on the evolution of submarine channels. However, advances in data acquisition and concomitant step-changes in conceptual understanding necessitate further work to understand how these systems evolve. In this thesis, three themes that represent gaps in contemporary understanding of channel initiation, evolution, and deposit formation are addressed:

1.1.1 Theme 1: Controls on the architecture and evolution of axial channel and overbank deposits in compressional basins

Within the broad classification of ‘compressional basins’ several sub-environments are commonly the loci for the formation of deep-water channels that run axially through elongate, structurally- or tectonically-confined troughs. In foreland settings, which result from the collision of two continental plates, deep-water channel deposits have been identified in foredeep basins, such as the Magallanes Basin in Chile (Hubbard et al., 2008, 2009, 2014, 2020), or in thrust-top basins that are confined by thrust-cored anticlines and form on top of thrust sheets, such as the South Pyrenean Foreland Basin in Spain (Mutti, 1985; Pickering and Bayliss, 2009; Dakin et al, 2013; Bell et al., 2018b; Tek et al., 2020) and the Gorgoglione Basin in Italy (Casciano et al., 2019). At subduction zones, where oceanic crust is being subducted, deep-water channels and their deposits are observed in subduction trenches (McArthur and Tek, 2021), such as the Hikurangi Trench offshore New Zealand (Tek et al., 2021a, b), or in elongate thrust-

confined trench-slope mini-basins that occur in the accretionary wedge, such as in the East Coast Basin, offshore New Zealand (Crisostomo Figueroa et al., 2020).

The two case studies presented herein represent end members at opposing ends of the spectrum of structurally-bound axial channel systems found at compressional margins. The Arro turbidite system sits within the well-studied Aínsa Depocentre, within the South Pyrenean Foreland Basin. The system contains the deposits of one of a series of ancient deep-water channel systems located in thrust-top basins on thrust sheets bounded by thrust-cored anticlines formed on the orogenic wedge (Mutti, 1977, 1985; Clark et al., 2017). Compared with the younger channel and overbank deposits in the depocentre, the Arro system has received very little attention, with its distal expression in the basin essentially unstudied. Therefore, the first case study (Chapter 3) presented herein contains descriptions of the sedimentology and architecture of understudied axial channel and overbank deposits in a well-studied basin, and interpretations of channel initiation and evolution.

Although the study of outcropping axial channel and overbank deposits is commonplace, comparisons to modern axial channel and overbank systems are not. Of the foreland basins on Earth today (Nyberg and Howell, 2015), none are traversed by axial channel and overbank systems, making direct comparison impossible. Deep-ocean trenches are sometimes traversed by trench-axial channels (McArthur and Tek, 2021), offering potential comparators to deposits that fill outcropping and buried foredeeps such as the Magallanes Basin (Hubbard et al., 2008, 2009, 2014, 2020) and Austrian Molasse Basin (De Ruig and Hubbard, 2006; Hubbard et al., 2009; Bernhardt et al., 2012; Masalimova et al., 2015; Kremer et al., 2018) respectively. However, due to their inaccessible oceanographic settings, the data available from deep-ocean trenches is typically limited to bathymetry and low-resolution two-dimensional seismic data. The integrated dataset used in the second case study, from the Hikurangi Channel, offshore New Zealand (Chapters 4 and 5), encompasses high-resolution bathymetry, backscatter, two-dimensional seismic data, and the first three-dimensional seismic dataset to image an axial channel and overbanks system in a deep-ocean trench. Although not all of the Hikurangi Channel is trench-confined (Lewis, 1994; Lewis et al., 1998), examination of the three-dimensional architecture of the trench-axial portion can be used to interrogate what effects its setting may exert on its architecture.

The case studies herein differ in their interpreted scale, water depth and tectonic setting; the relatively short (~40 km long) channels that formed the Arro turbidite system are interpreted to have traversed a relatively shallow water thrust-top basin in the orogenic wedge of a foreland basin, while the exceptionally long (~2000 km long) Hikurangi Channel traverses a deep-ocean subduction trench at water depths in excess

of 2500 m. However, comparing controls on the architecture of the channel and overbank deposits in tectonically-confined axial channel systems with different tectonic and oceanographic settings can allow the assessment of what controls may be common to axial channel and overbank systems in confined, compressional basins generally.

1.1.2 Theme 2: Linking seafloor geomorphology to channel and overbank deposit architecture

Comparing modern and ancient turbidite systems has long been a goal in deep-water sedimentology (Mutti and Normark, 1987), but its attainment has been undermined by a lack of process-to-product understanding in both modern and ancient systems (Peakall and Sumner, 2015). However, a recent increase in the use of data acquisition techniques such as repeat bathymetric surveying (Hughes Clarke et al., 2012, 2014), direct flow monitoring (Azpiroz-Zabala et al., 2017; Clare et al., 2020; Heerema et al., 2020), and analysis of shallow cores (Hage et al., 2018, 2020; Maier et al., 2019), has revolutionised our understanding of how submarine channel and overbank systems evolve over annual to decadal timescales. Specifically, the role of geologically-transient, upstream-migrating features such as knickpoints (Heijnen et al., 2020; Guiastrenec-Faugas et al., 2020, 2021) and cyclic steps (Paull et al., 2018; Vendettuoli et al., 2019; Chen et al., 2021) in sculpting the seafloor within submarine channels has become apparent. Increasingly, the depositional products of migrating cyclic steps are being identified in outcropping channelised successions (Hage et al., 2018; Englert et al., 2020; Slootman and Cartigny, 2020; Ghienne et al., 2021; Postma et al., 2021). However, the stratigraphic preservation of larger scales of upstream-migrating features such as knickpoints and knickpoint-zones (*sensu* Heijnen et al., 2020) remains poorly understood. Furthermore, cyclic-steps and knickpoints in modern channel systems, have been shown to interact with one another (Chen et al., 2021), yet the stratigraphic response of this interaction remains understudied. Nested scales of concave-up surfaces are commonly identified in cross-sections through channelised stratigraphy from seismic (Mayall et al., 2006) and outcrop (Sprague et al., 2005; Di Celma et al., 2011) data, leading to the interpretation of 'hierarchy' in channel deposits (Cullis et al., 2018). With the recognition that some scales of concave-up surface can be generated by upstream-migrating features, the role such features may play in generating apparent hierarchy also warrants attention.

The aforementioned knowledge gaps expose another question related to the study of modern and ancient submarine channel and overbank systems: how useful is the modern seafloor as a predictor of channel deposit architecture? This question has implications for the validity of comparisons between modern submarine channel and overbank morphologies, and the morphologies of stratigraphy and surfaces observed in

ancient channel and overbank deposits. Although repeat bathymetric mapping, flow monitoring and analysis of shallow cores are not used in this thesis, recent insights from active channel systems are applied herein to interpret the genesis of surfaces and packages of stratigraphy observed in the studied deposits. Key to this application of insights from modern systems is the integration of bathymetric and seismic data in the Hikurangi Channel (Chapters 4 and 5), where seafloor features such as knickpoints, knickpoint-zones identified on the modern channel-floor are assumed to act in a similar way to other settings, and therefore provide information on channel evolution.

1.1.3 Theme 3: The effect of mass-transport deposits (MTDs) on channel and overbank formation and evolution

In this thesis, 'mass-transport deposit' (MTD) is used as a catch-all term for the product of *en masse* transport and deposition initiated and facilitated by gravity (Posamentier and Martinsen, 2011); this includes the products of debris flow, slumping, and sliding, but excludes the products of turbidity currents. The role of turbidity currents in the formation and evolution of submarine channels has long been studied using experimental and numerical modelling (Keevil et al., 2006; Peakall et al., 2007; Kane et al., 2008; Dorrell et al., 2013b, 2014; Peakall and Sumner, 2015), and analysis of deposits at outcrop and in the subsurface (Kneller, 2003; Wynn et al., 2007; Gong et al., 2013; Hubbard et al., 2014, 2020); however, the role of MTDs is less well studied.

That the topography on top of large, regionally-extensive MTDs can control the routing of turbidity currents and therefore the location of inception of submarine channels is well documented (Ward et al., 2018). However, the effect of the interaction of smaller, but more frequent MTDs with turbidity currents, on the process of channel inception, particularly in confined basins, is poorly understood. In the Arro turbidite system, the relationship between numerous MTDs with turbidity current deposits of multiple architectures allows the effect of MTD emplacement on the channelisation process to be investigated, in order to fill this knowledge gap (Chapter 3).

When an MTD is emplaced into an established submarine channel, its effects on the surrounding deposits have been noted (Bernhardt et al., 2012; Masalimova et al., 2015; Corella et al., 2016; Kremer et al., 2018). However, the impact of MTD emplacement on the evolution of submarine channel systems is less well understood. In the Hikurangi Channel, numerous large MTDs are observed in the subsurface alongside other submarine channel deposits, allowing the investigation of how the emplacement of these MTDs affected channel evolution at large scales and over long time periods (Chapter 4).

1.2 Thesis aims and objectives

The aims of this thesis are fundamentally to provide insight into the themes introduced above: controls on the architecture and evolution of axial channel and overbank deposits in compressional basins; linking seafloor geomorphology to channel and overbank deposit architecture; and the effect of mass-transport deposits (MTDs) on channel and overbank formation and evolution. These insights are gained through achieving a series of chapter-specific aims and objectives:

1.2.1 Chapter 3

The primary aim of this chapter is to discern how syn-depositional tectonics and MTD emplacement affect the process of channelisation and evolution, and the formation of channelised deposits. The primary objective of this chapter is to provide a detailed sedimentological and architectural categorisation of the Arro turbidite system, in the Aínsa Depocentre, South Pyrenean Foreland Basin. This overarching objective is achieved through the following specific objectives:

- Gathering sedimentological, stratigraphic and structural field data from outcrops in the unstudied distal part of the Arro turbidite system.
- Categorising the outcropping deposits into sedimentary facies, facies associations, and depositional elements using detailed sedimentary logs and outcrop photographs acquired from the ground, and from an uncrewed aerial vehicle (UAV or 'drone').
- Mapping the distributions of depositional elements through the outcrops from the proximal to distal parts of the basin.
- Analysing structural and paleocurrent data to investigate the relationship between structural trends and sediment routing.
- Interpreting the evolutionary history of channel and overbank deposits in key outcrops: Sierra de Soto Gully, Barranco de la Caxigosa, and Muro de Bellos.
- Using the results from these evolutionary interpretations to inform generic models of how tectonic structures and MTDs affect channelisation and channel evolution.
- Identifying potential seafloor analogues for the deposits in the Arro turbidite system.

1.2.2 Chapter 4

The primary aim of this chapter is to elucidate the role of geologically-transient seafloor features such as channel-damming mass-transport deposits, and upstream migrating knickpoints and knickpoint-zones in generating channelised deep-water deposits and surfaces. The primary objective of this chapter is to link observations and interpretations made using bathymetric data to those from three-dimensional seismic data that image the Hikurangi Channel and its subsurface deposits. This overarching objective is achieved through the following specific objectives:

- Categorising the seafloor geomorphology of the Hikurangi Channel within the area of interest, identifying features such as terraces, channel-damming MTDs, sediment waves, cyclic-steps, knickpoints and knickpoint-zones associated with the channel.
- Categorising the subsurface architecture through the identification of commonly occurring seismofacies, seismic surfaces, and depositional elements.
- Performing a three-dimensional correlation of deposits and surfaces using MTDs as chronostratigraphic markers, to establish the relative ages of the deposits.
- Integrating detailed observations of seismic reflector character in the shallowest studied stratigraphy, with observations from the overlying seafloor, to establish relationships between seafloor features and subsurface deposits.
- Providing a new model of submarine channel evolution and deposit formation, informed by observations in the seafloor and subsurface.
- Discerning the barriers to, and ways to reduce uncertainty in, reconciling seafloor geomorphology and subsurface architecture in deep-water channel systems.

1.2.3 Chapter 5

The primary aim of this chapter is to ascertain the controls on overbank flow processes and associated deposit architecture on the overbanks of trench-axial channels. The primary objective of this chapter is to integrate qualitative and quantitative observations and interpretations made from the analysis of sediment waves on the overbanks of the Hikurangi Channel, with the architecture of the subsurface overbank deposits. This overarching objective is achieved through the following specific objectives:

- Conducting seismic interpretation of the trench-fill, categorising it into commonly occurring seismofacies, and identifying and tracing regionally-traceable horizons through a two-dimensional and three-dimensional seismic dataset.
- Developing and implementing novel methodologies for the extraction and analysis of data pertaining to the morphology and analysis of sediment waves on the seafloor, and on traced horizons in the subsurface.
- Analysing the size, orientation and distribution of sediment waves using quantitative and qualitative methods.
- Establishing the controls on sediment wave size, orientation and distribution, and using these interpretations to infer controls on modern overbank flow and palaeoflow processes.
- Identifying the controls that led to the formation of enigmatic sediment waves on inner-bend overbanks.

1.3 Thesis Structure

1.3.1 Chapter 2 – Literature review

This chapter provides a brief synthesis of the theoretical background that underpins the concepts discussed in this thesis. This synthesis first gives an overview of historical and contemporary understanding of subaqueous sediment gravity flow processes, and their depositional products. To contextualise the flow- and deposit-scale understanding above, a review of the large-scale sedimentary environments and sub-environments built by these flows and their deposits is provided. As the focus of this thesis is on submarine channels, a more detailed review of their geomorphology and the architecture of their deposits is then provided, with a specific focus on their developmental controls. In addition to this introductory review, each ‘data chapter’ (Chapters 3 – 5) provides a more in-depth review of the literature specific to the data and concepts addressed therein.

1.3.2 Chapter 3 – Syn-depositional tectonics and mass-transport deposits control channelised, bathymetrically complex deep-water systems (Aínsa depocenter, Spain)

This chapter presents a case study of outcropping channelised deep-water deposits from the Aínsa depocenter, in the South Pyrenean Foreland Basin. Traditional field techniques such as sedimentary logging and mapping were used in addition to digital techniques such as drone-based photography and photogrammetry to collect data on the sedimentology and architecture of the deposits. Characterisation of the sedimentology and architecture of the deposits was conducted, to inform interpretations of channel initiation and evolution. Evolutionary models were formulated based on observations from three key outcrops. The key findings of this chapter relate to how seafloor topography, and MTD emplacement affect the process of channelisation, and channel evolution. This work is published in the *Journal of Sedimentary Research* (Tek et al., 2020).

1.3.3 Chapter 4 – Relating seafloor geomorphology to subsurface architecture: how mass-transport deposits and knickpoint-zones build the stratigraphy of the deep-water Hikurangi Channel

This chapter integrates observations from bathymetry and 3D seismic data imaging a 150 km long reach of the Hikurangi Channel, offshore New Zealand. Observations of channel geomorphology made using multibeam bathymetry data and a seafloor horizon rendered from the 3D seismic data were interpreted, and commonly occurring seafloor features were identified. Subsurface deposits were categorised based on observations of seismic character into seismofacies and depositional elements, and

were correlated across the survey. Observations and interpretations from the seafloor were then integrated to discern the relationship between seafloor features, and subsurface deposits and surfaces. This work is published in *Sedimentology* (Tek et al., 2021a).

1.3.4 Chapter 5 – Controls on the architectural evolution of deep-water channel overbank sediment wave fields: insights from the Hikurangi Channel, New Zealand

This chapter integrates observations from multibeam bathymetry, 2D and 3D seismic data imaging 21,000 km² of the floor of the Hikurangi Trench. The architecture of the overbank deposits adjacent to the Hikurangi Channel is categorised, and sediment waves on the banks of the modern Hikurangi Channel, and their expression in the subsurface, are analysed. Novel methodologies for the quantitative analysis of sediment wave size, orientation and distribution are presented and applied. These quantitative analyses, combined with qualitative analysis, are used to interpret the controls on the orientation and magnitude of overbank flow, and how the influence of these controls has changed through time. This work is in press with the *New Zealand Journal of Geology and Geophysics* (Tek et al., 2021b).

1.3.5 Chapter 6 – Discussion

This chapter synthesises the findings of the three data chapters, and is divided in accordance with the research themes outlined in section 1.1. Discussion of each theme incorporates results and discussions presented in the data chapters above, and insights from the published literature.

1.3.6 Chapter 7 – Conclusions and future work

This chapter presents the key findings of this thesis and makes recommendations for further work to address outstanding research questions.

2 Literature Review

This review has two constituent parts:

1. A review of Sediment Gravity Flows, the processes associated with their formation and evolution, and of deposition from them (Section 2.1).
2. An overview of deep-water sedimentary environments and the architectures of sedimentary bodies found in these settings, with a specific focus on submarine channels (Section 2.2).

2.1 Subaqueous sediment gravity flows and their deposits

2.1.1 *An introduction to sediment gravity flows and their classification*

Deep-water clastic sedimentation is controlled by the interaction of a range of processes (Fig. 2.1). Subaqueous sediment gravity flows (SGFs) are volumetrically the most significant sediment transport process on earth (Talling et al., 2015), and exhibit a wide range of flow behaviours and leave a diverse range of deposits. The naming of subaqueous flows and their respective deposits has a complex history. Kuenen (1937), and Kuenen and Migliorini (1950) defined turbidity currents as ‘turbid’ (sediment-laden) flows which travelled below an ambient fluid due to the contrast in density, under the influence of gravity. Kuenen and Migliorini (1950) also posited that normally graded beds found in many ‘flysch’ (Mutti et al., 2009) outcrops worldwide were deposited by ancient turbidity currents. Following further work on turbidity current deposits, ‘turbidites’ (Kuenen, 1957; Bouma, 1962), and the processes associated with their formation (Walker, 1967; Middleton and Hampton, 1973), turbidite deposits have become associated with deposition from turbulent flows. The term ‘turbidity current’ has now become colloquially synonymous with turbulent flows that act below storm wave base (Talling et al., 2012).

Prior to a relatively recent uptake in direct monitoring of active deep-water sedimentary systems (Xu, 2011; Clare et al., 2020), process-product understanding and classification of SGFs and their deposits has relied on integrating observations from experimental modelling, and from outcropping deposits. The classification of SGFs and their deposits is generally based on one of two approaches: using flow character to infer deposit type, and using deposit type to infer flow character.

Flow rheology (Gani, 2004), and the parameters that control flow rheology (Mulder and Alexander, 2001), such as particle-support mechanism (Middleton and Hampton, 1973, 1976) have been used to classify SGFs. The rationale behind a flow character-based approach is to provide an at-a-point definition of a flow without the complications of spatiotemporal flow variability and transformation. However, two

problems limit the application of flow character-based classifications: unambiguous inference of flow parameters from ancient rocks is not possible, and some parameters cannot be measured through direct monitoring (Talling et al., 2012).

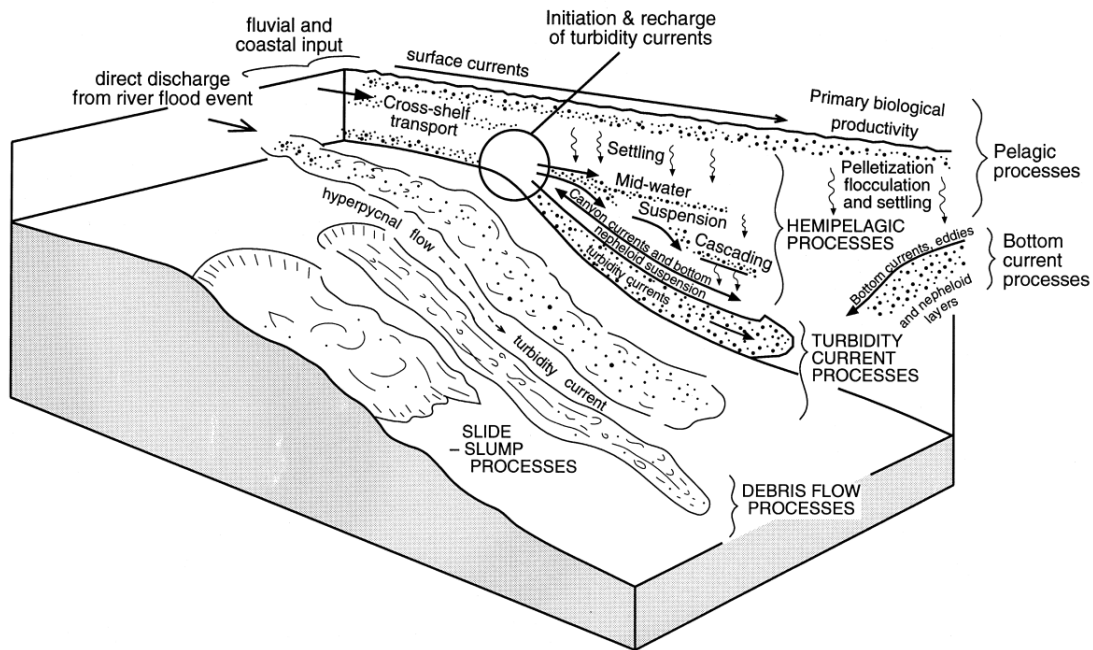


Figure 2.1 – Environmental diagram illustrating the range of processes that transport and deposit sediment into deep-water (Stow and Mayall, 2000).

Consequently, most authors prefer classifications that are fundamentally deposit-based, but are supported by observations from experiments and direct monitoring (Bouma, 1962; Walker, 1978; Lowe, 1982; Mutti, 1992; Mutti et al., 1999, 2003). Sedimentary ‘facies’ are used to categorise SGF deposits at outcrop and in core. Walker and Mutti (1973) define a ‘facies’ (based on earlier work by Walker, 1970 and Mutti and Ricci Lucchi, 1972) as: “the sum of all primary lithological and palaeontological characteristics of a body of rock which differentiate it from adjacent bodies of rock, both laterally and vertically”. The ‘classic’ turbidite facies model of ‘the Bouma sequence’ (Fig. 2.2A; Bouma, 1962), contains an idealised vertical trend in sedimentary structures within beds, which was explained by incremental deposition from a gradually decelerating, turbulent flow. Bouma (1962) also recognised a spatial control on facies: finer-grained facies were expected to be more prevalent further from the sediment source (Fig. 2.2B). These ideas were developed by Walker (1967) who allocated the terms ‘proximal’ and ‘distal’ into their facies model. The recognition of subaqueous debris flows (Johnson, 1970; Hampton, 1972), conglomeratic turbidites, traction carpets and inverse grading (Mutti and Ricci Lucchi, 1972) suggested that a single flow type could not explain the

diversity of deposits found within deep-water systems. Middleton and Hampton (1973, 1976) showed how five deposit types can be produced from a combination of two flow states (fluidal and plastic) sub-divided into four flow types, each with a different sediment support mechanism (Fig. 2.3A; Lowe, 1979). Mutti and Ricci Lucchi (1975) and Walker (1978) then incorporated these concepts into their observation-grounded model (Fig. 2.3B).

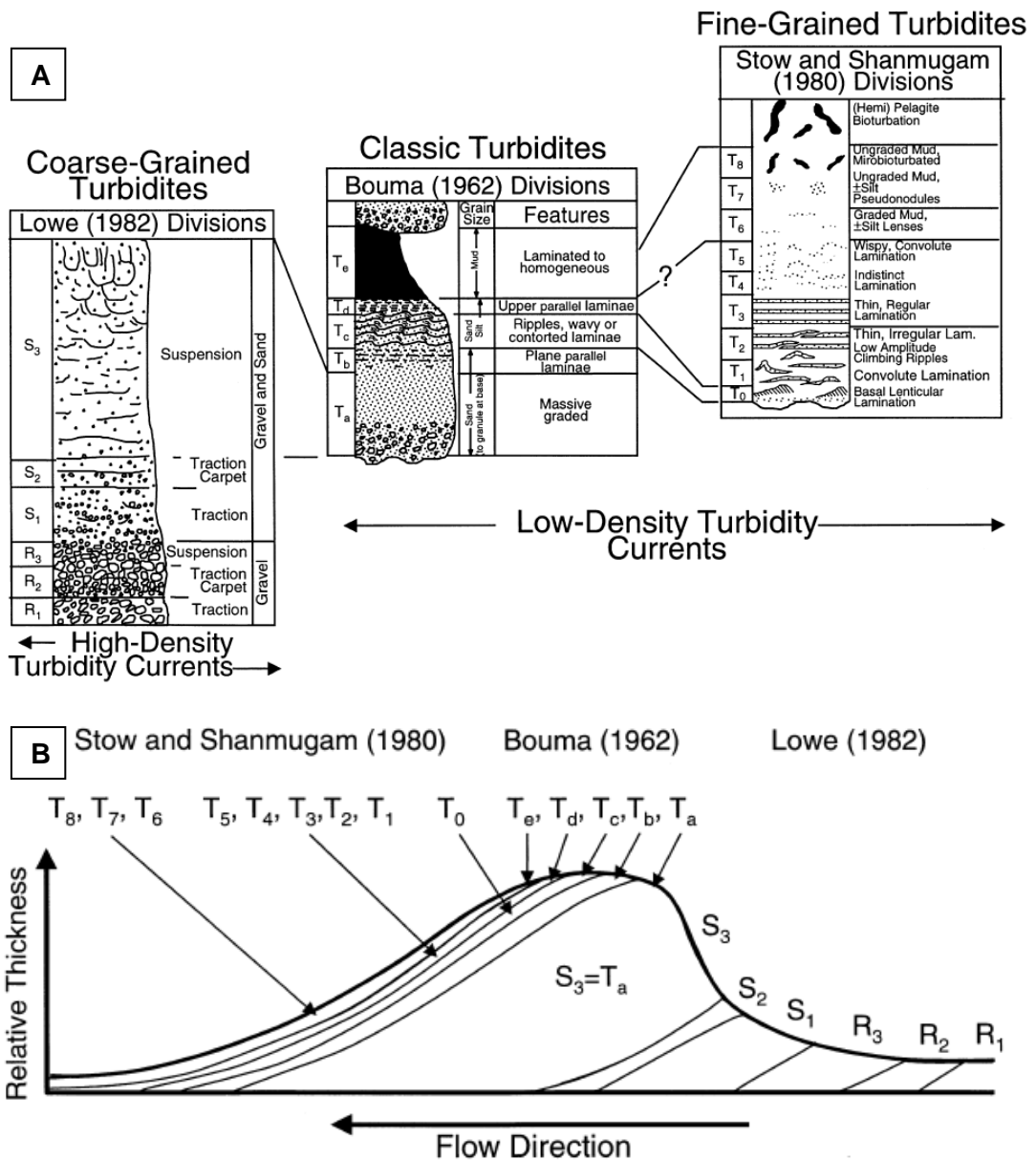


Figure 2.2 – Conceptual diagrams from Shanmugam (2000), based on original work by Lowe (1982), Bouma (1962) and Stow and Shanmugam (1980), showing: (A) Composite figure combining the facies models and their comparative divisions; (B) Idealised downflow facies transitions based on original diagram of Lowe (1982).

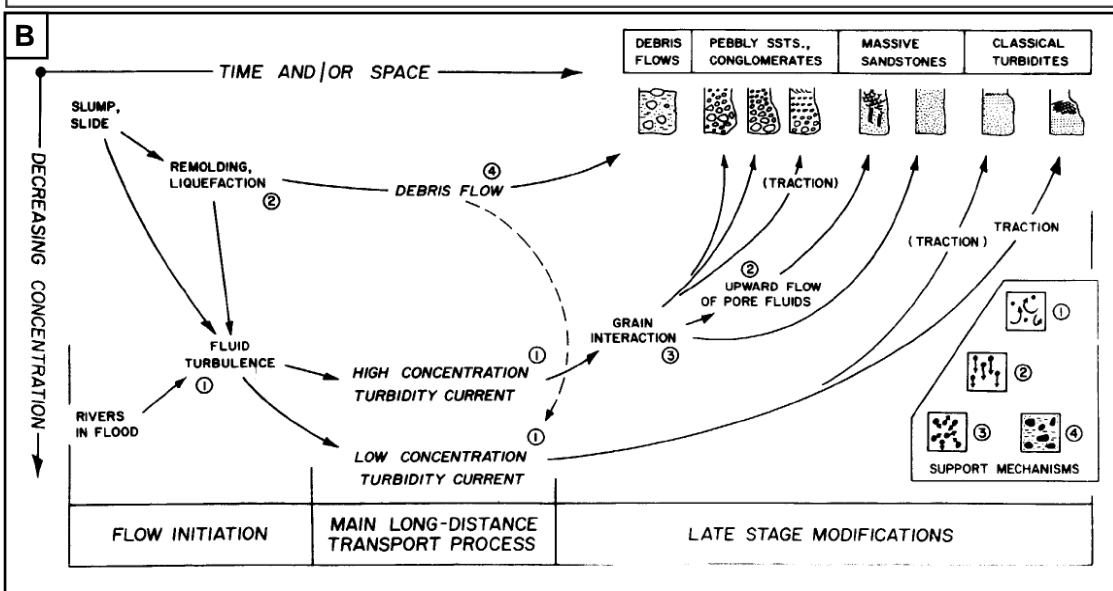
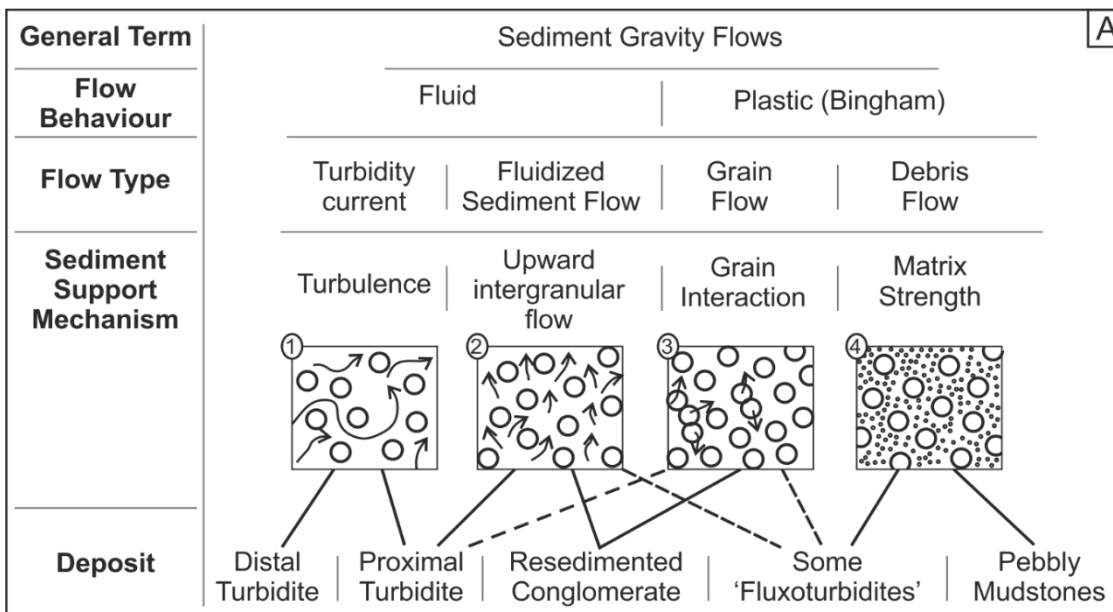


Figure 2.3 – (A) Sediment gravity flow classification scheme based on sediment support mechanism (modified after Middleton and Hampton, 1973; ‘flow behaviour’ added from Lowe, 1979); (B) classification diagram of Walker (1978) linking deposits to: flow initiation mechanism, long-distance transport process, late stage modification, and sediment support mechanism (numbered in accordance with those in A).

Process-product understanding advanced with the in-depth study of coarse- (Lowe, 1982) and fine-grained (Stow and Shanmugam, 1980) turbidite systems (Fig. 2.2). Lowe (1979; 1982) distinguished rocks deposited by laminar flows from rocks deposited from turbulent flows. He also interpreted a fundamental difference between sedimentary structures found in the basal (R2-S3 in Fig. 2.2) and upper (Tbc-Te in Fig.

2.2) parts of a turbidity current deposit. The Tbc-Te divisions represent deposition from, and re-working of, sediment by a dilute, fully turbulent flow.

Talling et al (2012) present a simple classification scheme based partially on the early facies schemes of Bouma (1962) and Lowe (1982) with complementary detailed process interpretations, which also incorporates the concepts of grain-size segregation and flow efficiency (Mutti, 1992). Three different end-member bed types are categorised based on flow velocity, effective concentration, and cohesive clay content:

1. 'High-density turbidites', which are formed by 'high-density turbidity currents' (see 'turbidity currents' section below)
2. Low-density turbidites, which are formed by 'low-density turbidity currents' (see 'turbidity currents' section below)
3. 'Debrites', which are formed by 'debris flows' (see 'mass-transport deposits' section below)

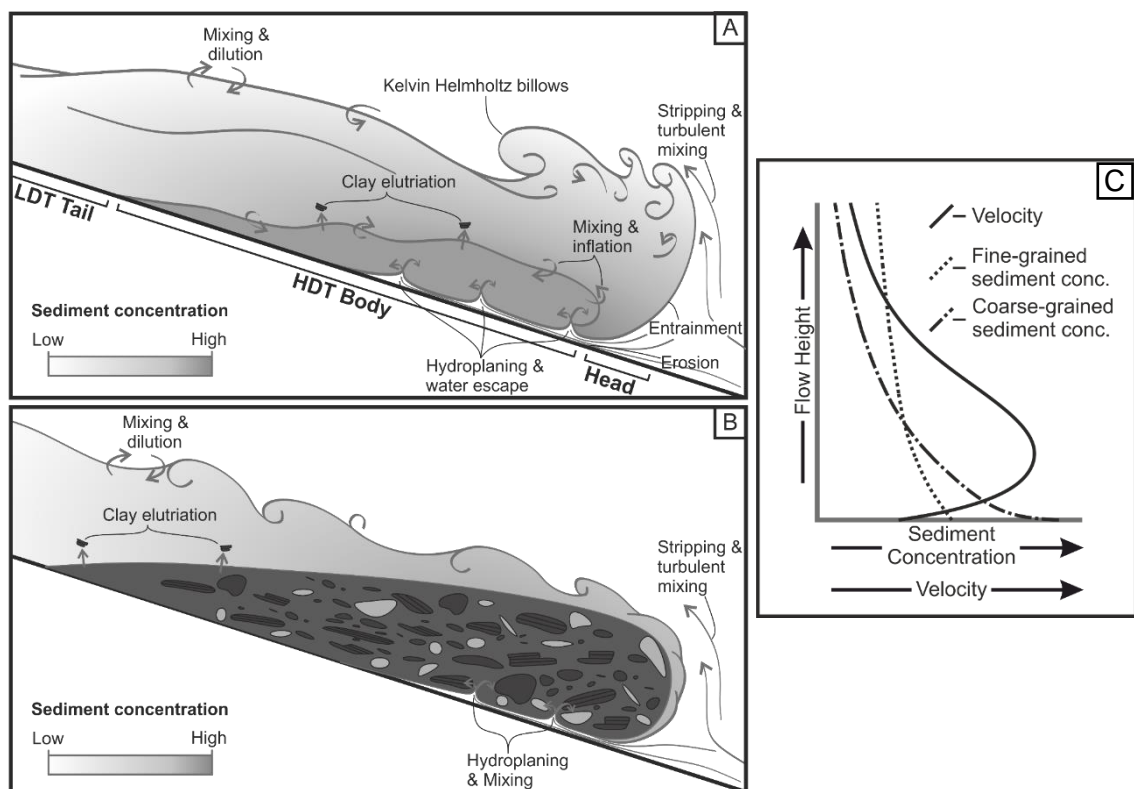


Figure 2.4 – Structure of, and processes acting within: (A) a bi-partite sediment gravity flow (Modified after Postma et al., 1988, Breien et al., 2010, and Manica, 2012), and (B) a cohesive debris flow (inspired by Hampton, 1972, Sohn, 2000, Mohrig and Marr, 2003); (C) Schematic plot showing the velocity and concentration structure of a typical stratified flow following a Russian stratification profile (after Kneller and Buckee, 2000).

2.1.2 Turbidity currents and turbidites

The work of Lowe (1982) suggests that turbidity currents typically exhibit a 'bi-partite' structure (*sensu* Sanders, 1965) comprising:

1. A basal layer with dampened turbulence due to its high velocity (a function of slope, grain-size, particle-fluid ratio and column height) and high effective sediment concentration (Sanders, 1965; Postma et al., 1988; Breien et al., 2010), i.e., a High-Density Turbidity Current (HDTC) (Fig. 2.4A).
2. An upper, lower velocity, low fluid-particle ratio, fully turbulent layer (Sanders, 1965; Britter and Simpson, 1978), i.e., a Low-Density Turbidity Current (LDTC) (Fig. 2.4A).

Deposits from HDTCs and LDTCs are termed High-Density Turbidites (HDTs) and Low-Density Turbidites (LDTs) respectively (*sensu* Lowe, 1982). Following the classification of Talling et al (2012), a vertical section through a HDT can contain:

1. Traction Carpets (T_{b-2} & T_{b-3})
2. Ungraded to normally graded sandstone (T_a)
3. Upper stage parallel laminations (T_{b-1})

An LDT can contain:

1. Ripple cross-lamination (T_c) (and potentially dune cross-stratification; Arnott, 2012)
2. Lower stage parallel laminations (T_d & T_{e-1})
3. Graded to un-graded mud (T_{e-2} & T_{e-3})

The idealised anatomy of a bi-partite flow (Fig. 2.4A) consists of a LDTC 'head' formed from entrainment of water followed by a HDTC 'body' at the flow base, which is itself topped and followed by another LDTC. The idea of a LDTC 'tail' is supported by the abundance of grain-size breaks between the S3 and T_{b-c} divisions in ancient (Mulder and Alexander, 2001; Talling et al., 2012) and modern (Stevenson et al., 2014) deposits. Missing grainsizes suspended in a LDT may bypass and re-work a recently deposited LDT until favourable depositional conditions are maintained (Talling et al., 2012). Direct monitoring of turbidity currents also supports a bi-partite flow model, with instruments such as Acoustic Doppler Current Profilers recording dense, high-velocity layers at the base and front of natural turbidity currents (Azpiroz-zabala et al., 2017; Paull et al. 2018; Wang et al., 2020). However, the nature of these basal layers remains poorly understood.

Turbulent dilute suspensions have been shown to be stratified with respect to their sediment concentration (Fig. 2.4C; Kneller and McCaffrey, 1999). Within stratified polydisperse turbidity currents (those carrying a range of grain sizes), fine sediment is typically more evenly distributed than coarse sediment, which displays a more

pronounced vertical decay profile (Garcia, 1994; Peakall et al., 2000a, b; Kneller and Buckee, 2000; Fig. 2.4C), making the base of the gravity flow poorly sorted relative to its top. Furthermore, sediment in such flows can also be stratified in terms of density, with the densest particles being most abundant at the base of the flow (Pohl et al., 2020a; Bell et al., 2021).

At a point on the seafloor, a turbidity current (or MTD) can deposit sediment, bypass (e.g. Stevenson et al., 2013), or erode the substrate it flows over. The threshold between erosion and deposition (from suspension fallout) in turbidity currents can be modelled using either flow capacity (the amount of particulate material it can support) or competence (the largest transportable grainsize) (Kuenen and Sengupta, 1970; Dorrell et al., 2018). A flow may become depositional because of a reduction in velocity (Kneller, 2003), potentially at a break in slope (Pohl et al., 2020b) or after a loss of fine-grained material from the top of a flow by overspill (see Section 2.3.4), leading to the flow dropping the coarsest fraction of the flow as it attempts to maintain its concentration structure.

2.1.3 Mass-transport and Mass-Transport Deposits

The term Mass-Transport Deposit (MTD) (Carter, 1975; Nelson et al., 2011; Kneller et al., 2016) is used here as 'catch-all' term for the product of *en masse* transport and deposition initiated and facilitated by gravitational influence (Posamentier and Martinsen, 2011). MTD was originally used as a seismic-sedimentary term (Weimer and Slatt, 2006) and, due to the limitations of outcrop-based studies (mainly that of scale and tectonic overprinting), seismic is still the most commonly used method for interpreting the external, and large-scale internal geometries found in MTDs (Ogata et al., 2012). Outcrop-based studies are used to determine the internal structure and deformation style observed within part of, or the whole of, an MTD (Butler and McCaffrey, 2010). Both process- (Stow, 1986; Nemeč, 1990; Martinsen, 1994) and deposit-based (Dott, 1963; Nardin et al., 1979; Moscardelli et al., 2006) sub-classifications are commonly adopted to name MTDs. Here, a process-based classification is favoured (Fig. 2.5A), comprising:

1. Creep, where effectively in-situ sediments constituting a submarine slope gradually deform and move down-slope.
2. Sliding a gravity-driven mass movement of sediments with little or no internal deformation above one or multiple bedding-concordant sheared horizons, typically with an extensional up-dip domain, a translational middle, and compressional toe domain (Fig. 2.5B).
3. Slumping (*sensu* Jones, 1939) forms part of a continuum between sliding and debris flow. As with sliding, a mass of re-mobilised stratigraphy moves over a basal shear horizon, but the overriding stratigraphy is contorted and rotated during transport.

However, unlike debris flow, the original stratification remains intact during the slumping event (Heezen and Drake, 1964; Stow, 1986; Strachan, 2002, 2008; Cardona et al., 2020). As such, the deposits formed by slumping, 'slumps', contain faulted and folded, but still traceable strata derived from the source of the slump (Jones, 1939; Woodcock, 1979; Strachan, 2002, 2008; Sharman et al., 2015).

4. Debris flow, which exhibits a laminar flow state and deposits sediment en masse from flow 'freezing' (Lowe, 1982), forming 'debrites'. At a point in space, debris flows display a relatively uniform velocity and concentration structure from the base to the top (Fig. 2.4B; Hampton, 1972), with a high basal shear layer commonly lubricated by hydroplaning (Fig. 2.4B; Mohrig et al., 1998, 1999). Sediment is supported by a cohesive matrix (Middleton and Hampton, 1973, 1976). The strength of this matrix is dependent on the effective concentration of the flow (Johnson, 1970; Iverson, 1997; Mutti et al., 2003; Baas et al., 2009), the proportion (Baas and Best, 2002; Mohrig and Marr, 2003) and type of cohesive (clay) particles it carries (Baker et al., 2017), and the flow velocity. Debrites are often ungraded, however their nature is highly variable and grading (usually inverse) can occur (Mulder and Alexander, 2001; Hodgson, 2009). Large rafts of mudstone, sandstone, or heterolithic material are commonly observed in debrites (Haughton et al., 2003; Talling et al., 2010; Patacci et al., 2014; Southern et al., 2015; Fonnesu et al., 2015).

Mass-transport will initiate when the critical shear strength (controlled primarily by rheology) of a rock is overcome by an exerted shear stress (controlled by rheology, mass and slope angle) (Posamentier and Martinsen, 2011). For a given shear stress, strain rate and internal deformation are controlled by the competence of the rock or sediments (Laubach et al., 2009), such that thin, interbedded competent and weak beds will break up to form a slump (Ogata et al., 2012) at low shear strains. Hence, MTDs in deep-water systems commonly comprise un- to semi-lithified, heterogeneous, mud-rich deposits (Festa et al., 2012). The deformation mechanisms associated with mass-transport, and the resultant deposits, form a continuum between one another (Fig. 2.5A; Moscardelli and Wood, 2008; Bull et al., 2009; Posamentier and Martinsen, 2011). Flow transformation occurs with increasing shear strain, resulting in increased internal disaggregation (Ogata et al., 2012) and increased flow velocity (Posamentier and Martinsen, 2011), meaning a flow may sequentially transform into more deformed flow states (Fig. 2.5B; Strachan, 2008; Bull et al., 2009). Alternatively, a single flow may synchronously contain multiple flow types (Fig. 2.5B), and multiple kinematic domains, including extensional, translational and compressional (Bull et al., 2009; Ortiz-Karpf et al., 2017).

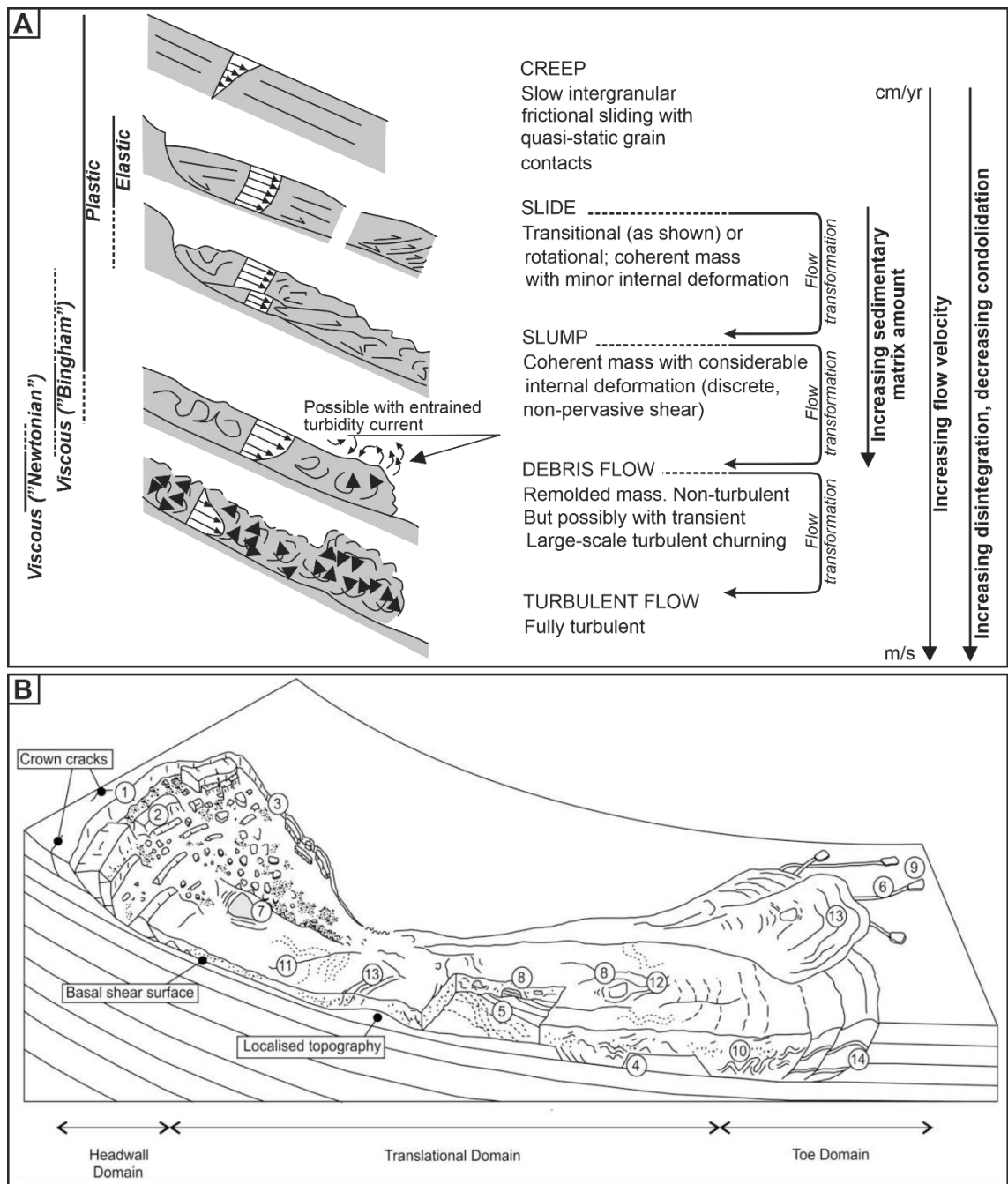


Figure 2.5 – (A) Scheme for the classification of mass transport deposits showing how different flow types transition to one another with increasing flow velocity and disaggregation, and their respective flow behaviours (Compiled from Nemeč, 1990; Posamentier and Martinsen, 2011; Ogata et al., 2012); (B) schematic figure (from Bull et al., 2009) showing anatomy of, and kinematic features within a typical MTC: (1) Headwall scarp, (2) Extensional ridges and blocks, (3) Lateral margins, (4) Basal shear surface ramps and flats, (5) Basal shear surface grooves, (6) Basal shear surface striations, (7) Remnant blocks, (8) Translated blocks, (9) Outrunner blocks, (10) Folds, (11) Longitudinal shears / first order flow fabric, (12) Second order flow fabric, (13) Pressure ridges, (14) Fold and thrust system.

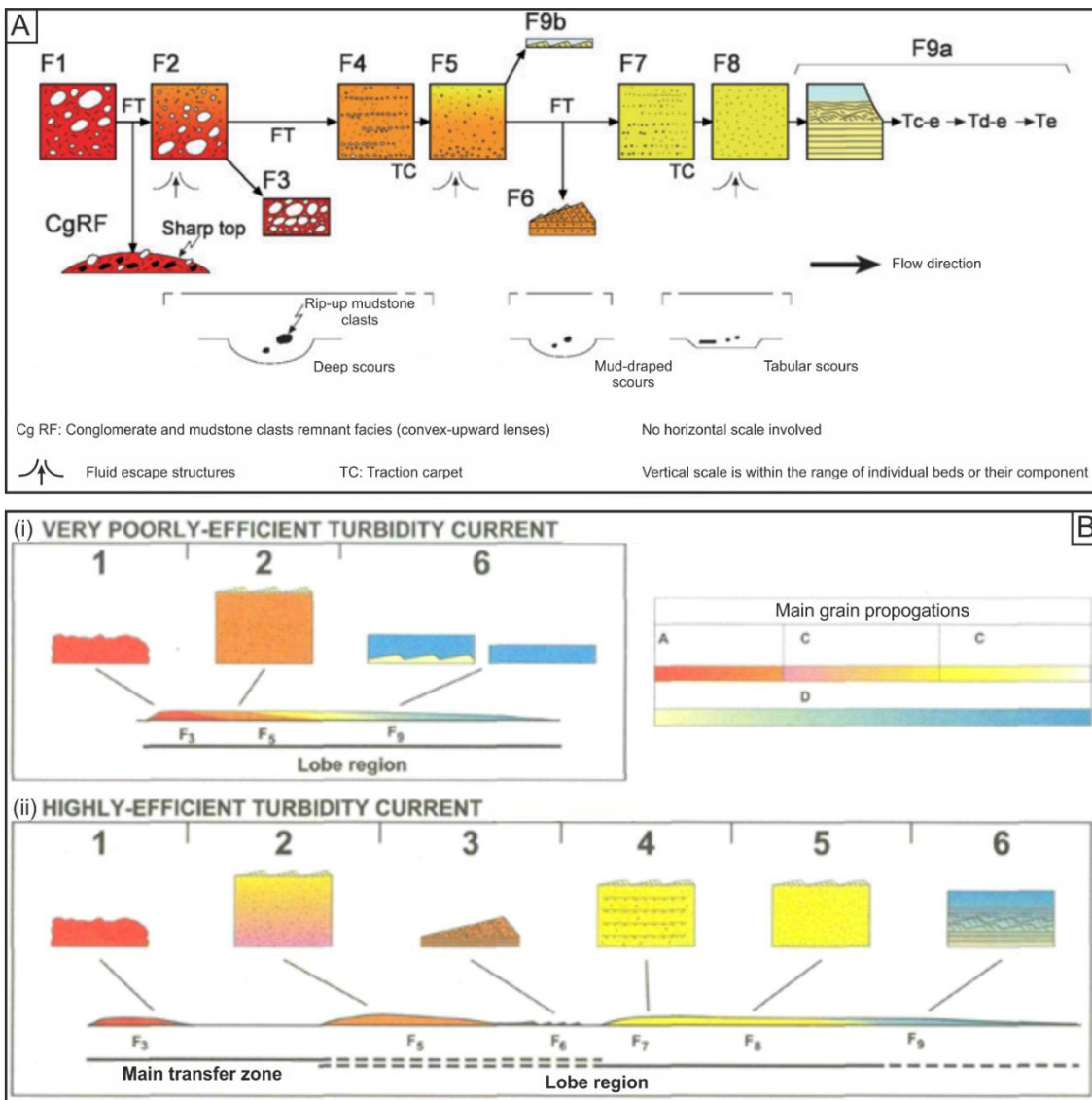


Figure 2.6 – (A) Turbidite facies classification scheme originally from Mutti et al. (1999) showing 9 commonly observed facies, alongside common erosional features seen alongside these facies (from Mutti et al., 2009); (B) facies tracts and the effects of flow efficiency on downstream facies segregation (Mutti et al., 1999): (i) a poor efficiency flow; (ii) a high efficiency flow.

2.1.4 Facies tract analysis and flow transformation

That a flow's character varies temporally as it passes a point on the seabed has long been recognised (Bouma, 1962). However, flows may also vary temporally and spatially within a single event (Kneller and Buckee, 2000; Kneller and McCaffrey, 2003; Mohrig and Marr, 2003; Talling et al., 2012). Based on the recognition of proximal to distal trends in deposit type, grain-size and sedimentary structures observed in many outcropping deep-water successions, a systematic facies scheme was developed (Fig. 2.6), in which 9 common facies and three common erosional features are recognised

(Mutti, 1992). Facies tract analysis (*sensu* Mutti, 1992) builds on earlier facies models (Fig. 2.2B; Bouma, 1962; Lowe, 1982), and is based on predictive proximal-to-distal trends in observed sedimentary facies. The concept is founded on the idea that a single bed will, both vertically and along its length, record the temporal and longitudinal expression of a passing flow, thereby recording its evolution (Mutti, 1992; Kneller and Branney, 1995; Mutti et al., 2003, 2009): debrites and coarse-grained facies are more abundant in proximal locations, and progressively finer grained sediments are deposited distally as the flow evolves (Fig. 2.6B). The ability of a flow to laterally segregate grain-size is termed its 'efficiency' (Mutti, 1979; Mutti et al., 1994). An efficient facies tract will have strong lateral segregation and its deposit will generally record a single flow type at any one location, whereas a low efficiency flow deposit may record the stacking of many facies (Fig. 2.6B; Mutti et al., 1994, 1999, 2003).

Just as transitions can occur between MTDs of different flow states, and between HDTCs and LDTCs, transitions between MTDs and turbidity currents also occur distally and through time: a process called 'flow transformation'. Multiple transformations between turbulent and laminar flow can occur within a single flow event (Talling et al., 2007).

A proposed mechanism for the initiation and sourcing of turbidites in some deep-water systems, is the disaggregation of large 'submarine landslides' (Talling, 2014). These landslides occur on the continental slope or in a submarine canyon, initially as slumps or slides, then transition distally into debris flows, and finally into turbidity currents (Piper et al., 1999a; Strachan, 2008; Clare et al., 2014, 2015; Mountjoy et al., 2018). In outcropping deep-water successions, flow transformation from debris flows to turbidity currents can be recorded by proximal-to-distal and vertical transitions between debrites and turbidites (Talling et al., 2004; Felix et al., 2009), and by sole structures found on the bases of turbidites (Peakall et al., 2020). Transformations from debris flows into turbidity currents can occur through the incorporation of ambient water at the head or top of a flow, or through a hydroplaning layer (Fig. 2.4). This can reduce the fluid-particle ratio sufficiently to transform an MTD into a turbidity current (Fig. 2.4B; Hampton, 1972; Mohrig et al., 1998, 1999; Sohn, 2000; Mohrig and Marr, 2003; Mutti et al., 2003; Felix and Peakall, 2006).

Vertical and proximal-to-distal transitions between debrites and turbidites observed in outcropping (Hodgson, 2009; Sychala et al., 2017; Fonnesu et al., 2015, 2016, 2018) and subsurface (Lowe and Guy, 2000; Haughton et al., 2003; Kane et al., 2017; Southern et al., 2017) successions, and quaternary deposits on the seafloor (Talling et al., 2007, 2010), suggest that flow transformation from turbidity currents to debris flows can also occur. Individual beds (termed 'hybrid event beds') that show

vertical transitions from a basal high-density turbidite, through a debrite in their middle, to a low-density turbidite on top, record this type of flow transformation (Haughton et al., 2009; Talling, 2013); this process can also be recorded by sole structures (Peakall et al., 2020). Turbulence modulation by clay (Baas and Best, 2002) can hinder mixing with, and dilution by, ambient fluid (Mohrig and Marr, 2003). Therefore, increasing clay concentration in a turbidity current can dampen turbulence and lead to flow transformation (Baas and Best, 2002; Baas et al., 2009; Haughton et al., 2009; Sumner et al., 2009). Through the early deposition of coarse, non-cohesive sediment at its base (Tinterri et al., 2003; Baas et al., 2009), and potentially the erosion of a clay-rich substrate (Fig. 2.4A; Mutti, 1977; Ricci Lucchi and Valmori, 1980; Mutti and Nilsen, 1981; Haughton et al., 2003, 2009; Hodgson, 2009; Muzzi Magalhaes and Tinterri, 2010; Kane and Pontén, 2012; Southern et al., 2015; Fonnesu et al., 2016), an originally fully turbulent flow may become enriched with clay through time, and distally. This progressive enrichment forms a laminar ‘plug’ that rides on top of a turbulent basal layer, which eventually freezes and is deposited (Baas et al., 2009; Kane and Pontén, 2012). Besides increasing the clay content this type of flow transformation can be triggered by a decrease in flow velocity (Barker et al., 2008; Sumner et al., 2009; Baas et al., 2011), leading to a strong topographic control on hybrid event bed deposition (Patacci et al., 2014; Tinterri and Tagliaferri, 2015; Southern et al., 2017).

2.1.5 SGF interaction with basin topography

Kneller (1995) and Kneller and Branney (1995) present a simplified account, based on outcrop and experimental data, of how flow velocity (and resulting deposit expression) may change in response to flow interaction with basin topography. Along a downflow transect, a flow may be accumulative (increasing in velocity), uniform (constant velocity), or depletive (decreasing in velocity). At a fixed location, a flow can be waxing (increasing in velocity), steady (constant velocity), or waning (decreasing in velocity).

Stratified turbidity currents can be divided vertically upon interaction with topography. The ratio of inertial and gravitational forces in a flow may be expressed in terms of its internal Froude number, \mathbf{Fr}_i :

$$\mathbf{Fr}_i = \frac{U}{\left(\frac{g}{\rho} \frac{\partial \rho}{\partial z}\right)^{\frac{1}{2}} h}$$

Where U is the depth-averaged velocity, $\frac{\partial \rho}{\partial z}$ is the vertical density gradient, g is gravitational acceleration, ρ is a reference density (e.g. the ambient fluid) and h is a reference length (Kneller and McCaffrey, 1999; Hansen et al., 2015). The ability of a flow to divide vertically, and the position at which it does so, depends on the flow’s \mathbf{Fr}_i number

and the height of the topography (Fig. 2.8): a flow with a large Fr_i (and consequently poorly stratified) is unlikely to divide (Fig. 2.8); a flow with a small Fr_i will divide along a plane termed the ‘dividing streamline’ (Kneller and McCaffrey, 1999).

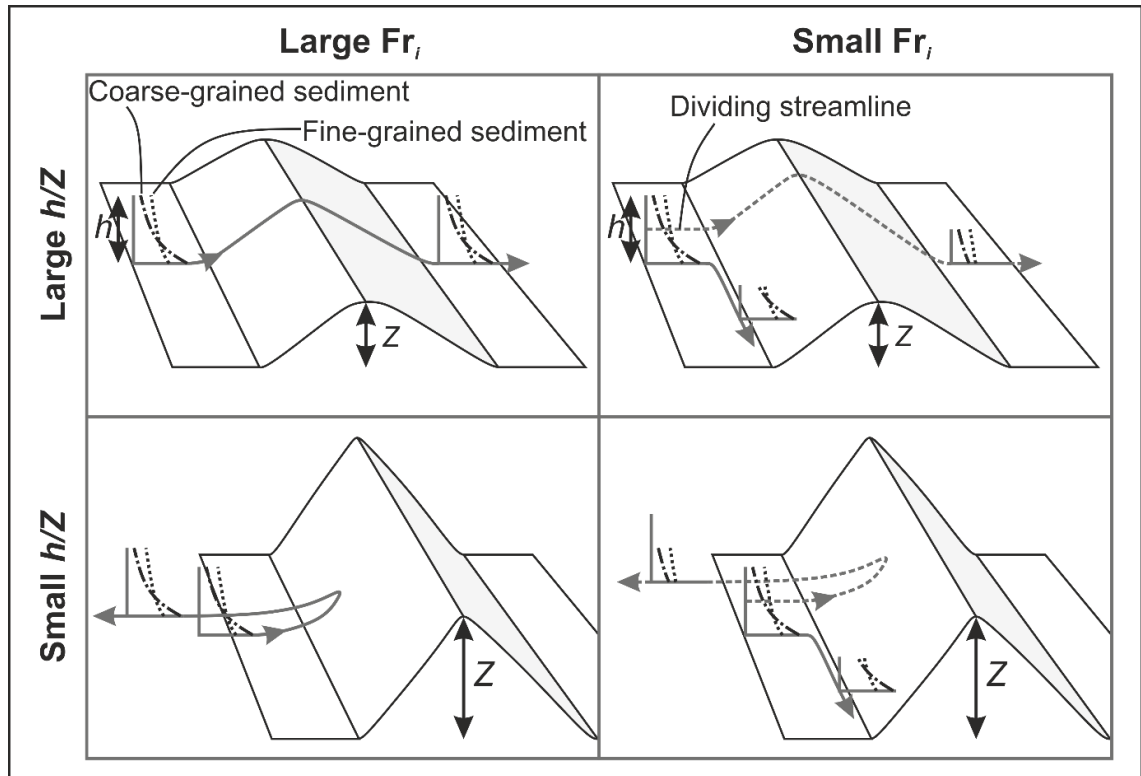


Figure 2.7 – Schematic diagrams showing the interplay between the height of frontal topography and the internal Froude number (Fr_i) on the reflection and division of a stratified turbidity current (modified from Kneller and McCaffrey, 1999 with grain-size segregation from Hansen et al., 2015).

Non-uniformity associated with flows interacting with prominent seafloor topography generated by tectonic structures (Fig. 2.8) has been invoked to explain turbidite expression in topographically complex basins (e.g. McCaffrey and Kneller, 2001; Amy et al., 2004; Howlett et al., 2019; Privat et al., 2021). The topography on top of MTDs can also impact the flow pathways of, and deposition by turbidity currents that traverse them. MTD-top topography can create ponded mini-basins which can be subsequently filled by thick turbidite successions (Kneller et al., 2016). Conversely, MTDs can themselves be influenced by underlying topography, in some cases contributing to slope ‘healing’ (see Prather, 2003 for definition; e.g. McArthur et al., 2021), and in others contributing to further seafloor excavation (Moscardelli et al., 2006; Ortiz-Karpf et al., 2017).

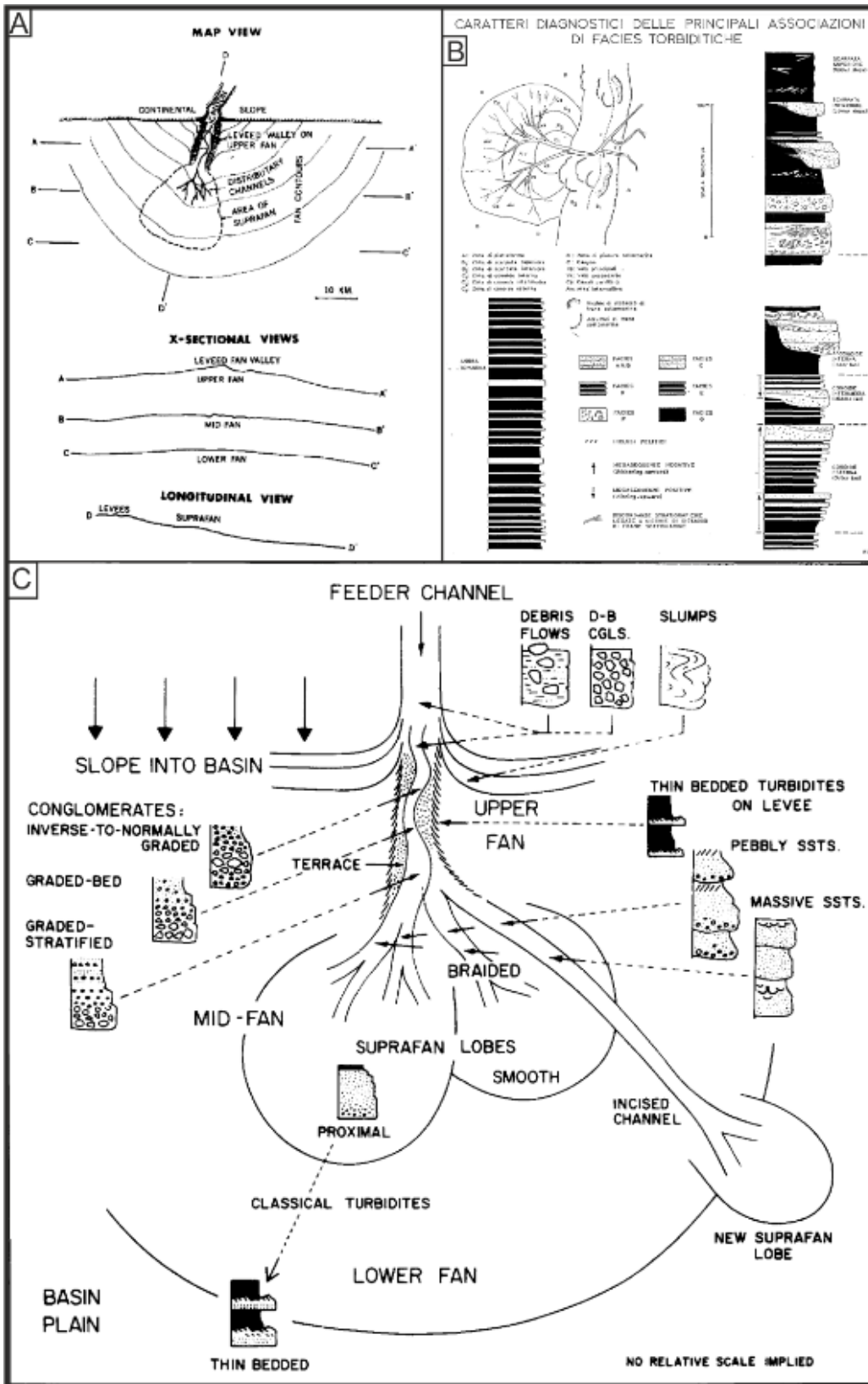


Figure 2.8 – Early generic fan models: (A) the ‘suprafan model’ based on observations from modern systems (Normark, 1970); (B) turbidite fan model from Mutti and Ricci Lucchi (1972) based on ancient turbidite deposits; (C) model from Walker (1978) showing a schematic drawing of a fan with the expected facies in each location.

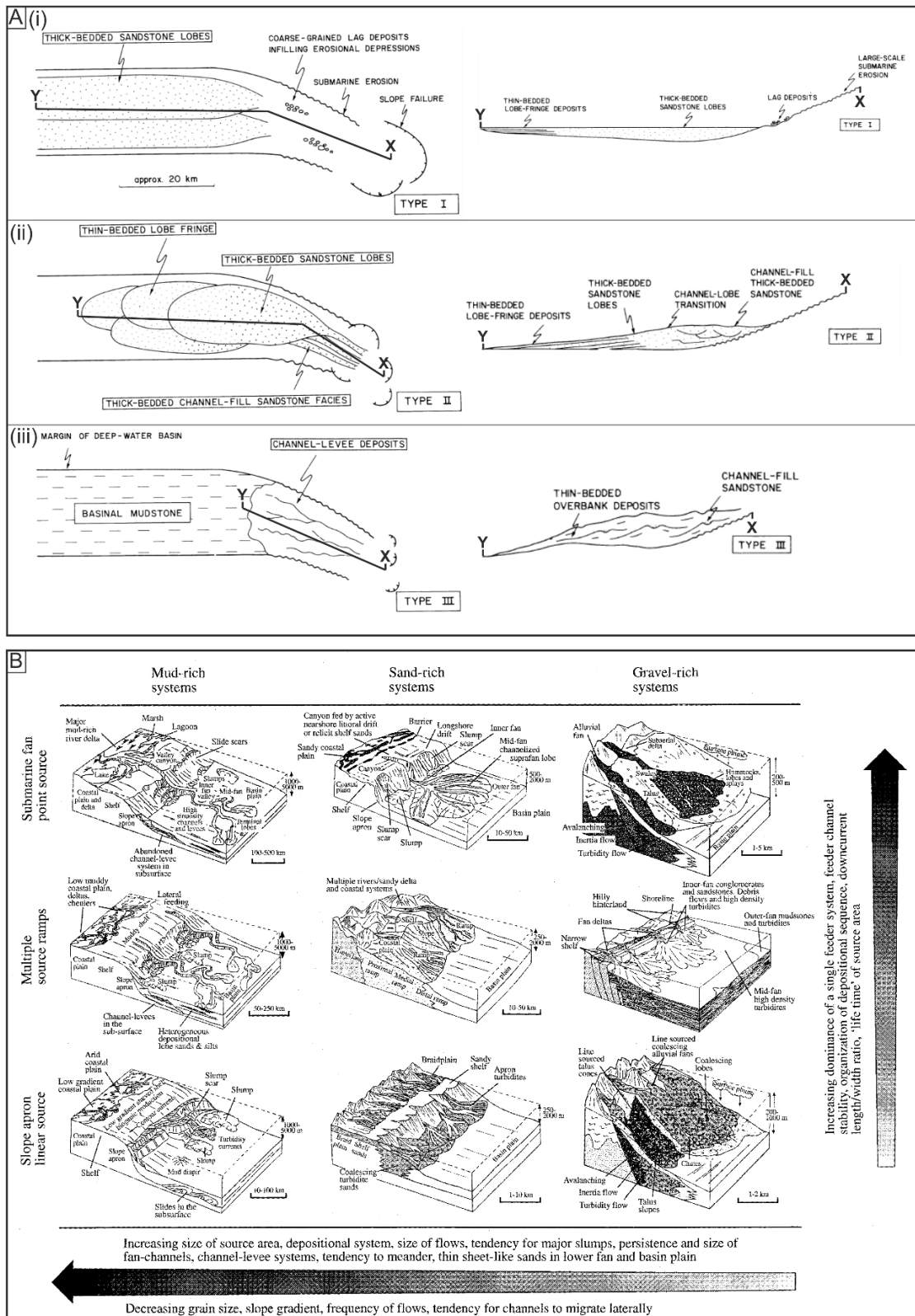


Figure 2.9 – (A) Three types of turbidite depositional system observed within the South Pyrenean Foreland Basin in plan-view and longitudinal section (after Mutti, 1985). Type I was attributed to falling sea level, type II to sea level lowstand, and type III to rising sea level. (B) Nine types of deep-water systems (Stow and Mayall, 2000) based on classification by Reading and Richards (1994; original authors identified 12 types). Key controls are input source type and grain-size.

Although conceptually useful, the models proposed by Kneller (1995) and Kneller and Branney (1995) do not account for important factors such as the shape of the topographic obstacle (Howlett et al., 2019; Soutter et al., 2021), inertia (Hay, 1987), superelevation (Dorrell et al., 2013a), cohesive clay content (Mulder and Alexander, 2001; Baas et al., 2009), and the potential interaction of multiple sedimentary systems that are common in topographically complex deep-water basins (Hansen et al., 2021; Privat et al., 2021).

The influence of both tectonic and MTD-derived topography on turbidity current flow processes and turbidite deposition is explored in more detail in Chapters 3, 4 and 5, and these concepts are reviewed in Chapter 3 (see Sections 2.3.10 and 2.3.11). The interaction of stratified flows with topography is also fundamentally important to the process of overspill (Hansen et al., 2015), which will be discussed later in this literature review (see Section 2.3.4).

2.2 Deep-water sedimentary environments

2.2.1 *Fan models and architectural element analysis*

Most oceanic continental margins exhibit a downslope geometric evolution from terrestrial to shelf, slope, rise and finally abyssal environments (Heezen et al., 1959; Hedberg, 1970). Although gravity-driven sedimentary processes may operate anywhere along this profile, “deep-water sediments” are defined as those deposited below storm wave base, and are here considered primarily to be deposited on the slope, rise or abyssal plain. Many reviews have attempted to document the classification history of deep-water sedimentary environments (Normark et al., 1993; Stow et al., 1996; Stow and Mayall, 2000; Shanmugam, 2000, 2016). This section will swiftly review these efforts, noting only key theoretical developments, with the aim to provide context for the discussion in the following sections.

Following early work on commonly observed stratigraphic trends (Kuenen and Migliorini, 1950; Bouma 1962; Walker 1967), Normark (1970) and Mutti and Ricci Lucchi (1972) assembled detailed environmental models, describing depositional trends in modern (Fig. 2.8A) and ancient turbidite systems (Fig. 2.8B) respectively. Based on similarities between ancient and modern systems, such as their fan-like shape, and the presence of channels and feeder canyons, the modern and ancient ‘turbidite fan models’ were combined by Walker (1978) into a ‘general fan model’ (Fig. 2.8C; Shanmugam, 2000, 2016). Although early models temporarily provided a unified descriptive template, further work revealed remarkable diversity between modern and ancient deep-water fans (Barnes and Normark, 1985; Shanmugam and Moiola, 1988; Pickering et al., 1995; Kenyon et al., 2002). Much of this perceived diversity is due to the poor preservation potential of large passive margin systems like the Amazon or Congo fans compared to

smaller, coarser grained systems on compressional margins (Kenyon et al., 2002); similarly, continental foreland basins, responsible for the deposition of many preserved ancient turbidite successions, such as the south Pyrenees (Mutti, 1985), are largely absent in the present-day (Shanmugam and Muiola, 1988; Nyberg and Howell, 2015). Generic fan models were consequentially abandoned (Shanmugam, 2000, 2016) for more descriptive models inclusive of the controls on internal architecture. Informed by stratigraphic trends seen in the South Pyrenean Foreland Basin, Mutti (1985) defined three types of 'turbidite depositional system' (Fig. 2.9A) acknowledging that sea level may affect the internal architecture of a deep-marine system, as well as the shelf-to-basin floor partitioning of sediment. Reading and Richards (1994) and Richards et al. (1998) devised a classification containing 12 'system types' (Fig. 2.9B), derived from qualitative analysis of 97 modern and ancient turbidite systems. Variability in system character was primarily attributed to dominant grain-size and the nature of the feeder system. Subsequent authors have sought to quantify the influence of specific controls on deep-water system through:

1. comparison of a single parameter across many systems (Covault and Graham, 2010; Covault et al., 2011; Covault et al., 2012)
2. quantitative analysis of multiple parameters across multiple systems (Sømme et al., 2009; Jobe et al., 2016).

However, full comprehension of the influence of all controls on all sub-environments (such as lobes and channels) across an entire deep-water system is likely impossible from a single study.

Mutti and Normark (1987, 1991) pioneered an approach to divide deep-water fans into distinct erosional and depositional 'elements'. Such 'architectural elements' (*sensu* Miall, 1985), are defined by commonly identified facies associations and their three-dimensional geometries (Pickering et al., 1995). Different types and classifications of architectural elements have been identified by many authors (Mutti and Normark, 1987, 1991; Normark et al., 1993; Pickering et al., 1995; Clark and Pickering, 1996; Piper and Normark, 2001; Posamentier, 2003). The earliest architectural analyses (Mutti and Normark, 1987, 1991) outlined seven principal types of architectural element that form the most common building blocks of modern and ancient deep-water systems: major erosional features, channels, overbank deposits, channel-lobe transition deposits, lobes, basin-plain deposits, and chaotic deposits; in principle, these were thought to be identifiable in seismic, bathymetric and outcrop data.

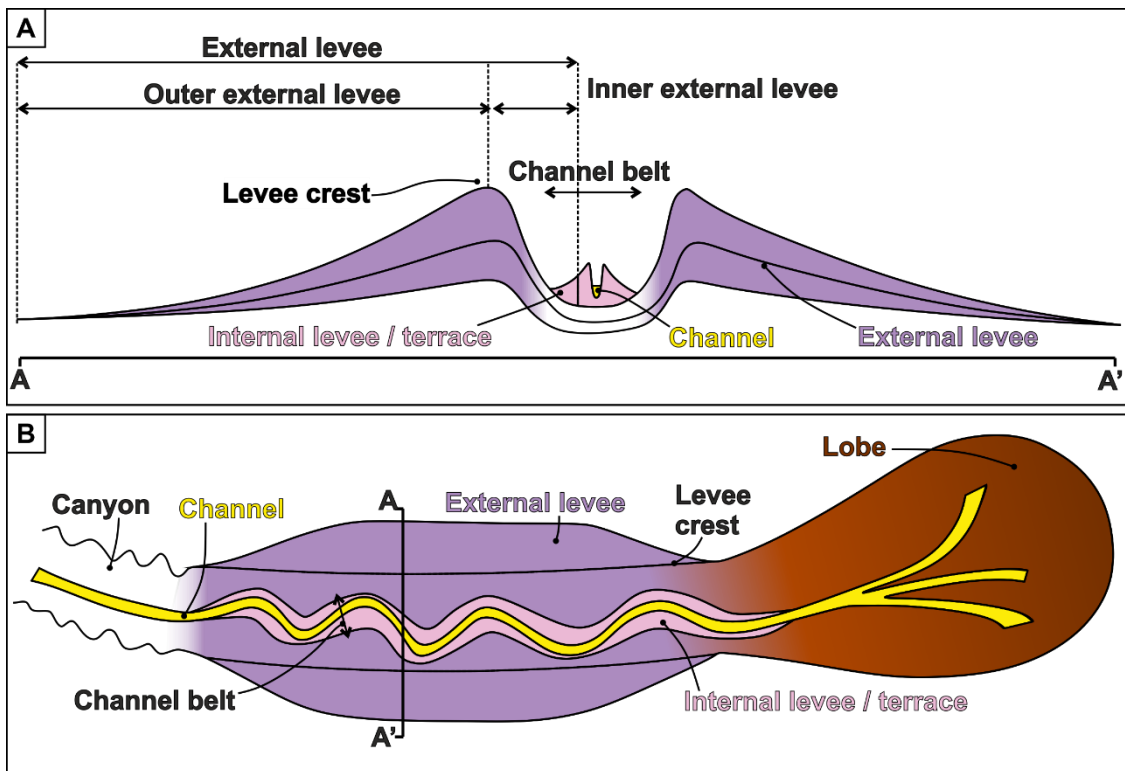


Figure 2.10 – Summary figure showing the anatomy of an idealised deep-water depositional system in cross-section (through a mixed erosional and depositional, levee confined channel), plan view, and longitudinal section (modified after Kane et al., 2007). Note that a given deep water system may not contain one or more of the features shown.

2.2.2 Anatomy of a deep-water depositional system

The lateral and stratigraphic relationships between these depositional elements allows the presentation of environmental models describing the anatomy of a ‘typical’ deep-water sedimentary system. Figure 2.10 contains a simple but robust model taken from Kane et al. (2007), displaying the depositional elements and associated sub-environments that will be referred to in this thesis and review. Moving from proximal-to-distal, the depositional elements that constitute a simple deep-water sedimentary system are as follows:

1. Submarine canyons were the first identified submarine geomorphic features (Lindenkehl, 1885; Spencer, 1905; Daly, 1936), and are defined as “steep-walled, sinuous valleys with V-shaped cross-sections, axes sloping outward as continuously as river-cut land canyons and relief comparable to even the largest of land canyons”, Shepard (1963). The deposits formed in submarine canyons are called ‘canyon deposits’. They feed most types of deep-water system (Reading and Richards, 1994)

and are commonly connected to long run-out deep-water channels (e.g. Lewis, 1994; Mountjoy et al., 2018).

2. Channels and channel belts generate channel-fills and channel complexes, which contain channel-fills and internal levee / terrace deposits, respectively. These elements will be reviewed in Section 2.3.6.
3. Overbank deposits form outside of and laterally adjacent to channel complexes from overflow from the channel belt. These elements will be reviewed in Section 2.3.4.
4. Channel-lobe transition zones represent the transition from confined, channelised flow and deposition, to unconfined flow and deposition, and are commonly characterised by an abundance of erosive scours (Normark, 1978; Wynn et al., 2002; Droz et al., 2020). As such, they are interpreted as areas of dominantly bypass and erosion and their deposits are rarely preserved (Mutti and Normark, 1987; Hofstra et al., 2015; Brooks et al., 2018a).
5. Lobes form at the end of channels. They are formed by dominantly depositional, unconfined flows and typically contain stacked or amalgamated high-density turbidity current deposits at their axes and stacked low-density turbidites and hybrid event beds toward their fringes (Bouma, 1962; Lowe, 1982; Mutti and Normark, 1987; Mutti, 1992; Hodgson et al., 2006; Hodgson, 2009; Prélat et al., 2009; Macdonald et al., 2011; Sychala et al., 2017). However, they exhibit a diverse range of architectures, from so called 'frontal splays' containing pervasive networks of distributary channels (Posamentier and Kolla, 2003; McHargue et al., 2021), to those essentially devoid of distributary networks (Gervais et al., 2006; McHargue et al., 2021).

2.2.3 Cyclicity in deep-water deposits

Stratigraphic 'order' is defined as "some arrangement of facies or unit thickness that has a discernible trend or pattern that is unlikely to occur by chance" (Burgess, 2016, p.148). Repeated patterns of stratigraphic order have led to the common interpretation that the processes that form deep-water deposits are cyclical (Hajek and Straub, 2017). In deep-water lobe deposits, stratigraphic order is usually identified in packages of beds that display a trend of coarsening- and thickening-up, followed by a trend of thinning- and fining-up. This is usually interpreted to represent a progradation (basinward migration) and retrogradation (landward migration) of the lobe, recording deposition from the frontal lobe fringe, to the lobe axis, back to the fringe (e.g. Hodgson et al., 2016). However, other situations, such as the lateral migration of a lobe (e.g. Prélat and Hodgson, 2013), or the progradation from lobe to a levee (e.g. Hodgson et al., 2016) can explain the same stratal patterns. In channel deposits evidence for cyclicity comes from the formation and infill of concave-up surfaces commonly observed in outcrop (e.g. Di Celma et al., 2011) and seismic (e.g. Deptuck et al., 2003, 2007) data. The formation of

such surfaces is typically attributed to repeated periods of incision by erosive flows, and filling by depositional flows (Mayall et al., 2006): commonly termed 'cut-and-fill' (Gardner et al., 2003).

2.2.4 External forcing

A suite of forcing mechanisms (Sømme et al., 2009) including climate (Gong et al., 2016a), sediment supply (Jobe et al., 2015) and eustatic sea level (Flint et al., 2011) have been cited as influences on deep-water sedimentary architecture and cyclicity; many of these are inherently linked (for example climate and eustasy; Miller et al., 2005). These factors act collectively to control the volume and calibre of sediment which enters a given deep-water system (Stow et al., 1996). In 'sequence stratigraphic' models (see Vail et al., 1977; Van Wagoner et al., 1988) nested cycles of lobe progradation and retrogradation, or channel 'cut and fill', are attributed to eustatic sea level fluctuations of different magnitudes (e.g. Flint et al., 2011); during periods of high sea level more sediment is trapped on the shelf forming deltas, during low sea level periods sediment bypasses the shelf and a 'lowstand fan' is created (Vail et al., 1977). However, numerous other factors influence the volume, calibre and timing of sediment input to deep-water systems, including: the triggering mechanisms of sediment gravity flows (Piper and Normark, 2001, 2009), basin physiography (Covault et al., 2013; Gong et al., 2016b), the nature of the feeder system (Covault et al., 2007; Clift et al., 2014), the presence and strength of a littoral transport cell (Allin et al., 2017), the nature of the overall source to sink routing system (Sømme et al., 2009; Clift et al., 2014), and the effects of tectonism (Georgiopoulou and Cartwright, 2013) and halokinesis (Gee and Gawthorpe, 2006; Kane et al., 2012). Therefore, sequence stratigraphic models cannot be applied universally.

2.2.5 Internal forcing

Furthermore, natural patterns of progradation (Macdonald et al., 2011), retrogradation, and lateral movement of channel and lobe deposits (Picot et al., 2016; Dennielou et al., 2017) may arise without external forcing. For example, lobate deposition at the mouth of a channel may generate a topographic obstacle with a convex-up top at the channel-lobe transition zone that blocks, and causes backfilling in, the channel and causes retrogradation of the lobe (McHargue et al., 2011). The topography generated by the downstream blockage makes flow pathways lateral to the original path more efficient, and therefore an 'avulsion' may occur, whereby abrupt lateral (flow-perpendicular) shift in the position of the lobe, and the connecting channel is observed (Prélat et al., 2010; Fig. 2.11). Repeated iterations of this process can generate cross-sectional stacking patterns in lobe (Prélat et al., 2009) and channel-levee deposits (Picot et al., 2016), whereby the point of maximum thickness of each channel-levee or lobe deposit is laterally offset from that of the deposits stratigraphically above and below it: a process

called 'compensational stacking' (*sensu* Mutti et al., 1994; Fig. 2.11). The interplay between these internal sedimentary forcing mechanisms, and the aforementioned external forcings can generate complex patterns, and the depositional controls are often difficult to discern (Ferguson et al., 2020).

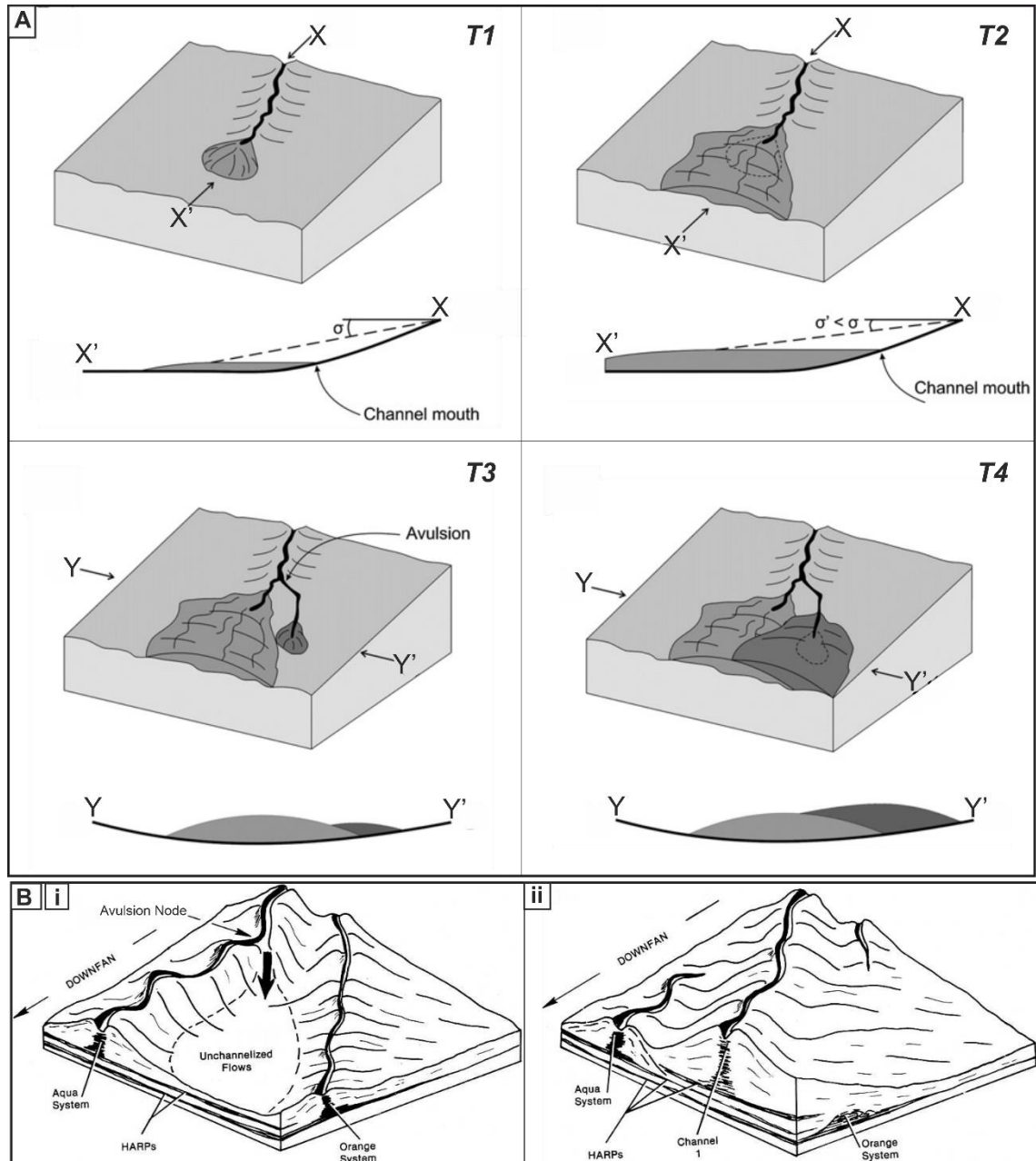


Figure 2.11 – (A) Figure summarising the process of compensational stacking, whereby avulsion leads to a lateral offset in the maximum thicknesses of two lobes (Prélat et al., 2010); (B) post breach evolution of an avulsion through: (i) the escape of unconfined turbidity currents, through the breach point at the avulsion node into the inter-channel low point depositing HARPs; (ii) progressive flow confinement leads to the accretion of levees and the establishment of a second channel (Flood et al., 1991).

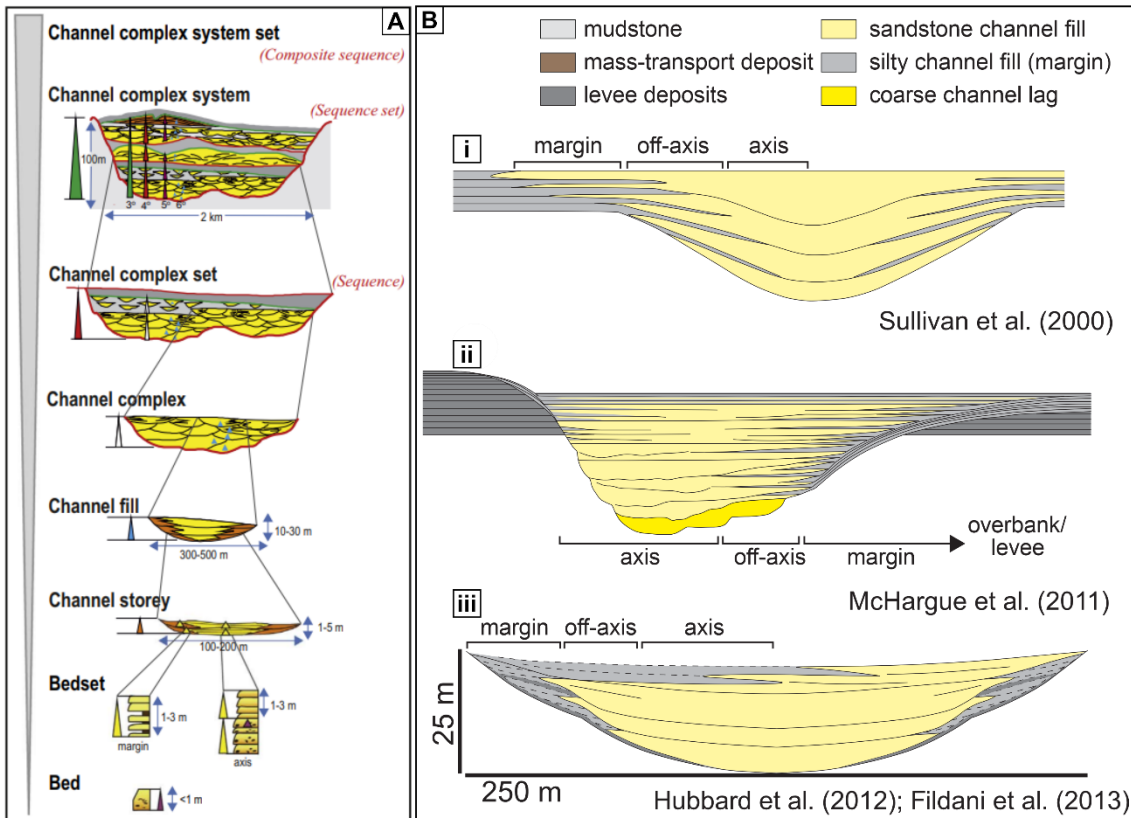


Figure 2.12 – (A) Hierarchical classification scheme for deep-water channel deposits used in this review (from Cullis et al., 2018 after Sprague et al., 2005); (B) variety of different types of channel-fill, showing lateral and vertical trends with relatively symmetrical (i and iii), and asymmetrical (ii) facies distributions (after Hubbard et al., 2014).

2.2.6 Stratigraphic hierarchy

The apparent recognition of multiple, nested scales of distinct stratigraphic orders led to the adoption of ‘hierarchical’ classifications of deep-water deposits (Mutti and Normark, 1987, 1991). Most hierarchical classifications are case-study specific. They can be based on outcrop data, which encourages a ‘bottom-up’ (starting with the smallest scale of stratigraphic order) approach (e.g. Gardner et al., 2003; Prélat et al., 2009), or seismic data, which encourages a ‘top-down’ (starting with the largest scale of stratigraphic order) approach (e.g. Mayall et al., 2006; Deptuck et al., 2008). Hierarchical schemes are commonly developed separately for channels (e.g. Campion et al., 2005) and lobes (e.g. Prélat et al., 2009). Descriptive hierarchical classifications of whole deep-water systems have been attempted (e.g. Mutti and Normark, 1987), but are not usually possible. Alternatively, Flint et al (2011) applied a three-level sequence stratigraphic hierarchy to an entire deep-water system in the outcropping Laingsburg depocentre

(Karoo Basin). However, in a recent review, Cullis et al (2018) concluded that complete reconciliation of hierarchical schemes is not possible, with the principle obstacle being the number of ‘orders’ recognised in each system. The scheme of Sprague et al. (2005) is used herein (Fig. 2.12).

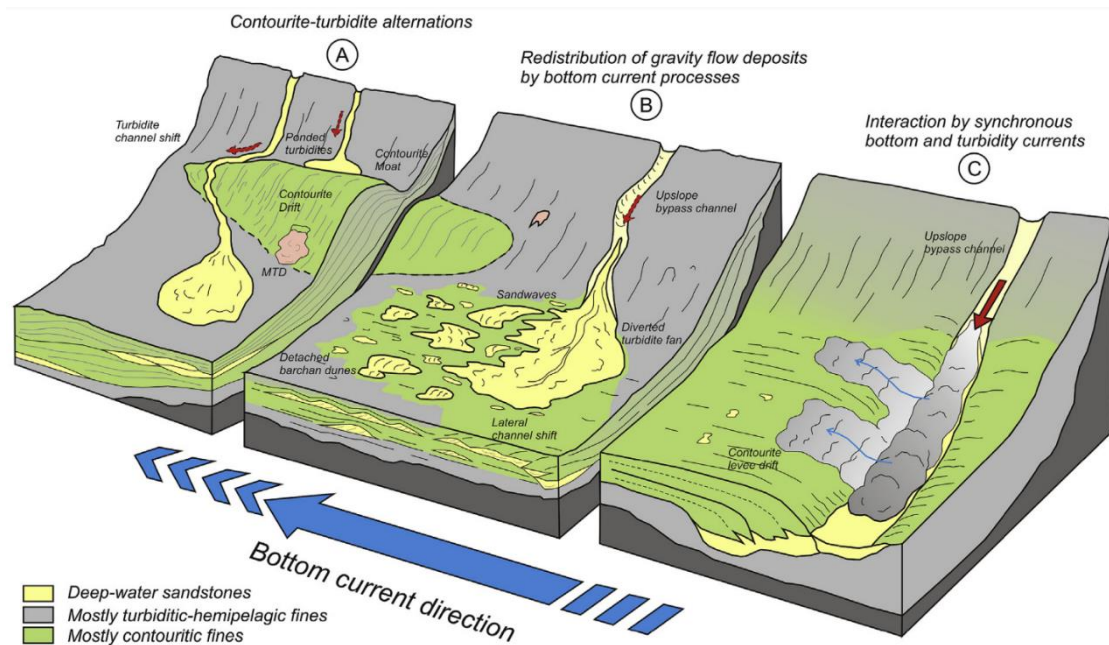


Figure 2.13 – Conceptual depositional and process models for the interaction of gravity flows and bottom currents at different temporal scales (Fonnesu et al., 2020).

2.2.7 Contour currents and contourites

Thermohaline ‘contour currents’ have long been simulated and measured in oceanographic studies (Wüst, 1933; Swallow and Worthington, 1961), and are the product of dense fluid input, flowing beneath less-dense ambient fluid. Thus, the formation and nature of a contour current is dependent on an interplay between the temperature and salinity of both the input and ambient fluid, as well as the circulation potential, sea-floor topography and interaction with other currents in the receiving basin (Faugères et al., 1999; Stow et al., 2008). Temperature-driven contour currents tend to initiate in polar seas and flow towards the equator (Rebesco et al., 2014); salinity-driven currents tend to initiate in warmer, confined basins (e.g. the Mediterranean; Hernández-Molina et al., 2014). Once initiated, contour currents flow parallel to the contours of the continental slope or rise and, as such, typically flow normal or oblique to turbidity

currents, which typically flow perpendicular to slope contours (Fuhrmann et al., 2020). Contour currents can travel at any height within the water column, and are deflected, rightwards in the North Hemisphere and leftwards in the Southern, by the Coriolis force (Faugères et al., 1999).

The ability of contour currents to re-work and deposit sediments was first recognised by Heezen and Hollister (1964). Sedimentary successions deposited or re-worked by deep-water contour currents are termed 'contourites' (Faugères and Stow, 1993). Although sandy contourites have been documented, contour current influence on deep-water deposits has typically been associated with fine-grained sediments (Stow and Piper, 1984). However, their identification in ancient successions is contentious (Stow et al., 1998), as contourites can contain many of the same structures seen in shallow and deep marine environments (Stow et al., 2008). Inverse grading and pervasive bioturbation have been postulated as potentially diagnostic of contourite deposition (Rebesco et al., 2014), however these characteristics may also be observed in hyperpycnal flow deposits (see discussion of Mulder et al., 2001, 2002, and Shanmugam, 2002) or a 'pulsing' flow (Kneller and McCaffrey, 1999, 2003; Ho et al., 2018). The identification of contourites at larger, architectural, scales is easier than at deposit scale, as contourites can form cause impressive 'mounded drift' deposits (Faugères et al., 1999), and erosional 'moats' (Hernández-Molina et al., 2014).

Fonnesu et al. (2020) present three models for how turbidity currents and contour currents, and their resultant deposits can interact (Fig. 2.13):

1. Alternating periods when (a) turbidity currents are dominant and contour currents are weak or inactive, and (b) contour currents are dominant and turbidity currents are infrequent or inactive (Faugères and Stow, 2008; Brackenridge et al., 2013; Fuhrmann et al., 2020).
2. Contour currents have a relatively minor on turbidity currents that occur periodically during the deposition of turbidites, but these turbidite deposits are subsequently re-worked by contour currents (Faugères and Stow, 2008; Gong et al., 2013).
3. Synchronously active contour currents and turbidity currents interact. Contour currents capture the finer-grained sediment from the upper parts of stratified turbidity currents, transporting it in the direction of the flow of the contour current (Miramontes et al., 2020; Fuhrmann et al., 2020).

Where deep-water channel systems are crossed by perpendicularly-flowing contour currents, their interaction can lead to strong asymmetry in the height and width of a channel's levees, and hence the volume of its overbank deposits (Fig. 2.13).

2.3 Deep-water channels

2.3.1 Introduction and terminology

'Deep-water channels' are elongate sediment conduits that transport sediment from shallow to deep-water, and as such this term refers only to the geomorphic features observed on the floors of Earth's oceans and seas (Carter, 1988; Peakall and Sumner, 2015). The classification scheme of Peakall and Sumner (2015) is used hereafter to distinguish different types of deep-water channel.

'Deep-water channel deposits' are the product of the evolution of deep-water channels. They are recognised by the presence of concave-up surfaces that are typically filled by dominantly coarse-grained, high-density turbidites and debrites, are concave-up in cross-section, and typically truncate other surfaces (Gardner et al., 2003; Deptuck et al., 2003, 2007; Hodgson et al., 2011; Fig. 2.14A).

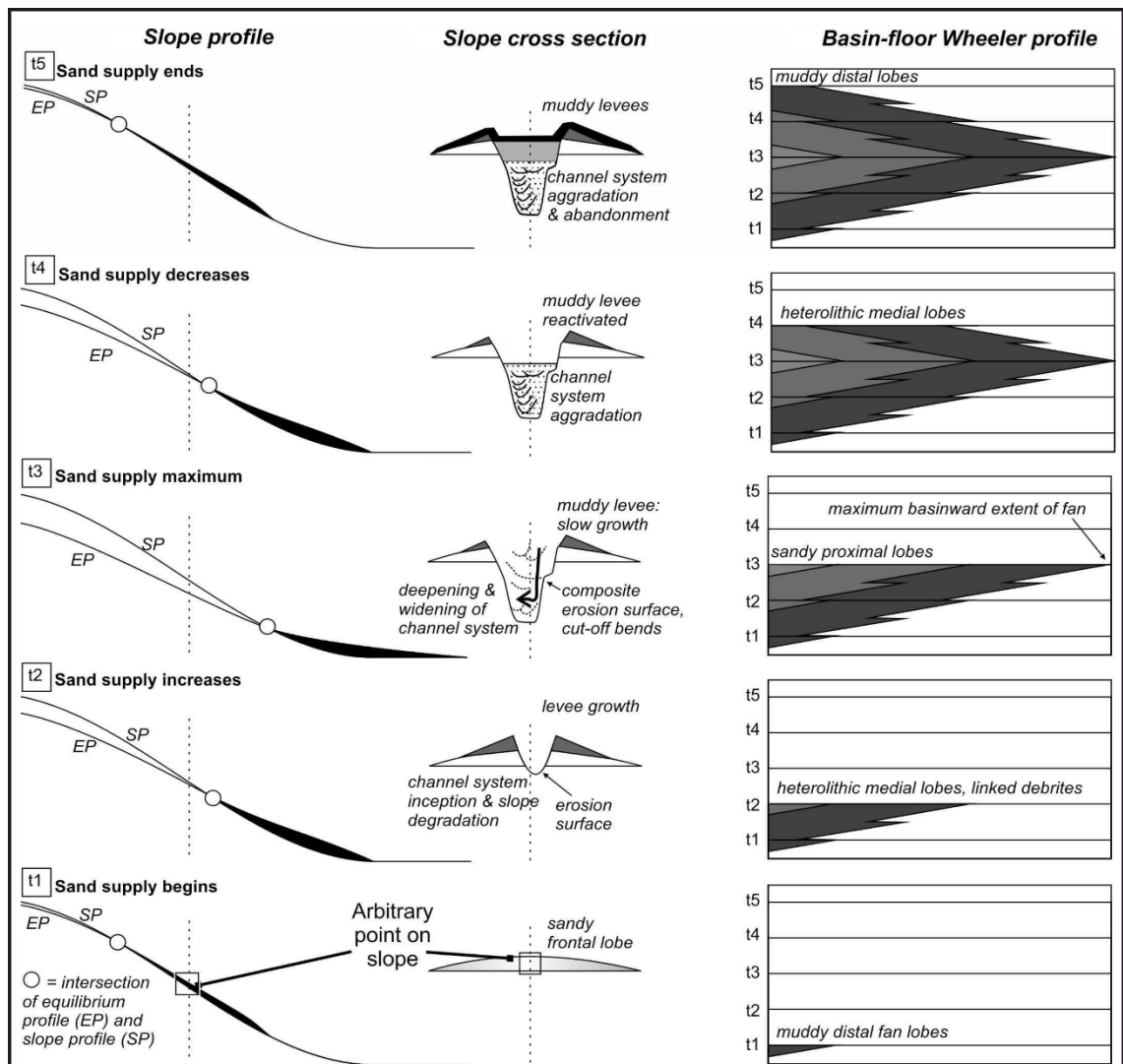


Figure 2.14 – Schematic diagram explaining the concept of cut-and-fill and its effects on a whole depositional system (Hodgson et al., 2016).

On the seafloor, an idealised deep-water channel system will comprise a broad ‘channel belt’ that is bound by two ‘external levees’ (see Section 2.3.4; Fig. 2.10). Within this channel belt, a ‘channel’ with a higher sinuosity (see Section 2.3.5) than the broader belt is bound by ‘terraces’ or ‘internal levees’, which are stepped areas that can be essentially flat or slope gently away from the channel, respectively (see Section 2.3.6; Fig. 2.10).

The deposits formed on external levees, internal levees, and terraces are called ‘external levee deposits’ (see Section 2.3.4; Fig. 2.10), ‘internal levee deposits’ (see section 2.3.6; Fig. 2.10), and ‘terrace deposits’ (see Section 2.3.6; Fig. 2.10) respectively; the deposits formed in channels are called ‘channel-fill’ deposits (see Section 2.3.6; Fig. 2.10).

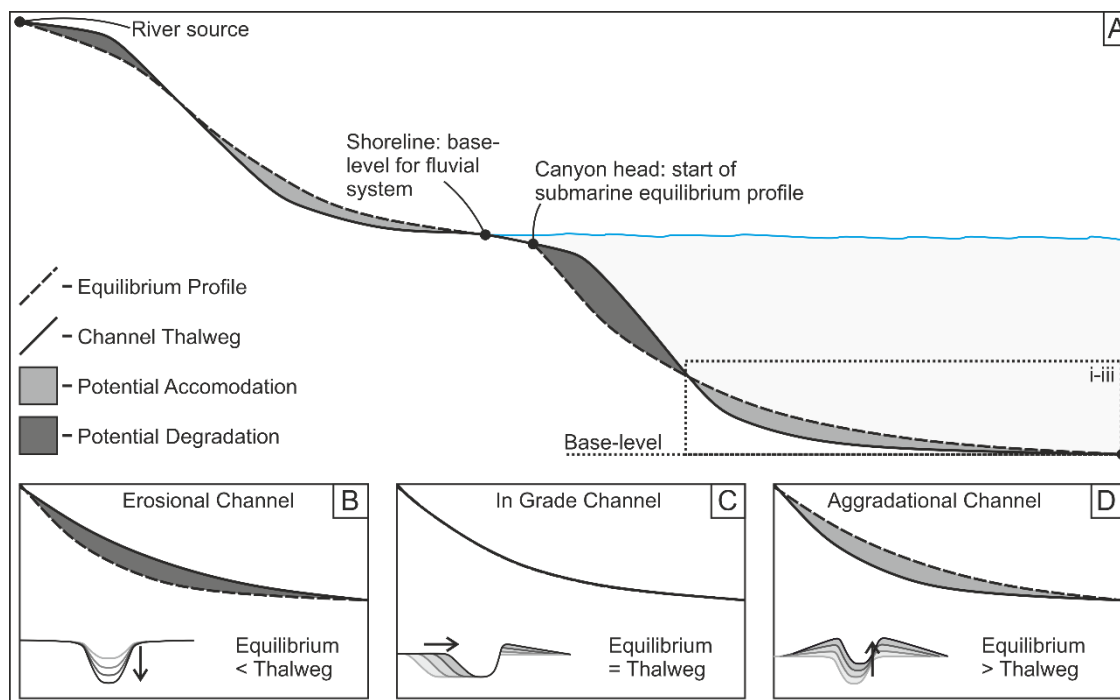


Figure 2.15 – (A) Summary diagram of the concept of channel equilibrium profiles with a focus on submarine channels; (B)-(D) show the response of a channel in pursuit of its equilibrium profile relative to its current position (modified after Kneller, 2003 with inspiration from Georgiopoulou and Cartwright, 2013).

2.3.2 Deep-water channel equilibrium model

Dailly (1982) applied the concepts of ‘grade’ (*sensu* Gilbert, 1877) and ‘baselevel’ (*sensu* Davis, 1902), which have long been prevalent in fluvial sedimentology, to subaqueous systems, advocating a sea-level independent ‘slope readjustment’ model. Subaerial and subaqueous systems will trend towards an idealised ‘equilibrium profile’

(Pirmez et al., 2000), representing the most efficient path between the primary sediment source, which in subaqueous systems typically represents the head of a canyon (Ross et al., 1994), and a baselevel, which is typically located at the terminal lobe. Erosion into the shelf and upper slope by the canyon or most proximal channel reaches, coupled with filling of accommodation at the base of slope (Fig. 2.15B), are the mechanisms by which a channel may reach equilibrium (Pirmez et al., 2000).

Deep-water depositional elements are the compound product of the many flows that erode, bypass and deposit within the constituent parts of a system over its lifecycle (Stevenson et al., 2013). Therefore, the nature of the flows that traverse the system over long periods controls where erosion and deposition are likely to occur, and hence the geometry of a system's equilibrium profile (Kneller, 2003). Thus, the shape of a channel's equilibrium profile can change through time.

Kneller (2003) related this concept to the stratigraphic record, postulating that: a channel with its thalweg below its idealised equilibrium profile will aggrade; a channel with its thalweg following its equilibrium profile will be 'in grade' and remain vertically static, usually accompanied by sinuosity enhancement; a channel with its thalweg above its equilibrium profile will incise (Fig. 2.15B). Therefore, a channel may undergo distinct periods of aggradation and incision as it adjusts to changes in its equilibrium profile caused by variations in the nature of the flows that traverse it (Pirmez et al., 2000; Kneller, 2003), potentially driven by external forcings (see Section 2.2.4).

Alternatively, the shape of a channel's longitudinal profile may be modified by the influence of tectonics (Georgiopoulou and Cartwright, 2013), mass transport deposits (Tek et al., 2021), and avulsion (Pirmez et al., 2000). Therefore, even with a static equilibrium profile, local or system-scale perturbations about this profile can cause incision and aggradation in different locations, as the channel attempts to maintain equilibrium (Georgiopoulou and Cartwright, 2013). Ultimately, the interaction between the nature of the flows that traverse a deep-water system, and modifications of a channel's longitudinal profile, can generate complex patterns of erosion and deposition temporally and along a deep-water system (Pirmez et al., 2000; Prather, 2003; Georgiopoulou and Cartwright, 2013; Prather et al., 2017; Brooks et al., 2018b).

2.3.3 Cut-and-fill

Channels may initiate through:

1. the quasi-instantaneous evacuation of, and excavation by, a submarine landslide failure on the continental slope (Hodgson et al., 2016; Ortiz-Karpf et al., 2017; Brooks et al., 2018c; Gomis-Cartesio et al., 2018)

2. the formation of trains of cyclic-steps (see Section 2.3.12), which then connect to produce a through-going conduit (Ridente et al., 2007; Fildani et al., 2006, 2013; Covault et al., 2014; Droz et al., 2020)
3. preferential bypass in the (cross-sectional) centre and deposition at the lateral edges of unconfined flows, which build topography that confines subsequent flows, sequentially providing more central bypass and lateral confinement, thus initiating a 'channelisation feedback' (Eggenhuisen et al., 2011; De Leeuw et al., 2016)

Through the initiation of a channel, a given point on the seafloor may experience dominantly bypass and erosion, until an incised channel becomes established when overspill and deposition is permitted on its overbanks (Deptuck et al., 2003, 2007; Hansen et al., 2017a; Kneller et al., 2020). Alternatively, progradation of the channel-lobe transition zone can cause a channel to incise into unconfined lobe deposits that formed prior to, and basinward of, the location of incision (Macdonald et al., 2011; Hodgson et al., 2016; De Leeuw et al., 2016; Fig. 2.14).

A deep-water channel can be filled through:

1. the loss of fine-grained material from the top of a flow through the process of overspill (see Section 2.3.4), which forces a flow out of equilibrium, reduces its capacity, and causes the coarsest grains to fall out of suspension (Peakall et al., 2000a, b).
2. backfilling of a conduit, where the terminal lobe deposit retrogrades and sediment is sequestered in the channel, causes the channel to fill with coarse-grained sediment that would have been deposited in the lobe axis first, followed by a general fining-up trend often observed within channel elements (Gardner et al., 2003).
3. abandonment after an avulsion, whereby the channel abruptly jumps laterally to a new location, after plugging by an MTD upstream, or after the cut-off of a meander bend (Deptuck et al., 2003, 2007), causing the channel to fill with fine-grained sediment (Barton et al., 2010; Alpak et al., 2013).

Repeated increases and decreases in the velocity or magnitude of flows that traverse a channel can cause repeated periods of incision then deposition. Therefore, the formation of concave-up surfaces in deep-water channel deposits are typically interpreted as the product of the periodic formation and subsequent infill of deep-water channels (Mayall and Stewart, 2000; Gardner et al., 2003; Mayall et al., 2006; Deptuck et al., 2003, 2007; Di Celma et al., 2011; Hodgson et al., 2011; Flint et al., 2011; Hubbard et al., 2009, 2014; Fig. 2.14). Repetition of the processes described below are responsible for the generation of nested scales of concave-up surfaces (see Section 2.2.6). For example, a large, incised master conduit that hosts the deposits of a channel belt with multiple channel fills may be formed during a period of significant incision and bypass, and then be filled gradually, through the formation and fill of multiple channels

(e.g. Deptuck et al., 2007). Alternatively, the progressive widening and deepening of a master conduit may be achieved through progressive alteration during the formation and infill of multiple channels, meaning that the master conduit need not have existed as a geomorphic feature at any time (e.g. Hodgson et al., 2011, 2016; Fig. 2.14).

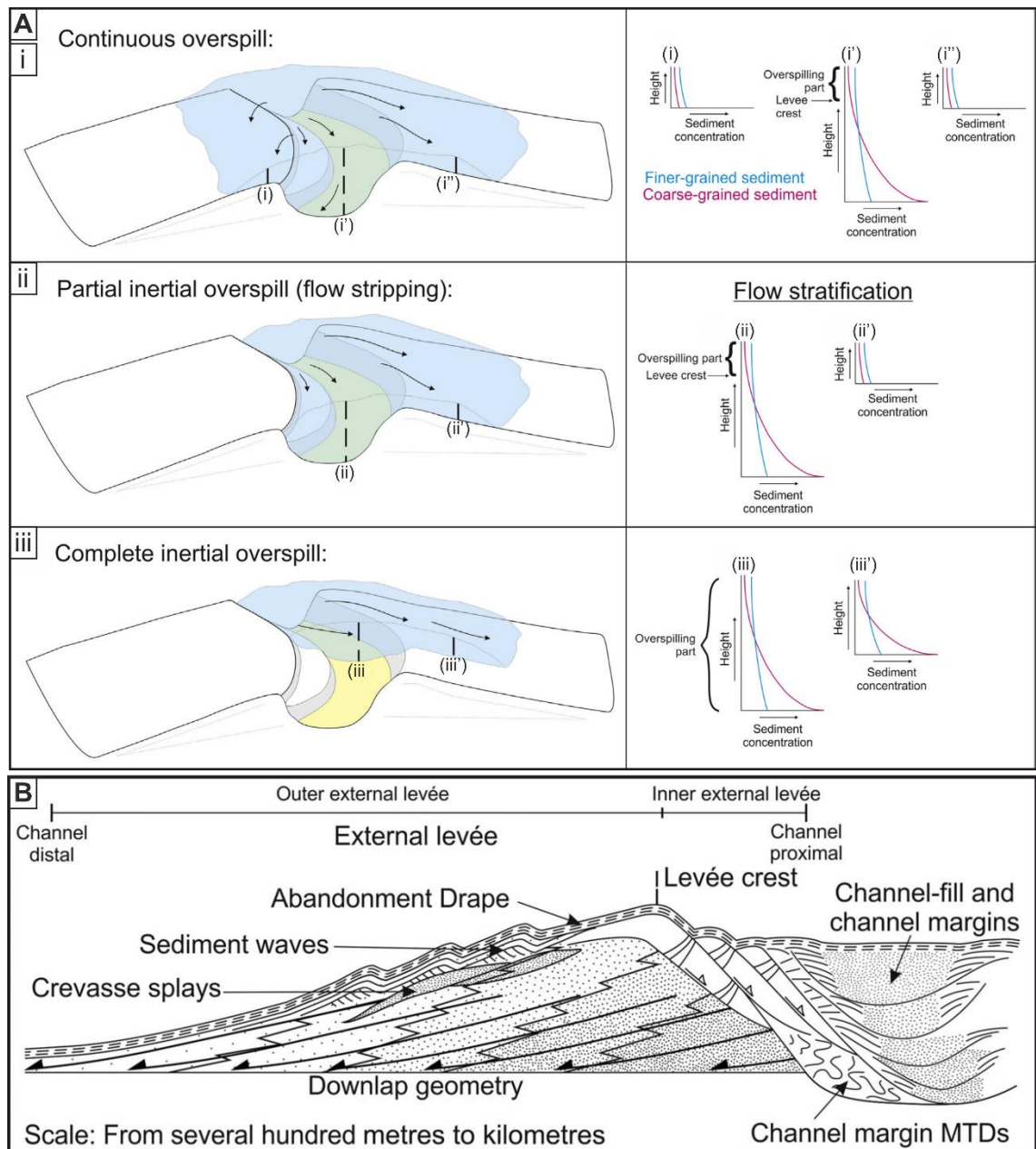


Figure 2.16 – (A) Summary figure explaining the overspill processes responsible for the formation of levees and the effect of flow stratification in controlling their grain-size (after Hansen et al., 2015): (i) continuous overspill, (ii) partial inertial overspill, and (iii) complete inertial overspill; (B) sketch of a fine-grained submarine levee from the Karoo Basin (from Morris et al., 2014a) showing common features, grain-size trends and stratal terminations; denser dot spacing indicates coarser grains.

2.3.4 *Overspill*

Turbidity currents that are thicker than the deep-water channel they traverse can 'overspill' (Clark and Pickering, 1996) onto their overbank areas. Due to the effect of flow stratification (Migeon et al., 2012), finer sediment is more abundant in the upper parts of turbidity currents, meaning a finer-grained portion of a flow will overspill than that traversing the channel. Three types of overspill can occur (Hansen et al., 2015):

1. Continuous overspill (Fig. 2.16A): in straight channels (Felix, 2002) the material suspended above the channel walls will naturally 'overspill' evenly onto both overbanks as confinement is lost. This leads to deceleration and deposition of thin, usually low density turbidites (Hiscott et al., 1997), and the formation of symmetric levees. Flow dilution from ambient fluid entrainment will occur as sediment is lost to overspill and thalweg deposition (due to re-equilibration; Peakall et al., 2000a, b) which will increase flow height (Pirmez and Imran, 2003), thus initiating a feedback mechanism allowing continuous overspill and deposition along long channel reaches (Hesse, 1995).
2. Partial inertial overspill: at a meander bend, due to the centrifugal force, superelevation and flow stratification, flow above the height of confinement will preferentially spill onto the outer bend bank whilst at least part of the flow remains in confinement (Fig. 2.16A; Piper and Normark, 1983; Hay, 1987; Peakall et al., 2000a, b).
3. Complete inertial overspill – In extreme cases, such as at very tight channel bends, increased inertia and resultant flow superelevation may cause the velocity maxima of a turbidity current to exceed the height of confinement (Straub et al., 2011), hence causing the entire flow to overspill (Fig. 2.16A; Hay et al., 1983; Hay, 1987).

Deep-water channel deposits are commonly bounded by sedimentary accumulations that form from progressive deposition by overspilling turbidites over long periods. These accumulations commonly progressively reduce in thickness away from a 'crest', producing 'wedge-shaped' deposits and produce 'winged' seafloor cross-sections through modern deep-water channel systems (Flood et al., 1991; Pirmez and Flood, 1995; Babonneau et al., 2002), and are termed 'external levees' (*sensu* Kane and Hodgson, 2011; Fig. 2.16B). Where these accumulations are not wedge shaped, these deposits are simply termed overbank deposits (Tek et al., 2021b). Overspill and overbank deposition can occur during channel incision and infill (Pickering et al., 1995; Deptuck et al., 2003; Hodgson et al., 2011; Sylvester et al., 2011; Khan and Arnott, 2011). Levee deposits usually comprise primarily thin-bedded turbidites less than 10cm thick (Mutti, 1977; Hansen et al., 2015), which generally fine (Morris et al., 2014a, b) and thin (Kane et al., 2007) away from the levee crest (Fig. 2.16B). As the levee grows, the

point of overspill will naturally migrate away from the channel, causing a lateral stepping of the thin beds and a resultant migration of the levee crests and causing complex grain-size trends (Kane et al., 2007; Kane and Hodgson, 2011; Morris et al., 2014a). The presence of sinuosity accompanied by partial inertial overspill causes the outer bend levee to contain thicker and coarser beds than those of the inner bend, and the levee to be thicker around outer bends (Pirmez et al., 2000; Khan and Arnott, 2011). The palaeocurrents in external levees can show variability between perpendicular and parallel to the flow of the channel (Kane et al., 2010a). However, overspill and overbank deposition can be affected by a channel's sinuosity (Kane et al., 2010b; Khan and Arnott, 2011), the Coriolis force at mid to high latitudes (Chough and Hesse 1980; Imran et al., 1999), contour currents (Rebesco et al., 2014; Miramontes et al., 2020), and evolving seafloor topography (Clark and Cartwright, 2011).

The large (seismic) scale architecture of overbank deposits, the variability of and controls on their architecture, and the nature of bedforms such as sediment waves that are commonly observed on channel overbanks, are discussed and reviewed in depth in Chapter 5.

2.3.5 Deep-water channel morphologies

2.3.5.1 Length, width, and depth

The length, width and depth of deep-water channels on the seafloor vary between different channel systems, and the width and depth can vary significantly along a given channel system (Deptuck et al., 2003; Sømme et al., 2009; Covault et al., 2012; Konsoer et al., 2013; Pettinga et al., 2018; Shumaker et al., 2018; Palm et al., 2021).

Covault et al. (2012) identified the volume and type of sediment supplied to a continental margin, and the relief of the margin as key controls on deep-water channel length. This insight allowed generalisations about the relationship between channel length and margin type to be made: channels on high-relief passive margins with large, fine-grained feeder systems exhibit longer lengths than low-relief, low supply systems on active margins.

Performing a morphometric analysis on 36 channels, Shumaker et al. (2018) determined that, due to stark variability between different systems, that channel width and depth are likely controlled by external forcings such as the type and volume of sediment supplied to the channel. While dramatic variations channel width, which can range from <100 m to >10 km, and channel depth, which can range from metres to >100 m, were observed between different systems, their aspect ratios remained within a range of 10:1 to 100:1, suggesting that this parameter is naturally (internally) modulated.

Furthermore, Shumaker et al. (2018) observed a general proximal-to-distal decrease in channel width and depth, attributing this to the maturity of the channel, with younger, more distal parts of the channel being smaller than well-established proximal parts. However, their analysis suggests that a channel may grow to a stable width relatively early in its evolution, whereas its depth may continue to change throughout its lifecycle. While these findings hold for established channels on deep-water fans, channels traversing topographically complex slopes may exhibit more localised morphometric variability (Deptuck et al., 2007; Shumaker et al., 2018). Even more locally, Palm et al. (2021) observed systematic width variations around channel bends with the greatest widths being located at bend apices.

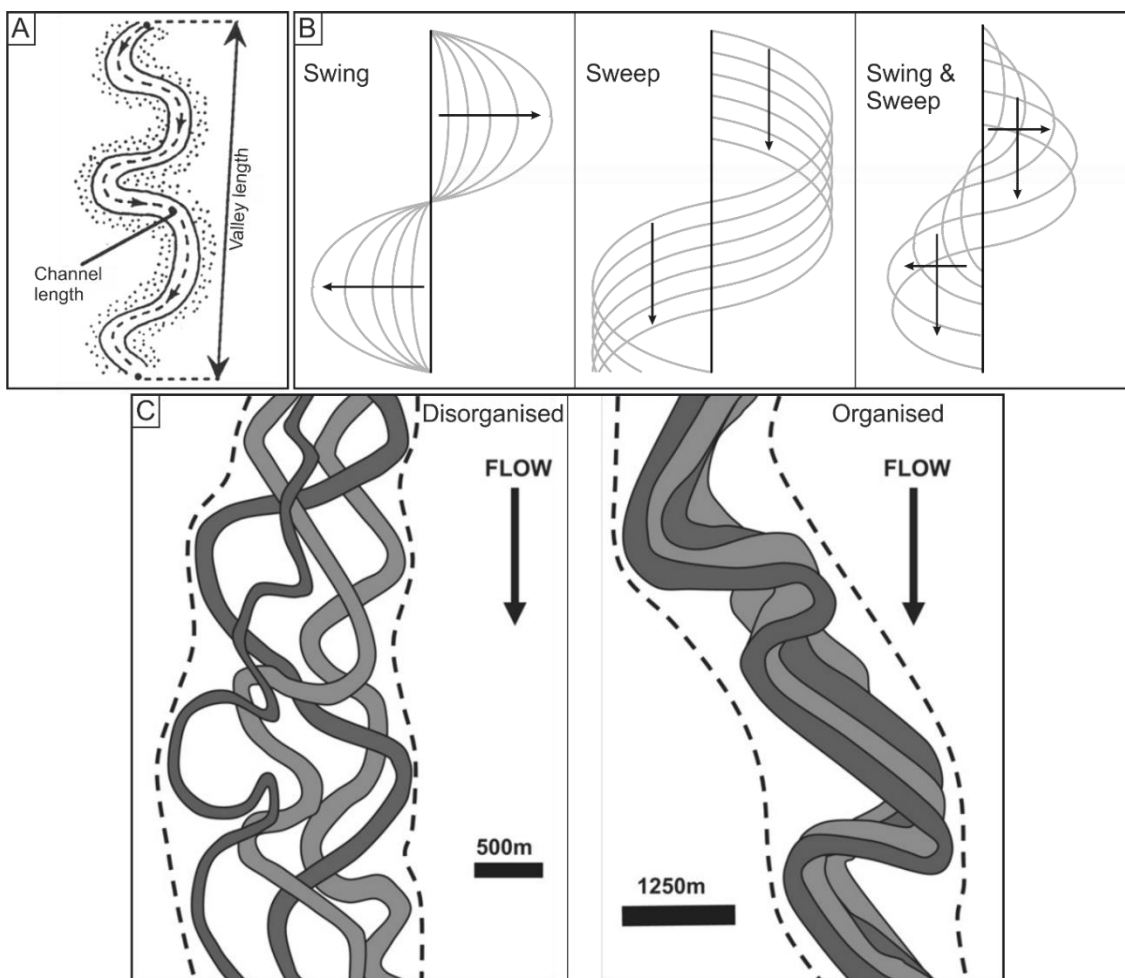


Figure 2.17 – (A) Schematic drawing of a sinuous fluvial channel highlighting the parameters of channel length and valley length (modified after Friend and Sinha, 1993); (B) three mechanisms for meander bend expansion and translation (modified from Peakall et al., 2000b); (C) contrasting styles of sinuosity in plan-view: disorganised and organised (after McHargue et al., 2011).

2.3.5.2 Sinuosity

Sinuosity is a measure of the plan-view degree of curvature of a channel. It affects the architecture, heterogeneity and sediment distribution within channel-fills and channel complex fills (Mayall and Stewart, 2000; Abreu et al., 2003; Mayall et al., 2006; Wynn et al., 2007), flow behaviour (Peakall et al., 2007; Straub et al., 2011; Peakall and Sumner, 2015), and overbank process and deposition (Straub et al. 2008; Kane et al., 2010b). Sinuosity can be calculated using the equation:

$$\text{Sinuosity} = \text{Chanel length} / \text{Valley length}$$

in both fluvial (e.g. Friend and Sinha, 1993) and submarine channels (e.g. Janocko et al., 2013; Hansen et al., 2017a), where channel length is the length of the meandering channel thalweg and valley length is the overall length of the host channel belt (Fig. 2.17).

Channel bend evolution may occur through swing (lateral translation), sweep (downstream translation), or a combination of the two (Fig. 2.17; Peakall et al., 2000a, b). Controls on sinuosity development are contentious. Comparing deep-water channels on 16 fans, Clark et al. (1992) interpreted slope gradient and sediment calibre as the primary control on channel sinuosity. However, further quantification of the data presented in Clark et al. (1992) shows that correlation of peak sinuosity and latitude is stronger than that of slope (Peakall et al., 2012). This trend is interpreted to be due to the effect of the Coriolis force, which has long been shown to effect flow within submarine channels (Imran et al., 1999) and their overbanks (Chough and Hesse, 1980). At low latitudes, the effects of the Coriolis force are negligible, and therefore centrifugal forces dominate at bends, allowing sinuosity development through swing and sweep. At high latitudes, the Coriolis force becomes dominant over centrifugal forces, pushing flow toward the right channel wall in the Northern Hemisphere, and the left channel wall in the Southern Hemisphere and inhibiting sinuosity development (Peakall et al., 2012; Wells and Cossu, 2013; Cossu et al., 2015; Davarpanah Jazi et al., 2020).

2.3.6 Channel-fill

Like-for like comparison between channel deposits in different systems is extremely difficult due to complications that arise from differences in scale (Deptuck et al., 2007; Macauley and Hubbard, 2013; Bell et al., 2020), and hierarchical categorisations of channel-fill deposits and the concave-up surfaces they contain and sit within (see Section 2.2.6; Cullis et al., 2018; Fig. 2.12A). However, attempts can be made to reconcile commonly identified orders has been attempted (e.g. McHargue et al., 2011; Hubbard et al., 2020).

The smallest scales of identified deposits are beds and bedsets (Sprague et al., 2005; Champion et al., 2005; Di Celma et al., 2011; Pickering and Cantalejo, 2015). The

organisation and distribution of different bed and bedset types ultimately controls the architecture of all larger scales of channel deposit (Fig. 2.12B).

Channel stories (*sensu* Sprague et al., 2005) are repeated stratigraphic units hosted within concave-up surfaces. Vertical and lateral changes in bed type and sedimentary facies occur across channel stories. Fine-grained deposits can line the bases of channel stories, which are typically formed by flows which mostly bypass a given location, leaving deposits from their fine-grained tails and sometimes coarse-grained lag deposits (Barton et al., 2010; Alpak et al., 2013; Stevenson et al., 2015; Hubbard et al., 2014, 2020; Fig. 2.12B). The 'axis' of a channel story, which is located at the deepest point of the host surface, typically contains debrites and coarse high-density turbidites, including conglomerates and coarse sandstones, and exhibits the most amalgamation. Logs or cores through the axis of a channel story typically contain conglomerates, debrites and amalgamated coarse sandstones at their base, and exhibit a fining-up trend to finer-grained sandstones. In the 'margins' of a channel story, located at the shallower lateral edges of the concave-up surface, the deposits typically comprise finer grained high- and low-density turbidites, exhibiting much less amalgamation (Mutti and Normark, 1987; Sprague et al., 2005; Campion et al., 2005; Kane et al., 2009a; Di Celma et al., 2011; Mchargue et al., 2011; Brunt et al., 2013a; Macauley and Hubbard, 2013; Pickering and Cantalejo, 2015; Casciano et al., 2019; Hubbard et al., 2014, 2020; Fig. 2.12B).

The internal architecture of a 'channel-fill' (*sensu* Sprague et al., 2005) is a result of the stacking of its constituent channel stories. Similarly to channel stories, their host surface can be lined by a package of fine-grained bypass deposits (Barton et al., 2010; Alpak et al., 2013; Fig. 2.12B). The axis of a channel-fill typically contains the coarsest deposits, as it is usually the location where the axes of the channel stories stack. A progressive fining-up trend is also typically observed in the channel axis (Mutti and Normark, 1987; Sprague et al., 2005; Campion et al., 2005; Kane et al., 2009a; Di Celma et al., 2011; Mchargue et al., 2011; Brunt et al., 2013a; Macauley and Hubbard, 2013; Pickering and Cantalejo, 2015; Casciano et al., 2019; Hubbard et al., 2014, 2020; Fig. 2.12B), because channel stories become progressively finer-grained vertically, due to the effective widening of the u-shaped conduit as it is filled (Hubbard et al., 2014); however exceptions do exist (Jobe et al., 2010). While channel margins are typically finer than in the axis, vertical trends in channel margins are unpredictable, such that beds may fine and thin upward (e.g. Bell et al., 2020), or may thicken and coarsen upward (e.g. Hubbard et al., 2014, 2020). As channel-fill architecture is determined by the stacking of stories, a cross-section through a channel fill can be:

1. symmetrical, whereby the deepest part of the host surface and of the position of the axis are located in the centre of the channel-fill (e.g. Fildani et al., 2013; Macauley and Hubbard, 2014; Pickering and Cantalejo, 2015; Casciano et al., 2019; Hubbard et al., 2014, 2020; Fig. 2.12B)
2. asymmetrical, whereby the deepest part of the host surface and axial position is skewed towards one edge of the channel-fill (e.g. Sullivan et al., 2000; Sprague et al., 2005; Jobe et al., 2010; McHargue et al., 2011; Alpak et al., 2013; Fig. 2.12B).

The symmetry of a channel-fill may change along its length, as cross-sections through the apices of meanders are more likely to exhibit asymmetry (Jobe et al., 2010).

These models of channel-fill facies and architecture have mostly been developed from outcropping ancient deep-water channel systems. However, they do not typically account for deposits formed by highly sinuous deep-water channels (Kolla et al., 2007; Wynn et al., 2007). The progressive expansion of channel bends, driven by outer-bank erosion ('bank-pull'; Palm et al., 2021), is commonly accompanied by deposition on the inner bends (Peakall et al., 2007; Peakall and Sumner, 2015). In cross-section, inner-bend deposits take the form of sigmoidal, laterally stacked beds or seismic reflectors that dip in the direction of channel migration, and in plan-view are arcuate and exhibit a similar geometry to the channel bend. Although relatively rare, these 'lateral accretion deposits' have been identified in both outcrop and seismic data (Elliott, 2000; Abreu et al., 2003; Arnott, 2007; Janbu et al., 2007; Wynn et al., 2007; Kolla et al., 2007, 2012; Peakall and Sumner, 2015; Arnott et al., 2021). On outer bends, deposits with similar sigmoidal geometries that exhibit opposing dips to lateral accretion surfaces, termed 'outer-bank bars', can form (Kane et al., 2008; Straub et al., 2008; Nakajima et al., 2009; Peakall and Sumner, 2015). Furthermore, some authors have recognised mounded deposits that contain little internal structure, termed 'nested mounds', on outer bends (Clark and Pickering, 1996; Peakall et al., 2000a, b; Wynn et al., 2007; Kane et al., 2008); however their origin remains unclear (Peakall and Sumner, 2015).

Despite recognition of deposits associated with sinuous channels in outcrop (Elliott, 2000; Arnott, 2007; Janbu et al., 2007; Arnott et al., 2021), seismic (Nakajima et al., 2009; Janocko et al., 2013; Kolla et al., 2012) and experimental data (Peakall et al., 2007; Kane et al., 2008; Straub et al., 2008), such deposits seldom feature in hierarchical classifications of channel deposits, at least not at channel-fill scale (Abreu et al., 2003).

2.3.7 Internal levee and terrace deposits

Internal levees and terraces (*sensu* Kane and Hodgson, 2011) - also referred to as low levees (Piper et al., 1999b) and inner levees (Deptuck et al., 2003) - are bound by external levees (Kane and Hodgson, 2011) and are differentiated by their geometries;

internal levees form a wedge shape, whereas terraces do not (Hansen et al., 2015; 2017a). Although, like external levees, they contain thin bedded turbidites, their crests are lower, allowing the overspill of coarser grain-sizes (due to flow stratification), meaning thicker beds are more common, as are erosional features such as scours. Lateral flow confinement imposed by external levees causes flow reflection, leading to less predictable grain-size and facies trends and higher palaeocurrent variability (Kane and Hodgson, 2011). Internal levees and terraces are common in sinuous channel belts (e.g. Deptuck et al., 2003; Hansen et al., 2017a), with terraces often forming on the inside of meander bends. The initiation of a terrace may be achieved through the failure of the channel wall (Deptuck et al., 2003, 2007; Hansen et al., 2017a) or the presence of remnant lateral accretion deposits (Barton et al., 2010; Sylvester et al., 2011; Alpak et al., 2013); both of which will create a plateau onto which overspill deposits can accumulate.

2.3.8 Channel complex architecture and channel-fill stacking

Channel-fills stack to form 'channel complexes' (*sensu* Sprague et al., 2005). If channel-fills represent the fill of individual channels observed in an ideal sedimentary system (Fig. 2.10; Section 2.3.1), channel complexes would represent the compound fill of the wider channel belt (Fig. 2.10; Section 2.3.1) deposited through the lifecycle of multiple channels (Mayall and Stewart, 2000; Mayall et al., 2006; Hubbard et al., 2009; Macauley and Hubbard, 2013). As such, channel complexes contain both channel-fill deposits, and internal levee or terrace deposits (Kane and Hodgson, 2011; Macauley and Hubbard, 2013).

In plan-view, lateral stacking of channel-fills can produce either an organised stacking pattern, where progressively younger channel-fills follow a modified path of their predecessors, or a disorganised stacking pattern, where the path followed by each channel-fill is drastically different its predecessors (McHargue et al., 2011; Fig. 2.17C). Both swing (Fig. 2.17B; Peakall et al., 2000a, b; Kolla et al., 2012), and sweep (Fig. 2.17B; DeRuig and Hubbard, 2006; Hubbard et al., 2009) can result in an organised stacking pattern.

In cross-section, the stacking of channel-fills in channel complexes can range from essentially horizontal to essentially vertical (Clark and Pickering, 1996). A common cross-sectional stacking trend in sinuous deep-water channels, whereby an initial phase of horizontal stacking caused by lateral migration is followed by a vertical stacking phase caused by aggradation (Peakall et al., 2000a, b; Jobe et al., 2016). Peakall et al. (2000a, b) suggest that after an initial cutting phase, sinuosity development leads to increased flow stripping which, through levee growth, restricts further lateral migration. A concomitant loss of suspended sediment was inferred to force the flow into

disequilibrium, encouraging deposition and thalweg aggradation (Fig. 2.18). The cross-sectional expression of a sinuous channel complex fill will depend on the position of the section relative to a bend apex, as the degree of lateral stacking generally increases towards the bend apex (Peakall et al., 2000a, b; Fig. 2.18), which may also migrate downstream through time to cause complex stacking patterns (DeRuig and Hubbard, 2006; Hubbard et al., 2009). Furthermore, repeated periods of incision causing amalgamation and the overprinting of previous phases of channel development can occur (Deptuck et al., 2003, 2007; McHargue et al., 2011; Fig. 2.18B).

Mayall and Stewart (2000), Mayall et al. (2006) and Cronin et al (2007) show, contrary to the trends described above, that in some highly entrenched channel systems sinuosity develops in the late stages of channel fill, generally initiating when the flows become levee confined (Fig. 2.19). These models also show the importance of mass transport and debris flow deposition, particularly within early stages channel fill, which are seen to make up a large portion of the fill in some channelised basins (e.g. the South Pyrenees; Pickering and Corregidor, 2005; Bayliss and Pickering, 2015).

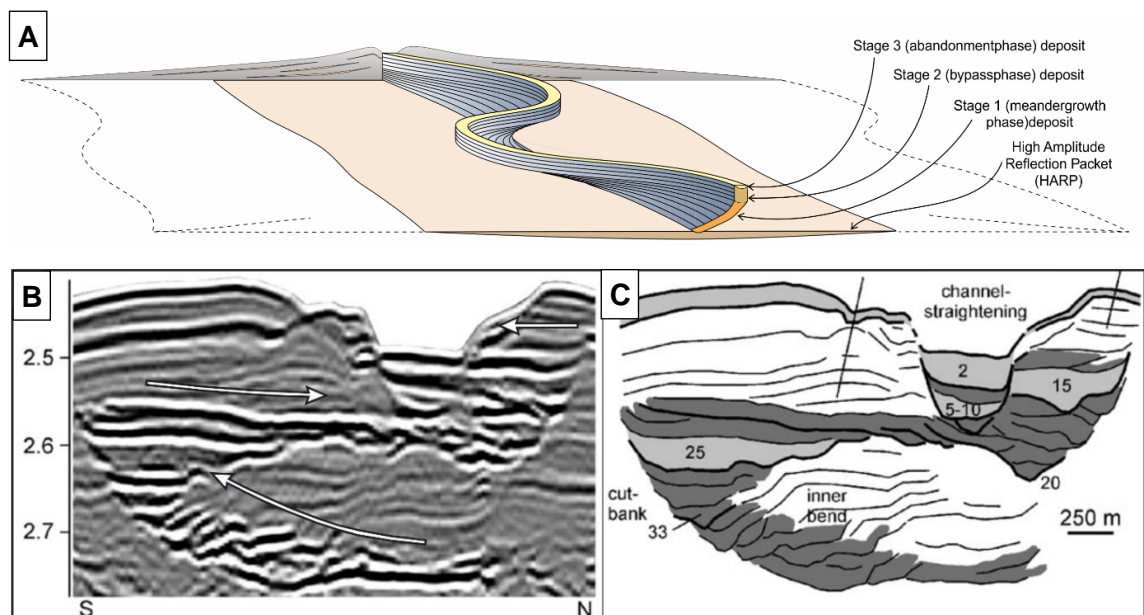


Figure 2.18 – (A) Block model showing the three-dimensional architecture of a sinuous channel formed by swing, with channel aggradation being facilitated by overspill (Peakall et al., 2000b); (B) seismic image and (C) interpretation of a cross-section through a sinuous submarine channel in the Benin Major Canyon, western Niger Delta Slope (after Deptuck et al., 2007); Arrows have been added to show the switches in channel migration direction. This channel has experienced multiple stages of cut, widening and aggradation.

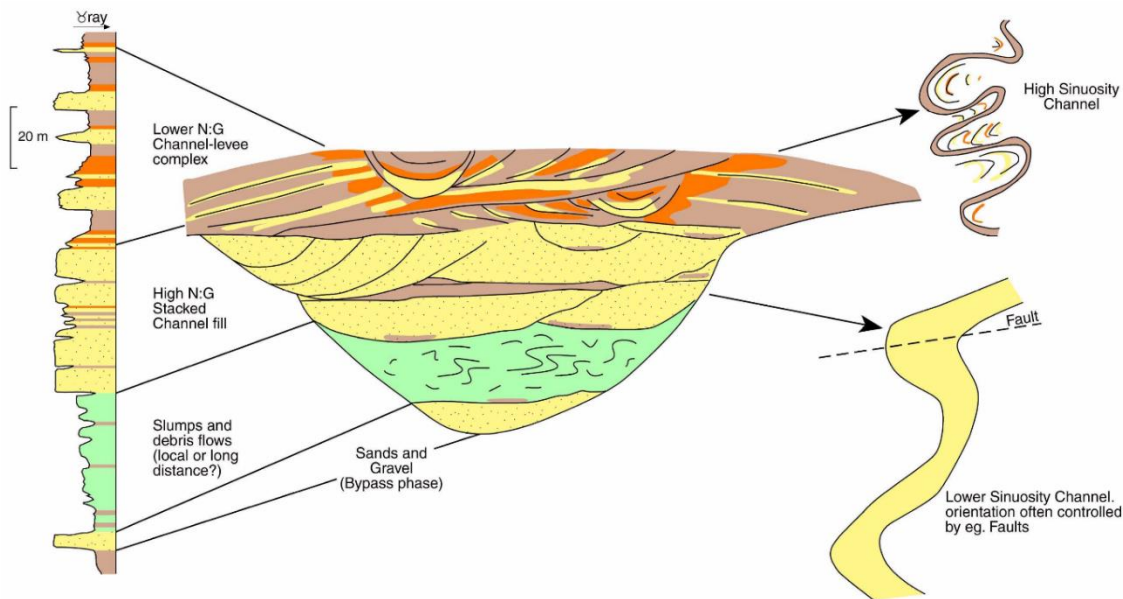


Figure 2.19 – Idealised sequence for the fill of a submarine slope valley (from Mayall and Stewart, 2000) showing (from base to top): lag deposits at the base as remnants of the cutting and bypass of the channel; slump or debris flow plugging of the channel; coarse grained sandy channel facies typically with lower sinuosity; a high sinuosity channel belt bound by levees and containing more fine-grained material.

2.3.9 Avulsion

Lateral jumps in channel-fill and channel complexes are caused by avulsions, whereby a channel or channel belts is abandoned and a new one is formed channel outside of the original belt, and outside of its bounding levees (see Pirmez and Flood, 1995 for definition and distinction from ‘bifurcation’). Deep-water avulsion facilitates compensational stacking at lobe element and channel story scale and above, hence aiding lateral sediment transfer (Picot et al., 2016; Dennielou et al., 2017). Repeated avulsions and the effects of compensational stacking (see Section 2.2.5) ultimately produces a fan-like plan-view distribution of channels and channel complexes radiating from a common feeder canyon, which typifies the world’s large deep-water fans such as the Amazon (Flood et al., 1991, 1995; Jegou et al., 2008). Based on the 3D distribution and relative ages of channels on the Congo fan, Marsset et al. (2009) and Picot et al. (2016) recognised multiple hierarchical scales of avulsion and compensational stacking; the largest being the presence of three separate ‘fans’, each being divided by smaller hierarchical levels that are formed by smaller downstream avulsion events.

Backfilling a channel through either sea level rise (Gardner et al., 2003; Fig. 2.14) or autogenic backfilling related to a break in slope (Prélat et al., 2010) will eventually lead to flow diversion along one edge of the obstructing sedimentary body (Fig. 2.11A). If the elevation of a channel thalweg is higher than the base of its levees, a breach in its confinement may lead to an avulsion. Levee failure due to structural weakness in external levees (*sensu* Kane and Hodgson, 2011), particularly in tectonically active regions, lead to a quasi-instantaneous avulsion (Ortiz-Karpf et al., 2015). Alternatively, levee breaching due to oversized flow is thought to be a more likely trigger in tectonically quiescent settings (Kolla, 2007). Results from 2D numerical modelling of aggradational channels suggests that, due to a natural decrease in flow confinement through time, levee breaching by an oversized flow will eventually become inevitable (Dorrell et al., 2015).

Not all levee breaches lead to a successful avulsion; depositional healing of the breach can occur, often leaving submarine crevasse splays (Posamentier and Kolla, 2003) or crevasse channels (Posamentier, 2003) as their remnant expression. Providing the breach is sufficiently deep (Posamentier and Kolla, 2003), the flow passing through the breach location will be initially unconfined, forming high amplitude reflection packages (HARPs; Flood et al., 1991) commonly seen underlying aggradational channels and thought to be formed from sheet-like turbidites (Kenyon et al., 1995; Fig. 2.11B). Once initiated, the post-avulsion (secondary) channel will incise into these deposits and ultimately a new terminal deposit will prograde (Armitage et al., 2012). The secondary channel will then connect the new terminal deposit to the point of departure from the primary channel; the avulsion node (Fig. 2.11B).

Channel sinuosity may have a profound influence on deep-water avulsion (Kolla, 2007). The presence of linearly aligned cyclic steps originating at the outside of sharp meander bends in the Monterey East Channel (Fildani et al., 2006, 2013; Covault et al., 2014) and Eel Canyon, offshore California (Lamb et al., 2008) suggest that progressive erosion by overspilling flows may eventually cause an avulsion.

2.3.10 MTDs and deep-water channels

At the largest scale, MTDs can control the plan-form and cross-sectional distribution and architecture of channel-levee complexes (e.g. the Amazon Fan; see Piper et al., 1997; Jegou et al., 2008), and can aid the formation of large submarine canyons (Nelson et al., 2011). More locally, the collapse of canyon walls is a vital process for the evolution and maintenance of, and the delivery of sediment to, the canyon (Sawyer et al., 2007). MTDs formed from the collapse of heterogenous levee deposits have also been shown to control the location of avulsion points on active continental margins (Ortiz-Karpf et al., 2015).

At a given point in a deep-water channel, MTDs can be sourced ‘longitudinally’, meaning they have travelled down the channel prior to emplacement, or ‘laterally’ where MTDs have been locally emplaced from a lateral source (Kremer et al., 2018; Fig. 2.20). Potential source locations for MTDs include: the walls of the system’s feeder canyons (Nelson et al., 2011), the continental shelf or slope (Ortiz-Karpf et al., 2017), lateral slopes that dip toward the channel formed by channel-parallel structures (Arbues et al., 2007a, b), or collapse of the channel-walls adjacent to MTD emplacement (Hansen et al., 2015; Fig. 2.20).

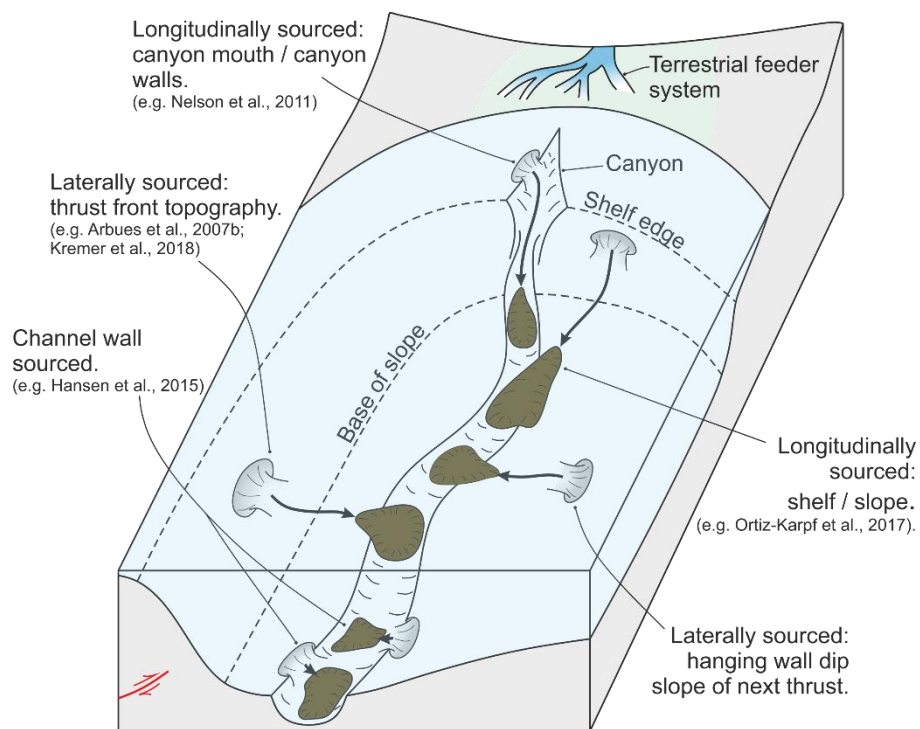


Figure 2.20 – Schematic diagram showing the potential sources of MTDs in a channel system in a structurally confined basin

2.3.11 Deep-water channels and seafloor topography

This theme is reviewed and discussed extensively in Chapter 3, and the fundamental concepts underpinning them are reviewed in Section 2.1.5. However, the concepts not explicitly covered in those sections are briefly covered here. The course of an established channel can be affected by normal faulting (e.g. Kane et al., 2010c; Georgiopoulou and Cartwright, 2013; Cullen et al., 2019), thrusting (e.g. Clark and Cartwright, 2011; Bayliss and Pickering, 2015; Jolly et al., 2016), or halokinesis (e.g. Gee and Gawthorpe, 2006; Mayall et al., 2010). Evolution of seafloor topography may affect the depth to which a channel can incise the substrate (Georgiopoulou and Cartwright, 2013), the geometry and type of deposits within a channel (Kane et al., 2010c) or of its

levees (Clark and Cartwright, 2011), and the stacking of a channel fills (Mayall et al., 2010; Clark and Cartwright, 2011).

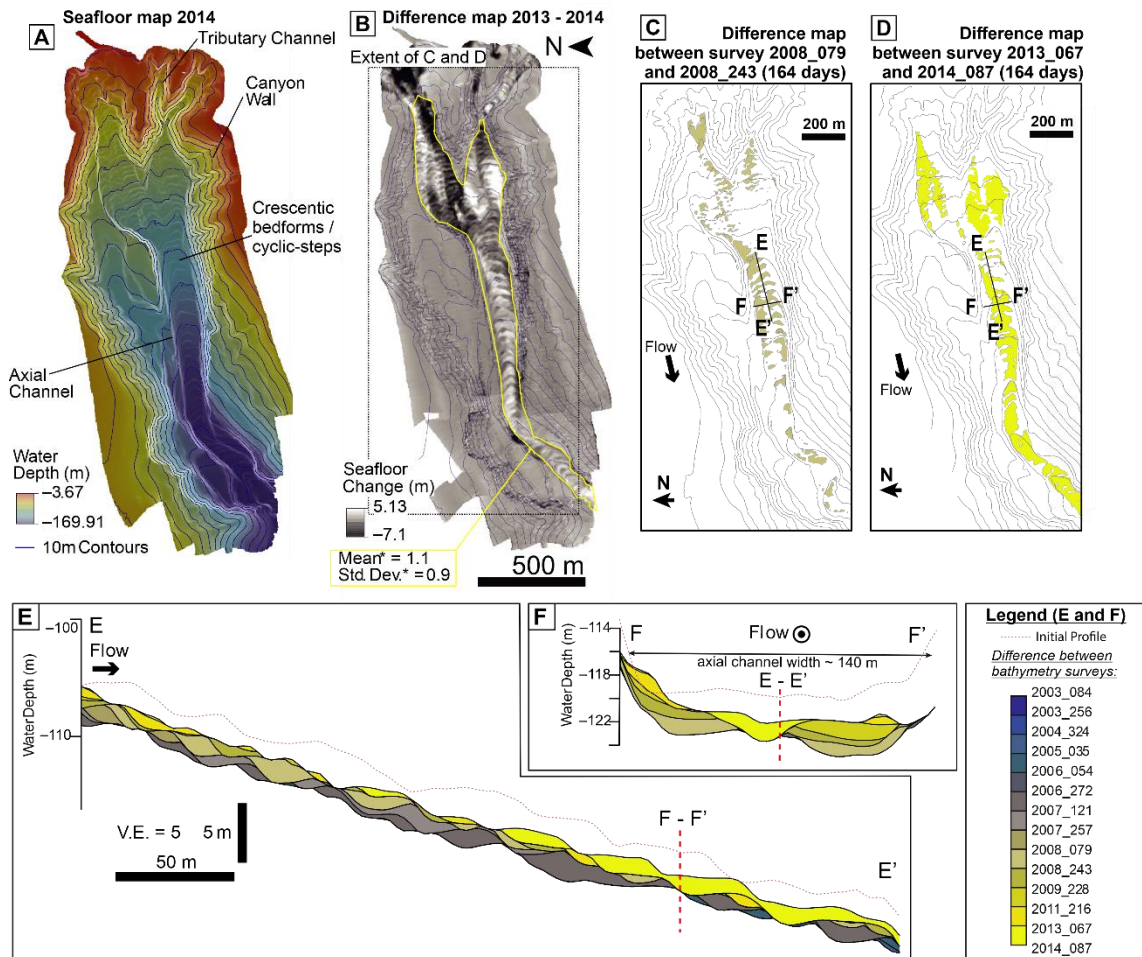


Figure 2.21 – Figure showing the plan-view expression of cyclic-steps in the Monterey Canyon, how they migrate and generate stratigraphy and surfaces (modified after Englert et al., 2021): (A) seafloor map of the Monterey Canyon and its axial channel, displaying the distribution and spacing of the cyclic-steps.; difference map of area in A, between bathymetry data collected in 2013 and 2014, showing areas of erosion and deposition; (C) and (D) seafloor change between two surveys in 2008 (C), and surveys in 2013 and 2014 (D), showing the distribution of deposits shown in E and F; (E) longitudinal profile and (F) cross-section (both located in C and D) showing areas of erosion and deposition between different bathymetry surveys, with the deposits and surfaces generated by migrating cyclic-steps coloured according to their survey interval.

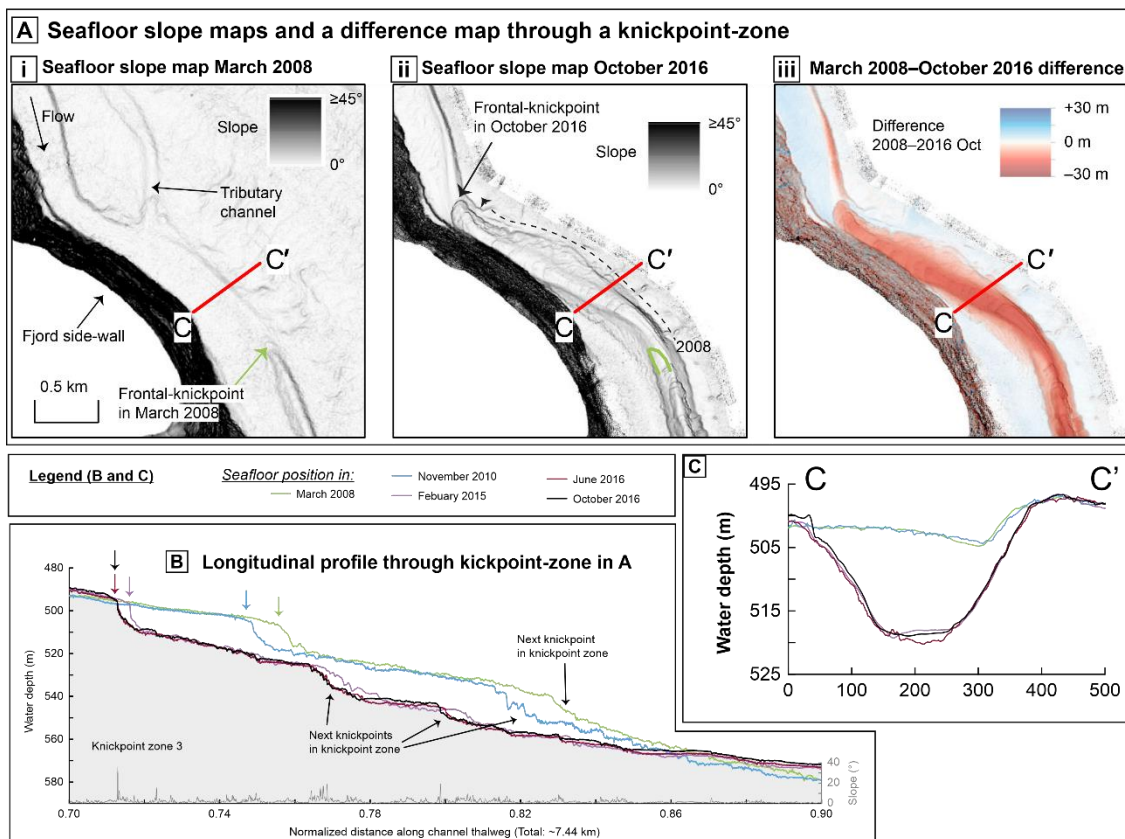


Figure 2.22 – Figure showing the plan-view expression of knickpoints in Bute Inlet, Canada, how they migrate and generate stratigraphy and surfaes (modified after Heijnen et al., 2020): (A) slope maps generated from bathymetry collected in 2008 (i), and 2016 (ii), and a difference map between them showing how upstream knickpoint / knickpoint-zone migration causes local erosion and deposition; (B) longitudinal profile and (C) cross-section showing areas of erosion and deposition between different bathymetry surveys, with the seafloor position at the time of each survey highlighted by a different colour.

2.3.12 Bedforms in deep-water channels

A recent increase in efforts to directly monitor naturally occurring turbidity currents (see Clare et al., 2020 and references therein) has resulted in a concomitant increase in the application of ‘repeat bathymetric mapping’ (*sensu* Hill, 2012) to investigate their effect on the seafloor. Two bedform types are commonly identified in bathymetry data imaging modern deep-water channels:

- ‘Cyclic-steps’ (Cartigny et al., 2014; Slotman and Cartigny, 2020) or ‘crescentic bedforms’ (Hage et al., 2018; Vendettuoli et al., 2019), which are small-scale (up to a few metres relief) bedforms that are typically crescent-shaped (widening downstream) in plan-view; in long-section they are characterised by a short, steep

upstream side that slopes down-channel, and a longer downstream side that slopes more gently upstream (Fig. 2.21).

- 'Knickpoints' (Hill, 2012; Corella et al., 2016; Gales et al., 2018; Heijnen et al., 2020; Guiastrannec-Faugas et al., 2020, 2021), which are larger (metres to tens of metres relief) features that are typically crescentic or v-shaped in plan-view; in long-section they possess an upstream side that slopes steeply downstream and a downstream side that slopes gently downstream (Fig. 2.22).

Comparing bathymetric data imaging the same area obtained years to decades apart have revealed how the upstream migration of such bedforms can shape the seafloor over annual to decadal timescales (Hill, 2012; Vendettuoli et al., 2019; Heijnen et al., 2020). In cross-section, the migration of cyclic-steps can generate filled, concave-up surfaces that incise < 3 m into underlying stratigraphy (Englert et al., 2021). In longitudinal section, they generate beds that dip upstream and are truncated in complex patterns (Hage et al., 2018; Englert et al., 2021).

The interaction between different scales of seafloor features, as has been documented in Bute Inlet, Canada, where knickpoints and cyclic-steps interact (Chen et al., 2021), and in Capbreton Canyon, where knickpoints interact with 'plunge pools' that form downstream of them (Guiastrannec-Faugas et al., 2021). These concepts will be discussed and reviewed in more detail in Chapter 4.

3 Syn-depositional tectonics and mass-transport deposits control channelised, bathymetrically complex deep-water systems (Aínsa depocenter, Spain)

3.1 Summary

The inception and evolution of channels in deep-water systems is controlled by the axial gradient and lateral confinement experienced by their formative flows. These parameters are often shaped by the action of tectonic structures and/or the emplacement of mass-transport deposits (MTDs). The Arro turbidite system (Aínsa depocenter, Spanish Pyrenees) is an ancient example of a deep-water channelised system from a bathymetrically complex basin, deposited in an active tectonic setting. Sedimentological fieldwork and geological mapping of the Arro system has been undertaken to provide context for a detailed study of three of the best-exposed outcrops: Sierra de Soto Gully, Barranco de la Caxigosa, and Muro de Bellos. These locations exemplify the role of confinement in controlling the facies and architecture in the system. Sedimentological characterisation of the deposits has allowed the identification of fourteen facies and eight facies associations; these form a continuum and are non-unique to any depositional environment. However, architectural characterisation allowed the grouping of facies associations into four depositional elements: (i) weakly confined, increasing-to-decreasing energy deposits; (ii) progradational, weakly confined to overbank deposits; (iii) alternations of MTDs and turbidites; (iv) channel fills. Different styles of channel architecture are observed. In Barranco de la Caxigosa, a master surface which was cut and subsequently filled hosts three channel stories with erosional bases; channelisation was enhanced by quasi-instantaneous imposition of lateral confinement by the emplacement of MTDs. In Muro de Bellos, the inception of partially levee-confined channel stories was enhanced by progressive narrowing of the depositional fairway by tectonic structures, which also controlled their migration. Results of this study suggest that deep-water channelisation in active tectonic settings may be enhanced or hindered due to: (1) flow interaction with MTD-margin topography or; (2) MTD-top topography; (3) differential compaction of MTDs and/or sediment being loaded into MTDs; (4) formation of megascours by erosive MTDs; (5) basin-floor topography being reset by MTDs. Therefore, the Arro system can be used as an analogue for ancient subsurface or outcropping channelised deposits in bathymetrically complex basins, or as an ancient record of deposits left by flow types observed in modern confined systems.

3.2 Introduction

Deep-water depositional elements are the product of flows that erode, bypass, and deposit along the constituent parts of a deep-water sedimentary system (Kneller, 2003; Stevenson et al., 2013). The architecture (geometry, distribution, and size) of these elements can be captured in seismic data (e.g. Mayall and Stewart, 2000; Posamentier, 2003; Posamentier and Kolla, 2003; Prather, 2003; Schwenk et al., 2005; Mayall et al., 2006; Wynn et al., 2007; Deptuck et al., 2003, 2007, 2008; Marsset et al., 2009); however, a flow-scale understanding of their constructional mechanisms is essential to inform generic models of their evolution (Peakall and Sumner, 2015). Despite recent advancements in experimental (De Leeuw et al., 2016) and numerical (Dorrell et al., 2018) modelling, direct flow monitoring (Xu et al., 2013; Clare et al., 2016; Hughes Clarke, 2016; Azpiroz-Zabala et al., 2017; Paull et al., 2018; Maier et al., 2019), flow reconstruction (Talling et al., 2007; Stevenson et al., 2013, 2018; Mountjoy et al., 2018), and repeat bathymetry surveying (Hizzett et al., 2018; Vendettuoli et al., 2019), process-informed outcrop studies still provide the most detailed account of system evolution over geological timescales.

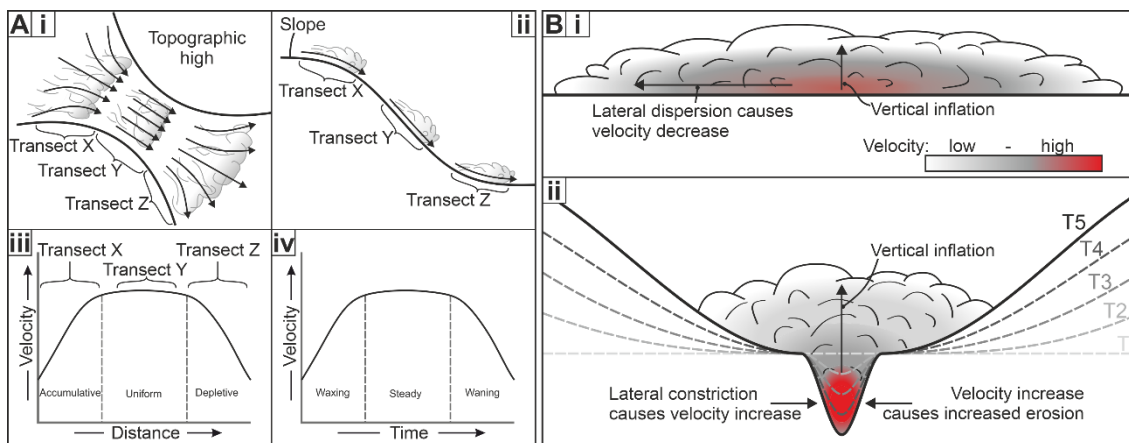


Figure 3.1 – Schematic diagrams showing the effect of axial gradient and lateral confinement on flow velocity. A) Lateral constriction and release of a flow, or (ii) increasing and decreasing the axial flow gradient can (iii) increase or decrease flow velocity over a longitudinal transect of a flow, or (iv) temporally at the base of a passing flow (modified from Kneller, 1995). B) Velocity response of an unconfined flow (i) as it undergoes progressive lateral confinement (ii).

A central parameter of the erosion-deposition threshold of suspended sediment in turbidity currents is velocity (Kuenen and Sengupta, 1970; Kneller, 2003; Stevenson et al., 2015; Dorrell et al., 2013b, 2018). Substrate morphology is among the most significant factors which control flow velocity. Kneller (1995) provided a summary

overview of topographic effects on flow velocity (Fig. 3.1A), whereby a flow may change its velocity along a downstream transect due to a change in its down-flow gradient or lateral flow constriction (Fig. 3.1). However, the complexity of turbidity current “run-up” (Kneller and McCaffrey, 1999) and interaction with asymmetrical (Bell et al., 2018a) and oblique (McCaffrey and Kneller, 2001) obstacles must be acknowledged.

Frontal confinement is defined as a reversal in the dip direction of the down-flow gradient along a longitudinal transect of a basin or flow pathway (Fig. 3.1A). Flow-scale frontal confinement can cause sufficient velocity reduction to initiate deposition and promote channel backfilling (Pickering et al., 2001). Where deceleration is rapid, it may generate hydraulic jumps (commonly at the ends of channels; Mutti and Normark, 1987, 1991; Hofstra et al., 2018) or cause the formation of hybrid event beds (Haughton et al., 2009). At larger (architectural) scales, down-flow gradient is considered a primary variable in studies of slope grading (Prather et al., 1998, 2017) and submarine channel equilibrium profiles (Kneller, 2003; McHargue et al., 2011; Georgiopoulou and Cartwright, 2013). Lateral confinement occurs due to the presence of two elongate surfaces situated at both lateral edges of a basin or flow pathway, each orientated quasi-parallel to input flow or regional palaeocurrent (Fig. 3.1B). The architectural effect of lateral confinement is manifested at multiple scales. A flow may be partially or fully confined by prominent basin-floor topography, or by a channel-wall composed of incised substrate or overspill deposits. These overspill deposits (commonly referred to as terraces or internal levees; Hansen et al., 2015) may themselves be confined within larger external levees (Kane and Hodgson, 2011), a canyon wall (Kane et al., 2009a), or by confining structures (Casciano et al., 2019). At flow scale, substrate erosion (Eggenhuisen et al., 2011), construction of depositional topography (e.g., levees) from preceding flows (De Leeuw et al., 2016), or both (Hodgson et al., 2016), can progressively generate lateral confinement, increasing the velocity, and hence bypass potential of subsequent flows (Fig. 3.1B). Continued flow input may trigger a positive feedback mechanism (a “channelisation feedback” sensu Eggenhuisen et al., 2011; De Leeuw et al., 2016), whereby elevated flow velocities lead to increased basal erosion and lateral overspill, hence imposing greater lateral confinement leading to channelisation. The onset of this feedback mechanism occurs as a “channelisation threshold” is crossed (sensu Eggenhuisen et al., 2011; De Leeuw et al., 2016). Understanding what controls this threshold, when it is crossed, and whether imposition of externally derived lateral confinement may influence this, is crucial to understanding deep-water channel inception.

The processes of deep-water channel initiation and infill have a varied architectural expression (Clark and Pickering, 1996; Deptuck et al., 2003; Macauley and

Hubbard, 2013), and a large range of potential autogenic and allogenic controlling factors (Pickering and Corregidor, 2005; Clark and Cartwright, 2011; Flint et al., 2011; Jobe et al., 2015; Gong et al., 2016). In structurally active settings, the influence of protruding structures and mass-transport deposits (hereinafter MTDs) is particularly prevalent.

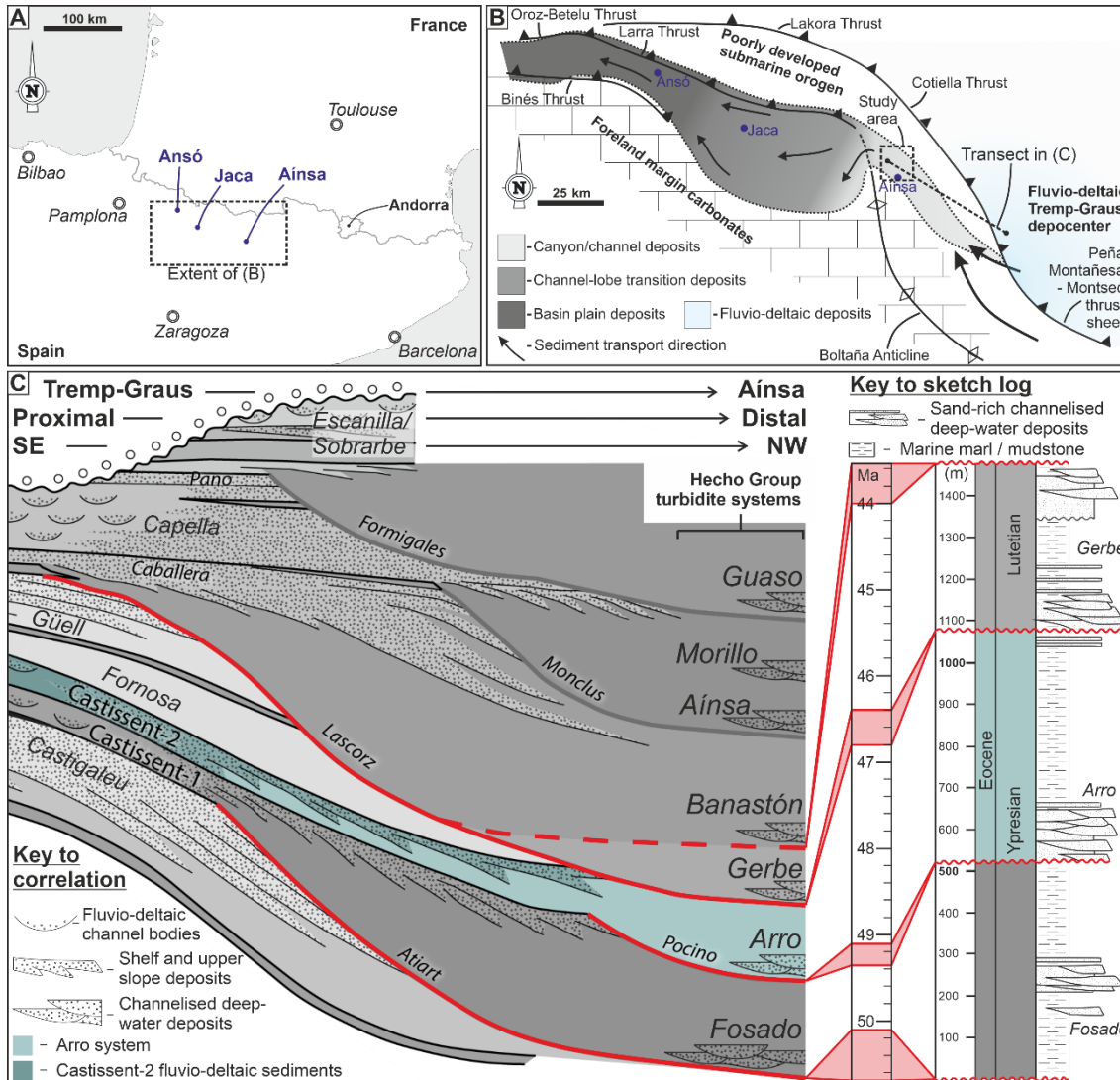


Figure 3.2 – A) Map showing broad location of the South Pyrenean Foreland Basin in northern Spain. B) Schematic map showing the sediment routing system from Tremp-Graus (east) to Jaca depocenter (west) in the Eocene, modified from Remacha and Fernández (2003) and Caja et al (2010). C) Depositional dip section showing the correlation of fluvio-deltaic units in the distal part of the Tremp-Graus depocenter to their contemporaneous deep-water units in the Ainsa depocenter, with inset showing the chronostratigraphy of the Fosado, Arro and Gerbe systems (modified from Clark et al., 2017).

Channels can be blocked or diverted by a growing structure, or incise through it, depending on: (i) rate of relative sedimentation to structural growth, (ii) timing of

structuration, and (iii) geometry and interaction of different structures (Gee and Gawthorpe, 2006; Mayall et al., 2010; Clark and Cartwright, 2011; Jolly et al., 2016). The growth of syn-sedimentary fault-derived folds may also result in palaeoflow directions to be oriented parallel to the structures; in such cases, progressive lateral confinement may be generated by the development of these structures (Clark and Cartwright, 2011).

Herein, MTD is used as a term to describe any of the products of en masse transport and deposition (Nelson et al., 2011; Kneller et al., 2016). The term encompasses a continuum of deposits, distinguished by the degree of internal deformation or disaggregation (Moscardelli and Wood, 2008; Bull et al., 2009; Ogata et al., 2012), and named in accordance with their deformational processes: slides (least internal deformation), slumps, and debris flows (most internal deformation). In tectonically active basins, longitudinally emplaced MTDs (see Kremer et al., 2018 for definition) may be sourced from the headwall or sidewalls of a feeding canyon (Nelson et al., 2011) or from a proximal shelf or slope failure (Ortiz-Karpf et al., 2017); transversely emplaced MTDs may be sourced from the local collapse of channel-walls (Hansen et al., 2015) or from a laterally confining slope (Arbués et al., 2007a). MTDs can have a profound influence on the evolution and architecture of submarine channels through: (i) quasi-instantaneous imposition of lateral confinement by MTD-top or -margin topography (Schultz et al., 2005; Hansen et al., 2013; Kneller et al., 2016; Masalimova et al., 2016; Kremer et al., 2018; Ward et al., 2018) and/or the development of evacuation scars (Dakin et al., 2013; Hodgson et al., 2016; Qin et al., 2017) leading to channelisation; (ii) the perturbation of flows leading to backfilling (Posamentier and Kolla, 2003; Nelson et al., 2009; Bernhardt et al., 2012; Corella et al., 2016); (iii) thalweg plugging, facilitating lateral channel migration (Kremer et al., 2018), diversion (Nelson et al., 2011; Kneller et al., 2016), or avulsion (Ortiz-Karpf et al., 2015); (iv) affecting channel sinuosity (Deptuck et al., 2007).

To help bridge the resolution gap between event-bed and seismic scale, outcrops from ancient structurally complex basins are commonly used as analogues (e.g., McCaffrey et al., 2002; Brunt et al., 2007; Leren et al., 2007; Janbu et al., 2007; Hubbard et al., 2008; Bernhardt et al., 2011, 2012; Casciano et al., 2019; McArthur and McCaffrey, 2019). One such “natural laboratory” is the Eocene Hecho Group, in the Aínsa depocenter (South Pyrenean Foreland Basin, Spain), where the effect of structures and mass-transport deposits on deep-water channels has been well documented (Pickering and Corregidor, 2005; Arbués et al., 2007a, 2007b; Pickering and Bayliss, 2009; Dakin et al., 2013; Bayliss and Pickering, 2015). This study provides a sedimentological and architectural characterisation of the Arro turbidite system, in the Hecho Group (see Scotchman et al., 2015 for definitions; Fig. 3.2), describing, for the first time, its distal

expression in the Aínsa depocenter. The study is used to investigate the extent to which mass-transport- and thrust-related structures influence the establishment, evolution, and infill of axial submarine channels, and the scales at which this control is exerted. A particular line of enquiry is whether the channelisation process may be enhanced or hindered by the imposition of frontal or lateral confinement during the emplacement or growth of these features. Investigating the sedimentological and architectural response to evolving basin-floor topography in channelised deep-water systems is important for elucidating how channels are initiated and what controls their presence and distribution. The findings herein may therefore be used to inform studies in other ancient and modern confined basins.

3.3 Geological Setting

The Lower Eocene stratigraphy of the Aínsa depocenter is part of the fill of the South Pyrenean Foreland Basin, formed on the southern margin of the doubly verging Pyrenean Orogen (Fig. 3.2; Séguret, 1972; Cámara and Klimowitz, 1985; Puigdefàbregas and Souquet, 1986; Muñoz, 1992; Bentham and Burbank, 1996; Barnolas and Gil-Peña, 2001; Fernández et al., 2004; Arbués et al., 2011). The South Pyrenean Foreland Basin comprises three parts: the terrestrial-to-shallow-marine “Trempe-Graus depocenter”; the channelised deep-water “Aínsa depocenter”; the unconfined, deep-water “Jaca depocenter”. The Aínsa depocenter is located in an oblique transfer zone between the Montsec-Peña Montañesa and Cotiella thrust units (Fernández et al., 2004, 2012; Muñoz et al., 2013). This “relay” forms a wider zone of smaller-wavelength thrust-related SE-NW structures propagating through Cretaceous-Neogene carbonate and clastic sedimentary rocks from a Triassic decollement (Séguret, 1972; Cámara and Klimowitz, 1985; Choukroune, 1992; Muñoz, 1992; Clark et al., 2017).

During the Ypresian, channelised deep-water deposits in the Aínsa depocenter were connected to unconfined deposits in the downstream Jaca depocenter (Fig. 3.2), hence their collective name: the Hecho Group (Mutti, 1984). Here, the scheme presented by Clark et al. (2017) is followed, wherein the Hecho Group is divided into seven turbidite systems (Fig. 3.2C). However, inconsistency in the naming and dating of deposits in the fill of the deep-water Aínsa depocenter is rife (cf. Mutti, 1985; Fernández et al., 2004; Pickering and Corregidor, 2005; Arbués et al., 2007a; Das Gupta and Pickering, 2008; Heard and Pickering, 2008; Pickering and Bayliss, 2009; Muñoz et al., 2013; Heard et al., 2014; Pickering and Cantalejo, 2015; Scotchman et al., 2015; Cornard and Pickering, 2019; Cantalejo et al., 2020a, b; Honegger et al., 2020).

Sediment in the turbidite systems of the Hecho Group was derived predominantly from the fluvio-deltaic environments in the Trempe-Graus depocenter to the east, entering the Aínsa depocenter through a series of submarine canyon systems to the southeast

(Fig. 3.2B). Shelfal deposits of the Castigaleu Group are incised by the Atiart surface, a large submarine unconformity, which is filled by deep-water sediments of the Castissent Group (time equivalent to the Fosado and Arro systems) (Soler-Sampere and Garrido-Megías, 1970; Puigdefàbregas and Souquet, 1986; Mutti et al., 1988; Muñoz et al., 1994; Scotchmann et al., 2015; Chanvry et al., 2018). The Arro system, which was active during the Ypresian (Fig. 3.2C), was fed through the Pocino surface, a subtle canyon first recognised by Mutti et al. (1988, see also Sgavetti, 1991; Millington and Clark 1995a, 1995b) which was in turn incised by the Lascorz surface (the feeder of the overlying

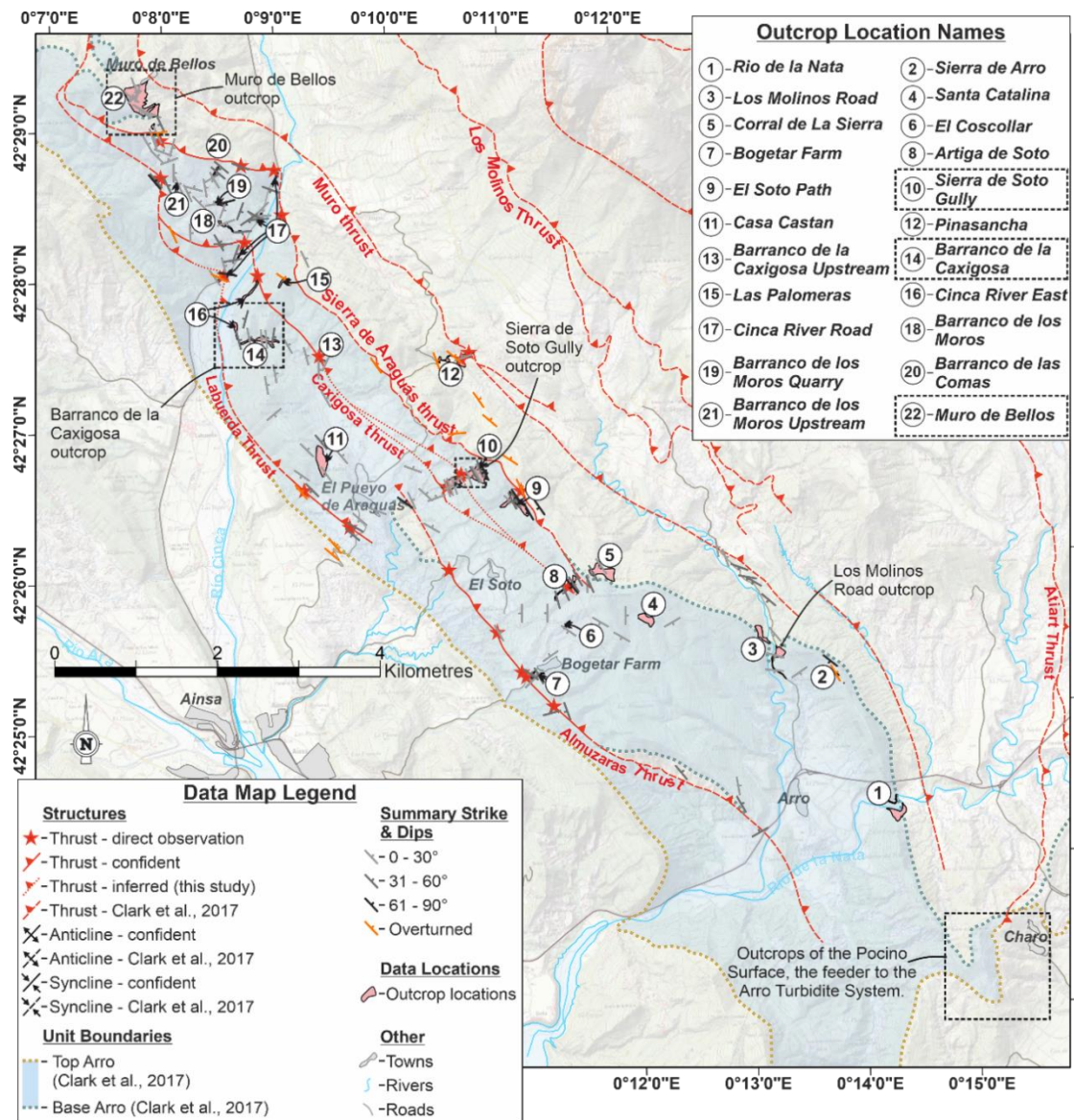


Figure 3.3 – Map of the Arro turbidite system modified from Clark et al. (2017) with data from this study, showing locations and names of major tectonic structures, the top and base of the Arro turbidite system, some summary structural data, and the twenty-two locations used to inform this study with Sierra de Soto Gully, Barranco de la Caxigosa, and Muro de Bellos highlighted. Grid is in degrees, minutes, and seconds, georeferenced in European Datum 1950 UTM zone 30N. Basemap at 1:25,000 scale courtesy of Instituto Geográfico Nacional.

Gerbe system) (Muñoz et al., 1994; Payros et al., 2009; Poyatos-Moré, 2014; Castelltort et al., 2017).

To date, detailed sedimentological and stratigraphic analysis has been conducted only on the most proximal Arro outcrops, i.e., those of Charo (exposing part of the Arro's feeder canyon fill), Rio de la Nata, Los Molinos Road, and Santa Catalina (Millington and Clark, 1995a, 1995b; Arbués et al., 2007a, 2007b) (Fig. 3.3). The Los Molinos Road has commonly been used as the "type locality" for the Arro system (Das Gupta and Pickering, 2008; Caja et al., 2010). Van Lunsen (1970), Castelltort et al. (2017), and Honegger et al. (2020) present data from more distal outcrops, but the sedimentology and stratigraphy remain undescribed. This study is focused on the sedimentological characterisation of the more distal parts of the Arro system in the Aínsa depocenter (Fig. 3.3).

3.4 Data and Methods

The field area, located N-NE of the town of Aínsa, covers approximately 40 km² (Fig. 3.3) along an ~ 13-km-long transect oriented SE-NW (parallel to regional palaeocurrent). A revised version of a geological map by Clark et al. (2017) is used; structural amendments are informed by 448 strike and dip measurements of bedding (Fig. 3.4C) and the tracing of some of the larger, depocenter-scale structures (Fig. 3.3). Detailed sedimentological analysis of twenty-two outcrops was undertaken using traditional field methods, augmented by study of aerial photographs acquired using an unmanned aerial vehicle. A total of 230 palaeocurrent measurements were taken from flute casts, and ripple and cross-bed foresets (Fig. 3.4). Fifty-six logs totalling 1,088 m of stratigraphy were measured with centimetre resolution and drawn at 1:10 to 1:50 scale to capture vertical facies and grain-size variations at multiple scales; a high-precision Jacob's staff (Patacci, 2016) was used. As the Charo area and the most proximal outcrops (1, 3, and 4 in Fig. 3.3) have been studied in detail previously (Millington and Clark, 1995a, 1995b; Arbués et al., 2007a, 2007b), this study is focused primarily on three outcrops in the more distal part of the Arro system in the Aínsa depocenter: Sierra de Soto Gully, Barranco de la Caxigosa, and Muro de Bellos (Fig. 3.3; outcrops 10, 14, and 22 respectively). At these locations, multiple laterally offset logs, field sketches, and interpreted photomosaics (from ground and aerial photographs) have been used to generate architectural panels.

3.4.1 Large-Scale Trends

The trend of palaeocurrents for the Arro system is dominantly to the NW (Fig. 3.4), which is consistent with the findings of Millington and Clark (1995a, 1995b) and Arbués et al. (2007a, 2007b), who present data from the proximal localities and feeder

system. The regional trend of strike orientation of thrusts and related folding within the area is also NW-SE, which is consistent with the trend of the larger, depocenter-bounding structures, such as the Mediano, Anisclo, and Boltaña anticlines (Millington and Clark, 1995a, 1995b; Arbués et al., 2007a; Muñoz et al., 2013). It is possible that these structures have undergone clockwise rotation along with the regional structures (Muñoz et al., 2013). Regardless, the correspondence of the regional palaeocurrents (from flutes, ripples, and cross beds; Fig. 3.4B) and the structural trend (Fig. 3.4C) allow the Arro system to be classified as an axial deep-water system.

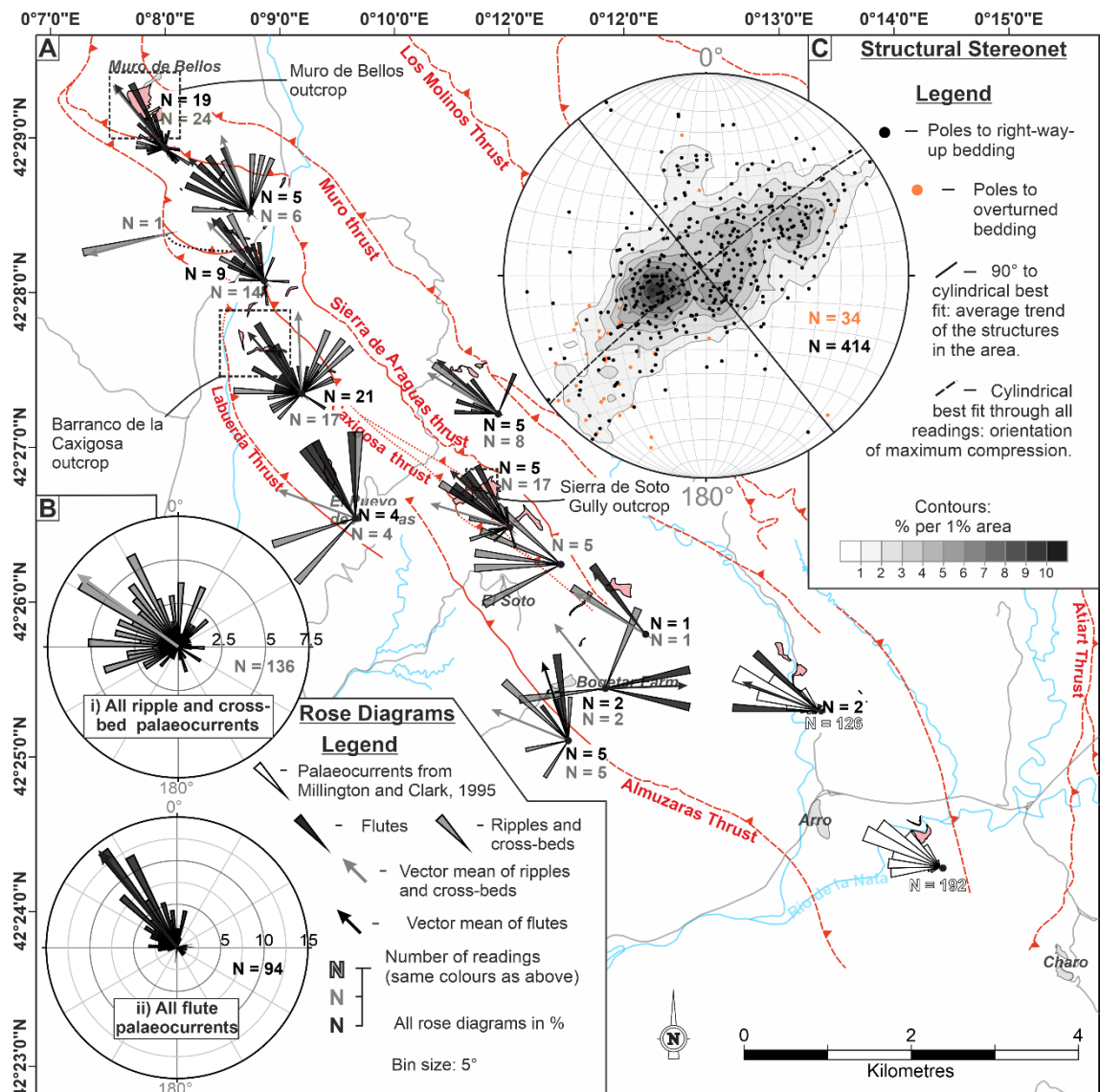


Figure 3.4 – A) Map presenting palaeocurrent data from fourteen of the visited locations illustrating their relationship with the basinal structures. B) Regional palaeocurrent data measured from (i) ripples and cross beds, and (ii) flute casts. C) All strike and dip measurements of bedding, indicating the average structural trend.

Lithofacies	Lithology	Description	Thickness	Process Interpretation	Photo
Lf1 – Structureless mudstone	Carbonate mudstone containing silt.	No obvious grading or structure, weathers with a texture comprising loose spheroids < 10 cm long. Concretionary horizons occur with variable spacing (0.5-10 m).	No clear bedding or laminae	Hemipelagic suspension fallout.	Fig. 3.5A
Lf2 – Graded siltstone	Sometimes graded from very fine-grained sand to mud, typically silt to mud.	Usually structureless, however parallel lamination and starved ripples are sometimes present.	0.1-4 cm	Fine-grained, dilute-gravity-current deposits, equivalent to a coarse T _e division of Bouma (1962) or a T ₆ division of Stow and Shanmugam (1980).	Fig. 3.5B
Lf3 – Lenticular sandstone	Very fine- to medium-grained sandstone, occasionally coarse silt or coarse sandstone.	Lenses of sandstone typically 3-7 cm wide, separated laterally by 0.1-10 cm. Lenses are aligned along bedding-conformable horizons which can usually be traced laterally for over 10 m and often over 20 m.	0.1-1.5 cm	Deposition from a dilute, dominantly bypassing turbidity current.	Fig. 3.5C
Lf4a – Rippled sandstone	Very fine- to coarse-grained sandstone.	Unless they are eroded, rippled bed tops are usually preserved, commonly with internal ripple cross lamination observed, both of which may be disturbed by dewatering effects. Where Lf4a occurs as isolated beds, bases are usually flat but some exhibit basal scouring, making the beds pinch and swell. Ripple heights (crest to trough) typically range from 1.5-5 cm. Ripple lengths (trough to trough) typically range from 7 to 30 cm. In the thinnest intervals the facies nears a lenticular geometry.	1.5-10 cm	Deposition and tractional reworking by dilute, low-density gravity current (Allen, 1973, 1982).	Fig. 3.5D

Lf4b – Hummocky-cross-stratified sandstone	Very fine- to medium-grained sandstone.	Characterised by undulating laminae with wavelengths ranging from 5 to 25 cm and amplitudes ranging from 0.5 to 5 cm, comprising internal lamination truncations and dip changes. Bed tops display 3D bedforms with no dominant inferred paleocurrent direction. Always located at the tops of sandstone beds, sometimes overlying ungraded, cross-stratified (< 7-cm-thick foresets, typically pervasive through an event bed or scour fill), cross-laminated (> 7-cm-thick foresets) or parallel-laminated sandstones.	2-6 cm	Deposition and reworking from reflected or deflected dilute flows, typically in the bypassing part of a bipartite flow (Mutti, 1992; Mulder et al., 2009; Muzzi Magalhaes and Tinterri, 2011; Bell et al., 2018a).	Fig. 3.5E
Lf4c – Planar-cross-stratified sandstone	Fine- to medium-grained sandstone.	Foreset heights range from 7 to 50 cm, commonly infilling concave-convex scoured surfaces, sometimes exhibiting positive depositional relief, and sometimes both. Foreset angles vary significantly from ~ 10° to ~ 40°. Fluted bases and rippled tops are also seen. Cross stratification can be pervasive throughout isolated beds or occur above ungraded structureless sandstones.	7-50 cm	(1) Dunes or mega ripples formed by traction and fallout from a dilute flow (Tinterri, 2011; Peakall et al., 2020); (2) 'pseudo dunes' formed from scour derived instabilities in a unidirectional flow (Arnott and Al-Mufti, 2017; Peakall et al., 2020).	Fig. 3.5F
Lf5 – Parallel-laminated sandstone	Very fine- to coarse-grained sandstone.	Parallel laminae spaced 0.1-1 cm apart which may underlie or overlie any other sandstone-rich facies. Can be disturbed or convoluted in parts due to bioturbation and dewatering.	5-50 cm	Traction carpets from upper-stage plane beds or lower-stage plane beds (Talling et al., 2012).	Fig. 3.5G
Lf6a – Graded, structureless sandstone	Large grain-size range with some beds fining from granules to very fine sand. Typically coarse or medium or medium to fine sand.	Bedded, internally structureless sandstone except for dish structures. Some beds are capped with siltstone, whereas others are bounded by amalgamation surfaces. At amalgamation surfaces and bedding boundaries, load balls and flame structures are seen; flutes, some of which loaded, are common on bed bases, but grooves are rare.	0.1-2.75 m	Bouma (1962) sequence T _a division deposited from a depositional, and potentially erosional, high-density turbidity current (Lowe, 1982), often with subsequent dewatering. Where present, grooves were formed by a debris flow that bypassed this area prior to turbidite deposition (Peakall et al., 2020).	Fig. 3.5H

Lf6b – Ungraded, structureless sandstone	Fine to coarse-grained sandstone.	Lack of grading characterises this facies. Flames, load balls, and flutes are found on many bed bases. Amalgamation surfaces and intense internal deformation relating to dewatering are common.	0.04-1.25 m	Bouma (1962) sequence T _a division deposited from a depositional, and potentially erosional, high-density turbidity current (Lowe, 1982; Peakall et al., 2020).	Fig. 3.5I
Lf6c – Sandstone with mudclasts	Fine to coarse sandstone.	Bedded sandstone similar to Lf6a and Lf6b, but containing up to 40% rounded to subangular mudclasts, sometimes armored with sand and granules. Mudclasts may be concentrated at bed bases, tops, or distributed throughout. Amalgamation surfaces exhibiting scouring geometries are sometimes lined with mudclasts. In some cases mudclasts are concentrated on distinct planar, inclined horizons within beds, potentially highlighting cross strata.	0.2-4 m (upper limit possibly a series of amalgama- ted beds)	Erosional and depositional high-density turbidity current (Lowe, 1982) carrying “rip-up clasts” (Mutti and Nilsen, 1981; Mutti, 1992).	Fig. 3.5J
Lf7a – Extraclast conglomerate	Granule- to cobble- size extraclasts and bioclasts supported by very poorly sorted, polymictic, argillaceous usually coarse-grained sandstone.	Characterised by the presence, and dominance, of rounded to subangular extrabasinal lithic fragments composed of limestone, quartzite, or other mineral aggregates. The silt and clay content of the matrix varies significantly between and within (laterally and vertically) individual beds. Mudclasts, rounded clasts of sandstone and local heterolithics, and bioclasts such as <i>Nummulites</i> and shell fragments (of oysters, other bivalves, and brachiopods) are common yet not in dominant quantities. Extraclasts are almost always matrix supported but may be locally clast supported.	8-70 cm	Deposition from the traction carpet of dominantly bypassing flow(s) (Mayall et al., 2006; Stevenson et al., 2015) due to frictional freezing (Mutti et al., 2000).	Fig. 3.5K
Lf7b – Mudclast conglomerate	Pebble-size mudclasts supported by sandy matrix of varying texture and grain size.	Size (0.5-20 cm long axis), rounding (rounded to subangular), and proportion (typically > 75% of clasts) of mudclasts varies between and within (laterally and vertically) beds; some mudclasts are armored with coarse sand. Extraclasts and bioclasts are often present. The matrix composition ranges	5-30 cm	A high-energy erosional and dominantly bypassing flow containing abundant “rip-up clasts” (Mutti and Nilsen, 1981; Mutti, 1992) deposited as a lag (Mayall	Fig. 3.5L

		from well-sorted medium and coarse sandstone to poorly sorted, clay- and silt-rich sandstone.		et al., 2006; Stevenson et al., 2015); type A1 and B1 of Johanssen and Stow (1995).	
Lf8a – Chaotic mudstone	Chaotic mud-rich deposit supporting rafts of heterolithic stratigraphy, blocks of sandstone, extraclasts, and bioclasts	A clay-rich matrix with variable silt and sand content contain: deformed, disaggregated blocks (up to 5 m long axis) of fine-grained heterolithic sediment which exhibit internal structure similar to stratigraphy found elsewhere in the basin; bioclasts such as <i>Nummulites</i> and shell fragments; 5-20 cm rounded to subrounded blocks of coarse sandstone, sometimes nummulite and shell rich, similar to that seen in the proximal (shelfal) Castissent Formation; 3-40 cm rounded to subrounded clasts of well-sorted fine to coarse sandstone resembling Lf4-6; and granule- to pebble-size extrabasinal lithic fragments (see Lf7a). The presence and relative proportions of these components is highly variable between deposits.	0.2-20 m	<i>En masse</i> deposition from debris flows and highly disaggregated slumps (termed “blocky beds” by Ogata et al., 2012). The formative material was sourced from: local stratigraphy, possibly due to a growing basin-floor structure (Arbués et al., 2007a, 2007b) or channel-bank collapse (Barton et al., 2010); or from the proximal fluvio-deltaic and shelf deposits of the Castissent Formation (Nijman and Puigdefabregas, 1977; Mutti et al., 1996, 2000; Nijman, 1998).	Fig. 3.5M
Lf8b – Deformed heterolithics	Deformed, not disaggregated local heterolithic stratigraphy.	Folded heterolithic packages with wavelengths between 0.1 and 3 m, sometimes overlying a heavily deformed basal surface. The constituent stratigraphy can be easily matched to the adjacent or underlying stratigraphy and is therefore generally devoid of shelf material.	0.5-6 m	Slumped local stratigraphy. A continuum exists between these and Lf8a distinguished by the degree of disaggregation (Posamentier and Martinsen, 2011; Ogata et al., 2012).	Fig. 3.5N
Lf9 – Polymictic, bioclastic sandstone	Ranging from very poorly sorted polymictic coarse- to very coarse-grained (average) sandstone with abundant bioclasts.	This bedded facies can exhibit normal grading and scouring bases, sometimes with flutes and sometimes overlying amalgamation surfaces. <i>Nummulites</i> (0.2-2.5 cm diameter) are the dominant bioclast with fragmented oyster shells (0.2-4 cm long axis) also abundant; gastropods are rarely found. Relative and absolute bioclast proportions vary between beds and (vertically and laterally) within beds, sometimes over < 5 cm. In some cases bioclasts occur in such abundance that this facies can be classed as a carbonate packstone.	0.03-1m	Sandstones and bioclasts introduced by turbidity currents (Peakall et al., 2020), sourced from the Castissent shelf (Marzo et al., 1988; Nijman, 1998).	Fig. 3.5O

Table 3.1 – Descriptions of the fifteen facies and sub-facies recognised in the stratigraphy of the Arro system, including their lithologies, typical thicknesses and interpretations of their depositional processes.

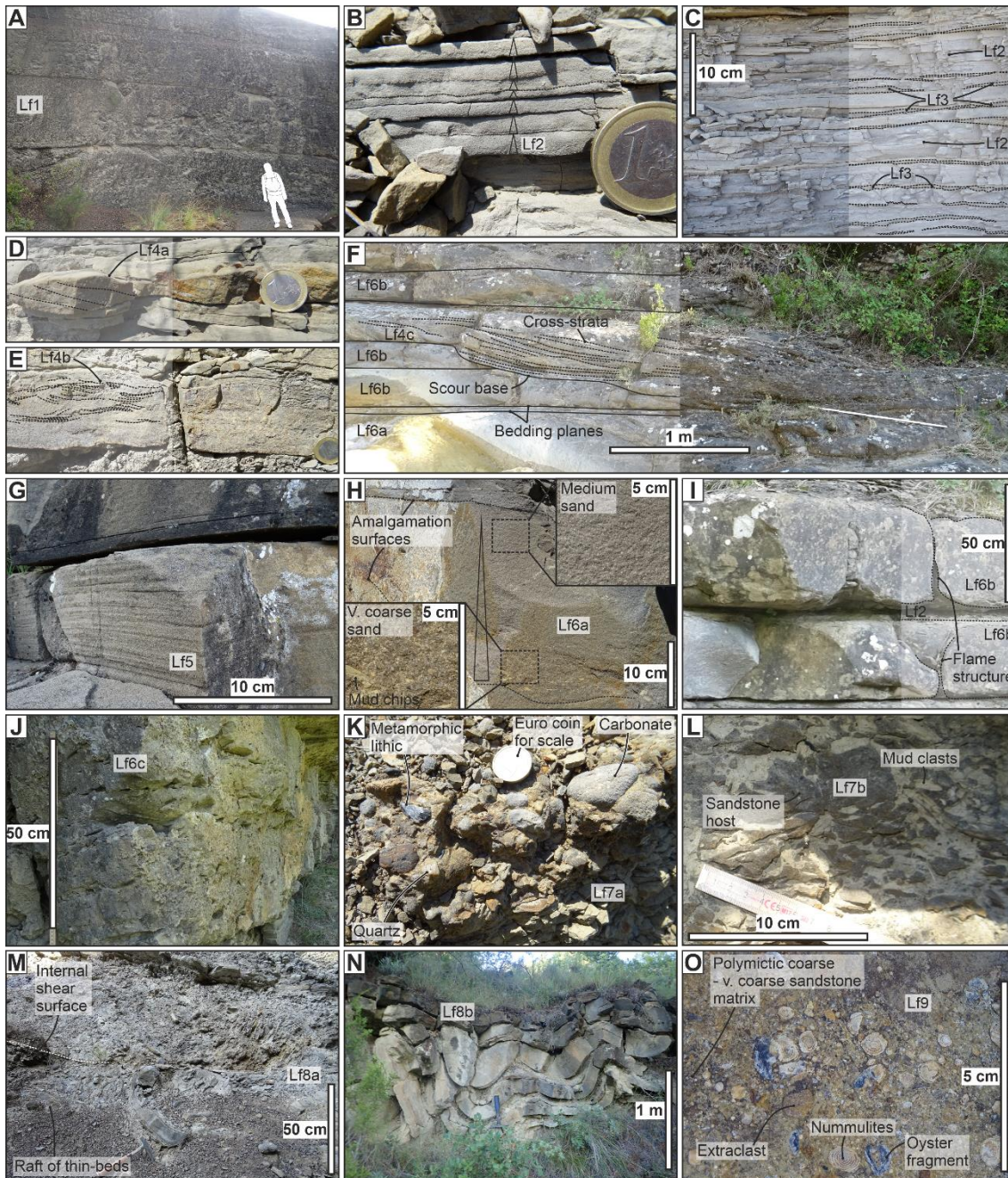


Figure 3.5 – Photographs of all fifteen facies and sub-facies which constitute the stratigraphy of the Arro system; descriptions are provided in table 1. A) Lf1 - structureless mudstone; B) Lf2 - graded siltstone; C) Lf3 - lenticular siltstone; D) Lf4a - rippled sandstone; E) Lf4b – hummocky-cross-stratified sandstone; F) Lf4c – planar-cross-stratified sandstone; G) Lf5 – parallel-laminated sandstone; H) Lf6a - graded, structureless sandstone; I) Lf6b - ungraded, structureless sandstone; J) Lf6c - sandstone with mudclasts; K) Lf7a - extraclast conglomerate; L) Lf7b - mudclast conglomerate; M) Lf8a - chaotic mudstone; N) Lf8b - deformed heterolithics; O) Lf9 - polymictic, bioclastic sandstone.

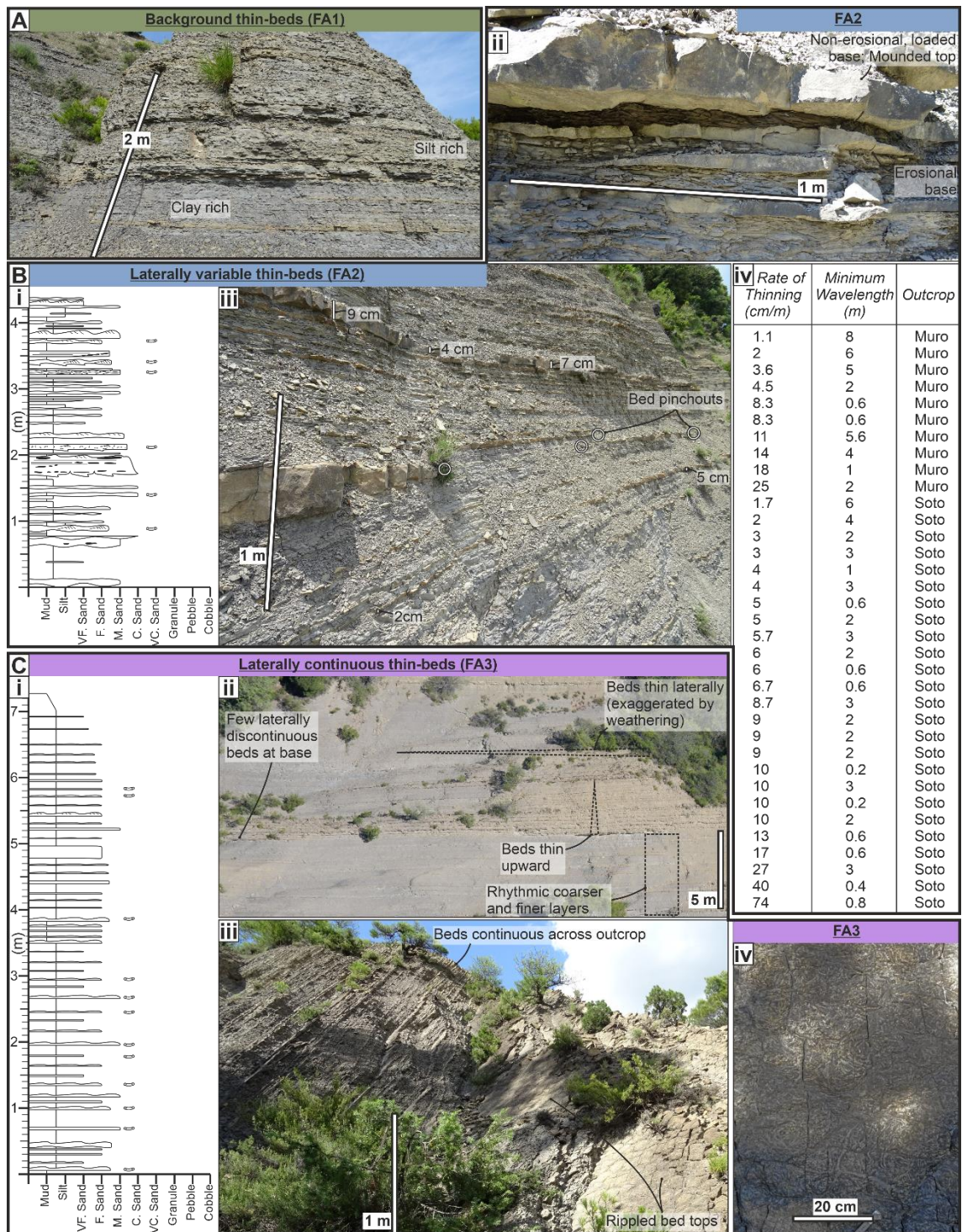
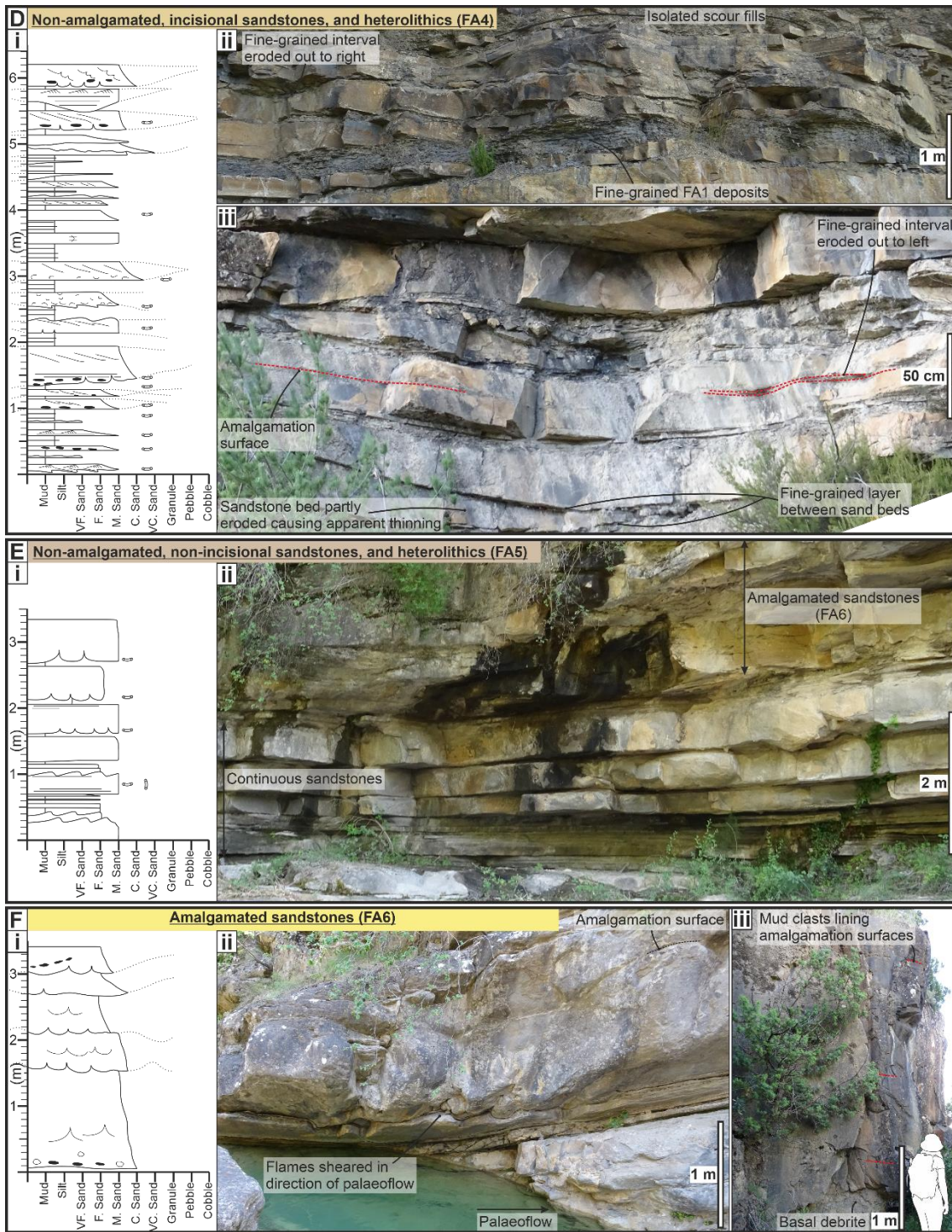


Figure 3.6 – A – H) Typical nature of facies associations 1 to 8 (FA1 – FA8) respectively. A, Bii-iii, Cii-iii, Dii-iii, Eii, Fii-iii, Gii and Hi) Representative photographs of all eight facies associations; Bi, Ci, Di, Ei, Fi and Gi) representative logs through idealised sections of FA2 – FA7 respectively; Biv) thinning rates and wavelengths of pinching and swelling beds in FA2; Ci) bed top in FA3 covered by Scolicia; Hi) debris mass-transport deposit of FA7 forming a steep-walled scour surface into an underlying sandstone bed.



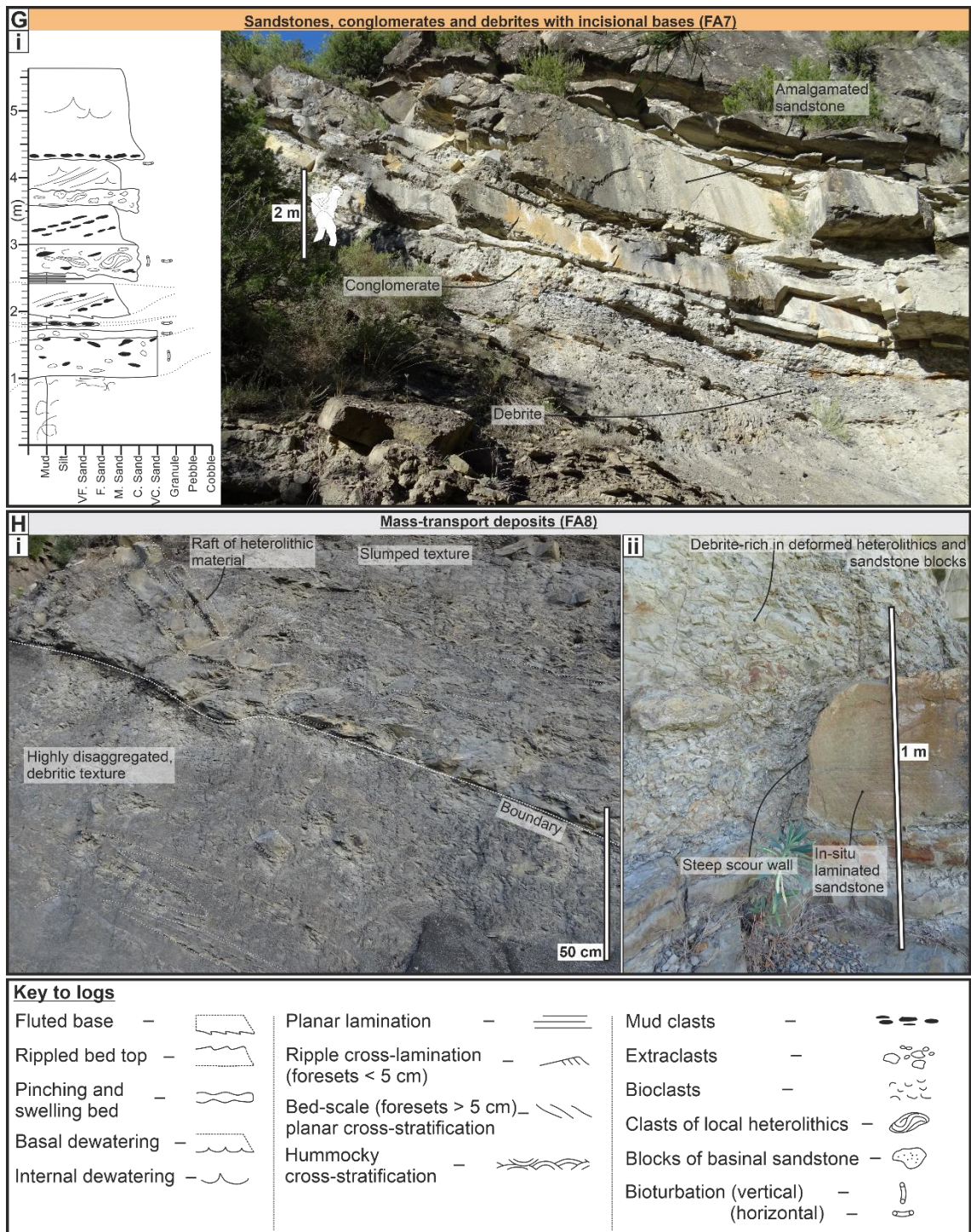


Figure 3.6 – Continued.

3.5 Results

3.5.1 Facies Analysis

The fifteen facies and sub-facies defined in the Arro turbidite system are described in Table 3.1, with photographs presented in Figure 5. These facies and sub-facies are defined according to lithology, grain size, and composition, the presence and type of sedimentary structures, and grading.

The facies are grouped together to form eight facies associations (FA1-8) that can be widely recognised in the Arro system (Fig. 3.6). These facies associations are not unique to a single depositional environment and often exhibit gradational transitions between one another; the observed continuum prevented any meaningful quantitative facies-association definition based upon facies proportions. The logs displayed in Figure 6 are from representative sections. The interpretation of depositional elements (DE1-4) was therefore based on the combination of facies association occurrence and the presence of key bounding surfaces (see “depositional elements” section).

Turbidite and MTD character is a record of the velocity, concentration, magnitude, and grain size (and modality thereof) of flows traversing the depocenter. As the specific role of each of these parameters is generally indiscernible, the term “energy” will be used such that high-energy flows are those of high velocity, concentration, and magnitude, and coarse grain size (and vice versa for low-energy flows).

3.5.1.1 Facies Association 1 (FA1) – Background Thin Beds

Description:

Constituting most of the depocenter fill, this facies association contains very thin (typically < 3 cm, average thickness ~ 1 cm) very fine- to medium-grained beds of lenticular (Lf3), rippled (Lf4a), and ungraded, structureless (Lf6b) sandstone, which alternate with finer-grained siltstone and mudstone facies of structureless mudstone (Lf1) and graded siltstone (Lf2) (Table 3.1); Lf2 is dominant. The thickness of mudstone and siltstone layers in FA1 varies from 3 to 25 cm (average: 7 cm), with variable proportions of clay and silt (Fig. 3.6A). Bedding-concordant packages (a few decimetres to ten metres thick) of alternating grain size can be traced for tens to hundreds of metres. In some outcrops, such as Muro de Bellos (Fig. 3.7), wedging geometries in these packages are observed. Bioturbation on sandstone bed tops and bases is seldom observed (possibly due to outcrop limitations), but sand-filled burrows are found in finer-grained layers. Distinct beds of fully disaggregated debrites (Lf8a) are rare, but FA1 is often highly deformed because of syn-sedimentary remobilisation or due to later tectonic activity; subtle deformation can be hard to detect at outcrop scale. The two causes are distinguished by the presence of calcite veining along shear horizons (or faults), which are taken as an indicator of tectonic deformation. FA1 can be found as heterolithic packages between incisional and non-incisional sandstone beds of FA4 and FA5. Lateral and vertical transitions into laterally variable (FA2) and laterally continuous (FA3) thin beds are observed; a continuum exists between these three facies associations.

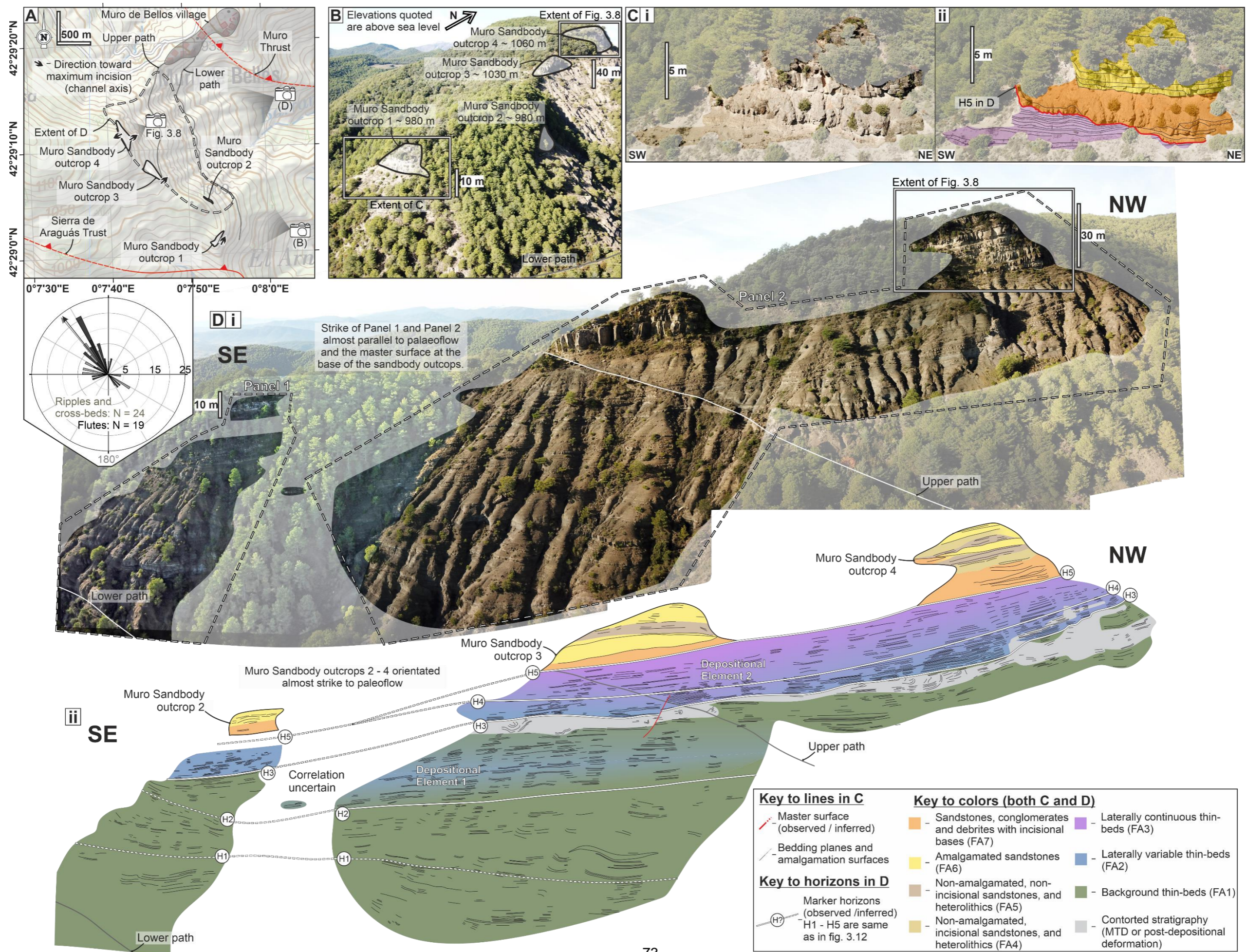


Figure 3.7 – Architecture of the Muro de Bellos outcrop. A) Locations of the Muro Sandbody outcrops 1 – 4 and the inferred direction towards their axes, the Muro and Sierra de Araguás thrusts, panels 1 and 2 in part D, and a rose diagram showing all palaeocurrents collected from the outcrop (channelised and non-channelised stratigraphy combined). B) Drone photograph from the east showing the relationship between sandbody outcrops 1 – 4 and their respective elevations; C) Raw (i) and interpreted (ii) photograph of Muro Sandbody outcrop 1. Di) Photomosaic showing the location of panels 1 and 2. Dii) Interpretation of the photopanel shown above (panel numbers and marker horizons are the same as in figure 3.12).

Interpretation:

FA1 comprises the deposits of dilute, low-density flows (Mutti, 1977), which experienced periodic variations in silt and sand content, together with hemipelagites. The vertical distribution of FA1 between and within other facies associations (FA4 and FA5) suggests that it represents the dominant background sedimentation, but not necessarily from hemipelagic settling alone, as has also been recognised in the deep-water strata of the Tanqua depocenter, Karoo Basin (Boulesteix et al., 2019). The formative flows may have been derived from: (i) small sediment failures on the shelf, on the upper slope, or in the feeder canyon (Clare et al., 2016); (ii) hyperpycnal flows associated with direct sediment input from a canyon-connected river mouth, whereby variations in grain size may reflect variations in the flux of the feeding river (Mulder et al., 2003; Mutti et al., 2003; Zavala et al., 2011); (iii) the down-slope flow of sediment plumes that build at the mouth of a feeding river and collapse upon attainment of a critical density (Hizzett et al., 2018; Mutti, 2019). The presence of FA1 lateral to, and gradational with, FA2 and FA3 suggests that FA1 may also represent distal-most or lateral-most fan or levee deposits. In periods of contemporaneous fan or levee deposition, laterally or upstream, this facies association may therefore have experienced increased rates of aggradation.

3.5.1.2 Facies Association 2 (FA2) – Laterally Variable Thin Beds

Description:

FA2 is highly variable with respect to its constituent facies, bed thickness, and bed nature. It is composed of mainly fined-grained packages (3-50 cm thick) of Lf1, Lf2, and Lf3, interbedded with sandstone beds (> 1 cm, < 50 cm, typically 3-25 cm thick) comprising: rippled (Lf4a), hummocky (Lf4b), and planar cross-stratified (Lf4c), parallel-laminated (Lf5), graded, structureless, and mudclast-bearing (Lf6a-c) and polymictic, bioclastic sandstone (Lf9) (Table 3.1). Lf4a and Lf6b (Fig. 3.5) are the dominant sandstone facies (Fig. 3.6B); Lf4b is particularly prevalent in Sierra de Soto Gully. Bioclasts in beds of Lf9 are fragmented and do not display organisation; Nummulites typically exhibit a lower degree of fragmentation than bivalve and gastropod bioclasts. Chaotic mudstone (Lf8a) is very rarely observed and, where present, occurs as < 50 cm beds. Ophiomorpha, Nereites, and Scolicia traces are found on some sandstone bed tops, Thalassinoides burrows are found on some sandstone bed tops and bases, and other undifferentiated sand-filled burrows are found in some of the fine-grained intervals; no single trace is dominant.

The characteristic feature of this facies association is the geometry of its constituent sandstone beds. Some beds form isolated lenses, some form lenses that pinch out along distinct horizons, and others subtly pinch and swell without forming

lenses (Fig. 3.6B). Bed thinning rates and minimum pinch-and-swell wavelengths (constrained by bed exposures) have been calculated from thirty-five measured beds (average thinning rate: 11.3 cm/m; average minimum wavelength: 235 cm) from the Muro de Bellos (average thinning rate: 9.6 cm/m; average minimum wavelength: 348 cm; N = 10) and Sierra de Soto Gully (average thinning rate: 12 cm/m; average minimum wavelength 190 cm; N = 25) outcrops. Ripple-scale bed thickness variations (7-30 cm wavelength) are sometimes superimposed onto the aforementioned, larger-wavelength, pinching and swelling trends (see Fig. 3.6B (iv)); the two are usually distinguishable. Bed bases can be flat, lightly incisional (< 10 cm), or exhibit a concave-up geometry which is non-erosional and concordant with bedding below; bed tops can be mounded or flat.

FA2 occurs in all locations and is observed in every depositional element (DE1-4; see “depositional elements”), forming lateral transitions with non-amalgamated, incisional sandstones, and heterolithics (FA4) and background thin beds (FA1), and a vertical transition with laterally continuous thin beds (FA3). In some locations, gradational lateral transitions from a package of FA2 in the center to FA1 are observed in both directions. The nature of the bed tops and bases may change dependent on the depositional element in which they are found.

Interpretation:

The presence and fragmented nature of bioclasts in Lf9 suggests that some of the original sediment was derived from a shallow-marine domain. Hummocky cross stratification (Lf4b), interpreted as the product of combined flow, could indicate current reflection or deflection by the interaction with syn-depositional basin-floor topography (Tinterri, 2011). Beds with erosional bases could represent either the tail deposits of a bypassing turbidity current that deposited coarser-grained material downstream, or the deposit of a lower-energy flow that infilled an erosional surface left by a preceding, higher-energy flow (Kane et al., 2009b). Bedding-concordant (non-erosional) bed bases, still concave-up, are interpreted to have filled some substrate topography formed by local tectonic deformation or slumping. Mounded bed tops suggest a bedform-related origin, particularly in beds containing planar or hummocky cross stratification (Lf4b-c). In beds with concave-up bases these bedforms may have formed in relation to the infilling of depressions (*sensu* Arnott and Al-Mufti, 2017); however, this process does not account for those with flat bed bases. Another possible formative mechanism is deposition and tractional reworking of sediment forming dunes (Mutti, 1977) or megaripples (Tinterri, 2011). Postdepositional loading and deformation may also cause or enhance the lateral thickness variability observed in these beds (e.g., Owen, 2003; Oliveira et al., 2011).

FA2 exhibits multiple modes of occurrence. Lateral and vertical transitions into a range of other associations means a number of formative scenarios are possible; these are presented in the “depositional elements” section.

3.5.1.3 *Facies Association 3 (FA3) – Laterally Continuous Thin Beds*

Description:

FA3 comprises fine-grained intervals (2-30 cm thick) of structureless mudstone (Lf1), graded siltstone (Lf2), and lenticular sandstone (Lf3) punctuated by beds (typically 2-8 cm thick, average thickness ~ 3 cm) of rippled sandstone (Lf4) which tend to weather proud. Hummocky and planar cross stratified (Lf4b-c), and ungraded, structureless (Lf6b) sandstone beds are also common. Graded (Lf6a) and mudclast-bearing (Lf6c) sandstones are rare. Chaotic mudstone (Lf8a) beds are rare (but more common than in the laterally variable thin beds; FA2) and, where present are < 75 cm thick. Packages of deformed heterolithics (Lf8b), up to 2 m thick, can be found in FA3. Sand-filled burrows are found in the finer-grained intervals, and *Thalassinoides* is occasionally present on sandstone bed bases (< 10% of beds); however *Scolicia* is the dominant trace in FA3. Where bed tops are exposed, they are commonly (> 50% of beds) pervasively bioturbated with *Scolicia* (Fig. 3.6C).

While the facies assemblage may resemble that of FA2, sandstone beds of FA3 do not pinch and swell, aside from undulations related to their rippled tops (7-30 cm wavelength). Thin (< 8 cm) sandstone beds are largely observed to maintain their thickness laterally over ~ 20 m (Fig. 3.6C). However, in outcrops with exposures greater than tens of metres, a systematic lateral thinning of these beds is observed. Concomitant with this lateral thinning, FA3 transitions gradationally into background thin beds (FA1; Fig. 3.6C). FA3 also grades upwards into FA1.

Interpretation:

The regular, thin-bedded nature and systematic thinning of the rippled and structureless sandstone beds is consistent with overbank deposition from dilute turbidity currents which overspill a contemporaneous lateral conduit (Mutti, 1977; Mutti et al., 1988; Millington and Clark, 1995a, 1995b; Bayliss and Pickering, 2015). Susceptibility to slumping and remobilisation is common in overbank deposits (Kane and Hodgson, 2011; Hansen et al., 2015), and the intensity of *Scolicia* bioturbation also supports this interpretation (Heard et al., 2014).

3.5.1.4 *Facies Association 4 (FA4) – Non-Amalgamated, Incisional Sandstones, and Heterolithics*

Description:

In this facies association, heterolithic packages of graded siltstone (Lf2) and thin (< 5 cm) beds of lenticular (Lf3) and rippled (Lf4a) sandstone are interbedded predominantly with thin to thick beds (highly variable from 5 to 100 cm thick, typically 20-50 cm) of: planar-cross-stratified (Lf4c), parallel-laminated (Lf5), structureless (Lf6a-b), mudclast-bearing (Lf6c) and bioclastic (Lf9) sandstone. Beds (< 50 cm) of extraclast (Lf7a) and mudclast (Lf7b) conglomerates, and debrites (Lf8a) are observed less commonly. The relative proportions of sandstone beds and fine-grained intervals vary between outcrops (Fig. 3.6D).

Lateral variability in sandstone bed thickness is related to the presence of erosional surfaces that incise the tops of underlying sandstone beds and into the fine-grained intervals, and that host thicker sediment accumulations in the loci of maximum incision (Fig. 3.6D). These surfaces are almost always filled mainly by sandstone beds (Lf4c, Lf5 and Lf6a-c) or debrites (Lf8a), and they are often draped by finer-grained deposits (Lf2, Lf3 and < 5 cm beds of Lf4a and Lf6b) that also thicken towards the locus of maximum incision. On rare occasions, the fine-grained deposits are observed to heal the erosional surface completely. FA4 forms a continuum between laterally variable thin beds (FA2) and amalgamated sandstones (FA6). The tendency for the erosional surfaces to cut one another (and lateral transitions into FA2 and FA6) makes measurements of their width and relief problematic, but bed thinning rates (which can be used as proxies) range from ~ 4 to 20 cm/m. Sand-filled burrows are observed in the finer-grained intervals, and Ophiomorpha traces are observed.

Interpretation:

The diversity of sandstone facies (similar to that of FA2) and presence of Lf7a, Lf7b, and Lf8a suggests deposition from flows of various concentrations, magnitudes, grain sizes, and velocities. Fine-grained drapes on scoured surfaces likely represent combined accumulation from the fine-grained remnants of bypassing flows (which formed the scour) and possibly subsequent ones (e.g., Mutti and Normark, 1987; Mutti, 1992; Kane et al., 2009b; Stevenson et al., 2015; Bell et al., 2018a), and a temporary return to background sedimentation (respectively the “bypass” and “abandonment” drape of Barton et al., 2010; Alpak et al., 2013). The erosional nature of FA4 was attained either by unconfined to weakly confined scouring flows which were not fully contained by their lateral confinement but were still able to scour and bypass coarse sediment fractions, and/or as the lateral expression of higher-energy channelised deposits.

3.5.1.5 *Facies Association 5 (FA5) – Non-Amalgamated, Non-Incisional Sandstones, and Heterolithics*

Description:

This facies association consists of medium-bedded (10-100 cm) rippled (Lf4a), parallel-laminated (Lf5), and structureless (graded and ungraded; Lf6a-b) sandstones interbedded with finer-grained heterolithic packages. These packages (typically < 20 cm thick) comprise graded siltstone (Lf2) and thin (< 5 cm) beds of lenticular (Lf3), rippled (Lf4a) and graded, structureless (Lf6a) sandstone. Sandstone beds usually exhibit a sharp basal boundary followed by a thickening-upward and sometimes a coarsening-upward trend (Fig. 3.6E). Both sandstone beds and fine-grained packages maintain their thickness for up to 40 m laterally, unless incised by an erosional surface underlying another facies association (Fig. 3.8). FA5 is observed solely in outcrops containing channelised deposits (locations 3, 18 and 22; Fig. 3.2), wherein it may both overlie and underlie non-amalgamated, incisional sandstones, and heterolithics (FA4) or amalgamated sandstones (FA6) (Figs. 3.6E, 3.8).

Interpretation:

Laterally continuous, non-erosional sandstone beds associated with channel deposits may form when a channel has filled its confining surface (the “spill” phase; Gardner et al., 2003), or from the deposition of sand “sheets” from flows which were fully laterally confined but possessed insufficient energy to erode (McCaffrey et al., 2002). The latter interpretation is favored due to the sharp base and upward thickening. The presence of a sharp basal contact with underlying FA4 and FA6 (Fig. 3.8) deposits which, internally, contain more evidence of erosion, is interpreted to be due to a rapid drop in local sedimentation rate, likely due to an upstream blockage, or avulsion causing an abrupt lateral shift in the channel axis. Vertical transitions into overlying FA4 and FA6 deposits represent a return to high-energy flow conditions, potentially accompanying an increase in local sedimentation rate (McCaffrey et al., 2002).

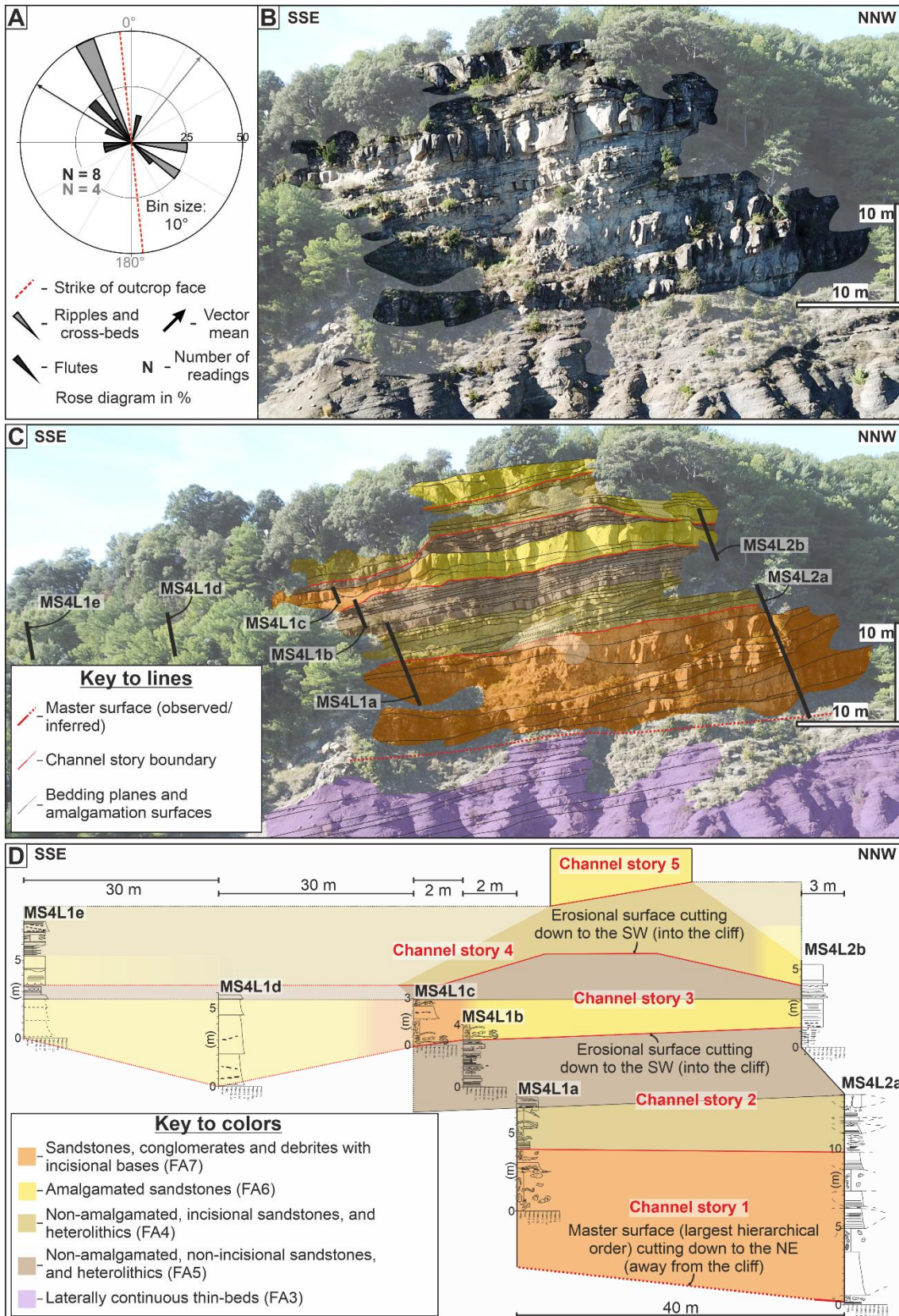


Figure 3.8 – A) Rose diagram showing local palaeoflow and its relationship with the strike of the outcrop face. B) Drone photograph of the Muro Sandbody outcrop 4. C) Interpretation of photograph in part B, showing bedding planes, facies associations, and log locations. D) Correlation panel built from the logs in part C.

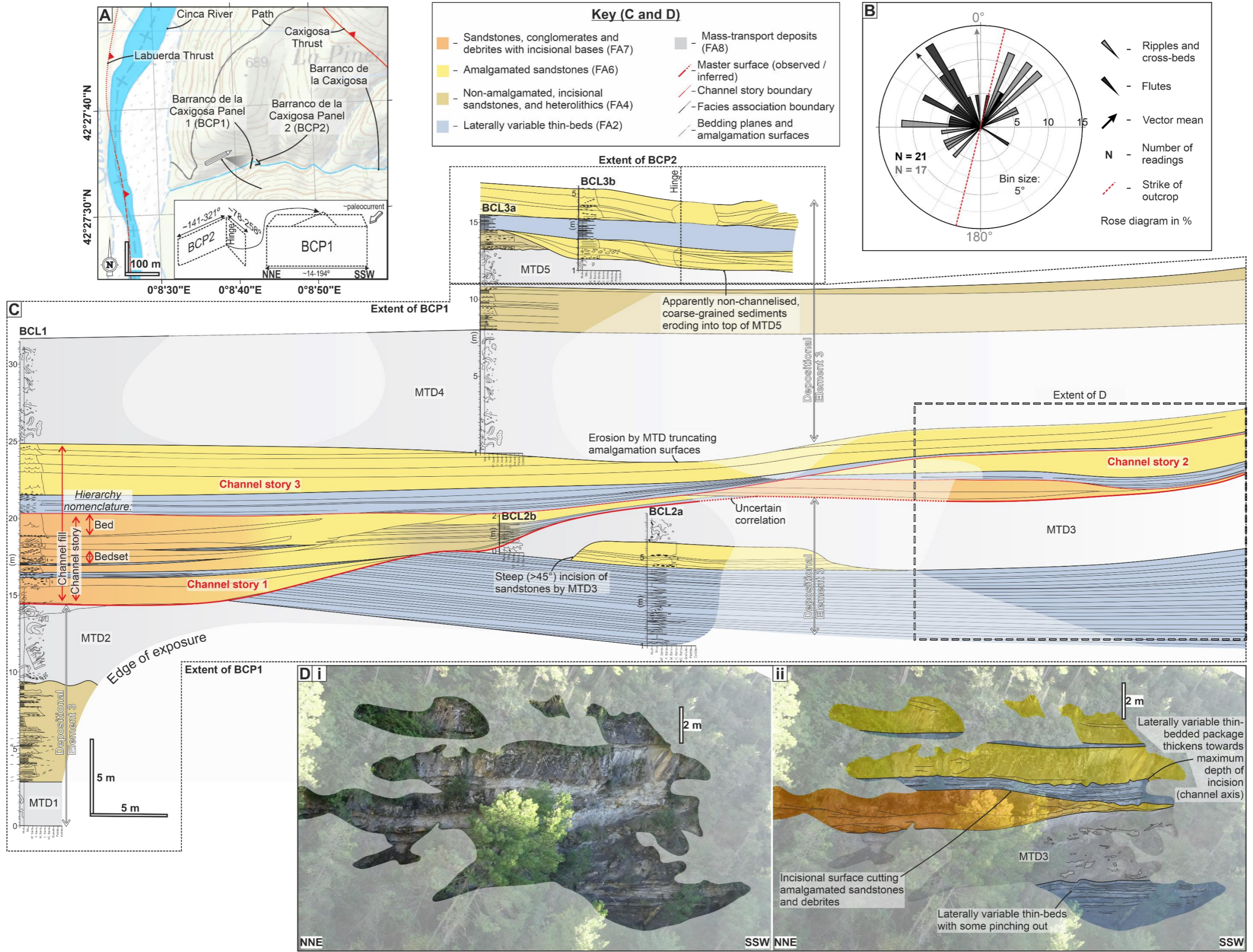


Figure 3.9 – Architecture of the Barranco de la Caxigosa outcrop: A) Summary map showing the locations and orientations of the panels in part C, and the Labuerda and Caxigosa thrusts. B) Rose diagram showing local palaeoflow and its relationship with the strike of panel BCP1. C) Correlation panel built from logs and interpreted photographs, such as in part D, showing bedding planes, facies associations, and channel stories. D) Raw (i) and interpreted (ii) photograph forming the basis for the correlation in the WSW of panel BCP1.

3.5.1.6 Facies Association 6 (FA6) – Amalgamated Sandstones

Description

FA6 is composed solely of sandstone facies, comprising rippled (Lf4a), planar-cross-stratified (Lf4c), parallel-laminated (Lf5), structureless (graded and ungraded; Lf6a-b) and mudclast-bearing (Lf6c) sandstones. Among these, Lf6a-c appear dominant, but its common pervasive dewatering may obscure the identification of sedimentary structures (Fig. 3.6F). Sandstone packages of FA6 can be > 5 m thick, but internal amalgamation surfaces picked out by grain-size breaks or horizons of aligned mudclasts are ubiquitous (Fig. 3.6F); these erode into and are filled by sandstone beds. Amalgamation surfaces are concave-up and typically exhibit dips of up to 40° (corrected for local bedding). In outcrops oriented quasi-perpendicular (60-90°) to local palaeoflow (e.g., locations 3 and 14; Fig. 3.2), the wavelength of scouring varies from ~ 1.5 m to > 25 m. In such outcrops, the locus of maximum incision of successive scours switches laterally in both directions; however, scour walls dipping towards higher-energy sandstones, conglomerates, and debrites with incisional bases (FA7) are preferentially preserved. In outcrops orientated subparallel (0-30°) to local palaeoflow (e.g., locations 18 and 19; Fig. 3.2), scour walls exist in the same dip range, but do not have a preferential orientation of preservation. In FA6, packages of Lf6b can be up to 4 m thick without development of any obvious amalgamation surfaces, although dewatering might obscure them. Where dewatering is not present, maximum bed thickness (between amalgamation surfaces) is rarely > 1.2 m, and is never greater than 2 m, in keeping with typical channel bed thicknesses quoted in Fryer and Jobe (2019). This facies association lies in a continuum between non-amalgamated, incisional sandstones, and heterolithics (FA4) and (FA7).

Interpretation

FA6 is the result of deposition from recurrent, sand-rich turbidity currents that locally eroded, bypassed, and deposited. Common amalgamation surfaces may have been filled by their formative flows or represent periods of sustained bypass (e.g., Kane et al., 2009b; Bell et al., 2018a). Surface-lining mudclasts likely represent residual lag deposits (Stevenson et al., 2015), possibly derived externally (from a proximal source), or locally, from the erosion of a fine-grained drape (Mutti, 1992; Kane et al., 2017). The frequency and/or magnitude of events increased towards a depositional low (i.e., channel axis), causing the preferred preservation of axis-dipping scour walls in cross section, but not longitudinal, palaeoflow-parallel sections.

3.5.1.7 *Facies Association 7 (FA7) – Sandstones, Conglomerates, and Debrites with Incisional Bases*

Description:

FA7 comprises rippled (Lf4a), cross-stratified (Lf4c), parallel-laminated (Lf5), structureless (graded and ungraded; Lf6a-b), mudclast-bearing (Lf6c) and bioclastic (Lf9) sandstones, and extraclast and mudclast conglomerates (Lf7a-b), and MTDs (Lf8a-b) (Fig. 3.6G). MTDs in FA7 are sometimes stacked (Fig. 3.8). They mostly occur as < 1-m-thick debrites of variable composition, with a silt- and clay-rich matrix containing a combination of: (i) sandstone (< 40 cm long axis) and local heterolithic (< 1 m long axis) blocks; (ii) bioclasts (< 1.5 cm long axis); (iii) extraclasts (< 3 cm long axis, typically comprising lithic fragments and clasts of rounded carbonate). In distinguishing debrites within FA7 from those comprising FA8, their architectural context is used: debrites in package-bounding confining surfaces (such as channel-walls; cf. DE3 and DE4; see “depositional elements”) are classified as FA7 deposits (Fig. 3.9).

FA7 displays internal erosion, with bed bases of each lithofacies incising into one another. Bed thicknesses increase towards the maximum depth of the bounding erosional surface (Fig. 3.9). In longitudinal, palaeoflow-parallel sections, some erosional bed bases are asymmetric, steeper upflow (maximum dip ~ 40°) than downflow (maximum dip ~ 20°). These surfaces can contain a higher concentration of imbricated mudclasts against the steep side, dipping down-flow; they are interpreted as megaflutes (Elliott, 2000; Kane et al., 2009b). FA7 forms a continuum with amalgamated sandstones (FA6).

Interpretation:

Erosional, generally coarse-grained lags and debrites are commonly observed in channel thalwegs (Mayall et al., 2006; Hubbard et al., 2009; Kane et al., 2009a; Bell et al., 2018b). These build incrementally through repeated scouring, bypassing, and deposition from passing, possibly supercritical flows (Froude number > 1, Komar, 1971).

3.5.1.8 *Facies Association 8 (FA8) – Mass-Transport Deposits (MTDs)*

Description:

FA8 is composed solely of MTDs exhibiting debritic (Lf8a) and slumped (Lf8b) textures, found outside of confining surfaces that bound packages (see FA7 for distinction); they are typically > 1 m thick and sometimes stack up to > 22 m thick (Fig. 3.6H). The composition of the debrites (Lf8a) is highly variable, with blocks or clasts derived from any of the other lithofacies in the system (see Table 3.1) hosted within a heterolithic matrix. Blocks of conglomerate (Lf7) and bioclastic, polymict sandstone (Lf9)

are observed amongst isolated extraclasts and bioclasts. Deformed, isolated blocks (a few decimetres to metres) of background (FA1), laterally variable (FA2) and laterally continuous (FA3) thin beds are common in FA8. The composition of Lf8b is almost exclusively fine-grained heterolithic, thin-bedded deposits.

Basal contacts of FA8 packages can incise up to 3 m into underlying deposits, and are sometimes manifested as broad erosional surfaces (Fig. 3.9) with the MTD thickening towards the maximum incision depth, or as steep (up to 90° in some cases) walled scours (Fig. 3.6H). The tops of FA8 packages are commonly eroded and filled by FA2, FA4, FA6, and FA7 (Fig. 3.9).

Interpretation:

The formative flow type and the resultant depositional character of an MTD depends mainly on the composition (mainly its clay content) and degree of disaggregation (controlled principally by its transport history; Moscardelli and Wood, 2008; Bull et al., 2009; Ogata et al., 2012). Because the MTDs of FA8 are highly variable in their texture and composition, determining transport distance is problematic. Furthermore, compositional indicators often used to determine source, such as dispersed bioclasts and extraclasts, might all be derived from their feeding lithologies or have been incorporated through basal substrate erosion. Isolated extraclasts and bioclasts may have been incorporated from the disaggregation of blocks of Lf7 and Lf8 during transportation.

Arbués et al. (2007a, 2007b) attributed the < 20 m thick, stacked MTDs at Los Molinos Road to failures on a structurally controlled, laterally confining slope. Mutti (1985) and Dakin et al. (2013), however, recognise longitudinally emplaced MTDs in the Aínsa channel systems. The data presented herein do not allow conclusive determination of whether the thick (> 1 m) MTDs of FA8 (Fig. 3.9) were derived dominantly from transverse sources, such as growing structures (Arbués et al., 2007a) or the collapse of a confining surface (Hansen et al., 2015), or from more proximal sources such as the head or wall of a feeding canyon (Nelson et al., 2011), the shelf or upper slope (Ortiz-Karpf et al., 2017). Furthermore, an MTD that may appear (based on composition and/or degree of disaggregation) to have been emplaced longitudinally may have been derived from a transverse source in a more proximal location, potentially kilometres upstream. Based on the (slumped) character and composition (all apparently derived from local stratigraphy) of the deposits, a transverse source is favored for the emplacement of the MTDs in FA8.

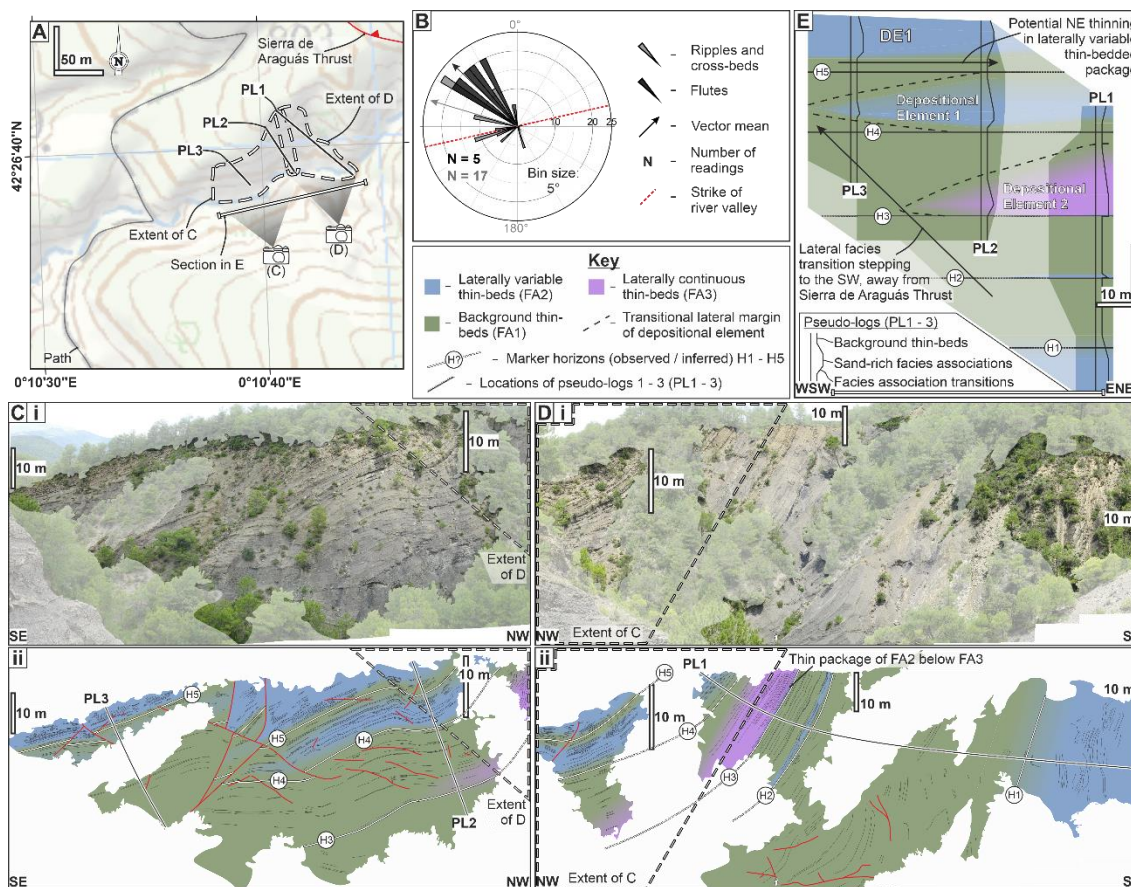


Figure 3.10 – Architecture of the Sierra de Soto Gully outcrop: A) Summary map showing the extent of the panels in parts C and D, and the locations of the pseudo-logs in part E and Sierra de Araguás Thrust. B) Rose diagram showing local palaeoflow and its relationship with the strike of the gully. C) Photomosaic (i) and interpreted line drawing (ii) of the western outcrop panel. D) Photomosaic (i) and interpreted line drawing (ii) of the eastern outcrop panel. E) Correlation panel showing DE1 and DE2, and their constituent vertical and lateral facies association transitions, built from pseudo-logs created using outcrop panel interpretations supported by measured log data.

3.5.2 Depositional Elements

Classification of depositional elements is useful in systems where facies associations are not unique to a single depositional environment. The following depositional elements are derived from groups of facies associations on the basis of systematically recurring vertical or lateral interrelationships, or of relationships with key bounding surfaces.

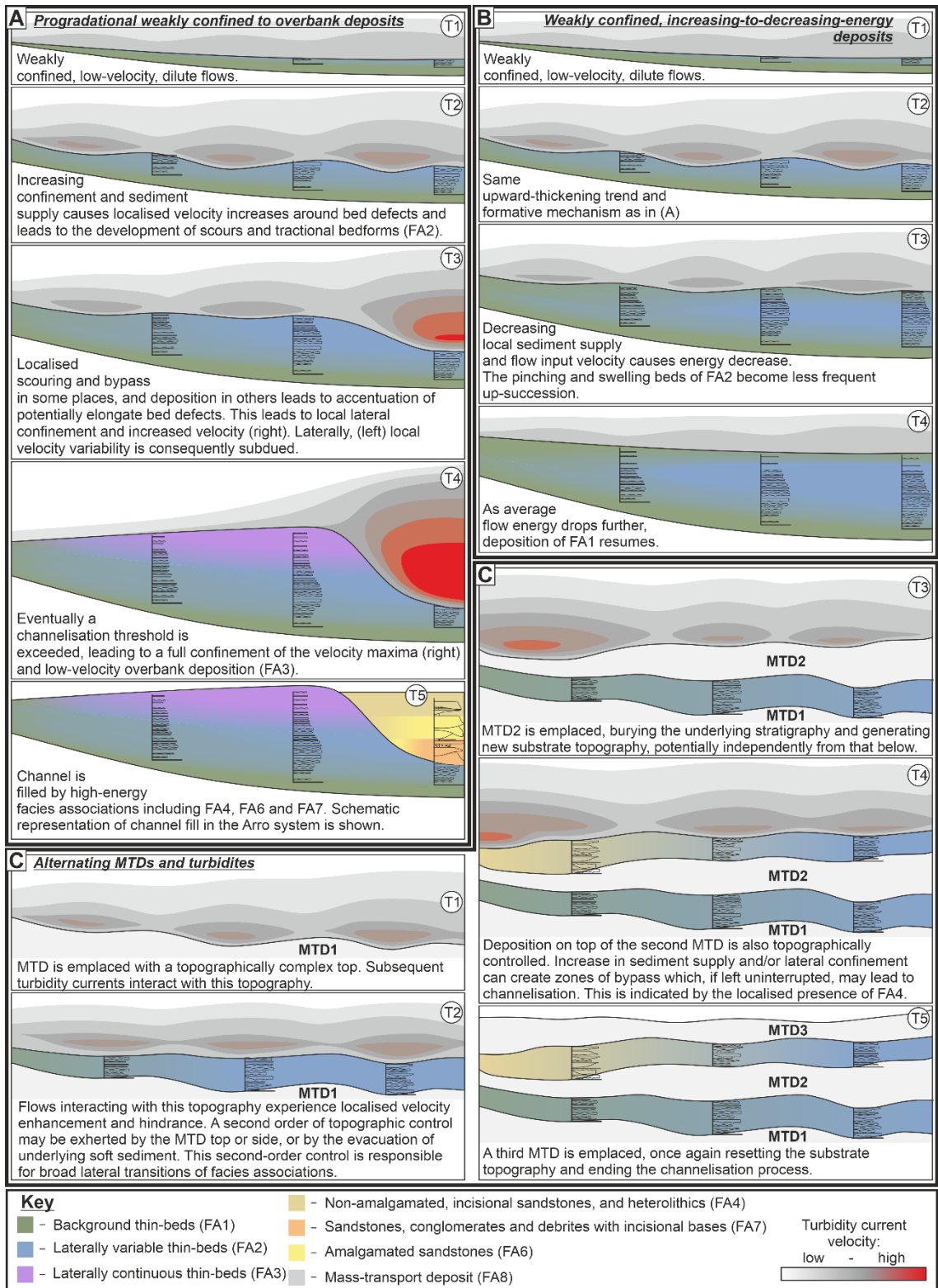


Figure 3.11 – Schematic diagrams showing the interpreted formation and evolution of depositional elements 1 – 4: A) DE1; B) DE2 and DE4; C) DE3.

3.5.2.1 *Depositional Element 1 (DE1) – Weakly Confined, Increasing-to-Decreasing-Energy Deposits*

Observations:

The base, top, and lateral edges of DE1 (best observed in Sierra de Soto Gully; between H4 and H5 in Fig. 3.10) are transitional. Within its basal transition, background thin beds (FA1) grade into laterally variable thin beds (FA2) over 1-4 m. At its top, FA2 grades into FA1 over 2-6 m. Laterally, FA2 transitions into FA1 over tens of metres away from the depositional locus (the location of maximum net sandstone thickness and average sandstone bed thickness). Lateral transitions show a gradual upward increase, followed by a subsequent decrease, in the extent of sandstone beds. While in some outcrops both lateral margins are observed, in most well exposed locations only one margin is preserved. The longitudinal expression of DE1 is poorly constrained, but it is assumed to be elongate in a down-flow orientation. Constituent sandstone beds exhibit all bed geometries recognised in FA2: flat, lightly incisional, or concave-up but non-erosional bases; flat or mounded tops. No common lateral thickening trend is recognised in the sandstone beds, but their average thickness increases towards the depositional locus. From tracing FA2 packages laterally, aggradation in the depositional locus appears to be comparable to that of the margins and surrounding FA1 deposits. Non-amalgamated, incisional sandstones, and heterolithics (FA4) are sometimes present within the depositional locus, transitioning laterally and vertically into FA2.

In Sierra de Soto Gully (Fig. 3.10), the lateral transition from FA2 to FA1 migrates towards the WSW, away from the Sierra de Araguás thrust; palaeoflow directions based on the ripples and cross beds therein also show a western deflection, relative to the flute casts (Fig. 3.10B). At Muro de Bellos, the same lateral facies transition occurs towards the Muro and Sierra de Araguás Thrusts, which laterally bound the stratigraphy (Fig. 3.7).

Interpretation:

No master confining surface bounds DE1 at the outcrop scale, so the velocity maxima of the formative flows of constituent FA2 deposits were effectively unconfined. However, the constituent sandstones are thinner, laterally more variable, and less amalgamated than those typical of unconfined, sand-rich deposits (cf. Remacha et al., 2005; Liu et al., 2018; Fryer and Jobe, 2019); evidence for compensation is also lacking. The pinching and swelling geometries and bypassing nature of constituent sandstone beds, and the lack of amalgamation and compensation, suggests these are unlike classical “lobes” (Mutti et al., 1994; Prélat et al., 2010). Facies and bed geometries in FA2 deposits show evidence for tractional reworking and scouring (Fig. 3.6B). However,

coarse-grained lag deposits and mud-draped scours indicative of bypassing, high-concentration flows (Barton et al., 2010; Alpak et al., 2013; Stevenson et al., 2015) are largely absent. Therefore, FA2 deposits in DE1 represent low-concentration, generally fine-grained but dominantly bypassing flow deposits.

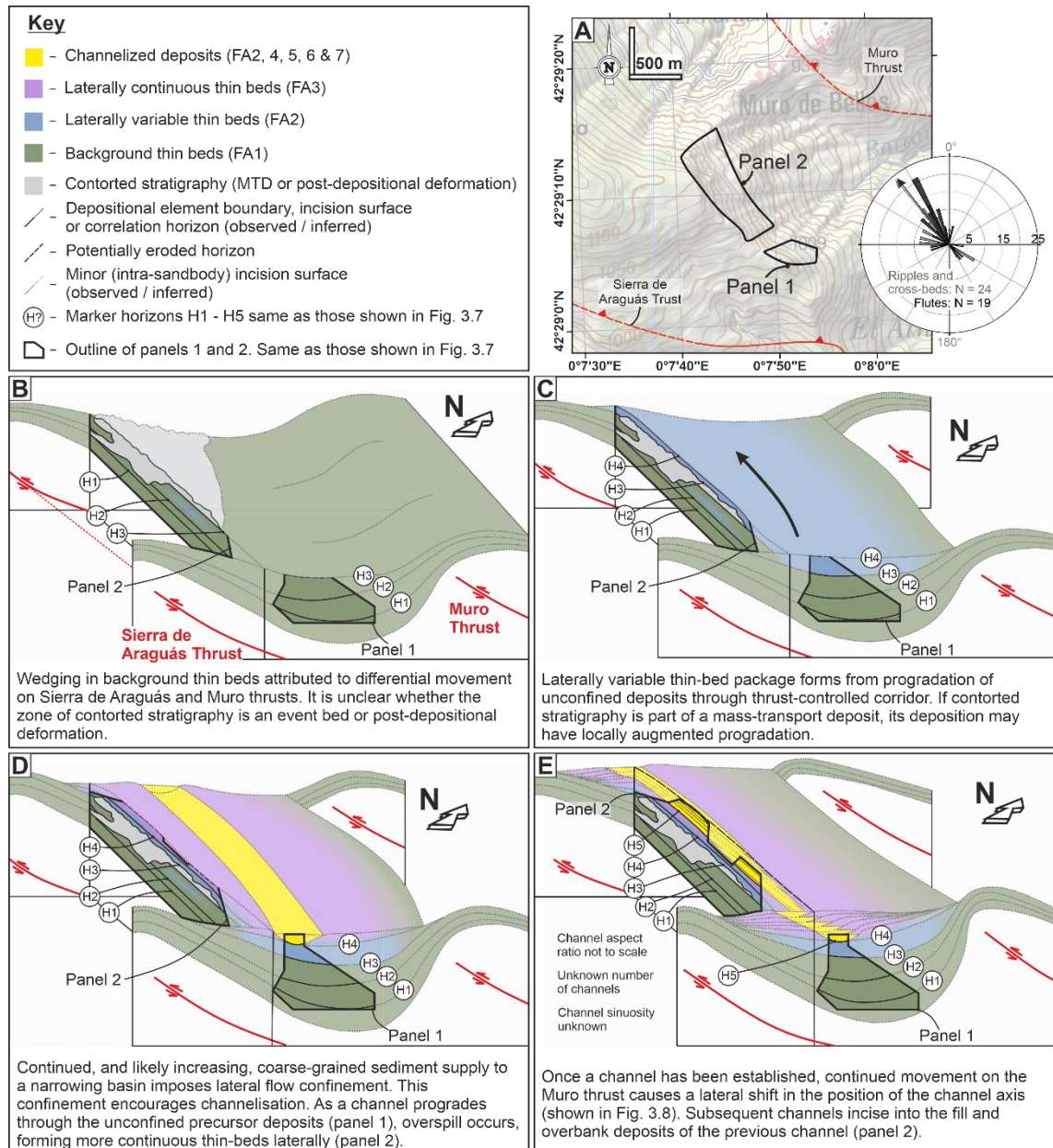


Figure 3.12 – A) Map showing the locations of panels 1 and 2, the Sierra de Araguás and Muro thrusts, and local palaeocurrent (rose diagram same as in Fig. 3.7A); B – E) sketch diagrams showing the evolution of the channels in Muro de Bellos through four time steps. Interpreted panels 1 and 2 presented in Fig. 3.7 have been used to inform the interpretation and are displayed herein.

Observed vertical transitions within DE1 represent increasing and subsequently decreasing flow energy. This motif arises in response to variations in local sediment delivery (Fig. 3.11), due either to an upstream levee crevasse (formed from a failed avulsion), or driven by basinal supply (Lowe et al., 2019). The relationship with structures suggest that the depositional axes of DE1 coincided with the deepest part of elongate topographic lows, which also controlled the location of lateral facies transitions. Movement (dominantly forward propagation) of fairway-bounding structures is inferred to be responsible for the lateral shifts in the depositional axis and subtle lateral facies association transitions as seen in Sierra de Soto Gully (Fig. 3.10). Lateral facies transitions are associated with increasing local sand input, as the high-velocity sand-rich part of flows was able to spread over a wider area, whilst still contained within the fairway (Fig. 3.11b).

Increases in velocity on steep axial gradients may allow a weak flow to exceed its bypass threshold, causing it to erode or bypass, and leaving a thin deposit or no deposit (Stevenson et al., 2015; Dorrell et al., 2018). Elongate sediment pathways provide subtle lateral confinement, which may also cause flow velocity to increase (Fig. 3.1). At the bases of these weakly confined flows, substrate topography (metres to tens of metres in wavelength) generated by previous flows, sediment loading or small structures cause localised velocity variability (Eggenhuisen et al., 2010; Dorrell et al., 2019), which leads to the formation of tractional bedforms and scours (Fig. 3.11). Modern canyons (Paull et al., 2018) and fjord-head delta slopes (Hughes Clarke, 2016) also experience broad lateral confinement (a few kilometres across). Turbidity currents monitored in such settings commonly die out only kilometres from the source (e.g., Paull et al., 2018). DE1 may provide an ancient analogue for these weak flows.

3.5.2.2 *Depositional Element 2 (DE2) – Progradational, Weakly Confined to Overbank Deposits*

Observations:

DE2 is observed in Muro de Bellos (Fig. 3.7) and Sierra de Soto Gully (Fig. 3.10). Similarly to the increasing-to-decreasing-energy deposits of DE1, there is a basal vertical transition from background thin beds (FA1) into laterally variable thin beds (FA2) over 1-4 m; the same lateral transition as in DE1 (from FA2 to FA1 over tens of metres away from the depositional locus) is also observed (Fig. 3.11). Above this, another transition is observed, with a gradual upward decrease in pinching and swelling of beds (of FA2), and a proportional increase in laterally continuous thin beds (FA3). The boundary between the two is arbitrary; however, the FA3 part tends to be thicker (> 20 m) than the FA2 part (> 10 m). FA3 deposits grade vertically into FA1 at the top of DE2. Constituent FA3 deposits can span a wider depositional area than the underlying FA2, leading to

some vertical sections showing FA3 grading to FA1 above and below, with an apparently sharp base (see PL1 and PL2, Fig. 3.10). In Muro de Bellos panel 2 (Fig. 3.7), DE2 is mostly underlain by a zone of contorted stratigraphy containing folds of metres to tens of metres in wavelength, faults with up to 2 m displacement, and blocks measuring up to several metres. This deformed stratigraphy appears to be composed of, and contained within, FA1 deposits, but locally ramps up and down through the stratigraphy.

Interpretation:

DE2 is interpreted to represent the transition from weakly confined deposits (FA2), into overbank deposits (FA3), possibly lateral to the position where a nearby channel was forming (Fig. 3.11); this is comparable to the transition zone from levee to lobe fringe (Normark et al., 1979; Kane and Hodgson, 2011). With locally increasing sediment delivery, weakly confined deposits will prograde; once flow magnitude in the depositional axis crosses the erosional threshold, a channelisation feedback may be initiated (Eggenhuisen et al., 2011; De Leeuw et al., 2016) (Fig. 3.1B). Accordingly, greater proportions of successive flows will become laterally confined, meaning that progressively lower-energy, finer-grained, and better-sorted flows will deposit on the margins (Fig. 3.11). The progressive nature of this process is reflected in the transitional nature of the contact between FA2 and FA3. DE1 and DE2 represent end members of a continuum controlled by channel development. It is unclear whether the disturbed interval beneath DE2 in Muro de Bellos was emplaced as a large MTD, or is a postdepositional product of tectonically or gravitationally driven deformation (Fig. 3.12). If the former is true, the contorted zone may have influenced progradation and channel inception. However, due to the fact that this contorted zone is not constrained to a stratigraphic interval and ramps into overlying stratigraphy, the deformation is likely postdepositional.

3.5.2.3 Depositional Element 3 (DE3) – Alternating MTDs and Turbidites

Observations:

DE3 comprises packages (1-8 m thick) of turbiditic facies associations (background (FA1) or laterally variable (FA2) thin beds, or non-amalgamated, incisional sandstones, and heterolithics (FA4) between stacked or single MTDs (FA8) (< 20 m)). It is best observed in Barranco de la Caxigosa, where five MTDs (MTD1-MTD5; Fig. 3.9) are interbedded with ~ 3–10-m-thick, dominantly turbiditic, packages, one of which (between MTD3 and MTD4) is obviously channelised and is not included within DE3 (see DE4). Any of the turbidite packages (FA1, FA2 or FA4), which exist in a continuum with each other, can overlie and underlie sharp basal and top contacts with MTDs of FA8. Lateral transitions exist between FA1 and FA2, and between FA2 and FA4. Where lateral transitions are visible, the higher-energy facies associations overlie the deepest part of

the basal contact (MTD top), transitioning laterally into thinner, lower-energy packages. The contacts with the overlying MTDs are commonly erosional. Exposure of MTDs in the Arro system is insufficient to trace their full extent. Millington and Clark (1995a, 1995b) and Arbués et al. (2007a, 2007b) describe DE3 at Los Molinos Road, where the turbidite-prone intervals dominantly thin towards the NE, with one notable exception thinning to the SW.

Interpretation:

The nature of DE3 is interpreted to be controlled by the interplay between an underlying MTD and the magnitude, concentration, and grain size of overpassing turbidity currents. The response of turbidity currents to this MTD-top topography is recorded in the overlying turbidite deposits. Depositional lows present on the top of MTDs, or left behind by erosive MTDs, can either generate partial ponding or provide lateral confinement which may enhance channelisation (Fig. 3.11; Schultz et al., 2005; Bull et al., 2009; Hansen et al., 2013; Kneller et al., 2016; Ward et al., 2018). The reason turbidite packages in DE3 may not have crossed a channelisation threshold and formed DE4 may be that the lateral confinement or axial gradient provided by the underlying MTD were insufficient, or the emplacement of a subsequent MTD may have interrupted the process and reset the basin-floor topography (Fig. 3.11). The interplay of the aforementioned factors means that DE3 can form a continuum with increasing-to-decreasing-energy deposits (DE1), progradational-to-overbank deposits (DE2) and channels (DE4).

Arbués et al. (2007a, 2007b) interpreted deposits of this type at Los Molinos Road as the lateral expression of non-exposed channel bodies to the SW of the outcrop. Therein, FA2 deposits (their “TS” facies association) are interpreted as marginal deposits associated with channel bodies, which are formed in response to the emplacement of MTDs. Definitive distinction of the aforementioned interpretations is not possible based on field data due to limited outcrop exposure in both Los Molinos Road and Barranco de la Caxigosa. However, it is likely that a continuum exists between DE3 and DE4, whereby the early stages of channelisation in locations prone to MTD emplacement are similar to those responsible for the deposition of the turbiditic intervals in DE3.

3.5.2.4 Depositional Element 4 (DE4) – Channels

DE4 comprises sandbodies which are characterised by nested erosional surfaces (see below) and that contain non-amalgamated, incisional sandstones, and heterolithics (FA4), non-amalgamated, non-incisional sandstones, and heterolithics (FA5), amalgamated sandstones (FA6), and sandstones, conglomerates, and debrites with incisional bases (FA7).

Four sandbody exposures crop out at the Muro de Bellos location (Muro Sandbody outcrops 1 – 4; Fig. 3.7) above a thick (> 150 m) succession of predominantly background thin beds (FA1), but with laterally variable (FA2) and laterally continuous (FA3) thin beds in the upper ~ 30 m (Fig. 3.7D). While all four outcrops contain DE4 elements, sandbody outcrop 4 exhibits the greatest exposure, therefore allowing the most detailed analysis (Fig. 3.8). In the Barranco de la Caxigosa outcrop (described above), one of the five turbidite packages (up to 11 m thick) contains FA2, FA4, FA6, and FA7 (Fig. 3.9) and multiple nested erosional surfaces; this package is therefore classed as DE4.

Because of their characteristic nested erosional surfaces and sandy fill, DE4 deposits are interpreted as the fill of submarine channels. Further description and discussion of these deposits is presented below.

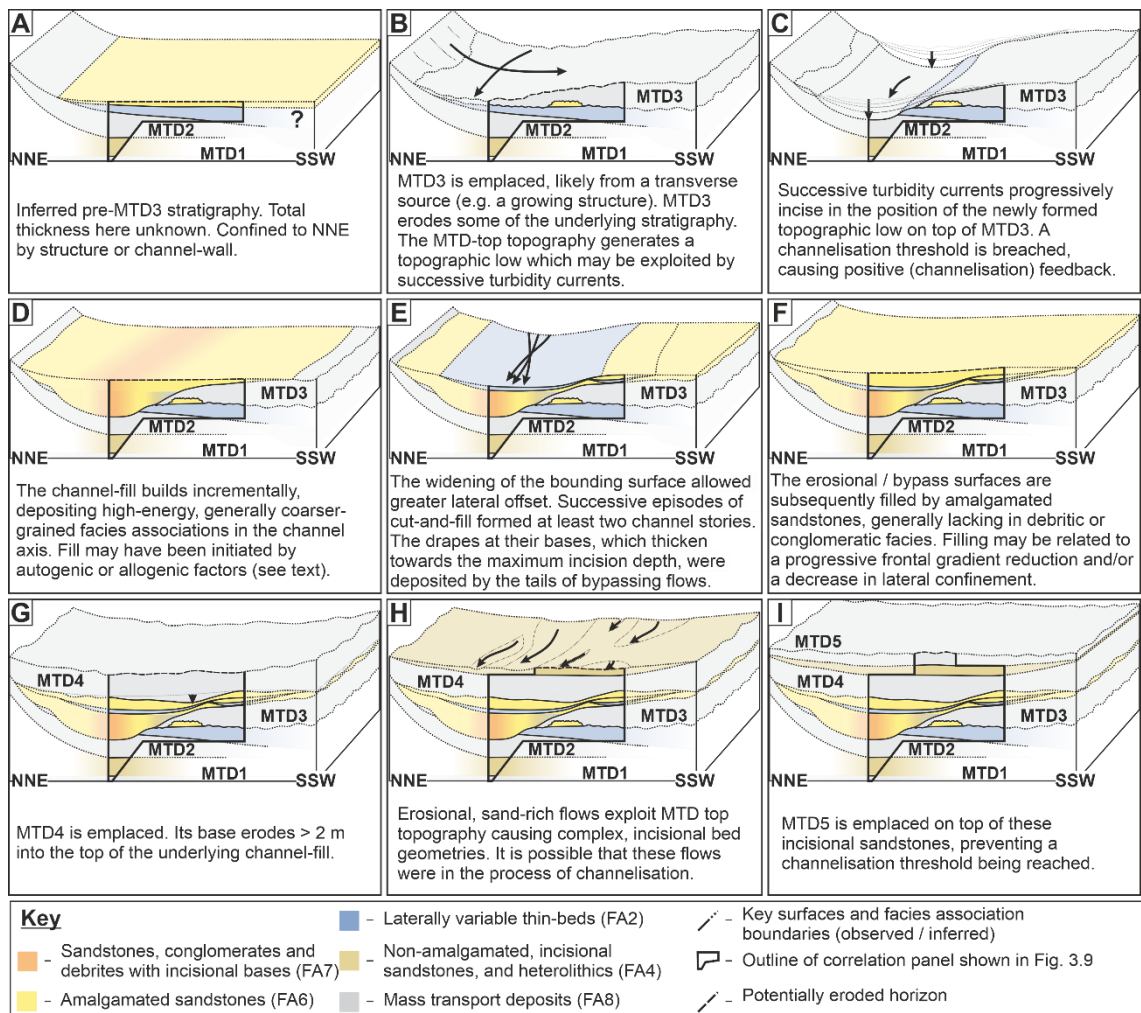


Figure 3.13 – Sketch block models showing the evolution of Barranco de la Caxigosa through nine time steps (A – I). Interpretation is informed by panels presented in Fig. 3.9 and displayed herein.

Key Surfaces and Hierarchy:

Channelised deposits are hosted within concave-up surfaces which may be generated by erosion and/or cogenetic thin-bedded turbidites formed from overspill (Hodgson et al., 2011; Brunt et al., 2013b). At least three hierarchical orders of confining surface are observed, which are named according to the hierarchical nomenclature scheme of Sprague et al. (2005; Fig. 3.9). These orders are distinguished based on scale and the recognition of nested surfaces starting at the smallest: bed bases. While key surfaces are used to define each hierarchical order, in areas where bed truncation is not apparent, these surfaces are picked out by major changes in facies associations:

(1) Bed / bedset surfaces (< 3 m deep) with scour-like geometries are observed in palaeoflow-parallel and -perpendicular sections (Figs. 3.8, 3.9); in sections subparallel to flow (SE-NW; e.g., location 18, Fig. 3.2) megaflutes can be observed. Scours were cut by the erosive part of an unsteady flow (Kneller, 1995), or by wholly erosive or bypassing flows. They were filled by the depositional part of the scour-forming flow, or by a subsequent depositional flow (e.g., Kane et al., 2009b; Stevenson et al., 2015; Bell et al., 2018a). The process of cut and fill builds stratigraphy incrementally in deep-water channels.

(2) Channel story surfaces (3-10 m deep at axis) are concave-up and elongate (in the direction of local palaeoflow), and are best observed at Barranco de la Caxigosa (Fig. 3.9). These cut through bed and/or bedset fills and exist within larger channel-fill surfaces (below). Ranges for the typical depth of incision of bedsets and channel stories overlap, such that these two scales can be difficult to distinguish (Sprague et al., 2005; Cullis et al., 2018). However, at least three channel stories are identified at Barranco de la Caxigosa (Fig. 3.9), and at least five in Muro Sandbody outcrop 4 (Fig. 3.8). Sprague et al. (2005) quote typical channel story thicknesses of 3-5 m, meaning that scale overlap with channel fills (10-30 m) is unlikely. However, the basal 10 m of Muro Sandbody outcrop 4 is interpreted to belong to a single channel story. In axial sections, distinguishing bed- or bedset-scale amalgamation within a story from a story bounding surface is difficult. Therefore it is possible that, within this package, more stories are hidden due to the cliff striking at a low angle to local palaeoflow, or that an overlap may exist between the channel story scale and the channel-fill scale.

(3) Channel-fill surfaces (10-50 m deep at axis). At Barranco de la Caxigosa, vertically and laterally stacked channel stories are confined at both margins by a master basal concave-up surface, and collectively constitute the channel-fill. At Muro de Bellos, the master confining surface may simply be a compound surface resulting from vertical and lateral amalgamation of the bases of channel stories towards the SW. In both cases

this master surface also acts as the confining surface to channel stories (Figs. 3.12, 3.13).

Vertical and Lateral Facies Variability:

Channel story 1 in Barranco de la Caxigosa (Fig. 3.9) exhibits a lateral facies transition from high-energy deposits of FA7 towards the “axis”, through lower-energy “off-axis” deposits of FA4 and FA6, to fine-grained, laterally variable thin-bedded FA2 deposits at its “margin” (sensu McHargue et al., 2011; Hubbard et al., 2014). Sandstone beds of marginal FA2 deposits thin towards (and sometimes onlap onto) their confining surface; towards the axis they thicken or are truncated by the incisional bases of overlying beds. The channel margin thin beds in Barranco de la Caxigosa represent the interplay between (i) marginal deposits of dominantly bypassing flows that did not deposit along the palaeo-thalweg, (ii) the marginal expression of fully depositional flows which thickened towards the channel axis, where some were subsequently eroded, (iii) deposits left by the tails of bypassing flows, and hosted within scours, and (iv) fine-grained drapes which formed during quiescent periods. Lenses of FA2, independent of the aforementioned margin deposits, exist within the axial fill. These overlie bedset- and channel-story-scale surfaces; they are thickest in the deepest point of the surface and pinch out towards the margin (Fig. 3.9). Constituent sandstone beds thicken towards the axis of the lens, with thickness variations due to incision at their base. These lenses may represent bypass drapes (Barton et al., 2010; Alpak et al., 2013; Stevenson et al., 2015), whereby sediment from the tail of a dominantly bypassing flow filled topography generated by the flow itself or by a precursor flow. At the base of channel story 1, a single rippled sandstone likely represents reworking during a relatively short bypassing stage, after channel incision (Fig. 3.9). The bases of channel stories 2 and 3 are overlain by thick (> 1.5 m) bypass drapes that thicken towards the maximum depth of the confining surfaces, partially healing them. These are overlain by amalgamated sandstones (FA6), which are thickest in the axis of the confining surface and gradually thin away from it. Unlike in channel story 1, lateral transitions into marginal FA2 or axial FA7 deposits are not observed; transitions between axis and margin are accommodated by thinning of FA6 deposits and bypass drapes (Fig. 3.9). The infill of all stories in Barranco de la Caxigosa exhibit vertical trends associated with an upward decrease of energy. In story 1 this is represented by an upward decrease in debritic and conglomeratic facies. In stories 2 and 3 it is marked by the basal bypass drape and gradual fining-up of the overlying amalgamated sandstones (Fig. 3.9). In the margin of story 1, however, coarsening- and thickening-up is observed as beds and bedsets become progressively wider up-succession (Fig. 3.9; Hubbard et al., 2014). An apparent upward increase in the interpreted energy of facies at channel story margins may not be reflective of the

nature of the flows that filled it. As a concave-up surface is filled, widening of the conduit causes the margin pinch-out of coarse-grained beds to step away from the channel axis, leading to the superposition of thicker beds onto thinner beds.

In Muro Sandbody outcrop 4 (Fig. 3.8) FA4, FA6, and FA7 are seen transitioning laterally into one another, and are thought to exhibit a similar axial-to-marginal trend as in Barranco de la Caxigosa, except without laterally variable thin beds (FA2). Fining-up patterns of individual channel stories are also more subtle in Muro de Bellos. At their tops, channel stories 2 and 3 contain > 5 m packages of non-amalgamated sandstones (FA5) which are tabular across the outcrop. These overlie a sharp basal transition and are commonly incised by overlying, higher-energy facies associations (FA4, FA6, and FA7). In Muro Sandbody outcrop 4, the presence of FA5 in channel stories 2 and 3 marks a decrease in average flow energy, possibly due to autogenic processes, in response to a partial upstream blockage (potentially from an MTD) or to an upstream avulsion.

At channel-fill scale, an overall upward decrease in energy is inferred in Muro Sandbody outcrop 4. However, in Barranco de la Caxigosa, vertical facies trends are complex, as they are influenced by the stacking of the constituent channel stories.

Architecture and Migration Patterns:

The exposures at Muro de Bellos all strike at a low angle to local palaeoflow, making the architecture of the constituent channel stories difficult to ascertain. Therefore, extrapolation of architectures in the Muro de Bellos outcrop has been attempted using geometric relationships between confining surfaces and underlying stratigraphy, and assuming that channel stories exhibit similar axis-to-margin facies-association transitions as in Barranco de la Caxigosa (Fig. 3.9). Muro Sandbody outcrops 1 and 2 are along strike, at similar elevations (~ 980 m) and can be connected along palaeoflow. The master confining surfaces beneath outcrop 1 (Fig. 3.7C), outcrop 3, and outcrop 4 (Fig. 3.8) truncate progressively older underlying thin beds towards the NE (Fig. 3.7A). Muro Sandbody outcrop 3, which comprises dominantly axial FA7 and off-axis FA6 deposits, is laterally (perpendicular to palaeoflow) offset ~ 200 m and vertically offset ~ 50 m (not restored for local tilt of ~ 11 - 16°) from outcrop 2, which contains axial FA7 deposits. Muro Sandbody outcrop 4 is ~ 50 m laterally (perpendicular to palaeoflow) and ~ 30 m vertically offset from sandbody outcrop 3. In sandbody outcrop 4, four incision surfaces are observed, two of which cut progressively older underlying beds to the SW (into the cliff), the direction opposite to the incision at the base of the outcrop (NE); the cutting direction of the other two surfaces is not obvious (Fig. 3.8). While a general vertical decrease in the energy of the facies associations in Muro Sandbody outcrop 4 (Fig. 3.8) is interpreted, the base of channel stories 3 and 5 comprise dominantly off-axis FA6 deposits, interpreted as higher energy than the FA4 deposits that constitute the

basal part of their underlying channel stories (2 and 4 respectively). This variability may reflect changes in the overall energy of the fill of successive channel stories, or variability of channel story stacking, superimposing more axial onto more marginal facies associations.

McHargue et al. (2011) define two contrasting styles of stacking observed (in plan view) at channel-fill scale (therein “channel elements”): (i) disorganised, whereby successive channels do not resemble each other; (ii) organised, where successive channels modify the course of the previous element. Herein, this terminology is applied to describe the stacking of channel stories. The channel stories in Muro Sandbody outcrops 1–4 are interpreted to stack vertically and laterally to the southwest, generally in an organised manner (Fig. 3.12), based principally on the vertical and lateral offset of axial FA7 deposits between outcrops 2, 3, and 4, and the vertical change from the NE truncation of older underlying stratigraphy to SW truncation in outcrop 4. However, the superposition of channel stories containing high-energy FA6 deposits (stories 3 and 5) onto those containing lower-energy FA4 deposits (stories 2 and 5; Fig. 3.8) suggests that local variability may exist.

Compounded erosion of these channel stories may create a through-going surface on their southwestern side (represented by H5; Fig. 3.7); the architecture on the northeastern margin cannot be constrained (Fig. 3.12).

In Barranco de la Caxigosa, channel stories 1 and 2 are offset at least 70 m laterally and 6 m stratigraphically. Stories 2 and 3 are laterally offset by ~ 50 m, and the maximum depth of the confining surface of story 3 is ~ 50 cm stratigraphically lower than that of story 2. Although none of the stories is fully exposed, story 1 appears to have a lower aspect ratio than story 3. The master bounding surface, containing the channel-fill, displays a concave-up geometry which then abruptly flattens to the SSW; the concave-up part is ~ 6 m thick. The increase in lateral offset (relative to vertical) of channel story axes, and vertical increase in aspect ratio is concomitant with the widening and flattening of the master bounding surface (Fig. 3.9).

The channel-fill at Barranco de la Caxigosa is situated within an erosional bounding surface (Figs. 3.9, 3.13), in which the channel stories are stacked in a disorganised or compensational manner. Changes in lateral stacking and aspect ratio were potentially controlled by a widening of the master confining surface: stories 2 and 3, situated above the wider and shallower part of the master confining surface, experienced greater offset and formed channel deposits of higher aspect ratios, likely because their confinement was not dictated by the presence of a steep channel-wall.

3.6 Discussion

3.6.1 Timing of the Structures in the Arro System

The western deflection of ripples and cross beds (relative to flutes) and westward stepping of the lateral facies transitions in Sierra de Soto Gully (Figs. 3.4, 3.10) suggest that the formative flows interacted with growing seafloor topography to the east, likely caused by growth of the Sierra de Araguás thrust. Wedging geometries of the background thin beds (Fig. 3.7) and the onset of channelisation in Muro de Bellos are attributed to movement on the Muro and Sierra de Araguás thrusts (Fig. 3.12). Previous works suggest that structures in the most proximal outcrops were active at the time of deposition, with the growth of the Los Molinos Thrust as the cause of MTD emplacement at Los Molinos Road (Millington and Clark, 1995a, 1995b; Arbués et al., 2007a, 2007b). It is therefore also possible that the origin of the MTDs in Barranco de la Caxigosa was linked to the activity of the nearby Caxigosa thrust. Furthermore, cross sections through the Aínsa depocenter fill (e.g., Muñoz et al., 2013; Clark et al., 2017) commonly show a thinning of Arro stratigraphy towards the depocenter-bounding thrust-cored anticlines, suggesting that these structures were growing during deposition.

3.6.2 Controls on Variability in Channel-Deposit Architecture

Multiple autogenic and allogenic controls dictate the architecture and facies distribution of deep-water deposits (Clark and Cartwright, 2011). For example, sequence stratigraphy is built on various scales of external forcing (Vail et al., 1977; Gardner et al., 2003; Flint et al., 2011), whereas other studies focus on the stratigraphic response of autogenic processes (Pirmez et al., 2000; McHargue et al., 2011). Furthermore, studies from modern deep-water channel systems (e.g., Vendettuoli et al., 2019) are beginning to reveal the true complexity of seabed deposition. However, although it can be challenging to discern the extent to which individual factors control the nature of ancient sedimentary successions, it is possible to assess the relative importance of a suite of controls at various hierarchical scales.

At bed to bedset scale, local scouring and filling builds stratigraphy incrementally in a channel. Scours may be filled by their formative flow or by successive flows (Kane et al., 2009b). The preserved deposit of a flow may be present only in the axis or margin of a channel, or across its entirety (Hubbard et al., 2014, 2020). Variations in scour depth and fill between individual beds is likely due to random variations in the type and magnitude of individual flows.

Because there may be scale overlap between bedset and channel story surfaces, the relative likelihood of different factors controlling their inception may also vary, rather than being fixed for each level. Both Muro de Bellos and Barranco de la Caxigosa display

incision at the bases of their constituent channel stories, and a general upward decrease in the inferred energy of their constituent facies associations (Figs. 3.8, 3.9). Therefore, they are interpreted to result from repeated incision and filling of the surfaces that confine them. Repeated “cut and fill” can be attributed to:

- Increases (cut) and subsequent decreases (fill) in average flow magnitude and erosive potential arising from variations in sediment delivery rate and/or caliber enhanced by relative sea-level changes and/or climatic variations (Gardner et al., 2003; Flint et al., 2011).
- Surfaces being generated by erosive flows trying to maintain equilibrium, potentially after an upstream avulsion (Pirmez et al., 2000). In this case fill is initiated by backfilling due to a downstream blockage (Pickering et al., 2001) or a decrease in flow efficiency (Mutti et al., 1999; Hodgson et al., 2011, 2016), or by aggradation of a below grade channel, seeking its equilibrium profile (Pirmez et al., 2000; Kneller, 2003; Prather, 2003).
- The upstream migration of cyclic-steps (Hage et al., 2018; Vendettuoli et al., 2019; Englert et al., 2020) and/or knickpoints (Heiniö and Davies, 2007; Gales et al., 2019; Heijnen et al., 2020; Guiastrenec-Faugas et al., 2020, 2021) as seen in modern submarine channels, may produce an erosional surface. Immediately downstream of crescentic bedforms and knickpoints (commonly the location of hydraulic jumps) flow efficiency is reduced, resulting in deposition of higher-energy sediments from flows which would previously have bypassed (Postma and Cartigny, 2014; Hage et al., 2018; Vendettuoli et al., 2019; Heijnen et al., 2020; Guiastrenec-Faugas et al., 2020, 2021). As channel-floor topography is healed and the bedform or knickpoint migrates farther upstream, flow efficiency is reattained. This may cause a general upwards decrease in inferred flow energy as the higher-energy parts of flows bypass with increasing efficiency.
- Quasi-instantaneous erosion by a bypassing MTD (Dakin et al., 2013) or an oversized turbidity current may generate the confining surface. The infill is progressive: as the narrowest and deepest part of a concave-up surface (axis) is filled with high-energy facies, the effective conduit size widens. Lateral confinement is relieved, leading to a decrease in efficiency of the next flow, which may form a feedback mechanism, depositing progressively lower-energy facies.

The relative likelihood of these formative mechanisms can be determined based on the architecture of the channel-fill more generally. The architectural interpretation of Muro de Bellos is that of partially overbank-confined channel stories, whose southwestern migration is accommodated by small-scale avulsions (Fig. 3.12). Therefore, their architectural expression is likely due to (structurally derived) changes in

lateral confinement and axial gradient. In contrast, the internal architecture of the channel-fill at Barranco de la Caxigosa is less well organised; the bounding surface likely resulted from cut and fill. In this scenario, any of the aforementioned mechanisms may have formed its channel stories. However, the Barranco de la Caxigosa outcrop contains multiple MTDs with incisional bases, interbedded with channelised and non-obviously channelised turbidite deposits. Due to the MTD-prone nature of the deposits, it is possible that the confining surfaces of channel stories 2 and 3 were excavated partially or fully by large, erosive MTDs. The surface originally generated by this large flow may have been partially filled by the deposit of the formative MTD, and is likely to have been modified, progressively, by successive flows that shaped its preserved geometry (Fig. 3.9). Progressive incision alone, however, cannot be ruled out.

The master confining surface of the channel-fill at Muro de Bellos is interpreted to represent a compound surface. This did not exist as a basin-floor feature in its entirety at any point, but instead formed by the lateral and vertical migration (stacking) of its channel stories in response to movement on the Muro thrust (Fig. 3.12). The basal incision at Barranco de la Caxigosa is interpreted to have formed from the cut and fill of a steep-sided conduit, at channel-story hierarchical order. Once this basal story was filled, channel stories formed within a much larger conduit, potentially derived from structural confinement or a lower order channel surface. The evolution away from flow-scale lateral confinement was responsible for the increase in the ratio of horizontal to vertical stacking and lower-energy facies in stories 2 and 3 (Fig. 3.13). At the lowest order, an overall increase then decrease in the rate of delivery of coarse-grained sediment to each location is necessary for the inception, fill, and occlusion of these channels.

Observations from outcropping deep-water channel systems such as those in the Laingsburg (Di Celma et al., 2011), Capistrano (Campion et al., 2005) and Tres Pasos (Macauley and Hubbard, 2013) formations has led to the development of predictive models, wherein laterally offset stacking is observed at channel-fill scale, whereas channel stories are assumed to stack vertically with little or no lateral offset (McHargue et al., 2011). In both Muro de Bellos and Barranco de la Caxigosa, and in other systems of the Aínsa depocenter (Pickering and Cantalejo, 2015), lateral stacking of channel stories is observed. In Barranco de la Caxigosa, disorganised lateral channel-story stacking was driven by the interplay between MTDs and turbidites (Fig. 3.13); in Muro de Bellos, organised lateral channel-story stacking was driven by thrust-derived shifting of the depositional fairway (Fig. 3.12). It is possible that, in exceptionally tectonically active and MTD-prone areas like the Aínsa depocenter, the processes which typically affect the lateral stacking of channel fills, such as avulsion, MTDs and tectonic structure,

may act at smaller temporal scales. This may result in less predictable channel-story stacking patterns, and may obscure the distinction between channel stories and channel fills, making hierarchy-based comparisons with other systems difficult.

Despite their differences in architecture, vertical sections through the channel-fill in Barranco de la Caxigosa and Muro de Bellos (Muro Sandbody outcrop 4) show a similar facies trend: high-energy facies at the base, which gradually decrease upwards, with channel stories providing nested higher-order trends. In Muro de Bellos, this trend arises from the progressive superposition of off-axial deposits on top of axial facies associations. The presence of debritic and conglomeratic material at the base of both Muro Sandbody outcrops 1 and 4 (Fig. 3.7) suggests that the fill of the successive channel stories was similar. Therefore, observed vertical facies transitions are more likely to reflect the progressive migration of the channel-story axes, than a decrease in input flow energy between successive channel stories (Fig. 3.12). In Barranco de la Caxigosa, the trend in channel-fill is interpreted to be partly due to a marked widening of the master confining surface, leading to a decrease in flow efficiency in the axis. However, this widening allowed subsequent channel stories to stack with greater lateral offset (Fig. 3.13; Li et al., 2018). Axial deposits of channel stories 2 and 3 were superimposed onto the margin of channel story 1, leading to a local upward increase in inferred flow energy (Figs. 3.9, 3.13). The fill of channel story 1 exhibits the same pattern. While a section through the axis of channel story 1 (BCL1 in Fig. 3.9C) records an upward decrease in inferred flow energy, a section through the margin (in the position of BCL2b in Fig. 3.9C) records upward bed thickening (Fig. 3.9). This marginal trend is interpreted to be due to the widening of the depositional fairway as the channel was progressively filled, meaning that the sand-rich part of the flows could deposit over more of the channel floor (Hubbard et al., 2014). The decrease in flow-scale lateral confinement accompanying conduit widening may also have inhibited the bypass potential at the axis of the channel, causing an autogenic decrease in the inferred energy of channel-axis facies. Therefore, at this scale, vertical facies trends may be more influenced by filling of sea-floor topography rather than records of energy changes. At channel-fill scale (see Fig. 3.9), one-dimensional facies trends recording an upward decrease in inferred energy may be generated by the vertical and lateral migration of constituent channel stories (Muro de Bellos) (Figs. 3.7, 3.8, 3.12) or by the widening of the master confining surface (Barranco de la Caxigosa) (Figs. 3.9, 3.13). Therefore, stacking-pattern analysis is best undertaken at the channel-story scale. However, at channel-story scale, axial facies trends recording upward decreasing flow energies may be associated with marginal facies which record the opposite. Architectural information is therefore required when imposing environmental interpretations onto non-unique facies associations.

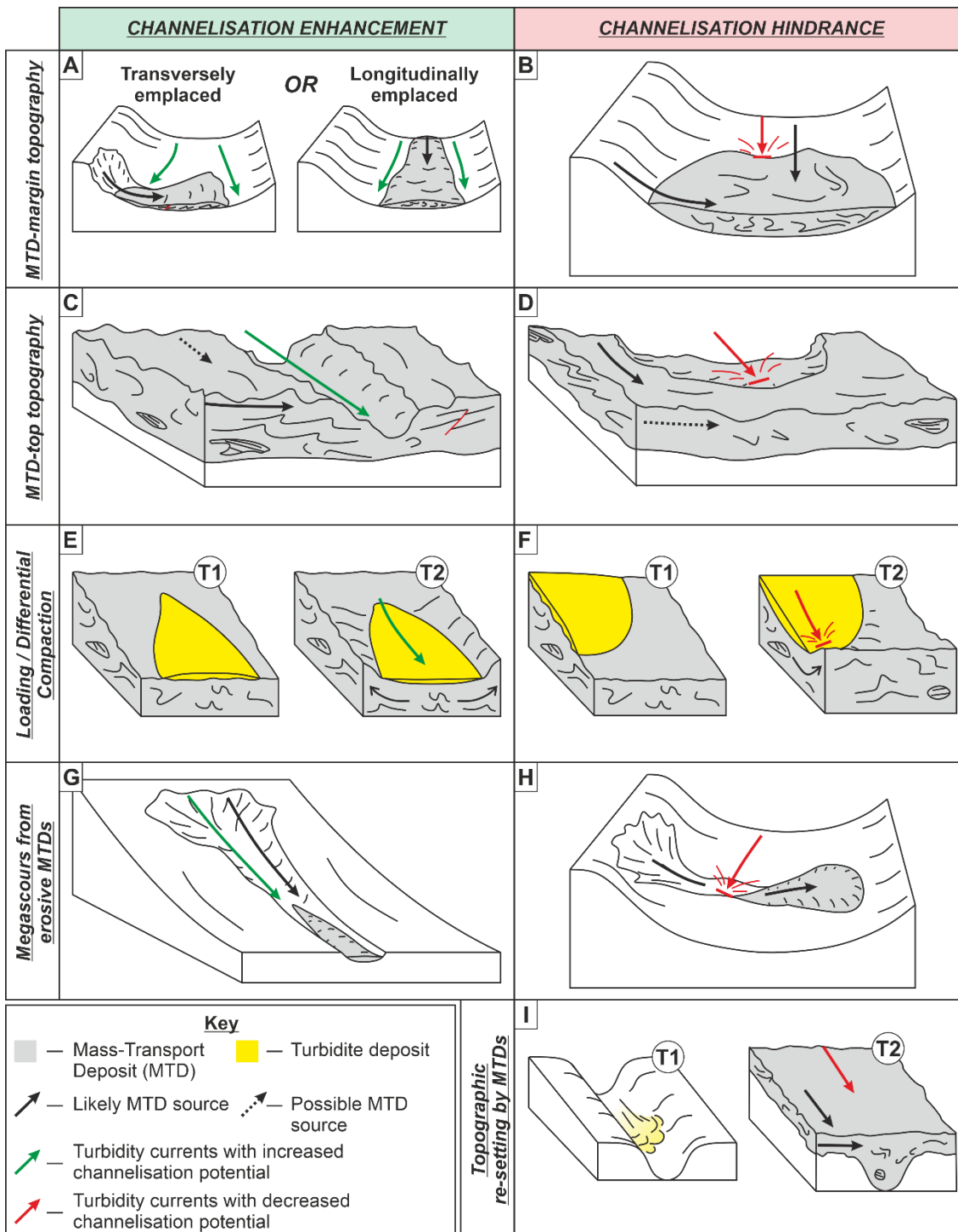


Figure 3.14 – Conceptual diagram showing the mechanisms by which MTD emplacement can help (A, C, E, G) or hinder (B, D, F, H, I) channelisation: A, B) interaction with MTD-margin topography; C, D) interaction with MTD-top topography; E, F) syndepositional substrate deformation and/or differential compaction; G, H) megascours excavated by erosive MTDs; I) MTDs filling a fully or partially channelised pathway and resetting basin-floor topography.

3.6.3 Influence of MTDs on Channelisation and Channel-Deposit Architecture

Previous studies have focused mainly on the effect of MTDs on established channel forms (e.g., Masalimova et al., 2015; Kremer et al., 2018). Mass-transport deposits can form blockages which may lead to backfilling (Posamentier and Kolla, 2003; Nelson et al., 2009; Bernhardt et al., 2012; Corella et al., 2016) or avulsion (Ortiz-Karpf et al., 2015). Less attention has been given to how MTDs may lead to, or prevent, the formation of channelised flow pathways. In the Arro system, the interplay between sediment supply, axial gradient and lateral confinement may be the principal drivers of channelisation at the channel-fill hierarchical scale, whereas MTDs may have a profound influence on the channelisation process at the channel-story scale. Five processes are proposed below, to describe the ways MTDs can enhance or hinder channelisation (Fig. 3.14) in elongate confined settings (bounded by a large-scale erosional surface or tectonic structures). Although the origin of the MTDs in the Arro system is unknown, it should be noted that each mechanism can be associated with either longitudinally or transversely emplaced mass-transport deposits. These process may co-occur.

3.6.3.1 MTD-Margin Topography

Arbués et al. (2007a) propose a model in which relief on the margin of transversely emplaced MTDs provides lateral confinement that is responsible for the formation of channels. A similar model may be invoked in Barranco de la Caxigosa: channel initiation, and formation of the bounding surface for channel story 1 (Fig. 3.13), likely formed in response to MTD-margin topography (Fig. 3.14A). In the case of transversely emplaced MTDs, either the margin farthest from the source (e.g., Arbués et al., 2007a) or the near-source margin (e.g., Kremer et al., 2018) can provide this confinement (Fig. 3.14A). Other studies from the Austrian Molasse Basin (Bernhardt et al., 2012; Masalimova et al., 2015) show how the lateral edges of longitudinally emplaced MTDs can have the same effect (Fig. 3.14a). Pickering and Corregidor (2000, 2005) show how the upstream margin of an MTD can frontally confine or reduce the axial gradient of subsequent turbidites, causing a loss of efficiency which may hinder channel development (Fig. 3.14B).

3.6.3.2 MTD-Top Topography

The effects of MTD-top and -margin topography are similar. MTDs, particularly large slumps and slides, often exhibit very complex topography on their tops (Armitage et al., 2009; Kneller et al., 2016; Brooks et al., 2018b; Ward et al., 2018; Bull et al., 2020). Depressions elongate in the direction of palaeoflow provide lateral confinement and are likely to encourage channelisation (Fig. 3.14C). Thickness variations and localised scouring in turbidite deposits that overlie MTDs in Barranco de la Caxigosa (comprising

DE3 deposits) are interpreted as the result of interaction with such depressions (Figs. 3.11, 3.13). Depressions which have no elongation or are elongate in a palaeoflow-perpendicular orientation may provide frontal confinement and therefore hinder channelisation (Fig. 3.14D).

Accentuation or hindrance of channelisation can be achieved by either transversely or longitudinally emplaced MTDs. However, the typical distribution and orientation of structures on large MTDs, with secondary ridges striking at a high angle to the emplacement direction (Sharman et al., 2015), means that transversely emplaced MTDs are more likely to encourage channelisation, whereas longitudinally emplaced MTDs are likely to hinder it.

3.6.3.3 *Syn-depositional Substrate Deformation and/or Differential Compaction*

The complexity of the composition of MTDs dictates the spatial distribution of mechanically strong and weak areas. Lithological zones of varying competence and the presence of large mostly undeformed blocks may allow higher compaction rates on top of weak zones (Alves, 2010; Dykstra et al., 2011; Ward et al., 2018). Furthermore, the depositional weakness of mud-rich MTDs may be sufficient for evacuation of substrate material below subsequently deposited turbidites (Kneller et al., 2016). If the initial MTD-top deposits are elongate and aligned with local palaeoflow, differential compaction may cause lateral confinement and hence encourage channelisation (Fig. 3.14E). If the deposits and the depression formed by their presence are elongated in a palaeoflow-perpendicular orientation or are not elongated, frontal confinement and ponding may arise, inhibiting channel formation (Fig. 3.14F). Substrate deformation and/or differential compaction is likely responsible for the lateral facies transitions observed in the turbidite packages which are underlain and overlain by MTDs (DE3) and may have augmented channelisation in Barranco de la Caxigosa.

3.6.3.4 *Megascour Excavation by Erosive MTDs*

Dakin et al. (2013) show how longitudinally sourced, erosive-mass-transport deposits in the Upper Hecho Group can create “megascours”, which may show cross-sectional profiles similar to submarine channels (see also Moscardelli and Wood, 2008; Brooks et al., 2018b; Soutter et al., 2018). The proximal-distal longitudinal section of Dakin et al. (2013) through the Aínsa II fan passes from a fully evacuated elongate megascour on the slope, through a zone filled with chaotic deposits at the base of slope, ending distally in turbidite deposition. These quasi-instantaneously generated pathways can provide sufficient lateral confinement to subsequent turbidity currents for a channelisation threshold to be exceeded (Fig. 3.14G). A similar process has been documented at larger scales, where lateral confinement and a local increase in the axial

gradient can be provided by the proximal headwall scar of a large MTD (Qin et al., 2017). The stratigraphic and architectural context of channel stories 2 and 3 in Barranco de la Caxigosa (below erosive MTD4; Fig. 3.9) suggest that their confining surfaces may have been formed or initiated by mass-transport-derived megascours. These megascours may have been exploited and possibly significantly modified by subsequent bypassing, and potentially erosive, flows, which formed channel-base drapes, and were eventually filled by amalgamated sandstones (Fig. 3.13E, F). If the axial orientation of the erosional surface is perpendicular to local palaeoflow, the downstream wall of the erosional surface may cause a decrease in axial gradient and block, or deviate, successive turbidity currents (Fig. 3.14H). Commonly, the erosional basal surfaces of MTDs on the lower slope and basin-floor are partially or fully filled by the remnant deposit of their formative flow (e.g. MTD4, Fig. 3.9; Dakin et al., 2013). The lack of remnant MTD at the base of channel stories 2 and 3 may be because: (i) Barranco de la Caxigosa was sufficiently proximal, or possessed a sufficient axial gradient, for MTDs to have fully evacuated their basal surface (Gomis-Cartesio et al., 2018), (ii) the flows that formed the basal surfaces of channel stories 2 and 3 were abnormally large and were therefore able to erode and bypass for longer distances downstream, or (iii) the remnant MTD has been eroded and replaced by subsequent turbidity currents and their deposits (e.g., Qin et al., 2017).

3.6.3.5 Topographic Resetting by MTDs

Of the five turbidite packages that separate the MTDs in Barranco de la Caxigosa, only one is obviously channelised. The mechanism invoked to explain the hindrance of channelisation in these non-channelised intervals (which, together with their associated MTDs, form DE3) is burial by subsequent MTDs. A large depositional MTD may fill the elongate flow pathway, suppressing and effectively resetting the basin-floor topography (Figs. 3.11C, 3.14I); the channelisation process is thereby halted and must then start again (McArthur and McCaffrey, 2019).

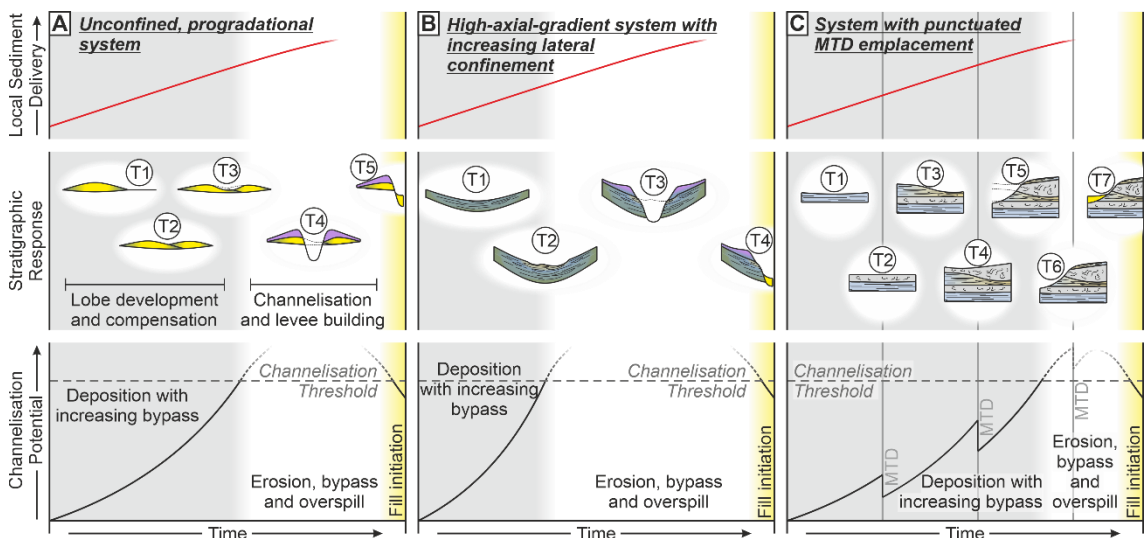


Figure 3.15 – Conceptual diagrams showing how progressive, structurally derived lateral confinement, and the punctuated emplacement of MTDs can affect channel inception and resultant sedimentary architecture: A) in an unconfined, progradational system experiencing increasing local coarse-grained sediment delivery, a channel will incise through unconfined precursor deposits after a channelisation threshold is crossed (sketches based on Hodgson et al., 2016); B) imposed lateral confinement from growing tectonic structures allows the channelisation threshold to be crossed earlier and at lower rates of delivery of coarse-grained sediment, inhibiting the development of sand-rich unconfined precursor deposits (example from Muro de Bellos); C) regular input of MTDs can interrupt the channelisation process by periodically removing the previously formed lateral confinement, which leads to delayed crossing of the channelisation threshold and the formation of DE3 deposits in replacement of sand-rich unconfined precursor deposits (example from Barranco de la Caxigosa).

3.6.4 Precursor Deposits and Channel Initiation

Examples of lobate, unconfined deposits cut by a channel that progrades over them are well documented (e.g., Gardner et al., 2003; Macdonald et al., 2011; Hodgson et al., 2011, 2016). Deposits from the Laingsburg depocenter, Karoo Basin, South Africa, record evidence of channel progradation cutting into unconfined deposits (Hodgson et al., 2011, 2016), and are herein compared with examples from the Arro system (Fig. 3.15). To first order, for fine-grained background deposits (FA1) to be overlain or incised by coarse-grained channelised deposits requires an increase in local delivery of coarse-grained sediment to the particular outcropping location (not necessarily to the whole basin). Channelisation in an unconfined, progradational system will typically be preceded by deposition of lobes (deposited by unconfined flows) followed by progressive channelisation, caused by incision and levee construction (Burgreen and Graham, 2014; Hodgson et al., 2016). If assuming time-transgressive flow confinement in submarine channels is the norm, the absence of precursor lobate deposits is enigmatic. Such cases may arise when: (i) a master erosional surface has completely eroded through the axis or the thinner marginal parts of a precursor lobe (more likely where lateral architectural control is limited), (ii) the conduit was formed (and filled) quasi-instantaneously, negating the requisite for frontal lobe development and channel progradation, or (iii) precursor unconfined deposits are absent or are not in the form of classical lobes, potentially because the axial gradient or externally imposed lateral confinement was sufficient to promote bypass.

Muro de Bellos is an example of where lobate precursor deposits are apparently absent. Progradation and channelisation are interpreted to have arisen from steadily increasing local delivery of coarse-grained sediment through a corridor confined by the Muro and Sierra de Araguás thrusts, both of which were active at the time of deposition (Fig. 3.12B). The assumed high axial gradient of the depositional fairway and broad lateral confinement imposed by these structures is thought to be partially responsible for the bypass-prone nature of the laterally variable thin-bed deposits (FA2) that form part of both increasing-to-decreasing-energy deposits (DE1), and progradational-to-overbank (DE2) deposits. Enhanced velocities related to high axial gradients and lateral confinement likely prevent the formation of thick and continuous lobate deposits (Fig. 3.12C). Contemporaneous narrowing of this (high gradient) corridor and increasing local delivery of coarse-grained sediment is then thought to have initiated a channelisation feedback mechanism and the formation of Muro Sandbody outcrops 1 and 2 (Fig. 3.12D). Subsequent migration of partially levee-confined channels to the SW arose due to movement of the inboard Muro Thrust (located to the NE) predominating over movement on the outboard Sierra de Arguas thrust (located to the SW) (Fig. 3.12D). In this example, the lack of well-developed, sand-rich, unconfined precursor deposits is therefore likely due to the elevated bypass potential experienced by the formative flows of turbidites of FA2. By extension, thrust-derived, progressive lateral confinement may have augmented the effects of a high axial gradient in lowering the channelisation threshold, allowing channelisation to occur earlier, and at lower coarse-grained sediment delivery rates, than in an unconfined setting (Fig. 3.15). Therefore, less sand is sequestered in the pre-channelisation stratigraphy, and more is transported down dip.

A delay in crossing the channelisation threshold can be caused by the regular deposition of MTDs that reset topography (Fig. 3.14I), because of their effect of removing the lateral confinement developed by preceding flows (Fig. 3.15). The result of this process is the development of pre-channelisation interbedded packages of MTDs and turbidites (DE3), such as those seen in Barranco de la Caxigosa (Fig. 3.9). These might represent the equivalent deposits in an MTD-prone setting to the pre-channelisation precursor lobes deposited in the absence of MTDs (cf. those shown by Hodgson et al., 2016). In areas where MTD and turbidite deposition occur concurrently, decreasing the frequency of MTD input or increasing the frequency or magnitude of turbidity-current input may lead to conditions favorable for channelisation.

3.6.5 *The Arro System as an Analogue*

Much of the research on the younger channelised systems in the Aínsa depocenter, principally the Banastón, Aínsa, and Morillo systems, is centered around the role of syn-depositional structures (Pickering and Bayliss, 2009; Bayliss and Pickering,

2015) or MTDs (Pickering and Corregidor, 2005; Dakin et al., 2013) in controlling the sedimentology and architecture of turbidite deposits; deposition in the Arro system was influenced by, and records the effects of, both. The processes discussed in this article can be exported to other exhumed topographically complex basins traversed by axial sediment routing systems such as the Magallanes foreland basin (Hubbard et al., 2008; Bernhardt et al., 2011, 2012), the Sinop basin (Leren et al., 2007; Janbu et al., 2007), the Grès du Champsaur (McCaffrey et al., 2002; Brunt et al., 2007), and the Gorgoglione Flysch (Casciano et al., 2019). Studies concerning interplay between structures, MTDs, and turbidite deposition in the Austrian Molasse basin (Bernhardt et al., 2012; Masalimova et al., 2015; Kremer et al., 2018) may provide a subsurface analogue.

The Arro system formed in an elongate corridor with high axial gradients bound by structures or canyon walls, similar to that of the younger Aínsa systems (Cornard and Pickering, 2019). The deposits therein can therefore be compared with those deposited in modern high-gradient confined systems such as large canyons (e.g., the Monterrey Canyon; Paull et al., 2018) or fjord-head delta slopes (e.g., the Bute Inlet, British Columbia; Hughes Clark, 2016). Comparing the results of this study to these modern systems allows (i) evaluation of the possible depositional signature of modern seafloor processes, and (ii) postulation of new mechanisms for the formation of recognised deep-water facies associations that have not hitherto been interpreted or have been attributed to other processes. For example, the dilute flows which form the background thin beds (FA1) of the Arro system have three possible origins, all of which have been monitored directly in fjord-head systems: (a) hyperpycnal flows, (b) small sediment failures on the shelf, upper slope, or in the feeder canyon (Clare et al., 2016), and (c) plume related density currents, which generate so-called “plumites” (Hizzett et al., 2018; Mutti, 2019). Weak, partially bypassing flows are inferred to have created the bedforms in laterally variable thin beds (FA2), specifically in increasing-to-decreasing-energy (DE1) and progradational-to-overbank (DE2) deposits. These may be analogous to some of the short-run-out flows observed by Hughes Clark (2016) and Paull et al. (2018), which do not reach the terminal deposits of the system. Traditionally, models accounting for the formation of channel stories invoke episodic variations in sediment supply and/or equilibrium gradients. Upstream-migrating knickpoints and crescentic bedforms are commonly recognised in modern submarine channels (Heiniö and Davies, 2007; Hughes Clark, 2016; Hage et al., 2018; Gales et al., 2019; Vendettuoli et al., 2019; Heijnen et al., 2020; Guiastrennec-Faugas et al., 2020, 2021; Englert et al., 2020; Chen et al., 2021), indicating that more spatio-temporally complex patterns of incision and deposition may be involved in building submarine-channel stratigraphy (Vendettuoli et al., 2019; Guiastrennec-Faugas et al., 2021). Crescentic bedforms have been shown to generate erosive surfaces that are concave-up in cross-section and incise underlying stratigraphy

by up to 3 metres (Vendettuoli et al., 2019; Englert et al., 2020). Similarly, knickpoints have been shown to generate concave-up surfaces that incise up to tens of metres into underlying stratigraphy (Heijnen et al., 2020; Guiastrennec-Faugas et al., 2020, 2021; Tek et al., 2021). Furthermore, in modern systems, different scales of bedforms have been observed to interact with one another. In the Bute Inlet, British Columbia, Canada, crescentic bedforms that exhibit sub-metre to metre-scale relief are observed to interact with larger knickpoints, which exhibit reliefs of metres to tens of metres (Chen et al., 2021). It is possible that, at a given point along a channel, the passage of these two scales of bedforms may generate nested scales of concave-up surface. In the channelised units (DE4) of the Arro system, cut and fill at bed and bedset scale may result from the passing of upstream-migrating crescentic bedforms, whereas channel-story scale cut and fill may result from the passing of upstream-migrating knickpoints; other causes however, cannot be discounted.

No interpretation is given for the source or triggers of flows that formed the Arro turbidite system because its constituent facies associations (from background thin beds, FA1, to sandstones, conglomerates, and debrites with incisional bases, FA7) exist as part of a continuum with non-unique representations. If the formative flows were initiated by a single process (e.g., hyperpycnal flows or instability-driven sediment failures) that acted at a large range of magnitudes, a natural lack of distinction between different facies assemblages and bed types might be expected. Alternatively, if flows of overlapping magnitude were initiated by different trigger mechanisms, a range of processes may result in deposits with similar sedimentological character. Flow genesis cannot, therefore, be differentiated using the methodologies employed here and in the current state of knowledge.

3.7 Conclusions

The Arro turbidite system is confirmed as a channelised, axial sedimentary system that traversed the SE-NW-oriented Aínsa depocenter during the Eocene (Ypresian). It records a complex interplay between tectonic structuration, emplacement of mass-transport deposits (MTDs), and routing of turbidity currents. The principal findings from this field-based study are that:

- The locations of sandy turbidite and muddy debrite pathways were controlled by the development of tectonic structures that were active at the time of deposition.
- The deposits of the Arro system can be grouped into eight facies associations. These form a continuum of constituent facies and bed geometries attributed principally to variations in the velocity, magnitude, and grain size of their

formative flows. In the Arro system, facies associations are non-unique to single depositional elements. Four depositional elements are recognised by the combined observation of groupings of facies associations, their lateral and vertical transitions, and the presence or absence of key surfaces: i) Weakly confined, increasing-to-decreasing-energy deposits (DE1), ii) progradational, weakly confined to overbank deposits (DE2), iii) alternating MTDs and turbidites (DE3), and iv) submarine-channel deposits (DE4). The different styles of observed channel architecture contain at least three orders of hierarchical organisation.

- Tectonic structuration and emplacement of MTDs can affect the timing and nature of channel inception, and may inhibit the formation of precursor sand-rich, lobe deposits of the type typically observed in unconfined, progradational systems. Thus 1) high axial gradients and lateral confinement (e.g., due to thrust-related fairway narrowing) can promote higher flow velocities, allowing the onset of channelisation earlier (and at lower rates of local delivery of coarse-grained sediment) than would be expected in an unconfined system, resulting in the development of discontinuous, thin-bedded deposits below the channelised deposits (as seen in the Muro de Bellos outcrop). 2) Extra-channel MTD emplacement may act to delay the onset of channelisation due to the punctuated healing of substrate topography and eradication of lateral confinement. The stratigraphic response to this is the presence of alternating MTDs and packages of non-channelised turbidites, below the channelised deposits (as observed in the Barranco de la Caxigosa outcrop).

- Five mechanisms describe how the emplacement of extra-channel MTDs can affect seafloor topography and therefore channelisation: (i) flow interaction with MTD-margin topography or; (ii) MTD-top topography; (iii) differential compaction of MTDs and/or syn-sedimentary loading into them; (iv) formation of megascours by erosive MTDs; or (v) resetting of basin-floor topography by MTDs that occlude fully or partially channelised pathways. Apart from the last, which may only impede it, any of these mechanisms may accelerate or hinder the channelisation process.

In this study confinement imposed by tectonic structures and by MTDs is seen to exert significant control on the inception, evolution, and fill of deep-water channels. The controlling processes are likely analogous to those observed or inferred in both modern and ancient confined systems. Therefore, in basins traversed by axial channel systems, the bathymetric expression of tectonic structures and MTDs may dictate the presence, distribution, architecture, and internal sedimentological character of channelised units and their precursor deposits.

4 Relating seafloor geomorphology to subsurface architecture: How mass-transport deposits and knickpoint-zones build the stratigraphy of the deep-water Hikurangi Channel

4.1 Summary

Monitoring of modern deep-water channels has revealed how migrating channel-floor features generate and remove stratigraphy, improving understanding of how channel morphologies relate to their deposits. Here, seafloor and subsurface data are reconciled through an integrated study of high-resolution bathymetry and three-dimensional seismic data imaging a ~ 150 km stretch of the trench-axial Hikurangi Channel, offshore New Zealand. On the seafloor, terraced channel-walls bound a flat, wide, channel-floor, ornamented with three scales of features that increase then decrease in longitudinal gradient downstream, and widen downstream: cyclic-steps, knickpoints and knickpoint-zones (in increasing size). Mass-transport deposits (MTDs) derived from channel-wall collapse, are bordered by wide and flat reaches of channel-floor upstream and by knickpoint-zones (reaches containing multiple knickpoints) downstream. In the subsurface, recognition of ten seismofacies and five types of surface enables identification of four depositional elements: channel-fill, sheet or terrace, levee, and mass-transport deposits. Integration of subsurface and seafloor interpretations reveals knickpoint-zones initiate on the downstream margins of channel-damming mass-transport deposits; they migrate and incise through the mass-transport deposits and weakly-confined deposits formed upstream, as the channel tends toward equilibrium. Downstream of a knickpoint-zone, a flat channel-floor is bounded by newly-formed terraces. Knickpoints migrate by eroding upstream and depositing downstream, generating filled concave-up (cross-sectional) surfaces in their wake. Within knickpoint-zones, knickpoint-generated surfaces are re-incised by subsequently-passing knickpoints to produce a composite bounding surface; this surface does not delineate the morphology of any palaeo-conduit. The Hikurangi Channel's subsurface architecture records the localised erosional response to mass-transport deposit emplacement via knickpoint-zone migration, showcasing how transient seafloor features can build channelised stratigraphy. This model provides an additional mechanism to conventional models of channel deposit formation through 'cut-and-fill' over long stretches of channel. These findings may aid subsurface interpretation in systems lacking a contemporary self-analogue or with poor data coverage.

4.2 Introduction

Deep-water channels are conduits formed by erosion, bypass and deposition from turbidity currents and other sediment-laden flows (Peakall & Sumner, 2015). Alongside terrigenous sediment deep-water channels also transport, and potentially sequester, pollutants (Zhong & Peng, 2021), organic carbon (Hage et al., 2020) and nutrients (Heezen et al., 1955). Their deposits can provide archives of environmental change (e.g. Prins & Postma, 2000; Castelltort et al., 2017) and catastrophic events such as earthquakes (e.g. Goldfinger, 2011; Mountjoy et al., 2018). Deep-water channels on the seafloor can reach thousands of kilometres in length (Covault et al., 2012, Shumaker et al., 2018). Their scales and morphologies vary along an individual channel and between channels; channel heights range from metres to hundreds of metres, and widths range from tens of metres to kilometres (Shumaker et al., 2018; Jobe et al., 2020). Deep-water channel deposits are hosted within elongate (longitudinally), concave-up (in cross-section) surfaces that can be identified in outcrop or seismic data and exhibit a broad range of cross-sectional architectures (Clark & Pickering, 1996; Deptuck et al., 2003; Macauley & Hubbard, 2013). Multiple, stacked concave-up surfaces may be hosted within larger surfaces (Clark & Pickering, 1996; McHargue et al., 2011). The common observation of multiple nested scales of surfaces has led to the categorisation of the hierarchical organisation of the deposits of many channel systems (Cullis et al., 2018). Resolution constraints of conventional seismic data make it difficult to distinguish filled palaeo-conduits from composite, diachronous surfaces formed by amalgamation of multiple smaller surfaces (Hodgson et al., 2016; Hubbard et al., 2020). Reconstructing palaeo-conduit morphologies from deep-water channel deposits is therefore problematic.

Bathymetry and shallow subsurface data reveal how features such as sediment waves and cyclic-steps (Hughes Clark, 2016; Hage et al., 2018; Mountjoy et al., 2018; Vendettuoli et al., 2019; Englert et al., 2020), knickpoints (Heiniö & Davies, 2007; Heijnen et al., 2020; Guiastrenec-Faugas et al., 2020, 2021), terraces (Babonneau et al., 2002, 2004, 2010, Hansen et al., 2015, 2017a) and mass-transport deposits (MTDs) (Hansen et al., 2015, 2017a; Watson et al., 2020), generate longitudinal variability in channel morphology. Repeat seafloor surveying has shown how migrating cyclic-steps and knickpoints are instrumental in constructing channelised stratigraphy. Cyclic-steps are crescent-shaped (widening downstream) in plan-view, and in long section possess a short, steep, downstream-dipping upstream side, and a longer, flat or upstream-dipping downstream side (Cartigny et al., 2011, 2014). Cyclic-steps in deep-water channels are typically regularly-spaced, exhibit wavelengths of tens of metres, metre-scale relief, and generate packages of stratigraphy at bed- to bedset-scale (up to a few metres thick; Hage et al., 2018; Vendettuoli et al., 2019; Englert et al., 2020). Knickpoints are crescent-

shaped or V-shaped (widening downstream) features that exhibit steep upstream sides, and shallower, downstream-dipping downstream sides. They are larger than cyclic-steps, are typically spaced hundreds of metres to a few kilometres apart, exhibit metres to tens of metres of relief, and generate larger-scale stratigraphic packages (tens of metres; Heijnen et al., 2020). Knickpoints migrate upstream by headward incision and downstream deposition. They can either exist as solitary channel-floor features, or as part of knickpoint-zones (sensu Heijnen et al., 2020; Guiastrenec-Faugas et al., 2020, 2021) within which, multiple, closely-spaced knickpoints collectively form longer reaches of elevated average longitudinal gradient. The formation of knickpoints and knickpoint-zones may allow deep-water channels to attain or maintain an idealised 'equilibrium profile' (Pirmez et al., 2000; Kneller, 2003; Guiastrenec-Faugas et al., 2020). However, their subsurface manifestation and preservation potential at larger architectural scales are less well understood.

Seismic studies of channel deposits on convergent margins (e.g. Ortiz-Karpf et al., 2015; McArthur & McCaffrey, 2019) are rarer than on passive margins (Deptuck et al., 2003; 2007; Jegou et al., 2008; Janocko et al., 2013; Jobe et al., 2015; Hansen et al., 2017a), with the three-dimensional architecture of axial channel-fills in deep-ocean trenches even less studied (McArthur & Tek, 2021). Here, high-resolution bathymetry and 3D seismic data from the trench-axial Hikurangi Channel, offshore New Zealand (Fig. 4.1) are integrated. This study aims to: (i) investigate how common seafloor surfaces and transient features (for example, MTDs, terraces and knickpoints) are manifested in channelised stratigraphy, how they interact with each other, and at what scales; (ii) compare the mechanisms of knickpoint formation and migration with those in other subaqueous channel systems; (iii) identify the barriers to, and ways to reduce uncertainty in, reconstructing the palaeo-seafloor from subsurface channel deposits. The objectives of this study are to: (i) provide the most detailed description, to date, of the three-dimensional subsurface architecture of a trench-axial channel system; (ii) use the modern Hikurangi Channel as a self-analogue to reconcile observations from the seafloor and subsurface, and link seafloor features (and inferred processes) to their deposits; (iii) generate three-dimensional palaeo-seafloor reconstructions through the formation of subsurface channel architecture, accounting for longitudinal variability. Bridging the disconnect between seafloor morphology and preserved stratigraphy is important for understanding how deep-water channels evolve, how they transport and sequester sediment, and how accurately their deposits may record palaeoenvironmental signals. The interpretations, models and principles presented herein challenge existing concepts of how channelised strata is built and may be exported to aid interpretation in other deep-water channel systems.

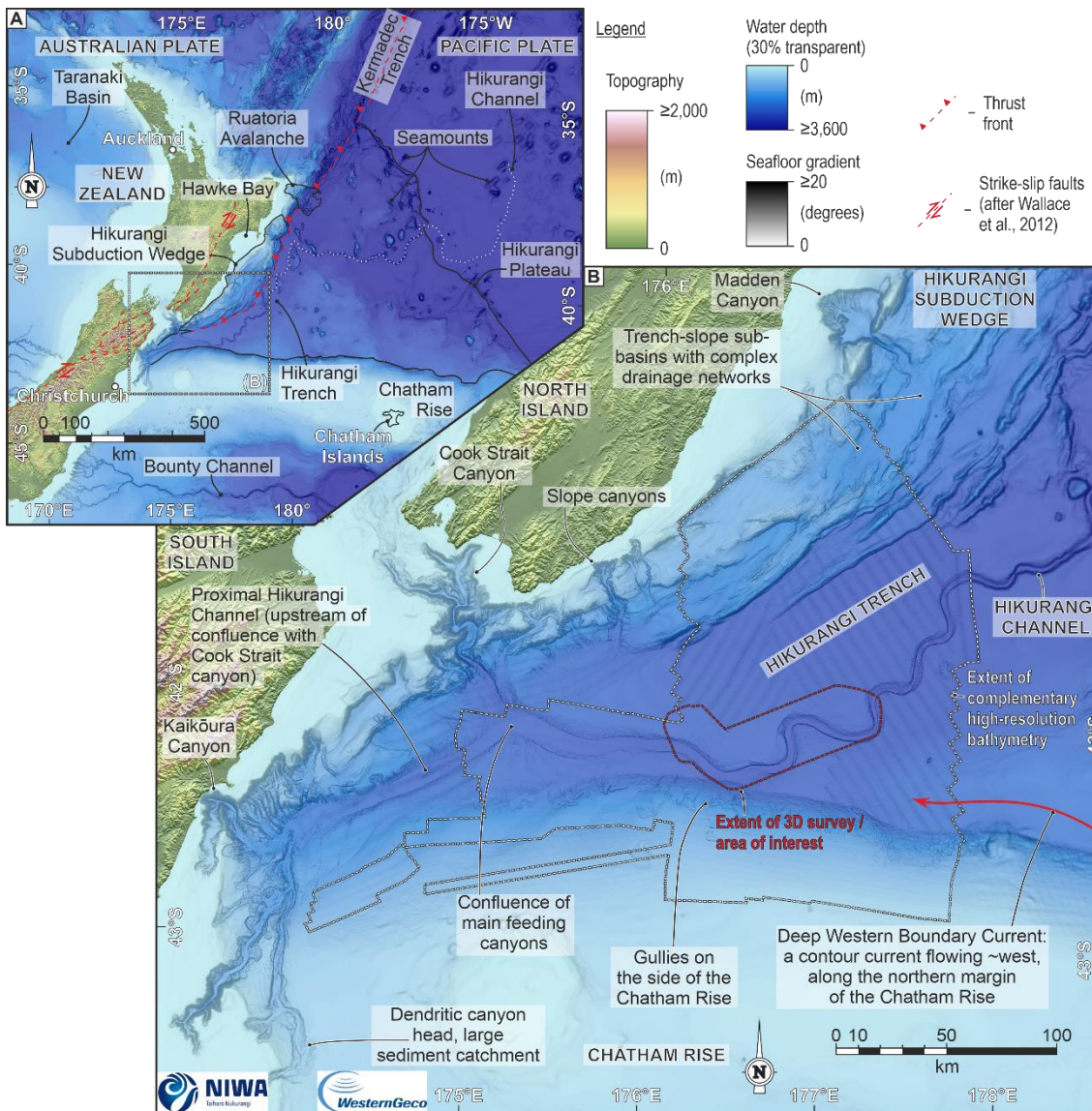


Figure 4.1 – Location maps showing: (A) the location of the Hikurangi Margin, and plate-scale features and structures; (B) the most proximal reach of the Hikurangi Channel, showing its relationship with its feeder canyons, slope-traversing trench-perpendicular systems, the Chatham Rise, Hikurangi Trench, and the Hikurangi Subduction Wedge. Bathymetry were provided by the New Zealand National Institute for Water and Atmosphere (NIWA), and bathymetry is displayed as slope gradient maps with transparent water depth overlays.

4.3 Geological Setting

The ~ 1800 km long Hikurangi Channel (Lewis & Pantin, 2002; Mountjoy et al., 2009, 2018) is located at the Hikurangi subduction margin, offshore New Zealand. The

subduction of the Pacific Plate beneath the Australian Plate (Fig. 4.1) began at ~ 27 Ma (Ballance, 1975; Nicol et al., 2007; Barnes et al., 2010; Lamb, 2011; Jiao et al., 2015), generating a north-east/south-west orientated trench (the 'Hikurangi Trench') and an adjacent subduction complex (Davey et al., 1986; Lewis & Pettinga, 1993; Nicol et al., 2007; McArthur et al., 2019). Towards its southern end, the deformation becomes increasingly oblique, eventually transitioning into the transpressive Marlborough and Alpine Fault systems (Wallace et al., 2004, 2012). Most of the fill of the trench and construction of the accretionary prism has occurred in the last ~ 3.5 Ma (Barnes & Mercier de Lepinay, 1997; Barnes et al., 2010; Ghisetti et al., 2016). The trench fill decreases in thickness from ~ 6 km in the south-west to ~ 1 km in the north-east (Lewis et al., 1998; Barnes et al., 2010; Plaza-Faverola et al., 2012). The fill dominantly comprises turbidites resulting from overbank deposition from the Hikurangi Channel, and transverse drainage networks that traversed the bounding slope (Lewis, 1994; Lewis et al., 1998; Mountjoy et al., 2009; McArthur et al., 2021).

The Hikurangi Channel is fed by a network of canyons, which incise the continental shelf and capture sediment from the North and South Islands (Fig. 4.1; Carter, 1992; Lewis, 1994; Lewis et al., 1998; Lewis & Barnes, 1999; Mountjoy et al., 2009, 2018). The channel is dominantly fed by the flushing of canyons during earthquake-triggered failure events (Carter et al., 1982; Carter, 1992; Lewis, 1994; Lewis et al., 1998; Lewis & Barnes, 1999; Mountjoy et al., 2009, 2018). Downstream of the confluence of its feeder canyons, the channel flows east for ~ 130 km along the northern margin of the Chatham Rise (Fig. 4.1; Wood & Davy, 1994; Davy et al., 2008). The channel then runs north-east for ~ 500 km through the trench before abruptly changing direction offshore of Hawke Bay (~ 110° in <10 km), due to subducting seamounts and submarine landslides blocking the trench (Fig. 4.1; Lewis et al., 1998; Collot et al., 2001; Lewis & Pantin, 2002). Downstream of its departure from the trench, the channel continues for ~ 550 km east across the Hikurangi Plateau before continuing for a further ~ 600 km across the Pacific abyssal plain to its terminus (Fig. 4.1; Lewis & Pantin, 2002). Leftward flow deflection by the Coriolis force and the presence of deep-ocean currents (particularly a shallow branch of the Deep Western Boundary Current) have been interpreted to impact overbank flow processes and sedimentation within the trench (McCave & Carter, 1997; Lewis et al., 1998; Lewis & Pantin, 2002; Bailey et al., 2020). Submarine landslides at the Hikurangi Margin range in scale from large margin collapses (Lewis et al., 1998; Collot et al., 2001; Couvin et al., 2020) to smaller collapses of the walls of the Hikurangi Channel (Lewis & Pantin, 2002; Watson et al., 2020).

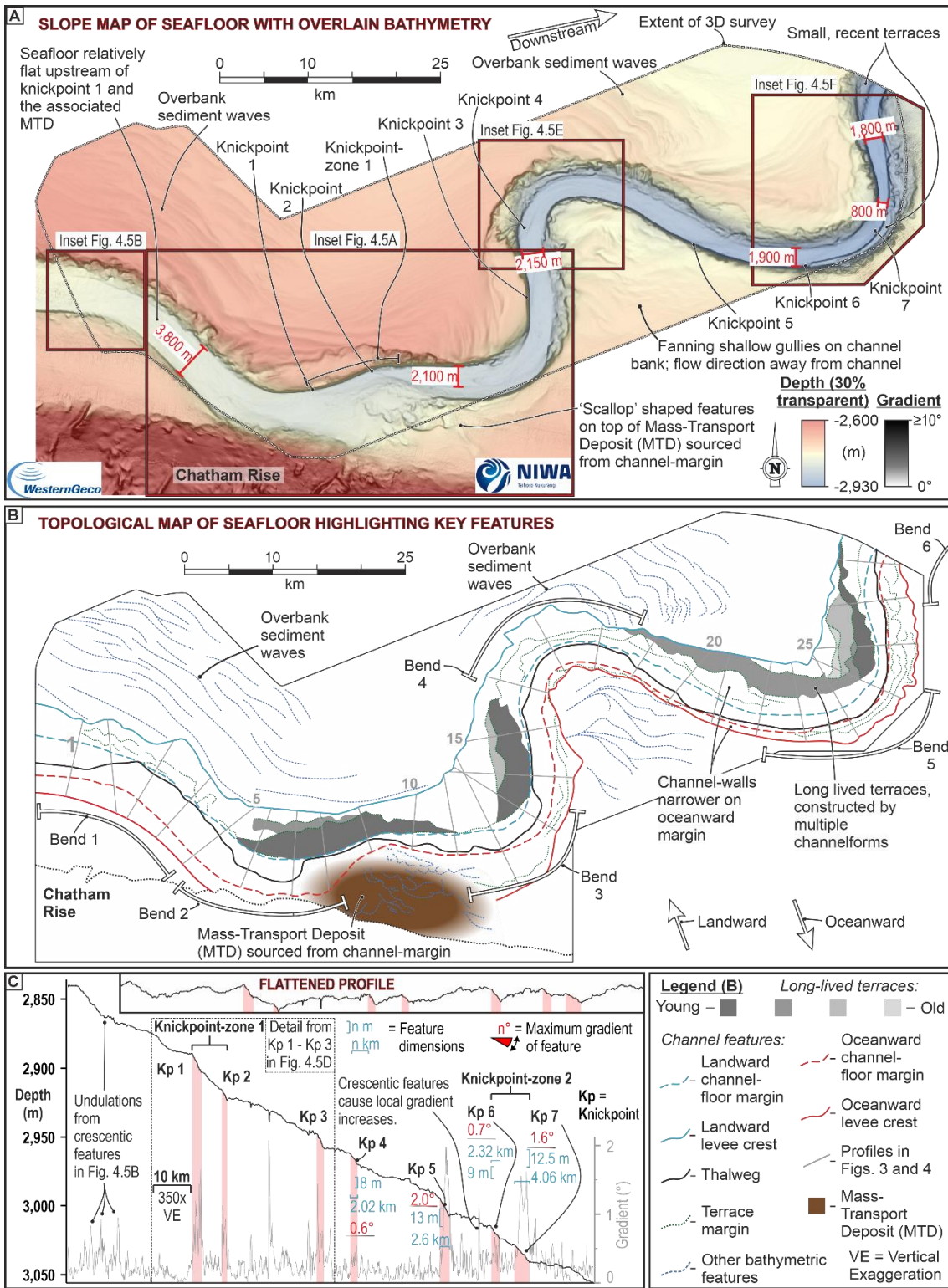


Figure 4.2 – (A) Gradient map with bathymetric overlay of the modern Hikurangi Channel within the study area. (B) Interpreted topological line drawing highlighting the location of bends 1 to 6 referenced in the text, main overbank and channel-wall features, and the locations of the profiles and morphometric features shown in Figs 4.3 and 4.4. (C) Detailed longitudinal depth and gradient profile along the thalweg of the channel showing the locations of the two knickpoint-zones, seven knickpoints, and other channel-floor features detailed in Fig. 4.5.

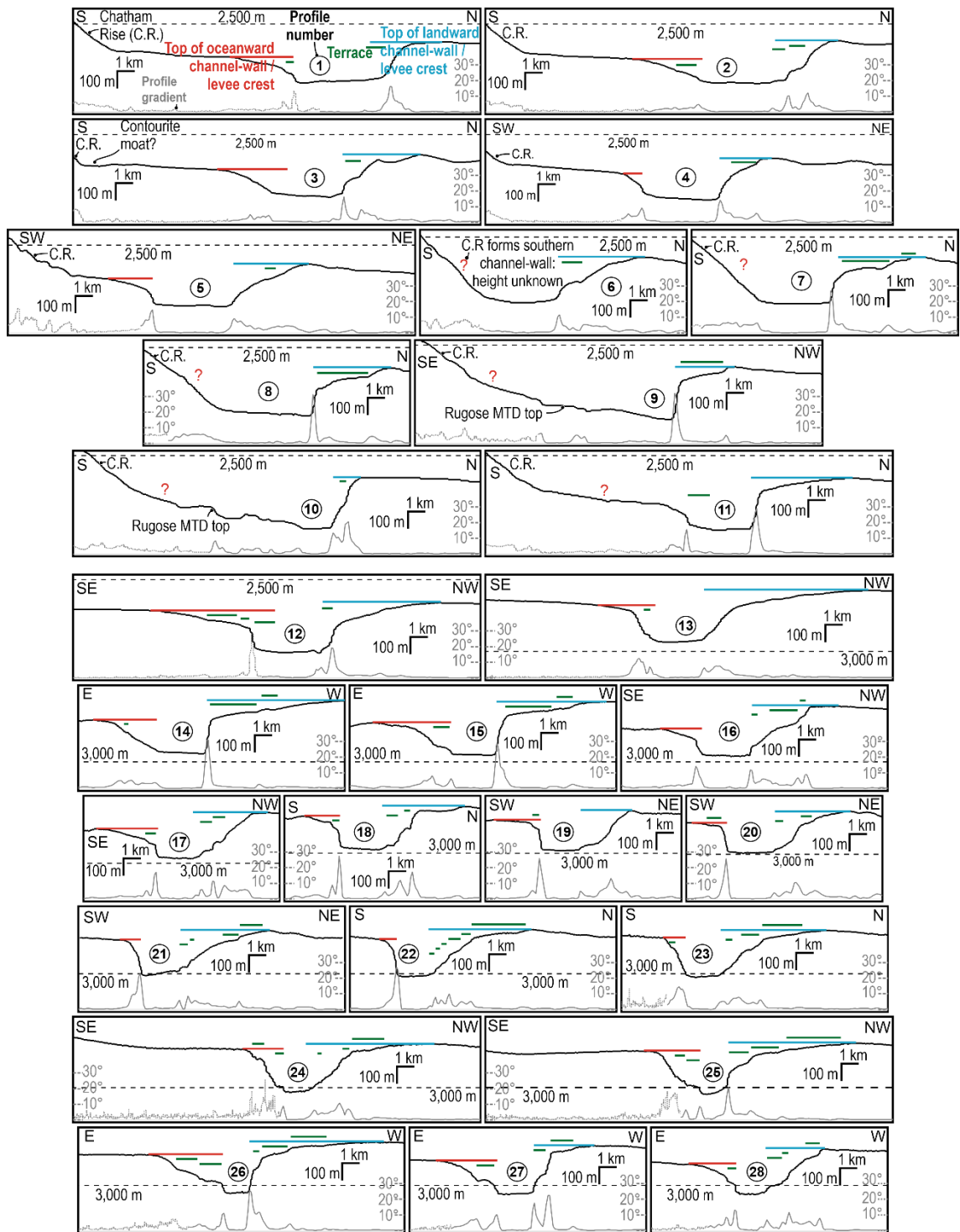
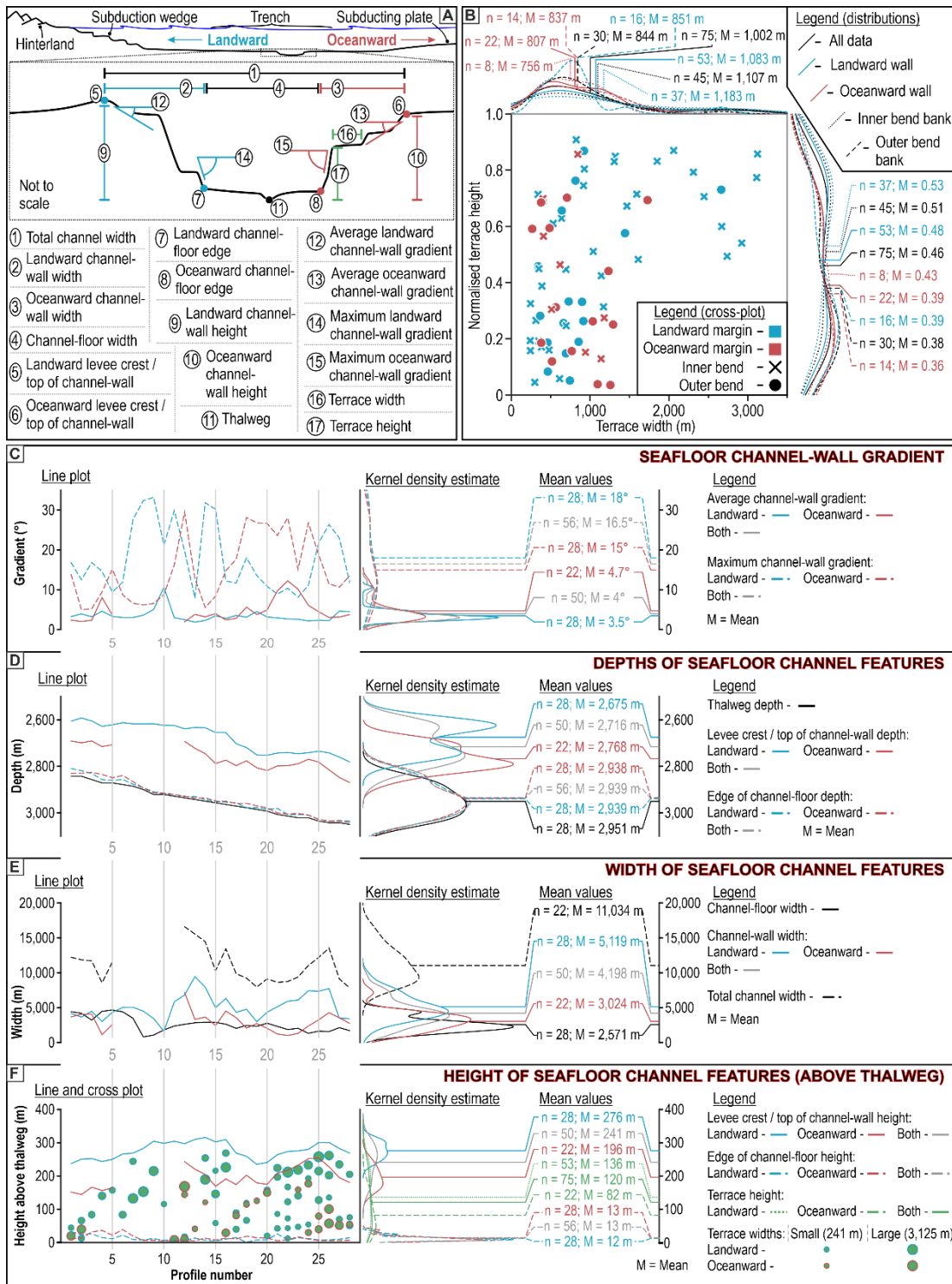


Figure 4.3 (above) – Cross-sectional seafloor profiles 1 to 28 (see Fig. 4.2 for locations), highlighting the features shown in Fig. 4.4.

Figure 4.4 (below) – (A) Summary sketch of the nomenclature used in the text and the parameters presented in parts (B) to (F). (B) Plot of terrace width versus normalised terrace height (its vertical position between the base and top of the host channel-wall), and the kernel density estimations thereof, derived from profiles 1 to 28 (Fig. 4.3). (C) Average and maximum channel-wall gradients against profile (a proxy for along-channel distance, which totals 140 km), and distributions and means

thereof. (D) Depth versus distance (profile number) plot of the thalweg, channel-floor edges and tops of the channel-walls, and the distributions thereof. (E) Width versus distance (profile number) plot showing the width of the channel-floor, channel-walls, and total channel width, and distributions thereof. (F) Plot showing the height of the channel-floor edges, channel-wall tops and the height, width and abundance of terraces above the thalweg, and distributions thereof. Note that a section (profiles 6 to 11 inclusive) of the oceanward channel-wall top is outside of the survey extent, measurements in this section are therefore missing in (C) to (F).

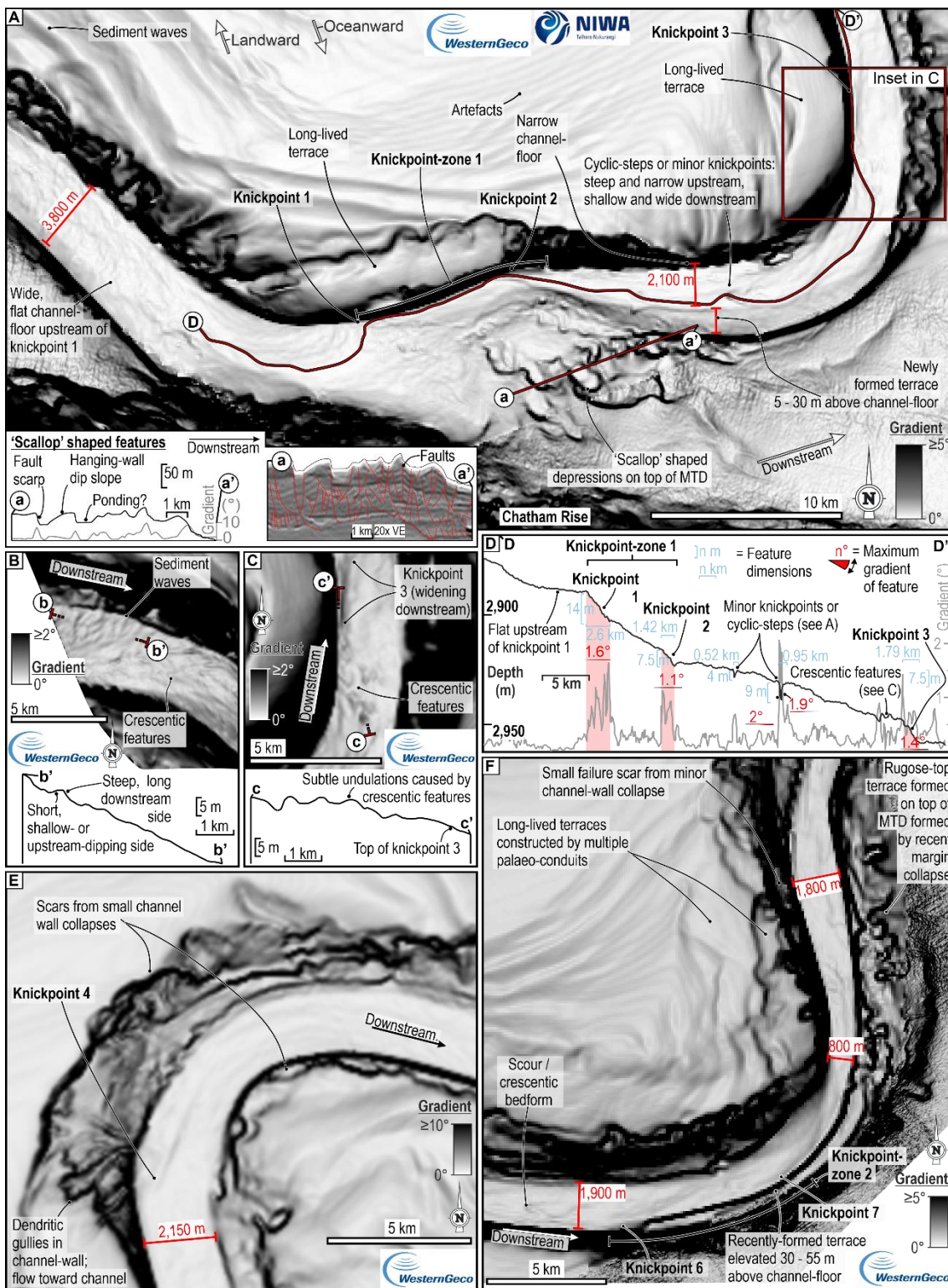
Data are provided in appendices 1, 2 and 3.



4.4 Data

This study primarily utilises 2600 km² of pre-stack Kirchhoff depth migrated (broadband) 3D seismic data, acquired in 2017 by WesternGeco. This dataset images a ~ 150 km long stretch of the Hikurangi Channel (Figs. 4.1 and 4.2). Full stack data are displayed SEG positive; a downward decrease in acoustic impedance is shown as a trough (white reflection). The horizontal resolution of the survey is ~ 25 m and the vertical resolution is ~ 7 m (values accurate at seafloor; Crisóstomo-Figueroa et al., 2020). High-resolution bathymetry rendered from the 3D seismic data is augmented with 25 m grid bathymetry data, provided by New Zealand Petroleum and Minerals (NZPM). This bathymetry data was collected by the National Institute of Water and Atmospheric Research (NIWA) using an EM302 multibeam echosounder at a frequency of 30 kHz, in 2012 and 2013 (see Bland et al., 2014). Collectively, these surveys cover ~ 32,000 km² and contain a ~ 320 km long stretch of the Hikurangi Channel (Fig. 4.1). The study focuses on the shallowest ~ 500 m of the trench fill, which contains several large (kilometres across) channelforms, each of which follows a similar path to their predecessor.

Figure 4.5 (below) – *Seafloor gradient maps and profiles from various features in the channel-floor, walls and banks. (A) Map showing the downstream-narrowing channel-floor containing knickpoints 1 to 3 and knickpoint-zone 1, bound by steep channel-walls with terraces of varied widths, adjacent to an area of overbank (to the south) containing scallop-shaped depressions; a seafloor and interpreted seismic profile are provided as insets to aid interpretation of the scallop-shaped features (uninterpreted dip map in appendix 5). (B) Map and longitudinal profile showing thalweg-perpendicular ridges interpreted as sediment waves and a train of crescentic features on the channel-floor. (C) Map and longitudinal profile through a train of crescentic features upstream of knickpoint 3. (D) Longitudinal profile through section in (A), showing: a low gradient upstream of knickpoint-zone 1; the sizes and gradients of knickpoint-zone 1; knickpoints 1 to 3; and crescentic features. (E) Map of bend 4 showing knickpoint 4 present on the outer bend, a number of small terraces on the inner bank and one larger terrace with dendritic gullies on the outer bank. (F) Map bend 5 showing: the channel-floor narrowing as it passes knickpoint 6 and 7, where it is bound by a newly formed terrace, and widening further downstream; numerous large terraces situated near the top of the inner bend channel-wall.*



4.5 Methods

Seismic interpretation, horizon mapping, surface extraction and attribute analysis (Root Mean Squared [RMS] amplitude, variance, spectral decomposition) were conducted in Petrel© and PalaeoscanTM. Seafloor maps and profiles were prepared using ArcGISTM and Python. Most of the bathymetric analysis, including the extraction of all seafloor profiles, was conducted using a seafloor horizon generated from the

seismic survey; outside the area covered by the seismic survey, complementary bathymetry data were used.

The interpretation herein is based on the identification of seismofacies and related surfaces, whose interrelations allow the classification of depositional elements. Descriptions of the seafloor, and subsurface seismofacies and surfaces are permitted by high-resolution imaging of the channel. Where reflector terminations hinder correlation, relationships between concave-up surfaces and packages of deformed reflectors interpreted as MTDs were used to determine a relative age framework and infer correlation.

4.6 Results

4.6.1 Seafloor expression

Description:

Within the study area, twenty-eight thalweg-perpendicular cross-sections (Figs. 4.2B, 4.3 and 4.4), a longitudinal profile (Fig. 4.2C), and bathymetric and gradient maps (Figs. 4.2 and 4.5) are used to quantify the seafloor expression of the Hikurangi Channel. The channel is concave-up in cross-section, with a relatively flat channel-floor and steep channel-walls (Fig. 4.3). The channel exhibits a moderate sinuosity (calculated as channel thalweg length divided by the straight line separation of the channel end-points; see Friend & Sinha, 1993) of 1.3 (cf. Peakall et al., 2012; Figs. 4.1 and 4.2). Landward channel-walls, on the inside and outside of meander bends, are consistently higher than oceanward walls (Figs. 4.3, 4.4D and 4.4F). Landward channel-walls shallow upward before reaching a levée crest, where the gradient reverses to form a wider (tens to 100 km) outer levée surface that dips away from the channel at $<2^\circ$ (Fig. 4.3). On the oceanward walls, levée crests and concomitant gradient reversals are largely absent, with the overbank dipping gently ($<0.5^\circ$) towards the channel, before steepening at the edge of the Chatham Rise or subducting plate (Fig. 4.3); in profiles 6 to 8 the Chatham Rise forms the oceanward channel-wall (Figs. 4.2B and 4.5B). Channel-walls dip between 2° and 12° (mean 4°) towards the thalweg (Fig. 4.4). Both walls are stepped, with steeper parts (up to 33°) connecting gentler parts ($<4^\circ$) that form terraces (sensu Babonneau et al., 2004) (Figs. 4.2 and 4.4). The oceanward channel-wall is narrower (mean 3024 m) and steeper (mean 4.7° ; measured from the top of the channel-wall to the thalweg) than the landward one (mean 5119 m and 3.5° , respectively); the landward wall exhibits steeper maximum gradients than the oceanward one (mean 18° and 15° , respectively) (Fig. 4.4C). Terraces occur from <10 m to 269 m above the thalweg, and range in width from 242 m to 3123 m (mean 1002 m). Terraces are: (i) wider towards the top of their host wall, (ii) more commonly located towards the base of the channel-wall and become more abundant distally, and (iii) wider and more abundant on the landward

side and inner meander bends (Figs. 4.4B, 4.4F and 4.5). At any given location a channel-wall may contain multiple terraces that may coalesce, upstream or downstream, with adjacent terraces (forming a larger terrace), the channel-floor, or overbanks (Figs. 4.2, 4.3, 4.4 and 4.5F). A variety of overbank features, such as two large fields of sediment waves that are concentric around bends 1 and 4, shallow fanning gullies inside of bend 4, and an area containing 'scallop-shaped' features (Figs. 4.2 and 4.5) may obscure the identification of terraces and levée crests.

The widths of the channel-floor (mean 2571 m) and the wider channel (including channel-walls; mean 11,034 m) generally decrease from ~ 4650 m and ~ 16,600 m (respectively) in proximal parts, to ~ 1700 m and ~ 7800 m (respectively) at the distal end of the survey (Figs. 4.2 and 4.4). Within the broader area of bathymetric coverage (Fig. 4.1), the channel thalweg exhibits an asymptotic longitudinal profile, with an average longitudinal gradient (measured from the mouth of the Kaikōura Canyon; Fig. 4.1B) of 0.23°; the longitudinal gradient within the study area (averaged over 140 km) is much shallower: 0.09° (Fig. 4.2C). Locally, both channel-floor width, and longitudinal gradient vary substantially over kilometre scales (Figs. 4.2C, 4.4E and 4.5).

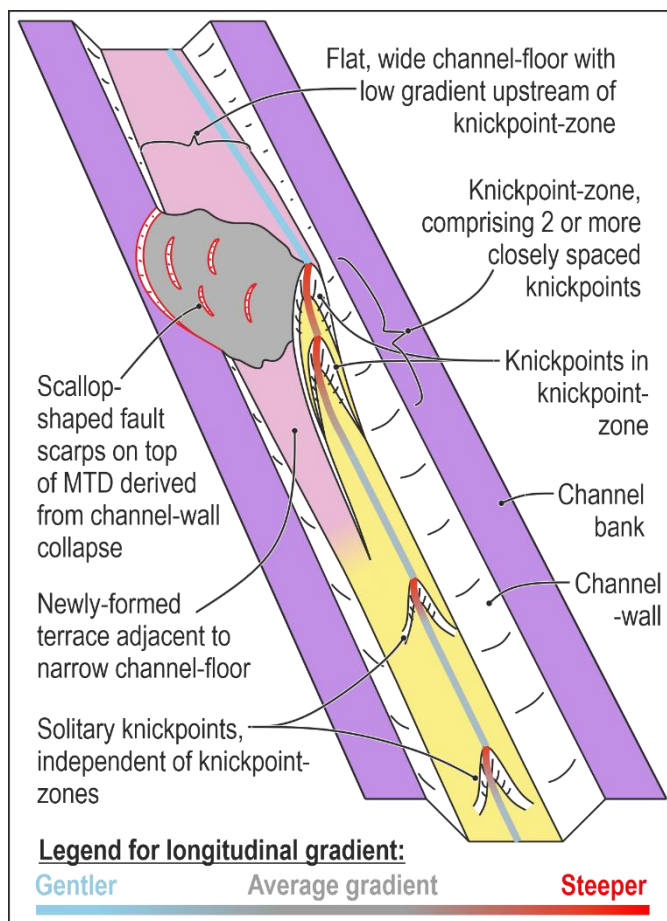


Figure 4.6 – Schematic 3D diagram showing the relationships between the various described seafloor features. The diagram is modelled on the area in Fig. 4.5A but the channel is displayed as straight, rather than sinuous as in reality, and the positions of solitary knickpoints are further upstream than in reality.

The largest scale longitudinal gradient variations occur in two steep knickpoint-zones (1 and 2, Fig. 4.2C), which are ~ 10,000 m long and ~ 35 m tall with downstream

gradients of $\sim 0.2^\circ$ (Fig. 4.2C; appendix 4); knickpoint-zone 1 is slightly steeper (0.212°) than knickpoint-zone 2 (0.191°). Seven smaller-scale steep areas, knickpoints 1 to 7, are also observed within the studied channel section (knickpoints 1 to 7 in Fig. 4.2C). Knickpoint-zones 1 and 2 contain two knickpoints each (knickpoints 1 and 2, and knickpoints 6 and 7 respectively; Fig. 4.2C), that superimpose higher magnitude gradient increases onto their host knickpoint-zone (Figs. 4.2, 4.5 and 4.6). Three solitary knickpoints (knickpoints 3 to 5; Fig. 4.2C), that exist independently of knickpoint-zones, are spaced at ~ 5 to 25 km intervals between knickpoint-zones 1 and 2 (Figs. 4.2, 4.5 and 4.6). Knickpoints are 1420 to 4060 m long (mean 2401 m), 7.5 to 14 m tall (mean 10 m), with maximum gradients of 0.6° to 2.0° (mean 1.3°) (appendix 4). In plan-view knickpoints and knickpoint-zones are narrowest upstream, at the point of maximum gradient increase. Knickpoint-zone 1 marks an abrupt change in channel morphology over <10 km longitudinally (Figs. 4.5A and 4.6). Upstream of knickpoint-zone 1 (and hence knickpoint 1) the channel-floor is 3500 to 4000 m wide and relatively flat; immediately downstream of the head of knickpoint-zone 1, the channel is effectively V-shaped with a very narrow (<200 m) channel-floor; ~ 10 km downstream of the head of knickpoint-zone 1, ~ 5 km of knickpoint 2, the channel-floor widens to ~ 2000 m and is adjacent to a flat, <1000 m wide, terrace elevated 5 to 30 m above the thalweg that gets progressively shorter, and eventually disappears distally over ~ 15 km (Figs. 4.5A and 4.6).

Knickpoint-zone 1 is north of and adjacent to the aforementioned area of 'scallop-shaped' depressions. These ~ 1 to 5 km wide (long axis), <25 m deep features dip steeply ($<10^\circ$) north on their southern side, and are shallower ($<5^\circ$) to flat on their northern side (Figs. 4.5A and 4.6). Into the subsurface, the scallop-shaped features can be traced to lineaments against which reflectors abruptly terminate and / or change in dip, all hosted within a chaotic <120 m thick package with a sharp basal contact with undisturbed underlying reflectors (Fig. 4.5A). Knickpoint-zone 2 (which hosts knickpoints 6 and 7) is ~ 5 km upstream of a locally narrow (800 m) stretch of channel-floor bordering a flat, <500 m wide terrace elevated 30 to 50 m above the channel-floor upstream of the narrowest point; downstream it borders a highly rugose, <2500 m wide terrace (Fig. 4.5F).

Subtle features are common on the channel-floor. The most common are crescentic features that are steep ($<2^\circ$) and narrow upstream but widen and shallow downstream (Fig. 4.5B and 4.C). They most commonly occur as thalweg-aligned trains of <500 m long, <5 m deep features, spaced <1 km apart, often near the head of knickpoints (Fig. 4.5B and 4.C). Where crescentic features are isolated (spaced <5 km apart), they are longer (<1 km) and deeper (<7.5 m) (Fig. 4.5F). Thalweg-perpendicular

ridges with straight <1 km long crests, steep and long (<750 m) upstream sides, and short (<300 m), shallowly-dipping or upstream-dipping sides are also present on parts of the channel-floor (Fig. 4.5B).

Interpretations:

Terraces may have initiated through: (i) the establishment of a new conduit that is laterally offset from the axial fill of a precursor conduit (punctuated channel migration; e.g. Maier et al., 2012); (ii) the formation of lateral accretion deposits in a migrating conduit (progressive channel migration; e.g. Abreu et al., 2003; Deptuck et al., 2007); or (iii) the local emplacement of an MTD from the collapse of a channel-wall (Hansen et al., 2017a,b). They subsequently aggraded by the marginal deposition of finer grained sediment from the overspilling upper parts of flows that traversed the newly formed conduit (Kane & Hodgson, 2011; Hansen et al., 2015). Narrow terraces with low elevations above the channel-floor formed recently on top of MTDs derived from the local collapse of a channel-wall, or the incision of a narrow conduit into the fill of a precursor, likely at the edge (Maier et al., 2012; Hansen et al., 2015, 2017a,b; Figs 4.5A, 4.5E, 4.5F and 4.6). These processes likely co-occur, causing the abundance of small terraces near the channel-floor. Larger terraces near the top of the channel-walls (Fig. 4.5F) are longer-lived features that likely formed during the establishment and infill of palaeo-conduits. Long-lived terraces can receive sediment from multiple sequentially-active palaeo-conduits (Fig. 4.2B), and are preferentially preserved on inner bends and destroyed on outer bends, as meanders expand (Fig. 4.5A and F).

Scallop-shaped features on the oceanward channel bank are interpreted as fault scarps on top of a quasi-instantaneously emplaced MTD that formed through channel-wall collapse (Figs. 4.2 and 4.5; see also Lewis & Pantin, 2002; Watson et al., 2020). It partially filled and dammed the channel, likely causing a reduction in flow velocity and deposition upstream (Pickering & Corregidor, 2000, 2005; Tek et al., 2020; Soutter et al., 2020), to form the wide, flat channel-floor upstream of knickpoint-zone 1 (Figs. 4.2, 4.5D and 4.6). Knickpoint-zone 1 formed because of increased flow velocities and erosive power in response to an increase in longitudinal gradient (Kneller, 1995) on the downstream side of the MTD. Upstream migration of knickpoints is interpreted as the primary erosive mechanism in the studied reach of the Hikurangi Channel, and operates at a smaller hierarchical scale than that of knickpoint-zones. The migration of knickpoint-zones (and their constituent knickpoints) allows the channel to re-attain its equilibrium after alteration (Heiniö & Davies, 2007; Guiastrennec-Faugas et al., 2020a). A narrow channel-floor and adjacent terrace may be formed downstream of a migrating knickpoint-zone (Deptuck et al., 2007; Heiniö & Davies, 2007; Guiastrennec-Faugas et al., 2020, 2021, Heijnen et al., 2020), as is observed downstream of knickpoint-zone 1 (Fig. 4.5A).

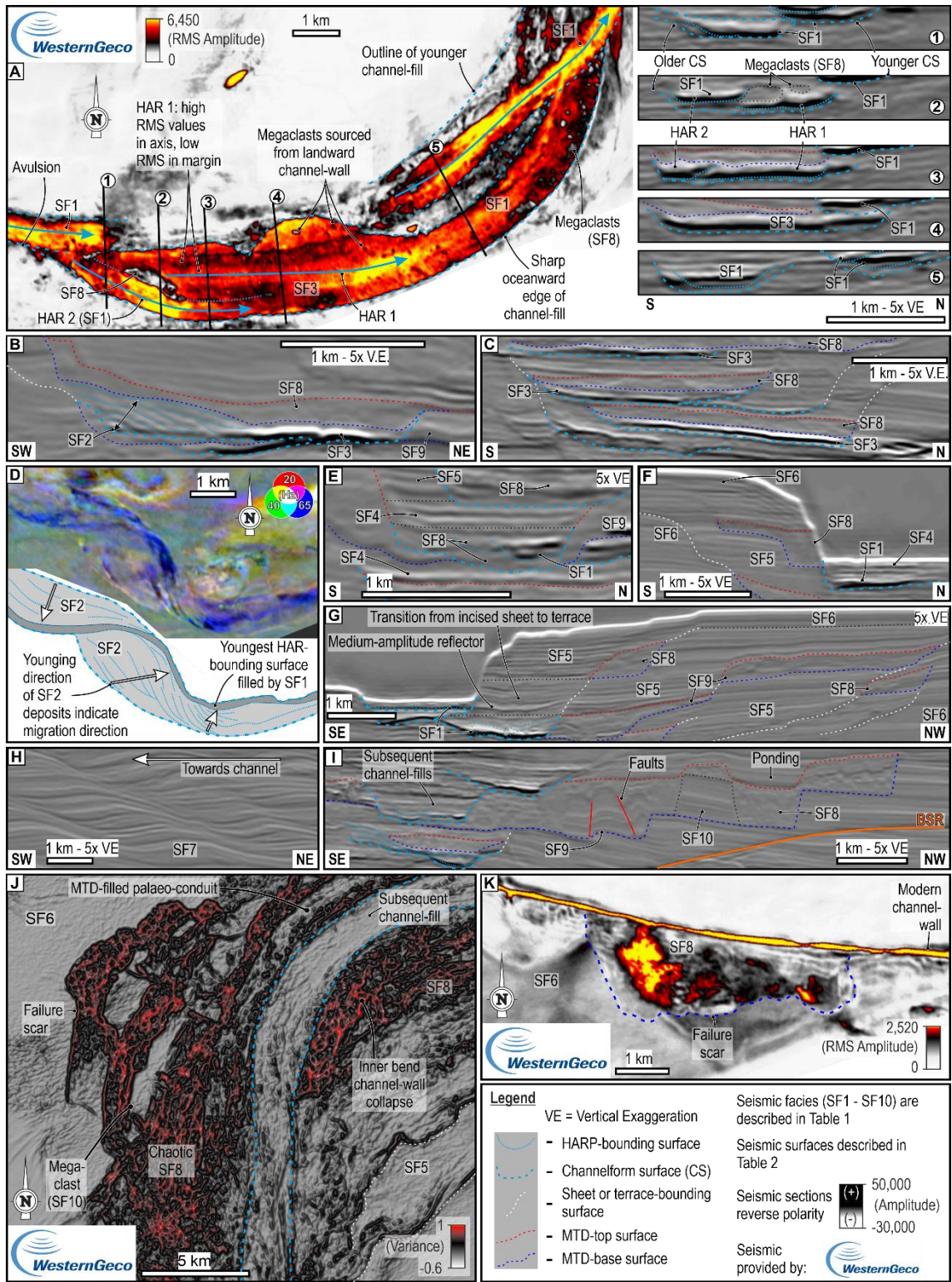
As knickpoint-zones migrate, they may shallow and lengthen until the conduit attains equilibrium. While knickpoint-zone 2 is also interpreted to have formed after the quasi-instantaneous emplacement of a channel-wall-derived MTD (Fig. 4.5F), it is shallower and longer than knickpoint-zone 1 (Figs. 4.2, 4.5A and 4.5F). Having migrated farther upstream, knickpoint-zone 2 has formed a long terrace where it has successively incised through the MTD (forming the rugose part of the terrace on the oceanward channel-wall in Fig. 4.5F), and the wide, partially ponded deposits that formed upstream of it (forming the flat part of the terrace on the oceanward channel-wall in Fig. 4.5F). Once a knickpoint-zone has passed, the newly-formed terrace will then aggrade as finer parts of flows are deposited on it. Knickpoints may initiate in response to a localised modification of a longitudinal profile (e.g. Heiniö & Davies, 2007), potentially by small MTDs derived from channel-wall collapse, effectively making them small knickpoint-zones. Alternatively, knickpoints may occur naturally through the exploitation of channel-floor relief or by longitudinal variations in flow velocity (Heijnen et al., 2020).

At the smallest scale, crescentic features interpreted as cyclic-steps (Cartigny et al., 2011, 2014), and ridge-like features interpreted as sediment waves (Mountjoy et al., 2018) are observed in discrete areas of the channel-floor (Fig. 4.5C); they may be more widespread but undetectable at the resolution of the dataset.

4.6.2 Seismofacies, surfaces and depositional elements

Ten seismofacies, categorised on the properties of their reflectors and/or their terminations, are described in Table 4.1. Five seismic surface types distinguished by abrupt changes in seismofacies, or reflector character, dip or thickness, are described in Table 4.2. Surfaces can be concave-up, or unidirectionally dipping (from sub-horizontal to vertical). For concave-up surfaces, reflectors above or inside the surface will be described hereafter as 'inboard'; reflectors outside will be described as 'outboard'. For unidirectionally dipping surfaces, reflectors on the down-dip side will be described as 'inboard' and on the up-dip side as 'outboard'. Interrelationships between seismofacies and surfaces have allowed the establishment of four types of depositional elements:

Figure 4.7 (below) – Seismic sections and z-slices displaying the ten seismofacies and five seismic surfaces observed in the area, containing: (A) RMS amplitude z-slice, from 3000 m depth, and seismic sections showing dominantly SF1, SF2, SF8, HAR-bounding surfaces and channelform surfaces; (B) section showing SF2, SF3, SF8, HAR-bounding surfaces, channelform surfaces, MTD-bases and MTD-tops; (C) section showing SF2, SF8, channelform surfaces, sheet or terrace-bounding surfaces, MTD-bases and -tops; (D) spectral decomposition and interpreted line drawing showing SF3, SF1, HAR-bounding surfaces, channelform surfaces; (E) section showing SF1, SF4, SF5, SF8, HAR-bounding surfaces, channelform surfaces, MTD-bases and MTD-tops; (F) section showing SF1, SF5, SF4, SF5, SF6, SF8, channelform surfaces, sheet or terrace-bounding surfaces, MTD-bases and MTD-tops; (G) section showing SF1, SF5, SF6, SF8, SF9, HAR-bounding surfaces, channelform surfaces, sheet or terrace-bounding surfaces, MTD-bases and MTD-tops; (H) section showing SF7; (I) section showing aerially extensive SF8, SF9 and SF10 deposits, HAR-bounding surfaces, channelform surfaces, MTD-bases and MTD-tops (BSR: Bottom Simulating Reflector); (J) variance attribute z-slice showing aerially extensive SF8 and SF10 deposits and their context with SF5, SF6, MTD-bases, sheet or terrace-bounding surfaces, channelform surfaces; (K) RMS amplitude z-slice showing a aerially non-extensive SF8 deposit and bounding MTD-base, and SF6.



Facies	Seismic properties	Description, distribution and variability	Interpretation
Lens-like HARs / HARPs (SF1) - Fig. 4.7A - Sand-rich channel-floor deposits.	<ul style="list-style-type: none"> - One to five variably stacked reflectors. - High to very high amplitude (positive or negative). - Reflectors < 20 m, in packages < 80 m thick. - 100 m – 1 km wide. - Laterally variable package thickness. - Reflectors lens-like in cross-section and decrease in thickness and amplitude toward the margins; elongate downstream. 	Each HAR (High Amplitude Reflector) or HARP (High Amplitude Reflector Package) sits within a HARP-bounding surface or a channelform surface, but may also be cut by another HARP-bounding surface or channelform surface. HARs or HARPs may juxtaposed against chaotic / transparent zones (SF8) stratigraphically higher or lower. These reflectors form a continuum with flat, wide, HARs / HARPs (SF3). Distinct HARs / HARPs may converge upstream or downstream to form a through-going package of SF1 or SF3 (Fig. 4.7A).	Coarse-grained sediments, likely sand-rich with high porosity (and therefore fluid content) that elicits a strong amplitude response (Flood and Piper, 1997; Mayall and Stewart, 2000; Posamentier, 2003; Posamentier and Kolla, 2003; Deptuck et al., 2003, 2007). Reflector geometries are interpreted as deposits infilling incised surfaces at a smaller scale than their host channelform surface (Mayall et al., 2006; Deptuck et al., 2007). Incision and infill may be due to (a) time-transgressive seafloor degradation (Hodgson et al., 2011, 2016) creating HARP-bounding surface-scale palaeo-conduits, that were subsequently filled (Janocko et al., 2013; Hansen et al., 2017a) in response to a drop in input flow energy or a downstream blockage; (b) knickpoints that incised and infilled locally (longitudinally) as they migrated upstream (Heijnen et al., 2020).
Inclined reflector packages (SF2) - Fig. 4.7B, D - Unilaterally stacked margins of sand-rich channel-floor deposits.	<ul style="list-style-type: none"> - One to ten, inclined reflectors, stacked laterally and vertically. - Low to high amplitude. - Reflectors < 15 m, in packages < 50 m thick. - Reflectors and packages < 1.5 km wide. - In cross-section reflectors increase in thickness and amplitude in direction of inclination; elongate downstream. 	Reflectors consistently dip (at 2 – 7 degrees) towards one margin of the confining channelform surface (Fig. 4.7B). At their base, these reflectors coalesce to form a through-going, flat based, generally laterally continuous HAR (SF3). In some sections, the stacking of inclined reflectors is less consistent and two are observed, dipping in opposing directions forming a lens-like HAR (SF1). In plan-view (Fig. 4.7D) they form linear features that generally follow the path of the channelform but become progressively more arcuate and eventually mirror the form of the youngest stacked reflector. The youngest reflector is usually most sinuous and has a lens shape in cross section.	These deposits either represent: (a) deposits formed by progressive lateral channel migration, which produces these 'point bars' (Abreu et al., 2003; Arnott., 2007; Alpak et al., 2013) or 'oblique accretion deposits' (Peakall and Sumner, 2015) on inner-bends; (b) the unidirectional, lateral migration of palaeo-conduits at HARP-bounding surface scale that formed and were infilled sequentially, preferentially destroying one margin of its precursor and preserving the other (Peakall et al., 2000a, b; Kolla et al., 2001, McHargue et al., 2011); (c) the product of sequentially migrating knickpoints (see SF1) that preferentially hugged one side of a wider palaeo-conduit, thus preferentially preserving one margin (Heijnen et al., 2020). Definitive distinction is impossible, but due to their scale, presence on outer bends and occasional inconsistencies in stacking direction, (a) is unfavourable. Through-going basal HARs likely contain similar coarse-grained sediments as in SF1.
Flat, wide, HARs / HARPs (SF3) - Fig. 4.7A, C - Laterally stacked sand-rich channel-floor deposits below seismic resolution.	<ul style="list-style-type: none"> - One to four vertically stacked reflectors. - High to very high amplitude. - Reflectors < 20 m, in packages < 40 m thick. - Typically 1 – 3 km wide. - Laterally continuous package thickness. - Reflectors tabular (thickness maintained across ~ 80 % of width) in cross-section, elongate downstream. 	Reflectors terminate abruptly at both margins against their confining surface; SF3 is virtually always confined by a channelform surface, and / or cut by a subsequent channelform surface (Fig. 4.7C). SF3 deposits form a continuum with the SF1. A narrow HAR or HARP may widen, or multiple may converge to form an apparently through-going reflector (Fig. 4.7A). A narrow (< 500 m wide), elongate, lens-shape (in cross-section) pathway is commonly preserved beneath the otherwise flat base of SF3 deposits.	Same coarse-grained sediments as in SF1. Relationships with SF1, SF2 and SF8 suggest that these may represent amalgamated 'sandbodies' (Millington and Clark, 1995a; Pickering et al., 1995) with internal variability below seismic resolution (Schwab et al., 2007). Unresolvable HARP-bounding surfaces, each hosting lithologically similar deposits, stacked laterally in an 'organised' or 'disorganised' manner (<i>sensu</i> McHargue et al., 2011) and underwent little vertical aggradation. Stacking and migration may have occurred in response to sequential palaeo-conduit formation and infill or the passage of migrating knickpoints (SF1 and SF2).

<p>Non-truncated tabular reflector packages (SF4) - Fig. 4.7E, F - Sheet deposits.</p>	<ul style="list-style-type: none"> - One to seven vertically stacked reflectors. - Typically low to medium (rarely high) amplitude. - Reflectors < 10– 20 m, in packages < 50 m thick. - 1 – 4 km wide. - Packages taper towards edge of their bounding surface (constituent reflectors widen upwards). - Reflectors tabular (thickness maintained across ~ 80 % of width) in cross-section, elongate downstream. 	<p>Continuous (SF4) and truncated (SF5) tabular reflector packages are distinguished based on their relationships with their lateral bounding surfaces. Reflectors of SF4 terminate abruptly, at both margins, against sheet- or terrace-bounding surfaces or an MTD-top that dip in opposing directions. SF4 deposits commonly gradationally overlie SF1 deposits (Fig. 4.7E, F).</p>	<p>Sheet deposits (Pickering et al., 1995; Tókéš and Patacci, 2018; Liang et al., 2020) from flows that deposited across the entirety of their host palaeo-conduit. Sheet deposits may be a product of: (a) passive palaeo-conduit fill, probably representing a systematic decrease in input flow energy accompanying abandonment (Haughton, 2000; Deptuck et al., 2003), or (b) confined flows that were dominantly depositional (McCaffrey et al., 2002) because of a shallow longitudinal gradient, or a release of lateral confinement, potentially in response to partial ponding upstream of an MTD (Kneller et al., 2016; Liang et al., 2020), or downstream of a knickpoint (Heijnen et al., 2020). Sediments within these reflector packages may be sand-rich (Posamentier and Kolla, 2003), mud-rich (Mayall et al., 2006), or heterolithic (Janocko et al., 2013). The apparent gradation from underlying SF1 deposits suggests an overall upward fining (McHargue et al., 2011).</p>
<p>Truncated, tabular reflector packages (SF5) - Fig. 4.7F, G - Incised sheets or terrace deposits.</p>	<ul style="list-style-type: none"> - One to tens of vertically stacked reflectors. - Typically low (rarely very low) to medium (rarely high) amplitude. - Reflectors < 10 m – 20 m thick, in packages < 300 m thick. - 1 - 5 km wide (widening-up). - Packages (and reflectors therein) subtly widen upward. - Reflectors tabular or taper slightly away from channel-fills in cross-section, elongate downstream. 	<p>SF5 comprises the same reflector styles as SF4 but terminate, on their outboard side, against a sheet- or terrace-bounding surface or an MTD-top. However, on their inboard side, reflectors in SF5 terminate against a subsequently formed channelform surface, an MTD-base or a sheet- or terrace-bounding surface, which can lead to their juxtaposition against younger SF1, SF3 or SF4 deposits. SF5 deposits commonly gradationally overlie SF1 or SF4 deposits, and underlie (also gradationally) SF2 deposits (Fig. 4.7F, G).</p>	<p>These deposits may represent: (a) sheet deposits (SF4) that have been incised; (b) terrace deposits, formed during the formation and fill of a subsequent channelform, by overspill onto a high confined by a sheet- or terrace-bounding surface (Babonneau et al., 2004; Deptuck et al., 2003, 2007; Hansen et al., 2015, 2017). A descriptive distinction between SF4 and SF5 is provided, based on the relationship with subsequently formed surfaces: continuous reflectors that terminate, at both margins, against sheet- or terrace-bounding surfaces or MTD-tops that dip in opposing directions are classified as SF4; reflectors that terminate on one side against a sheet- or terrace-bounding surface or MTD-top, but are truncated on the other side by a surface that dips in the same direction are classed as SF5.</p>
<p>Continuous reflectors without undulation (SF6) - Fig. 4.7F, G, I - Levees without sediment waves.</p>	<ul style="list-style-type: none"> - Vertically stacked reflectors. - Very low to medium amplitude. - Reflectors < 10 – 25 m, in packages hundreds of meters thick. - Packages traceable for < 50 km away from the channel. - Laterally continuous package thickness or slight tapering away from channel. - Reflectors tabular in all directions or tapering away from channel. 	<p>On the landward channel margin they thin away from the channel. On the oceanward margin the reflectors typically maintain their thickness. Packages of SF6 are continuous for < 45 km on the landward margin, and on the oceanward margin they widen upward from ~ 20 – 50 km.</p>	<p>Interpreted as external levee deposits (Pirmez and Flood, 1995; Posamentier and Kolla, 2003; Deptuck et al., 2003; Kane and Hodgson, 2011; Nakajma and Kneller, 2013).</p>

<p>Continuous reflectors with undulation (SF7)</p> <ul style="list-style-type: none"> - Fig. 4.7H - Levees with sediment waves. 	<ul style="list-style-type: none"> - Vertically stacked reflectors. - Very low to medium amplitude. - Reflectors < 10 m – 25 m, in packages hundreds of metres thick. - Packages traceable for < 40 km away from the channel. - Slight tapering away from channel. - Sigmoidal reflector geometries. 	<p>Reflectors systematically pinch and swell to form sigmoidal, wave like geometries (Fig. 4.7H) with sediment wave wavelengths varying from ~ 300 m to 4 km and amplitudes from < 10 m to ~ 75 m. These deposits are mainly observed on the landward channel margin where the thick limbs of the sigmoidal waves dip towards the channel. In plan-view, the waves are concentric around outer meander bends.</p>	<p>External levee deposits with sediment waves (Normark et al., 1980, 2002, Flood, 1988; Nakajima and Satoh, 2001; Wynn and Stow, 2002; Migeon et al., 2004, Posamentier, 2003; Posamentier and Kolla, 2003). Based on their dimensions they are interpreted to be formed by fine grained turbidity currents overspilling from a channel or palaeo-conduit (Normark et al., 1980; Wynn and Stow, 2002). Fine grained sediment waves aggrade and migrate towards the channel by accretion on their upstream side (Flood, 1988; Nakajima and Satoh, 2001).</p>
<p>Chaotic / transparent zones (SF8)</p> <ul style="list-style-type: none"> - Fig. 4.7A, E, J, K - Slump and / or debris flow deposits, or megaclasts. 	<ul style="list-style-type: none"> - Low amplitude zones with no coherent internal reflectivity. - Three modes of occurrence: <ul style="list-style-type: none"> - (1) Within depositional element 1 deposits: <ul style="list-style-type: none"> • Zones less than 10 m (below data resolution) to ~ 50 m thick. • Zones up to 2 km across. • Usually no preferred elongation. - (2) Distinct from and overlying depositional element 1 deposits: <ul style="list-style-type: none"> • Typically between 30 and 100 m thick. • 1 – 4 km wide. • Elongate and mounded downstream. - (3) Distinct from depositional element 1 deposits, lateral to and between zones of SF9 and SF10: <ul style="list-style-type: none"> • Typically between 50 and 150 m thick. 	<p>(1) SF8 may exist adjacent to any SF1, SF2 or SF3 deposit (Fig. 4.7A, E). These may sit within, or be cut by, HARP-bounding surfaces or channelform surfaces. In plan-view these zones sometimes form relatively undefined patches, but they commonly form defined polygons that usually have no preferred orientation and are typically < 100 m across, but can reach 1 km. (2) SF8 overlying SF1 deposits that are underlain by a pre-existing channelform surface. They thicken to the deepest part of the channelform surface and pinch out to the edges (Fig. 4.7C). (3) SF8 may form part of much larger, areally-extensive MTDs and therefore exhibit a complex planform distribution (Fig. 4.7J; see depositional element 4). A continuum exists between the three modes of occurrence.</p>	<p>Chaotic zones that form discrete polygons (mode of occurrence (1)) are interpreted as megaclasts (Posamentier and Martinsen, 2011; Ortiz-Karpf et al., 2017; Casson et al., 2020; Naranjo-Vesga et al., 2020). Those without a defined polygonal planform are interpreted as debris flow or slump deposits (see Moscardelli and Wood, 2008; Bull et al., 2009; Ogata et al., 2012 for definition). Either may have been proximally sourced from the shelf or feeder canyon (Nelson et al., 2011; Bernhardt et al., 2012; Masalimova et al., 2015; Ortiz Karpf et al., 2017) or locally sourced from the palaeo-conduit walls and adjacent overbank (Clark and Pickering, 1996; Deptuck et al., 2007; Hansen et al., 2017; Kremer et al., 2018); the latter is favoured for both due to the abundance of failure scars observed in the channel-walls.</p>
<p>Folded and faulted reflectors (SF9)</p> <ul style="list-style-type: none"> - Fig. 4.7I - Slump and / or slide deposits. 	<ul style="list-style-type: none"> - Vertically stacked reflectors. - Very low to medium amplitude. - Reflectors < 10 – 20 m, packages < 200 m thick. - Highly variable lateral extent and complex planform distribution. - Packages may or may not be elongate downstream. - Reflectors highly variable in their continuity and dip. 	<p>SF9 comprises: (a) folded reflectors, with fold wavelengths from 100 m to 1 km, amplitudes 10s of m to 100 m; (b) straight reflectors of varying dips that terminate against sub-vertical normal and reverse faults (Fig. 4.7I). The strike of kinematic indicators (folds and faults) is typically sub-parallel to the trend of adjacent channelforms.</p>	<p>Interpreted as the product of slumping and sliding (Moscardelli and Wood, 2008; Bull et al., 2009; Ogata et al., 2012) during the collapse of terrace (SF5) or levee deposits (SF6 and SF7).</p>
<p>Steep sided blocks of coherent reflectors (SF10)</p>	<ul style="list-style-type: none"> - Vertically stacked reflectors. - Very low to medium amplitude. - Reflectors < 10 - 20 m, packages < 200 m thick. - Reflectors tabular but terminate abruptly against steep sides. 	<p>Steep sided blocks of reflectors resembling those of SF4, SF5 and SF6. Dip and strike of reflectors is concordant with underlying stratigraphy. Blocks are sometimes underlain and / or overlain by chaotic zones (SF8), but not always (Fig. 4.7I). Blocks are</p>	<p>Interpreted as megaclasts (Jackson, 2011; Posamentier and Martinsen, 2011; Ortiz-Karpf et al., 2017; Hodgson et al., 2018; Nugraha et al., 2020a, b) formed during channel-wall collapse composed of in-tact terrace or levee stratigraphy, some of which moved on a sub-seismic scale decollement horizon. These</p>

- Fig. 4.7I, J - Megaclasts	- Polygonal in plan-view, up to 6 km wide.	typically elongate in the orientation of adjacent channelforms (Fig. 4.7J). Steep block sides usually separate SF10 from SF8 and SF9 deposit.	megaclasts differ from those of chaotic / transparent zones as they possess internal reflectivity.
--------------------------------	--	---	--

Table 4.1 (above) – Descriptions and interpretations of the ten seismofacies observed within the studied stratigraphy.

Seismic surface	Description	Bounded by / bounding:	Interpretation
HARP-bounding surface - Fig. 5.7A, B, D, E	<ul style="list-style-type: none"> - Concave-up in cross-section except when truncated by a younger surface. - Surfaces truncate < 60 m of stratigraphy, and are always < 2 km wide, typically < 500 m. - Elongate downstream, traceable for 100s of m to 10s of km until they are truncated, or disappear because they are unresolvable in the data or they become part of another surface. - HARP-bounding surfaces form the lens like geometry of lens like HARs / HARP (SF1) and separate reflectors in inclined reflector packages (SF2). Parts of a HARP-bounding surfaces form sections of channelform surfaces that bound channel-fill deposits. 	<p>Inboard – Channel-fill deposits of any type (SF1, SF2, SF3, SF8).</p> <p>Outboard - Reflectors of older channel-fill deposits are truncated. HARP-bounding surfaces within a given channelform surface incise to similar maximum depths (< 50 m of each other).</p> <p>Top - Can be overlain by flat reflectors of sheet or terrace deposits.</p> <p>Truncation - Can be truncated by a younger HARP-bounding surface, channelform surface or MTD-base.</p> <p>Nomenclature - Where a HARP-bounding surface also forms part of (or all of) a channelform surface, it is classified as a channelform surface (Fig. 5.7A, B, E).</p>	The smallest resolvable elongate, concave-up surface ('channel-forms' of Deptuck et al., 2003, 2007). They are formed by incision and infill caused by local blockages and / or diversions, or variations in the nature of the formative flows. Avulsions and confluences form the cross-cutting relationships between surfaces and deposits of different ages and the longitudinally discontinuous nature of these surfaces (Fig. 5.7A). They may represent buried palaeo-conduits (Janocko et al., 2013), or the passage of upstream-migrating channel floor features such as knickpoints (Heijnen et al., 2020; Guiastrennec-Faugas et al., 2020).
Channelform surface - Fig. 5.7A, B, C, D, E	<ul style="list-style-type: none"> - Concave-up except when truncated by a younger surface. Surface typically shallows in both directions from a thalweg, before abruptly steepening at both sides. - Surfaces truncate < 80 m of stratigraphy, and are typically < 3 km wide. - Elongate downstream, most continuous surfaces in the dataset, traceable for 10s of km to > 100 km. - Two or more HARP-bounding surfaces commonly coalesce to form a through-going channelform surface. 	<p>Inboard - Channel-fill deposits (SF1).</p> <p>Outboard - reflectors of channel-fill, sheet or terrace, MTDs, or, less commonly, levee deposits can be truncated.</p> <p>Top - Transitions into a sheet- or terrace-bounding surface.</p> <p>Truncation - can be truncated by a subsequent channelform surface, sheet- or terrace-bounding surface, or MTD-base.</p> <p>Nomenclature - Where a channelform surface is also an MTD-top, the surface is classed as a channelform surface (Fig. 5.7E, G, I).</p>	Records the compound result of the diachronous modification of the base and sides of a longer lived palaeo-conduit through the formation and infill of one or more HARP-bounding surface (Sylvester et al., 2011; Hodgson et al., 2016). Channelform surface bases are interpreted to incise into underlying MTDs or sheet or terrace deposits. However, in some cases aggradation of the palaeo-channel-floor may juxtapose channel-fill deposits against terrace deposits that formed earlier in the history of the same palaeo-conduit (Hodgson et al., 2011; Brunt et al., 2013b).

<p>Sheet- or terrace-bounding surface - Fig. 5.7C, F, G</p>	<ul style="list-style-type: none"> - Straight or slightly curved dipping surface. A sheet- or terrace-bounding surface can only be unequivocally identified where it is inclined, as the base and top of the surface either transitions into: another surface, a channelform surface or MTD-top, or into through-going, sub-horizontal reflectors with concordant dips. - Surfaces are < 200 m thick, typically 100 m to 2 km wide (one inclined surface, not concave-up). - Elongate downstream, traceable 100s of m to 10s of km (traceable until incised by a subsequent channelform or MTD). - As a sheet- or terrace-bounding surface is defined based on the presence of sheet or terrace deposits on its inboard side, vertical transitions from channel-fill to sheet or terrace deposits are accompanied by a transitional boundary between a channelform surface and overlying sheet- or terrace-bounding surface. 	<p>Inboard - reflectors of sheet or terrace deposits terminate against a sheet- or terrace-bounding surface.</p> <p>Outboard - reflectors of channel-fill, sheet or terrace or levee deposits can terminate against a sheet- or terrace-bounding surface.</p> <p>Base - A sheet- or terrace-bounding surface can: (a) terminate against or transition into an MTD-top, (b) transition into a channelform surface, or (c) transition into throughgoing sheet or terrace deposits.</p> <p>Top - sheet- or terrace-bounding surfaces gradually flatten as the inboard sheet or terrace deposits grade into overlying sheet or terrace or levee deposits.</p> <p>Truncation - Can be truncated by a younger channelform surface, sheet- or terrace-bounding surface, or MTD-base.</p> <p>Nomenclature - Reflectors of sheet or terrace deposits may also terminate against an MTD-top. Where a sheet- or terrace-bounding surface is also an MTD-top (see below), the surface is classed as an MTD-top (Fig. 5.7G).</p>	<p>Formed by: (a) erosion of pre-existing sheet or mass-transport deposits by a channelform, followed by aggradation, and resultant juxtaposition, of sheet and / or terrace deposits from a subsequent channel against an originally erosional surface (Hodgson et al., 2011); (b) the construction of a depositional terrace that created bathymetric surface which was then filled by sheet deposits of that channel, and / or by terrace deposits from a subsequent channel (Hansen et al., 2015); (c) aggradation of terrace or levee deposits on both sides of a pre-existing sheet- or terrace-bounding surface. As the deposits outboard and inboard of the surface aggrade independently, eventually the inboard deposits will be juxtaposed against a surface generated solely by deposition.</p>
<p>MTD-base - Fig. 5.7C, F, G, I, J, K</p>	<ul style="list-style-type: none"> - If the overlying MTD fills a concave-up surface (Fig. 5.7C, J), the MTD-base usually overlies channel-fill or sheet (SF4) deposits at the base and truncates reflectors of sheet or terrace (SF4) and / or levee deposits at the sides. MTD-bases below large, aerially extensive MTDs are usually: much wider (higher aspect ratio) than those overlying channel-fills or confined to the overbank; have flat bases and steep, stepped sides; are asymmetric about the surface they fill; are overlain by thick deposits of folded or faulted reflectors (SF8), or megaclasts (SF10; Fig. 5.7I). If the overlying MTD is confined to the overbank (Fig. 5.7F, K), the MTD-base exists as an isolated, inclined surface. - Surfaces are variable in scale: < 300 m thick, < 7 km wide. - Elongate downstream, traceable for 2 to 10s of km (albeit with variable depths). - MTD-bases are commonly 'stepped' in cross-section, with abrupt changes in dip (up to 90°) occurring over < 100 m laterally. 	<p>Inboard (above) - Always an MTD; any of the 'zones' recognised may be present.</p> <p>Outboard (below) - Reflectors of any seismic facies or any other seismic surface can be truncated or terminate.</p> <p>Top - An MTD-base merges with the MTD-top surface as the MTD between them pinches out or is eroded.</p> <p>Truncation - An MTD-base can be truncated by a channelform surface, sheet- or terrace-bounding surface or another MTD-base.</p> <p>Nomenclature - Where an MTD-base apparently forms the continuation of a channelform surface, the surface is classed as an MTD-base (Fig. 5.7C).</p>	<p>The stepped nature of an MTD-base is produced by deformation localisation along sub-vertical faults or 'scars' at the sides and sub-horizontal decollements at the base of the failing stratigraphy (Nugraha et al., 2019, 2020; Nwoko et al., 2020a, b). Where an MTD-base overlies channel-fill deposits and follows the shape of the channelform surface underlying the channel-fill deposits, the overlying MTD is interpreted to be filling a pre-existing surface. Where evidence of erosion at the base of an MTD is absent, the MTD-base may record the instantaneous morphology (predominantly the width) of a palaeo-conduit it filled.</p>

	- Where reflectors below and above the MTD-bases are concordant (e.g. below a megaclast) the 3D context is used to differentiate.		
MTD-top - Fig. 5.7C, F, G, H, I	<p>- If the underlying MTD fills a channelform surface (Fig. 5.7C, I), the MTD-top is usually concave-up in cross-section; if it is confined to the overbank (Fig. 5.7F, K), it occurs as an isolated, inclined surface. MTD-tops can be irregular, and packages of concordant (usually flat) reflectors of sheet or terrace, or levee deposits thicken into lows on both sides.</p> <p>- Surfaces are variable in scale: < 200 m thick, < 7 km wide.</p> <p>- MTD-top surfaces are topographically complex, but are generally elongate and mounded in longitudinal section. Traceable downstream for 2 to 10s of km (variable depths).</p> <p>- Because the MTD between a MTD-top and MTD-base usually thickens towards the lowest part of a MTD-base, MTD-tops show a similar but subdued concave-up profile relative to their associated MTD-base. MTD-tops generally show less abrupt changes in dip than their associated MTD-base.</p> <p>- Where reflectors below and above the MTD-top are concordant (e.g. above a megaclast) the 3D context is used to differentiate.</p>	<p>Inboard (above) - Reflectors of any seismic facies.</p> <p>Outboard (below) - Always an MTD; any of the 'zones' recognised may be present.</p> <p>Top - An MTD-top can: (a) terminate abruptly against overlying, throughgoing reflectors of sheet or terrace or levee deposits, or (b) transition abruptly into a sheet- or terrace-bounding surface.</p> <p>Truncation - An MTD-top can be truncated by a younger channelform surface, sheet- or terrace-bounding surface, or MTD-base. MTD-tops on top of large, aerially extensive MTDs are more commonly truncated by a channelform surface (Fig. 5.7I).</p>	<p>MTDs heal the topography at their base making depth and dip changes on MTD-tops smaller and less abrupt. Small scale local rugosity, larger, deposit scale topography (concave-up cross-section and mounded longitudinal profile), and / or post depositional loading may cause: (a) ponding on an MTD-top, and / or (b) the focusing of subsequent flows leading to erosion and the truncation of an MTD-top (Armitage et al., 2009; Alves, 2010; Dykstra et al., 2011; Kneller et al., 2016; Brooks et al., 2018b; Ward et al., 2018; Bull et al., 2020; Tek et al., 2020). The presence of analogous channel-blocking MTDs on the seafloor, and their sharp tops and lack of associated rotated, fanning reflectors on their tops in the subsurface, suggests that the underlying MTDs were formed quasi-instantaneously; non-eroded MTD-tops are therefore reliable chronostratigraphic markers.</p>

Table 4.2 – Descriptions and interpretations of the five seismic surfaces observed within the studied stratigraphy.

4.6.2.1 *Depositional Element 1 – Channel-fill*

Description:

Channel-fill comprises: (i) High-Amplitude Reflectors (HARs) and HAR Packages (HARPs) that can be narrow (<1 km wide) and lens shaped (SF1; Fig. 4.7A and E) or wide (1 to 3 km) and flat (SF3; Fig. 4.7B and C); (ii) laterally stacked, unidirectionally inclined reflector packages (SF2; Fig. 4.7B and D); (iii) chaotic/transparent packages (SF8; Fig. 4.7A and E). Channel-fill deposits sit within channelform surfaces (Table 4.2; Fig. 4.7B). At smaller scales, one or more packages of SF1, SF2, SF3 and SF8, themselves bounded by HARP-bounding surfaces, constitute the broader channel-fill (for example, Fig. 4.7C). A channelform surface can be truncated by a younger channelform surface or MTD-base (Fig. 4.7B, C and G). If the thalweg of a subsequent channelform is sufficiently deep, older channel-fills may be juxtaposed against the sheet or terrace-bounding surface formed by a younger channelform. Channel-fills can be overlain by a relatively flat MTD-base that spans the width of the underlying fill (Fig. 4.7B and C), or be gradationally overlain by tabular reflectors (Fig. 4.7G).

Interpretations:

The presence of SF1 and SF2 (sand-rich channel-floor deposits), SF3 (laterally stacked marginal deposits of SF1), and SF4 (megaclasts or debrites sourced from palaeo-conduit walls) (Table 4.1), and the occurrence of HARP-bounding surfaces within channel-fills suggests at least two orders of hierarchy are present. Incision and infill at HARP-bounding surface scale may have formed in response to: (i) erosion and deposition in palaeo-conduits (Janocko et al., 2013; Hansen et al., 2017), possibly in response to increases and decreases in input flow energy (Gardner et al., 2003; Flint et al., 2011); or (ii) may represent the stratigraphic manifestation of the passage of channel-floor features such as knickpoints (Heijnen et al., 2020, Guiastrennec-Faugas et al., 2020, 2021). Local blockages or diversions caused by the emplacement of megaclasts (SF8) (Deptuck et al., 2003; 2007) may have also caused incision and infill by either of the aforementioned mechanisms.

A channelform surface is a composite surface of a larger hierarchical order than a HARP-bounding surface (Table 4.2). Degradation and infill at channelform surface scale is caused by the system adjusting to its idealised equilibrium profile (Pirmez et al., 2000; Kneller, 2003). Channelform surfaces likely start off as smaller, narrower surfaces (HARP-bounding surface scale), that are filled and modified during successive iterations of formation and infill of HARP-bounding surfaces (Hubbard et al., 2020). Time-transgressive modification by widening and deepening of the bounding channelform surface is achieved by the erosion and/or collapse of one or both walls of a palaeo-conduit.

4.6.2.2 *Depositional Element 2 – Sheet or Terrace*

Description:

Sheet or terrace deposits comprise two seismofacies constituting tabular reflectors, distinguished based on whether they are (SF5) or are not (SF4) truncated by a younger surface (Fig. 4.7E, F and G; Table 4.1). On the outboard side, sheet or terrace deposits are bounded laterally by a sheet or terrace-bounding surface or an MTD-top (Fig. 4.7E, F and G). On the inboard side, reflectors in SF5 terminate against younger channelform surfaces, sheet or terrace-bounding surfaces, or MTD-bases (Fig. 4.7F and G). At their base, sheet or terrace deposits may grade from channel-fill deposits or overlie an MTD-top. Adjacent packages of truncated tabular reflectors can converge upward to form a larger, through-going reflector package, and eventually either transition upward into overlying levée deposits, or be overlain by an MTD-base (Fig. 4.7F and G).

Interpretations:

Reflectors that are continuous across their bounding surfaces (SF4; Fig. 4.7C, E and F) represent sheet deposits formed from passive fill or weakly confined, depositional flows in response to a decrease in or reversal of the downstream gradient and/or lateral confinement (Table 4.1). Where reflectors are truncated by a younger surface (SF5; Fig. 4.7F and G), they may represent incised sheet deposits or terrace deposits formed by overspill from a younger palaeo-conduit (Table 4.1). Sheet or terrace-bounding surfaces may have formed during both the fill of a palaeo-conduit and subsequent incision forming a HARP-bounding surface or channelform surface, or by contemporaneous aggradation of two terraces, or a terrace and a levée; as such, they cannot be tied to any one channelform. A vertical transition likely exists between incised sheet and terrace deposits (from sheet deposits at the base to terrace deposits toward the top), making their definitive distinction difficult based on seismic character alone (Deptuck et al., 2003). The upward convergence of two terraces to form a larger one, and gradational vertical transition into overlying levée deposits suggests terraces closer to the thalweg aggrade faster and may heal terrace-top topography; this concept is supported by an observed upward increase in terrace width and decrease in terrace frequency on the modern channel-walls (Fig. 4.4B).

4.6.2.3 *Depositional Element 3 – Levées*

Description:

Levée deposits comprise laterally continuous packages of reflectors which may be devoid of (SF6; Fig. 4.7F, G and I), or contain (SF7; Fig. 4.7H) sediment waves. Towards the channel, reflectors terminate against channelform surfaces, sheet or terrace-bounding surfaces, or MTD-bases (Fig. 4.7F, G and I). Away from the channel,

on the landward side, they interfinger with wedging reflector packages that thicken towards the subduction margin (McArthur et al., 2019). On the oceanward side, reflectors terminate against the Chatham Rise or Hikurangi Plateau (Fig. 4.1).

Interpretations:

Where reflectors decrease in amplitude and thickness away from the channel, they are interpreted as unconfined external levées (Pirmez & Flood, 1995; Posamentier & Kolla, 2003; Deptuck et al., 2003; Nakajima & Kneller, 2013). Where reflectors terminate against the Chatham Rise or Hikurangi Plateau, they are interpreted as confined external levées (Clark & Cartwright, 2011). Reflector tapering, however, does not necessarily correspond to depositional relief (Fig. 4.3), as transversely sourced trench filling sediment may enhance aggradation near the subduction front, therefore leading to relatively even aggradation across the trench-floor, and the suppression of wedge shaped levée development.

4.6.2.4 Depositional Element 4 – Mass-transport deposits from channel-wall collapse

Description:

MTDs comprise a variety of reflector styles: chaotic / transparent intervals (SF8), folded and faulted reflectors (SF9), and steep-sided blocks of coherent reflectors (SF10) (Table 4.1). Chaotic/transparent intervals that sit among channel-fill deposits (Fig. 4.7A) are classified as channel-fill (Depositional Element 1, see above). Deformed reflectors within MTDs were originally sheet or terrace and/or levée deposits. They usually overlie and thicken towards the fill of a pre-existing channelform, and thin into adjacent sheet or terrace and/or levée deposits. Transitions between seismofacies and thickness changes can be very abrupt (Fig. 4.7I).

Mass-transport deposits are bound below (and/or laterally) by an MTD-base (Fig. 4.7B, C, F, G and I; Table 4.2). Above (and/or laterally), they are bound by an MTD-top (Fig. 4.7B, C, F, G and I), by the base of a younger MTD (Fig. 4.7G), or are incised by a channelform surface (Fig. 4.7G, I and J; Table 4.2). They are commonly cut by a younger channelform surface, often to or through their underlying MTD-base, but rarely more than 20 m below (Fig. 4.7E, G and I). MTDs may be present on both sides of an incising channelform surface (Fig. 4.7G), or on just one side (Fig. 4.7I). If the depth of incising channelform is sufficient, a sheet or terrace-bounding surface may be juxtaposed against an MTD-top (Table 4.2).

Mass-transport deposits have three modes of occurrence: (a) Areally extensive (Fig. 4.7I and J), containing a part overlying pre-existing channel-fill deposits, and a part preserved within in adjacent terrace or levee deposits; these parts may be spatially separated by a sheet or terrace-bounding surface (Fig. 4.7G; Table 4.2). These MTDs

can span over 300 km² and be up to 200 m thick; they are usually thicker and more laterally extensive on one side of the channel-fill they overlie (Fig. 4.7J). (b) Deposits that overlie pre-existing channel-fill but have no expression in the adjacent overbank. SF8 and heavily folded SF9 reflectors dominate (Fig. 4.7C). (c) Deposits that are confined to terrace or levée stratigraphy; they are less areally extensive (typically <50 km²) than those described in 'a' (Fig. 4.7F and K). MTDs confined to overbank (c) or above channel-fill (b) may transition up or downstream into areally extensive MTDs (a). A marked scale gap is apparent between large, areally extensive MTDs ('a' above), with maximum thicknesses >100 m and areal extent >100 km², and smaller, typically localised MTDs ('b' and 'c' above) with maximum thicknesses typically <100 m and areal extent <50 km². At least five very large MTDs, are observed in the studied stratigraphy. These deposits can be sourced from either channel-wall and there appears to be no preferred location for their source.

Interpretations:

The MTDs formed by the remobilisation of sheet, terrace, or levée deposits (Deptuck et al., 2003, 2007; Hansen et al., 2017). Deposits comprise the product of en masse transport and deposition via a continuum of processes (Moscardelli & Wood, 2008; Bull et al., 2009; Ogata et al., 2012; Wu et al., 2020) distinguished based on the degree of internal deformation or disaggregation. MTDs here record the product of debris flow (SF8), slumping (SF8 and SF9), and sliding and spreading (SF9); blocks of coherent reflectors are megaclasts (SF10). The diversity of processes interpreted from these deposits is greater than typically observed from channel-wall collapse (cf. Sawyer et al., 2007, 2014; Hansen et al., 2017). A lack of fanning reflectors within or above the deposits (Tables 4.1 and 4.2) suggests these failures were not progressive like in some other systems (e.g. Sawyer et al., 2014). They are akin to the large MTD seen partially filling the modern Hikurangi Channel (Figs. 4.2 and 4.5; Lewis & Pantin, 2002; Watson et al., 2020), which was emplaced quasi-instantaneously.

Where MTDs deposits are confined to the channelform they fill, they may have been sourced from the collapse of a confining terrace or levée where the source has been fully 'evacuated' (Kremer et al., 2018; Nugraha et al., 2020), or transported from more proximal locations (Bernhardt et al., 2012; Masalimova et al., 2015). Due to the presence of small, fully evacuated scars on the modern channel-wall (Fig. 4.7E and F), the former is favoured. MTDs confined to the overbank may have initially had a counterpart filling the adjacent channelform that has since been eroded by channel-traversing flows; remnants of these deposits may form local debrites or slumps within the channel-fills.

Upstream → Downstream

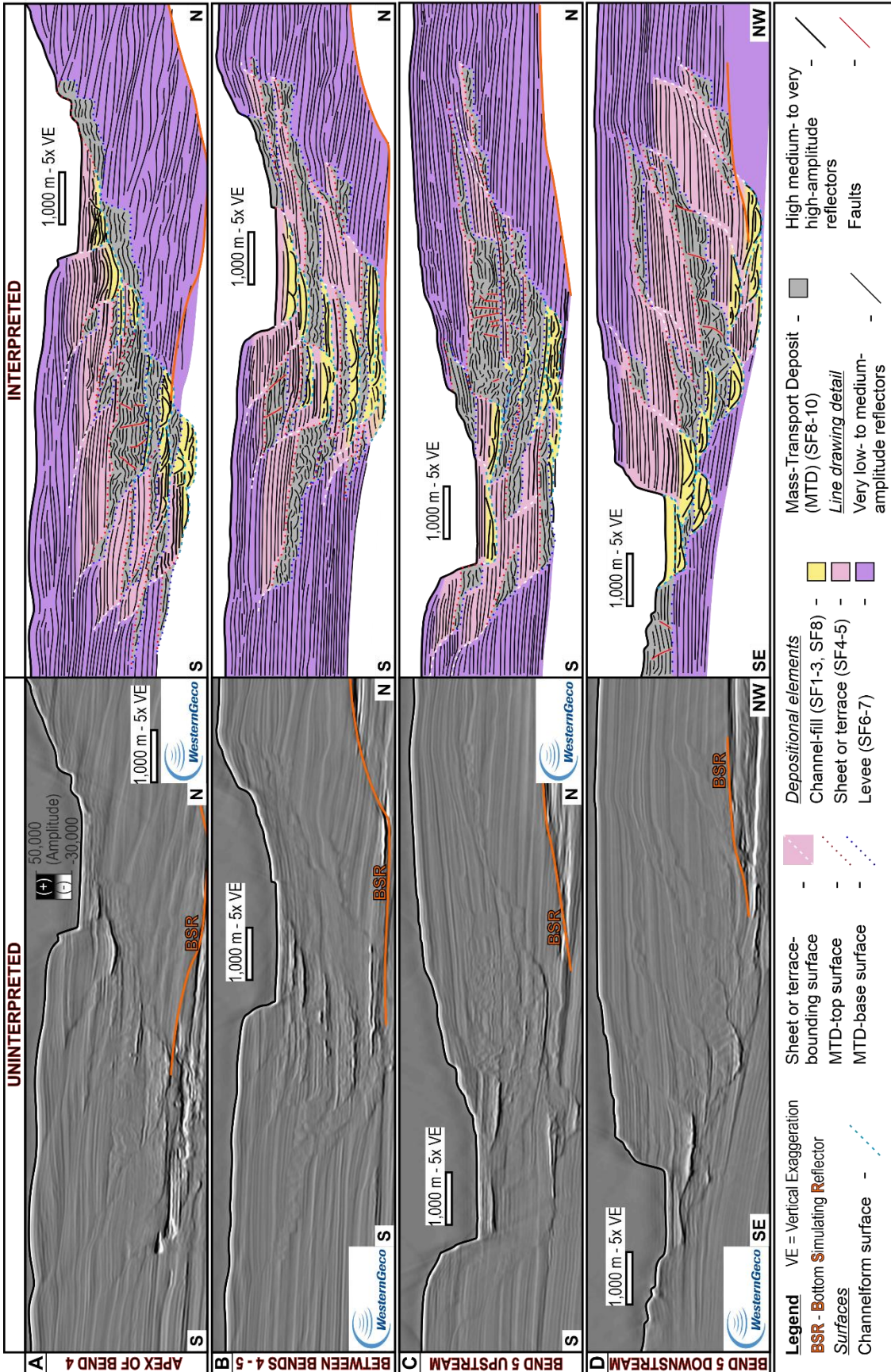


Figure 4.8 (above) – Uninterpreted images (left) and interpreted line drawings (right) of seismic sections from: (A) the apex of bend 4; (B) the straight section between bends 4 and 5; (C) upstream of the apex of bend 5; (D) downstream of the apex of bend 5. Note: all sections displayed looking upstream.

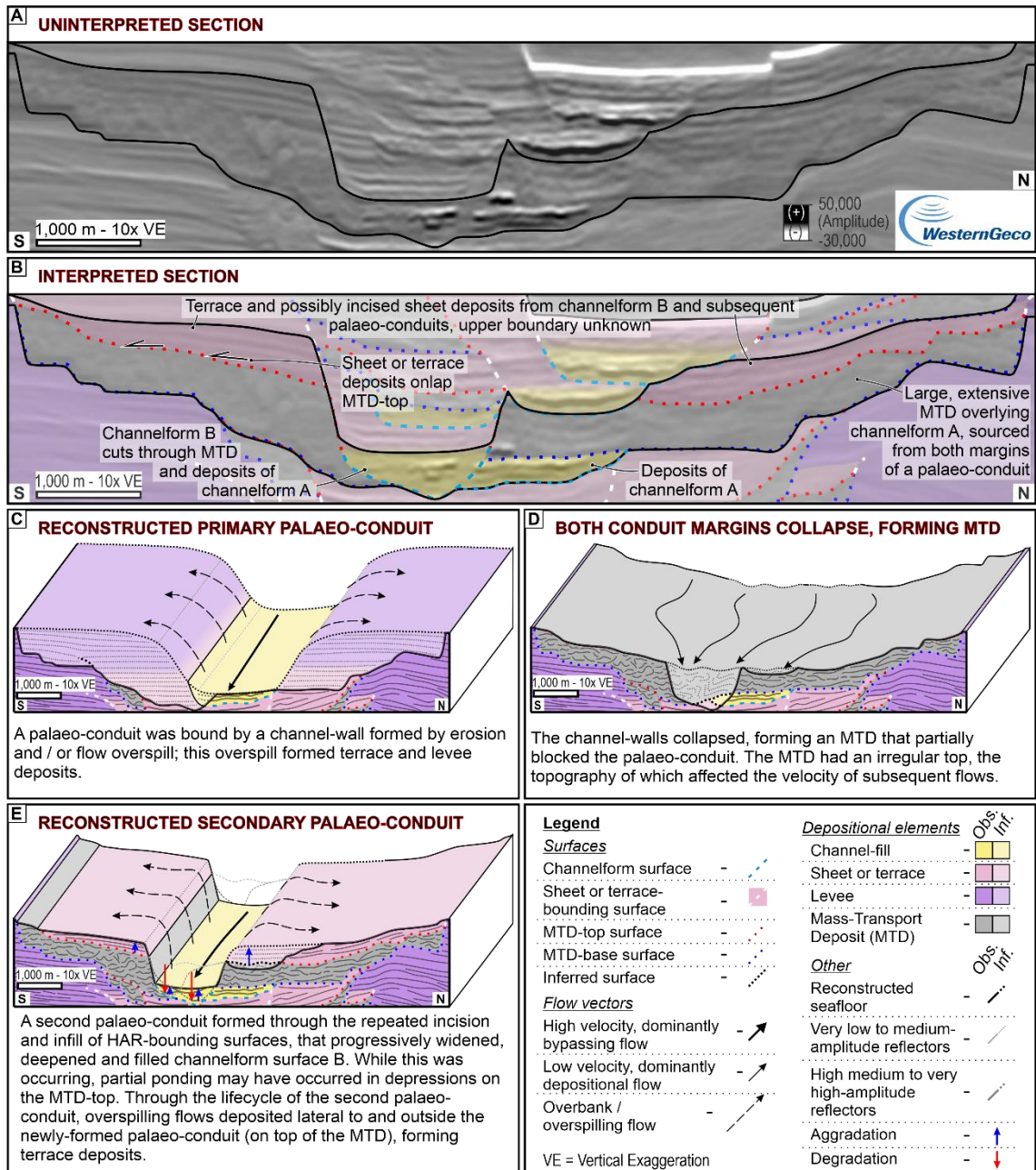


Figure 4.9 (above) – (A) Minimally interpreted and (B) interpreted sections showing 'sequence-type 1' (described in the text). (C), (D) and (E) Evolutionary block diagrams showing the formation of 'sequence-type 1'.

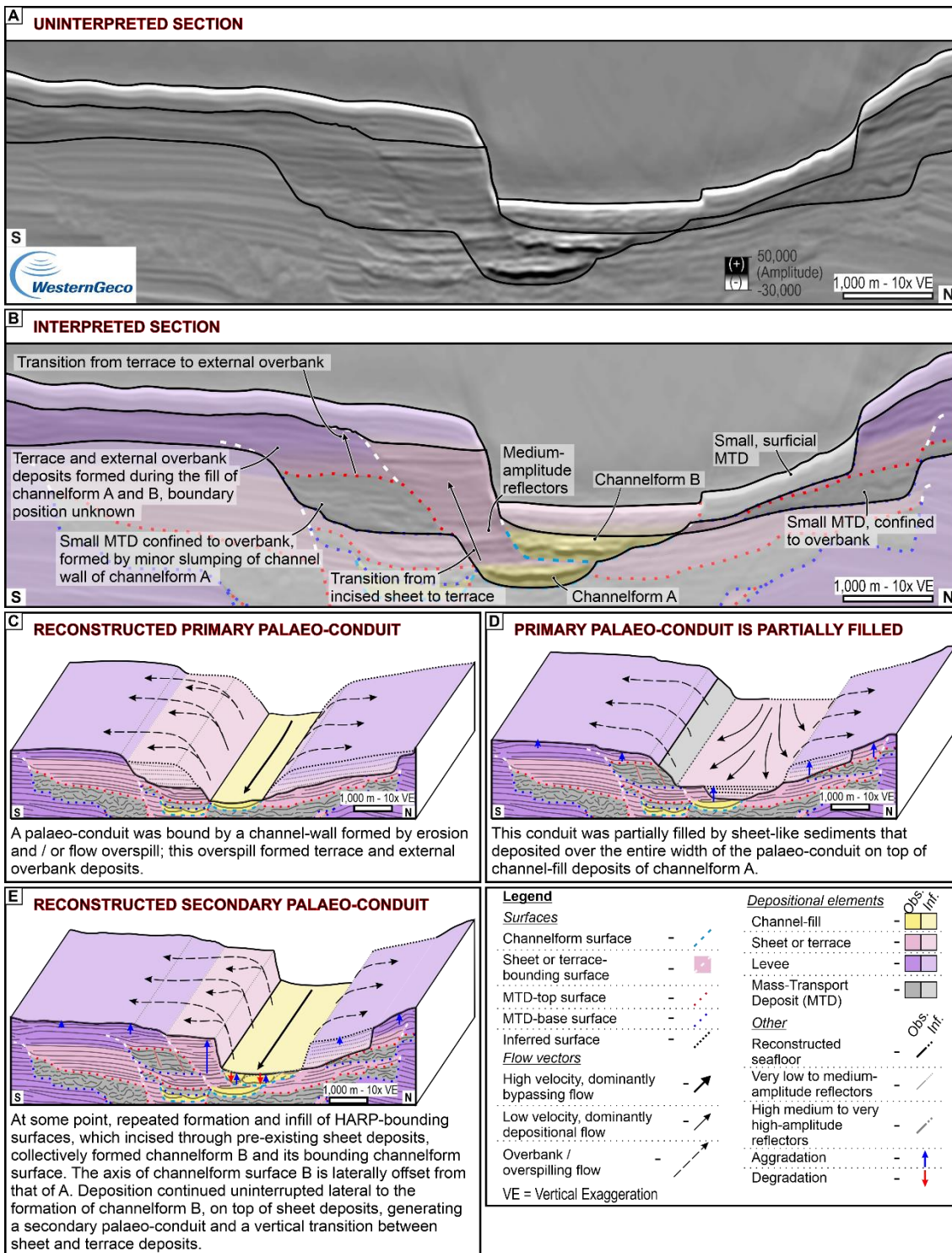


Figure 4.10 – (A) Minimally interpreted and (B) interpreted sections showing 'sequence-type 2' (described in the text). (C), (D) and (E) Evolutionary block diagrams showing the formation of 'sequence-type 2'.

4.6.3 Stratigraphic relationships and three-dimensional correlation

The classifications of seismic facies, surfaces and depositional elements allow the lithological interpretation of the studied stratigraphy, and the lateral and vertical

transitions between them can be used to establish the relative ages of the deposits (Fig. 4.8). The two sequence types presented below describe the cross-sectional evolution through the fill and abandonment of a primary channelform surface (hereunder 'channelform surface A') and the establishment of a second channelform surface (hereunder 'channelform surface B'), the result of which formed two distinct channel-fills ('channelform A' and 'channelform B').

4.6.3.1 *Sequence-type 1*

Description (Fig. 4.9A, B):

Channelform surface A, partially filled by channel-fill deposits, is overlain by an areally extensive MTD. The top, and sometimes the base, of the MTD are incised by channelform surface B, which is also filled by channel-fill deposits. Tabular reflectors overlie the MTD outboard of channelform surface B. On their inboard side they are usually truncated by channelform surface B, and/or a sheet or terrace-bounding surface that channelform surface B has transitioned into. On their outboard side, they terminate against the MTD-top and, if present, a sheet or terrace-bounding surface. Rarely, non-truncated, tabular reflectors that onlap an MTD-top at both sides are preserved below incised sheet or terrace deposits. Sequence-type 1 can occur upstream or downstream of the thickest part of the MTD.

Interpretations (Fig. 4.9C, D and E):

A palaeo-conduit existed on the seafloor. Conduit-traversing flows were laterally confined by steep channel-walls that consisted of terrace, levée and/or incised sheet deposits formed by erosion and overspill of flows that formed channelform A. They flowed over a wide, flat channel-floor formed by channel-fill deposits that partially filled channelform surface A. The channel-walls then collapsed (collapses of one or both channel-walls are observed in different parts of the stratigraphy), forming an MTD with an irregular top, which partially dammed the conduit. Partial ponding may have occurred in depressions formed by rugose MTD-top topography (Armitage et al. 2009; Kneller et al. 2016; Ward et al. 2018; Tek et al., 2020). Following MTD emplacement, sheet deposits formed upstream and downstream of the thickest part of the MTD due to changes in longitudinal gradient and lateral confinement, and downstream flow perturbation related to upstream ponding. Subsequently, channelform surface B was formed through the repeated formation and infill of small HARP-bounding surfaces, which progressively widened and deepened channelform surface B; the initial location of incision was determined by the MTD-top topography. Through the time-transgressive formation and infill of channelform surface B, overspilling parts of palaeo-conduit-traversing flows deposited laterally to and outside of the conduit, forming terrace deposits on top of the MTD and/or precursor incised sheet deposits. Definitive distinction between

incised sheets on top of the MTD and terrace deposits formed by flows that generated channelform surface B is not usually possible.

4.6.3.2 *Sequence-type 2*

Description (Fig. 4.10A and B):

The fill of channelform A is overlain by, and transitions into, tabular reflectors. These terminate, on their outboard side, against a sheet or terrace-bounding surface that channelform surface A transitions into vertically, or an MTD-top. The inboard side of these tabular reflectors, and sometimes the underlying channel-fill and parts of channelform surface A, are truncated by channelform surface B, a sheet or terrace-bounding surface that it transitions into, or a subsequently formed MTD-base. Rarely, non-truncated, tabular deposits that terminate at both sides against a sheet or terrace-bounding surface are preserved above the channelform A fill and below the axis of channelform surface B.

Interpretations (Fig. 4.10C, D and E):

An existing palaeo-conduit was filled by sheet deposits formed on top of pre-existing channel-fill deposits. Some of these sheets were incised during the establishment of channelform surface B, that formed by the repeated formation and infill of multiple HARP-bounding surfaces. During the formation of channelform surface B, overflowing flows deposited terrace deposits on top of incised sheet deposits, generating a (likely complex) vertical transition between channel-fill, incised sheet and terrace deposits (Deptuck et al., 2003; Hubbard et al., 2020). These overflowing flows deposited sediment on two adjacent, vertically offset terraces.

4.6.3.3 *Three-dimensional stratigraphic correlation*

The interpretations of the depositional sequence-types allow distinction of the relative ages of depositional elements in cross-section, which have been traced upstream and downstream. Where this was not possible, MTDs, which are interpreted to have been emplaced quasi-instantaneously, are used as chronostratigraphic markers. Non-eroded MTD-tops are useful stratigraphic markers as MTDs mobilised after deposition of their constituent stratigraphy and before their onlapping strata. Where younger concave-up surfaces truncate the MTD-tops the surfaces and their fill must be younger than the underlying MTD. Where a concave-up surface is filled by an MTD, or the reflectors hosted within that surface are incorporated into an overlying or adjacent MTD, the MTD must be younger. These relationships have allowed 3D stratigraphic correlation (Fig. 4.11) through areas where channel-fills are discontinuous, incised by subsequent channel-fills, or obscured by the presence of MTDs. Through the piecemeal linking of segments of channel-fills and their surrounding deposits, and using MTDs as

chronostratigraphic markers, ten channelform surfaces containing channel-fills (hereafter termed 'channelforms 1 – 10') were traced across the entire study area (Fig. 4.12).

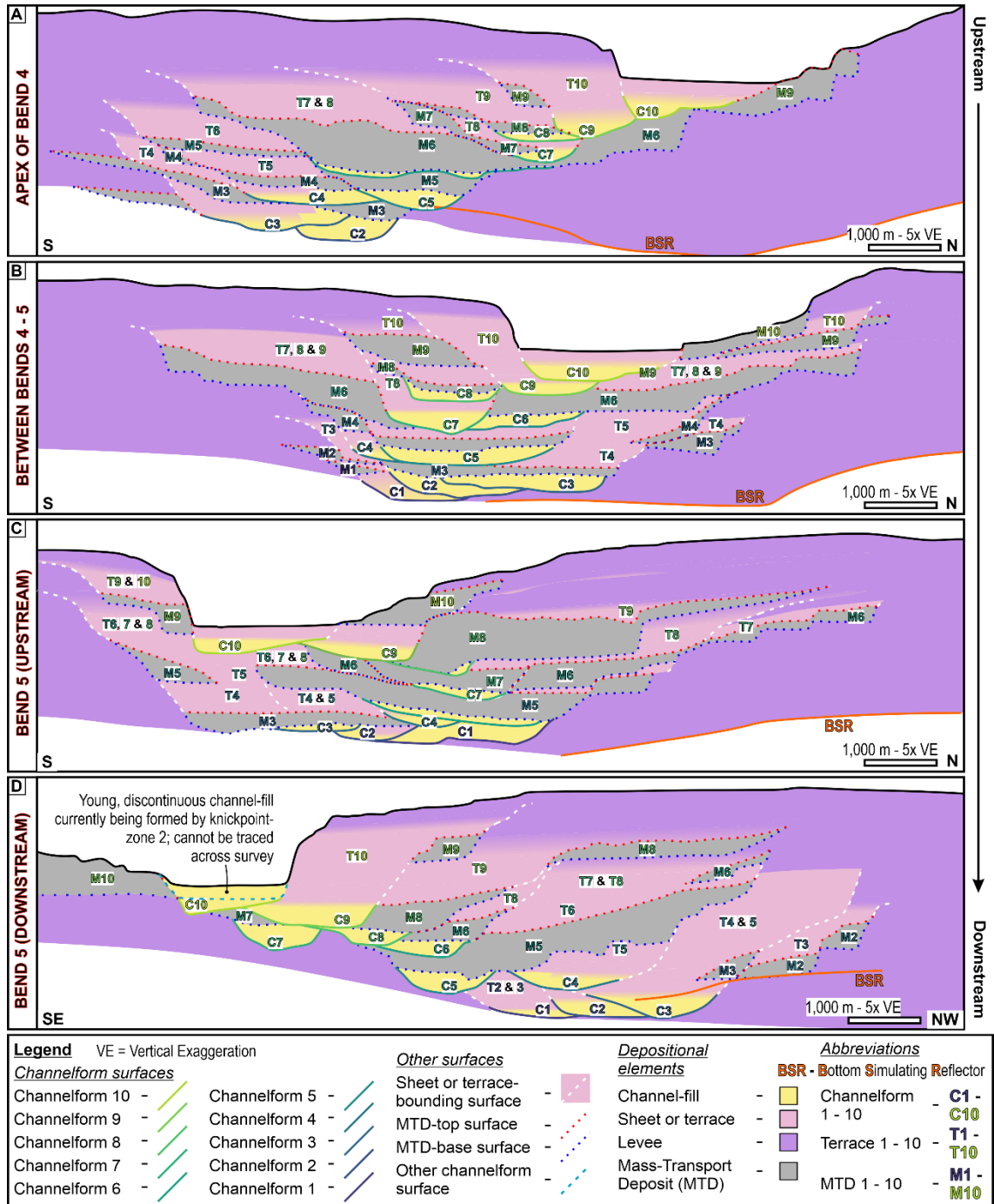


Figure 4.11 – Interpretations of sections in Fig. 4.8 showing the relative ages of the different depositional elements, T, and their longitudinal correlations.

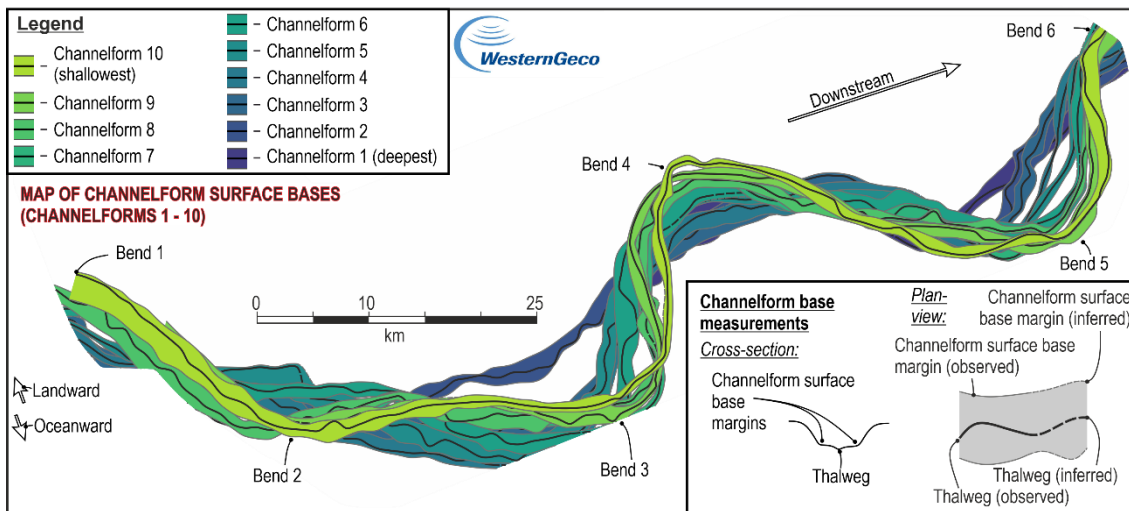


Figure 4.12 – Map of the thalwegs and edges of the flat bases of channelform surfaces 1 to 10 that have been traced across the area.

4.6.4 Architectural variability and integration with seafloor observations

While the categorisation of depositional elements and interpretation of sequence-types 1 and 2 provide a framework for subsurface interpretation, integration with seafloor observations can inform models of architectural genesis. In this section, the seismic character of recent deposits is linked to geomorphological features. Subtle variability in the seismic character of depositional elements, and the nature of transitions between them and their seismofacies, are then linked to observations from the shallow subsurface immediately below prominent seafloor features.

Description

The seismic character within the transition from channel-fill to terrace and sheet deposits is variable. In this transition, tabular reflectors commonly vary in amplitude and thickness, and contain transparent patches (Fig. 4.7E). Sometimes, <50 m above the transition, one to three medium to high-amplitude reflectors are observed. These exhibit insufficient amplitudes to be classified as another seismofacies, but are anomalously higher than most sheet or terrace deposits (Figs. 4.7E, 4.7G and 4.10B). These reflectors are only present upstream of large MTDs. Upstream of the large, recently emplaced MTD observed on the modern seafloor (Fig. 4.5A), a ~ 50 m thick succession of tabular reflectors with highly variable thicknesses and amplitudes and containing distinct transparent patches overlies channelform 10 (Fig. 4.13B). These are topped by a ~ 20 m thick medium to high-amplitude reflector that is present immediately below the seabed and spans the entire 3800 m wide, flat channel-floor (Figs. 4.5 and 4.13B).

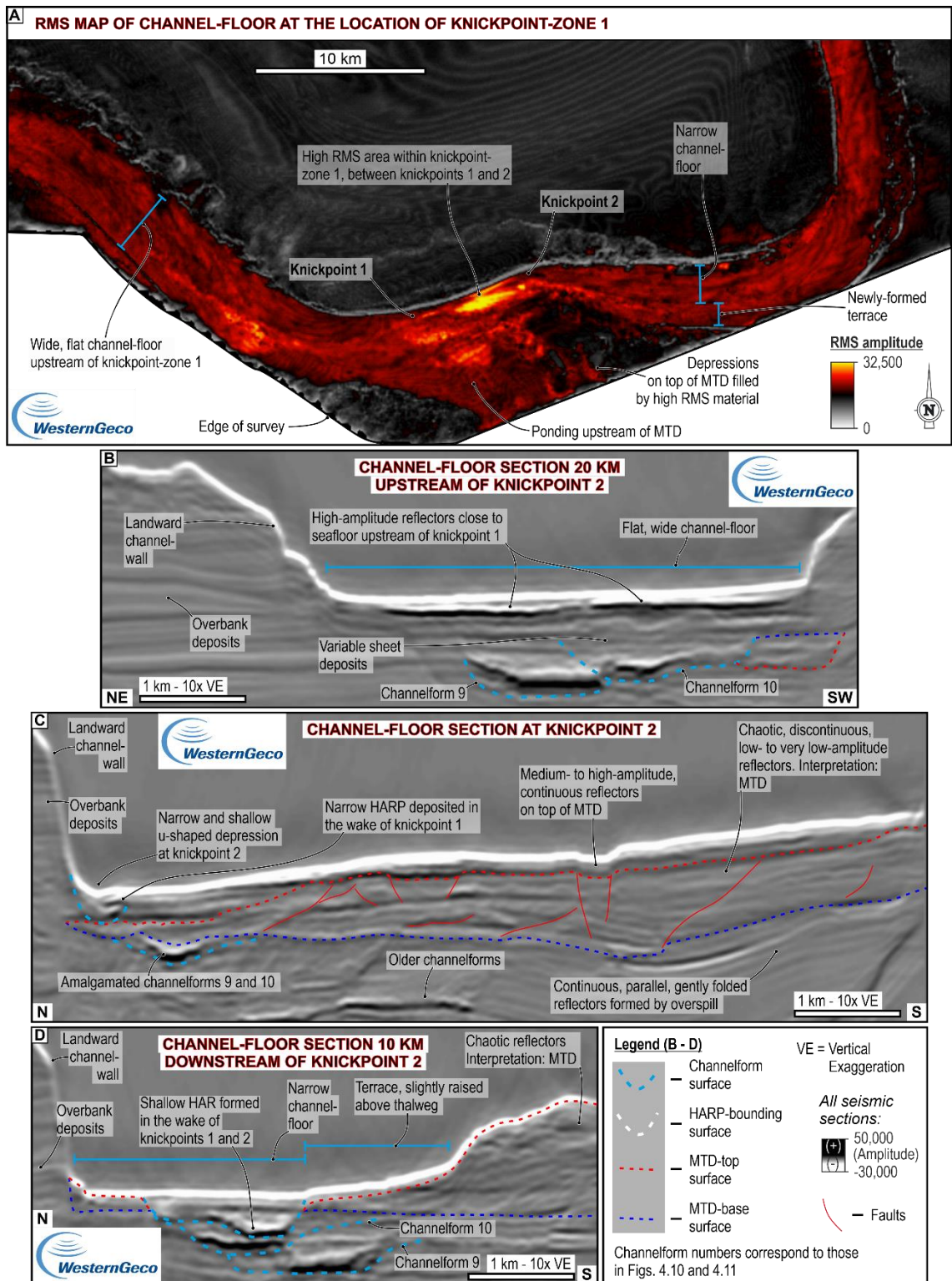


Figure 4.13 – (A) Root Mean Square (RMS) amplitude map of the seafloor showing the location of knickpoint-zone 1 (delineated by an area of high RMS amplitude), the flat, wide channel-floor upstream of knickpoint-zone 1, and the narrow channel floor bound by a newly formed terrace downstream of knickpoint-zone 1. (B), (C) and (D) Seismic sections from the shallow subsurface (B) in the area with a wide, flat channel-floor, ~ 15 km upstream of thalweg of knickpoint-zone 1, (C) immediately (~ 300 m) downstream of knickpoint 2 and (D) ~ 7.5 km downstream of knickpoint 2.

At the head of knickpoint 2 (Figs. 4.2 and 4.5), within knickpoint-zone 1, the aforementioned MTD has a maximum thickness of ~ 90 m (Fig. 4.13C). It systematically thins away from the oceanward channel-wall, and pinches out on top of channelforms 9 and 10, which are amalgamated at that point. On top of the MTD and channelforms 9 and 10, a ~ 55 m thick package of tabular reflectors with variable amplitudes is incised by a ~ 40 m deep, ~ 500 m wide, HARP-bounding surface cutting down from the landward edge of the channel-floor (Fig. 4.13C); the high-amplitude deposits within this surface are exposed on the seafloor, exhibiting high RMS amplitude values (Fig. 4.13A). This surface shallows and disappears ~ 500 m upstream of the head of knickpoint 2. At the head of knickpoint 2, the channel-floor contains a ~ 300 m wide U-shaped depression that is also confined to the north by the oceanward channel-wall (Fig. 4.13C). This depression sits within a 1300 m wide, subtler depression, below which tabular reflectors are exposed. Laterally adjacent to the southern margin of this depression, a 6 km wide mound of medium to high-amplitude reflectors is present between the MTD-top and the seabed.

When the HARs exposed just upstream of knickpoint 2, and their associated HARP-bounding surface, are traced ~ 7.5 km downstream, the surface becomes ~ 55 m deep and 1500 m wide, and partially truncates channelform 10 (Fig. 4.13D). At this location the MTD has a maximum thickness of 150 m, but thins dramatically northward before the top flattens out to form a ~ 1300 m wide terrace (Fig. 4.13D). The location of knickpoint formation on the seafloor is on the landward side, opposite the source of the formative MTD.

Interpretations

Amplitude variability and transparent intervals in sheet deposits upstream of a conduit-damming MTD may result from initial partial ponding as flows rapidly decelerate upon encountering the MTD (Liang et al., 2020). Deceleration may lead to the formation of more chaotic, yet still weakly-confined flow deposits. Anomalously high-amplitude reflectors observed above sheet deposits with variable amplitudes may reflect sand-rich deposits from weakly-confined flows (McArthur et al., 2021) after initial MTD-margin topography was healed, leaving a less severe reduction in longitudinal gradient. These deposits formed immediately prior to, and during, re-incision and may mark the transition from incised sheet to terrace deposits.

As little remnant MTD is preserved on the landward side of the channel, it is unclear whether the modern MTD was deposited across the full channel-floor width; it is inferred that it did due to its relationship with deposits upstream. Knickpoints 1 and 2 (constituting knickpoint-zone 1) are in the process of upstream migration. They have incised through the thickest part (longitudinally) of the MTD, and any initial downstream

deposits, and are currently incising weakly-confined deposits upstream (Fig. 4.13). If MTDs are sourced from one channel-wall, the locus of incision into MTD-tops in the subsurface is typically on the side opposite its source. Both knickpoints create concave-up depressions in cross-section that widen downstream. At its head, knickpoint 1 is dominantly erosional. In its downstream wake (upstream of knickpoint 2) knickpoint 1 generated a HARP-bounding surface containing channel-fill deposits that exhibit high RMS amplitude values where exposed at the seafloor. Knickpoint 2 is interpreted to be presently incising into the deposits formed downstream of knickpoint 1.

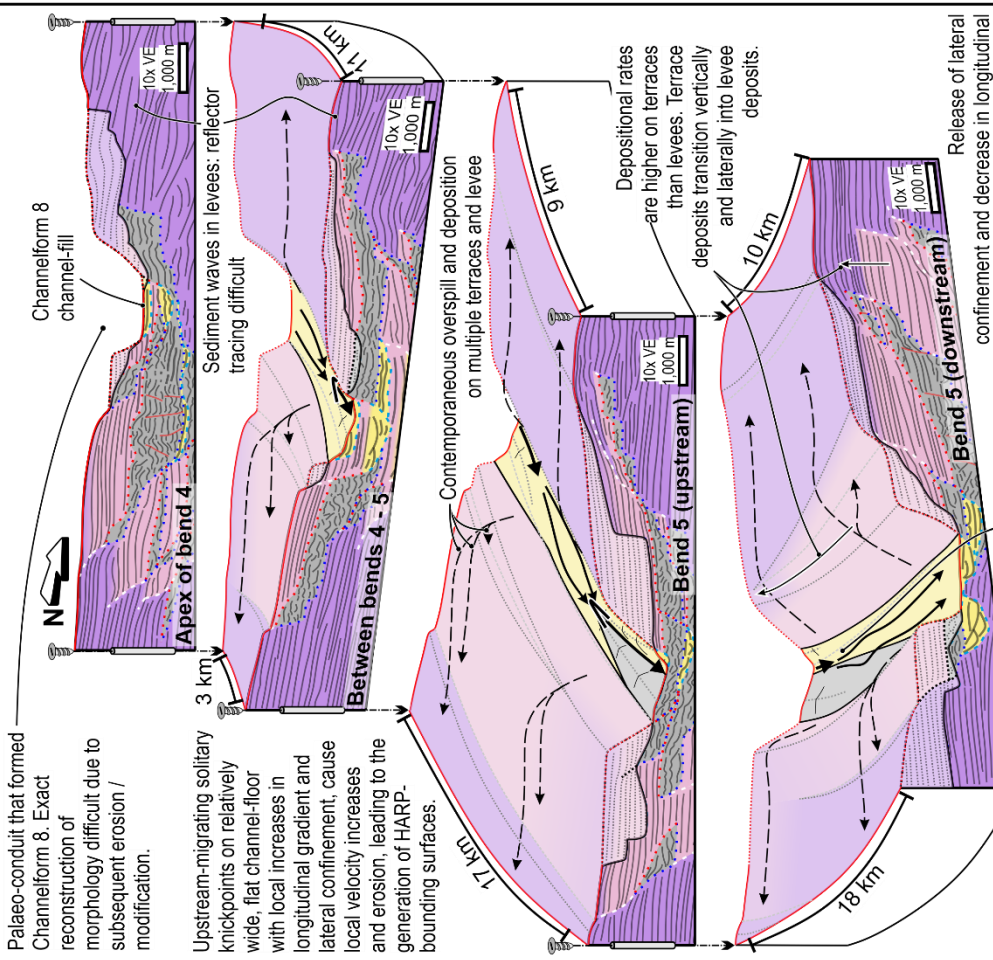
4.7 Discussion

4.7.1 An alternative model for the stratigraphic evolution of deep-water channels

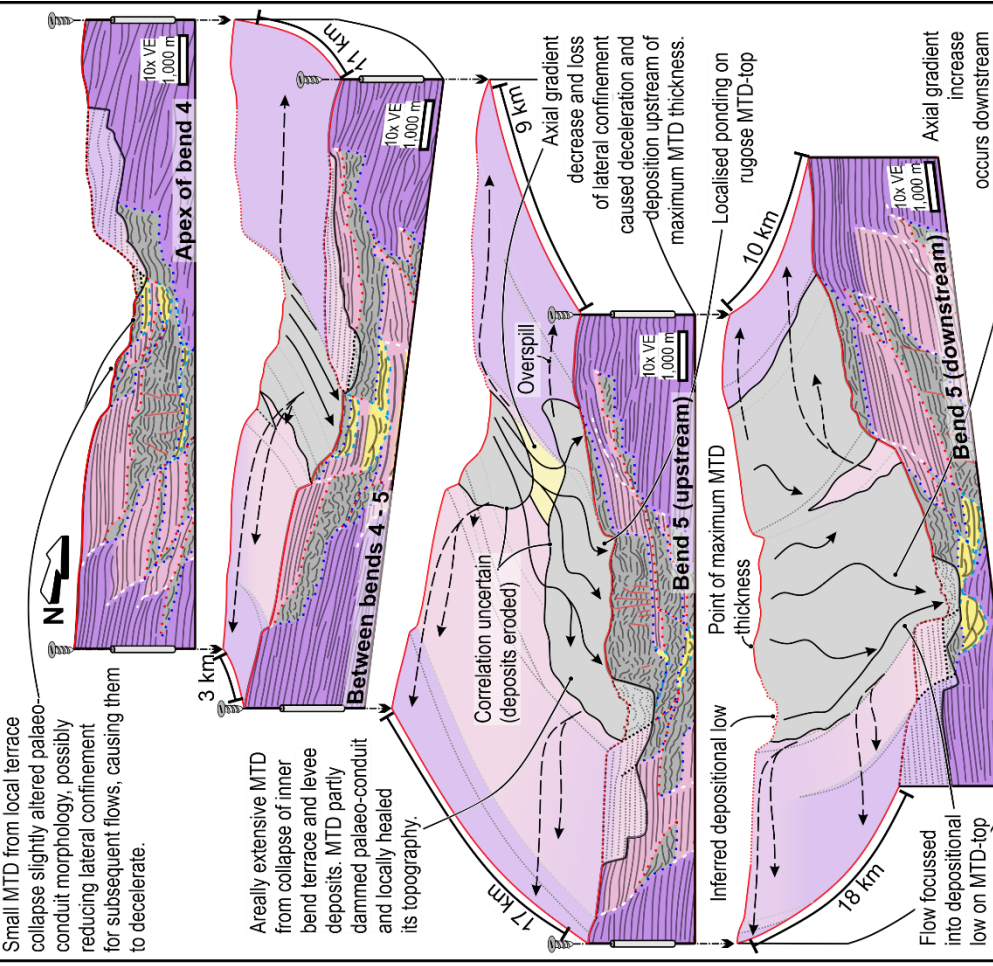
The currently active state of the channel (Mountjoy et al., 2018) together with the young age (<2 Ma) of the studied stratigraphy (Ghisetti et al., 2016) and the correspondence of features identified on the seafloor with seismic surfaces and seismofacies in the subsurface validate the use of the modern Hikurangi Channel as a 'self-analogue' for its deposits (Fig. 4.14). This article presents a new model for the stratigraphic evolution of deep-water channels that may help explain complexities in observed channel-fills and complement existing models of channel cut and fill.

Figure 4.14 (below) – *Interpreted seafloor reconstructions detailing the processes by which one palaeo-conduit is infilled and a subsequent one is created through five time-steps: (A) T1 – palaeo-conduit overlying channelform 8 has a wide channel-floor containing regularly spaced knickpoints; (B) T2 – collapse of the channel-wall forms an MTD that partially dams the channel, eliciting a decrease in longitudinal gradient upstream, and an increase downstream; (C) T3 – a knickpoint-zone forms and begins to migrate upstream, incising through, and leaving terrace deposits on top of, the MTD; (D) T4 – the knickpoint-zone migrates further upstream, incising through, and leaving terrace deposits on top of sheet deposits that formed upstream of the blockage but were contemporaneous to initial knickpoint-zone incision; (E) a new palaeo-conduit is formed in the downstream wake of the knickpoint-zone.*

A T1 - RECONSTRUCTED PALAEO-CONDUIT DURING DEPOSITION OF CHANNELFORM 8.

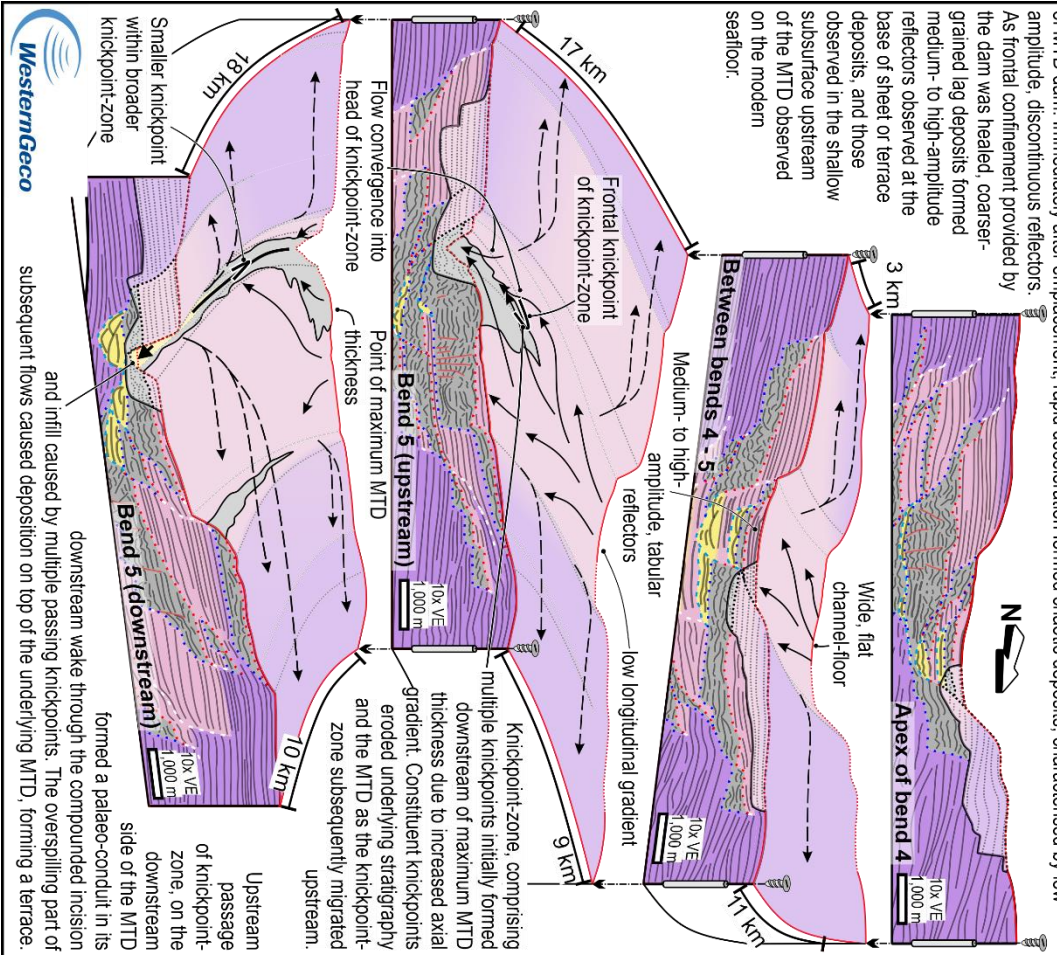


B T2 - COLLAPSE OF CONDUIT WALLS AND CHANNEL DAMMING.



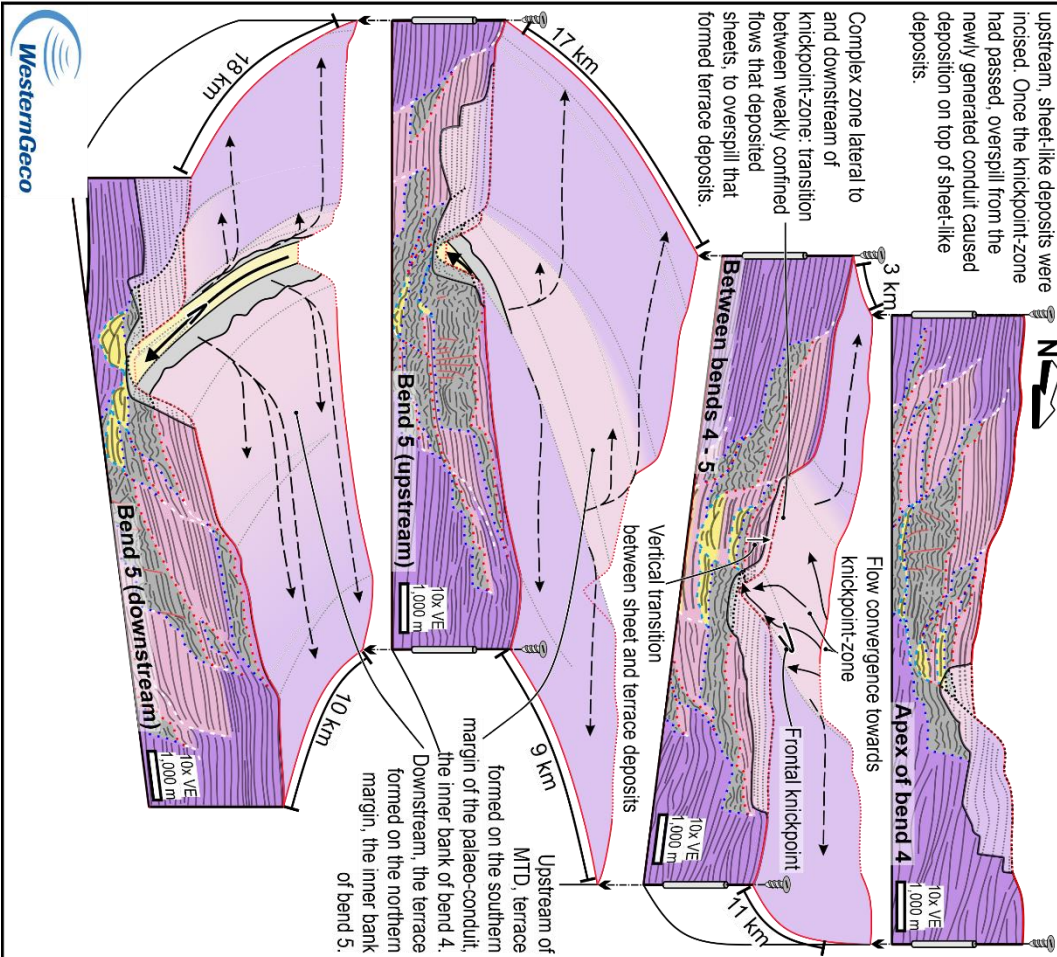
C T3 - DEPOSITION UPSTREAM AND KICKPOINT-ZONE FORMATION DOWNSTREAM.

Longitudinal gradient decrease and palaeo-conduit widening led to deceleration and widespread deposition upstream of MTD dam. Immediately after emplacement, rapid deceleration formed chaotic deposits, characterised by low amplitude, discontinuous reflectors. As frontal confinement provided by the dam was healed, coarser-grained lag deposits formed reflectors observed at the base of sheet or terrace deposits, and those observed in the shallow subsurface upstream of the MTD observed on the modern seafloor.



D T4 - UPSTREAM MIGRATION OF KICKPOINT-ZONE AND NEW CONDUIT FORMATION.

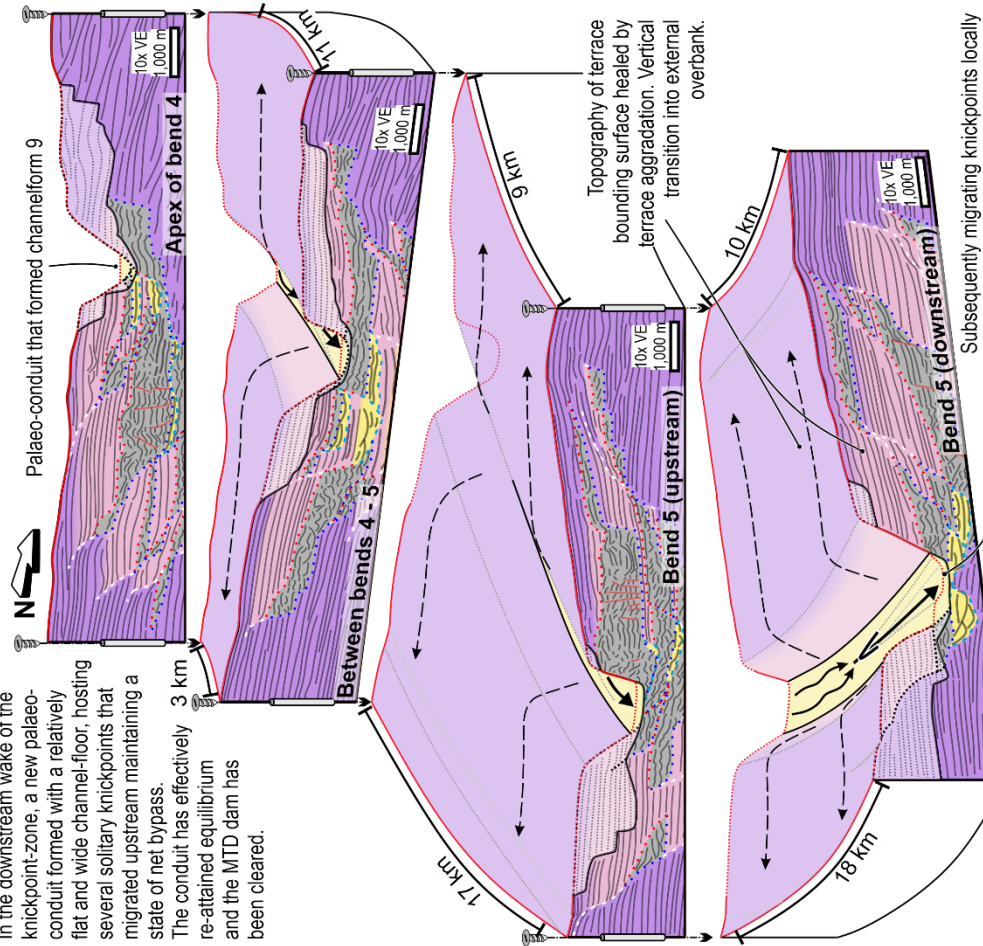
As knickpoint-zone migrated further upstream, sheet-like deposits were incised. Once the knickpoint-zone had passed, overspill from the newly generated conduit caused deposition on top of sheet-like deposits.



E T5 - RECONSTRUCTED PALAEO-CONDUIT DURING CHANNELFORM 9 DEPOSITION.

In the downstream wake of the knickpoint-zone, a new palaeo-conduit formed with a relatively flat and wide channel-floor, hosting several solitary knickpoints that migrated upstream maintaining a state of net bypass.

The conduit has effectively re-attained equilibrium and the MTD dam has been cleared.



Topography of terrace bounding surface healed by terrace aggradation. Vertical transition into external overbank.

Subsequently migrating knickpoints locally incised and filled, generating HARP-bounding surfaces and contributing to the widening and deepening of a larger, channelform surface.



Legend	Surfaces	Depositional elements	Flow vectors	Preserved / observed	Eroded / inferred
VE = Vertical Exaggeration					
Channelform surface	-	Channel-fill	-	Yellow box	Yellow box
Sheet or terrace-bounding surface	-	Sheet or terrace	-	Pink box	Pink box
MTD-top surface	-	Levee	-	Purple box	Purple box
MTD-base surface	-	Mass-Transport Deposit (MTD)	-	Grey box	Grey box
Inferred surface	-	Other	-	Red line	Red line
High velocity, dominantly bypassing flow	→	Reconstructed seafloor	-	Black line	Black line
Low velocity, dominantly depositional flow	→	Very low to medium-amplitude reflectors	-	Grey line	Grey line
Overbank / overspilling flow	→	High medium to very high-amplitude reflectors	-	Black line	Black line
		Knickpoints	-	Black line	Black line
		Faults	-	Black line	Black line

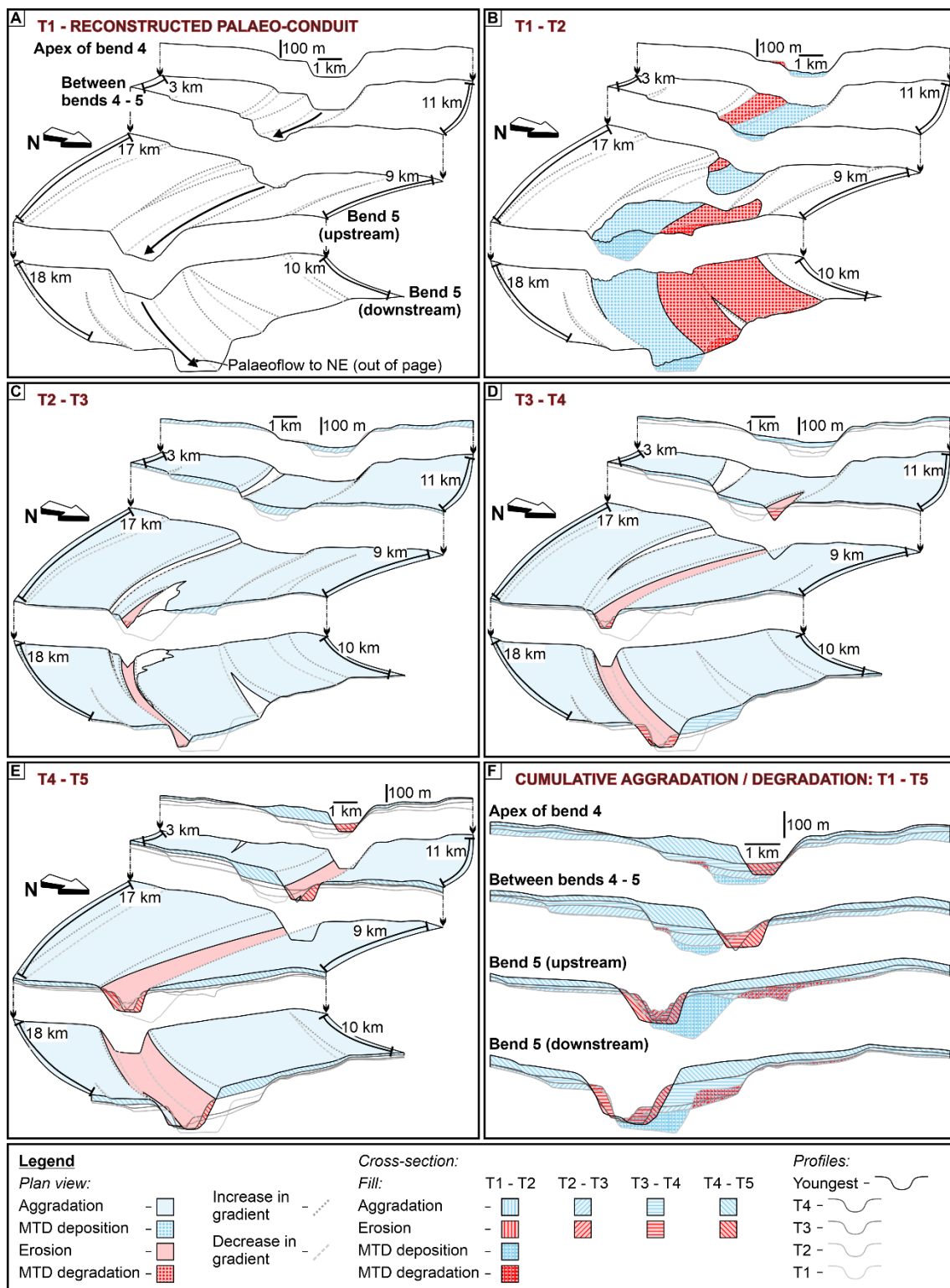


Figure 4.15 – Relative change diagrams showing the location of interpreted seafloor aggradation and degradation between the five time steps shown in Fig. 4.14: (A) T1, the initial surface; (B) T1 – T2; (C) T2 – T3; (D) T3 – T4; (E) T4 – T5; (F) cumulative product of T1 – T5.

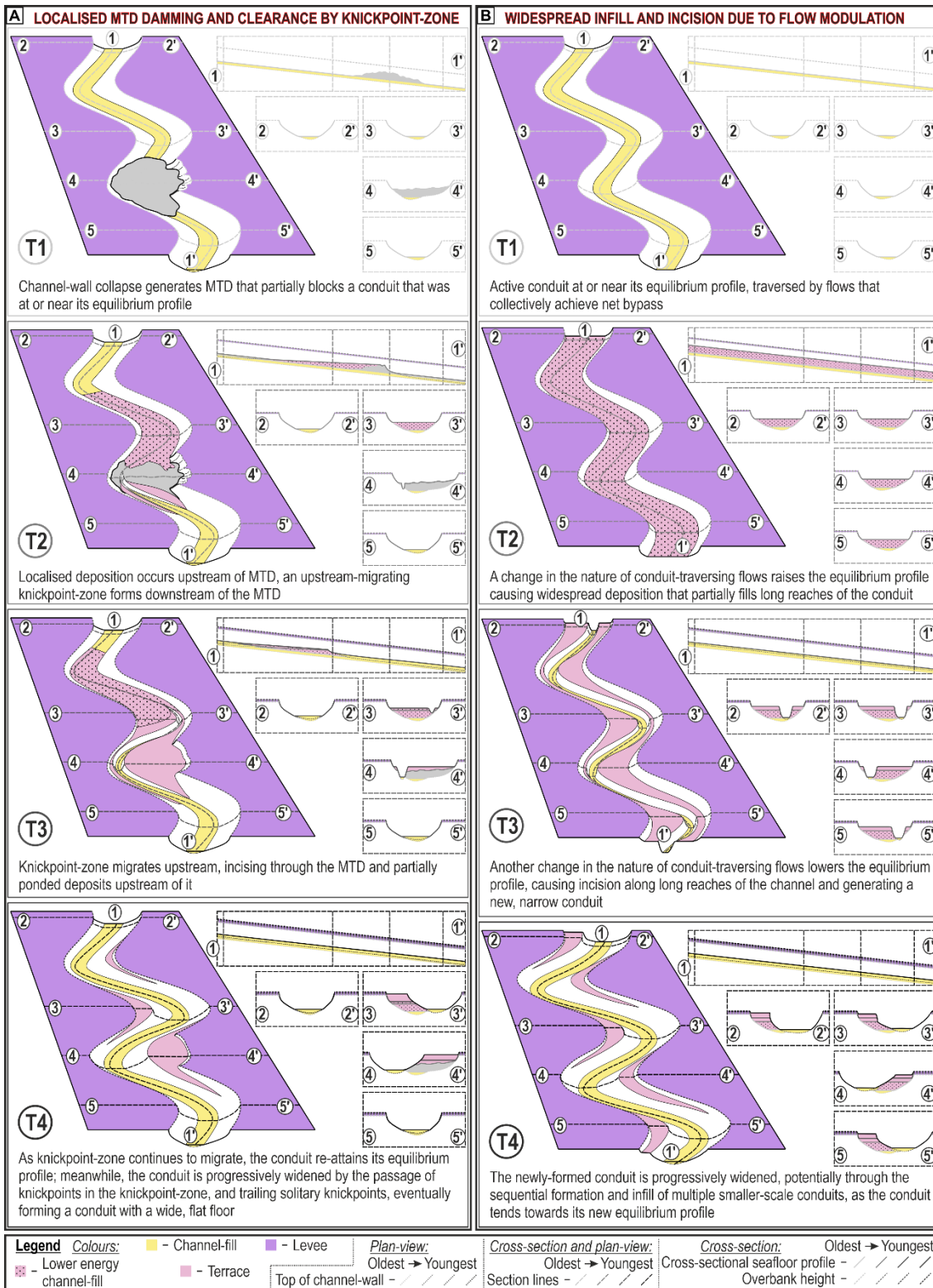


Figure 4.16 – Two schematic models of channel evolution, explaining the potential processes responsible for the infill of a composite channelform surface, and the establishment of another. (A) Channel damming by an MTD, then clearance by an upstream-migrating knickpoint-zone causing a localised morphodynamic response. (B) Variations in the nature of the channel-traversing flows causing widespread deposition then incision along the entire channel reach (roughly the same as the studied reach of the Hikurangi Channel). ‘Lower energy channel-fill’ encompasses a

range of possible architectures, from weakly confined sheet deposits (this study) to isolated, meandering channels (e.g. Kneller et al., 2020).

Upstream of the emplacement of a wall-derived MTD, flow deceleration accompanying a reduction in longitudinal gradient and lateral confinement caused deposition (Corella et al., 2016; Liang et al., 2020; Tek et al., 2020), filling the palaeo-conduit and widening the palaeo-channel-floor (Figs. 4.14B, 4.14C and 4.15B). Potentially sand-rich 'sheet-like' deposits in this area are preserved as medium to high-amplitude, tabular reflectors (Figs. 4.7E, 4.7G, 4.10B and 4.13B). Downstream of MTDs, sheet deposition may have occurred initially due to flow disequilibrium related to increased overspill (Peakall et al., 2000a, b) resulting from the shallowing of the partially-filled palaeo-conduit, and/or flow perturbation by their interaction with rugose MTD-top topography (e.g. Kneller et al., 2016; Ward et al., 2018; Bull et al., 2020). As partial ponding started healing short-wavelength MTD-top topography and upstream aggradation partially healed longer-wavelength topography, flow velocities increased downstream (Fig. 4.14C). Further velocity increase due to an increased longitudinal gradient led to the formation of a knickpoint-zone (Figs. 4.14C, 4.14D, 4.15C and 4.15D).

The knickpoint-zone, that comprised multiple, closely-spaced knickpoints, migrated upstream, sequentially incising first sheet-like deposits downstream of the MTD, then the MTD, and finally the sheet-like deposits upstream of the MTD (Figs. 4.14 and 4.15). The 'frontal' (furthest upstream; sensu Heijnen et al., 2020) knickpoint marks the highest and most upstream point of a knickpoint-zone. The elevation of the head of the frontal knickpoint of the knickpoint-zone was dictated by the longitudinal profile of the channel immediately upstream of it. The elevation of the most downstream knickpoint in the knickpoint-zone was likely situated at or near the channel's equilibrium profile (Guiastrenec-Faugas et al., 2020). As the knickpoint-zone migrated upstream, and the difference between the actual longitudinal profile upstream of the knickpoint-zone and its equilibrium profile decreased, so did the overall height of the knickpoint-zone (Fig. 4.16A). Eventually, as equilibrium was re-attained, the knickpoint-zone may have disappeared, or formed a solitary knickpoint.

Downstream of the knickpoint-zone, a channel-form surface was buried beneath a new, flat channel-floor that likely hosted a series of relatively regularly-spaced solitary knickpoints as seen on the seafloor, bound by a newly-formed terrace (Figs. 4.2C and 4.14E). The position of knickpoint-zone 2 (comprising knickpoints 6 and 7 on the seafloor; Figs. 4.2C and 4.5F), over 20 km upstream of its causative blockage, suggests that knickpoint-zones are non-static. However, due to the uncertainties in knickpoint

migration rates and lack of constraint of the timing of MTD emplacement, a detailed explanation of the migratory mechanism of knickpoint-zones is not possible. Studies have shown how large, composite concave-up surfaces (herein channelform surfaces) can form in response to widespread aggradation and degradation of the channel thalweg in response to variations in the nature (type, magnitude, velocity and grain size) of channel-traversing flows (Gardner et al., 2003; Kneller, 2003; Flint et al., 2011; Sylvester et al., 2011; Hodgson et al., 2016; Kneller et al., 2020). In such situations (commonly cyclical) periodic changes in flow nature alter the equilibrium gradient to which a channel tends to adjust, generating repeated periods of net erosion and deposition over long channel reaches (Kneller, 2003; Fig. 4.16B). Conversely, in the Hikurangi Channel, localised channel damming by MTDs induced modification of the actual channel profile, promoting deposition upstream and forcing the channel out of equilibrium. Through knickpoint-zone formation and migration, the longitudinal channel profile then tended towards re-attaining its equilibrium profile (Fig. 4.16A). Other mechanisms that can modify longitudinal channel profiles and induce similar, localised architectural motifs include structural growth (Heiniö & Davies, 2007; Georgiopoulou & Cartwright, 2013), halokinesis (Gee & Gawthorpe, 2006) and meander bend cut-off (Deptuck et al., 2007). However, none of these mechanisms affected the studied reach of the Hikurangi Channel.

While damming may be local at the scale of an entire channel, the low average longitudinal gradient of the channel (assumed similar throughout deposition), means that a 100 m thick blockage would, when restored to flat using simple trigonometry (a minimum estimate), cause aggradation up to ~ 64 km upstream. However, if sporadic episodes of localised channel-wall collapse, dam formation by MTDs, and clearance by knickpoint-zones (Fig. 4.16A) had been the only process responsible for the generation and infill of channelform surfaces, their subsurface distribution would have been complex and chaotic. Therefore, the fact that ten discrete channelform surfaces can be traced across the study area, suggests the existence of larger-scale cyclicity. Sediment supply to the canyons that feed the Hikurangi Channel is estimated to have been two to three times higher in glacial periods, when sediment was not trapped in glacial lakes (Lewis, 1994). Sediment supply-driven cyclicity may have resulted from periodic variations in the nature of flows that traversed the channel, causing repeated episodes of net aggradation followed by net erosion over long reaches of the channel, resembling a conventional 'cut-and-fill' model (Fig. 4.16B). More localised effects of channel damming (Fig. 4.16A) may be superimposed onto the effects of this broader cyclicity, generating the architecture observed in the Hikurangi Channel. Alternatively, apparent cyclicity could arise from repeated periods where the channel is particularly prone to channel-wall collapse, and periods of relative channel-wall stability. The aforementioned models likely interact.

However, additional data are required to discern the relative importance of factors such as sediment supply, seismicity, seafloor stability, and potential temporal variations in knickpoint and knickpoint-zone dynamics in controlling the evolution of the Hikurangi Channel.

Channel-wall collapse is common in submarine channels. However, the architecture of channel-wall derived MTDs in passive margin systems is commonly that of rotated blocks of coherent overbank stratigraphy (e.g. Sawyer et al., 2007, 2014), or relatively small slumps or debrites that comprise part of the channel-fill but are not preserved in adjacent overbank stratigraphy (e.g. Deptuck et al., 2003; Hansen et al., 2015). MTDs of similar scales and architectures to those in the Hikurangi Channel are observed in the axial channel deposits in the Northern Alpine Foreland Basin (Kremer et al., 2018). Furthermore, contrasting passive and active areas of the eastern continental margin of New Zealand, Watson et al. (2020) demonstrated that submarine landslides (including channel-wall collapses) are more prevalent and larger in active areas. Therefore, channels on seismically quiescent margins may experience less influence of MTDs on their architecture, when compared with channels on seismically active margins. However, a paucity of studies focused on the influence of channel-wall derived MTDs in channelised deep-water stratigraphy means data from more systems is needed to validate this relationship.

4.7.2 *The subsurface expression of knickpoints and knickpoint-zones*

Two nested scales of concave-up surfaces are observed in the subsurface of the Hikurangi Channel: small scale 'HARP-bounding surfaces' and larger 'channelform surfaces' (Table 4.2).

HARP-bounding surfaces truncate <60 m of stratigraphy, are <1 km wide (Fig. 4.7A and B), and are the smallest hierarchical order of surface preserved in the seismic data. They are interpreted to form from the passage of upstream-migrating knickpoints that incise upstream over short lengths (herein ~ 2.5 km) and deposit immediately downstream (Table 4.2; Fig. 4.17A).

Channelform surfaces truncate <80 m of stratigraphy, are <3 km wide, and represent composite surfaces that contain one or more HARP-bounding surfaces (Fig. 4.7A and B). Channelform surfaces initiate by the passage of knickpoint-zones (containing multiple knickpoints) that form in response to local damming by MTDs (Figs. 4.14 and 4.15). Channelform surfaces and their formative knickpoint-zones operate at a larger hierarchical order than HARP-bounding surfaces and their formative knickpoints (Fig. 4.17A).

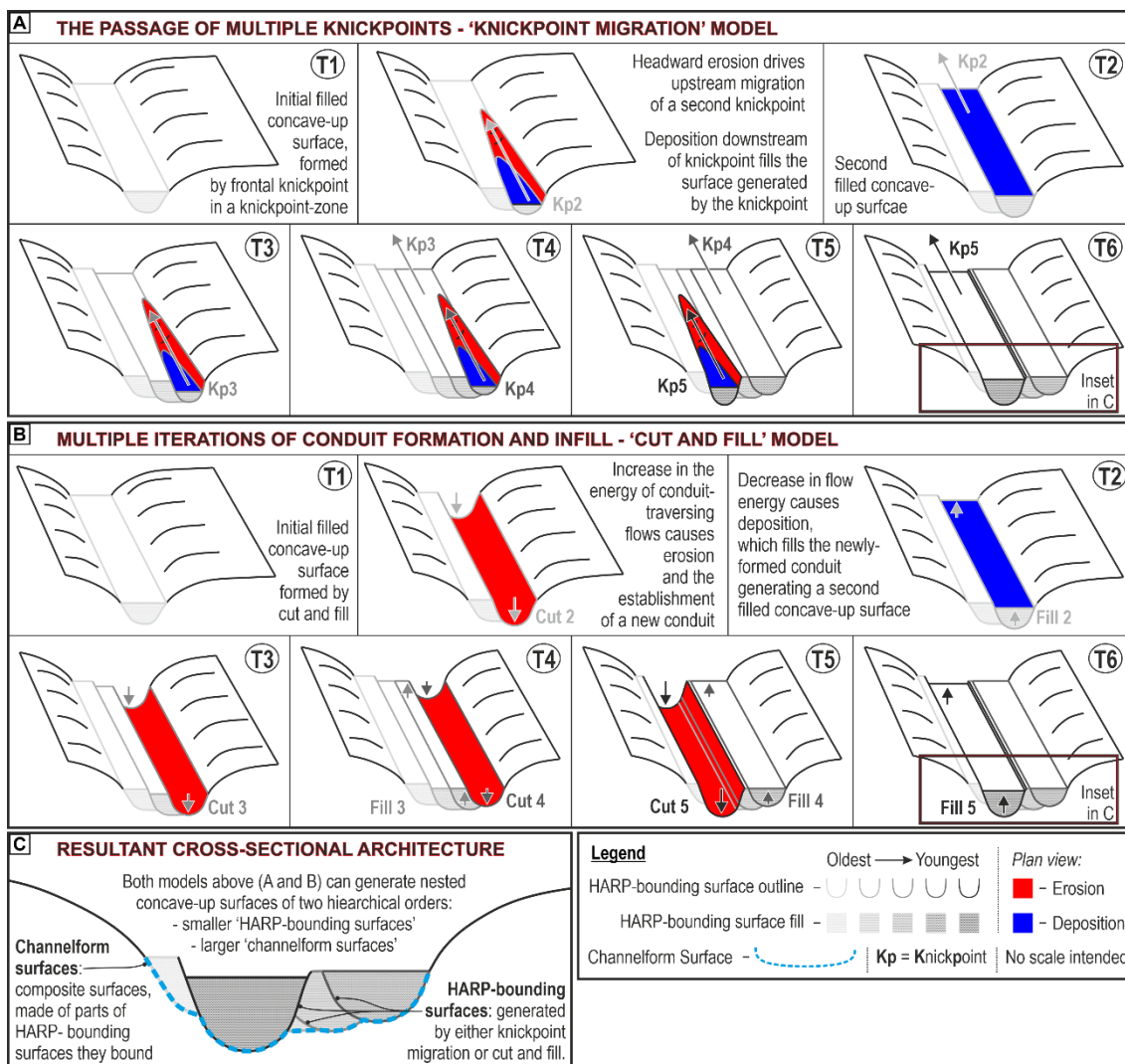


Figure 4.17 – Schematic diagrams showing two contrasting models for the generation of two nested scales of filled, concave-up surface in cross-section. (A) Multiple knickpoints, likely organised into a knickpoint zone, migrate upstream by headward erosion and deposition immediately downstream, leaving a series of concave-up surfaces (equivalent to HARP-bounding surfaces in the Hikurangi Channel), the edges of which constitute a larger-scale, composite surface (equivalent to a channelform surface in the Hikurangi Channel). (B) The formation and infill of multiple small-scale, incisional conduits generate a series of concave-up surfaces (HARP-bounding surface equivalent), the edges of which also constitute a larger, composite surface (channelform surface equivalent). (C) Schematic cross-section showing how both models could generate the same cross-sectional architecture.

In the Hikurangi Channel, as the frontal knickpoint in a knickpoint-zone migrated upstream, it generated an initial HARP-bounding surface (Fig. 4.17A). The initial surface was progressively deepened and widened by punctuated episodes of incision and infill by subsequent, passing knickpoints (Fig. 4.14C, D and E) forming a composite channelform surface (Fig. 4.17A). Channelform surfaces therefore record the protracted evolution of the channel system (Sylvester et al., 2011; Hodgson et al., 2016; Hubbard et al., 2014, 2020) attempting to re-attain equilibrium after modification (Kneller, 2003; Georgiopoulou & Cartwright., 2013; Guiastrennec-Faugas et al., 2020), whereas HARP-bounding surfaces record the remnant signature of a localised downstream transition from erosion to deposition in response to transient, upstream-migrating knickpoints. Because they both formed by longitudinally localised erosion and deposition by geologically transient features, neither scale of surface existed, in its entirety, as a geomorphic feature and neither delineates the instantaneous form of a palaeo-conduit at any one time. The generation of apparent stratigraphic hierarchy by the localised action of different scales of transient seafloor features (the 'knickpoint migration' model presented herein; Fig. 4.17A; see also Guiastrennec-Faugas et al., 2021) departs from conventional 'cut-and-fill' models (Gardner et al., 2003; Maier et al., 2012; Fig. 4.17B). Both models can generate two nested scales of concave-up (in cross-section) surfaces like those observed in the Hikurangi Channel (Fig. 4.17C). To form the smaller-scale surfaces (equivalent to HARP-bounding surfaces in the Hikurangi Channel), cut-and-fill models invoke the repeated excavation and infill of conduits in response to cyclical variations in the nature of channel-traversing flows (Hansen et al., 2017b; Bell et al., 2020; Fig. 4.17B). In such models, larger-scale surfaces (equivalent to channelform surfaces in the Hikurangi Channel) are generated by progressive widening and deepening, then infilling through the action of the smaller-scale conduits, in response to higher order variations in the nature of channel-traversing flows (Hodgson et al., 2011, 2016; Fig. 4.17B). While the formative mechanism of large-scale composite surfaces is comparable between the knickpoint-based and cut-and-fill models, the formative mechanisms of small-scale surfaces are very different.

At the smallest scale, the migration of features interpreted as cyclic-steps and sediment waves, observed on the floor of the modern Hikurangi Channel, may build and erase stratigraphy at the scale of a few metres (Vendettuoli et al., 2019; Englert et al., 2020). However, data with finer resolution are required to determine how pervasive these features may be in the studied reach of the Hikurangi Channel, as well as in other channels, and the impact these features may have on the preserved stratigraphy.

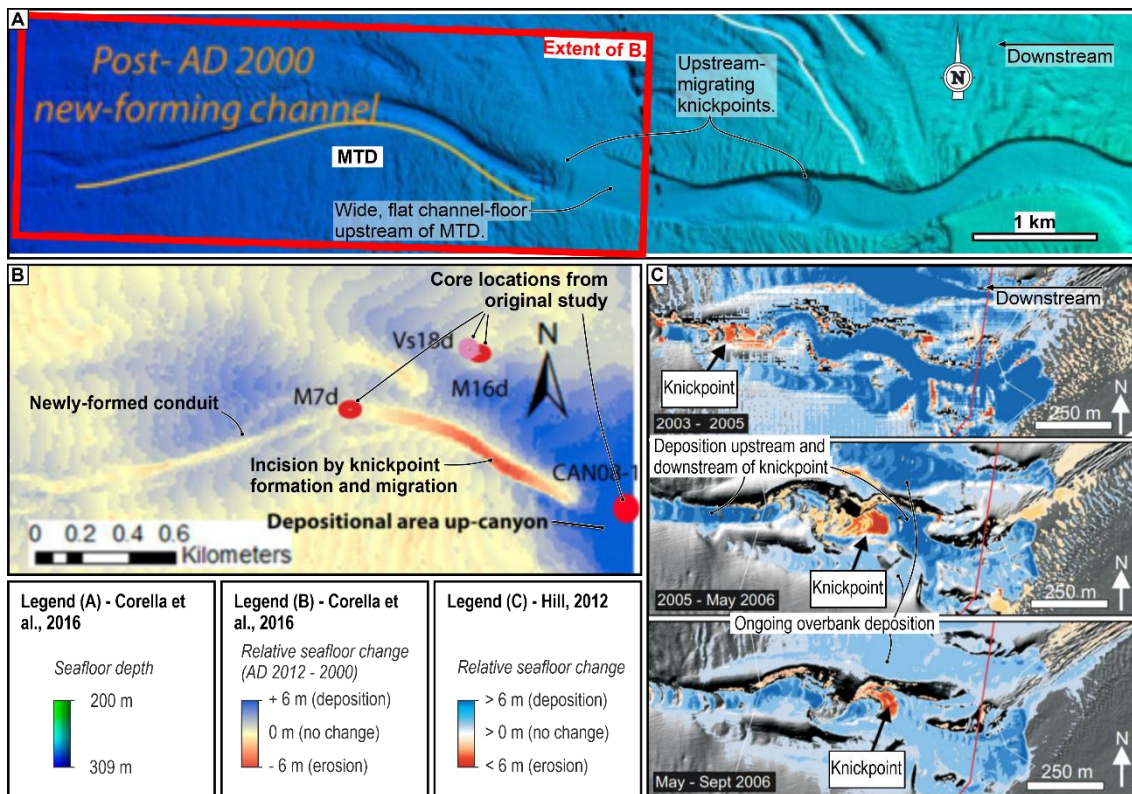


Figure 4.18 – (A) Bathymetry map from the Rhone Delta in Lake Geneva, modified from Corella et al. (2016; original bathymetry from Girardclos et al., 2012), showing a channel with a wide, flat channel-floor upstream of an MTD that is being incised by a knickpoint and a newly-formed conduit; reproduced with permission from Elsevier. (B) Map of sea floor change between AD 2000 and 2012 of the inset shown in (A), again modified from Corella et al. (2016), showing deposition upstream and erosion downstream of knickpoint; reproduced with permission from Elsevier. (C) Map of sea floor change between AD 2003 and 2006 on the Fraser River delta, modified from Hill (2012), showing ongoing deposition on the overbanks, and upstream and downstream of a migrating knickpoint, with erosion localised to the knickpoint head; reproduced with permission from the International Association of Sedimentologists (IAS).

4.7.3 Comparison with knickpoints and knickpoint-zones in other systems

Knickpoints and knickpoint-zones in deep-water channels can form in response to avulsions (Pirmez & Flood, 1995; Dennielou et al., 2017), structural growth (Heiniö & Davies, 2007; Mitchell et al., 2020), halokinesis (Gee & Gawthorpe, 2006), bend cut-off (Deptuck et al., 2007), longitudinal variations in substrate composition (Mitchell, 2004), MTD emplacement (Corella et al., 2016), or longitudinal variations in flow parameters (Heijnen et al., 2020). Ponding upstream and knickpoint generation downstream of MTDs has been observed in submarine canyon deposits (Paull et al., 2011; Corella et al.,

2016). Repeat bathymetry surveys on the Rhone Delta Canyon (Girardclos et al., 2012; Corella et al., 2016) show that in the 12 to 14 years after MTD emplacement widespread deposition (>6 m) occurred upstream, generating a flat, wide channel-floor, whilst a knickpoint formed downstream eroded >6 m into the substrate, forming a new conduit offset from the original one (Fig. 4.18A and B). In contrast, MTDs in the Hikurangi Channel cannot be thicker than the height of their source channel-wall, meaning they cannot fully occlude the channel, thereby allowing flows downstream to continue along the same path. Repeat surveying on the Fraser River Delta slope (Hill, 2012) shows how continual deposition on levées and terraces can occur during knickpoint migration, with deposition also occurring immediately upstream and downstream of knickpoints (Fig. 4.18C). Similar behaviours are interpreted to have contributed to the development of the Hikurangi Channel (cf. Figs. 4.14 and 4.15). Spatially localised erosion at the head of migrating knickpoints (and knickpoint-zones) may therefore contribute significantly to erosion in deep-water canyon and channel systems.

Knickpoints observed in the Hikurangi Channel appear shallower than those studied in systems with steep longitudinal gradients, where knickpoints may exceed 30° (e.g. Heijnen et al., 2020) and are similar to those observed in systems with shallow longitudinal gradients, which are all less than 5° (e.g. Babonneau et al., 2002). This may however be due to differences in data resolution, as gradients in datasets with finer horizontal resolution are more likely to be accurate. Knickpoints in the Hikurangi Channel may initiate in response to: (i) small-scale channel-wall collapse (a similar mechanism to knickpoint-zones); (ii) exploitation of smaller-scale bedforms; or (iii) longitudinal variability in flow parameters. Heijnen et al. (2020) present three mechanisms for knickpoint migration: (i) enhanced erosion by supercritical flow upstream of a hydraulic jump; (ii) mass failure in response to loading or shaking by a passing flow; and (iii) mass failure due to oversteepening by basal erosion. Knickpoint migration rates measured from repeat bathymetric surveys in canyon or channel systems in relatively shallow-water (up to ~ 500 m), namely on the Fraser River Delta (Hill, 2012), Rhone Delta (Corella et al., 2016), Capbreton Canyon (Guiastrennec-Faugas et al., 2020, 2021), and Bute Inlet (Heijnen et al., 2020), range between 50 and 600 m/yr. Channels in these highly active systems are traversed by one (Capbreton Canyon; Brocheray et al., 2014) to over thirty (Rhone Delta Canyon; Lambert & Giovanoli, 1988) flows per year. In contrast, earthquake-driven canyon flushing in the Kaikōura Canyon, generating turbidity currents large enough to reach the trench, is calculated to occur every ~ 140 years (Mountjoy et al., 2018). Furthermore, in a direct monitoring study from the Monterey Canyon, Paull et al. (2018) recorded fewer events at distal moorings than proximal ones per time period, suggesting distal parts of channel systems receive fewer events than their feeding canyons. Therefore, knickpoints in shallow-water, high-gradient reaches of channels and

canyons may be expected to migrate faster than distal, shallow-gradient reaches. However, because multiple canyons feed the Hikurangi Channel, knickpoint migration rates in distal, shallow-gradient parts of the channel may be accelerated. Furthermore, channel-traversing turbidity currents can accelerate as they entrain sediment from the substrate (Heerema et al., 2020), meaning the few flows that reach distal parts of the channel may exhibit larger average magnitudes, leading to knickpoints migrating further during each event.

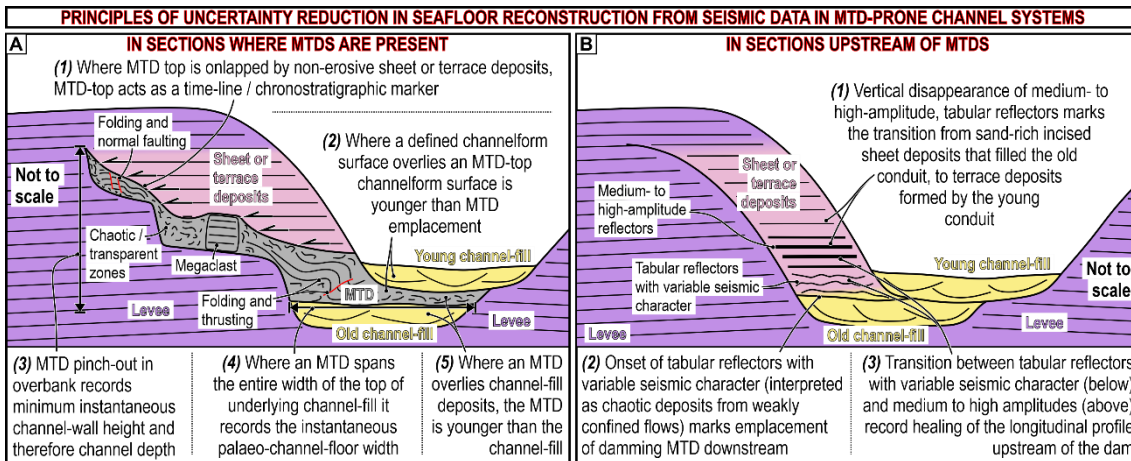


Figure 4.19 – Schematic cross-sections showing the principles by which uncertainty in seafloor reconstruction may be reduced in the presence of channel-damming MTDs. Sections either: (A) where MTDs are present; or (B) upstream of channel-damming MTDs, can be used to inform seafloor reconstruction.

4.7.4 Reconstructing the palaeo-seafloor from seismic data

Channels on the modern seafloor provide only a snapshot of the evolution of a channel system. In the absence of detailed chronostratigraphic control or thick hemipelagic drapes (e.g. Maier et al., 2011, 2012; Jobe et al., 2015), instantaneous reconstruction of the palaeo-seafloor from seismic data can be problematic because:

1) Surfaces elongate in the direction of palaeoflow with concave-up cross sections may be generated by the passage of transient features such as knickpoints and knickpoint-zones (Heijnen et al., 2020; Tek et al., 2020; this study). These surfaces are diachronous, did not exist in their entirety at any one time (Sylvester et al., 2011; Hodgson et al., 2016), and may represent the compound product of one or more upstream-migrating knickpoints (Guiastrenec-Faugas et al., 2020, 2021).

2) Synchronous deposition upstream, and erosion downstream, of an MTD dam hinders chronostratigraphic correlation, especially when upstream deposits are subsequently eroded and terrace deposits coalesce to form a single depositional element

(Figs. 4.14D and 4.15). As a result, concave-up surfaces may be progressively older downstream, making them less reliable as chronostratigraphic markers.

3) An upward transition can occur between the late-stage fill of a palaeo-conduit, and overlying terrace deposits formed by overspill from a secondary palaeo-conduit. In this case, a single surface does not provide a chronostratigraphic marker of the boundary between two successive palaeo-conduits (Deptuck et al., 2003; Figs. 4.7G, 4.10 and 4.14D).

4) Deposits on any one terrace may have formed through the lifecycle of multiple adjacent palaeo-conduits (Figs. 4.11, 4.14 and 4.15). Likewise, the overspill of a single palaeo-conduit may be manifested in multiple terraces (Droz et al., 2003; Babonneau et al., 2010; Kolla et al., 2012; Li et al., 2018; Figs. 4.2, 4.5, 4.11, 4.14A and 4.15). Furthermore, two adjacent terraces may merge, in time, through differential aggradation (Fig. 4.14). Attributing terrace deposits to a single formative palaeo-conduit can therefore be difficult.

5) Terrace bounding surfaces may be constructed by sustained, contemporaneous deposition on an inboard (towards the coeval palaeo-conduit) terrace and an adjacent, outboard terrace or levée (Table 4.1), thus obscuring estimates of terrace and levée height and width.

6) Failure of channel-walls and subsequent MTDs may significantly alter the morphology of a palaeo-conduit (Figs. 4.14B and 4.15B).

Therefore, deposits and surfaces in outcrop and subsurface provide the most reliable record of protracted channel evolution, and channel-margin and overbank deposits are the most complete as they are less prone to extended periods of erosion or non-deposition (Hubbard et al., 2020). In large, well imaged, long-lived channel systems prone to collapses of their channel-walls, such as the Hikurangi Channel, uncertainty related to some of the aforementioned factors can be mitigated by utilising:

1) Quasi-instantaneously emplaced MTDs as reliable chronostratigraphic markers. Five approaches to aid seismic interpretation and seafloor reconstruction from seismic sections containing MTDs are presented in Fig. 4.19A.

2) Subtle changes in reflector character akin to those observed in the shallow subsurface, which can be related to geomorphological features. Three seismic-stratigraphic relationships that can reduce uncertainty in evolutionary interpretations in sections upstream of MTD dams are presented in Fig. 4.19B.

Regardless, the cross-sectional morphology of the infill of ancient deep-water channels ultimately reflects the compound effect of various local, time-transgressive

processes which have affected an area of a specific channel, not necessarily the boundary conditions under which the channels formed. Care must be taken when extrapolating the dimensions of palaeo-seafloor features, specifically palaeo-conduits, from the dimensions of the depositional elements they generate in these inherently complex sedimentary systems.

4.8 Conclusions

This study uses high-resolution bathymetry and 3D seismic data to provide the most detailed description to date of the seafloor geomorphology and three-dimensional subsurface architecture of a trench-axial deep-water channel: the Hikurangi Channel. The identification of ten seismofacies and five surface types allowed categorisation of the stratigraphy into four depositional elements: channel-fill, sheet or terrace, levée, and mass-transport deposits (MTDs). Relationships between depositional elements, their constituent seismofacies and bounding surfaces, allowed three-dimensional correlation and interpretation of several depositional sequences. The modern Hikurangi Channel can be used as a self-analogue for its palaeo-incarnations; integration of seafloor and subsurface data enabled the role of seafloor features in deposit formation to be elucidated, facilitating the reconstruction of the palaeo-seafloor through time and development of a new model for the genesis of submarine channel deposits.

The subsurface architecture of the Hikurangi Channel is principally controlled by the response to the quasi-instantaneous emplacement of local MTD dams derived from channel-wall collapses. Following MTD emplacement sheet-like deposits formed upstream due to reduced longitudinal gradients and lateral confinement. Downstream a knickpoint-zone, comprising multiple smaller-scale, closely-spaced knickpoints formed due to increased longitudinal gradients. Knickpoint-zones and knickpoints are areas of steepened longitudinal gradient, that are concave-up in cross-section and widen downstream. The knickpoint-zone migrated upstream and eventually diminished as the channel approached equilibrium. Accompanying migration, the knickpoint-zone incised sequentially through the MTD and sheet-like deposits upstream, leaving a new, flat channel-floor bound by newly-formed terraces in its wake. These results are consistent with findings from studies of active channel systems.

At least two nested scales of elongate, concave-up surfaces are preserved, interpreted to be formed by two distinct scales of migrating channel-floor features: (i) HARP-bounding surfaces truncate <60 m of stratigraphy and are typically ~ 500 m wide. They are formed by upstream-migrating knickpoints that leave a filled, or partially-filled, surface in their wake as they erode upstream and deposit immediately downstream. (ii) Channelform surfaces truncate <80 m of stratigraphy and are <3 km wide, formed by knickpoint-zones. One or more HARP-bounding surfaces are contained within, and

constitute the edges of a channelform surface. Channelform surfaces are diachronous, composite surfaces that are initiated and modified by the passage of knickpoints within their formative knickpoint-zone; thus, they represent a larger hierarchical order than HARP-bounding surfaces. Both scales of surface form through the migration of transient features and were therefore never present as bathymetric features in their entirety at any time.

Reconstruction of palaeo-seafloor morphology from seismic data is problematic due to the time-transgressive and transitional nature of surface and deposit formation. However, the presence of quasi-instantaneously emplaced MTDs that can act as stratigraphic markers, and an active modern channel acting as a self-analogue for its subsurface deposits, mitigate uncertainty in this study.

By integrating sedimentary architecture and seafloor geomorphology, the data presented here permit a new model for the construction of channelised deep-water stratigraphy. This model complements existing models describing the formation and infill of deep-water channels, accounting for architectural complexity, and it is consistent with observations from the seafloor. Insights from this study may be used to aid interpretation in other channel systems where a direct seafloor analogue is lacking or data coverage is sparse.

5 Controls on the architectural evolution of deep-water channel overbank sediment wave fields: insights from the Hikurangi Channel, New Zealand

5.1 Summary

Deep-water channels can be bound by overbank deposits, resulting from overspilling flows, which are often ornamented with sediment waves. Here, high-resolution bathymetry, backscatter, and 2D and 3D seismic data are integrated to discern the controls on flow processes on the overbank areas of the Hikurangi Channel. Qualitative seismic interpretation and quantitative analyses of sediment wave morphologies and distributions are conducted through the shallowest 600 m of stratigraphy up to the seafloor. Four outer-bend wave fields are present throughout the studied stratigraphy on the landward margin (left margin looking down-channel) only. Originally closely spaced or combined, these fields evolved to become spatially separated; two of the separate wave fields became further subdivided into distinct outer- and inner-bend fields, whose constituent waves developed distinct differences in morphology and distribution. Sediment wave character is used to interpret the direction and strength of overbank flow. Nine controls on such flow and associated deposition are identified: flow versus conduit size, overbank gradient, flow tuning, Coriolis forcing, contour current activity, flow reflection, centrifugal forcing, interaction with externally derived flows, and interaction of overspill from different locations. Their relative importance may vary across parts of overbank areas, both spatially and temporally, controlling wave field development such that: (1) outer-bend wave fields only develop on the landward margin; (2) the influence of centrifugal force on outer-bend overbanks has increased through time, accompanying a general increase in channel sinuosity; (3) inner-bend wave fields on the landward margin form by the interaction of Coriolis-enhanced inner-bend overbank flow, and outer-bank flow from up-channel bends; (4) inner-bend fields on the oceanward margin form by the interaction of axial flow through wave troughs, and a transverse, toward-channel flow component. This work has implications for interpreting overbank flow from seafloor and seismic data, and for palaeogeographic reconstructions from outcrop data.

5.2 Introduction

Deep-water channels are subaqueous conduits through which turbidity currents and other sediment-laden flows transport sediment (Normark, 1970), which can contain pollutants (Kane et al., 2020; Zhong and Peng, 2021), organic carbon (Hage et al., 2020), fresh water (Kao et al., 2010), and nutrients (Heezen et al., 1955) to the deep seas. Turbidity currents thicker than the depth of the channel they traverse spill onto their overbank areas, depositing fine-grained ‘overbank’ sediments from dilute flows (Piper and Normark, 1983). Overbank deposits are accumulations of sediments that can reach almost one thousand metres in thickness and tens of kilometres in width (Pirmez and Flood, 1995; Nakajima and Kneller, 2013). These deposits can provide a more complete depositional record of channel evolution than deposits formed on the floors of palaeochannels, which are susceptible to being excavated by repeated episodes of incision (Morris et al., 2014). Previous studies have led to the development of models of overbank flow and architecture evolution in which progressive trends of diminishing grain size (typically from fine sand to mud) and deposit thickness are seen in transects away from the levee crest (Kane et al., 2007; Morris et al., 2014). However, these simple trends may be complicated by the influence of factors such as: variations in the size of turbidity currents relative to their host conduit (Dennielou et al., 2006), flow ‘tuning’ (Mohrig and Buttles, 2007; Kelly et al., 2019), variations in overbank slope gradient (Kane et al., 2010b; Nakajima and Kneller, 2013), sinuosity (Timbrell, 1993; Kane et al., 2008), structural confinement (Clark and Cartwright, 2011), the Coriolis force (Klaucke et al., 1998; Cossu et al., 2015), and contour currents (Fuhrmann et al., 2020; Miramontes et al., 2020).

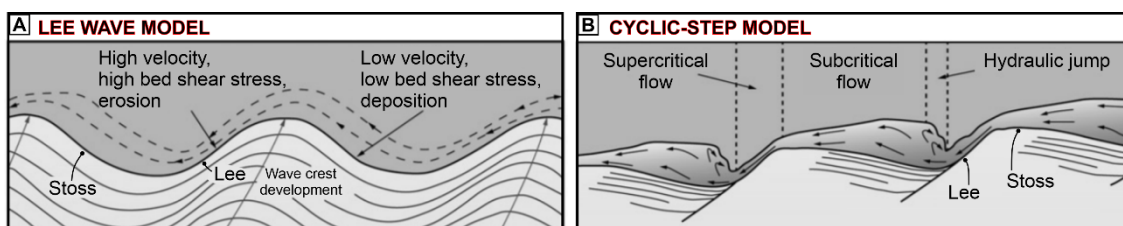


Figure 5.1 – Schematic diagrams showing how sediment waves migrate via: (A) the lee wave model (from Symons et al., 2016, after Flood, 1988), and (B), the cyclic-step model (from Symons et al., 2016, after Cartigny et al., 2011); flow direction is from right to left on both diagrams.

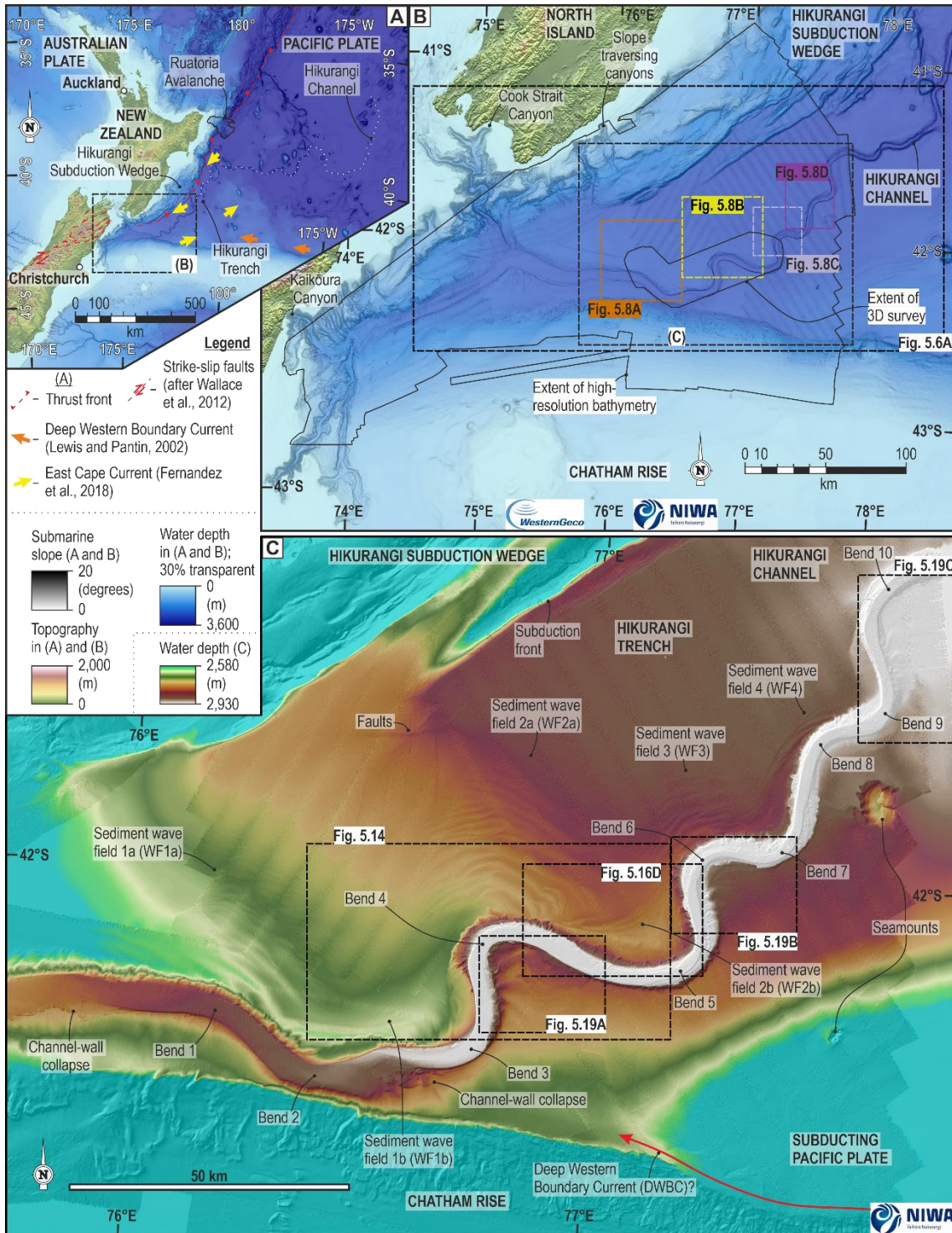
Channel overbank areas are often ornamented with sediment waves. Sediment waves are undulating bedforms that are commonly observed on the modern seafloor in a range of sedimentary environments (see Wynn and Stow, 2002; Symons et al., 2016).

The crests of sediment waves on channel overbanks are typically orientated parallel to the slope contours (Wynn and Stow, 2002), meaning they can range in orientation from parallel (e.g. Nakajima and Satoh, 2001) to perpendicular to their adjacent channel (e.g. Kuang et al., 2014). In crest-perpendicular transects overbank sediment waves have distinct stoss (upstream) sides that typically dip toward the channel and lee (downstream) sides that dip away from the channel, and typically exhibit wavelengths up to 7 km and heights up to 80 m (Wynn and Stow, 2002). They are found adjacent to reaches of channels that may extend hundreds of kilometres (e.g. Damuth, 1979; Migeon et al., 2004), and form fields that can extend for tens of kilometres (laterally) away from their formative channel (e.g. Normark et al., 1980; Carter et al., 1990). The upstream migration of sediment waves generates quasi-sinusoidal geometries commonly observed in seismic data imaging sediments beneath sediment wave fields. These depositional geometries can be present through hundreds of metres of stratigraphy (e.g. Migeon et al., 2000, 2001; Nakajima and Satoh, 2001). Two models have been proposed to explain the generation of such geometries: (a) flows with uniformly low Froude numbers, wherein increases in near-bed shear stresses on the lee sides inhibits deposition (the 'lee wave model'; Flood, 1988; Fig. 5.1A); or (b) flows with variable Froude numbers, wherein supercritical flow on the lee sides of the waves inhibits deposition, and a transition to subcritical flow occurs on the stoss side, essentially making the waves 'cyclic-steps' (Slootman and Cartigny, 2020; Fig. 5.1B).

It is commonly inferred that the crests of overbank sediment waves are orientated subperpendicular to the dominant local flow direction (Nakajima et al., 1998; Migeon et al., 2000), and their wavelengths and heights scale with the thickness, and velocity, of the overspilling flows that formed them (Normark et al., 2002). Therefore, the morphology of sediment waves can be valuable in inferring the dynamics of overspilling flow from modern deep-water channels (Normark et al., 1980; 2002). However, a lack of high-resolution, 3D seismic data imaging deep-water overbank deposits has hitherto inhibited analysis of their architectures and morphological analysis of buried sediment waves. This has hindered the capacity to infer the nature of, and controls upon, ancient overbank flow dynamics, and how the importance of different controls may change through time.

Figure 5.2 (below) – *Location maps showing: (A) the location of the Hikurangi Margin; (B) the proximal reach of the Hikurangi Channel, showing its relationship with its feeder canyons, the location of the study area slope-traversing trench-perpendicular systems, the location of the study area (see C) and the extent of the bathymetry and 3D seismic data used herein; (C) seafloor morphology in the study area, highlighting the ten channel bends referenced throughout the text, the sediment wave fields on the channel overbanks, and the channels' relationships*

with the Hikurangi subduction wedge, the Chatham Rise, and the Pacific Plate. Bathymetry data were provided by the New Zealand National Institute for Water and Atmosphere (NIWA) and WesternGeco.



Here, high-resolution bathymetry, and 2D and 3D seismic data, that images the seafloor geomorphology and subsurface architecture of the Hikurangi Channel and its overbanks, offshore New Zealand, are integrated to address this knowledge gap. This contribution complements Tek et al. (2021), which detailed the channel evolution; the

focus here is on the overbank areas. Lewis and Pantin (2002) described the seafloor expression of the Hikurangi Channel and its overbanks, using swath bathymetry and backscatter data. They interpreted centrifugal force, the Coriolis force, and the action of bottom currents as controls on flow dynamics on the overbanks. They also performed a subsurface interpretation, based on 2D seismic data and shallow (<5 m) cores, but did not possess 3D constraint to speculate on the evolution of the wave fields. This study aims to: (a) determine the controls on overbank flow processes, deposition, and resultant depositional architectures, through ~ 600 m of overbank stratigraphy, and compare these controls with those invoked by Lewis and Pantin (2002); (b) determine how these controls interact with one another, constraining the spatial variability of their influence, and how their relative importance has changed through the depositional period; (c) discern the origin of enigmatic wave-like features on inner-overbanks of channel bends. The objectives of this study are to: (a) characterise the seafloor geomorphology and subsurface architecture of the overbank stratigraphy; (b) identify, and categorise different overbank feature types, and interpret their genesis; (c) perform a quantitative analysis of sediment wave morphologies on the seafloor and subsurface stratigraphy. The results of this study have fundamental implications for determining controls on the evolution of deep-water channel-levee systems and can assist development of understanding of channel-levee evolution in other modern and ancient systems.

5.3 Geological Setting

The study area covers ~ 21,000 km² of the trench-floor, adjacent to the junction between the Chatham Rise and the subducting Pacific plate, containing a ~ 250 km stretch of the Hikurangi Channel (Fig. 5.2B). This study focuses on the upper ~ 600 m of trench-fill (upper trench fill in Fig. 5.3, 5.4), wherein ten channel-forms can be traced for the ~ 140 km length of the 3D seismic survey described in the 'data' section (Tek et al., 2021; Fig. 5.4).

The NE flowing ~ 1,800 km long Hikurangi Channel (Fig. 5.2; Lewis and Pantin, 2002; Mountjoy et al., 2009, 2018; Tek et al., 2021) sits within the NE-SW oriented Hikurangi Trench, which has developed over the last ~ 27 Ma due to the subduction of the Pacific plate beneath the Australian plate (Ballance, 1975; Nicol et al., 2007; Barnes et al., 2010; Lamb, 2011; Jiao et al., 2015). Most of the trench-fill has accumulated during the last 3.5 Ma (Fig. 5.3A; Ghisetti et al. 2016; Kroeger et al., 2019), and is interpreted to consist predominantly of turbidites associated with the Hikurangi Channel (Lewis, 1994; Lewis et al., 1998; McArthur and Tek, 2021) and with transverse drainage networks that traversed the slope and subduction wedge (Fig. 5.2B; Mountjoy et al., 2009; McArthur et al., 2021). In the SW of the trench, where this study is focused, the trench-fill is ~ 6 km thick; the top ~ 600 m of stratigraphy, studied herein (Fig. 5.3), is

dominated by overbank deposits from the Hikurangi Channel (McArthur and Tek, 2021). To the NE, the trench-fill thins to ~ 1 km (Lewis et al., 1998; Barnes et al., 2010; Plaza-Faverola et al., 2012).

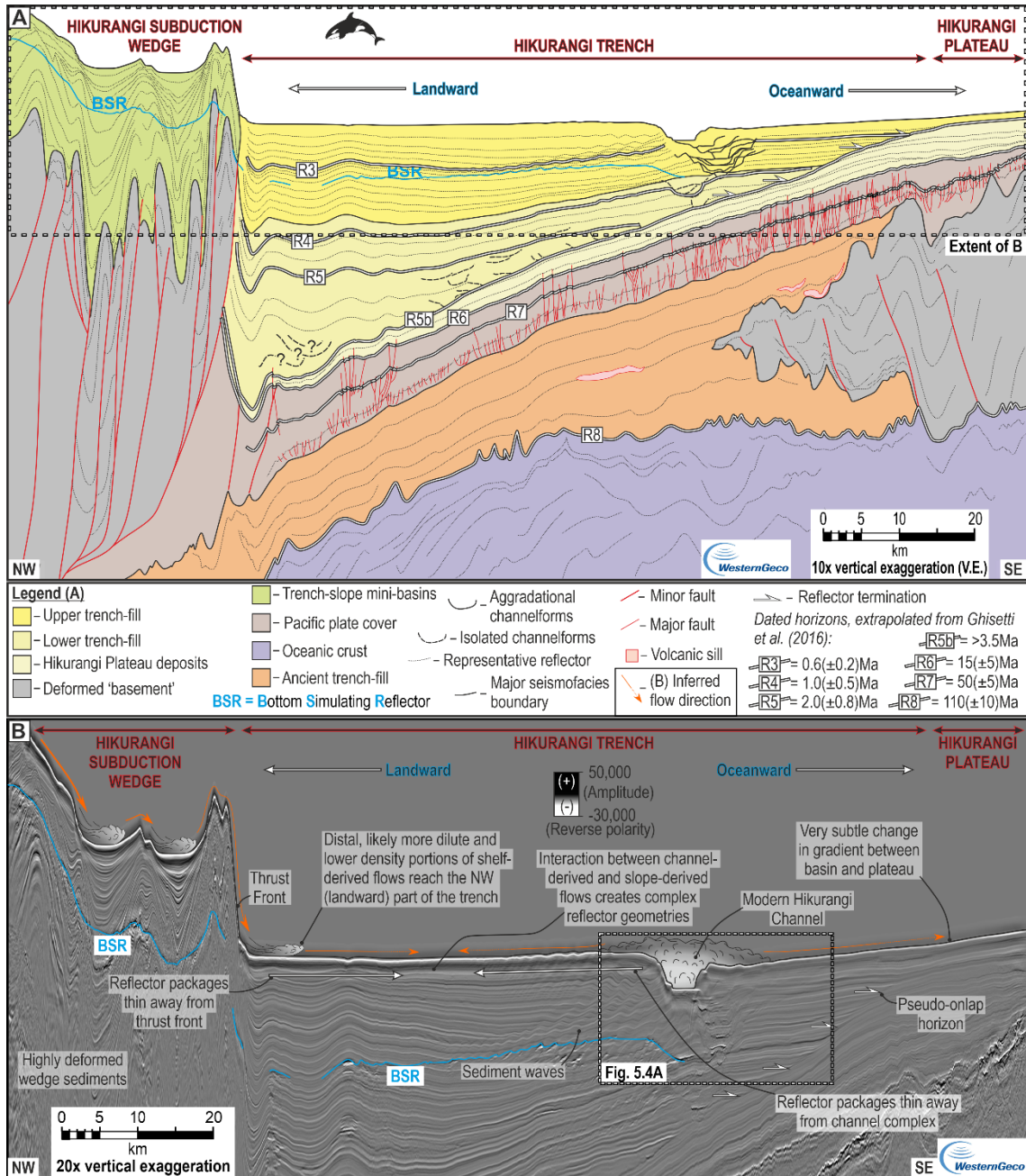


Figure 5.3 – (A) Interpreted seismic section through the Hikurangi Trench and its fill modified from McArthur and Tek (2021). (B) Annotated part of seismic section in A, showing the key geomorphic and seismic features present in and bounding the trench-fill and the potential sources of trench sedimentation.

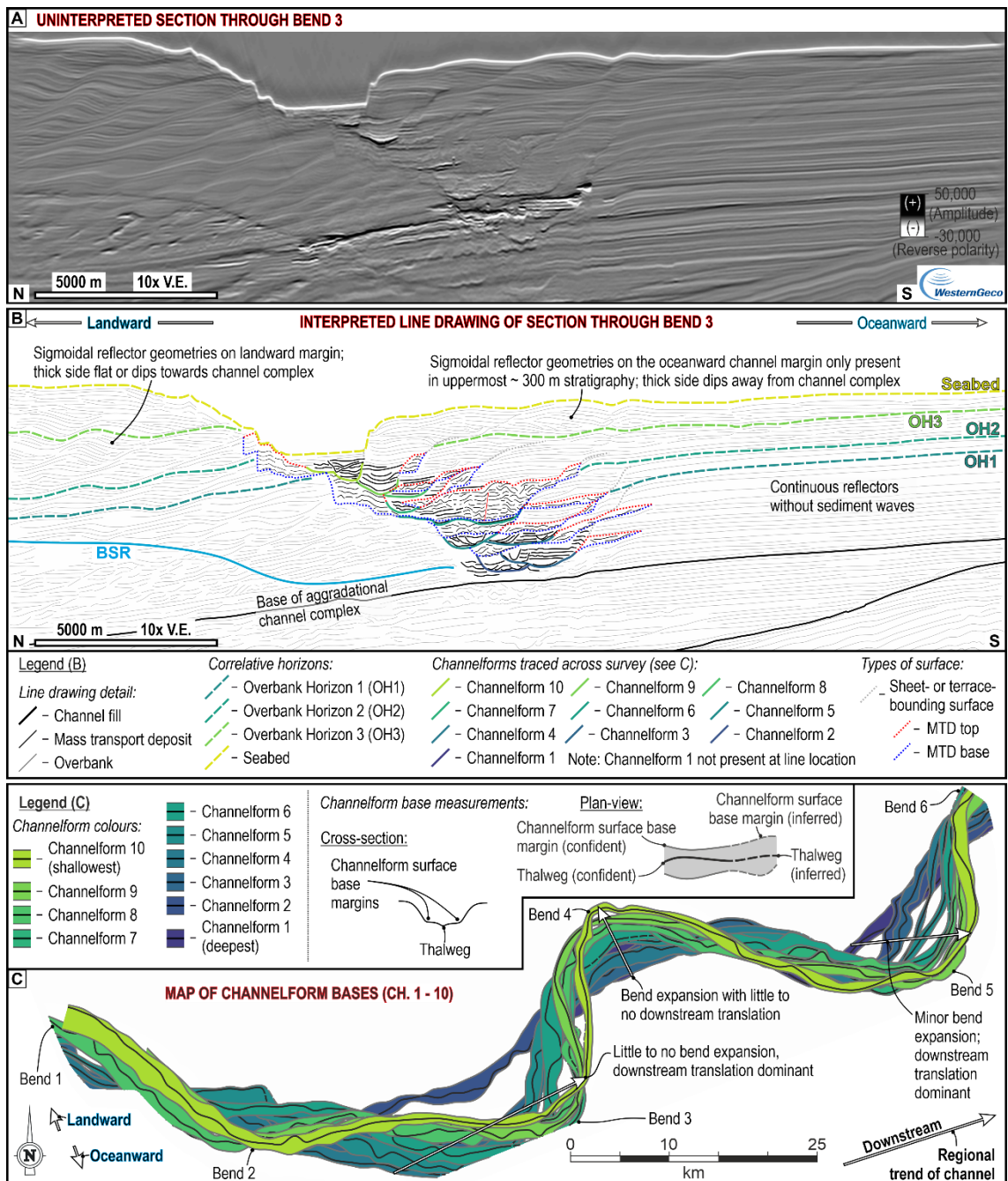


Figure 5.4 – (A) Uninterpreted seismic section (location on Fig. 5.3B) and (B) interpreted line drawing through the Hikurangi Channel and its landward and oceanward overbanks, highlighting the three subsurface horizons referenced in the text and nine of the ten channel-forms that have been traced across the study area. (C) Map of the thalwegs and edges of the flat bases of the ten traced channel-forms modified from Tek et al. (2021).

The Hikurangi Channel is fed by a network of shelf-incising canyons that capture sediment from the North and South Islands of New Zealand (Carter, 1992; Lewis, 1994; Lewis et al., 1998; Lewis and Barnes, 1999; Mountjoy et al., 2009), and are flushed by

earthquake-triggered failure events (Mountjoy et al., 2018; Howarth et al., 2021). Downstream of the confluence with the Cook Strait Canyon, the Hikurangi Channel flows east along the northern margin of the Chatham Rise (Wood and Davy, 1994; Davy et al., 2008) for ~ 130 km (Fig. 5.2). It then runs through the trench for ~ 500 km before abruptly changing direction and continuing a further ~ 1150 km across the Hikurangi Plateau and the Pacific abyssal plain (Fig. 5.2; Lewis et al., 1998; Collot et al., 2001; Lewis and Pantin, 2002). In the study area, in the proximal part of the trench, where the channel departs from the Chatham Rise, the overbank areas of the channel are ornamented by the scars from numerous channel-wall failures (Watson et al., 2020; Tek et al., 2021) and by sediment waves (Lewis et al., 1998; Lewis and Pantin, 2002).

A change in the nature of the trench-fill (Fig. 5.3) is observed between ~600 – ~800 m depth (above R4 in Fig. 5.3), from deeper isolated channel-forms that exhibit significant lateral offsets, to shallower aggradational channel-forms that each follow a similar course to their predecessor (Fig. 5.3A; McArthur and Tek, 2021). The stratigraphy of interest is located above this transition, where the trench-fill comprises thick, compound overbank deposits that bound the aforementioned aggradational channel-forms.

Contour currents have been identified in the Hikurangi Trench but their locations and orientations are poorly constrained, and their effects have likely changed through time (Carter et al., 2002; Lewis and Pantin, 2002; Fernandez et al., 2018; Bailey et al., 2020). For example, based on seafloor geomorphology and seismic architecture, Lewis and Pantin (2002) inferred that a shallow branch of the Deep Western Boundary Current (DWBC) flowed WNW along the northern edge of the Chatham Rise (Fig. 5.2A). The DWBC is interpreted to generate waves on the oceanward channel margin, and to have been active during glacial periods (Lewis and Pantin, 2002). However, modern oceanographic data show that the East Cape Current (ECC) is currently the dominant contour current in the study area (Carter et al., 2002; Fernandez et al., 2018). The ECC flows SW following the subduction front before turning anti-clockwise and crossing the channel near or within the study area (Fig. 5.2A); the exact location of its crossing with the channel is unclear.

5.4 Data

Analysis of the seafloor was conducted using high-resolution multibeam bathymetry and backscatter data covering ~ 47,000 km² (Fig. 5.2A), collected by the National Institute of Water and Atmospheric Research (NIWA) between 2001 and 2013; the data are provided by New Zealand Petroleum and Minerals (NZPAM) as part of their 2017 datapack. Within the study area (Fig. 5.2B), data from two cruises (TAN1207 and TAN1307 respectively) acquired in 2012 and 2013 using an EM302 multibeam

echosounder at 30 kHz with a 25 m grid size, are primarily used (Bland et al., 2014; Fig. 5.2B).

Subsurface analysis was conducted using three seismic datasets acquired by Westerngeco: (a) 2600 km² of pre-stack Kirchhoff depth migrated (broadband) 3D seismic data (acquired in 2017) with horizontal resolution of ~ 25 m and vertical resolution of ~ 7 m (values accurate at seafloor; Crisóstomo-Figueroa et al., 2020); (b) depth converted 2D seismic data (3 to 200 Hz frequency), acquired in 2014; (c) time domain 2D seismic data (30 to 40 Hz frequency), acquired in 2009. Full stack data are displayed SEG positive; a downward decrease in acoustic impedance is shown as a trough (white reflection). All presented seismic sections are shown in depth.

5.5 Methods

5.5.1 Bathymetry analysis and seismic interpretation

Analysis of the bathymetry and backscatter data, including the generation of depth, slope and hillshade maps, digitisation and segmentation of sediment wave crests and the channel trendline, and the generation of seafloor profiles, were conducted using ArcGISTM.

Three regionally traceable horizons (Overbank Horizons 1 – 3) form the basis for the subsurface interpretation. Seismic interpretation, including the tracing of reflectors, surface generation, the mapping of sediment wave fields, and the generation of three-dimensional images was conducted in Schlumberger Petrel©. Reflectors were first traced throughout the 3D seismic volume, then extrapolated along the 2D seismic lines for the purpose of mapping the extents of the wave fields; ties between the time- and depth-domain data were conducted by identifying marker horizons present in both surveys, and interpreting the position of the reflector of interest between those marker horizons. Analysis of sediment waves, which was only conducted within the boundaries of the 3D survey, was achieved by importing the subsurface horizons into ArcGISTM, where they were analysed in the same way as the bathymetry data: generation of depth and slope maps, and digitisation and segmentation of wave crests.

To ensure consistency in the resolution and spatial extent of the data, and to negate the potential effect of the migration of overbank features related to the 2016 Kaikōura canyon flushing event and its associated turbidity current (Mountjoy et al., 2018), a seafloor horizon generated from the 3D seismic data is used when comparing the orientations and morphologies of overbank features in the subsurface, to those on the seafloor.

When referring to the position of waves or profiles along a channel, those in more proximal channel reaches are referred to as ‘up-channel’ when compared to more distal,

'down-channel' reaches. Within a wave field, along an overbank transect normal to the channel, features located close to the channel are referred to as 'upstream', whereas features that are further away from a channel are referred to as 'downstream'.

5.5.2 Sediment wave orientations and flow analysis

The plan-view morphology of outer-bend sediment waves was used to infer modern overbank flow and palaeocurrent directions, and investigate how the orientational spread of a sediment wave field relates to the morphology of the adjacent channel (Fig. 5.5A - C). On the seafloor, this analysis was performed on four sediment wave fields present on the landward overbank (WF1a, WF2a, WF3 and WF4; Fig. 5.2). However, as WF2a is the only field that is imaged along its entire (up-channel to down-channel) width within the 3D seismic survey, subsurface analysis was limited to waves beneath WF2a; it should also be noted that only the upstream part of WF2a is imaged by the 3D survey.

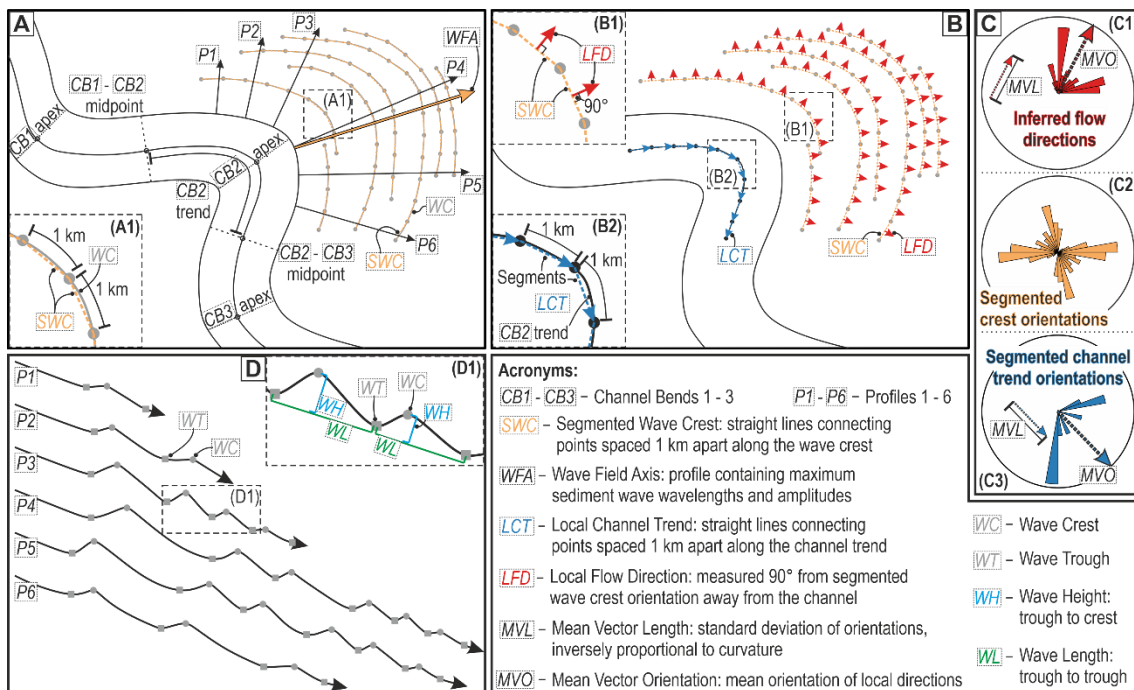


Figure 5.5 – Schematic, fictitious example showing the methodologies applied on the seafloor and subsurface horizons for sediment wave orientation and flow analysis, and morphological analysis of the sediment waves. (A) Shows the segmentation of wave crests shown in B and C, the distributions of the representative longitudinal profiles used to extract wave measurements in D, and how channel bends are defined. (B) Shows the segmentation of the channel bend and how inferred palaeocurrents are extracted from the segmented wave crests. (C) Rose diagrams illustrating analysis of the orientations of overbank flow directions, of wave crests and of channel trend (data from segments in B). (D) Shows how sediment wave heights and wavelengths are calculated in the profiles shown in A.

Sediment wave crests and the trend of the adjacent channel bend were digitised and divided into 1 kilometre long segments using ArcGISTM (Fig. 5.5A, B); the extent of each bend is defined as the along-channel connection from the midpoint between the apex of the relevant bend and the adjacent up-channel bend, to the midpoint between the apex of the relevant bend and the adjacent down-channel bend (Fig. 5.5A). Channel trend segments were vectorised via connection to their down-channel neighbour, their directions were then extracted using Python programming and plotted as rose diagrams in Stereonet 10 (Cardozo and Allmendinger, 2013; Fig. 5.5B, C). The spread of segment directions is inversely proportional to the mean vector length of the orientations (Fig. 5.5C); hence, the inverse of mean vector length is used hereafter as a direct measure of channel bend curvature. The local overbank flow direction is assumed to be perpendicular to the local orientation of the sediment wave crests (Migeon et al., 2000; Normark et al., 2002); vectors approximating local flow direction were therefore generated at 90° to each sediment wave crest segment (directed away from the channel; Fig. 5.5B) using Python. When local overbank flow directions are plotted on rose diagrams, the mean vector orientation indicates the mean flow direction, and the mean vector length provides an inverse measure of the bulk curvature of the sediment wave crests (Fig. 5.5C). The relationship between channel bend, and sediment wave curvature on the seafloor and in the subsurface is examined in the ‘outer-bend sediment waves’ sections.

5.5.3 Morphological analysis of sediment waves

To analyse the size distribution of sediment waves within each outer-bend wave field and on each subsurface horizon, six longitudinal profiles, distributed incrementally along the up- to down-channel width of the field, were digitised perpendicular to the dominant wave crest orientation (Fig. 5.5A). Along each profile, wave crests and troughs were interpreted (Fig. 5.5D), with the interpretations validated against the plan-view expression of the identified waves. Sediment wave wavelengths are calculated as the distance between two consecutive troughs. Wave heights are calculated as the distance from a wave crest to a straight line connecting two consecutive troughs, measured normal to the trough-connecting line (Fig. 5.5D; Ribó et al., 2016). Sediment wave dimensions, and their position in their host wave field were extracted using PythonTM from profiles digitised in CoreIDRAW®. Wave lengths and heights are assumed to scale with increasing flow thickness (Normark et al., 2002), and hence with (unidirectional) flow velocity, meaning they can provide insight into modern flow and palaeoflow dynamics across the wave fields. A longitudinal profile through the ‘axis’ of each wave field, defined as the profile containing the largest overall wavelengths and wave heights, was also digitised but was not used in the morphometric analysis.

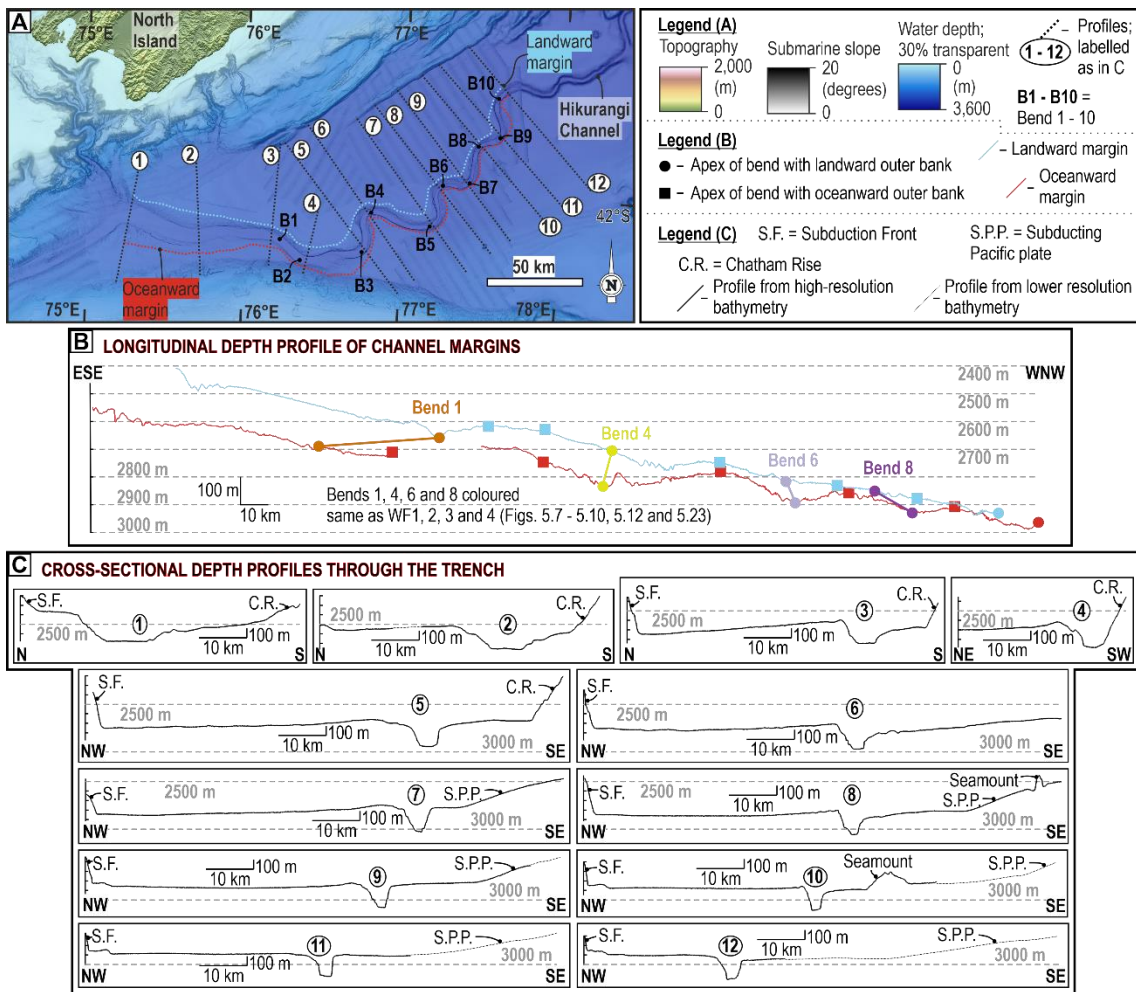


Figure 5.6 – (A) Map (location shown in Fig. 5.2B) showing locations of the trench profiles shown in B and C. (B) – (C) Longitudinal profiles through the trench showing the seafloor morphology of: (B) the tops of the channel walls, highlighting the depth difference between the two channel margins along the channel; (C) trench-perpendicular profiles, each through the apex of successive bends, showing the channel-perpendicular seafloor expression of the channel overbanks on both margins.

5.6 Results

5.6.1 Large-scale seafloor morphology and seismic stratigraphy

5.6.1.1 Observations

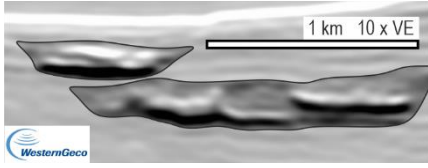
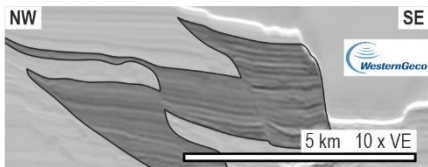
The ~ 250 km reach of the Hikurangi Channel in the study area exhibits steep (up to 35°) channel-walls and a relatively flat channel-floor that progressively narrows from ~ 6.5 km in the most proximal parts, to ~ 1 km distally (Fig. 5.2B, 5.6). In the most proximal region of the study area (Fig. 5.2B) the channel is situated near (e.g. Bend 1; profiles 1 – 3, Fig. 5.6) or at (e.g. Bend 2; profile 4, Fig. 5.6) the northern margin of the Chatham Rise. Further down-channel, the channel is located close to the margin of the

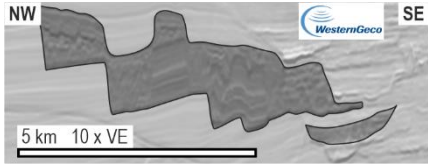
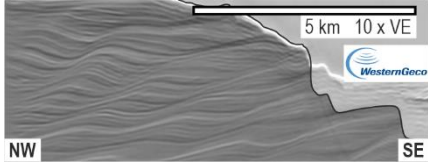
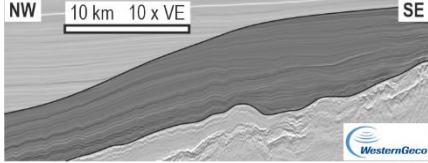
subducting Pacific plate, but becomes gradually more central within the trench distally (profiles 7 – 12, Fig. 5.6).

The landward (northern) channel overbank is consistently higher than the oceanward (southern) one, except where the channel is pinned against the Chatham Rise (Fig. 5.6); the height differential is greater on bends with landward outer-bend overbanks (profiles 3, 6, 8, 10 and 12, Fig. 5.6). The trench-floor on the landward overbank either: (a) dips gently (up to 0.8°), from a poorly defined levee crest away from the channel (NW) and toward the subduction front (e.g. profile 3, Fig. 5.6); (b) dips gently away from the channel for tens of kilometres before becoming subhorizontal (e.g. profile 9, Fig. 5.6); or (c) is subhorizontal across its entire width (e.g. profile 11, Fig. 5.6). In all cases an abrupt contact at the subduction front sees the seafloor dipping steeply (up to 35°) to the SE. The oceanward overbank either dips gently (up to 0.6°) toward the channel (NW) (e.g. profile 8, Fig. 5.6) or is subhorizontal (e.g. profile 7, Fig. 5.6). Where the trench-floor is bounded by the Chatham Rise, an abrupt steepening occurs at its boundary (e.g. profile 5, Fig. 5.6); where it is bound by the subducting Pacific plate, a subtle steepening occurs (e.g. profile 9, Fig. 5.6). In any trench-perpendicular transect in the study area, the thalweg of the channel is the deepest point of the trench (Fig. 5.6).

At its landward edge, the trench-fill is bound by deformed subduction wedge deposits (Table 5.1); the contact between the two is typically marked by a frontal thrust; however, minor folding is sometimes observed in the adjacent trench-fill (Fig. 5.3). At its oceanward edge, the trench-fill is bound proximally by the faulted strata that comprise the Chatham Rise (Table 5.1), and distally by strata imaged as low amplitude reflectors that top the subducting plate (Table 5.1). The trench-fill comprises deposits of the Hikurangi Channel, made up of channel-fill, sheet and terrace, and mass-transport deposits (Table 5.1; see Tek et al., 2021), and the overbank deposits studied here (Table 5.1, 5.2). The overbank deposits comprise most of the studied trench-fill, and can be categorised into three types (Table 5.2): overbank sediments with sediment waves; overbank sediments without sediment waves that terminate against the Chatham Rise or subducting place; overbank sediments without sediment waves that terminate against the subduction front, and that display compensational wedging patterns and terminate against the subduction front.

Table 5.1 (below) – *Descriptions and interpretations of the seven seismofacies observed within and adjacent to the studied trench-fill.*

Seismofacies name	Description	Amplitude	Geometry	Continuity		Bound by: toward channel	Bound by: away from channel	Dip / inclination	Internal structure	Interpretation	Example
				Trench-parallel	Trench-perpendicular						
Channel-fill	Lens-shaped High-Amplitude Reflector Packages (HARPs)	High	Lens-shaped, pinch and swell over 100s – m to kms laterally, reaching < 60 m thick	10s – 100s of km	< 3 km	N/A; lens-shaped	Older channel-fill, sheet or terrace, MTD or overbank	Concave-up cross section; very shallow (<1°), trench-parallel dip to NE	Concave-up surfaces within packages; unilaterally migrating reflectors; transparent areas	Coarse-grained channel-fill deposits (Flood et al., 1995)	
Sheet or terrace deposits	Narrow, tabular reflector packages adjacent to channel-fills	Low - medium	Tabular	Kms – 10s of km	Kms – 10s of km	Channel-fill, sheet or terrace, or MTD	Sheet or terrace, MTD, or overbank	Horizontal or very gently dipping (<1°) in any direction	Sometimes gullies toward their margin away from the channel	Weakly confined, sand-rich sheet-like deposits (Pickering et al., 1995) or heterolithic terrace deposits (Babonneau et al., 2004; Hansen et al., 2015)	

Mass-Transport Deposits (MTDs)	Deformed and chaotic reflector packages	Typically low to very low; can locally contain medium or high	Highly variable: contorted reflectors or transparent	Kms – 10s of km	Kms – ~ 10 km	Channel-fill, sheet or terrace, or MTD	Sheet or terrace, MTD, or overbank	Internal dips; overall dip toward channel	Folds; normal and thrust faults; and transparent zones	Mass-Transport Deposits, the product of debris flow, slumping, and sliding, comprising remobilised overbank and terrace deposits (Tek et al., 2021)	
Overbank	Laterally continuous, tabular or undulating reflector packages	Low to medium	Tabular or very subtle reflector thickening / thinning (ms over kms laterally)	10s – 100s of km	10s of km – ~ 100 km	Channel-fill, sheet or terrace, or MTD	Subduction front, subducting slab or Chatham Rise	Horizontal or gentle (<1°) landward (NW) dip	Sediment waves; gullies; sometimes faults	Fine grained (silt and clay), heterolithic external overbank deposits formed by overspill from channel-traversing turbidity currents (Normark et al., 1980; Pirmez and Flood, 1995; Migeon et al., 2004)	
Plate-top sediments	Low amplitude, very continuous reflector packages with subtle wedging	Low	Tabular or subtle wedging in all directions (ms vertically over kms laterally)	10s – 100s of km	10s – 100s of km	Reflectors that terminate against trench-fill are bound by overbank; reflectors that continue under the trench, terminate against the subduction front; SE termination not imaged	Consistent landward dip < 3°, sub-parallel to dip of subducting slab	Subtle wedging; sometimes faults	Muddy hemipelagites and contourites deposited on the pacific plate during subduction (Barnes et al., 2020)		

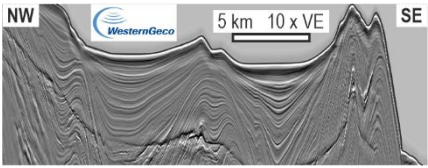
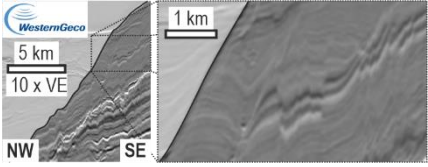
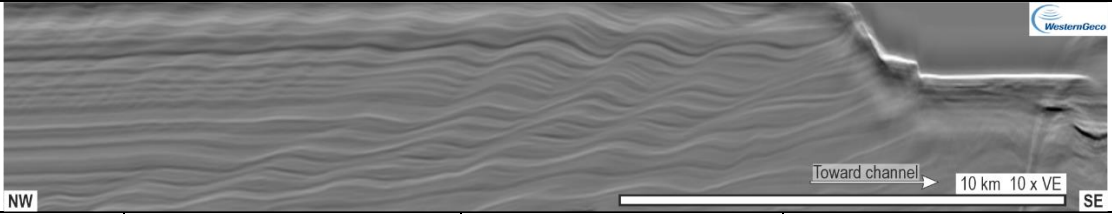
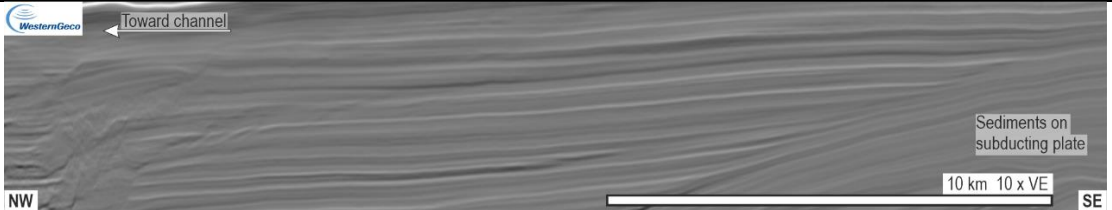
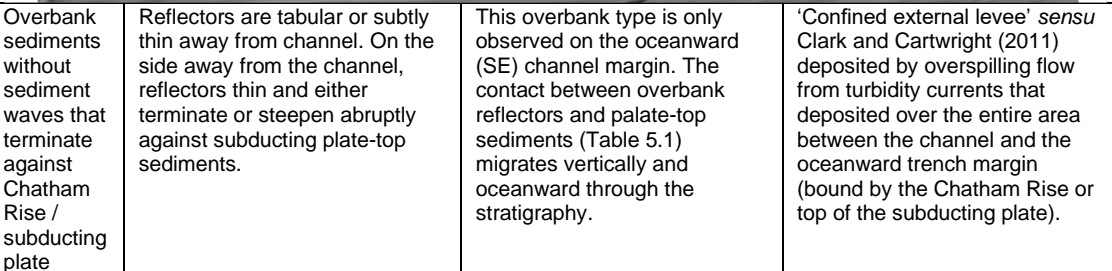
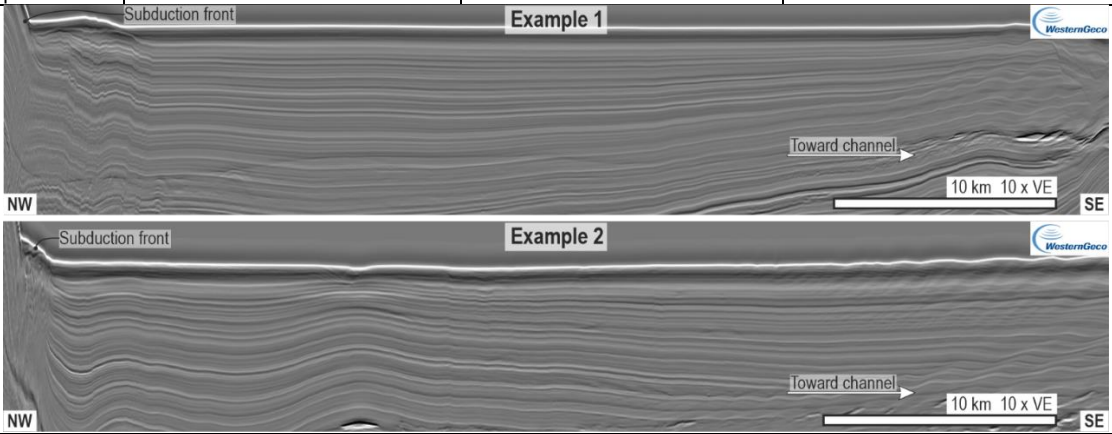
Subduction wedge deposits	Heavily folded reflector packages with variable thicknesses	Low to high; increases toward seabed	Highly variable in reflector thickness (ms vertically over kms laterally) and amplitude over metres to kms	Kms – 10s of km	Kms – 10s of km	Overbank	N/A; outside of study area	Highly variable dips due to structure; flat to sub-vertical and locally overturned reflectors	Thrust-cored anticlines, fanning reflectors, axis-thickening synforms	Coarse-grained deposits of trench slope mini-basins and the structures that bound them (McArthur et al., 2019)	
Chatham Rise deposits	Heavily faulted reflector packages with internal truncations	Low to high	Packages and reflectors traceable over 10s to 100s of km, subtly thinning toward subduction front; reflector displacement / abrupt dip changes common	10s – 100s of km	10s – 100s of km	Trench-fill of any type: channel-fill, sheet or terrace, MTD, or overbank	N/A; outside of study area	Packages follow dip of subducting plate, < 3° NW; dips of reflectors vary abruptly at faults	Pervasive normal faults (10s to 100s of m offset), spaced 100 m – 5 km apart	Sedimentary rocks that comprise the upper part of the Chatham Rise (Davy et al., 2008)	

Table 5.1 (below) – Descriptions, interpretations, and seismic cross-sections of the three types of overbank geometry observed within the studied

Overbank type	Description	Occurrence / context	Interpretation
	<p>Laterally continuous low to medium amplitude reflectors that systematically thicken and thin to form sigmoidal sediment waves. While some individual reflectors may disappear in the thin limb of the sediment waves, most reflectors can be traced across the length of the wave field.</p>	<p>Present through shallowest ~700 m of stratigraphy. Dominantly observed on the landward channel margin. Toward the channel, reflectors terminate abruptly against channel-fill, terrace deposits, or MTDs (Table 5.1). Away from the channel, reflectors transition into overbank sediments without sediment waves that terminate against the subduction front.</p>	<p>Fine grained overbank sediment waves formed by unidirectional overspilling flow from turbidity currents that traversed the Hikurangi Channel and its paleo-incarnations. Aggradation occurs faster on their upstream (toward the channel) limb and they migrate toward the channel.</p>
	<p>Reflectors are tabular or subtly thin away from channel. On the side away from the channel, reflectors thin and either terminate or steepen abruptly against subducting plate-top sediments.</p>	<p>This overbank type is only observed on the oceanward (SE) channel margin. The contact between overbank reflectors and palate-top sediments (Table 5.1) migrates vertically and oceanward through the stratigraphy.</p>	<p>'Confined external levee' <i>sensu</i> Clark and Cartwright (2011) deposited by overspilling flow from turbidity currents that deposited over the entire area between the channel and the oceanward trench margin (bound by the Chatham Rise or top of the subducting plate).</p>
	<p>Reflectors are generally laterally continuous and usually thicken away from the channel (example 1 above). However, reflectors and reflector packages thin, and occasionally pinch out onto highs and thicken into lows exhibited by deeper reflectors (example 2 above). In both cases, reflectors are deformed near to, and abruptly terminate against, the subduction front.</p>	<p>This overbank type is only observed on the landward (NW) channel margin. The expression of deep structures, typically thrust-cored anticlines, is muted toward the seafloor, which is generally subhorizontal. Structures are more common nearer the subduction front, sometimes causing packages of overbank reflectors to thin away from the channel.</p>	<p>These deposits likely represent a combination of fine-grained deposition from overspilling flow from the Hikurangi Channel, and the fine-grained, dilute, distal expression of flows that traverse the trench-slope basins of the Hikurangi Subduction wedge. Sediments from both sources collectively act to heal the expression of growing structures and maintain a relatively flat seafloor.</p>
			
<p>Overbank sediments without sediment waves that terminate against the subduction front</p>	<p>Reflectors are generally laterally continuous and usually thicken away from the channel (example 1 above). However, reflectors and reflector packages thin, and occasionally pinch out onto highs and thicken into lows exhibited by deeper reflectors (example 2 above). In both cases, reflectors are deformed near to, and abruptly terminate against, the subduction front.</p>	<p>This overbank type is only observed on the landward (NW) channel margin. The expression of deep structures, typically thrust-cored anticlines, is muted toward the seafloor, which is generally subhorizontal. Structures are more common nearer the subduction front, sometimes causing packages of overbank reflectors to thin away from the channel.</p>	<p>These deposits likely represent a combination of fine-grained deposition from overspilling flow from the Hikurangi Channel, and the fine-grained, dilute, distal expression of flows that traverse the trench-slope basins of the Hikurangi Subduction wedge. Sediments from both sources collectively act to heal the expression of growing structures and maintain a relatively flat seafloor.</p>

5.6.1.2 Interpretations

The observed channel-bank asymmetry is consistent with previous studies focused on the Hikurangi Channel (Lewis et al., 1998; Lewis and Pantin, 2002; Tek et al., 2021) and is interpreted to be dominantly due to leftward flow deflection by the Coriolis force. Local enhancement of overspill and aggradation on the landward margin and concomitant hindrance on the oceanward margin may be caused by flow reflection off the Chatham Rise and possibly the subducting plate, in addition to an overbank gradient that slopes towards the channel on the oceanward margin, and away from the channel on the landward margin. Elevated channel overbank heights on outer channel bends with landward outer-overbanks suggest that the centrifugal force of the flow field also enhances overspill and aggradation at these locations (Straub et al., 2008; Kane et al., 2010b).

Despite the lack of well-defined levees on the seafloor, the fact that the channel-forms throughout the studied stratigraphy are bounded laterally by compound overbank deposits, with no master incision surface hosting them (Fig. 5.3, 5.4; Table 5.2) allows their classification as 'aggradational' channel deposits. The lack of a 'wing-shaped', tapering cross-sectional profile (a common feature of levees adjacent to aggradational channels) is due to aggradation rates being similar across the entire trench-floor. On the narrow oceanward overbank, overspilling flows can reach the edge of the trench-floor (the Chatham Rise or subducting plate) and deposit over the entire overbank area (Fig. 5.3B). It is also possible that overbank flows may also deposit over the entirety of the wider landward overbank. aggradation near the subduction front may be accelerated by deposition from fine-grained distal parts of flows that traversed drainage networks on the bounding slope (Fig. 5.3B; Mountjoy et al., 2009; McArthur et al., 2019). Alternatively, overspill on the landward overbank may not reach the subduction front, with the interaction of overspilling flows and slope-traversing flows occurring somewhere in the trench.

5.6.2 Outer-bend sediment waves on the seafloor

5.6.2.1 Observations

The four prominent sediment wave fields (WF1a, WF2a, WF3 and WF4, Fig. 5.2B, 5.7, 5.8) present on the landward channel overbank collectively cover 3,300 km² of the channel overbank. Individual fields range from 130 km² to 1,400 km² and extend up to 28 km away from the channel. The size (area, length and width; Fig. 5.7) of the wave fields decreases down-channel (Fig. 5.7D, E, 5.8). Waves in WF1a, WF2a, WF3 and WF4 are concentric around the outer-overbanks of bends 1, 4, 6, and 8 respectively (Fig. 5.2C). On the seafloor, WF1a and WF2a are distinct from the wave fields present

on the inner-overbanks of bends 3 and 5 (WF1b and WF2b respectively; Fig. 5.2C). Each wave field is separate from its neighbours.

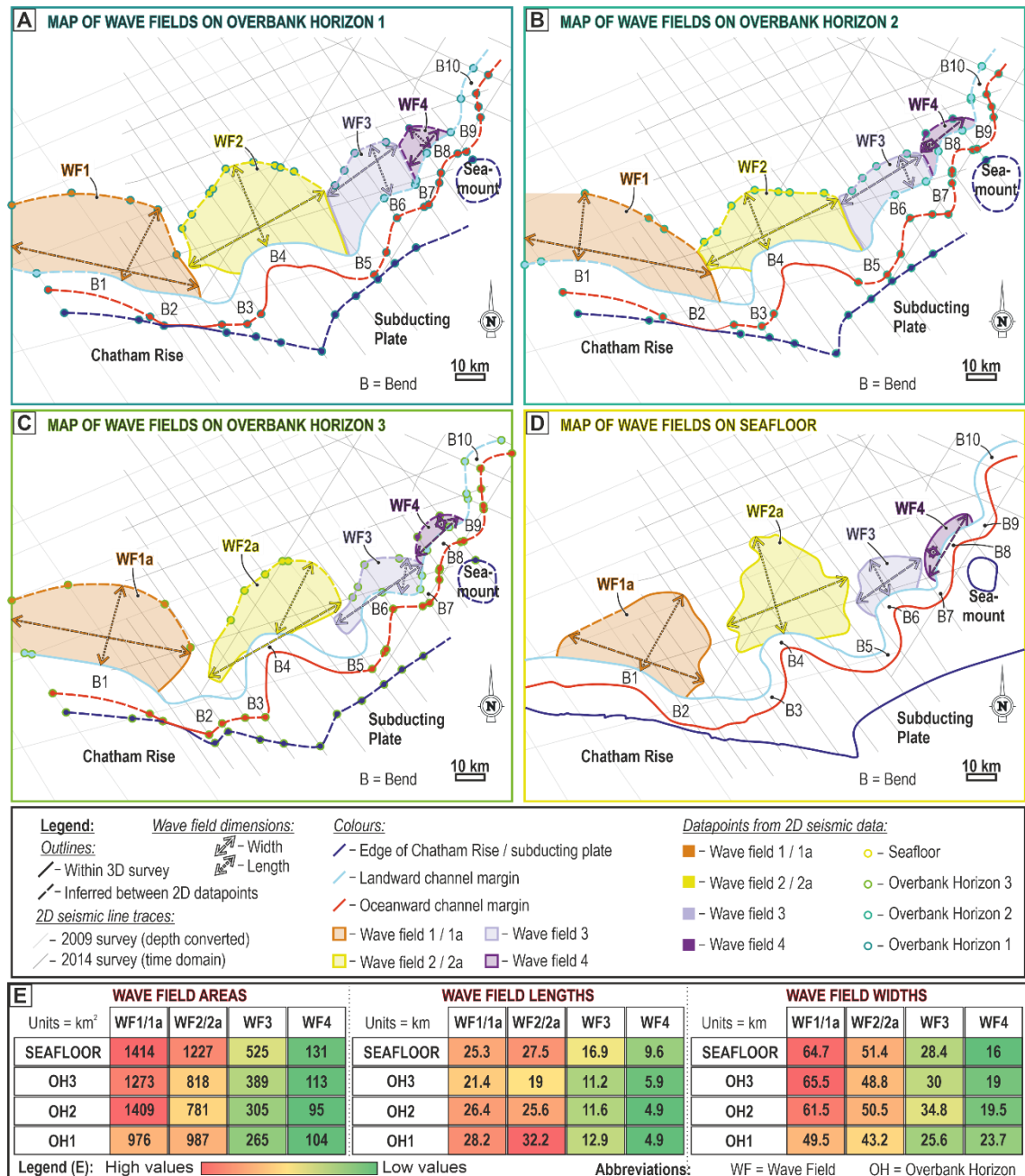


Figure 5.7 – (A) – (D) Topological maps of the four outer-bend wave fields on the landward channel margin, highlighting their stratigraphic evolution from Overbank Horizon 1 (A), through Overbank Horizons 2 (B) and 3 (C), to the seafloor (D). (E) Dimensions of the wave fields in A - D, showing area, length (measured away from the channel), and width (measured along the channel).

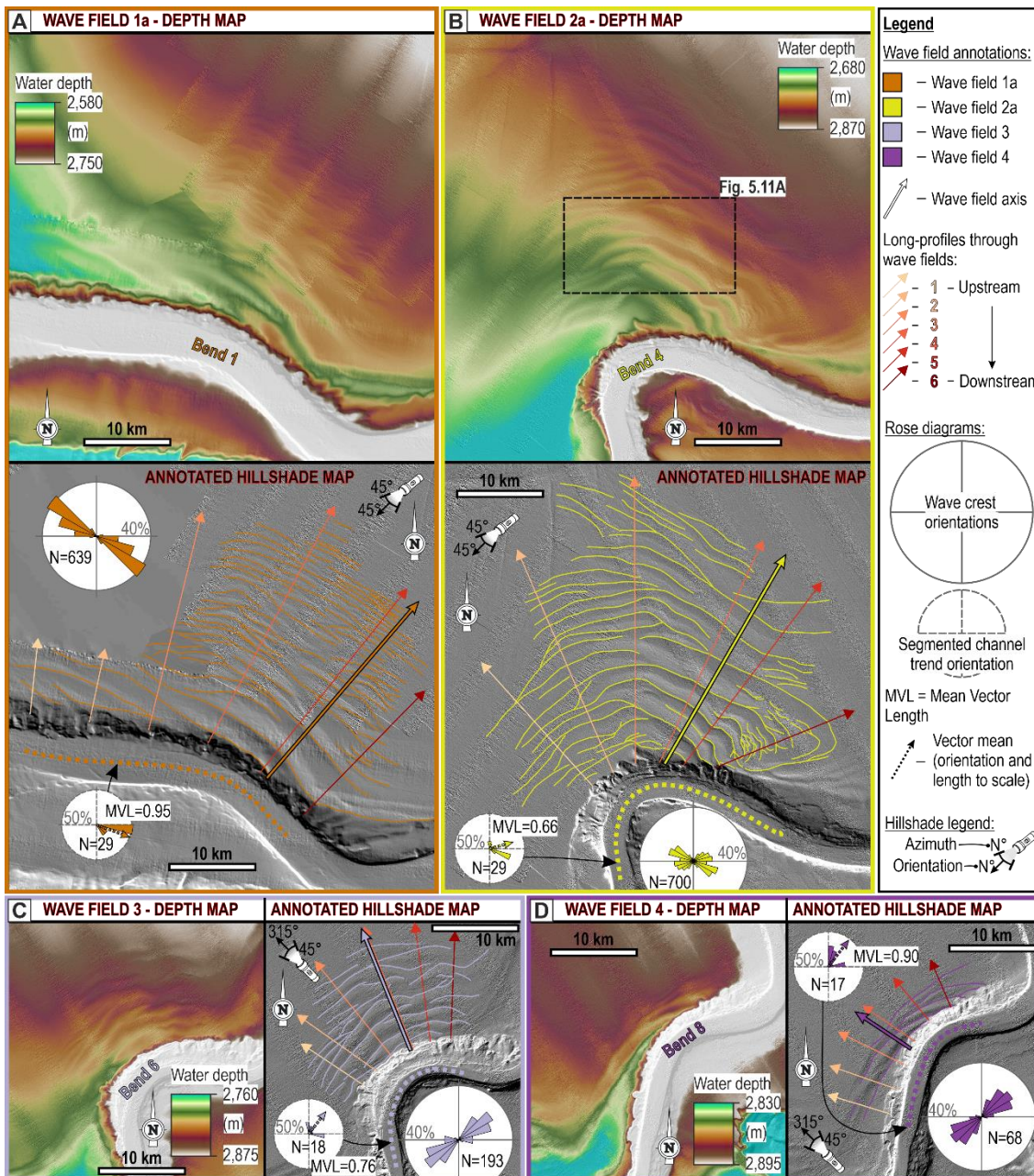


Figure 5.8 – Maps showing (A) the seafloor expression of wave field 1a, (B) wave field 2a, (C) wave field 3, and (D) wave field 4. For each wave field, an uninterpreted depth map and an interpreted hillshade map are displayed. On the interpreted map, the wave crests, the trend of the related channel bend, the locations of the longitudinal profiles shown in Fig. 5.10, including the wave field axis, and two inset rose diagrams showing the (bi-directional) orientations of the wave crest segments and the vector directions of the segmented channel bend trend are highlighted.

Bend 4 exhibits the greatest curvature (lowest mean vector length), followed by bends 6 and 8; bend 1 is the straightest (Fig. 5.8). The down-channel limit of WF2a and WF3 is further down-channel of the apex of their associated bends than the up-channel limits of the wave fields; WF1a and WF3 are more symmetric about the apex of their

associated bends (Fig. 5.7, 5.8). The orientations of the segmented wave crests, and therefore the inferred local flow directions, exhibit the greatest spread (inversely proportional to mean vector length) in WF2a, and the least in WF1a (Fig. 5.8, 5.9A, C). Except on WF4, the ‘axis’ of the wave field (the channel-perpendicular transect containing the largest waves; Fig. 5.5) is consistently orientated down-channel of the mean flow direction (mean vector orientation; Fig. 5.8, 5.9A).

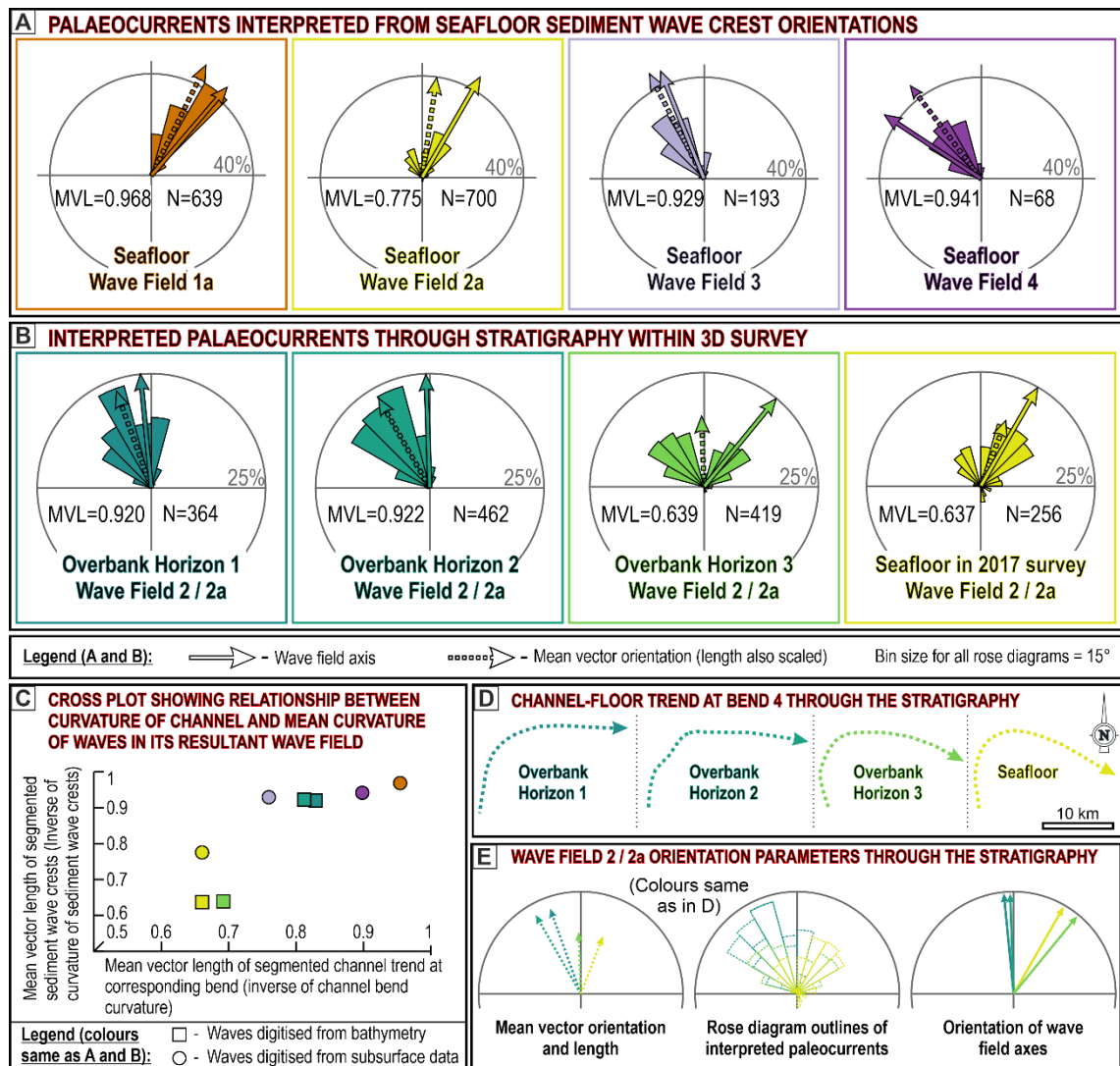


Figure 5.9 – (A) Rose diagrams showing the orientations of interpreted palaeocurrents from wave fields 1a, 2a, 3 and 4 on the seafloor, calculated from the segmented channel wave crests. (B) Rose diagrams showing the orientations of interpreted palaeocurrents from wave field 2 / 2a in the 3D seismic survey Overbank Horizon 1, 2, 3 and the seafloor. (C) Graph showing the relationship between the bend curvature, and the bulk curvature of the wave crests in their associated wave fields, calculated using the mean vector lengths of the segmented channel trend and the interpreted palaeocurrents from the segmented wave crests. (D) Plan-view of the trend of bend 4 through the stratigraphy, showing an overall increase in bend

curvature from Overbank Horizon 1 to the seafloor. (E) Hemispheric rose diagrams showing the mean vector orientation and length, interpreted palaeocurrents, and orientation of wave field axis through the stratigraphy, showing an overall clockwise rotation from the deep stratigraphy (Overbank Horizons 1 and 2), to the shallow stratigraphy (Overbank Horizon 3) and the seafloor.

In crest-perpendicular transects (see profiles 1 – 6; Fig. 5.8), sediment waves typically have narrow stoss sides that can be horizontal, or dip gently toward the channel, and wider lee sides that dip more steeply away from the channel (Fig. 5.10). Stoss sides exhibit higher backscatter reflectivity and Root Mean Squared (RMS) amplitude values than lee sides (Fig. 5.11A, B).

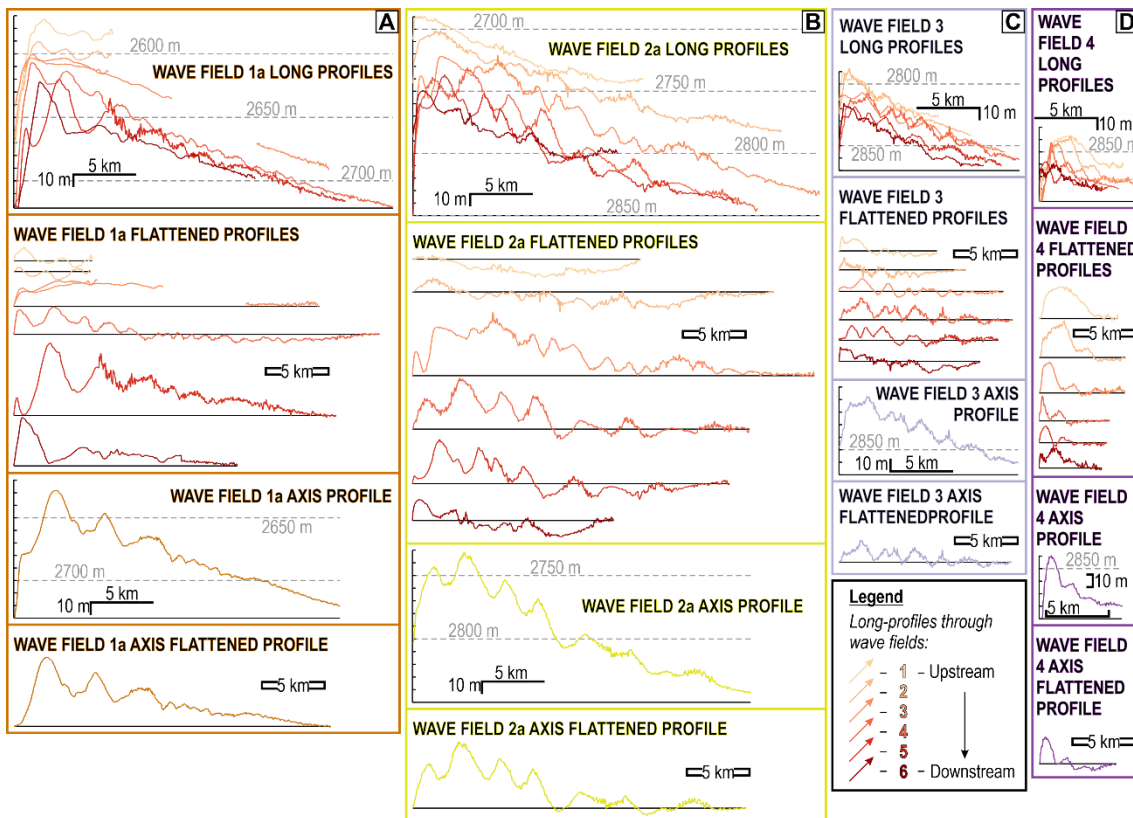


Figure 5.10 – Crest-perpendicular seafloor profiles (locations shown in Fig. 5.8) through wave fields 1a (A), wave field 2a (B), wave field 3 (C), and wave field 4 (D). For each wave field, the six profiles used for the extraction of wave dimensions in Fig. 5.12 are shown in depth and flattened to their upstream and downstream ends, and the wave field axis (profile containing the largest overall wavelength and wave heights), which is also shown in depth and flattened.

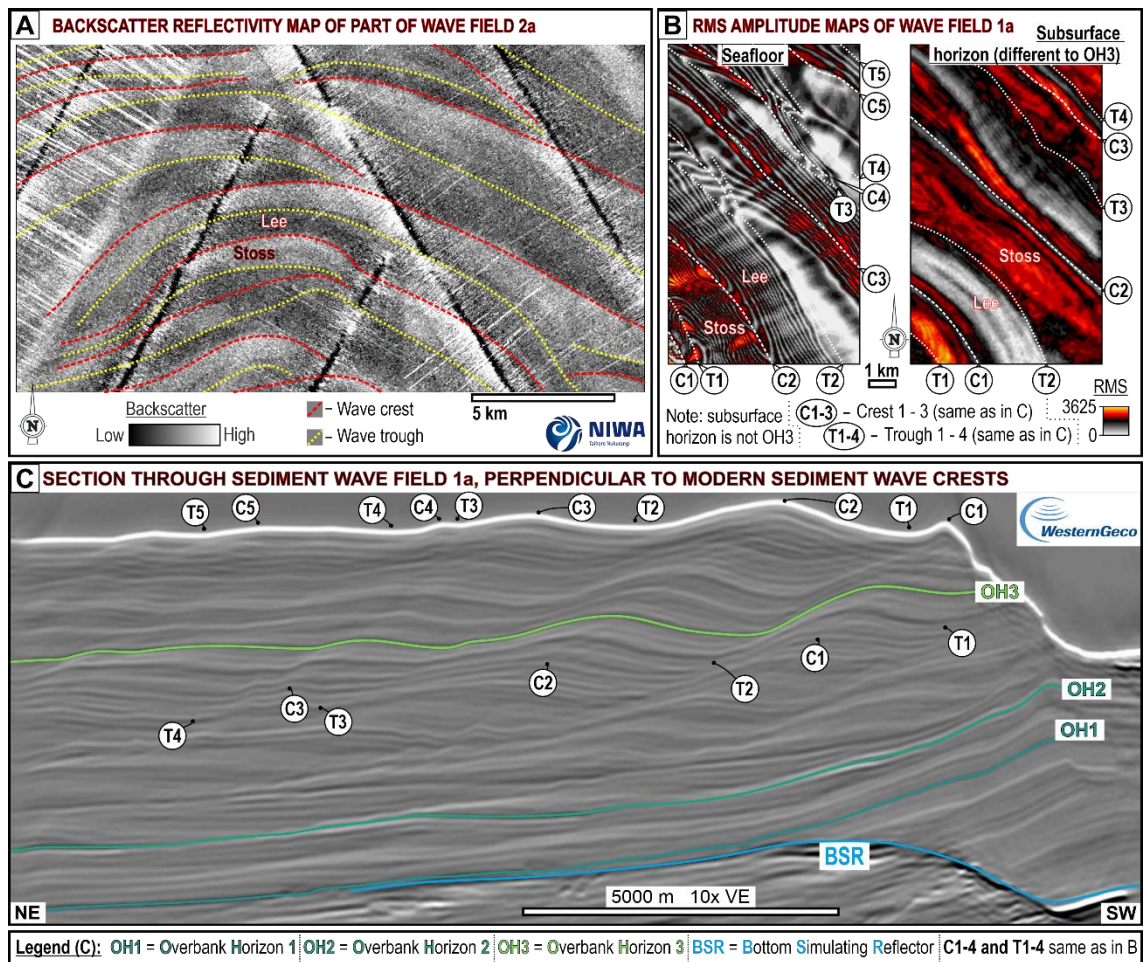
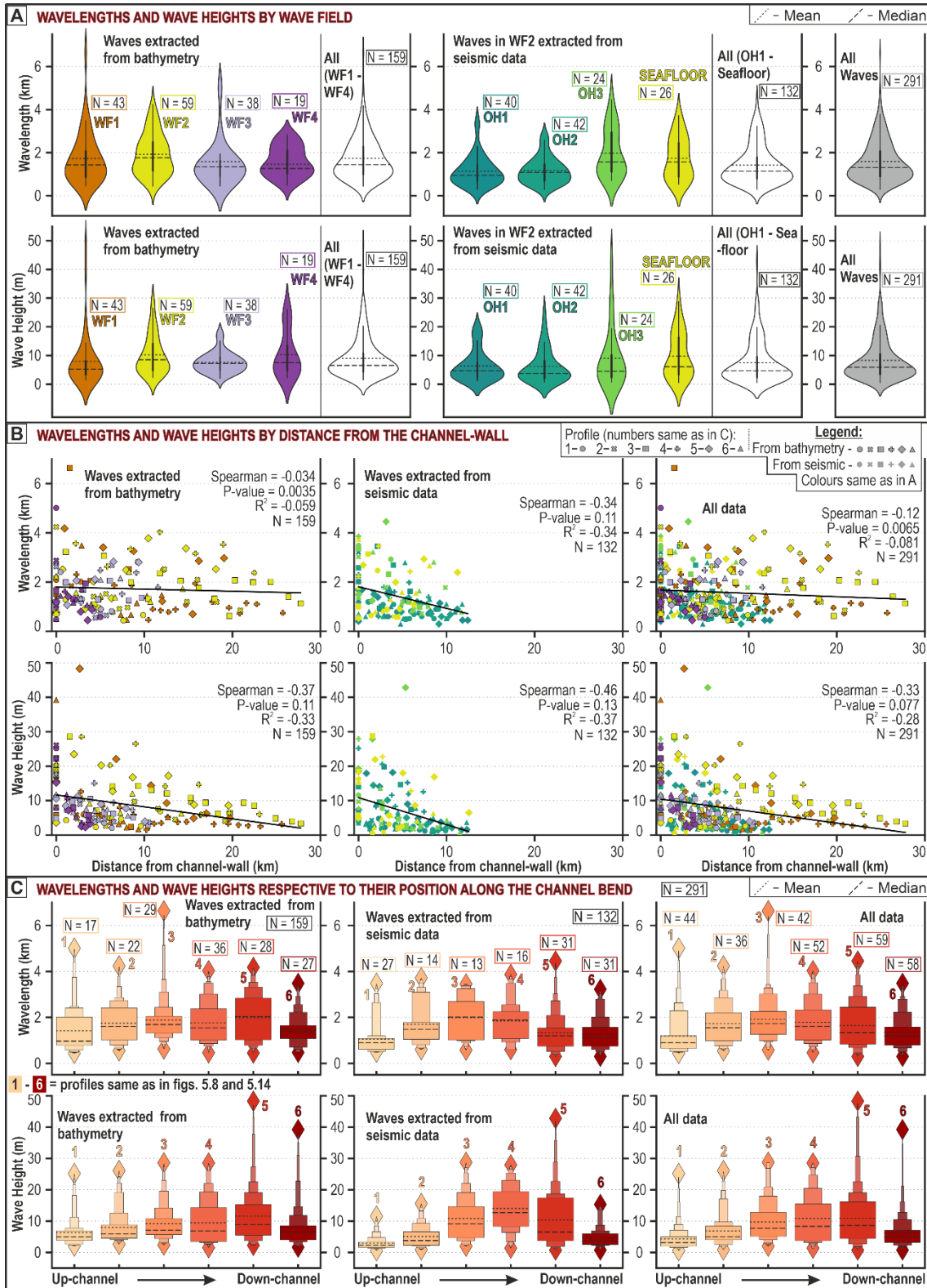


Figure 5.11 (above) – (A) Seafloor backscatter map imaging part of wave field 2a, showing that higher backscatter values occur on the upstream stoss sides of waves than on their lee sides. (B) Root Mean Squared (RMS) amplitude maps from the seafloor and the subsurface (depth shown in C) showing that, in general, RMS values are higher on the stoss (SW) sides of the waves in wave field 1. (C) Crest-perpendicular seismic section through wave field 1a, showing the locations of the three subsurface horizons and the locations of the horizons in B.

Figure 5.12 (below) – (A) Violin plots showing the distributions of sediment wave wavelengths and wave heights displayed by wave field on the seafloor and by measured Overbank Horizon in the subsurface for waves in wave field 2. (B) Scatterplots showing wavelengths and wave heights extracted from bathymetry data (coloured by wave field), seismic data from wave field 2 (coloured by the horizon they were extracted from), and all data. Separate plots of wave height versus distance from channel wall for each wave field and profile are displayed in Fig. 5.13. (C) Letter-value plots (Hofmann et al., 2017) showing wavelengths and wave heights displayed by profile number (profiles 1 – 6 in Fig. 5.8, 5.10) highlighting up-

to down-channel variability in the morphology of waves extracted from bathymetry, seismic, and all data; diamonds represent the minimum (resolvable) and maximum values, and boxes are scaled proportionally to number of datapoints.



Waves on the seafloor exhibit wavelengths that range from 6,639 m to 439 m with a mean wavelength of 1,734 m (Fig. 5.12; Tables 5.3 and 5.4). Wave heights range from 48 m to below the data resolution (< 1.5 m) with a mean height of 9 m (Fig. 5.12; Tables 5.3 and 5.4); smaller waves are likely present but undetectable at the resolution of the available data (Fig. 5.10, 5.12A). No systematic wavelength or wave height trends are observed between successive bends moving down-channel (Fig. 5.12A); however, the maximum wavelength and height in each wave field does decrease down-channel (Table 5.3, 5.4). Most profiles (Fig. 5.8) display a systematic downstream decrease in wave height (Fig. 5.10, 5.12B, 5.13A). In some profiles individual wavelengths and the overall range of wavelengths also decrease downstream (e.g. WF1a axis; Fig. 5.10, 5.12B, 5.13A); however, a systematic downstream variation in wavelength is not apparent (Fig. 5.12B, 5.13A). Wavelengths and wave heights decrease toward the up-channel and down-channel margins of each wave field, and therefore away from the bend apex (Fig. 5.8, 5.10, 5.12C). The decrease in wavelength and height is more abrupt at the down-channel margin of the field. The profiles containing the highest maximum and average wavelengths and heights (profiles 3, 4 or 5) are located toward the middle of each sediment wave field (Fig. 5.12C).

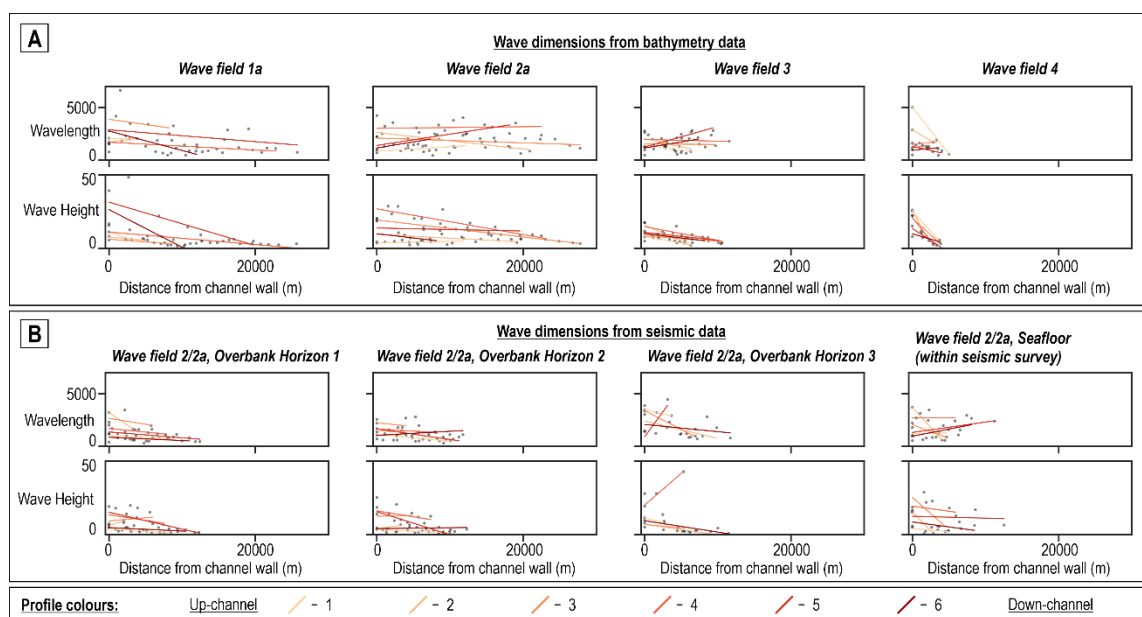


Figure 5.13 – Scatter plots showing wave dimensions (wavelengths and heights) versus distance from the channel wall for (A) each wave field on the seafloor, and (B) wave field 2/2a on each subsurface horizon. Best fit lines are coloured by profile (same as in Fig. 5.12; see Fig. 5.9 and Fig. 5.14 for locations). Note that most best fit trends show a general downstream decrease in wavelength and wave height.

	Name	Wavelength (m)				Wave Height (m)				No. of readings (N)
		Minimum	Maximum	Mean	Median	Minimum	Maximum	Mean	Median	
Measured From Bathymetry	Wave Field 1	460	6639	1730	1430	1.5	48.3	8.0	5.2	43
	Wave Field 2	439	4240	1919	1763	2.3	28.6	10.3	8.5	59
	Wave Field 3	484	2829	1589	1352	2.1	17.7	7.6	7.3	38
	Wave Field 4	447	5013	1461	1266	2.3	26.1	10.3	7.5	19
	All From Bathymetry	439	6639	1734	1439	1.5	48.3	9.0	6.6	159
Measured From Seismic	Overbank Horizon 1, Wave Field 2	299	3454	1142	949	1.2	19.8	6.3	4.7	40
	Overbank Horizon 2, Wave Field 2	299	2793	1172	1088	0.7	25.2	6.2	3.7	42
	Overbank Horizon 3, Wave Field 2	705	4455	1981	1571	0.7	42.8	9.0	4.5	24
	Seafloor, Wave Field 2	534	3718	1739	1571	0.6	28.8	9.8	6.1	26
	All From Seismic	299	4455	1422	1142	0.6	42.8	7.5	4.7	132
All Data		299	6639	1592	1314	0.6	48.3	8.3	5.9	291

Table 5.3 – Minimum (resolvable), maximum and average wavelengths and heights of the sediment waves in each wave field.

	Name	Wavelength				Wave Height				No. of readings (N)
		Minimum	Maximum	Mean	Median	Minimum	Maximum	Mean	Median	
Measured From Bathymetry	Profile 1	439	5013	1416	968	2.1	25.2	6.3	5.0	17
	Profile 2	546	4240	1747	1604	2.6	26.1	8.0	5.9	22
	Profile 3	622	6639	1878	1687	2.4	28.6	9.2	7.1	29
	Profile 4	460	4033	1764	1540	1.5	28.5	9.5	6.9	36
	Profile 5	447	4179	1993	2044	2.3	48.3	11.6	8.9	28
	Profile 6	473	3483	1462	1383	1.7	39.2	8.0	6.5	27
Measured From Seismic	Profile 1	490	3483	1049	896	0.6	11.6	3.0	2.3	27
	Profile 2	598	3718	1700	1482	0.8	15.6	5.1	3.8	14
	Profile 3	577	3454	1995	2016	2.0	28.8	10.9	9.1	13
	Profile 4	597	3868	1844	1887	1.4	28.0	14.0	12.7	16
	Profile 5	299	4455	1328	1194	0.7	42.8	10.4	6.5	31
	Profile 6	299	3227	1255	1109	0.7	15.3	4.7	3.6	31
All Waves	Profile 1	439	5013	1191	896	0.6	25.2	4.3	3.1	44
	Profile 2	546	4240	1729	1550	0.8	26.1	6.9	5.0	36
	Profile 3	577	6639	1914	1725	2.0	28.8	9.7	7.7	42
	Profile 4	460	4033	1789	1606	1.4	28.5	10.9	8.4	52
	Profile 5	299	4455	1644	1337	0.7	48.3	10.9	8.6	59
	Profile 6	299	3483	1351	1196	0.7	39.2	6.2	5.0	58

Table 5.4 – Minimum (resolvable), maximum and average wavelengths and heights of sediment waves across all fields, displayed by profile (shown in Fig. 5.8 and Fig. 5.14); profile 1 is furthest up-channel and profile 6 is furthest down-channel.

5.6.2.2 Interpretations

The exclusive presence of outer-bend wave fields on only the landward margin suggests that the velocity and / or magnitude of the overspilling flow was enhanced on the landward and hindered on the oceanward overbank. This may have occurred due to: (a) the influence of the Coriolis force (Wells and Cossu, 2013), or (b) overspilling flow reflecting (Kneller et al., 1991; Bell et al., 2018a) off the Chatham Rise and / or the subducting plate generating a transverse (landward; to the northwest) component of flow that likely counteracts overspill on the oceanward margin, and potentially aids overspill on the landward margin. scenario (a) likely affects the whole channel, whereas the effects of (b) are likely to be spatially variable. The observed down-channel decrease in wave field size is potentially a result of flow tuning, whereby the portion of a flow capable of overspilling systematically decreases down-channel as the flow thins due to material being lost from the upper part of the flow as it traversed successive up-channel bends (Mohrig and Buttles, 2007; Kelly et al., 2019). However, the East Cape Current, a contour current that flows SW along the subduction front before turning anti-clockwise and crossing the channel in the location of the study area (Fernandez et al., 2018), may counteract overbank flow on the landward margin in the distal parts of the study area, further inhibiting sediment wave development in WF3 and WF4.

The observed pattern of diminishing wave heights up- and down-channel from the wave field axis is interpreted as the result of overbank flow travelling sub-perpendicular to the wall of the channel bend it originates from, which typically occurs along most of the length of that bend. Thus, bulk wave curvature in a wave field generally scales proportionally with the curvature of its formative bend (Fig. 5.9C). However, the action of centrifugal force leads to increased overspill, and consequently the generation of larger waves, downstream of the bend apex, with overspill diminishing up- and down-channel from the wave field axis (Straub et al., 2008).

The wavelengths and heights of the outer-bend waves observed here are consistent with the ranges quoted by Wynn and Stow (2002) for those on levees (< 7 km and < 80 m respectively). Cores from the overbanks of the Hikurangi Channel examined by Lewis and Pantin (2002) and Mountjoy et al. (2018) contain thin-bedded turbidites that grade from fine sand or silt to mud (a mixture of silt and clay), which is also consistent with typical grain-sizes observed on submarine channel overbanks (Wynn and Stow, 2002). High backscatter and RMS amplitude values observed on the stoss sides of the waves (Fig. 5.11A, B) suggest that the stoss sides of the sediment waves contain coarser sediment than the lee sides; this finding is consistent with observations made by Lewis and Pantin (2002). These patterns may arise due to coarse grained sediment being preferentially bypassed on the lee sides where finer grained deposits form from the tails

of overspilling flows. Meanwhile, on the upstream-dipping stoss sides deposition of a wider grain-size range is permitted.

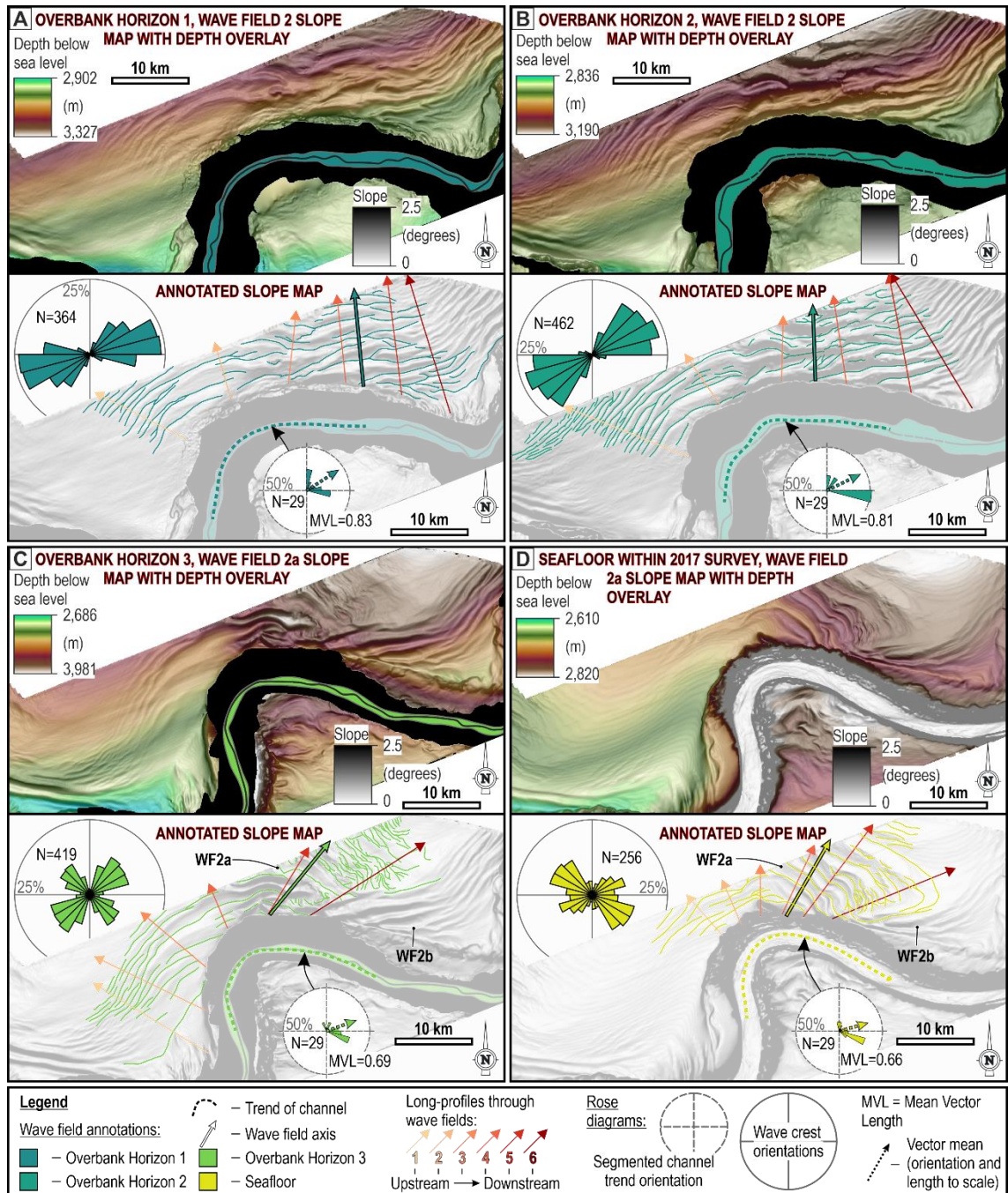


Figure 5.14 – Maps showing the seafloor expression of wave field 2 / 2a within the extent of the 3D seismic survey on Overbank Horizon 1 (A), Overbank Horizon 2 (B), Overbank Horizon 3 (C), and the seafloor (D). For each horizon, an uninterpreted slope map with depth overlay and an interpreted slope gradient map are displayed. On the interpreted map, the wave crests, the trend of the related channel bend, the locations of the longitudinal profiles shown in Fig. 5.15, including the wave field axis, and two inset rose diagrams showing the (bi-directional)

orientations of the wave crest segments and the vector directions of the segmented channel bend trend are highlighted.

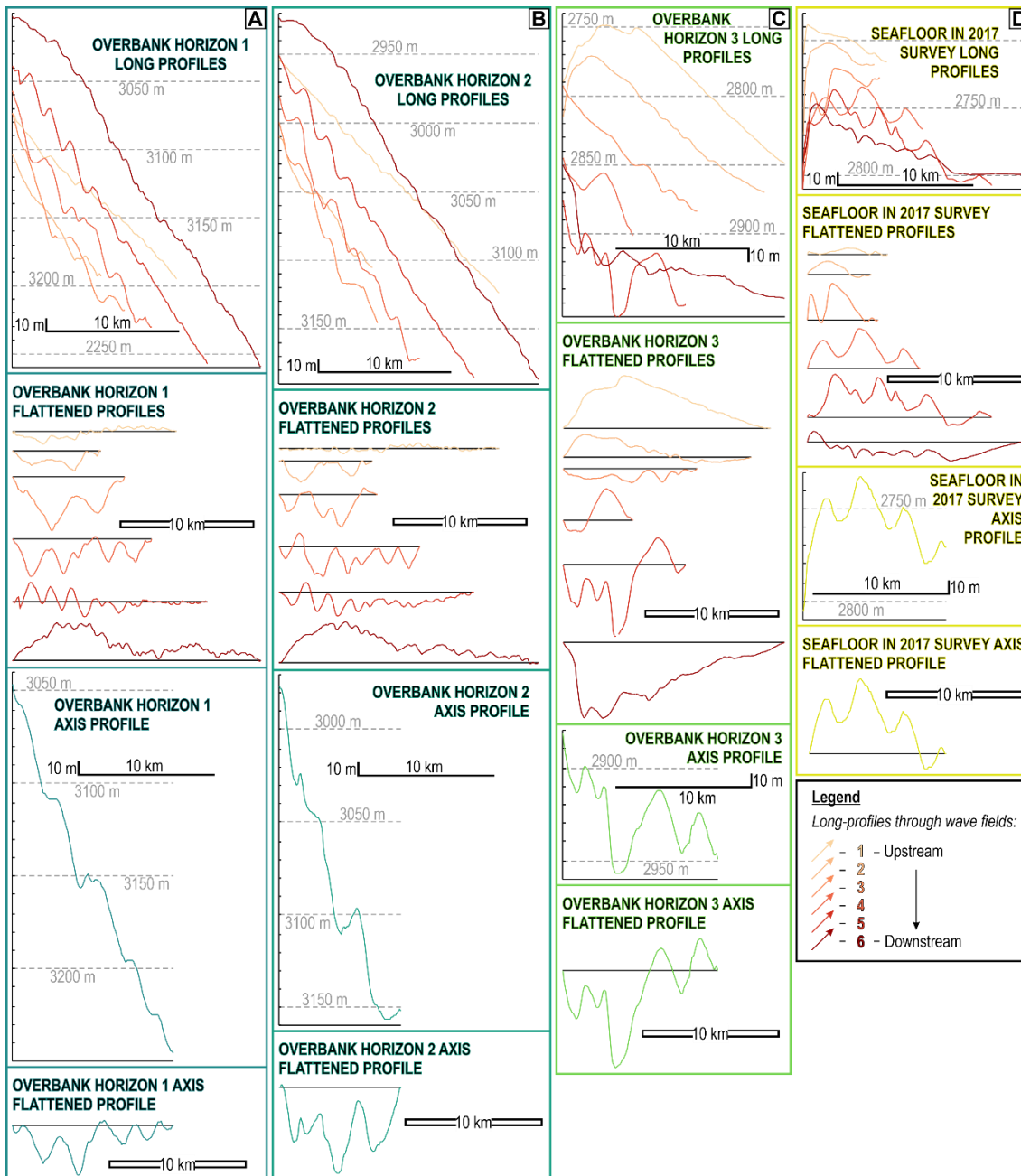


Figure 5.15 – Crest-perpendicular profiles (locations shown in Fig. 5.14) through wave field 2 / 2a, within the extent of the 3D seismic survey, measured on Overbank Horizon 1 (A), Overbank Horizon 2 (B), Overbank Horizon 3 (C), and the seafloor (D). For each wave field, the six profiles used for the extraction of wave dimensions in Fig. 5.12 are shown in depth and flattened to their upstream and downstream ends, and the wave field axis (profile containing the largest overall wavelength and wave heights), which is also shown in depth and flattened.

5.6.3 Outer-bend sediment waves in the subsurface

5.6.3.1 Observations

In the subsurface, waves are present through the shallowest 800 m of stratigraphy, although only the upper 600 m of stratigraphy is the focus of this study. In crest-perpendicular cross-sections, they exhibit sigmoidal geometries with thicker reflectors on their stoss sides, and their troughs and crests consistently stack toward the channel (Fig. 5.11C). Reflectors also exhibit higher RMS amplitudes on their stoss sides than their lee sides (Fig. 5.11B). The same four outer-bend wave fields observed on the seafloor have been mapped in the subsurface (WF1/1a, WF2/2a, WF3 and WF4; Fig. 5.7) on three subsurface horizons (Overbank Horizons 1 – 3; shallowing respectively; Fig. 5.4, 5.7). A down-channel decrease in wave field size is observed on all subsurface horizons (Fig. 5.7). The fields appear to show a general upward increase in area through the stratigraphy (Fig. 5.7E), but this may be due to diminished data resolution at depth impeding detection of smaller waves at the extremities of the field. The wave fields also change shape through the stratigraphy, from being relatively wide (along-channel) and short (distance away from the channel) fields that interfinger with their up-channel and down-channel neighbours in the deeper stratigraphy (Fig. 5.7A, B), to being narrow and long seafloor wave fields that are distinct from their neighbours (Fig. 5.7D).

Analysing the 3D distributions and morphologies of waves through the stratigraphy beneath WF2a permits an examination of the evolution of the wave field. The curvature of bend 4 (the formative bend of WF2a) increases through progressively shallower stratigraphy (Fig. 5.9D, 5.14), accompanied by: (a) an increase in the spread of the wave crest segment orientations and inferred palaeoflow (Fig. 5.9B, C, 5.14), (b) a down-channel shift and rotation of the up-channel and down-channel extent of the wave field, the mean palaeoflow orientation (mean vector orientation of palaeocurrents), and the wave field axis (Fig. 5.9B, E, 5.14). The axis of WF2/2a is consistently positioned down-channel of the mean palaeocurrent orientation and the apex of bend 4 (Fig. 5.9B).

The wave heights and wavelengths (Tables 5.3 and 5.4) in WF2/2a become larger through progressively shallower stratigraphy but appear to be smaller on the seafloor than in Overbank Horizon 3 (Fig. 5.12A, 5.14, 5.15). Similar trends of wave morphology to those observed on the seafloor are observed throughout the subsurface: crest-perpendicular transects typically display a downstream decrease in wave height (Fig. 5.12B, 5.13B, 5.14, 5.15), and wave heights and wavelengths generally increase toward the centre of the wave field (Fig. 5.12C, 5.14, 5.15).

5.6.3.2 Interpretations

The cross-sectional geometries of the waves are consistent with upstream-migrating sediment waves observed on the overbanks of many other submarine channel systems, wherein deposition on the shallow or upstream-dipping stoss sides occurs faster than on the lee sides, where bypass prevails (e.g. Nakajima and Satoh, 2001; Migeon et al., 2000, 2001; Normark et al., 2002). Observed reflector thickness trends (thicker stoss sides) and RMS amplitude trends (higher on the stoss sides) can be generated by either the 'lee wave' (Flood, 1988; Lewis and Pantin, 2002) or 'cyclic-step' (Slotman and Cartigny, 2020) models (Fig. 5.1).

At the time of Overbank Horizons 1 and 2, the channel was straighter compared to the modern channel and likely had steeper outer-levee gradients, allowing almost continuous overspill on the landward overbank, with a slight superimposed increase in overspill toward bend apices. Coriolis forcing likely enhanced overspill on the landward overbank. Through time, as the channel became more sinuous, centrifugal force became more dominant causing a focusing of thicker, faster overbank flow just downstream of the bend apices (Hay, 1987; Straub et al., 2011), leading to: (a) a separation of the wave fields from their up-channel and down-channel neighbours, (b) an increase in wave crest curvature, and (c) a down-channel shift in the wave field axis, the mean inferred flow orientation, and the up-channel, and down-channel limits of the wave fields. Effects of bend expansion may have been enhanced by diminishing outer levee gradients as trench sedimentation from transverse drainage networks became more voluminous and suppressed levee growth (see 'large scale trends' section above).

Up-stratigraphy increases in average wave heights and wavelengths (Fig. 5.12A) may reflect an enhancement in maximum overspilling flow velocities within each wave field due to increasing centrifugal influence, or combination of compactional effects and limits in data resolution; however, temporal variability in the average thickness of channel-traversing flows related to changes in sediment supply entering the system from the feeder canyons cannot be discounted.

5.6.4 Inner-bend overbank waves on landward channel margin

5.6.4.1 Observations

On the seafloor discrete wave fields are observed on the inner-overbanks of bends 3 and 5 (WF1b and WF2b; Fig. 5.2C); these are smaller (~ 105 km² and ~ 115 km² respectively) than adjacent outer-bend fields, and are not present in the deepest studied stratigraphy (Overbank Horizons 1 and 2). On Overbank Horizons 1 and 2, the down-channel ends of waves in WF2 interfinger with the up-channel ends of waves in WF3. Between Overbank Horizon 2 and 3, WF2 divides into two distinct fields (Fig. 5.16):

'WF2a', within which waves are arcuate and broadly concentric around the outside of bend 4 (Fig. 5.14), and 'WF2b', where waves are relatively straight and orientated at a high angle to the channel-wall (WSW-ENE) (Fig. 5.16D). WF1 shows a similar division into WF1a and WF1b. Wave crests at the down-channel end of WF2a are orientated sub-perpendicular to the crests of waves in WF2b, and terminate abruptly along a boundary that follows the crests of the waves in WF2b. In Overbank Horizon 3, waves in WF2b interfinger with waves in WF3, but on the seafloor WF2b and WF3 are distinct (Fig. 5.14, 5.16).

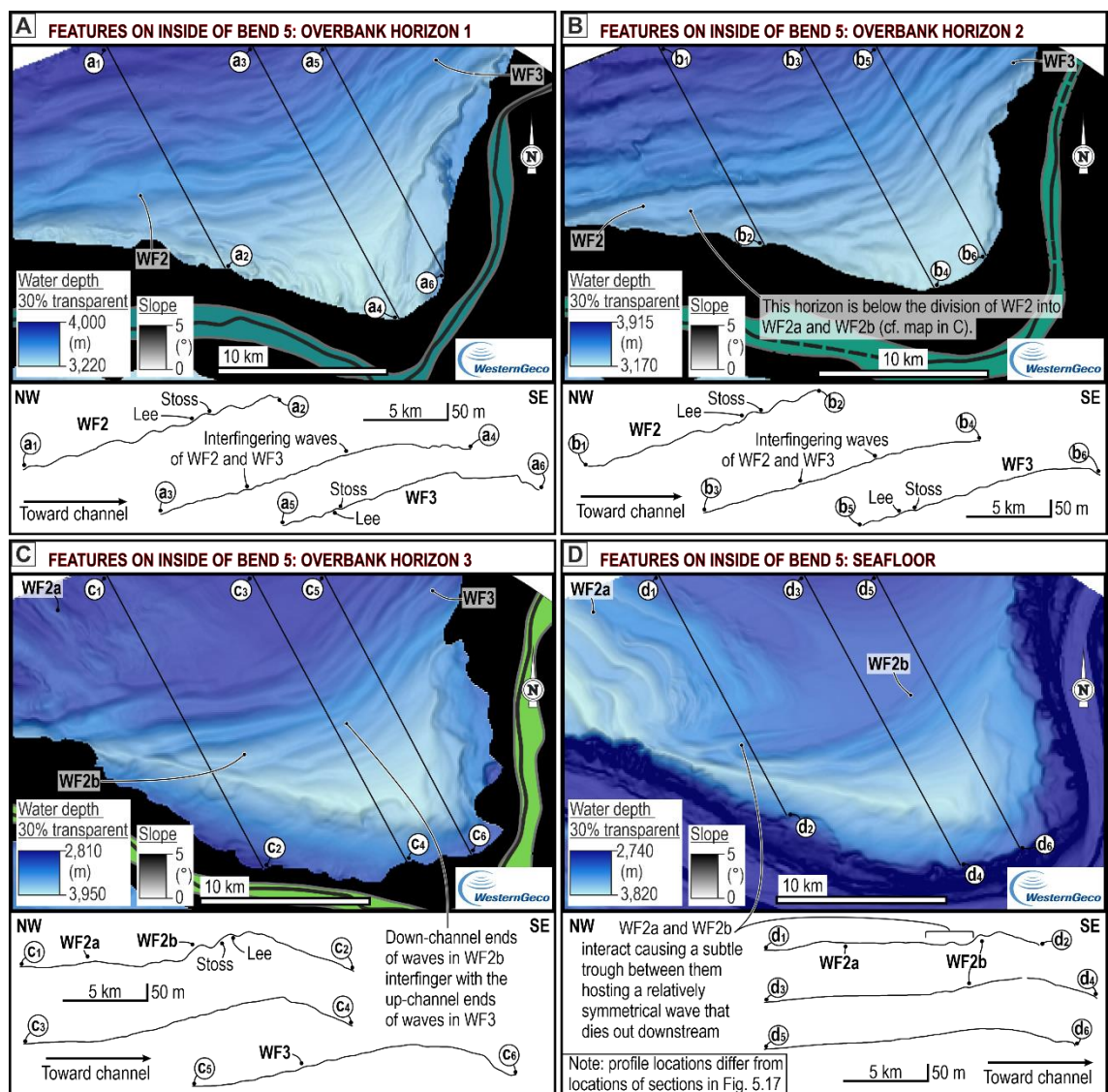


Figure 5.16 – (A) – (D) Slope maps with depth overlays centred on wave field 2 / 2b showing its relationship with field 2a and field 3, and three ~ crest-perpendicular profiles extracted from: Overbank Horizon 1 (A), Overbank Horizon 2 (B), Overbank Horizon 3 (C), and the seafloor (D).

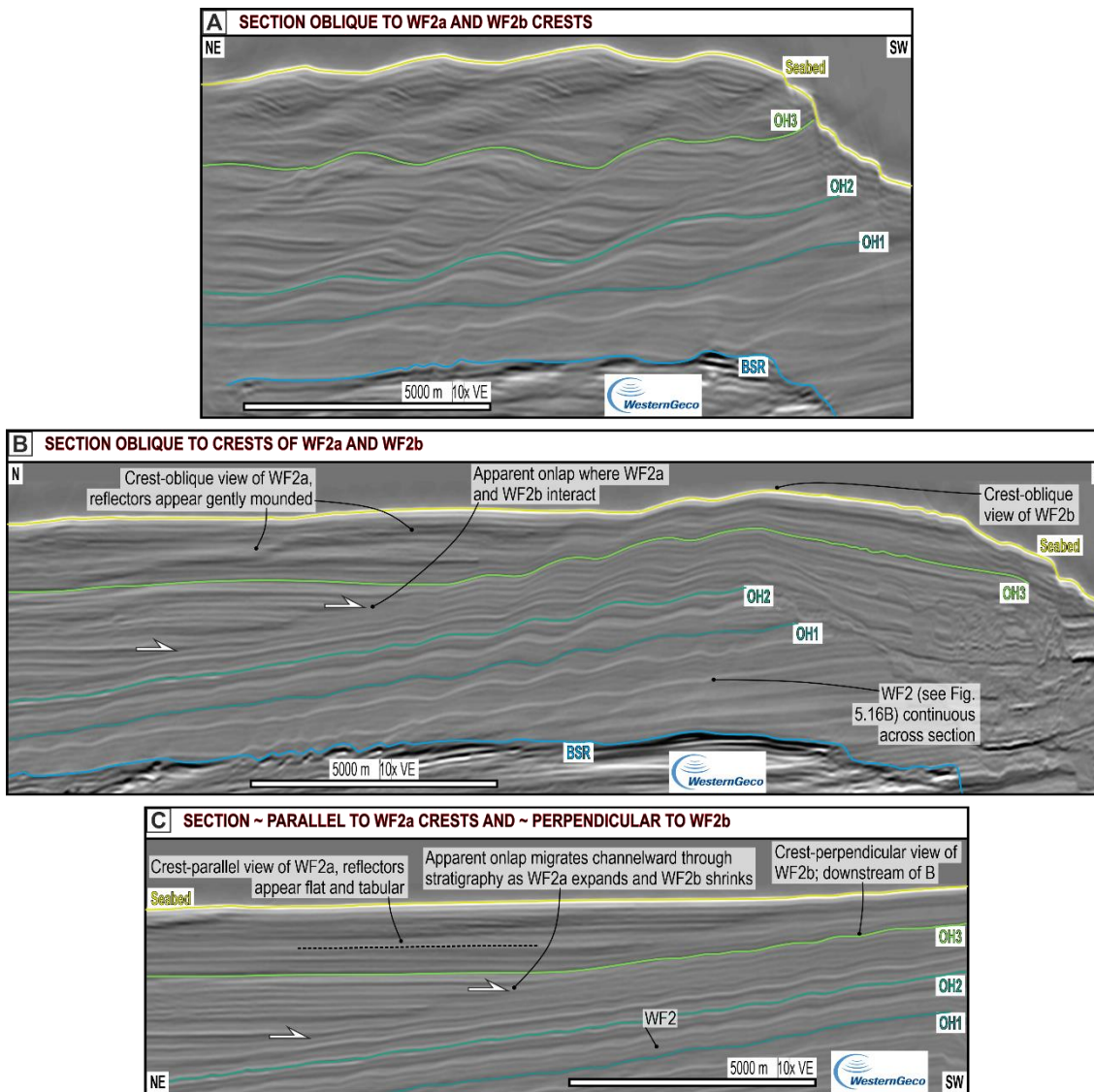


Figure 5.17 – Annotated seismic sections at different angles to the wave crests in wave field 2a and 2b: (A) is orientated oblique ($\sim 45^\circ$) to crests in both fields, (B) is orientated oblique to crests in both fields, but at a higher angle ($\sim 70^\circ$) to crests in field 2b, and a lower angle to those in field 2a, (C) is orientated \sim perpendicular to crests in field 2b and \sim parallel to those in field 2a. Differences in sediment wave height and wavelength are related to the sections being located at different positions along the channel. Note that these sections do not correspond to the profile locations in Fig. 5.16.

Waves in WF2b (visible on Overbank Horizon 3 and the seafloor) exhibit wavelengths of $< 1,500$ m (mean 1,250) and heights of < 20 m (mean 10) at their up-channel (WSW) end. Wavelengths and heights decrease downstream and down-channel (Fig. 5.16), where they branch into multiple smaller waves that interfinger with waves in WF3 (e.g. on Overbank Horizon 3; Fig. 5.16C) or diminish to heights below data resolution (e.g. on the seafloor; Fig. 5.16D). On the seafloor, immediately NE of

WF2a, is a broad, flat area devoid of sediment waves (Fig. 5.16D) that sits stratigraphically above buried waves. This area constituted the upstream part of WF3 in Overbank Horizon 3 (Fig. 5.16C).

In crest-perpendicular cross-section, waves in WF2b exhibit the same sigmoidal reflector geometries with upstream-stacking troughs and crests, similar to outer-bank wave fields (cf. Fig. 5.11C and Fig. 5.17). The crest and trough trajectories of waves in WF2b continue uninterrupted through ~ 500 m of stratigraphy, and the orientations of their peaks and troughs are concordant through the separation of WF2 into WF2a and WF2b (Fig. 5.17), suggesting the waves in WF2b have remained relatively static, while waves in WF2a have rotated clockwise. In cross-sections orientated oblique to wave crests in WF2a and WF2b, the waves from the two fields appear concordant (Fig. 5.17A). However, in sections orientated at higher angles to wave crests in WF2b, there is an abrupt lateral transition between sigmoidal wave-bearing reflectors of WF2b that dip away from the channel, to apparently flatter, mounded or tabular reflectors that represent the crest-parallel expression of waves in WF2a (Fig. 5.17B, C). Reflectors (and packages thereof) in WF2a are thicker than contemporaneous reflectors in WF2b, causing the transition between the wave fields to step channelward through progressively shallower stratigraphy, coinciding with the areal growth of WF2a and shrinkage of WF2b (cf. Fig. 5.16C and D). This transition is marked by a subtle trough (Fig. 5.16D), at which reflectors associated with both wave fields terminate, although the onlap of reflectors in WF2a onto those in WF2b may be mis-interpreted (Fig. 5.16B, C).

5.6.4.2 Interpretations

Accompanying the expansion of bend 4, WF2 divided into distinct outer-bend (WF2a) and inner-bend (WF2b) fields as overspill on the outer-bank of bend 4 became focused downstream of the bend apex due to an increase in the influence of centrifugal force.

Wave crest-perpendicular overbank flow at the location of WF2b is interpreted to have occurred consistently since sediment wave initiation (deeper than Overbank Horizon 1). The waves in WF2b formed and migrated upstream (SSE) through crest-perpendicular, NNW directed overspill on the inside of bend 5, in a similar manner to the outer-bank sediment waves described above. Overspill on inner-bend overbanks flowing away from the apex of bend 5 can only occur on the landward overbank, due to flow enhancement by the Coriolis force. As WF2a separated from WF2b and rotated, an area of flow interaction was generated between the two fields (Fig. 5.18). Thick overspilling flows that traversed WF2a likely spread out due to flow relaxation (Pohl et al., 2019), generating an ESE directed component of flow at the down-channel end of the wave field. This ESE-directed flow component interacted with NNW-directed flow traversing

WF2b, hindering the development of sediment waves, and forming a trough in which flow originating from both wave fields travelled ~NE (Fig. 5.18A, B, D). Such troughs may represent areas of higher velocity, and potentially contain deposits of coarser grain size.

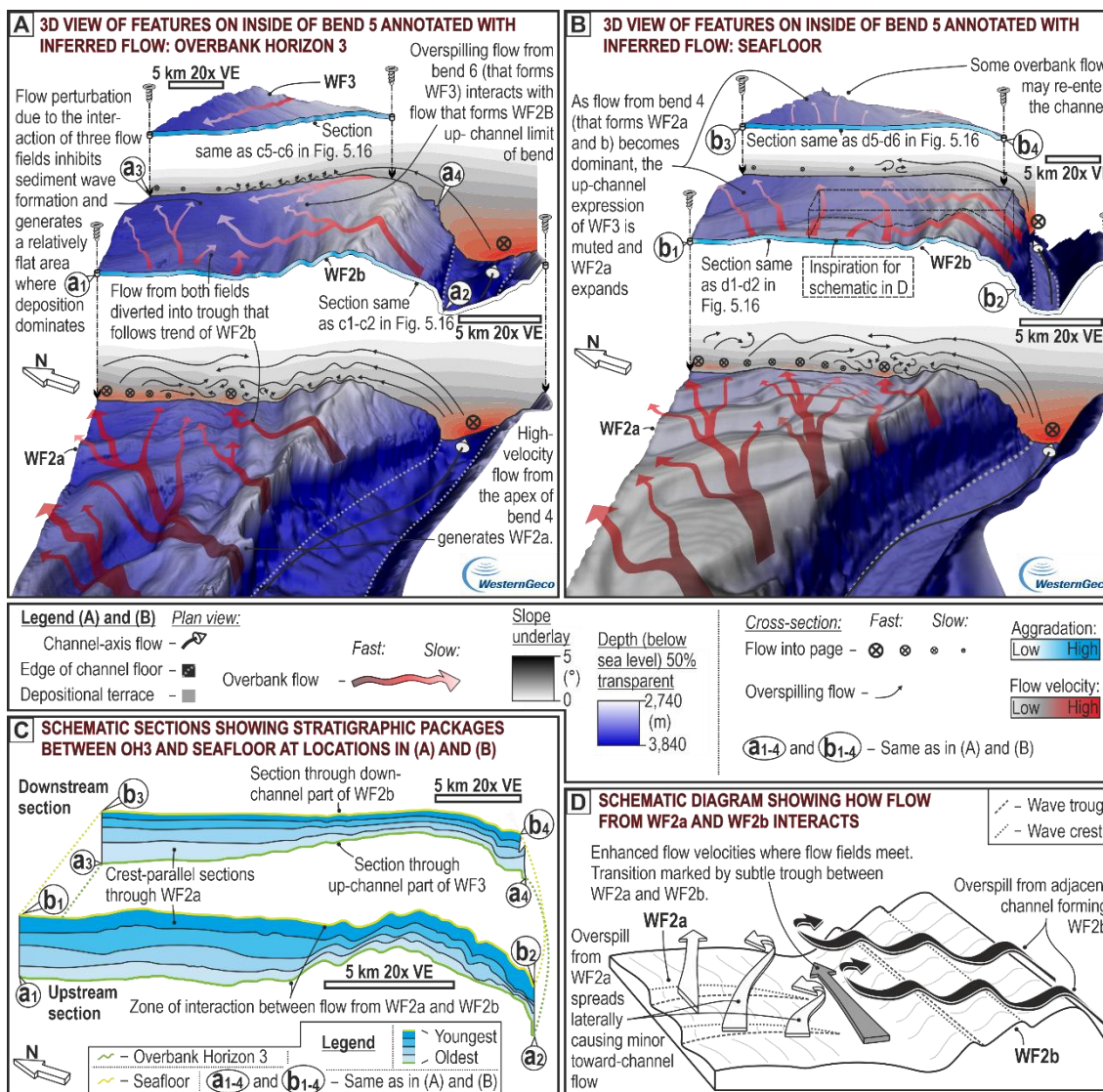


Figure 5.18 – (A) Part of Overbank Horizon 3 (same as shown in Fig. 5.16C) displayed in 3D looking down-channel over the inner-overbank of bend 5, annotated with interpreted overbank flow orientations and velocities, and locations of aggradation. (B) Part of the seafloor (same as shown in Fig. 5.16D) displayed and annotated in the same way as A. (C) Interpreted seismic sections through the locations displayed in A and B, showing the thickness of depositional packages between Overbank Horizon 1 and the seafloor, highlighting an overall down-channel decrease in package thickness and that reflector packages associated with wave field 2a are thicker than those of equivalent age in field 2b. (D) Schematic section showing the interpreted nature of overbank flow interaction between wave fields 2a and 2b.

Based on the thicknesses of contemporaneous reflector packages (Fig. 5.18B), sedimentation rates in WF2a are interpreted to be higher than in WF2b. As WF2a expanded, the outer-levee gradient on the landward channel margin was progressively healed. The disappearance of the up-channel part of WF3 and establishment of a large, waveless area likely occurred as combined overbank flow from WF2a and WF2b became dominant, inhibiting channel-perpendicular unidirectional flow on the up-channel outer-overbank of bend 6 (the formative bend of WF3) (Fig. 5.18A, B); down-channel focusing of overspill accompanying the expansion of bend 6 likely augmented this process. Some flow from WF2a and WF2b likely re-enters the channel at the down-channel end of WF2b; much of the sediment is, however, interpreted to be deposited in the flat areas on the up-channel outer-overbank of bend 6 (Fig. 5.18A, B, C).

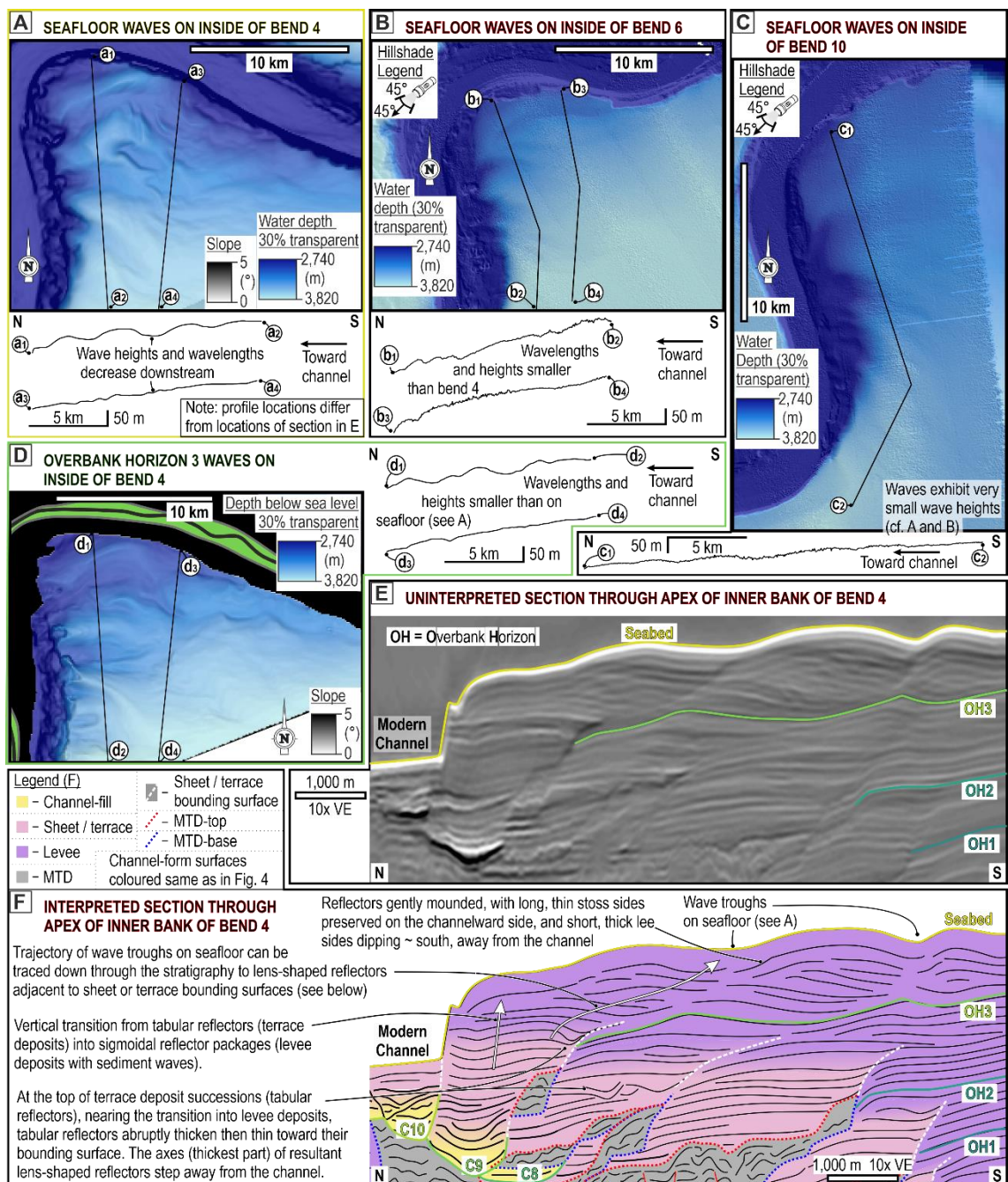


Figure 5.19 – (A) – (C) Seafloor maps displayed as slope (A), or hillshade (B and C) maps with depth overlays, showing inner-bend waves on the oceanward margin, on the insides of bends 4, 6 and 10; crest-perpendicular profiles are also included. (D) Slope map with depth overlay showing the waves on the inner-overbank of bend 4 on Overbank Horizon 3; two ~ crest perpendicular profiles included. (E) Annotated seismic section and (F) interpreted line drawing thereof, showing the seismic expression of the waves on the inner-overbank of bend 4 orientated perpendicular to the wave crests.

5.6.5 Inner-bend waves on oceanward channel margin

5.6.5.1 Observations

Sediment waves are also present on the oceanward margin, on the inner-overbanks of bends 4, 6 and 10 (Fig. 5.19A, B, C). Oceanward inner-bend waves are observed on the seafloor (Fig. 5.19A) and within Overbank Horizon 3 (Fig. 5.19D); they are likely present in deeper stratigraphy (to depths below Overbank Horizon 1) but their 3D geometries are uncertain. The crests of these waves are typically oriented SW-NE to NW-SE at the up-channel end of the field, where they are aligned at orientations sub-perpendicular to oblique to the channel. They curve down-channel and are typically oriented E-W to NW-SE at the down-channel end of the field, where they are aligned subparallel to oblique to the channel (Fig. 5.19). On the inner-overbank of bend 4, at their up-channel end, the troughs of these waves form depressions in the oceanward channel-wall on the straight reach between the apices of bends 3 and 4, reaching over 50 m deep where they intersect the channel-wall (Fig. 5.20A, B). The wavelengths and heights of these waves decrease down-channel, and waves branch to form multiple, smaller waves (Fig. 5.19A, B, C, 5.20A, B).

In wave crest-perpendicular cross-sections, at their up-channel end, the waves exhibit similar, sigmoidal geometries to those observed in waves on the landward margin (cf. Fig. 5.11C and 5.17 with Fig. 5.19E and 5.20C). However, on the oceanward margin the wave troughs and crests stack vertically and away from the channel (S to SE), with thicker reflectors on their lee sides, which dip away from the channel (Fig. 5.19E, F).

At the top of packages of terrace deposits, relatively tabular reflectors that form the main body of the terrace transition vertically into lenticular packages of reflectors that are thickest (up to 20 m) immediately channelward of the adjacent terrace-bounding surface (Fig. 5.19E, F). These reflectors thin abruptly (over tens to a couple of hundred metres) away from the channel and terminate against their adjacent terrace-bounding surface, and gradually thin and pinch out (over hundreds of metres to two kilometres)

toward the channel. The thickest part of these lens-like reflectors stacks vertically and away from the channel (southward) (Fig. 5.19E, F, 5.20C). Through progressively shallower stratigraphy, the deepest part of these lens-like reflectors transition into the troughs of the waves observed on the seafloor and Overbank Horizon 3; the reflectors themselves transition into the thick lee sides of the waves near the seafloor (Fig. 5.19E, F). The terrace-bounding surfaces, the deepest parts of lens-like reflectors, and the wave troughs follow a common trajectory that exhibits a progressively gentler inclination up-stratigraphy and away from the channel (Fig. 5.19E, F). Small waves in the down-channel parts of the field are relatively symmetrical, and do not appear to exhibit distinct differences in reflector geometries on their lee and stoss sides (Fig. 5.20C), although this could be due to geometric variability being below the resolution of the data

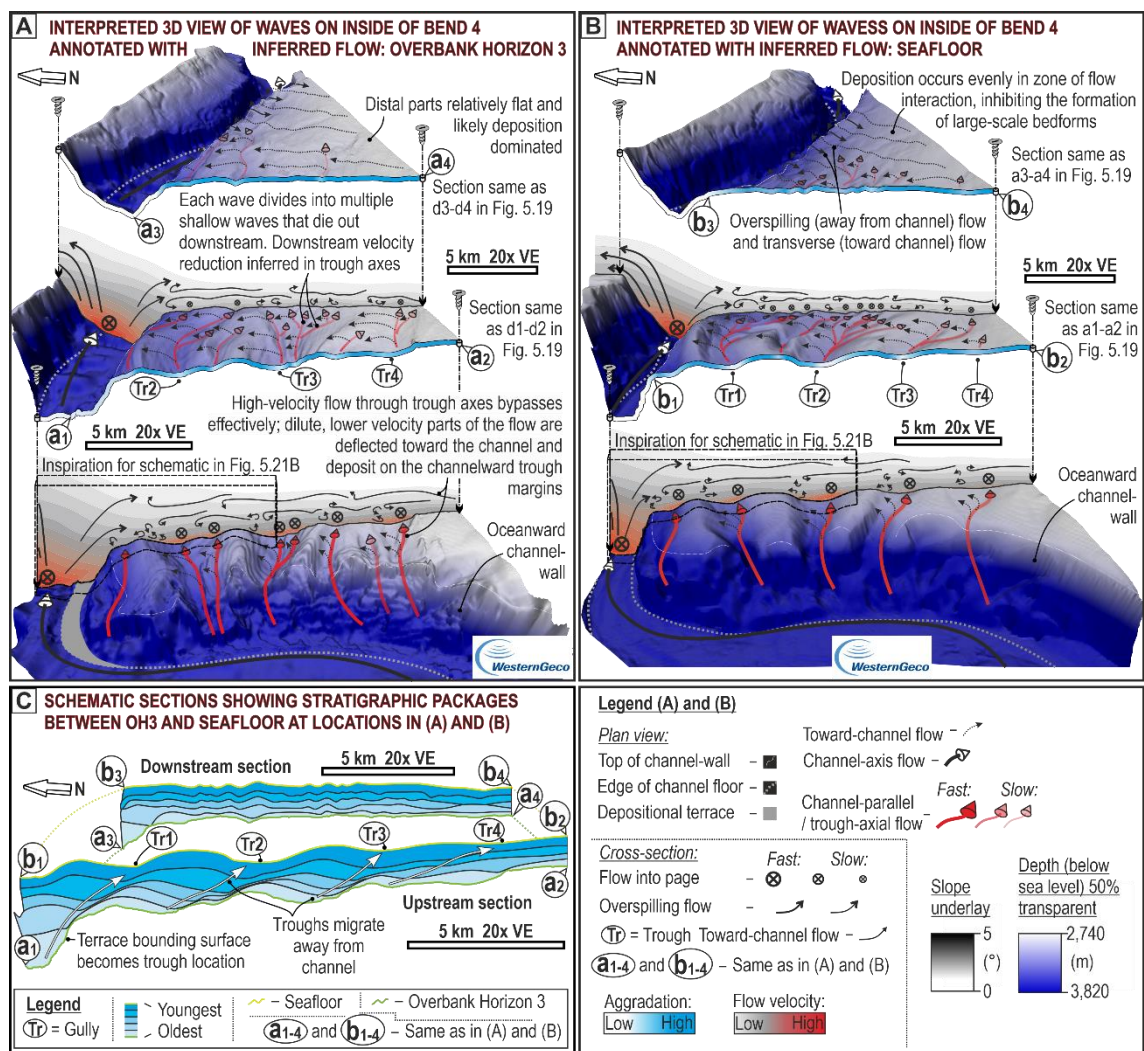


Figure 5.20 – (A) Interpreted part of Overbank Horizon 3 (same as shown in Fig. 5.19D) displayed in 3D looking down-channel over the inner-overbank of bend 4, annotated with interpreted overbank flow orientations and velocities, and locations of aggradation. (B) Interpreted part of the seafloor (same as shown in Fig. 5.19A)

displayed and annotated in the same way as A. (C) Interpreted seismic sections through the locations displayed in A and B, showing the thickness of depositional packages between Overbank Horizon 1 and the seafloor, highlighting an overall down-channel decrease in the sediment wave wavelengths and heights.

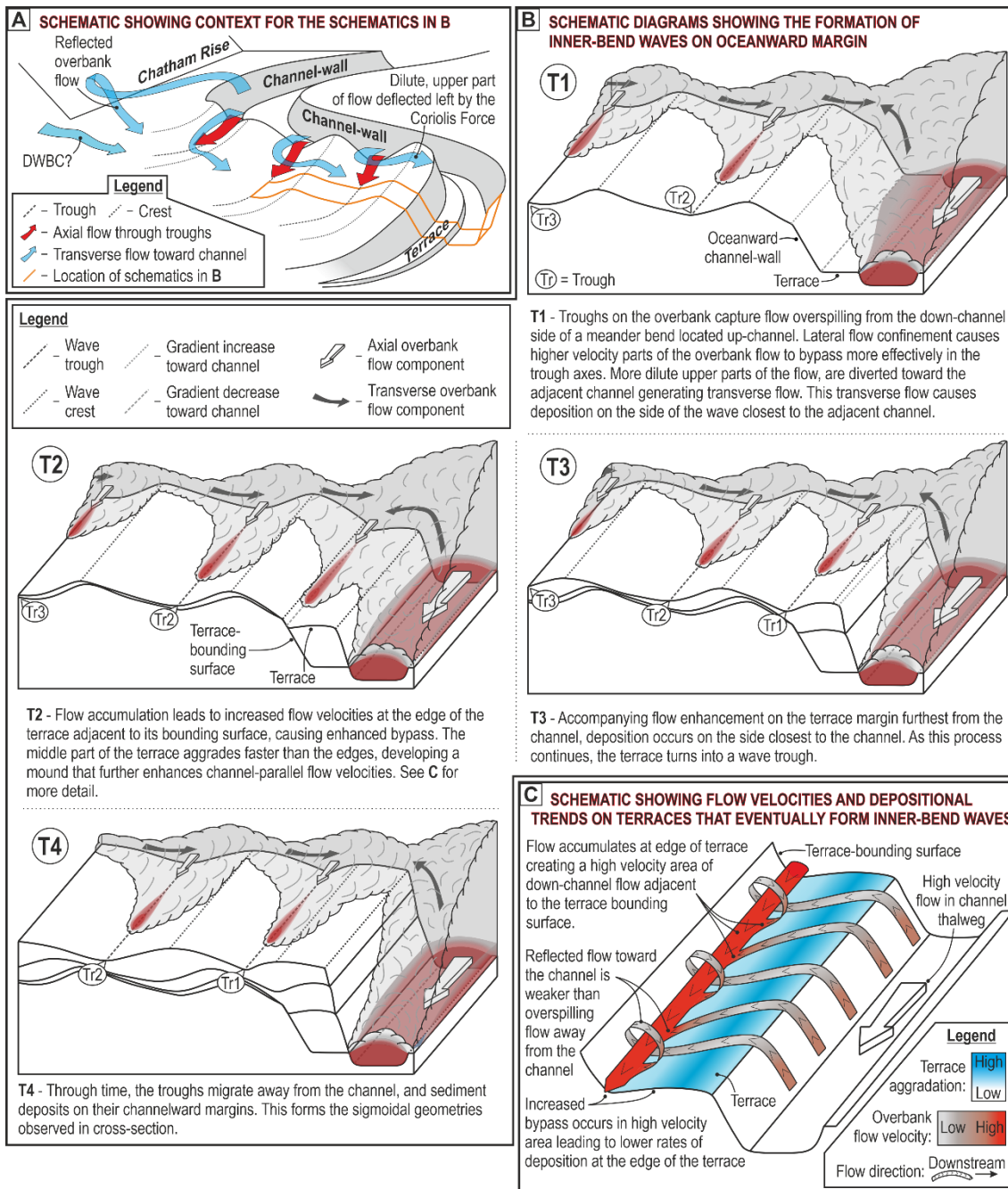


Figure 5.21 – Diagrams showing the formation and evolution of inner-bend waves on the oceanward overbank, specifically on the inside of bend 4. (A) Three-dimensional schematic showing the context of the inner-bend waves detailed in B, and the cause of transverse flow toward the channel and its relationship with trough-

axial flow. (B) Detailed schematic diagrams (location on Fig. 5.20A and B; stratigraphic evolution based on upstream section in Fig. 5.20C; note perspective change from Fig. 5.20 to looking up-channel) demonstrating how the sediment waves evolve from terraces, and how the interaction between axial flow through the wave troughs and transverse flow toward the channel causes sediment wave migration away from the channel. (C) Schematic showing how flow accumulation against the terrace-bounding surface generates a high-velocity component of down-channel flow leading to bypass at the terrace edge and mounding in the centre.

5.6.5.2 Interpretations

Overspill on the oceanward margin is enhanced in the straight channel section between bends 3 and 4 by the influence of centrifugal force downstream of the apex of bend 3. The point of maximum overspill may have also been shifted further down-channel by the influence of the Coriolis force, shifting the point of maximum shear stress on the outside of bend 3 further down-channel. Higher velocity and potentially coarser grained parts of the overbank flow on the inner-overbank of bend 4 were funnelled through the wave troughs that form depressions in the channel wall (Fig. 5.20A, B, 5.21A, B). On the channel overbank, higher concentration, higher velocity, dominantly bypassing parts of the overbank flow (McArthur et al., 2020) travel through the axis of the wave troughs. However, a more dilute component of flow, generated dominantly by deflection due to the Coriolis force and, potentially aided by flow reflected off the Chatham Rise and the subducting plate, and the influence of the DWBC, flows toward the channel (Fig. 5.21A). This transverse component of flow leads to faster deposition on the lee sides of the waves (away from channel), than on the stoss sides; deposition in the axis of troughs is suppressed by the axial flow component (Fig. 5.20A, B, 5.21B). Through time, these processes build the sigmoidal reflector geometries and troughs that stack away from the channel that are observed in the subsurface (Fig. 5.20C); this migration pattern differs from the interpreted toward-channel migration of waves on the oceanward overbank (Fig. 5.17).

The aforementioned waves evolve from terraces. Terraces aggrade faster than levees in the Hikurangi Channel, as evidenced by observed vertical transitions from terrace to overbank deposits (Fig. 5.19E, F; Tek et al., 2021). Flow on terraces is complex, commonly comprising a primary component that flows down-channel and away from the channel, and a secondary component that flows down-channel and toward the channel after being reflected off the terrace-bounding surface (Fig. 5.21C; Hansen et al., 2015). When a terrace has aggraded to near the height of its adjacent levee, the primary flow component dominates the reflected flow component, causing flow convergence

(sensu Kneller, 1995) adjacent to the terrace-bounding surface. Accumulative flow leads to a high velocity component of flow that travels down-channel, parallel to the confining terrace-bounding surface (Kneller and McCaffrey, 1999), where erosion and / or bypass is enhanced, and deposition is hindered (Fig. 5.21C). This process generates mounded reflectors on the terraces and concave-up surfaces adjacent to terrace-bounding surfaces, which are filled with lens-like reflectors (T2 in Fig. 5.21B). High velocity down-channel flow is also sheltered from a Coriolis-induced transverse component of overbank flow (potentially influenced by other processes) that travels toward the channel (responsible for deposition on the lee sides of the waves; see above) by the terrace-bounding surface. As the terrace aggrades further, the influence of this transverse flow component becomes greater. As such, the mounded, middle part of the terrace becomes an inner-overbank wave crest, and the area of enhanced bypass adjacent to the terrace-bounding surface becomes a trough (T3 and T4 in Fig. 5.21B).

Further down-channel, the influence of flow through the axis of the troughs is interpreted to diminish progressively, causing fanning of the waves and rotation of the wave crests to be oriented subparallel to the reach of channel downstream of the bend apex. The less well-pronounced waves in down-channel parts of the field are interpreted to have formed dominantly by the transverse, toward-channel component of flow (Fig. 5.20). The more symmetrical shape of these waves suggests that overbank flow away from the channel on the up-channel outer-overbank of bend 5 may have generated a competing component of flow, impeding strong unidirectional flow and leading to more even deposition (Fig. 5.20).

Figure 5.22 (below) – Schematic diagrams showing eight of the nine processes interpreted to control overspill from the Hikurangi Channel: (A) flow size relative to conduit size, (B) overbank gradient, (C) flow tuning, (D) the Coriolis force, (E) contour current, (F) centrifugal force, (G) flow reflection, (H) interaction with externally derived flows. The interaction of flows originating from different parts of the channel is demonstrated in Fig. 5.24.

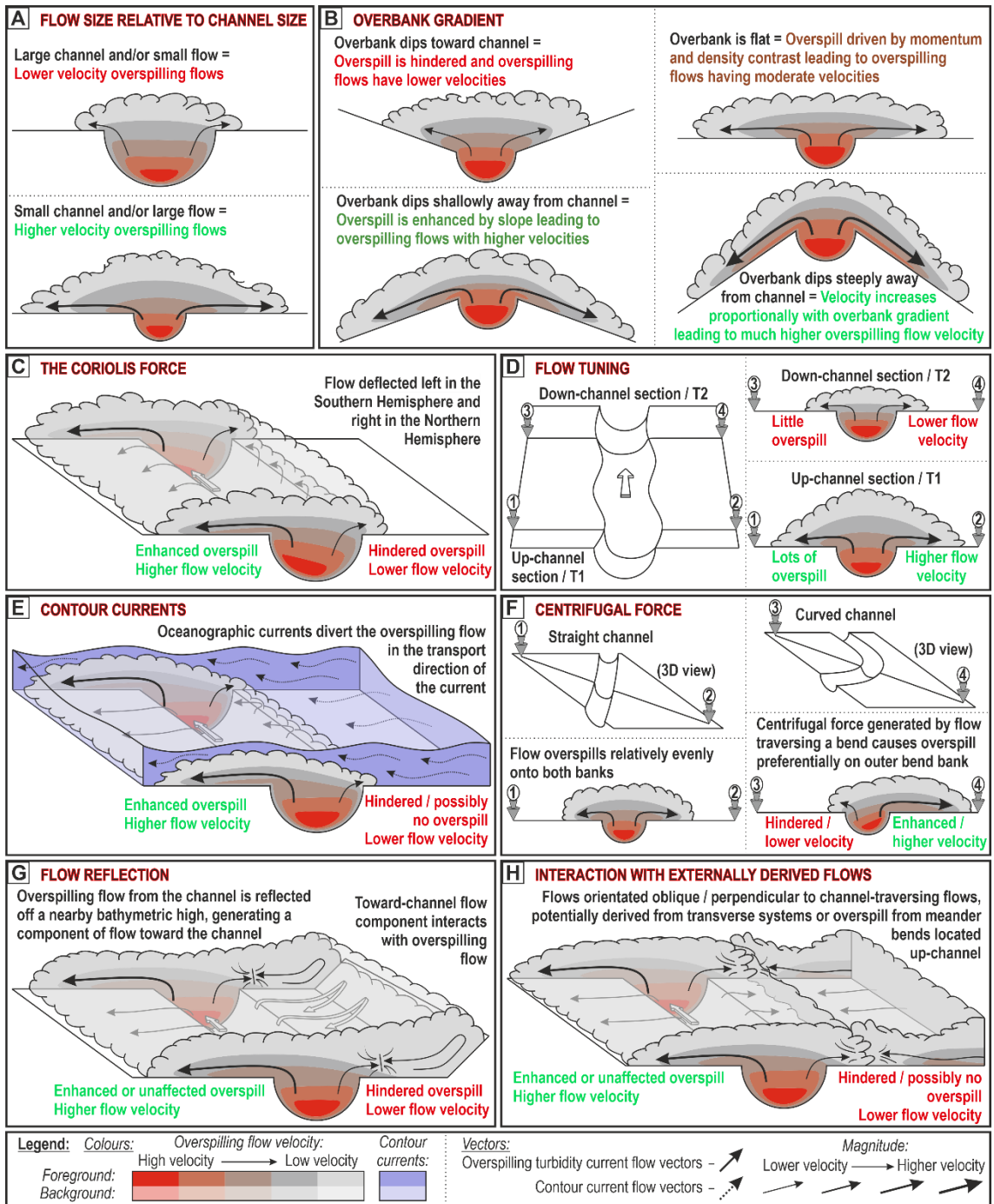
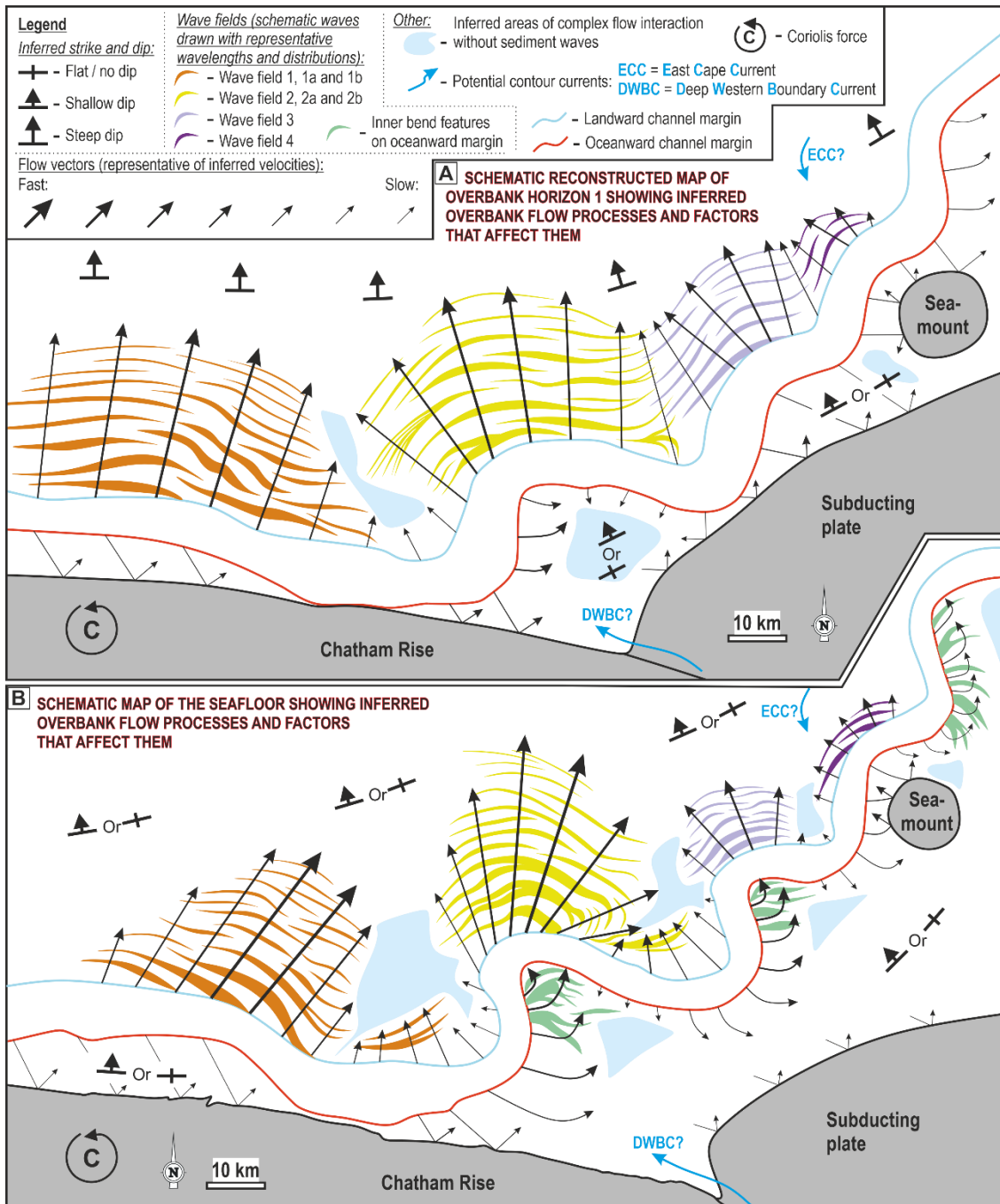


Figure 5.23 (below) – Schematic diagrams showing the distribution of sediment waves and interpreted overbank flow in the deep stratigraphy, on Overbank Horizon 1 (A), and on the seafloor (B).



5.7 Discussion

5.7.1 Controls on overspill processes on the overbanks of the Hikurangi Channel

Nine factors that control the nature of overbank flow and the resultant overbank depositional architecture of the Hikurangi Channel have been identified (Fig. 5.22).

5.7.1.1 Flow size versus conduit size

The thickness of a turbidity current relative to the depth of its host conduit is a fundamental control on the magnitude and velocity of overbank flow. Larger flows

generate thicker and likely higher velocity overbank flow, meaning coarser parts of stratified flows can escape the conduit (Fig. 5.22A; Dennielou et al., 2006).

5.7.1.2 *Overbank gradient*

Flow velocity may be enhanced on channel overbanks with steep outer-levee gradients that slope away from their conduit and hindered on overbanks that slope toward the channel (Fig. 5.22B; Kane et al., 2010b; Nakajima and Kneller, 2013). In the studied reach of the Hikurangi Channel, the oceanward overbank is horizontal, or slopes toward the channel throughout the studied stratigraphy. This appears to have hindered overbank flow and inhibited the formation of sediment waves on the oceanward overbank (Fig. 5.23). On the landward margin, the outer-levee gradient is interpreted to have shallowed progressively as slope-traversing drainage networks were established, and overbank flow downstream of the apex of expanding bends acted to redistribute sediment in the trench, leading to a largely flat trench-floor and gently-sloping to flat outer-levees (Table 5.2, Fig. 3B, 5.23).

5.7.1.3 *Flow 'tuning'*

A systematic down-channel decrease in the magnitude and velocity of overspill from the Hikurangi Channel is attributed to the process of flow 'tuning'. This arises from the loss of material from the dilute, upper parts of flows in up-channel locations, causing the range of flow heights to decrease down-channel as flows progressively lose material, with thicker flows losing more than thinner-ones (Fig. 5.22C; Mohrig and Buttles, 2007; Kelly et al., 2019). Flow tuning has generated a down-channel decrease in the size of the outer-bend wave fields (Fig. 5.23).

5.7.1.4 *The Coriolis force*

The leftward deflection of overbank (and potentially in-channel) flow characteristic of the Coriolis force in the southern hemisphere (Fig. 5.22D; Klaucke et al., 1998; Cossu et al., 2015) has exerted a significant control on overbank architecture throughout the depositional period along the studied channel reach (Fig. 5.23); this control was also recognised by Lewis and Pantin (2002). This flow deflection contributed to the generation of large, outer-bend wave fields solely on the landward overbank. It was also instrumental in the generation of transverse flow toward the channel that forms inner-bend waves on the oceanward channel margin (Fig. 5.20, 5.23), and in maintaining continual flow away from the channel on inner-bend overbanks on the landward margin (Fig. 5.18, 5.23).

5.7.1.5 Contour Currents

Contour currents may locally hinder overspill that flows counter to them and augment overspill in the same direction (Fig. 5.22E; Miramontes et al., 2020). While the locations and orientations of contour currents in the studied part of the Hikurangi Trench are poorly constrained, two currents have potentially affected the study area at different times. Lewis and Pantin (2002) inferred that a shallow branch of the DWBC flowed W along the northern edge of the Chatham Rise, which controlled the formation of inner-bend sediment waves on the oceanward margin (Fig. 5.2, 5.23). The detailed observations made herein allow for the interpretation that the DWBC helped generate a toward-channel component of overbank flow that contributes to the formation of inner-overbank waves (Fig. 5.21). However, the presence of similar waves on the inside of bends 6 and 10, where the DWBC would be unlikely to act, suggests that its effect may have been relatively minor. Furthermore, the DWBC is not observed to be presently active in the study area (Fernandez et al., 2018), meaning its potential effect would vary temporally. The ECC, in contrast, is currently active and likely flows SE across the channel in the study area, but the location of the crossing is unclear (Fig. 5.2). If the ECC crosses the down-channel parts of the studied channel reach, it may be partially responsible for the down-channel decrease in wave field size on the landward overbank (Fig. 5.23). If the ECC crosses the channel in a location further up-channel, its effects are likely negligible and are not recorded by the sediment wave distributions. Bailey et al. (2020) tentatively interpreted that a bottom current crossed the Hikurangi Channel at bend 4, which they inferred locally modified the channel and overbank wave field. However, analysis of the morphology and distribution of these sediment waves herein suggests they are more likely related to overbank flow, meaning that if the ECC crosses the channel at bend 4 it is unlikely to significantly affect overbank sediment wave development. Definitively determining the influence of contour currents on overbank sedimentation in the Hikurangi Trench requires additional oceanographic data.

5.7.1.6 Centrifugal force

Accompanying a channel bend's expansion, centrifugal force causes a focusing of overspill downstream of bend apices (Fig. 5.22F; Timbrell, 1993; Kane et al., 2008). Through time, as the channel became more sinuous, the wave fields on the landward channel overbank became spatially separated from one another, and some divided into distinct outer-bend and inner-bend fields (Fig. 5.23). The plan-view morphologies and distributions of wavelengths and wave heights in each field also changed concomitantly with increased channel sinuosity (Fig. 5.23). The effect of centrifugal force on sediment wave geometries on the seafloor in the study area was originally noted by Lewis and Pantin (2002).

5.7.1.7 Flow reflection

The Chatham Rise and the less prominent subducting Pacific plate generate seafloor topography that runs along the oceanward margin of the channel. Overbank flow reflects off this topography, generating (potentially in conjunction with other factors) a component of flow toward the channel (Fig. 5.22G, 5.23). This toward-channel component of flow may inhibit the formation of outer-bend sediment waves on the oceanward overbank, and contribute to the formation of inner-bend waves on the oceanward overbank (Fig. 5.21). The thickness of contemporaneously formed reflector packages (Table 5.2, Fig. 5.3) suggest deposition rates are generally higher on the flat trench floor than on the steep Chatham Rise and subducting plate. Therefore, largely tabular reflectors were generated, allowing the classification of the oceanward overbank deposits as 'confined external levees' (Table 5.2; Clark and Cartwright, 2011).

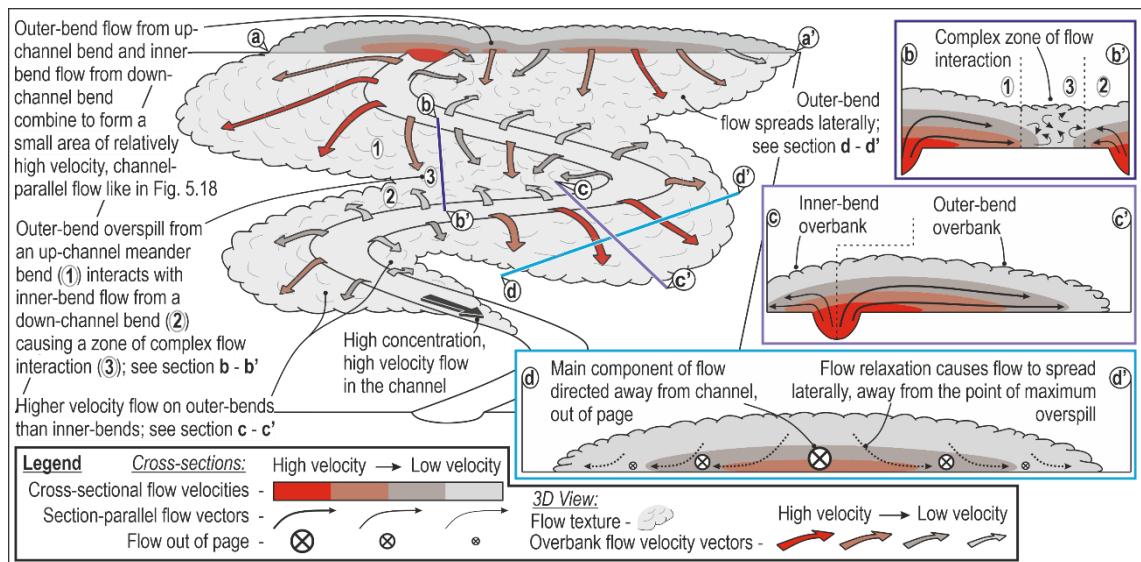


Figure 5.24 – Schematic diagram showing how overbank flow originating from different parts of a channel interacts on the overbanks.

5.7.1.8 Interaction with externally derived flows

The interaction with turbidity currents of different origins (Fig. 5.22H; Okon et al., 2021) may exert a control on overbank flow in the Hikurangi Channel. The dilute, distal parts of SE flowing, slope-traversing turbidity currents may interact with distal, NW flowing overbank flow near the subduction front (Fig. 5.2). Interaction of these turbidity currents may reduce the velocity of unidirectional overbank flow and restrict the size of outer-bend wave fields (Fig. 5.23). Alternatively, flow of these different origins may not

interact, but their deposits may stack compensationally; more data are needed to determine which process is dominant in the Hikurangi Trench. Regardless of whether the individual flows interact, combined deposition from slope-traversing and overbank flows may occur over the entire trench floor (outside of the channel), suppressing the development of steep outer-levee gradients and leading to a relatively flat trench floor (Table 5.2, Fig. 5.3, 5.6). In systems where two contemporaneously active channels run parallel to one another, overspill derived from the two channels may also interact on their mutual overbank, causing flow complexity.

5.7.1.9 Interaction of overspill from different locations

Overbank flows originating from different locations along the channel may generate areas of complex flow interaction, inhibiting the development of sediment waves. In the Hikurangi Channel, overspill down-channel of a landward facing bend may interact with lower velocity up-channel overspill from the next down-channel (landward facing) bend (Fig. 5.23, 5.24). This interaction could initially occur due to bend expansion causing a separation of the wave fields and focusing flow on the downstream sides of bends, generating a complex zone of flow interaction (Fig. 5.24). Consistent unidirectional flow does not occur in these zones and consequently they are devoid of sediment waves (Fig. 5.23). Interaction of flow from different bends is likely to be more common in channel systems with relatively flat, laterally-confined overbanks like the Hikurangi Channel, where the gradient of the outer-levee does not cause overspill to flow consistently away from the channel.

5.7.2 Spatio-temporal variability and interaction of controls

The subsurface architecture and seafloor expression of the studied overbank deposits are a product of the complex interaction between the controls listed above. The effect of most controls will also differ between individual flows as the flow height fundamentally dictates the volume of overspill (Fig. 5.22A); tuning effects may eventually suppress such differences. The influence of some controls, such as the Coriolis force, is also partially dependent on the nature of channel-traversing flows (Cossu et al., 2015; Davarpanah Jazi et al., 2020). Variations in flow thickness and nature can also occur cyclically, in response to sea-level fluctuations and climatic changes (Romans et al., 2016). The effect of some controls, such as contour currents, may also vary over a range of distinct timescales. For example, the ECC is highly variable on interannual and decadal timescales (Fernandez et al., 2018), and the shallow branch of the DWBC invoked by Lewis and Pantin (2002) may only be active during glacial periods. However, the analysis of sediment waves and seismic-scale architecture herein has allowed the spatio-temporal variability of the influence of different controls on net overbank flow and

sedimentation over longer timescales to be determined. This helps to mitigate uncertainty related to variability at timescales between individual flows.

Spatial variability in the magnitude at which controls operate is inferred on the seafloor and in the subsurface. Coriolis forcing (Fig. 5.22D) is the only control that is not spatially restricted at the scale of observation, and consistently affects overbank flow across the entire area. The effect of some controls changes up- or down-channel. For example, by definition, flow tuning (Fig. 5.22C) generates a down-channel decrease in the magnitude of overspill. However, some controls, such as centrifugal force (Fig. 5.22F), overbank gradient (Fig. 5.22B) and interaction of overspill from different locations (Fig. 5.24), are inherently linked to the morphology of the channel and its overbanks. As such, they can produce more localised effects and are subject to feedback effects. For example, the influence of centrifugal force is dependent on bend curvature, meaning its effect will vary between adjacent bends (tens of km) (Fig. 5.23). Other controls that present localised effects but are not directly related to channel morphology include contour currents (Fig. 5.22E) and flow reflection (Fig. 5.22A). For example, in this setting flow reflection is likely to influence flow dominantly on the oceanward overbank (Fig. 5.23). Additionally, as topography generated by the Chatham Rise is steeper, taller, and closer to the channel than the Pacific plate, the strength of reflected flow likely also decreases downstream.

Changes in sediment wave morphology are observed through the studied stratigraphy. These changes are caused by long-term temporal variations in the relative influence of some controls; other controls have affected overbank flow and sedimentation consistently throughout the depositional period. For example, the Coriolis force (Fig. 5.22D) has consistently affected overbank flow and sedimentation throughout deposition (Fig. 5.23). However, the influence of centrifugal force has increased with increasing channel sinuosity. The effect of other controls may have been constant throughout deposition in some areas, but variable in other areas. For example, the effect of toward-channel overbank gradients on the oceanward margin has been constant, whereas the away-from-channel gradient on the landward overbank is interpreted to have progressively shallowed through time, changing its influence on overbank flow (Fig. 5.23).

Multiple controls that influence overbank flow in a given location can either augment, or act against one another. For example, on the oceanward overbank the effects of the Coriolis force (Fig. 5.22D), an overbank gradient that sloped toward the channel (Fig. 5.22B), and flow reflecting off the Chatham Rise and the Pacific plate (Fig. 5.22G), combine to generate a component of flow that travels toward the channel (Fig. 5.21, 5.23). These three factors counteract the effect of centrifugal force on the

oceanward margin, inhibiting the formation of outer-bend sediment waves on the oceanward margin (Fig. 5.23). In addition to separate controls competing for dominance in a given area, the effect of some controls is directly dependent on the presence of others. For example, interaction of overspill originating from different bends (Fig. 5.24) is effectively dependent on channel sinuosity and the effect of centrifugal force; an increase in sinuosity, and therefore centrifugal force, will consequently increase interaction of down-channel overbank flow from up-channel bends, and up-channel flow from down-channel bends, leading to a progressive loss of sediment waves in the location of interaction.

Overall, the complex interaction between controls that have affected overspill on different parts of the overbank area consistently through time, vs. those that are temporally variable has led to the complex sediment wave distributions and depositional architectures described herein. It is therefore difficult to rank the importance of all controls. However, granted that overspill is occurring, evidence for leftward flow deflection is observed across the entire overbank area meaning that, while the effects of other controls locally augmented its effects, the Coriolis force is dominantly responsible for enhanced landward overbank flow and hindered oceanward overbank flow. Through progressively shallower stratigraphy, accompanying an increase in channel sinuosity, the morphologies of the waves on the landward margin have changed accordingly. Therefore, the interaction between Coriolis and centrifugal forcing are interpreted to have produced the most significant effect on overbank sediment wave distribution and overbank architecture, particularly on the landward overbank. These interpretations are generally in accordance with those of Lewis and Pantin (2002).

5.7.3 Inner-bend sediment wave fields

Identification of inner-bend wave fields on both sides of the channel was permitted by using high-resolution bathymetry and 3D seismic data. Inner-bend wave fields on each side of the channel are interpreted to have different mechanisms of formation, but both form as a result of multiple components of overbank flow originating in different locations and travelling in various orientations (Fig. 5.18, 5.20, 5.21). As such, they record more complex patterns of overbank flow and sedimentation than outer-bend waves and the morphologies of their constituent waves do not show simple relationships with the orientations of their formative flows.

Lewis and Pantin (2002) interpreted that waves that migrate away from the channel on the oceanward margin on the inside of bend 4 (this study), were produced solely by westward flowing contour currents (a shallow branch of the DWBC). However, in-depth analysis of these waves and their 3D subsurface architecture suggests that these waves are the product of the complex interaction between two different overbank

flow components: some overspilling flow generates an axial flow component that is funnelled through the wave troughs; some is deflected by the Coriolis force, reflected off the Chatham Rise or subducting plate, and possibly influenced by the DWBC, generating a transverse flow component toward the channel (Fig. 5.20, 5.21).

On the landward margin, inner-bend sediment wave fields have formed and become separated from wave fields on the outer-overbanks as the shape and distributions of outer-bend wave fields have progressively rotated and migrated down-channel (Fig. 5.7, 5.9, 5.14, 5.23). The inner-bend waves are formed and maintained by overspill on the inner-overbank of bends, the velocity of which in the study area is augmented by the Coriolis force. However, a subtle trough marks the contact between the outer- and inner-bend wave fields, which is interpreted to funnel relatively high-velocity parts of the flow (Fig. 5.18, 5.24); the crests of waves in the outer-bend fields are oriented normal to those in the inner-bend fields. The separation of outer bend fields and the complexity of inferred flow within them and at their boundary is due to the interaction of flow components originating from different parts of the channel (Fig. 5.24).

5.7.4 Sedimentological implications

The many controls listed above act to control flow processes and the development of sediment waves on the overbank areas of the Hikurangi Channel. The effect each control exerted on the overbank deposit architecture varied along the channel and through time, generating overbank deposits with a complex three-dimensional architecture. These deposits, their trends, and their sedimentary structures, may differ from those portrayed in conventional models derived from studies using outcrop, seafloor, or 2D seismic data.

On the seafloor, the Hikurangi Channel apparently lacks well-defined levees along much of its length. However, this bears no reflection on how effectively channel-traversing flows overspill, nor the nature of the channel and overbank deposits in the subsurface. It is merely a result of deposition by slope-traversing flows derived from the subduction margin and overspilling from the Hikurangi Channel occurring across the floor of a laterally-confined trench, and effectively filling the lateral accommodation space therein (Fig. 5.3); the Hikurangi Channel is highly aggradational (cf. Casciano et al., 2019). The fact that highly aggradational channels such as the Hikurangi Channel can be bordered by effectively flat overbank areas on the seafloor means the seafloor profile of submarine channel overbanks can be an unreliable predictor of subsurface channel and overbank architecture.

The orientation of overbank flow from the Hikurangi Channel is interpreted to vary substantially. On the oceanward and landward overbanks, interaction of flows

from different bends, flow reflection, and the Coriolis force generate areas with complex multidirectional flow. Deposits in these areas may exhibit highly variable palaeocurrents and may contain 'combined flow' bedforms such as hummocky cross-stratification (Muzzi Magalhaes and Tinterri, 2010). In outcrop, palaeocurrent variability has been used to distinguish 'internal levees' or 'terraces', which typically exhibit highly variable palaeocurrents, from 'external levees', which exhibit less variability (Kane and Hodgson, 2011). However, in outcropping confined channel systems with low overbank gradients, that are analogous to the Hikurangi Channel, this criterion may not be reliable.

In high latitude systems, the dominance of Coriolis forcing upon cross channel flow results in preferential deposition along one channel overbank (Cossu et al., 2015) and hinders sinuosity development (Peakall et al., 2012). In low latitude settings, Coriolis forces are negligible, and flow dynamics are dominated by centrifugal forces, leading to preferential overspill at bend apices on opposing sides of the channel, in successive bends (Keevil et al., 2006; Cossu and Wells, 2010). The overbank architecture of the mid-latitude (*sensu* Menard, 1955; Savoye et al., 1993) Hikurangi Channel displays evidence of the effect of both Coriolis and centrifugal forces on overbank architecture. The relative influence of these competing controls varied through time as a result of changing channel morphology, generating a more complex architecture than can be predicted by either of the aforementioned end member controls.

On the seafloor and in the subsurface of the Hikurangi Channel, evidence for the interaction of overbank flow and deposition from different locations along the channel are observed (Fig. 5.24). Interacting packages of overbank deposits can thin toward, and interfinger with, each other (Table 5.2, Fig. 5.17). In 2D seismic sections or in outcropping sections, these depositional architectures may be interpreted to be derived from an extra-channel source. Evidence for the interaction of contemporaneous overspill from different parts of the channel (Fig. 5.24) is also observed. In outcrop or core, these areas of interaction may exhibit complex paleocurrent variability and contain complex combinations of sedimentary structures and architectures that appear uncharacteristic of classic levee deposits.

Therefore, in the Hikurangi Channel, and probably in channels in other confined basins in mid-latitudes, simple models explaining bed thicknesses and sandstone distribution, palaeocurrent orientations, and sedimentary structures cannot be applied universally. This has implications for the interpretation of overbank deposits and therefore palaeogeographic reconstructions in outcropping ancient channel systems, but also for categorising channel types and inferring flow processes in channels and on their overbanks from bathymetric data alone.

5.8 Conclusions

Integration of high-resolution bathymetry, 2D, and 3D seismic data is used to investigate the controls on overbank flow processes and depositional architecture on the overbank areas of the Hikurangi Channel. Novel techniques for the quantitative analysis of sediment wave orientations and morphologies are conducted on the seafloor and on three, regionally-traceable subsurface horizons, and are used to interpret the three-dimensional subsurface architecture, and infer overbank flow processes.

Nine factors are interpreted to have controlled overbank flow processes on the overbanks of the Hikurangi Channel: flow size versus conduit size, overbank gradient (magnitude and orientation), flow tuning, the Coriolis force, contour currents, flow reflection, centrifugal force, interaction with externally derived flows, and interaction of overspill from different locations along the channel. These controls mutually interact, and their relative importance has varied significantly throughout the depositional period, and in different parts of the studied overbanks, generating complex patterns of overbank flow and sedimentation.

In deeper stratigraphy the Hikurangi Channel was straighter and was bordered on the landward margin by four sediment wave fields, with no wave fields preserved on the oceanward margin. Overspill that formed sediment waves on the landward margin occurred along the whole studied channel reach, and flowed away from the channel over relatively steep external levees; overbank flow velocities decreased down-channel and increased toward the apices of the then poorly-developed bends. Sediment wave formation was inhibited on the oceanward and enhanced on the landward margin by the combined effects of: the oceanward channel overbank sloping toward the channel, flow reflection off the Chatham Rise and the subducting plate, and leftward flow deflection by the Coriolis force.

Through progressively shallower stratigraphy, focusing of overbank flow downstream of bend apices led to the spatial separation of the four wave fields on the landward margin, the division of the most up-channel two wave fields into distinct inner- and outer-bend fields, and the development of inner-bend waves on the oceanward margin. These morphological trends chiefly arose due to an increase in channel sinuosity, augmented by a reduction in gradient on the landward margin as the trench-floor became flat; other controls such as the interaction of overbanks flow with slope-traversing turbidity currents near the subduction margin, and two contour currents (the East Cape Current and the Deep Western Boundary Current) may also have exerted some control.

This study builds on work by Lewis and Pantin (2002). However, detailed observations from high resolution data have permitted new quantitative analysis of wave morphologies and distributions, and interpretation of how the influence of each control has varied through time. It has also allowed the novel identification of distinct inner-bend wave fields. The nature of inner-bend fields on the landward margin is controlled by the interaction of Coriolis-enhanced overspill on wave-hosting inner-bends, and flow from the down-channel outer-bend overbank of the adjacent, up-channel bend. Inner-bend wave fields on the oceanward margin originate as terraces then evolve and migrate through the combined effects of axial flow funnelled through the wave troughs, and transverse flow toward the channel created by dilute overspill reflected off the Chatham Rise or subducting slab, and deflected by the Coriolis force.

Some or all of the controls on overbank flow and overbank deposit architectures identified in the Hikurangi Channel are common to most modern and ancient channel systems, and particularly those in mid-latitude and / or confined basins. This work has implications for the interpretation of overbank flow processes from seafloor data, and palaeoenvironmental reconstructions from ancient, outcropping overbank deposits.

6 Discussion

6.1 Comparison between the Arro turbidite system and the Hikurangi Channel

The Arro turbidite system (Chapter 3) and the studied stretch of the Hikurangi Channel (Chapters 4 and 5) are both examples of channelised deep-water sediment routing systems running axially through elongate, confined basins formed at convergent continental margins. Despite these similarities, the two systems exhibit significant differences in scale, tectonic and oceanographic setting, and depositional architecture. However, comparing systems of different scales, settings and architectures can allow the identification of architectural motifs or evolutionary trends that may be common to channels in such settings, or more generally.

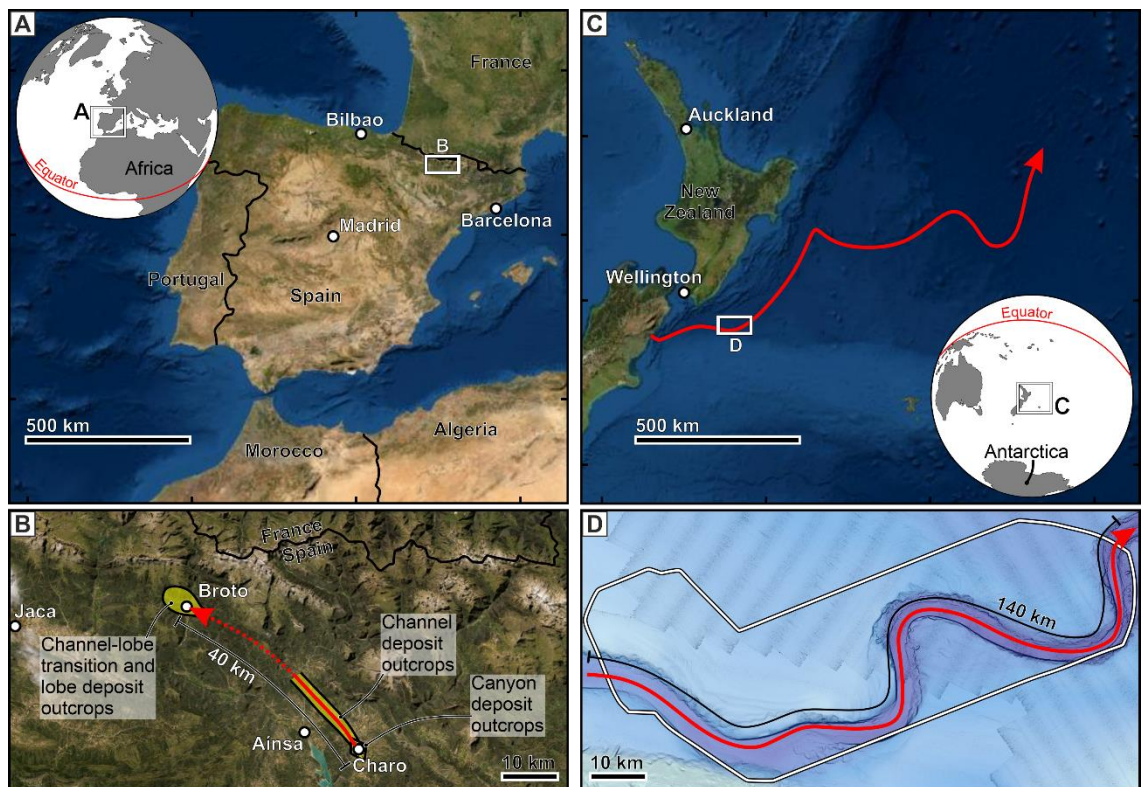


Figure 6.1 – Maps displaying the scale difference between the Arro turbidite system and the Hikurangi Channel: (A) map of the Iberian peninsula, showing the location of the Ainsa depocentre; (B) map of the east coast of northern New Zealand at the same scale as the map in A, showing the path of the Hikurangi Channel; (C) ~100 km by ~50 km map showing the reconstructed path of the Arro turbidite system between the outcrops of the Charo Canyon (Millington and Clark, 1995a, b), and the Broto lobes (Mutti, 1984); (D) map at the same scale as the map in C, showing the reach of the Hikurangi Channel imaged by the 3D seismic dataset herein.

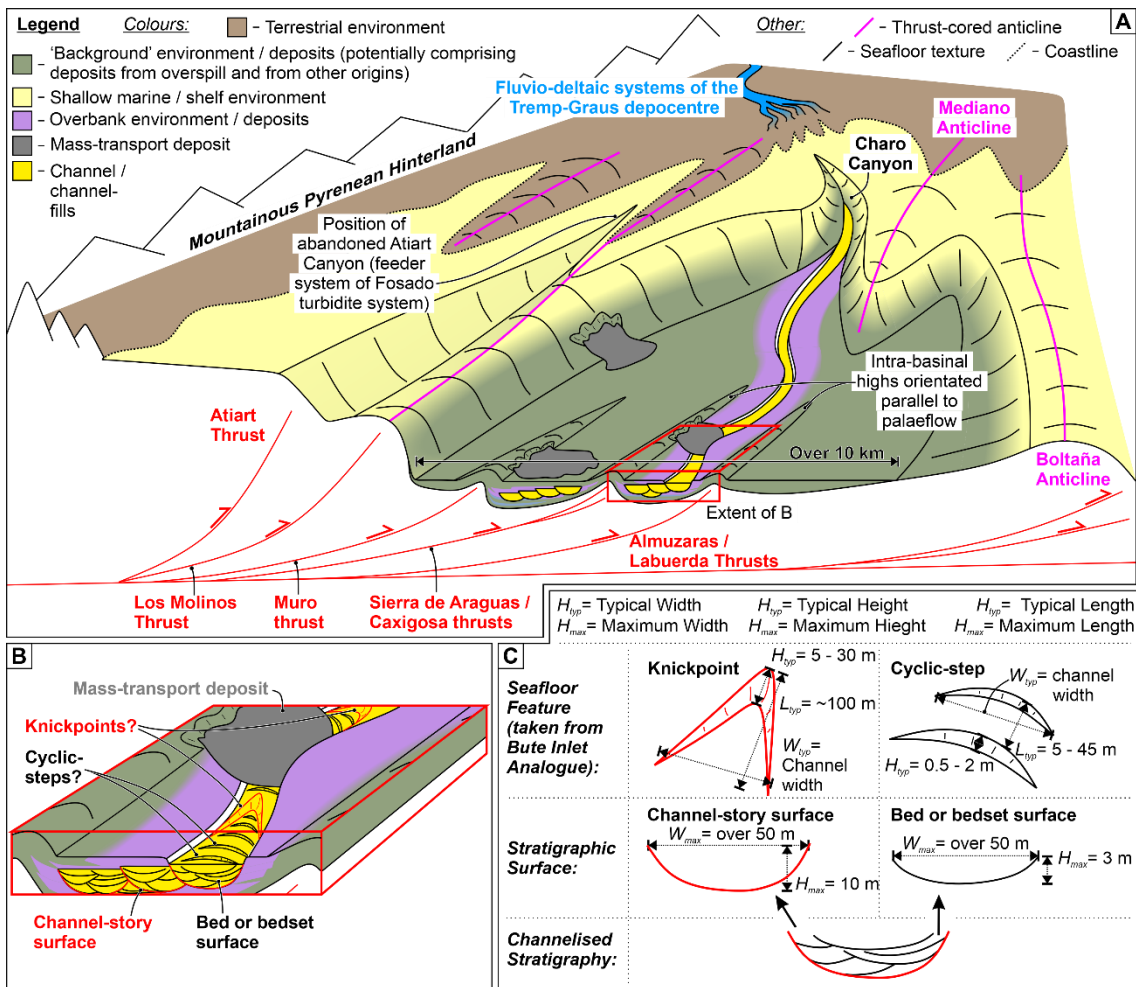


Figure 6.2 – (A) 3D depositional model of the Arro turbidite system, showing the reconstructed palaeogeography during the late stages of deposition, and the subsurface deposits; (B) zoomed-in insert from part A, showing the interpreted relationships between buried bed or bedset surfaces and channel-story surfaces, with seafloor bedforms such as cyclic-steps, and knickpoints; (C) scale relationships between the surfaces observed in the deposits of the Arro turbidite system and seafloor bedforms observed in a modern analogue: Bute Inlet, Canada (dimensions taken from Heijnen et al., 2020 and Chen et al., 2021).

6.1.1 Length

The channels that formed the deposits of the Arro turbidite system in the Aínsa depocentre are interpreted to have fed the unconfined lobe deposits of the Broto system in the Jaca depocentre. While these depocentres, which formed part of the larger 'South Pyrenean Foreland Basin', are now no longer contiguous, the distance measured along palaeoflow between the most proximal outcrops of the Arro turbidite system (deposits interpreted to have filled a shelf-incising canyon at 'Charo'; see Millington and Clark, 1995a, b Fig. 3.3) and the most proximal outcrops of the Broto system in the Jaca

depocentre (Mutti, 1984; Remacha and Fernandez, 2003; Bell et al., 2018b), is ~ 40 km (Fig 6.1). In contrast, the Hikurangi Channel is one of the longest deep-ocean channels in the world. Downstream of the confluence of its large network of feeder canyons (Mountjoy et al., 2009, 2018; Howarth et al., 2021), the channel runs along the Hikurangi Trench for ~ 600 km, before making a sharp (< 90°) right turn, escaping the trench, traversing the Hikurangi Plateau for a further ~ 550 km, and the Pacific abyssal plain for a further ~ 600 km, before reaching its terminus after ~ 1,750 km (Fig. 6.1). The length disparity between the two systems suggests that their axial setting within a confined basin has relatively little influence on channel length. This inference is supported by the wide range of the lengths of documented modern axial channels traversing active deep-ocean trenches (McArthur and Tek, 2021). For example, the Makran Trench is traversed by an ~ 185 km long channel (Bourget et al., 2011), and the Middle America Trench is traversed by small channels at the mouth of the Ometepe Canyon that run ~ 27 km along the trench (Moore et al., 1982); why channels such as the Hikurangi Channel extend so far remains a topic of active research (see review by Wells and Dorrell, 2021 and references therein).

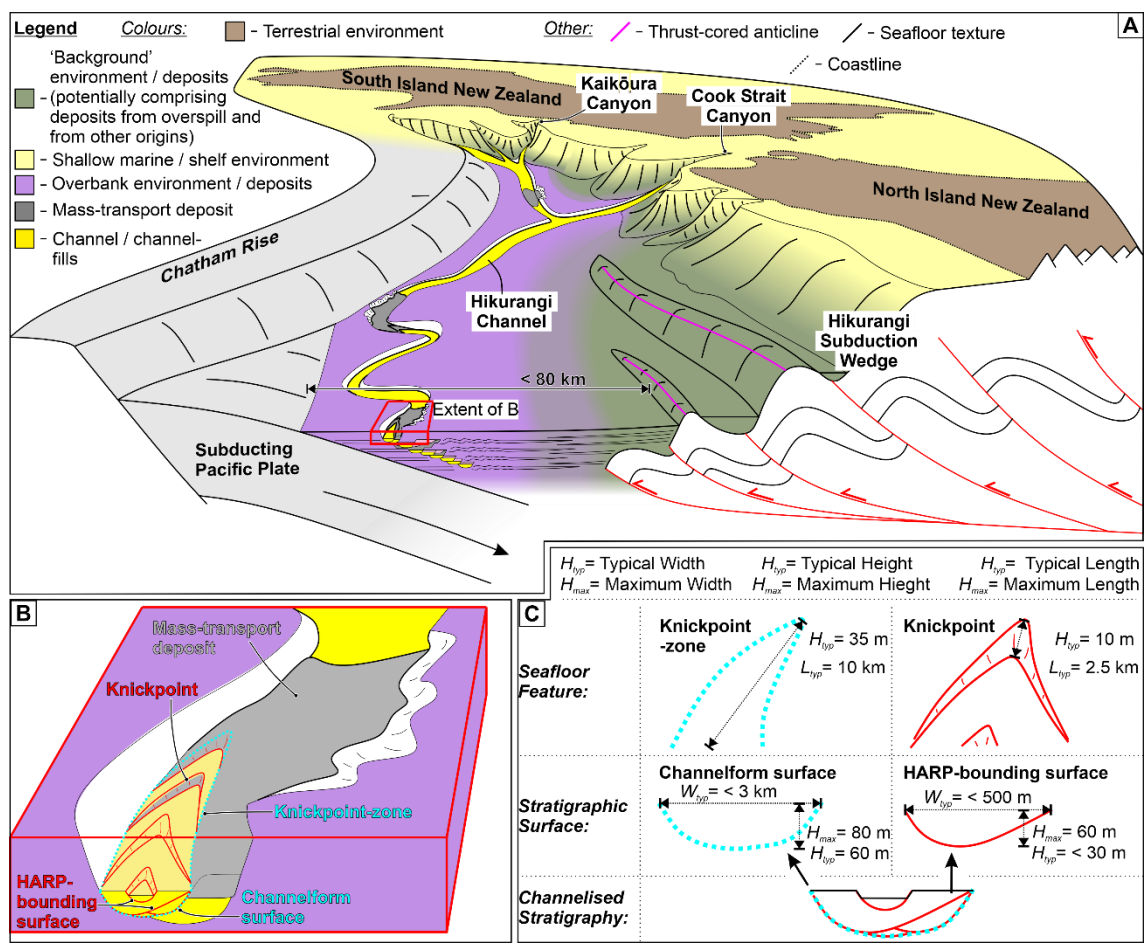


Figure 6.3 – (A) 3D depositional model of the proximal Hikurangi Trench showing a simplified version of the trench bathymetry and its relationship with the deposits imaged in the 2D and 3D seismic data presented in Chapter 4 and 5; (B) zoomed-in insert from part A, showing the interpreted relationships between HARP-bounding surfaces and channelform surfaces, with knickpoints and knickpoint-zones observed on the seafloor; (C) scale relationships between the surfaces observed in the deposits beneath the Hikurangi Channel, and the observed seafloor features.

6.1.2 Basin physiography and width

Both the Arro turbidite system and the Hikurangi Channel are / were confined by structures of tectonic origin, however the nature of their confinement differs: the Arro turbidite deposits sat within a thrust-top basin generated by the convergence of the Iberian and Eurasian continental plates (Muñoz, 1992), and the Hikurangi Channel sat within a deep-ocean trench generated by the subduction of the oceanic Pacific plate beneath the continental Australian plate (Balance, 1975).

Exposures of the Arro turbidite system sit within a 2-5 km wide, NW-SE oriented outcrop belt (Fig. 3.3). The structures that bound and dissect the outcrop belt (principally the ‘Sierra de Araguás’, ‘Muro’, ‘Caxigosa’, ‘Almazaras’ and ‘Labuerda’ thrusts; Fig. 3.3) are interpreted to have been active during deposition, based on the presence of combined flow bedforms (Tinterri, 2011; Fig. 3.5E), evidence of palaeoflow deflection near them, the stacking patterns of the channelforms at Muro De Bellos (Fig. 3.12), and the nature of wedging observed in packages of weakly confined thin-beds in the Sierra de Soto Gully (Fig. 3.10). However, as these structures deform thick (10s of m) successions of channelised sandstone and heterolithic deposits that form the Arro system, it is unlikely that these were the basin-bounding structures that confined the entire depositional system; instead, these structures likely generated intra-basinal topography. Due to the intense deformation that the deposits in the Arro system have undergone, the significant degree of erosion that has occurred post-deposition, and the limited outcrop exposure, reconstructing the basin physiography at the time of deposition is challenging. Nevertheless, based on extensive regional mapping, Clark et al. (2017) present a reconstructed cross-section through the entire Aínsa depocenter fill from Triassic to Oligocene. In this reconstruction, the structures that bounded the Arro turbidite system, and age-equivalent ‘background’ sediments found outside of the outcrop belt studied in Chapter 3, were the Boltaña Anticline in the west, and the Atiart Thrust in the east. The unrestored distance between the anticline’s crest and the thrust (measured perpendicular to the palaeoflow of the turbidites in the Arro system) is presently ~ 20 km. However, the Arro turbidite system is not interpreted to have

deposited over this entire area, given that it and time-equivalent outcrops cover ~ 10 km laterally (palaeoflow-perpendicular direction). Of course, these widths are minimum estimates as they have not been corrected for tectonic shortening. Therefore, the Arro turbidite system was likely formed in a structure-bound basin with an >10 km wide, relatively flat floor, albeit punctuated by intra-basinal highs (Fig. 6.2A). The interpreted physiography of the Aínsa depocentre at the time of the deposition of the Arro turbidite system is comparable to that inferred from deposits in other thrust-top basins formed by continental orogenies such as the Gorgoglione Flysch in Italy (Casciano et al., 2019). Furthermore, active channel systems in trench-slope mini-basins that form on accretionary wedges at oceanic subduction zones, such as the East Coast Basin offshore New Zealand (Crisostomo Figueroa et al., 2020), may provide a modern analogue for such basin fills; however, due to the lack of modern, channelised deep-water foreland basins (Nyberg and Howell, 2015) a direct analogue is not available.

The Hikurangi Trench, which hosts the Hikurangi Channel, is bound to the South by the Chatham Rise proximally and the subducting Pacific Plate distally, and to the North by the Hikurangi Subduction Margin (Fig 4.1, 5.2, 6.3A). In the broad area studied in Chapters 4 and 5 (Fig 4.1, 5.2), the trench's relatively flat floor ranges from 50 - 80 km wide, with the Hikurangi Channel located closer to the southeastern margin (Fig. 6.3A). The width of the trench is interpreted to have been slightly wider during deposition of the deepest studied stratigraphy than at the present day (McArthur and Tek, 2021); based on the deepest sediment being < 1 Ma (see Ghisetti et al., 2016, and McArthur and Tek, 2021) and the convergence rate at the studied location being ~ 30 mm/yr (Wallace et al., 2012) around 30 km of Pacific Plate has been subducted. However, it must be acknowledged that the effect that subduction would have had on the trench width remains uncertain. The Hikurangi Channel may provide a modern analogue to outcropping or buried axial channel deposits formed in ancient foredeeps such as the Magallanes Basin in Chile (Hubbard et al., 2008, 2009, 2014, 2020) and Austrian Molasse Basin (De Ruig and Hubbard, 2006; Hubbard et al., 2009; Bernhardt et al., 2012; Masalimova et al., 2015; Kremer et al., 2018). However, care should be taken when comparing the foredeeps formed in foreland basins with deep-ocean trenches at oceanic subduction zones as direct comparison of their physiography is impossible due to the lack of modern deep-water foreland basins containing axial channels (Nyberg and Howell, 2015).

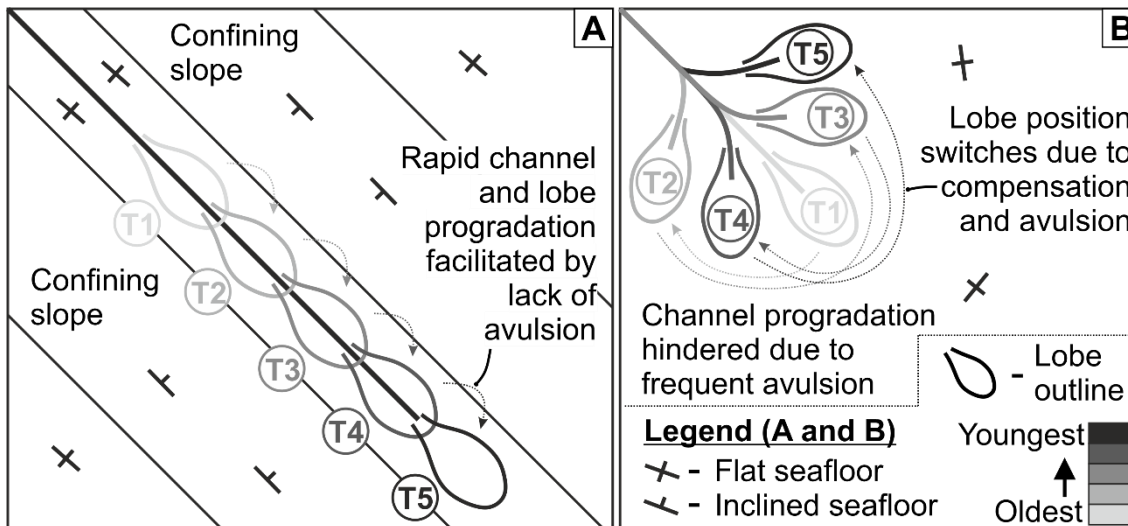


Figure 6.4 – Schematic showing the plan-view difference between: (A) a laterally confined system where avulsion is inhibited by the lateral confinement, leading the system to prograde quickly, and (B) an unconfined system where frequent avulsion leads to a more even lateral distribution of sediment and impedes progradation.

6.1.3 Channel stacking patterns and the absence of avulsion

In the subsurface beneath the Hikurangi Channel, the axes of ‘channelform surfaces’ (see Chapter 4) exhibit lateral offsets of < 5 km (typically 1 – 2 km; Fig. 4.12), and vertical offsets of < 150 m (typically < 60 m; Fig. 4.8). The effect of the emplacement of MTDs and superimposed cyclicity of unknown origin (see discussion in Section 4.7.1) are inferred to cause these offsets, which result in an ‘organised’ stacking pattern (*sensu* McHargue et al., 2011) in which through-going channel forms exhibit a gradual increase in channel sinuosity (rather than a pattern of radially fanning terminating channels, as might be seen in unconfined settings; Fig. 6.4). The overbank deposits that bound the channel-fill, sheet or terrace, and mass-transport deposits (see Chapter 4), which comprise most of the shallowest ~ 500 m of trench-fill, do not exhibit ‘wedge-shaped’ architectures (Fig. 6.5A) that are typical of overbank successions bounding large deep-water channels (e.g. those on the Amazon Fan: Flood et al., 1995; Pirmez and Flood, 1995). On the oceanward (southeastern) side of the channel, tabular overbank reflectors terminate against the subducting Pacific plate and Chatham Rise (Fig. 5.3); on the landward (northwestern) side, very laterally continuous overbank reflectors gradually taper away from the channel where they interfinger with reflectors that thicken toward the subduction front, which are interpreted to represent the distal expression of slope-traversing turbidites. Sedimentation derived from the channel and the subduction wedge

jointly act to fill the entire width of the trench (Fig. 6.5B). This process inhibits the growth of conventional 'wedge-shaped' levees leading to the development of a relatively flat trench-floor (Fig. 5.2, 5.3, 5.6, 6.5). Because the channel thalweg therefore remains the deepest point in the trench, i.e., is not superelevated relative to areas outside of its overbanks (Fig. 6.5), avulsion is effectively prevented.

The channelised deposits in the Arro turbidite system form an extensive 'sandbody' (*sensu* Millington and Clark, 1995a, b; Arbués et al., 2007a, b) that was interpreted by Clark et al. (2017) to span several kilometres of the basin's width (> 5 km; exact values cannot be calculated due exposure constraints). This sandbody sits within a 'channel-fill' surface, which hosts the channel-fill deposits found within the system. These deposits thin toward the anticlines and thrusts that dissect the basin and thicken into the synclines formed between them. Within the channel-fill deposits, numerous channel stories are observed, the axes of which stack with lateral offsets of 10s to 100s of metres, and vertical offsets of up to up to 5 m (Fig. 6.2A, B; see Chapter 3). The direction of this stacking is interpreted to have been controlled, in part, by movement of the depositional fairway between two parallel intra-basinal structures in response to their syn-depositional activity (see Fig. 3.12 and the "Architecture and Migration Patterns" part of Section 3.5.2.4). While these channel stories may be deflected around growing structures, as in the younger Banastón system (Bayliss and Pickering, 2015), they stacked in an organised manner (McHargue et al., 2011) through elongate, structure-bound corridors (Fig. 6.2), i.e., not developing a fan comprising radially-dispersing channels. Although reconstruction of the palaeo-physiography of the Arro turbidite system is more difficult, based on the lack of large avulsions, and the system's position between two large structures, the overbank areas are interpreted to have been flat, similar to those of the Hikurangi Channel (Fig. 6.2). As such, avulsion is also likely to have been inhibited by the basin confinement (Fig. 6.5).

Despite the differences in the interpreted widths of each basin floor, the channelised deposits beneath the Hikurangi Channel and in the Arro turbidite system stack in a relatively similar way. Abrupt shifts in the deepest cross-sectional points (axes) of the concave-up surfaces that host channelised deposits in both systems exhibit abrupt lateral and vertical shifts in the position of successive concave-up surfaces; lateral shifts are typically much greater than vertical shifts. However, in both systems the axis of each successive concave-up surface follows a modified version of its predecessor. Large shifts in the position of the depositional axis of either system to outside of the entire channel-overbank system are not observed. Therefore, avulsion in confined basins, where the position of the terminal lobe is shifted many kilometres or tens of kilometres

laterally, and the newly-formed post-avulsion channel is oriented at a relatively high angle to the pre-avulsion channel, is rare (Fig. 6.4; Casciano et al., 2019).

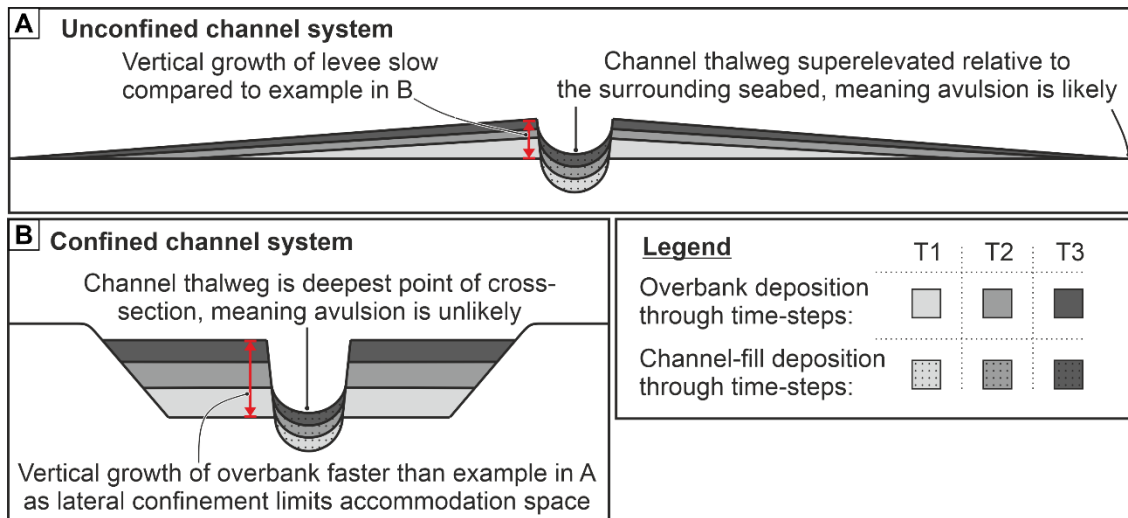


Figure 6.5 – Schematic showing the difference between: (A) an unconfined system where the development of levees that taper gradually away from the channel is permitted, and the channel thalweg is predisposed to become superelevated relative to the surrounding seabed and avulse, and (B) a confined system where overbank flows deposit over the entire basin-floor, leading to elevated vertical aggradation rates and the inhibition of the development of tapering levees, thalweg super-elevation, and hence avulsion.

6.1.4 Lateral confinement and aggradation and progradation rates

In addition to controlling the likelihood of avulsion, lateral confinement is likely to affect the rates of aggradation and progradation within confined basins. As there is less lateral accommodation on which deposition can occur, the aggradation rates are likely higher than they would be in an unconfined system with similar sediment supply (Fig. 6.5).

Furthermore, Chapter 3 explored the ability of structurally-imposed lateral confinement to promote the development and propagation of channelised deposits (see Section 3.6.4; Fig. 3.15). While the focus of that discussion was on the influence of intra-basinal structures, broader-scale lateral confinement may also exert a similar effect. In a system where avulsions occur freely (e.g. on large submarine fans like the Congo Fan; Babonneau et al., 2002; Marsset et al., 2009; Picot et al., 2016), large, regular lateral shifts in the position of the active channel and its terminal lobe cause the development of a radially distributed network of channels due to the effect of compensational stacking (Mutti et al., 1994; Prélat et al., 2010; Marsset et al., 2009). Conversely, in confined

systems, such as the Arro turbidite system or Hikurangi Channel, lateral confinement and the concomitant improbability of large avulsions means that less sediment is transported and sequestered laterally, and progradation along the basin axis is more important (Fig. 6.4). Therefore, in confined settings, rates of channel and lobe progradation are likely higher than would be expected for an unconfined system with similar sediment supply (Fig. 6.4).

6.1.5 Section summary

While there are significant differences between the length and width of the Arro turbidite system and the Hikurangi Channel, and the oceanographic and tectonic setting of the basins in which they formed, their laterally confined nature can lead to the development of similar architectural motifs. However, despite this first order influence, the nine controls on overspill and overbank deposition identified in Chapter 5 likely explains the development of considerable heterogeneity in the expression of these non-avulsing channels. Ultimately, the controls on the evolution of a channel system are likely a result of a complex interplay of factors that is largely specific to that system.

6.2 Relating seafloor geomorphology to subsurface architecture

6.2.1 Preservation of cyclic-steps, knickpoints and knickpoint-zones, and their inferred hierarchy

While the subsurface expression of cyclic-steps has recently been intensively investigated (Hage et al., 2018; Vendettuoli et al., 2019; Englert et al., 2021), to date the manifestation of larger scales of seafloor features such as knickpoints has been relatively understudied. Similarly, the stratigraphic patterns that may be formed by the interaction of different scales of bedforms (as documented by Chen et al., 2021, and Guiastranec-Faugas et al., 2021), and their potential link to the generation of apparent stratigraphic hierarchy remain understudied.

In the subsurface beneath the Hikurangi Channel, two nested scales of concave-up surfaces host high-amplitude reflectors that are interpreted to be sand-rich channel-floor deposits:

- High-Amplitude Reflector Package-(HARP)-bounding surfaces truncate up to 60 m (typically < 30 m) of stratigraphy, are typically < 500 m wide, and are traceable downstream up to tens of kilometres (Fig. 6.3B, C).
- Channelform surfaces truncate up to 80 m of stratigraphy, are typically < 3 km wide, and are traceable for > 100 km, across the entire 3D seismic survey (Fig. 6.3B, C).

The modern Hikurangi Channel provides a reliable self-analogue for the deposits formed in the subsurface below, offering a rare opportunity to relate features observed

on the modern seafloor, to their expression in the subsurface. On the seafloor, three scales of features are identified:

- Cyclic-steps, which are spaced relatively evenly from a few hundreds of metres to a kilometre apart, and exhibit relief of a few metres.
- Knickpoints (Fig. 6.3B, C), which are not evenly spaced, and occur as typically ~2.5 km-long reaches of channel with steep (up to 2°) longitudinal gradients that typically exhibit reliefs of ~10 m.
- Knickpoint-zones (Fig. 6.3B, C) are ~ 10 km-long reaches of channel containing closely spaced knickpoints that consequently exhibit elevated longitudinal gradients (typically around 0.2°), and relief of ~35 m.

Integration of seafloor and subsurface data in Chapter 4 led to the interpretation that HARP-bounding surfaces were generated by upstream-migrating knickpoints, and larger channelform surfaces were generated by the passage of knickpoint-zones, as the channel re-attained equilibrium after blockage by mass-transport deposit (MTD) dams (Fig. 6.3B, C); yet smaller-scale surfaces may be generated by cyclic-steps, which are observed to interact with the knickpoints, but these could not be observed in seismic data of this resolution.

In the Arro turbidite system, three nested scales of concave-up surface host 'channelised' deposits interpreted to have been deposited by high energy flows:

- Bed / bedset surfaces (Fig. 6.2B, C), which incise up to 3 m into the underlying stratigraphy, and the deposits within possess lens-like geometries in cross-section.
- Channel story surfaces (Fig. 6.2B, C), which incise up to 10 m into underlying stratigraphy, and are concave-up in cross-section.
- Channel-fill surfaces which can incise up to 50 m into the underlying stratigraphy and represent the master surface that bounds a set of stacked channel stories; a full channel-fill surface is not preserved so their geometries are uncertain.

Unlike the Hikurangi Channel, the Arro turbidite system (Chapter 3) does not have a modern counterpart to act as a self-analogue. Therefore, definitive distinction of the mechanisms by which multiple, nested scales of concave-up surfaces that host channelised deposits are formed and filled is not possible. Traditional models that invoke different scales of incision and infill along the entire channel in response to cyclical variability in the nature and/or volume of flows that traverse the system cannot be discounted. However, comparison with modern analogues of similar scales and physiographies suggests that upstream-migrating bedforms may play a significant role in the generation of channelised stratigraphy and surfaces in Arro turbidite system. One such analogue is the submarine channel that traverses the seafloor of Bute Inlet, Canada

(see Heijnen et al., 2020). This high-gradient channel and its flat overbank areas are laterally confined within a 1.5 – 3 km wide fjord, and is ~ 40 km long; the Arro turbidite system is also interpreted to have had a high axial gradient, was laterally confined within a > 10 km wide structure-bound basin, and was ~ 40 km long. Using Bute Inlet, wherein both cyclic-steps and knickpoints are observed, as an analogue for the Arro turbidite system, allows the interpretation that different scales of filled concave-up (in cross-section) surfaces were formed by different scales of seafloor feature: bed / bedset surfaces may have been formed by cyclic-steps (Fig. 6.2B, C); channel-story surfaces may have been formed by knickpoints (Fig. 6.2B, C); channel-fill surfaces may have been formed by the time-transgressive widening and deepening of a master bounding surface in response to the passage of multiple knickpoints, potentially organised into a knickpoint-zone (*sensu* Heijnen et al., 2020).

In both the Hikurangi Channel and the Arro turbidite system, filled concave-up (in cross-section) surfaces are interpreted to have been generated by transient, upstream-migrating seafloor features. In both systems, at least two nested scales of surface were generated by at least two scales of seafloor features (cf. Fig. 6.2, 6.3). The interaction between different scales of seafloor features (Chen et al., 2021; Guiastranec-Faugas et al., 2021) may therefore be capable of generating apparent stratigraphic hierarchy (*sensu* Mutti and Normark, 1987; 1991). Channel-story surfaces in the Arro turbidite system, and HARP-bounding surfaces have both been interpreted (in Chapters 3 and 4 respectively) to have been formed by knickpoints. However, while the fills of channel-story surfaces are between 3 and 10 m thick, HARP-bounding surfaces incise tens of metres of stratigraphy. This scale disparity between surfaces may be because:

- The knickpoints in the Hikurangi Channel are larger, and incise deeper, than the ones that formed the channel-story surfaces in the Arro turbidite system.
- The channelised deposits preserved in the Arro turbidite system represent only the remnant deposits downstream of multiple knickpoints, that re-incised into (albeit to a slightly laterally offset maximum depth) the deposits left downstream of the previous one.
- The surfaces that are preserved in the Hikurangi Channel represent only the largest knickpoint-related incisions, or those that are seismically resolvable, with the majority being unresolved. This resolution effect may be enhanced by the fact that an exceptionally strong impedance contrast between a relatively thin (< 10 m) layer of material located at the base of a HARP-bounding surface may produce a very high amplitude reflector that is thicker than said layer.

Further work is needed to (i) investigate the scales of deposits that are generated by upstream-migrating knickpoints, and (ii) investigate the variability of the scale of incision

of knickpoints in deep-ocean channels such as the Hikurangi Channel, versus those in shorter, high-gradient systems.

6.2.2 *Inferring levee deposit geometry from the seafloor expression of levees*

Deep-water channels traversing large submarine fans such as the Amazon or Danube are typically bordered by thick, 'wedge-shaped' overbank (levee) deposits that taper away from the top of the channel wall (Flood et al., 1995; Popescu et al., 2001). The seafloor cross-sectional expression of such channel levee systems is that of a U-shaped channel confined by two steep walls that shallow in gradient at their tops, toward a defined levee crest, where the gradient reverses and the outer levees dip gently (up to 2° but typically < 1°) away from the channel. This 'wing-shaped' profile type is therefore regarded as indicative of channels that are highly aggradational in nature, wherein the channel-fill deposits in the axis of the channel-levee deposit are dominantly hosted between the cogenetic levee deposits, instead of in a surface that cuts through the underlying stratigraphy.

However, channel-perpendicular seafloor profiles through the Hikurangi Trench show the overbanks of the Hikurangi Channel are essentially flat, or slope gently toward the channel (Fig. 5.6) despite the subsurface being highly aggradational in nature. The channel-fill deposits in the subsurface beneath the Hikurangi Channel, which each follow a modified version of the path of their precursor, are bordered on both sides by thick successions of overbank deposits, thus validating their classification as 'aggradational' channel deposits. Therefore, because the development of large, wedge-shaped levees is inhibited by the lateral confinement imposed by the trench, and the input of transversely-sourced sediment derived from the subduction margin, the seafloor expression of the Hikurangi Channel and its overbanks is a poor indicator of its subsurface architecture. This may also be true of channel systems in other confined settings (i.e. structurally-, canyon-, or fjord-confined), and in systems where significant quantities of sediment derived from transverse, externally-derived sources (i.e. from slope-traversing turbidite systems or overspill from an adjacent channel) are deposited on the overbanks.

6.3 The effect of mass-transport deposits on channel evolution and architecture

The effect of MTDs on deep-water channel deposits can be grouped into two categories: the depositional and evolutionary response of MTD emplacement in already established channels, and how MTDs control the processes of channel initiation and their location in basins without established channels.

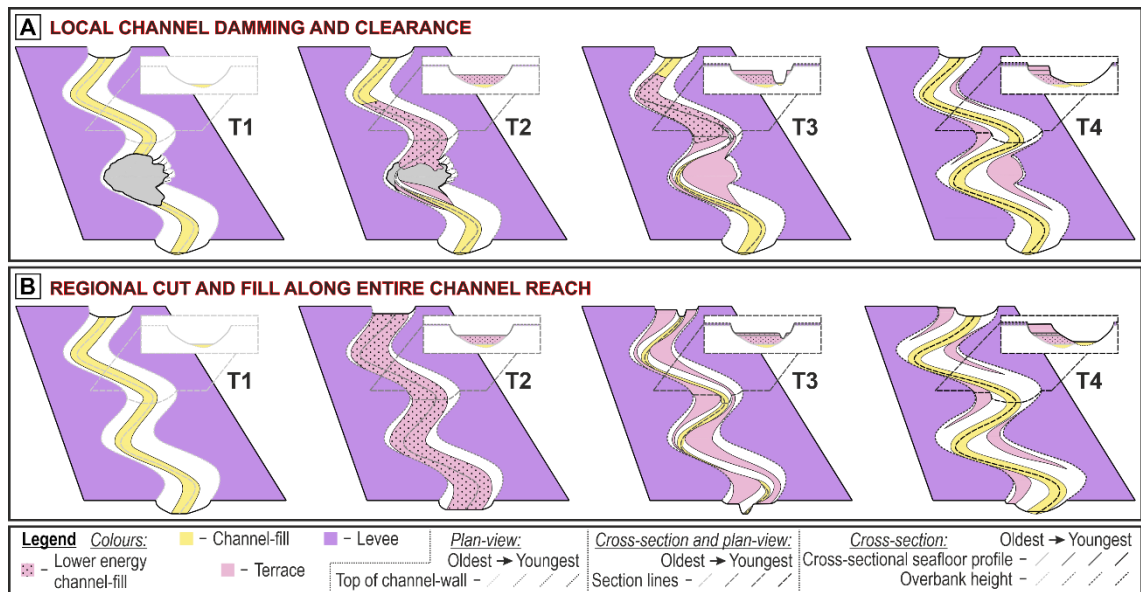


Figure 6.6 – Schematic diagrams (modified after Fig. 4.16) showing how, in some locations, similar cross-sectional stratigraphic motifs can be formed by: (A) the localised erosional response to MTD emplacement downstream of the section location, and (B) widespread deposition then erosion along long channel reaches.

6.3.1 Intra-channel MTDs

The large (over 100 m thick) MTDs preserved in the studied stratigraphy beneath the Hikurangi Channel are interpreted to have been sourced from the adjacent channel-walls (Fig. 4.8). In Chapter 4, comparison of the geomorphological response to a recently-emplaced MTD, with the deposits surrounding buried MTDs allowed the identification of a common evolutionary history following MTD emplacement:

- One or both of the channel-walls collapse generating an MTD that partially dammed the channel
- A decrease in longitudinal gradient upstream of the MTD caused rapid deposition of sheet deposits (also observed in Liang et al., 2020), whereas downstream a gradient increase caused a knickpoint-zone to form
- This knickpoint-zone migrated upstream, incising through the MTD and then the deposits formed upstream of the dam
- Continuing knickpoint-zone migration eventually allowed the channel to re-attain equilibrium

While this model departs from traditional ‘cut-and-fill’ models of channel evolution (Gardner et al., 2003), it can produce similar cross-sectional motifs (Fig 6.6). For

example, in areas upstream of the disappearance of a channel-wall-sourced MTD, a vertical transition between incised sheets and overlying terrace deposits, that are all truncated by a subsequently-formed channel-form surface, may have been formed by either process (Fig 6.6). While response of a deep-water channel system upstream of MTD dam emplacement was documented in the subsurface beneath the South China Sea by Liang et al. (2020), more comprehensive comparisons with the model presented in Chapter 4 can be made with modern systems, where repeat bathymetric surveys have revealed the dynamics of seafloor (or lake-floor) change next to recently emplaced MTDs. For example, the difference between two bathymetric surveys imaging a channel on the Rhone river delta in Lake Geneva (Corella et al., 2016) revealed that upstream of an MTD that occurred at some time between AD 1998 and 2000 that fully blocked the channel, widespread deposition occurred, generating a flat channel-floor. Downstream and on top of the MTD, a series of knickpoints formed and migrated upstream, incising through the MTD top.

In the Arro turbidite system, definite determination of the source of the MTDs is difficult. However, two modes of MTD occurrence are identified:

- (a) Debrisites that are typically < 1 m thick, are hosted within incisional 'bed' or 'bed-set' scale surfaces, are categorised as part of channel-fills and are interpreted to be dominantly longitudinally sourced
- (b) Thicker (> 1 m thick) slumps and debrisites that can exist within or outside of channel-fills, which were likely laterally sourced

Debrisites in channel-fills (see 'a' above) may have generated the incisional surfaces they sit within or filled surfaces generated by precursor channelised flows, and bypassing debrisites may have excavated some of the surfaces filled by sandy deposits. Therefore, in the Arro system, punctuated surface generation by, and / or emplacement of, debrisites may play an important role in controlling the bed to bed-set scale evolution of channel deposits. The surfaces they may generate, and/or the topography on their tops may interact with, or form a point of initiation for the formation of migrating bedforms such as cyclic-steps (Hage et al., 2018; Vendettuoli et al., 2019; Englert et al., 2020). Debritic deposits are also observed in channel-fill axes elsewhere in the Aínsa depocentre (e.g. Bayliss and Pickering, 2015), and in other ancient axial channel systems that traversed elongate compressional basins such as the Cerro Toro Formation in the Magallanes basin, Chile (Hubbard et al., 2008), and the Austrian Molasse basin (Hubbard et al., 2009).

The typically larger MTDs (see b above) with more slump-like textures in the Arro turbidite system are not only associated with channel-fills, but where they are (for example MTD4 in Barranco de la Caxigosa; Figs. 3.9, 3.13), they can fill incisional,

concave-up surfaces which they generate themselves. The presence of multiple scales of MTD overlying concave-up incisional surfaces leads to a less predictable channel-story stacking pattern than may be expected in systems that are less prone to MTD emplacement. The tops of larger MTDs in the Arro turbidite system healed the topography of their host surface, generating an irregular, but weakly confined channel-floor, likely leading to ponding upstream.

The collapse of deep-water levees (Ortiz-Karpf et al., 2015), and the emplacement of large, channel-damming MTDs (Corella et al., 2016) have both been invoked as the cause for deep-water channel avulsions with concomitant large lateral shifts in the position of any depositional lobe. In the studied location of the Hikurangi Channel, because the MTDs are sourced solely from the channel-wall, the resultant deposit is unlikely to exceed the height of the channel-walls, meaning filling of the entire conduit to the point where it 'spills' (sensu Gardner et al., 2003) is unlikely. And as noted above, due to the confined setting of the Hikurangi Channel and the Arro turbidite system inhibiting superelevation of the channels' thalwegs (see Section 6.1), avulsion is less likely to occur altogether.

6.3.2 Mass-transport deposits and channelisation

The studied stratigraphy beneath the Hikurangi Channel was all deposited after the establishment of an initial channel, that is interpreted to have been progressively modified, meaning that the effects of MTDs on initiation of channelisation in the Hikurangi Channel have not been studied. However, in the Arro turbidite system, the transition from non-channelised to channelised stratigraphy is recorded. In Chapter 3 (see Section 3.6.3), five ways in which MTD transport and emplacement have been shown to influence the channelisation process in deep-water systems, and potentially in the Arro too (Fig. 3.14):

1. Turbidity current velocity enhancement can occur along the margins of MTDs where a depression is oriented parallel to the flow direction. Velocity enhancement may also occur on the downstream margin of an MTD that partially blocks a channel, due to an increased longitudinal gradient on its downstream margin (Tek et al., 2021). Alternatively, turbidity current deceleration can be forced by interaction with the upstream margin of an MTD that partially or fully blocks a flow pathway (Liang et al., 2020).
2. The topography on top of large MTDs can control the location of channels that traverse their tops, as channelisation is more likely to occur along elongated lows on the MTD top (Kneller et al., 2016). Ridges on the MTD top that are oriented perpendicular to the flow direction of MTD top-traversing turbidity currents are likely

to inhibit channel formation. Alternatively, lows oriented parallel to turbidity current orientation can enhance flow velocity by providing lateral flow confinement.

3. Differential compaction on top of MTDs has been inferred as a control on the location of channelisation (Ward et al., 2018). Similarly to the processes on MTD tops, the loci of compaction, and the topographic geometries they generate can either enhance or slow turbidity current velocities, therefore promoting or hindering channelisation.
4. The erosive scars left behind by MTDs can generate elongate depressions that are typically partially filled by MTDs, but may be fully evacuated (Dakin et al., 2013). Elongate depressions formed by MTDs oriented with long axes parallel to the direction of basin-traversing turbidity currents may provide lateral confinement and a location for subsequent channelisation. Scars formed by MTDs that travel normal to turbidity current direction may hinder channelisation, but this is likely rare.
5. If a channel is in the process of forming, the emplacement of an MTD can fill that topography, effectively healing the basin floor. This process can delay the onset of channelisation as the process must essentially start again (Fig 3.15, 3.14; see Section 3.6.3.5).

7 Conclusions and future work

7.1 Conclusions

Three principal research themes carried in this thesis were outlined in Chapter 1. The conclusions relating to each theme are listed below.

7.1.1 Theme 1: Controls on the architecture and evolution of axial channel and overbank deposits in compressional basins

- Growing tectonic structures may form lateral bathymetric confinement to turbidity currents that can encourage channelisation and inhibit the formation of lobes prior to channel formation (Chapter 3).
- Lateral structural confinement can inhibit the development of wedge-shaped levees. Confined channels can, instead, be bound by flat overbank areas on the seafloor, and in the subsurface by laterally continuous packages of overbank sediments that terminate against the edge of their confinement (Chapters 3 and 5).
- Impeded development of wedge-shaped levees reduces the likelihood of a channel thalweg becoming superelevated with respect to overbank areas, and hence of channel avulsion (Chapter 6).
- With fewer avulsions channel and lobe progradation rates may be enhanced in confined systems (Chapter 6).
- Despite both being confined channel systems that run / ran axially through elongate, structurally-bound basins at convergent margins, the deposits of the Arro and Hikurangi systems differ in their scale and tectonic context. However, they exhibit similarities in architectural style due to their laterally confined nature and interpreted association with growing structures (Chapter 6), namely:
 1. in plan-view, channelforms do not stack to form a distributive network of radially fanning channels, but instead each channelform follows a modified version of the path of its predecessor
 2. the channelised deposits and their overbanks are both interpreted to have been bound by structures that confined their overbanks, meaning they were unlikely to develop thick, wedge-shaped levees and were thus unlikely to have had superelevated thalwegs
 3. in both settings channelforms contain mass-transport deposits (MTDs) of varying scales, that are interpreted to have a significant impact on subsequent turbidity currents, and channel evolution (see 7.1.3)
- Nine factors were interpreted to control flow processes and deposition on the overbanks of the Hikurangi Channel: flow versus conduit size, overbank gradient, flow tuning, Coriolis forcing, contour current activity, flow reflection, centrifugal

forcing, interaction with externally derived flows, and interaction of overspill from different locations.

7.1.2 Theme 2: Linking seafloor geomorphology to channel and overbank deposit architecture

- The deposits of the Arro turbidite system may provide an analogue for modern submarine channels in confined basins, including those in fjords.
- Channel-floor bedforms such as cyclic-steps and knickpoints may be responsible for generating the concave-up surfaces observed in the channelised stratigraphy of the Arro system (Chapter 3).
- Nested scales of concave-up surfaces preserved in the stratigraphy beneath the Hikurangi Channel (HARP-bounding surfaces and channelform surfaces) are interpreted to have been formed and filled by two scales of interacting seafloor features (knickpoints and knickpoint-zones) (Chapter 4).
- Evidence from both the Arro and Hikurangi case studies suggests that concave-up surfaces preserved in the stratigraphy may not represent the instantaneous morphology of a palaeochannel that existed on the seafloor (Chapters 3, 4 and 6).
- The deposits of Hikurangi Channel are aggradational in nature, yet the overbank areas are essentially flat. Therefore, the presence of large, tapering levees is not a requirement to infer that an observed channel has had an aggradational history (Chapters 5 and 6).

7.1.3 Theme 3: The effect of mass-transport deposits (MTDs) on channel and overbank formation and evolution

- MTDs in topographically complex basins can influence the channelisation process, controlling whether turbidity currents will form a channel, and when this will happen. This influence is determined by the relationship between the MTD and nature and direction of flows that traverse the basin post MTD emplacement (Chapter 3). Turbidity currents can interact with:
 1. Topography generated by the margins of an MTD
 2. Topography on top of an MTD
 3. Topography generated by differential compaction on top of an un- or partially-lithified MTD
 4. Megascours formed by erosive MTDs
- The erosional response of turbidity currents to the emplacement of MTDs in active submarine channels can generate the stratigraphic architectures commonly observed in channelised systems via the following sequence of processes (Chapter 4):

1. An MTD is emplaced that partially dams the channel
2. Partial ponding occurs upstream of the MTD due to a reduced longitudinal gradient; the resultant deposits are continuous across the channel
3. A knickpoint-zone forms downstream of the MTD due to a locally increased longitudinal gradient
4. The knickpoint-zone migrates upstream and incises through both the MTD and the deposits formed upstream of it
5. Eventually, the channel re-attains equilibrium and a new conduit is formed. Such channels are usually laterally and vertically offset from their predecessors.

7.2 Future work

Addressing the themes carried through this thesis has highlighted the requirement for further work to develop understanding of some key topics. These topics are highlighted in the 'General Recommendations' section immediately below (Section 7.2.1).

Additionally, the work on the two case studies presented in this thesis has highlighted the potential for further investigation specifically on them. Suggestions for further work on each case study are categorised according to work that could be performed with the existing data, and that which requires the collection of additional data. These suggestions are addressed for the Arro turbidite system in Section 7.2.2 and for the Hikurangi Channel in Section 7.2.3.

7.2.1 General Recommendations

7.2.1.1 The dynamics of deep-water channel-wall collapse

Work on the dynamics of deep-water channel-wall collapse is recommended, both in confined settings like the Hikurangi and Arro systems, but also in unconfined systems, where MTDs derived from channel-wall collapse have been documented, but not studied in detail. Specific questions related to this topic include:

1. What was the kinematic nature of these collapses? (i.e., quasi-instantaneous vs. creep-like failures)
2. Are there any systematic trends in channel-wall-derived MTDs character between channel systems in confined, tectonically-active basins, versus unconfined, tectonically-quiescent basins in terms of their kinematic nature, size or abundance?
3. What are the triggers of channel-wall collapse, and do they vary between channel systems?
4. Do overbank flow processes and/ or associated depositional trends control where a channel-wall collapse is likely to occur?

5. Is there a relationship between the locations of MTD failure and emplacement in plan-view and the stacking of the channel-form surfaces in the subsurface?

A mixture of case-studies using outcrop, core, bathymetry, and subsurface geophysical data, and comparative analyses across multiple systems would be required to fully answer these research questions. Seismic data that image large MTDs interpreted to be derived from the collapse of the walls of the Hikurangi Channel would provide an in-depth case study for looking at the dynamics of channel-wall collapse (see section 7.2.3.1). Repeat high-resolution bathymetry and shallow subsurface geophysical data imaging surficial channel-wall collapse deposits in the canyon systems that feed the Hikurangi Channel could be used to augment understanding of these processes in this case study. Results from the Hikurangi case study could then be compared with the results of Sawyer et al. (2007, 2014), who documented progressive channel-wall collapse of large (tens of km) stretches of the Mississippi Canyon. Hansen et al. (2017a) present bathymetry and 3D seismic data imaging channel-wall collapse deposits in the Mahin Channel system, offshore Nigeria, but their seismic character and hence their evolution was not studied in detail. This dataset could be used to perform a third geophysical case study on a passive margin system that is not affected by salt tectonics. Finally, an outcrop-based study looking at MTDs interpreted to be formed due to levee collapse in the Rosario Formation (Kane et al., 2007) could complement the proposed geophysical studies, providing control on the architecture and evolution of these deposits at smaller scales.

7.2.1.2 Progradation rates of channels and lobes in confined vs. unconfined basins

A testable hypothesis arose from the discussion in Chapter 6, stating that channel and lobe systems in confined basins might prograde faster than those in unconfined basins. A comparative analysis of progradation rates, containing at least one case study each from a confined and unconfined system, is recommended to test this hypothesis. Even in datasets imaging confined channel deposits in exceptional detail, such as the one used in Chapters 4 and 5, the evolution of the system's terminal deposits is seldom inferable. Therefore, a more suitable method for testing this hypothesis would be to use numerical and experimental modelling techniques. An experimental setup, similar to that presented in Soutter et al. (2021), whereby a sediment-laden turbidity was released from lateral confinement and deposited its sediment on a basin-floor with a shallow axial gradient, would be required. It is recommended for these experiments to first be run on a flat basin-floor with no obstacles to establish a control. Subsequently, lateral walls oriented parallel to flow with heights less than, equal or exceeding the flow thickness, with progressively diminishing lateral separations could be imposed. The difference in deposit geometries between different experimental configurations, and their evolution throughout the length of each experiment, would allow the testing of this hypothesis.

7.2.1.3 Plan-view channel-fill stacking patterns in confined vs. unconfined basins

Although the stacking of deep-water channel-fills in cross-section and plan-view are the focus of many studies of deep-water channel architecture, plan-view stacking patterns are usually examined at the scale of an individual channel bend, or a few consecutive bends. Differences in plan-view stacking at a system scale between channel-fills in confined basins, versus those in unconfined basins is comparatively understudied. A testable hypothesis that arose in Chapter 6 is that channels in confined basins are likely to follow a relatively organised stacking pattern, where each channel-fill follows the modified path of its predecessor, and terminates close to or at the same terminus as its predecessor; conversely, channel-fills in unconfined basins are likely to develop radially fanning plan-view distributions, with terminations significantly spatially separated from their predecessors. A comparative analysis of system-scale, plan-view channel-fill stacking patterns from at least one case study from a confined system, and one from an unconfined system, is therefore recommended. However, a key challenge is that while data on the system-scale stacking of fanning channel networks in certain unconfined systems (e.g. the Congo Fan) exists, datasets imaging system-scale stacking in confined systems are rare.

7.2.1.4 Comparing overbank geometries in confined and unconfined settings

The overbank deposits that bound the channelised deposits beneath the Hikurangi Channel are not wedges of sediment that taper away from the channel. While the large-scale geometry of the overbank deposits in the Arro system is less certain, they are inferred to have possessed similar geometries to those bounding the Hikurangi Channel. However, this relationship is yet to be tested globally, to determine whether deep-water overbank deposits in confined systems are universally inhibited from generating 'classical' wedge-shaped levees. A comparative analysis of the geometries of overbank deposits, containing at least one case study from a confined basin and one from an unconfined system, would help to answer this question. Due to the typically large lateral extent of submarine channel levees, such a study would be most feasible using seismic data. Nakajima and Kneller (2013) analysed the degree of taper in unconfined submarine levee deposits imaged in numerous seismic datasets. A similar statistical approach adding data from confined systems would simply require the addition of seismic datasets imaging some confined channel and overbank systems. Candidate datasets include 2D and 3D seismic datasets imaging: the Hikurangi Channel and its overbanks (this study), the channelised fill of the Austrian Molasse Basin (De Ruig and Hubbard, 2006; Hubbard et al., 2009), and smaller channel and overbank deposits on the Niger Delta slope (Clark and Cartwright, 2011).

7.2.1.5 Relationships between sediment wave orientation, channel-bend curvature, and submarine slope gradient

In Chapter 5, a relationship between the orientation and curvature of sediment wave crests on the overbanks of the Hikurangi Channel was established, with sediment wave crest curvature predominantly paralleling that of the adjacent channel bend. However, the Hikurangi Channel's overbank areas exhibit exceptionally low gradients, and in other case-studies sediment crest orientation is commonly reported to be parallel to the strike of the local seafloor gradient (see Wynn and Stow, 2002, and references therein). Accordingly, it would be worthwhile to determine what relationship between wave crest curvature and adjacent channel bend curvature holds in areas of elevated seafloor gradient. A comparative analysis using bathymetry data imaging sediment wave fields on the overbank areas of multiple channels with various overbank slope gradients is therefore recommended. Due to difficulties in identifying overbank sediment waves in outcrop, simulating their formation numerically or experimentally, and a general lack of 3D seismic datasets imaging entire overbank wave fields, performing this analysis on bathymetry data from many channel systems and comparing the results is advised. Candidate high-resolution bathymetric datasets imaging overbank sediment waves include the Toyoma Channel (Nakajima and Satoh, 2001), the Monterey Fan (Normark et al., 2002), the Bengal Fan (Kolla, 2012), and the Var Sedimentary Ridge (Migeon et al., 2001).

7.2.2 The Arro turbidite system

7.2.2.1 Using existing data

Petrographic and provenance analysis:

Samples were collected at all the major sandbody locations in the study area, and measurements of clast composition and texture were taken from conglomeratic lag deposits at the base of the channelised units. Petrographic analysis of these samples, used alongside the textural data collected from the lags, would help refine palaeogeographic reconstructions of the Arro system. The key aim of this work would be to determine whether the sediments in each outcrop share a similar axial provenance (principally from the Tremp-Graus fluvio-deltaic system), or whether a transverse component of sedimentation from the poorly-constrained northeastern margin was also responsible for sediment input in the basin. Gravel- to pebble-sized clasts in these lags are varied in their composition, but some are composed of blue coloured limestone that appears similar to limestone outcrops within the Peña Montañesa thrust sheet to the north, suggesting that some material may have entered the Arro system from transverse sources. Further investigation into the outcrops in the potential source terrains would be required, in combination with point-counting on thin-sections of collected samples, which

could be used to identify the likely source of clastic material in the Arro system. A secondary aim could be to investigate the proportions of organic carbon sequestered in the studied channelised deposits, by analysing organics in thin-sections or using established palynological analysis techniques.

7.2.2.2 Requiring additional data

Relationship of outcrops and structures:

While Chapter 3 presents a detailed study of the sedimentology of the deposits in the Arro turbidite system, and the architectural evolution of key outcrops, the relationship between these outcrops, and their relationships with the intra-basinal structures is less certain. Further detailed mapping of the structures and outcrops containing channelised deposits would be useful to constrain the effect of structural growth on the large-scale architecture of the system, and the distribution of different facies and sedimentary architectures in structurally-confined basins containing intra-basinal structures. The key aim of this work would be to determine whether the growth of structures could force large-scale avulsions, as has been documented in other systems in the Aínsa depocentre (Bayliss and Pickering, 2015), and to investigate the dynamics of such events if so (i.e., are structurally-forced avulsions likely to be quasi-instantaneous or more progressive in nature). At least one additional 2 to 4 week field season, specifically aimed at collecting structural data such as bedding measurements and thrust tracing would be required to conduct this work.

7.2.3 The Hikurangi Channel

7.2.3.1 Using existing data

3D stacking of the channelform surfaces beneath the Hikurangi Channel:

The evolution of the palaeo-Hikurangi Channel through the formation and infill of multiple channelform surfaces was not investigated in detail in Chapter 4, which focused on the process of filling a single primary channelform surface and establishing a younger one. Therefore, further work to analyse the 3D stacking patterns of the channelform surfaces preserved in the subsurface is recommended. The key aim of this work would be to determine whether the suite of nine controls identified in Chapter 5 to influence overbank flow processes and deposition also affect the stacking of the channelforms over longer timescales. For example, a map displaying the outlines of channelform surfaces presented in Figure 4.12 shows how progressively younger channelform surfaces record the evolution from relatively straight to more sinuous planform geometries. However, this map also shows how, while the apices of bends with landward outer banks (Bends 4 and 6) appear to remain fixed in their up- to down-channel position (and appear to expand via dominantly swing), the apices of bends with oceanward outer

banks (Bends 3 and 5) exhibit relatively little swing, and large components of down-channel migration (sweep). Determining the controls on the nature of bend expansion in the Hikurangi Channel could have fundamental implications for the understanding of bend evolution in mid-latitude deep-water channel systems where the Coriolis force has been shown to affect overbank sedimentation. Furthermore, parameterisation and statistical analysis of the trajectories of bend apices and inflection points, both in plan-view and vertically, is possible in this 3D seismic dataset. Such analyses could provide quantitative insight into the nature of bend expansion through the formation and infill of multiple channelform surfaces, and provide data for comparisons with other channel systems imaged in 3D seismic data.

Understanding deep-water channel-wall collapse in the Hikurangi Channel and its effect on channel stacking:

Tens of MTDs derived from local channel-wall collapse are preserved in the stratigraphic interval studied in Chapters 4 and 5. These MTDs vary significantly in their aerial extent and thickness. Detailed mapping of MTD tops and bases, which is permitted by the depth-domain 3D seismic data, would allow the extraction of the areas, thicknesses and volumes of these deposits, therefore permitting interrogation of their size distribution, and what proportion of the stratigraphy is dominated by MTDs. Detailed categorisation of the internal structure of the MTDs, and the non-remobilised sediments on top of and adjacent to them, would help answer the generic questions about channel-wall collapse highlighted in Section 7.2.1.1 above but would likely be feasible only on larger MTDs. One such MTD is traceable for over 50 km down-channel, contains material that appears to be derived from both channel-walls, and reaches over 250 m thick. Preliminary investigations into the internal structure of this deposit has revealed: (a) thick (up to 200 m) weakly or undeformed blocks of stratigraphy that are surrounded by areas of chaotic seismic character; these blocks internal reflectivity that is similar to undeformed reflectors below and adjacent to the MTD; (b) imbricated high-amplitude reflector packages located at, and dipping away from, the margin of the MTD opposite the interpreted location of channel-wall collapse; (c) no apparent fanning of reflectors into lows adjacent to coherent blocks suggesting failure occurred relatively rapidly.

Exploration of the deeper stratigraphy imaged by the 3D seismic dataset used in Chapters 4 and 5:

Chapters 4 and 5, and the further work suggested above, focus on the shallowest ~ 600 m of the trench stratigraphy, yet ~ 6 km of trench fill stratigraphy is preserved in the location of the 3D seismic survey. Although McArthur and Tek (2021) briefly investigated the expression of the palaeo-Hikurangi Channel deeper in the trench stratigraphy, many of the identified features have not been investigated. For example:

(a) The plan-view expression of the deeper channelform surfaces is less organised, and more ‘fan-like’ than that of the organised channelforms studied in Chapter 4. Comparing the 3D stacking patterns of the deep and shallow channelforms would be valuable, and might resolve an architectural signature of channel initiation that differs from that developed when the channel is established.

(b) At ~ 1 km below the seabed, a large (~ 8 km across) meander is imaged in spectacular detail exhibiting reflectors on the inside of the channel bend that are arcuate in plan-view and that dip toward the channel in cross-section. Investigating the process of their formation and the subsequent meander cut-off would be valuable as future work, both as an example of meander evolution at very large scales, and also for its value in giving generic insight into meander development.

(c) At ~ 1.2km below the seabed, a relatively straight channelform surface is filled with disaggregated patches of high-amplitude reflectors that are polygonal in plan-view, and sit within a seismically transparent matrix. Investigating the origin of this channelform surface fill, and determining whether it may be a large, channelised MTD would be an worthwhile investigation. A key characteristic of this deposit is that it is entirely confined within the channel; it may result from a “flow tuning” process of equilibration of flow to the channel form that has not been documented for debris flows hitherto.

7.2.3.2 Requiring additional data

Constraining the age and lithology of the deposits in the Hikurangi Trench:

In 2018, on IODP expeditions 372 and 375, four cores containing over 1 km of strata were collected from the northeastern sector of the Hikurangi Trench (see Barnes et al., 2020). When fully analysed, the information derived from these cores will allow better constraint on the type and ages of the sediments, and therefore on the evolutionary history of the channel, in that part of the trench. However, the IODP core sites are located ~ 300 km from the area studied in this thesis, with little high-resolution seismic data between them. Therefore, lithological and chronostratigraphic constraint in the studied area of the trench is currently lacking. Acquisition of a core through the trench stratigraphy, and concomitant characterisation of the sediment type and its age would allow quantification of the timing of each of the processes discussed in chapters 4 and 5, the evolution and aggradation rates of the channel and its overbanks, and the recurrence intervals of large channel-wall collapse events.

8 References

- Abreu, V., Sullivan, M., Pirmez, C. and Mohrig, D. 2003. Lateral accretion packages (LAPs): An important reservoir element in deep water sinuous channels. *Marine and Petroleum Geology*. **20**(6–8), pp.631–648.
- Allen, J.R.L. 1973. A classification of climbing-ripple cross-lamination. *Geological Society of London Journal*. **129**, pp.537–541.
- Allen, J.R.L. 1982. *Sedimentary Structures: Their Character and Physical Basis*. Amsterdam, The Netherlands: Elsevier, 592p.
- Allin, J.R., Hunt, J.E., Clare, M.A. and Talling, P.J. 2017. Eustatic sea-level controls on the flushing of a shelf-incising submarine canyon. *Bulletin of the Geological Society of America*. **130**(1–2), pp.222–237.
- Alpak, F.O., Barton, M.D. and Naruk, S.J. 2013. The impact of fine-scale turbidite channel architecture on deep-water reservoir performance. *American Association of Petroleum Geologists Bulletin*. **97**(2), pp.251–284.
- Alves, T.M. 2010. 3D Seismic examples of differential compaction in mass-transport deposits and their effect on post-failure strata. *Marine Geology*. **271**, pp.212–224.
- Amy, L.A., McCaffrey, W.D. and Kneller, B.C. 2004. The influence of a lateral basin-slope on the depositional patterns of natural and experimental turbidity currents. *Geological Society, London, Special Publications*. **221**(1), pp.311–330.
- Arbués, P., Mellere, D., Puig, M. and Marzo, M. 2007a. Los Molinos Road, Spain: The Effect of Slumping on Sandstone Distribution in the Arro Turbidites. In: T.H. Nilsen, R.D. Shew, G.S. Steffens and J.R.J. Studlick, eds. *Atlas of Deep-Water Outcrops*. AAPG *Studies in Geology*. **56**, pp.1-17.
- Arbués, P., Mellere, D., Puig, M. and Marzo, M. 2007b. The effect of slumping on sandstone distribution in the Arro Turbidites, Los Molinos Road, Spain. In: T.H. Nilsen, R.D. Shew, G.S. Steffens and J.R.J. Studlick, eds. *Atlas of Deep-Water Outcrops*. AAPG *Studies in Geology*. **56**, pp.333-335.

Arbués, P., Butillé, M., López-Blanco, M., Marzo, M., Monleon, O., Muñoz, J.A., and Serra-Kiel, J., 2011, Exploring the relationships between deepwater and shallow-marine deposits in the Aínsa piggy-back basin fill (Eocene, South-Pyrenean Foreland Basin). In: C. Arenas, L. Pomar and F. Colombo, eds. Post-Meeting Field Trips Guidebook, 28th International Association of Sedimentologists Meeting, Zaragoza. 8: Zaragoza, Spain: Sociedad Geológica. de España, pp.199–240.

Armitage, D.A., Romans, B.W., Covault, J.A., and Graham, S.A. 2009. The influence of mass-transport-deposit surface topography on the evolution of turbidite architecture: The Sierra Contreras, Tres Pasos Formation (Cretaceous), Southern Chile. *Journal of Sedimentary Research*. **79**, pp.287–301.

Armitage, D.A., McHargue, T., Fildani, A. and Graham, S.A. 2012. Postavulsion channel evolution: Niger Delta continental slope. *AAPG Bulletin*. **96**(5), pp.823–843.

Arnott, R.W.C. 2007. Stratal architecture and origin of lateral accretion deposits (LADs) and conterminous inner-bank levee deposits in a base-of-slope sinuous channel, lower Isaac Formation (Neoproterozoic), East-Central British Columbia, Canada. *Marine and Petroleum Geology*. **24**(6–9), pp.515–528.

Arnott, R.W.C. 2012. Turbidites, and the Case of the Missing Dunes. *Journal of Sedimentary Research*. **82**(6), pp.379–384.

Arnott, R.W.C., and Al-Mufti, O. 2017. Deep-marine pseudo dune cross-stratification—Similar, but completely different. *Journal of Sedimentary Research*. **87**(3), pp.312–323.

Arnott, R.W.C., Tilston, M., Fraino, P., Navarro, L., Dumouchel, G. and Miklovich, N. 2021. Laterally accreting sinuous channels and their deposits: The Goldilocks of deep-water slope systems. *Journal of Sedimentary Research*. **91**(5), pp.451-463.

Azpiroz-Zabala, M., Cartigny, M.J.B., Talling, P.J., Parsons, D.R., Sumner, E.J., Clare, M.A., Simmons, S.M., Cooper, C. and Pope, E.L. 2017. Newly recognized turbidity current structure can explain prolonged flushing of submarine canyons. *Science Advances*. **3**(10), pp.1–12.

Baas, J.H. and Best, J.L. 2002. Turbulence Modulation in Clay-Rich Sediment-Laden Flows and Some Implications for Sediment Deposition. *Journal of Sedimentary Research*. **72**(3), pp.336–340.

Baas, J.H., Best, J.L., Peakall, J. and Wang, M. 2009. A Phase Diagram for Turbulent, Transitional, and Laminar Clay Suspension Flows. *Journal of Sedimentary Research*. **79**(4), pp.162–183.

Baas, J.H., Best, J.L. and Peakall, J. 2011. Depositional processes, bedform development and hybrid bed formation in rapidly decelerated cohesive (mud-sand) sediment flows. *Sedimentology*. **58**(7), pp.1953–1987.

Babonneau, N., Savoye, B., Cremer, M. and Klein, B. 2002. Morphology and architecture of the present canyon and channel system of the Zaire deep-sea fan. *Marine and Petroleum Geology*. **19**(4), pp.445–467.

Babonneau, N., Savoye, B., Cremer, M. and Bez, M. 2004. Multiple terraces within the deep incised Zaire Valley (Zaïango Project): are they confined levees? *In: S.A. Lomas and P. Joseph, eds. Confined Turbidite Systems: Journal of the Geological Society of London Special Publication*. **222**, pp.91–114.

Babonneau, N., Savoye, B., Cremer, M. and Bez, M. 2010. Sedimentary architecture in meanders of a submarine channel: detailed study of the present Congo turbidite channel (Zaïango Project). *Journal of Sedimentary Research*. **80**, pp.852–866.

Bailey, W.S., McArthur, A.D. and McCaffrey, W.D. 2020. Distribution of contourite drifts on convergent margins: Examples from the Hikurangi subduction margin of New Zealand. *Sedimentology*. **68**(1), pp.294-323.

Ballance, P.F. 1975. Evolution of the India-Pacific plate boundary in North Island, New Zealand. *Bulletin of the Australian Society of Exploration Geophysicists*. **6**, pp.58-59.

Barker, S.P., Haughton, P.D.W., McCaffrey, W.D., Archer, S.G. and Hakes, B. 2008. Development of Rheological Heterogeneity in Clay-Rich High-Density Turbidity Currents: Aptian Britannia Sandstone Member, U.K. Continental Shelf. *Journal of Sedimentary Research*. **78**(2), pp.45–68.

Barnolas, A., and Gil-Peña, I. 2001. Ejemplos de relleno sedimentario multiepisódico en una cuenca de antepaís fragmentada. *La Cuenca Surpirenaica: Boletín Geológico y Minero*. **112**(3), pp.17– 38.

Barnes, N.E. and Normark, W.R. 1985. Diagnostic Parameters for Comparing Modern Submarine Fans and Ancient Turbidite Systems *In*: A.H. Bouma, W. R. Normark and N. E. Barnes, eds. *Submarine Fans and Related Turbidite Systems*. New York: Springer, pp.13–14.

Barnes, P. M., and Mercier de Lepinay, B. 1997. Rates and mechanics of rapid frontal accretion along the very obliquely convergent southern Hikurangi margin, New Zealand. *Journal of Geophysical Research*. **102**, pp.24,931– 24,952.

Barnes, P.M., Lamarche, G., Bialas, J., Henrys, S., Pecher, I., Netzeband, G.L., Greinert, J., Mountjoy, J.J., Pedley, K. and Crutchley, G. 2010. Tectonic and geological framework for gas hydrates and cold seeps on the Hikurangi subduction margin, New Zealand. *Marine Geology*. **272**, pp.26–48.

Barnes, P.M., Wallace, L.M., Saffer, D.M., Bell, R.E., Underwood, M.B., Fagereng, A., Meneghini, F., Savage, H.M., Rabinowitz, H.S., Morgan, J.K., Kitajima, H., Kutterolf, S., Hashimoto, Y., Engelmann de Oliveira, C.H., Noda, A., Crundwell, M.P., Shepherd, C.L., Woodhouse, A.D., Harris, R.N., Wang, M., Henrys, S., Barker, D.H.N., Petronotis, K.E., Bourlange, S.M., Clennell, M.B., Cook, A.E., Dugan, B.E., Elger, J., Fulton, P.M., Gamboa, D., Greve, A., Han, S., Hüpers, A. Ikari, M.J., Ito, Y., Kim, G.Y., Koge, H., Lee, H., Li, X., Luo, M., Malie, P.R., Moore, G.F., Mountjoy, J.J., McNamara, D.D., Paganoni, M., Screatton, E.J., Shankar, U., Shreedharan, S., Solomon, E.A., Wang, X., Wu, H-Y, Pecher, I.A. and LeVay, L.J. 2020. Slow slip source characterized by lithological and geometric heterogeneity. *Science Advances*. **6**(13), eaay3314.

Barton, M., Byrne, C.O., Pirmez, C., Prather, B., Vlugt, F. Van Der, Alpak, F.O. and Sylvester, Z. 2010. Turbidite Channel Architecture: Recognizing and Quantifying the Distribution of Channel-base Drapes Using Core and Dipmeter Data *In*: M. Poppelreiter, C. Garcia-Carballido and M. Kraaijveld, eds. *Dipmeter and borehole image log technology: AAPG Memoir 92.*, pp.195–210.

Bayliss, N. and Pickering, K.T. 2015. Transition from deep marine lower slope erosional channels to proximal basin floor stacked channel-levee-overbank deposits, and synsedimentary growth structures, middle Eocene Banaston System, Ainsa Basin, Spanish Pyrenees. *Earth-Science Reviews*. **144**, pp.23–46.

Bell, D., Stevenson, C.J., Kane, I.A., Hodgson, D.M., and Poyatos-Moré, M. 2018a. Topographic controls on the development of contemporaneous but contrasting basin-floor depositional architectures. *Journal of Sedimentary Research*. **88**, pp.1166–1189.

Bell, D., Kane, I.A., Pontén, A.S.M., Flint, S.S., Hodgson, D.M., and Barrett, B.J. 2018b. Spatial variability in depositional reservoir quality of deep-water channel-fill and lobe deposits. *Marine and Petroleum Geology*. **98**, pp.97–115.

Bell, D., Hodgson, D. M., Pontén, A. S. M., Hansen, L. A. S., Flint, S. S. and Kane, I. A. 2020. Stratigraphic hierarchy and three-dimensional evolution of an exhumed submarine slope channel system. *Sedimentology*. **67**(6), pp.3259-3289.

Bell, D., Soutter, E.L., Cumberpatch, Z.A., Ferguson, R.A., Sychala, Y.T., Kane, I.A., Eggenhuisen, J.T. 2021. Flow-process controls on grain type distribution in an experimental turbidity current deposit: Implications for detrital signal preservation and microplastic distribution in submarine fans. *The Depositional Record*. **00**, pp.1-24.

Bentham, P.A., and Burbank, D.W. 1996. Chronology of Eocene foreland basin evolution along the western oblique margin of the South-Central Pyrenees. *In*: P.F. Friend and C.J. Dabrio, eds. *Tertiary Basins of Spain*: New York, Cambridge University Press, pp.144–152.

Bernhardt, A., Jobe, Z.R., and Lowe, D.R. 2011. Stratigraphic evolution of a submarine channel-lobe complex system in a narrow fairway within the Magallanes foreland basin, Cerro Toro Formation, southern Chile. *Marine and Petroleum Geology*. **28**(3), pp.785–806.

Bernhardt, A., Jobe, Z.R., Grove, M., and Lowe, D.R. 2012. Palaeogeography and diachronous infill of an ancient deep-marine foreland basin, Upper Cretaceous Cerro Toro Formation, Magallanes Basin. *Basin Research*. **24**(3), pp.269–294.

Boulestex, K., Poyatos-Moré, M., Flint, S.S., Taylor, K.G., Hodgson, D.M., and Hasiotis, S.T. 2019. Transport and deposition of mud in deep-water environments: Processes and stratigraphic implications. *Sedimentology*. **66**(7), pp.1–32.

Bouma, A.H. 1962. *Sedimentology of Some Flysch Deposits: A Graphic Approach to Facies Interpretation*. Amsterdam/New York: Elsevier.

Bourget, J., Zaragosi, S., Ellouz-Zimmermann, N., Mouchot, N., Garlan, T., Schneider, J. L., Lanfumey, V. and Lallemand, S. 2011. Turbidite system architecture and sedimentary processes along topographically complex slopes: the Makran convergent margin. *Sedimentology*. **58**(2), pp.376-406.

Bland, K.J., Lamarche, G., Anderson, O., Barnes, P.M., Black, J., Bowden, D., Chiswell, S., Crutchley, G., Gorman, R., Mountjoy, J., Niel, H., Notman, P., Pallentin, A., Rowden, A., Stagpoole, V.M. and Strogon, D.P. 2014. Pegasus Basin Petroleum Prospectivity Screening Report. *GNS Science Consultancy Report 2014/103, NZP&M, Ministry of Business, Innovation & Employment (MBIE), New Zealand Unpublished Report PR(CR2014-103)*. 139 p.

Brackenridge, R. E., Hernandez-Molina, F. J., Stow, D. A. V. and Llave, E. 2013. A Pliocene mixed contourite-turbidite system offshore the Algarve Margin, Gulf of Cadiz: Seismic response, margin evolution and reservoir implications. *Marine and Petroleum Geology*. **46**, pp.36-50.

Breien, H., De Blasio, F. V., Elverhoi, A., Nystuen, J.P. and Harbitz, C.B. 2010. Transport Mechanisms of Sand in Deep-Marine Environments--Insights Based on Laboratory Experiments. *Journal of Sedimentary Research*. **80**(11), pp.975–990.

Britter, R.E. and Simpson, J.E. 1978. Experiments on the dynamics of a gravity current head. *Journal of Fluid Mechanics*. **88**(2), pp.223–240.

Brocheray, S., Cremer, M., Zaragosi, S., Schmidt, S., Eynaud, F., Rossignol, L. and Gillet, H. 2014. 2000 years of frequent turbidite activity in the Capbreton Canyon (Bay of Biscay). *Marine Geology*. **347**, pp.136–152.

Brooks, H. L., Hodgson, D. M., Brunt, R. L., Peakall, J., Hofstra, M. and Flint, S. S. 2018a. Deep-water channel-lobe transition zone dynamics: Processes and depositional architecture, an example from the Karoo Basin, South Africa. *Geological Society of America Bulletin*. **130**(9-10), pp.1723-1746.

Brooks, H.L., Hodgson, D.M., Brunt, R.L., Peakall, J. and Flint, S.S. 2018b. Exhumed lateral margins and increasing flow confinement of a submarine landslide complex. *Sedimentology*. **65**(4), pp.1067-1096.

Brooks, H.L., Hodgson, D.M., Brunt, R.L., Peakall, J., Poyatos-moré, M. and Flint, S.S. 2018c. Disconnected submarine lobes as a record of stepped slope evolution over multiple sea-level cycles. *Geosphere*. **14**(4), pp.1753–1779.

Brunt, R.L., McCaffrey, W.D., and Butler, R.W.H. 2007. Architectural Elements of the Grès du Champsaur: Chaillol Area, Haute Alpes, Southeast France. *In*: T.H. Nilsen, R.D. Shew, G.S. Steffens and J.R.J. Studlick, eds. *Atlas of Deep-Water Outcrops: American Association of Petroleum Geologists, Studies in Geology*, pp.1–17.

Brunt, R. L., Hodgson, D. M., Flint, S. S., Pringle, J. K., Di Celma, C. N., Prelat, A. and Grecula, M. 2013a. Confined to unconfined: Anatomy of a base of slope succession, Karoo Basin, South Africa. *Marine and Petroleum Geology*. **41**, pp.206-221.

Brunt, R.L., Di Celma, C.N., Hodgson, D.M., Flint, S.S., Kavanagh, J.P., and van der Merwe, W.C. 2013b. Driving a channel through a levee when the levee is high: An outcrop example of submarine down-dip entrenchment. *Marine and Petroleum Geology*. **41**(1), pp.134–145.

Bull, S., Cartwright, J. and Huuse, M. 2009. A review of kinematic indicators from mass-transport complexes using 3D seismic data. *Marine and Petroleum Geology*. **26**(7), pp.1132–1151.

Bull, S., Browne, G.H., Arnot, M.J. and Strachan, L.J. 2020. Influence of Mass Transport Deposit (MTD) surface topography on deep-water deposition: an example from a predominantly fine-grained continental margin, New Zealand. *Geological Society of London, Special Publication*. **500**(1), pp.147-171.

Burgess, P.M. 2016. Identifying Ordered Strata: Evidence, Methods, and Meaning. *Journal of Sedimentary Research*. **86**(3), pp.148–167.

Burgreen, B., and Graham, S. 2014. Evolution of a deep-water lobe system in the Neogene trench-slope setting of the East Coast Basin, New Zealand: Lobe stratigraphy and architecture in a weakly confined basin configuration. *Marine and Petroleum Geology*. **54**, pp.1–22.

Butler, R.W.H. and McCaffrey, W.D. 2010. Structural evolution and sediment entrainment in mass-transport complexes: outcrop studies from Italy. *Journal of the Geological Society*. **167**(3), pp.617–631.

Caja, M.A., Marfil, R., Garcia, D., Remacha, E., Morad, S., Mansurbeg, H., Amorosi, A., Martínez-Calvo, C., and Lahoz-Beltrá, R. 2010. Provenance of siliciclastic and hybrid turbiditic arenites of the Eocene Hecho Group, Spanish Pyrenees: Implications for the tectonic evolution of a foreland basin. *Basin Research*. **22**(2), pp.157–180.

Cámara, P., and Kilmowitz, J. 1985. Interpretación geodinámica de la vertiente centro-occidental surpirenaica (cuencas de Jaca-Tremp). *Estudios Geológicos*. **41**, pp.391–404.

Campion, K.M., Sprague, A.R.G., and Sullivan, M.D. 2005. *Architecture and lithofacies of the Capistrano Formation (Miocene–Pliocene), San Clemente, California*: Pacific Section, SEPM, Fieldtrip Guidebook, October 29, 2005, 42p.

Cardona, S., Wood, L.J., Dugan, B., Jobe, Z. and Strachan, L.J. 2020. Characterization of the Rapanui mass-transport deposit and the basal shear zone: Mount Messenger Formation, Taranaki Basin, New Zealand. *Sedimentology*. **67**, pp.2111–2148

Cardozo, N. and Allmendinger, R.W. 2013. Spherical projections with OSXStereonet. *Computers and Geosciences*. **51**, pp.193–205.

Carter, L. 1992. Acoustical characterisation of seafloor sediments and its relationship to active sedimentary processes in Cook Strait, New Zealand. *New Zealand Journal of Geology and Geophysics*. **35**, pp.289–300.

Carter, L., Carter, R.M., Nelson, C.S., Fulthorpe, C.S. and Neil, H.L. 1990. Evolution of Pliocene to Recent abyssal sediment waves on Bounty Channel levees, New Zealand. *Marine Geology*. **95**(2), pp.97-109.

Carter, L., Manighetti, B., Elliot, M., Trustrum, N. and Gomez, B. 2002. Source, sea level and circulation effects on the sediment flux to the deep ocean over the past 15 ka off eastern New Zealand. *Global and Planetary Change*. **33**(3-4), pp.339-355.

Carter, L., Gavey, R., Talling, P.J. and Liu, J.T. 2014. Insights into submarine geohazards from breaks in subsea telecommunication cables. *Oceanography*. **27**(2), pp.58–67.

- Carter, R. M. 1975. A Discussion and Classification of Subaqueous Mass-Transport with Particular Application to Grain-Flow, Slurry-Flow, and Fluxoturbidites. *Earth-Science Reviews*. **11**(2), pp.145-177.
- Carter, R.M. 1988. The nature and evolution of deep-sea channel systems. *Basin Research*. **1**(1), pp.41–54.
- Carter, R.M., Carter, L. and Griggs, G.B. 1982. Sedimentation in the Conway Trough, a deep near-shore marine basin at the junction of the Alpine transform and Hikurangi subduction plate boundary, New Zealand. *Sedimentology*. **29**, pp.475-497.
- Cartigny, M.J.B., Postma, G., Van den Berg, J.H. and Mastbergen, D.R. 2011. A comparative study of sediment waves and cyclic steps based on geometries, internal structures and numerical modelling. *Marine Geology*. **280**, pp.40–56.
- Cartigny, M. J. B., Ventra, D., Postma, G. and van den Berg, J. H. 2014. Morphodynamics and sedimentary structures of bedforms under supercritical-flow conditions: New insights from flume experiments. *Sedimentology*. **61**(3), pp.712-748.
- Casciano, C.I., Patacci, M., Longhitano, S.G., Tropeano, M., McCaffrey, W.D. and Di Celma, C. 2019. Multi-scale analysis of a migrating submarine channel system in a tectonically-confined basin: The Miocene Gorgoglione Flysch Formation, southern Italy. *Sedimentology*. **66**(1), pp.205-240.
- Casson, M., Calvès, G., Huuse, M., Sayers, B. and Redfern, J. 2020. Cretaceous continental margin evolution revealed using quantitative seismic geomorphology, offshore northwest Africa. *Basin Research*. **33**(1), pp.1–25.
- Castelltort, S., Honegger, L., Adatte, T., Clark, J.D., Puigdefàbregas, C., Spangenberg, J.E., Dykstra, M.L., and Fildani, A. 2017. Detecting eustatic and tectonic signals with carbon isotopes in deep-marine strata, Eocene Ainsa Basin, Spanish Pyrenees. *Geology*. **45**(8), pp.707–710.
- Chanvry, E., Deschamps, R., Joseph, P., Puigdefàbregas, C., Poyatos-Moré, M., Serra-Kiel, J., Garcia, D., and Teinturier, S. 2018. Impact of intrabasinal tectonics in the stratigraphic evolution of piggyback basin fills: an example from the Eocene South-Pyrenean Foreland Basin (Spain). *Sedimentary Geology*. **377**, pp.34-62.

Chen, Y., Parsons, D. R., Simmons, S. M., Williams, R., Cartigny, M. J. B., Hughes Clarke, J. E., Stacey, C. D., Hage, S., Talling, P. J., Azpiroz-Zabala, M., Clare, M. A., Hizzett, J. L., Heijnen, M. S., Hunt, J. E., Lintern, D. G., Sumner, E. J., Vellinga, A. J. and Vendettuoli, D. 2021. Knickpoints and crescentic bedform interactions in submarine channels. *Sedimentology*. **68**(4), pp.1358-1377.

Chough, S.K. and Hesse, R. 1980. The Northwest Atlantic Mid-Ocean Channel of the Labrador Sea; III, Head spill vs. body spill deposits from turbidity currents on natural levees. *Journal of Sedimentary Petrology*. **50**(1), pp.227–234.

Choukroune, P. 1992. Tectonic evolution of the Pyrenees. *Annual Review of Earth and Planetary Sciences*. **20**, pp.143–158.

Clare, M.A., Talling, P.J., Challenor, P., Malgesini, G. and Hunt, J. 2014. Distal turbidites reveal a common distribution for large (>0.1 km³) submarine landslide recurrence. *Geology*. **42**(3), pp.263–266.

Clare, M.A., Hughes Clarke, J.E., Talling, P.J., Cartigny, M.J.B. and Pratomo, D.G. 2016. Preconditioning and triggering of offshore slope failures and turbidity currents revealed by most detailed monitoring yet at a fjord-head delta. *Earth and Planetary Science Letters*. **450**, pp.208–220.

Clare, M., Lintern, D. G., Rosenberger, K., Hughes Clarke, J. E., Paull, C., Gwiazda, R., Cartigny, M. J. B., Talling, P. J., Perara, D., Xu, J., Parsons, D., Jacinto, R. S. and Apprioual, R. 2020. Lessons learned from the monitoring of turbidity currents and guidance for future platform designs. *Geological Society, London, Special Publications* **500**(1), pp.605-634.

Clark, I.R. and Cartwright, J.A. 2011. Key controls on submarine channel development in structurally active settings. *Marine and Petroleum Geology*. **28**(7), pp.1333–1349.

Clark, J.D. and Pickering, K.T. 1996. Architectural elements and growth patterns of submarine channels: Applications to hydrocarbon exploration. *AAPG Bulletin*. **80**(2), pp.194–221.

Clark, J.D., Kenyon, N.H. and Pickering, K.T. 1992. Quantitative analysis of the geometry of submarine channels: Implications for the classification of submarine fans. *Geology*. **20**, pp.633–636.

Clark, J.D., Puigdefàbregas, C., Castellort, S. and Fildani, A. 2017. *Propagation of Environmental Signals within Source-to-Sink Stratigraphy: SEPM Field Trip Guidebook No. 13*: Tulsa, Oklahoma, USA, 63p.

Clift, P.D., Giosan, L., Henstock, T.J. and Tabrez, A.R. 2014. Sediment storage and reworking on the shelf and in the Canyon of the Indus River-Fan System since the last glacial maximum. *Basin Research*. **26**(1), pp.183–202.

Collot, J.-Y., Lewis, K.B., Lamarche, G. and Lallemand, S. 2001. The giant Ruatoria debris avalanche on the northern Hikurangi margin, New Zealand: result of oblique seamount subduction. *Journal of Geophysical Research*. **106**, pp.271–297.

Corella, J. P., Loizeau, J. L., Kremer, K., Hilbe, M., Gerard, J., le Dantec, N., Stark, N., Gonzalez-Quijano, M. and Girardclos, S. 2016. The role of mass-transport deposits and turbidites in shaping modern lacustrine deepwater channels. *Marine and Petroleum Geology*. **77**, pp.515-525.

Cornard, P.H., and Pickering, K.T. 2019. Supercritical-flow deposits and their distribution in a submarine channel system, middle Eocene, Ainsa Basin, Spanish Pyrenees. *Journal of Sedimentary Research*. **89**, pp.576–597.

Cossu, C. and Wells, G.W. 2010. Coriolis forces influence the secondary circulation of gravity currents flowing in large-scale sinuous submarine channel systems. *Geophysical Research Letters*. **37**(7), pp.1-6.

Cossu, R., Wells, M.G. and Peakall, J. 2015. Latitudinal variations in submarine channel sedimentation patterns: the role of Coriolis forces. *Journal of the Geological Society*. **172**(2), pp.161-174.

Couvin, B., Georgiopoulou, A., Mountjoy, J. J., Amy, L., Crutchley, G. J., Brunet, M., Cardona, S., Gross, F., Böttner, C., Krastel, S. and Pecher, I. 2020. A new depositional model for the Tuaheni Landslide Complex, Hikurangi Margin, New Zealand. *In: A. Georgiopoulou, L.A. Amy, S. Benetti, J.D. Chaytor, M.A. Clare, D. Gamboa, P.D.W. Haughton, J. Moernaut, and J.J. Mountjoy, eds. Subaqueous Mass Movements and their Consequences: Advances in Process Understanding, Monitoring and Hazard Assessments, Geological Society, London, Special Publications*. **500**, pp.551-566.

Covault, J.A. and Graham, S.A. 2010. Submarine fans at all sea-level stands: Tectono-morphologic and climatic controls on terrigenous sediment delivery to the deep sea. *Geology*. **38**(10), pp.939–942.

Covault, J.A., Normark, W.R., Romans, B.W. and Graham, S.A. 2007. Highstand fans in the California borderland: The overlooked deep-water depositional systems. *Geology*. **35**(9), pp.783–786.

Covault, J.A., Fildani, A., Romans, B.W. and McHargue, T. 2011. The natural range of submarine canyon-and-channel longitudinal profiles. *Geosphere*. **7**(2), pp.313–332.

Covault, J.A., Shelef, E., Traer, M., Hubbard, S.M., Romans, B.W. and Fildani, A. 2012. Deep-Water Channel Run-Out Length: Insights from Seafloor Geomorphology. *Journal of Sedimentary Research*. **82**(1–2), pp.21–36.

Covault, J.A., Craddock, W.H., Romans, B.W., Fildani, A. and Gosai, M. 2013. Spatial and Temporal Variations in Landscape Evolution: Historic and Longer-Term Sediment Flux through Global Catchments. *The Journal of Geology*. **121**(1), pp.35–56.

Covault, J.A., Kostic, S., Paull, C.K., Ryan, H.F. and Fildani, A. 2014. Submarine channel initiation, filling and maintenance from sea-floor geomorphology and morphodynamic modelling of cyclic steps. *Sedimentology*. **61**(4), pp.1031–1054.

Crisóstomo-Figueroa, A., McArthur, A.D., Dorrell, R.M., Amy, L. and McCaffrey, W.D. 2020. A new modelling approach to sediment bypass prediction applied to the East Coast Basin, New Zealand. *Geological Society of America Bulletin*. **133**(7-8), pp.1734-1748.

Cronin, B.T., Celik, H. and Hurst, A. 2007. Sinuous channels in late stages of entrenched deep-water channel complexes, Hasret Mountain Main Channel, Turkey *In: Atlas of Deep-Water Outcrops: AAPG Studies in Geology* 56. pp.368–372.

Cullen, T. M., Collier, R. E. L., Gawthorpe, R. L., Hodgson, D. M. and Barrett, B. J. 2020. Axial and transverse deep-water sediment supply to syn-rift fault terraces: Insights from the West Xylokastro Fault Block, Gulf of Corinth, Greece. *Basin Research*. **32**(5), pp.1105-1139.

Cullis, S., Colombera, L., Patacci, M. and McCaffrey, W.D. 2018. Hierarchical classifications of the sedimentary architecture of deep-marine depositional systems. *Earth-Science Reviews*. **179**, pp.38–71.

Dailly, G.C. 1982. Slope Readjustment During Sedimentation on Continental Margins *In: AAPG Special Volume M34: Studies in Continental Margin Geology.*, pp.593–608.

Dakin, N., Pickering, K.T., Mohrig, D. and Bayliss, N.J. 2013. Channel-like features created by erosive submarine debris flows: Field evidence from the Middle Eocene Ainsa Basin, Spanish Pyrenees. *Marine and Petroleum Geology*. **41**(1), pp.62–71.

Damuth, J.E. 1979. Migrating sediment waves created by turbidity currents in the northern South China Basin. *Geology*. **7**(11), pp.520-523.

Daly, R.A. 1936. Origin of Submarine 'Canyons'. *American Journal of Science*. **31**(186), pp.401–420.

Das Gupta, K., and Pickering, K.T. 2008. Petrography and temporal changes in petrofacies of deep-marine Ainsa – Jaca basin sandstone systems, Early and Middle Eocene, Spanish Pyrenees. *Sedimentology*. **55**, pp.1083–1114.

Davarpanah Jazi, S., Wells, M. G., Peakall, J., Dorrell, R. M., Thomas, R. E., Keevil, G. M., Darby, S. E., Sommeria, J., Viboud, S. and Valran, T. 2020. Influence of Coriolis Force Upon Bottom Boundary Layers in a Large-Scale Gravity Current Experiment: Implications for Evolution of Sinuous Deep-Water Channel Systems. *Journal of Geophysical Research: Oceans*. **125**(e2019JC015284), pp.1-30.

Davey, F.J., Hamfton, M.A., Childs, J., Fisher, M.A., Lewis, K.B. and Pettinga, J.R. 1986. Structure of a growing accretionary prism, Hikurangi margin, New Zealand. *Geology*. **14**, pp.663-666.

Davis, W.M. 1902. Baselevel, Grade and Peneplain. *The Journal of Geology*. **10**(1), pp.77–111.

Davy, B., Hoernle, K. and Werner, R. 2008. Hikurangi Plateau: crustal structure, rifted formation, and Gondwana subduction history. *Geochemistry, Geophysics, Geosystems*. **9**, pp.1–31.

Davy, B., Hoernle, K. and Werner, R. 2008. Hikurangi Plateau: crustal structure, rifted formation, and Gondwana subduction history. *Geochemistry, Geophysics, Geosystems*. **9**, pp.1–31.

De Leeuw, J., Eggenhuisen, J.T. and Cartigny, M.J.B. 2016. Morphodynamics of submarine channel inception revealed by new experimental approach. *Nature Communications*. **7**, pp.1–7.

De Ruig, M. J. and Hubbard, S. M. 2006. Seismic facies and reservoir characteristics of a deep-marine channel belt in the Molasse foreland basin, Puchkirchen Formation, Austria. *American Association of Petroleum Geologists Bulletin*. **90**(5), pp.735-752.

Dennielou, B., Huchon, A., Beaudouin, C. and Berne, S. 2006. Vertical grain-size variability within a turbidite levee: Autocyclicity or allocyclicity? A case study from the Rhone neofan, Gulf of Lions, Western Mediterranean. *Marine Geology*. **234**(1-4), pp.191-213.

Dennielou, B., Droz, L., Babonneau, N., Jacq, C., Bonnel, C., Picot, M., Le Saout, M., Saout, Y., Bez, M., Savoye, B., Olu, K. and Rabouille, C. 2017. Morphology, structure, composition and build-up processes of the active channel-mouth lobe complex of the Congo deep-sea fan with inputs from remotely operated underwater vehicle (ROV) multibeam and video surveys. *Deep-Sea Research Part II*. **142**, pp.25–49.

Deptuck, M.E., Steffens, G.S., Barton, M. and Pirmez, C. 2003. Architecture and evolution of upper fan channel-belts on the Niger Delta slope and in the Arabian Sea. *Marine and Petroleum Geology*. **20**(6–8), pp.649–676.

Deptuck, M.E., Sylvester, Z., Pirmez, C. and O'Byrne, C. 2007. Migration-aggradation history and 3-D seismic geomorphology of submarine channels in the Pleistocene Benin-major Canyon, western Niger Delta slope. *Marine and Petroleum Geology*. **24**(6–9), pp.406–433.

Deptuck, M.E., Piper, D.J.W., Savoye, B. and Gervais, A. 2008. Dimensions and architecture of late Pleistocene submarine lobes off the northern margin of East Corsica. *Sedimentology*. **55**(4), pp.869–898.

Di Celma, C.N., Brunt, R.L., Hodgson, D.M., Flint, S.S. and Kavanagh, J.P. 2011. Spatial and Temporal Evolution of a Permian Submarine Slope Channel-Levee System, Karoo Basin, South Africa. *Journal of Sedimentary Research*. **81**(7–8), pp.579–599.

Dorrell, R.M., Darby, S.E., Peakall, J., Sumner, E.J., Parsons, D.R. and Wynn, R.B. 2013a. Superelevation and overspill control secondary flow dynamics in submarine channels. *Journal of Geophysical Research: Oceans*. **118**(8), pp.3895–3915.

Dorrell, R.M., Hogg, A.J. and Pritchard, D. 2013b. Polydisperse suspensions: Erosion, deposition, and flow capacity. *Journal of Geophysical Research: Earth Surface*. **118**(3), pp.1939–1955.

Dorrell, R.M., Darby, S.E., Peakall, J., Sumner, E.J., Parsons, D.R. and Wynn, R.B. 2014. The critical role of stratification in submarine channels: Implications for channelization and long runout of flows. *Journal of Geophysical Research: Oceans*. **119**(4), pp.2620–2641.

Dorrell, R.M., Burns, A.D. and McCaffrey, W.D. 2015. The inherent instability of leveed seafloor channels. *Geophysical Research Letters*. **42**(10), pp.4023–4031.

Dorrell, R.M., Amy, L.A., Peakall, J. and Mccaffrey, W.D. 2018. Particle Size Distribution Controls the Threshold Between Net Sediment Erosion and Deposition in Suspended Load Dominated Flows. *Geophysical Research Letters*. **45**, pp.1443–1452.

Dorrell, R.M., Peakall, J., Darby, S.E., Parsons, D.R., Johnson, J., Sumner, E.J., Wynn, R.B., Özsoy., E. and Tezcan, D. 2019. Self-sharpening induces jet-like structure in seafloor gravity currents. *Nature Communications*. **10**(1381), pp.1–10.

Dott, J. 1963. Dynamics of Subaqueous Gravity Depositional Processes. *AAPG Bulletin*. **47**(1), pp.104–128.

Droz, L., Marsset, T., Ondreas, H., Lopez, M., Savoye, B. and Spy-Anderson, F.-L. 2003. Architecture of an active mud-rich turbidite system: the Zaire Fan (Congo-Angola margin southeast Atlantic). Results from Zaiango 1 and 2 cruises. *American Association of Petroleum Geologists Bulletin*. **87**(7), pp.1145–1168.

Droz, L., Jégou, I., Gillet, H., Dennielou, B., Bez, M., Canals, M., Amblas, D., Lastras, G. and Rabineau, M. 2020. On the termination of deep-sea fan channels: Examples from

the Rhône Fan (Gulf of Lion, Western Mediterranean Sea). *Geomorphology*. **369**(107368), pp.1-23.

Dykstra, M., Garyfalou, K., Kertznus, V., Kneller, B.C., Milana, J.P., Molinaro, M., Szuman, M., and Thompson, P. 2011 Mass transport deposits: combining outcrop studies and seismic forward modeling to understand lithofacies distributions, deformation, and their seismic stratigraphic expression. *In: R.C. Shipp, P. Weimer and H.W. Posamentier, eds. Mass-Transport Deposits in Deepwater Settings: SEPM (Society for Sedimentary Geology), Special Publication*. **96**, pp.293–310.

Eggenhuisen, J.T., Caffrey, W.D.M.C., Haughton, P.D.W., and Butler, R.W.H. 2010. Small-scale spatial variability in turbidity-current flow controlled by roughness resulting from substrate erosion: field evidence for a feedback mechanism. *Journal of Sedimentary Research*. **80**(2), pp.129–136.

Eggenhuisen, J. T., McCaffrey, W. D., Haughton, P. D. W. and Butler, R. W. H. 2011. Shallow erosion beneath turbidity currents and its impact on the architectural development of turbidite sheet systems. *Sedimentology*. **58**(4), pp.936-959.

Elliott, T. 2000. Depositional Architecture of a Sand-Rich, Channelised Turbidite System: The Upper Carboniferous Ross Sandstone Formation, Western Ireland *In: GCSSEPM Foundation 20th Annual Research Conference, Deep-Water Reservoirs of the World.*, pp.243–373.

Englert, R. G., Hubbard, S. M., Cartigny, M. J. B., Clare, M. A., Coutts, D. S., Hage, S., Hughes Clarke, J., Jobe, Z., Lintern, D. G., Stacey, C. and Vendettuoli, D. 2021. Quantifying the three-dimensional stratigraphic expression of cyclic steps by integrating seafloor and deep-water outcrop observations. *Sedimentology*. **68**(4), pp.1465-1501.

Faugères, J.-C. and Stow, D.A.V. 1993. Bottom-current-controlled sedimentation: a synthesis of the contourite problem. *Sedimentary Geology*. **82**(1–4), pp.287–297.

Faugères, J.-C., Stow, D.A.V., Imbert, P. and Viana, A. 1999. Seismic features diagnostic of contourite drifts. *Marine Geology*. **162**(1), pp.1–38.

Faugères, J. C. and Stow, D. A. V. 2008. Contourite Drifts: Nature, Evolution and Controls. *In: M. Rebesco and A. Camerlenghi, eds. Contourites. Developments in Sedimentology*. **60**, pp.259-288. Elsevier Science, Amsterdam.

- Felix, M. 2002. Flow structure of turbidity currents. *Sedimentology*. **49**(3), pp.397–419.
- Felix, M. and Peakall, J. 2006. Transformation of debris flows into turbidity currents: mechanisms inferred from laboratory experiments. *Sedimentology*. **53**(1), pp.107-123.
- Felix, M., Leszczynski, S., Slaczka, A., Uchman, A., Amy, L. A. and Peakall, J. 2009. Field expressions of the transformation of debris flows into turbidity currents, with examples from the Polish Carpathians and the French Maritime Alps. *Marine and Petroleum Geology*. **26**(10), pp.2011-2020.
- Ferguson, R.A., Kane, I.A., Eggenhuisen, J.T., Pohl, F., Tilston, M., Spychala, Y.T. and Brunt, R.L. 2020. Entangled external and internal controls on submarine fan evolution: an experimental perspective. *The Depositional Record*. **6**(3), pp.605-624.
- Fernandez, D., Bowen, M.M. and Sutton, P.J.H. 2018. Variability, coherence and forcing mechanisms in the New Zealand ocean boundary currents. *Progress in Oceanography*. **165**, pp.168–188.
- Fernández, O., Muñoz, J.A., Arbués, P., Falivene, O., and Marzo, M. 2004. Three-dimensional reconstruction of geological surfaces: An example of growth strata and turbidite systems from the Ainsa basin (Pyrenees, Spain). *American Association of Petroleum Geologists Bulletin*. **88**(8), pp.1049–1068.
- Fernández, O., Muñoz, J.A., Arbués, P., and Falivene, O. 2012. 3D structure and evolution of an oblique system of relaying folds: the Ainsa basin (Spanish Pyrenees). *Geological Society of London Journal*. **169**(5), pp.545–559.
- Festa, A., Dilek, Y., Pini, G.A., Codegone, G. and Ogata, K. 2012. Mechanisms and processes of stratal disruption and mixing in the development of mélanges and broken formations: Redefining and classifying mélanges. *Tectonophysics*. **568–569**, pp.7–24.
- Fildani, A., Normark, W.R., Kostic, S. and Parker, G. 2006. Channel formation by flow stripping: Large-scale scour features along the Monterey East Channel and their relation to sediment waves. *Sedimentology*. **53**(6), pp.1265–1287.
- Fildani, A., Hubbard, S.M., Covault, J.A., Maier, K.L., Romans, B.W., Traer, M. and Rowland, J.C. 2013. Erosion at inception of deep-sea channels. *Marine and Petroleum Geology*. **41**, pp.48–61.

Flint, S.S., Hodgson, D.M., Sprague, A.R., Brunt, R.L., Van der Merwe, W.C., Figueiredo, J., Prélat, A., Box, D., Di Celma, C. and Kavanagh, J.P. 2011. Depositional architecture and sequence stratigraphy of the Karoo basin floor to shelf edge succession, Laingsburg depocentre, South Africa. *Marine and Petroleum Geology*. **28**(3), pp.658–674.

Flood, R.D. 1988. A lee wave model for deep-sea mudwave activity. *Deep-Sea Research Part I: Oceanographic Research Papers*. **35**, pp.973–983.

Flood, R.D. and Piper, D.J. 1997. Amazon Fan sedimentation: the relationship to equatorial climate change, continental denudation, and sea-level fluctuations. In: R.D. Flood, D.J. Piper, A. Klaus, L.C. Peterson, eds. *Proceedings-Ocean Drilling Program, Scientific Results, Amazon Fan, National Science Foundation*. **155**, pp.653–675.

Flood, R.D., Manley, P.L., Kowsmann, R.O., Appi, C.J. and Pirmez, C. 1991. Seismic facies and late quaternary growth of Amazon Submarine Fan In: P. Weimer and M. H. Link, eds. *Seismic facies and sedimentary processes of submarine fans and turbidite systems*. New York: Springer-Verlag, pp.415–433.

Flood, R.D., Piper, D.J.W., Klaus, A., Burns, S.J., Busch, W.H., Cisowski, S., Cramp, A., Damuth, J.E., Goni, M.A., Haberle, S.G., Hall, F.R., Hinrichs, K-U., Hiscott, R.N., Kowsmann, R.O., Kronen, J.D.J., Long, D., Lopez, M., McDaniel, D.K., Manley, P.L., Maslin, M.A., Mikkelsen, N., Nanayama, F., Normark, W.R., Pirmez, C., dos Santos, J.R., Schneider, R.R., Showers, W.J., Soh, W. and Thibaut, J. 1995. Leg 155 Introduction; Amazon Fan. In: J.A. Marin, ed. *Proceedings of the Ocean Drilling Program, Part A: Initial Reports. Vol. 155. Texas: Texas A & M University, Ocean Drilling Program, College Station*. pp.5-16.

Fonnesu, M., Haughton, P., Felletti, F. and McCaffrey, W. 2015. Short length-scale variability of hybrid event beds and its applied significance. *Marine and Petroleum Geology*. **67**, pp.583–603.

Fonnesu, M., Patacci, M., Haughton, P.D.W., Felletti, F. and McCaffrey, W.D. 2016. Hybrid Event Beds Generated By Local Substrate Delamination On A Confined-Basin Floor. *Journal of Sedimentary Research*. **86**(8), pp.929–943.

Fonnesu, M., Felletti, F., Haughton, P.D.W., Patacci, M. and McCaffrey, W.D. 2018. Hybrid event bed character and distribution linked to turbidite system sub-environments:

The North Apennine Gottero Sandstone (north-west Italy). *Sedimentology*. **65**(1), pp.151-190.

Fonnesu, M., Palermo, D., Galbiati, M., Marchesini, M., Bonamini, E. and Bendias, D. 2020. A new world-class deep-water play-type, deposited by the syndepositional interaction of turbidity flows and bottom currents: The giant Eocene Coral Field in northern Mozambique. *Marine and Petroleum Geology*. **111**, pp.179-201.

Friend, P.F. and Sinha, R. 1993. Braiding and meandering parameters *In*: J. L. Best and C. S. Bristow, eds. *Braided Rivers: Geological Society, London, Special Publications*. pp.105–111.

Fryer, R.C., and Jobe, Z.R. 2019. Quantification of the bed-scale architecture of submarine depositional environments. *The Depositional Record*. **5**(2), pp.192–211.

Fuhrmann, A., Kane, I.A., Clare, M.A., Ferguson, R.A., Schomacker, E., Bonamini, E. and Contreras, F.A. 2020. Hybrid turbidite-drift channel complexes: An integrated multiscale model. *Geology*. **48**(6), pp.562-568.

Gales, J.A., Talling, P.J., Cartigny, M.J.B., Hughes Clarke, J., Lintern, G., Stacey, C., and Clare, M.A. 2019. What controls submarine channel development and the morphology of deltas entering deep-water fjords? *Earth Surface Processes and Landforms*. **44**(2), pp.535–551.

Gani, M. 2004. From turbid to lucid: a straightforward approach to sediment gravity flows and their deposits. *The Sedimentary Record*. **2**(3), pp.4–8.

Garcia, M.H. 1994. Depositional Turbidity Currents Laden with Poorly Sorted Sediment. *Journal of Hydraulic Engineering*. **120**(11), pp.1240–1263.

Gardner, M.H., Borer, J.M., Melick, J.J., Mavilla, N., Dechesne, M. and Wagerle, R.N. 2003. Stratigraphic process-response model for submarine channels and related features from studies of Permian Brushy Canyon outcrops, West Texas. *Marine and Petroleum Geology*. **20**(6–8), pp.757–787.

Gee, M. J.R. and Gawthorpe, R.L. 2006. Submarine channels controlled by salt tectonics: Examples from 3D seismic data offshore Angola. *Marine and Petroleum Geology*. **23**(4), pp.443-458.

Georgiopoulou, A. and Cartwright, J.A. 2013. A critical test of the concept of submarine equilibrium profile. *Marine and Petroleum Geology*. **41**, pp.35–47.

Gervais, A., Savoye, B., Mulder, T. and Gonthier, E. 2006. Sandy modern turbidite lobes: A new insight from high resolution seismic data. *Marine and Petroleum Geology*. **23**(4), pp.485–502.

Ghienne, J.F., Normandeau, A., Dietrich, P., Bouysson, M., Lajeunesse, P. and Schuster, M. 2021. The depositional signature of cyclic steps: A late Quaternary analogue compared to modern active delta slopes. *Sedimentology*. **68**, pp.1502–1538.

Ghisetti, F.C., Barnes, P.M., Ellis, S., Plaza-Faverola, A. and Barker, D.H.N. 2016. The last 2 Myr of accretionary wedge construction in the central Hikurangi margin (North Island, New Zealand): Insights from structural modelling. *Geochemistry, Geophysics, Geosystems*. **17**, pp.2661–2686.

Gilbert, G.K. 1877. *Report on the geology of the Henry mountains*. Washington DC: United States Geological and Geographical Survey.

Girardclos, S., Hilbe, M., Corella, J.P., Loizeau, J.-L., Kremer, K., DelSontro, T., Arantegui, A., Moscariello, A., Arlaud, F., Akhtman, Y., Anselmetti, F.S. and Lemmin, U. 2012. Searching the Rhone delta channel in Lake Geneva since François-Alphonse Forel. *Archive des Sciences*. **65**(1–2), pp.103–118.

Goldfinger, C. 2011. Submarine Paleoseismology Based on Turbidite Records. *Annual Review of Marine Science*. **3**(1), pp.35–66.

Gomis-Cartesio, L.E., Poyatos-Moré, M., Hodgson, D.M. and Flint, S.S. 2018. Shelf-margin clinothem progradation, degradation and readjustment: Tanqua depocentre, Karoo Basin (South Africa). *Sedimentology*. **65**, pp.809–841.

Gong, C., Wang, Y., Zhu, W., Li, W. and Xu, Q. 2013. Upper Miocene to Quaternary unidirectionally migrating deep-water channels in the Pearl River Mouth Basin, northern South China Sea. *American Association of Petroleum Geologists Bulletin*. **97**(2), pp.285–308.

Gong, C., Steel, R.J., Wang, Y., Lin, C. and Olariu, C. 2016a. Grain size and transport regime at shelf edge as fundamental controls on delivery of shelf-edge sands to deepwater. *Earth-Science Reviews*. **157**, pp.32–60.

Gong, C., Steel, R.J., Wang, Y., Lin, C. and Olariu, C. 2016b. Shelf-margin architecture variability and its role in sediment-budget partitioning into deep-water areas. *Earth-Science Reviews*. **154**, pp.72–101.

Guiastrennec-Faugas, L., Gillet, H., Jacinto, R.S., Dennielou, B., Hanquiez, V., Schmidt, S., Simplet, L. and Rousset, A. 2020. Upstream migrating knickpoints and related sedimentary processes in a submarine canyon from a rare 20-year morphobathymetric time-lapse (Capbreton submarine canyon, Bay of Biscay, France). *Marine Geology*. **423**(106143), pp.1–18.

Guiastrennec-Faugas, L., Gillet, H., Peakall, J., Dennielou, B., Galliot, A. and Jacinto, R.S. 2021. Initiation and evolution of knickpoints and their role in cut-and-fill processes in active submarine channels. *Geology*. **49**(3), pp.314–319.

Hage, S., Cartigny, M. J. B., Clare, M. A., Sumner, E. J., Vendettuoli, D., Clarke, J. E. H., Hubbard, S. M., Talling, P. J., Lintern, D. G., Stacey, C. D., Englert, R. G., Vardy, M. E., Hunt, J. E., Yokokawa, M., Parsons, D. R., Hizzett, J. L., Azpiroz-Zabala, M. and Vellinga, A. J. 2018. How to recognize crescentic bedforms formed by supercritical turbidity currents in the geologic record: Insights from active submarine channels. *Geology*. **46**(6), pp.563-566.

Hage, S., Galy, V.V., Cartigny, M.J.B., Acikalin, S. Clare, M.A., Gröcke, D.R., Hilton, R.G., Hunt, J.E., Lintern, D.G., McGhee, C.A., Parsons, D.R., Stacey, C.D., Sumner, E.J. and Talling, P.J. 2020. Efficient preservation of young terrestrial organic carbon in sandy turbidity-current deposits. *Geology*. **48**(9), pp.882–887.

Hajek, E.A. and Straub, K.M. 2017. Autogenic Sedimentation in Clastic Stratigraphy. *Annual Review of Earth and Planetary Sciences*. **45**, pp.681–709.

Hampton, M.A. 1972. The role of subaqueous debris flow in generating turbidity currents. *Journal of Sedimentary Petrology*. **42**(4), pp.775–793.

Hansen, L., L'Heureux, J.S., Sauvin, G., Polom, G., Lecomte, I., Vaneste, M., Longva, O., and Krawczyk, C. 2013. The effect of mass-wasting on the stratigraphic architecture

of a fjord-valley fill: correlation of onshore, shear wave seismics and marine seismic data at Trondheim, Norway. *Sedimentary Geology*. **289**, pp.1–18.

Hansen, L.A.S., Callow, R.H.T., Kane, I.A., Gamberi, F., Rovere, M., Cronin, B.T. and Kneller, B.C. 2015. Genesis and character of thin-bedded turbidites associated with submarine channels. *Marine and Petroleum Geology*. **67**, pp.852–879.

Hansen, L.A.S., Janocko, M., Kane, I. and Kneller, B. 2017a. Submarine channel evolution, terrace development, and preservation of intra-channel thin-bedded turbidites: Mahin and Avon channels, offshore Nigeria. *Marine Geology*. **383**, pp.146–167.

Hansen, L.A.S., Callow, R., Kane, I.A. and Kneller, B.C. 2017b. Differentiating submarine channel related thin-bedded turbidite facies: Outcrop example from the Rosario Formation, Mexico. *Sedimentary Geology*. **358**, pp.19–34.

Hansen, L.A.S., Hodgson, D.M., Pontén, A., Thrana, C. and Obradors Latre, A. 2021. Mixed axial and transverse deep-water systems: The Cretaceous post-rift Lysing Formation, offshore Norway. *Basin Research*. **33**(4), pp.2229-2251.

Harris, P.T. and Whiteway, T. 2011. Global distribution of large submarine canyons: Geomorphic differences between active and passive continental margins. *Marine Geology*. **285**(1–4), pp.69–86.

Haughton, P.D. 2000. Evolving turbidite systems on a deforming basin floor, Tabernas, SE Spain. *Sedimentology*. **47**, pp.497–518.

Haughton, P.D.W., Barker, S.P. and McCaffrey, W.D. 2003. 'Linked' debrites in sand-rich turbidite systems - Origin and significance. *Sedimentology*. **50**(3), pp.459–482.

Haughton, P., Davis, C., McCaffrey, W. and Barker, S. 2009. Hybrid sediment gravity flow deposits - Classification, origin and significance. *Marine and Petroleum Geology*. **26**(10), pp.1900–1918.

Hay, A.E. 1987. Turbidity currents and submarine channel formation in Rupert Inlet, British Columbia: 2. The roles of continuous and surge-type flow. *Journal of Geophysical Research*. **92**(C3), pp.2883–2900.

Hay, A.E., Murray, J.W. and Burling, R.W. 1983. Submarine Channels in Rupert Inlet, British Columbia: I. Morphology. *Sedimentary Geology*. **36**(2–4), pp.289–315.

Heard, T.G., and Pickering, K.T. 2008. Trace fossils as diagnostic indicators of deep-marine environments, Middle Eocene Ainsa-Jaca basin, Spanish Pyrenees. *Sedimentology*. **55**(4), pp.809–844.

Heard, T.G., Pickering, K.T., and Clark, J.D. 2014. Ichnofabric characterization of a deep-marine clastic system: A subsurface study of the Middle Eocene Ainsa System, Spanish Pyrenees. *Sedimentology*. **61**(5), pp.1298–1331.

Hedberg, H.D. 1970. Continental Margins From Viewpoint of the Petroleum Geologist. *American Association of Petroleum Geologists Bulletin*. **54**(1), pp.3–43.

Heijnen, M. S., Clare, M. A., Cartigny, M. J. B., Talling, P. J., Hage, S., Lintern, D. G., Stacey, C., Parsons, D. R., Simmons, S. M., Chen, Y., Sumner, E. J., Dix, J. K. and Clarke, J. E. H. 2020. Rapidly-migrating and internally-generated knickpoints can control submarine channel evolution. *Nature Communications*. **11**(1), pp.1-15.

Hernandez-Molina, F.J., Llave, E., Preu, B., Ercilla, G., Fontan, A., Bruno, M., Serra, N., Gomiz, J.J., Brackenridge, R.E., Sierro, F.J., Stow, D.A.V., Garcia, M., Juan, C., Sandoval, N. and Arnaiz, A. 2014. Contourite processes associated with the Mediterranean Outflow Water after its exit from the Strait of Gibraltar: Global and conceptual implications. *Geology*. **42**(3), pp.227-230.

Heerema, C.J., Talling, P.J., Cartigny, M.J., Paull, C.K., Bailey, L., Simmons, S.M., Parsons, D.R., Clare, M.A., Gwiazda, R., Lundsten, E., Anderson, K., Maier, K.L., Xu, J.P., Sumner, E.J., Rosenberger, K., Gales, J., McGann, M., Carter, L., Pope, E. and Monterey Coordinated Canyon Experiment (CEE) Team. 2020. What determines the downstream evolution of turbidity currents? *Earth and Planetary Science Letters*. **532**(116023), pp. 1-11.

Heezen, B.C. and Hollister, C. 1964. Deep-sea current evidence from abyssal sediments. *Marine Geology*. **1**(2), pp.141–174.

Heezen, B.C., Ewing, M. and Menzies, R.J. 1955. The influence of submarine turbidity currents on abyssal productivity. *Oikos*, **6**(2), pp.170–182.

Heezen, B.C., Tharp, M. and Ewing, M. 1959. The floors of the oceans; I, the North Atlantic. *Special Papers of the Geological Society of America*. **65**, pp.1–122.

Heezen, B. C. and Drake, C. L. 1964. The 1929 Grand Banks slump. *American Association of Petroleum Geologists Bulletin*. **48**(2), pp.221-225.

Heiniö, P., and Davies, R.J. 2007. Knickpoint migration in submarine channels in response to fold growth, western Niger Delta. *Marine and Petroleum Geology*. **24**(6–9), pp.434–449.

Hesse, R. 1995. Continental slope and basin sedimentation adjacent to an ice margin: a continuous sleeve-gun profile across the Labrador-Slope, Rise and Basin *In*: K. T. Pickering, R. N. Hiscott, N. H. Kenyon, F. Ricci Lucchi and R. D. A. Smith, eds. *Atlas of Deep Water Environments; Architectural Style in Turbidite systems* [Online]. London: Chapman and Hall, pp.14–18.

Hill, P.R. 2012. Changes in submarine channel morphology and slope sedimentation patterns from repeat multibeam surveys in the Fraser River delta, western Canada. *In*: M.Z. Li, C.R. Sherwood and P.R. Hill, eds. *Sediments, Morphology and Sedimentary Processes on Continental Shelves, International Association of Sedimentologists Special Publications*. **44**, pp.47–70.

Hiscott, R.N., Hall, F.R. and Pirmez, C. 1997. 4. Turbidity-current overspill from the Amazon Channel: Texture of the silt/sand load, paleoflow from anisotropy of magnetic susceptibility and implications for flow process *In*: R. D. Flood, D. J. W. Piper, A. Klaus and L. C. Peterson, eds. *Proceedings of the Ocean Drilling Program, Scientific Results.*, pp.531–538.

Hizzett, J.L., Hughes Clarke, J.E., Sumner, E.J., Talling, P.J., and Clare, M.A. 2018. Which Triggers Produce the Most Erosive, Frequent, and Longest Runout Turbidity Currents on Deltas?. *Geophysical Research Letters*. **45**, pp.855–863.

Ho, V.L., Dorrell, R.M., Keevil, G.M. and Burns, A.D. 2018. Pulse propagation in turbidity currents. *Sedimentology*. **65**, pp.620–637.

Hodgson, D.M. 2009. Distribution and origin of hybrid beds in sand-rich submarine fans of the Tanqua depocentre, Karoo Basin, South Africa. *Marine and Petroleum Geology*. **26**, pp.1940–1956.

Hodgson, D.M., Flint, S.S., Hodgetts, D., Drinkwater, N.J., Johannessen, E.P. and Luthi, S.M. 2006. Stratigraphic evolution of fine-grained submarine fan systems, Tanqua depocenter, Karoo Basin, South Africa. *Journal of Sedimentary Research*. **76**(1-2), pp.20-40.

Hodgson, D.M., Di Celma, C.N., Brunt, R.L. and Flint, S.S. 2011. Submarine slope degradation and aggradation and the stratigraphic evolution of channel-levee systems. *Journal of the Geological Society*. **168**(3), pp.625–628.

Hodgson, D.M., Kane, I.A., Flint, S.S., Brunt, R.L. and Ortiz-Karpf, A. 2016. Time-Transgressive Confinement On the Slope and the Progradation of Basin-Floor Fans: Implications For the Sequence Stratigraphy of Deep-Water Deposits. *Journal of Sedimentary Research*. **86**(2), pp.73–86.

Hodgson, D.M., Browning, J.V., Miller, K.G., Hesselbo, S., Poyatos-More, M., Mountain, G.S. and Proust, J.-N. 2018. Sedimentology, stratigraphic context, and implications of Miocene bottomset deposits, offshore New Jersey. *Geosphere*. **14**, pp.95–114.

Hofmann, H., Wickham, H. and Kafadar, K. 2017. Letter-Value Plots: Boxplots for Large Data. *Journal of Computational and Graphical Statistics*. **26**(3), pp.469-477.

Hofstra, M., Hodgson, D.M., Peakall, J. and Flint, S.S. 2015. Giant scour-fills in ancient channel-lobe transition zones: Formative processes and depositional architecture. *Sedimentary Geology*. **329**, pp.98-114.

Hofstra, M., Peakall, J., Hodgson, D.M., and Stevenson, C.J. 2018. Architecture and morphodynamics of subcritical sediment waves in an ancient channel – lobe transition zone. *Sedimentology*. **65**(7), pp.2339–2367.

Howarth, J.D., Orpin, A.R., Kaneko, Y., Strachan, L.J., Nodder, S.D., Mountjoy, J.J., Barnes, P.M., Bostock, H.C., Holden, C., Jones, K. and Cağatay, M.N. 2021. Calibrating the marine turbidite palaeoseismometer using the 2016 Kaikōura earthquake. *Nature Geoscience*. **14**, pp.161–167.

Howlett, D.M., Ge, Z.Y., Nemeč, W., Gawthorpe, R. L., Rotevatn, A. and Jackson, C. A.L. 2019. Response of unconfined turbidity current to deep-water fold and thrust belt topography: Orthogonal incidence on solitary and segmented folds. *Sedimentology*. **66**(6), pp.2425-2454.

Hubbard, S.M., Romans, B.W., and Graham, S.A. 2008. Deep-water foreland basin deposits of the Cerro Toro Formation, Magallanes basin, Chile: Architectural elements of a sinuous basin axial channel belt. *Sedimentology*. **55**(5), pp.1333–1359.

Hubbard, S.M., Ruig, M.J. De and Graham, S.A. 2009. Confined channel-levee complex development in an elongate depo-center: Deep-water Tertiary strata of the Austrian Molasse basin. *Marine and Petroleum Geology*. **26**, pp.85–112.

Hubbard, S.M., Covault, J.A., Fildani, A. and Romans, B.W. 2014. Sediment transfer and deposition in slope channels: Deciphering the record of enigmatic deep-sea processes from outcrop. *Geological Society of America Bulletin*. **126**(5-6), pp.857-871

Hubbard, S.M., Jobe, Z.R., Romans, B.W., Covault, J.A., Sylvester, Z. and Fildani, A. 2020. The stratigraphic evolution of a submarine channel: linking seafloor dynamics to depositional products. *Journal of Sedimentary Research*. **90**(7), pp.673-686.

Hughes Clarke, J.E. 2016. First wide-angle view of channelized turbidity currents links migrating cyclic steps to flow characteristics. *Nature Communications*. **7**(11896), pp.1–13.

Hughes Clarke, J.E., Brucker, S., Muggah, J., Hamilton, T., Cartwright, D., Church, I. and Kuus, P. 2012. Temporal progression and spatial extent of mass wasting events on the Squamish prodelta slope *In: 11th International Symposium on Landslides, Conference Proceedings, June 2012*. Banff, pp.1091–1096.

Hughes Clarke, J., Marques, C.R.V. and Pratomo, D. 2014. Imaging Active Mass-Wasting and Sediment Flows on a Fjord Delta, Squamish, British Columbia. *In: S. Krastel, J.-H. Behrmann, D. Völker, M. Stipp, C. Berndt, R. Urgeles, J. Chaytor, K. Huhn, M. Strasser and C. B. Harbitz, eds. Submarine Mass Movements and Their Consequences. Advances in Natural and Technological Hazards Research, vol 37*. Cham: Springer, pp.249–260.

Imran, J., Parker, G. and Pirmez, C. 1999. A nonlinear model of flow in subaerial and submarine meandering channels. *Journal of Fluid Mechanics*. **400**, pp.295–331.

Iverson, R.M. 1997. The Physics of Debris Flows. *Reviews of Geophysics*. **35**(3), pp.245–296.

Jackson, C.A.-L. 2011. Three-dimensional seismic analysis of megaclast deformation within a mass transport deposit; implications for debris flow kinematics. *Geology*. **39**, pp.203–206.

Janbu, N.E., Nemeč, W., Kirman, E. and Özaksoy, V. 2007. Facies anatomy of a sand-rich channelized turbiditic system: the Eocene Kusuri Formation in the Sinop Basin, north-central Turkey *In*: G. Nichols, E. Williams and C. Paola, eds. *Sedimentary Processes, Environments and Basins: A Tribute to Peter Friend. Special Publications of the International Association of Sedimentologists*. **38**, pp.457–517.

Janocko, M., Nemeč, W., Henriksen, S. and Warcho, M. 2013. The diversity of deep-water sinuous channel belts and slope valley-fill complexes. *Marine and Petroleum Geology*. **41**, pp.7–34.

Jegou, I., Savoye, B., Pirmez, C. and Droz, L. 2008. Channel-mouth lobe complex of the recent Amazon Fan: The missing piece. *Marine Geology*. **252**(1–2), pp.62–77.

Jiao, R., Seward, D., Little, T.A. and Kohn, B.P. 2015. Unroofing of fore-arc ranges along the Hikurangi Margin, New Zealand: constraints from low-temperature thermochronology. *Tectonophysics*. **656**, pp.39–51.

Jobe, Z.R., Bernhardt, A. and Lowe, D.R. 2010. Facies and Architectural Asymmetry in a Conglomerate-Rich Submarine Channel Fill, Cerro Toro Formation, Sierra Del Toro, Magallanes Basin, Chile. *Journal of Sedimentary Research*. **80**(11–12), pp.1085–1108.

Jobe, Z.R., Sylvester, Z., Parker, A.O., Howes, N., Slowey, N. and Pirmez, C. 2015. Rapid Adjustment of Submarine Channel Architecture To Changes In Sediment Supply. *Journal of Sedimentary Research*. **85**(6), pp.729–753.

Jobe, Z.R., Howes, N.C. and Auchter, N.C. 2016. Comparing submarine and fluvial channel kinematics: Implications for stratigraphic architecture. *Geology*. **44**(11), pp.931–934.

Jobe, Z. R., Howes, N. C., Straub, K. M., Cai, D., Deng, H., Laugier, F. J., Pettinga, L.A. and Shumaker, L.E. 2020. Comparing aggradation, superelevation, and avulsion frequency of submarine and fluvial channels. *Frontiers in Earth Science*. **8**(53), pp.1–22.

Johansson, M. and Stow, D.A.V. 1995. A classification scheme for shale clasts in deep water sandstones. *In: A.J. Hartley and D.J. Prosser, eds. Characterization of Deep Marine Clastic Systems: Geological Society of London, Special Publication. 94*, pp.221–241.

Johnson, A.M. Physical processes in geology. Freeman and Cooper, San Francisco, 577p.

Jolly, B. A., Lonergan, L., & Whittaker, A. C. 2016. Growth history of fault-related folds and interaction with seabed channels in the toe-thrust region of the deep-water Niger delta. *Marine and Petroleum Geology. 70*, pp.58–76.

Jones, O.T. 1939. The geology of the Colwyn bay district: a study of submarine slumping during the Salopian period. *Quarterly Journal of the Geological Society of London. 380*, pp.335–382.

Kane, I.A. and Hodgson, D.M. 2011. Sedimentological criteria to differentiate submarine channel levee subenvironments: Exhumed examples from the Rosario Fm. (Upper Cretaceous) of Baja California, Mexico, and the Fort Brown Fm. (Permian), Karoo Basin, S. Africa. *Marine and Petroleum Geology. 28*(3), pp.807–823.

Kane, I.A. and Pontén, A.S.M. 2012. Submarine transitional flow deposits in the Paleogene Gulf of Mexico. *Geology. 40*(12), pp.1119–1122

Kane, I.A., Kneller, B.C., Dykstra, M., Kassem, A. and McCaffrey, W.D. 2007. Anatomy of a submarine channel-levee: An example from Upper Cretaceous slope sediments, Rosario Formation, Baja California, Mexico. *Marine and Petroleum Geology. 24*(6–9), pp.540–563.

Kane, I.A., McCaffrey, W.D. and Peakall, J. 2008. Controls on sinuosity evolution within submarine channels. *Geology. 36*(4), pp.287–290.

Kane, I.A., Dykstra, M.L., Kneller, B.C., Tremblay, S. and McCaffrey, W.D. 2009a. Architecture of a coarse-grained channel-levée system: The Rosario Formation, Baja California, Mexico. *Sedimentology. 56*(7), pp.2207–2234.

Kane, I.A., McCaffrey, W.D., and Martinsen, O.J. 2009b. Allogenic vs. autogenic controls on megaflute formation. *Journal of Sedimentary Research 79*(9), pp.643–651.

Kane, I.A., McCaffrey, W.D. and Peakall, J. 2010a. On the Origin of Paleocurrent Complexity Within Deep Marine Channel Levees. *Journal of Sedimentary Research*. **80**(1–2), pp.54–66.

Kane, I.A., McCaffrey, W.D., Peakall, J. and Kneller, B.C. 2010b. Submarine channel levee shape and sediment waves from physical experiments. *Sedimentary Geology*. **223**(1–2), pp.75–85.

Kane, I.A., Catterall, V., McCaffrey, W.D. and Martinsen, O.J. 2010c. Submarine channel response to intrabasinal tectonics: The influence of lateral tilt. *AAPG Bulletin*. **94**(2), pp.189–219.

Kane, I.A., McGee, D.T. and Jobe, Z.R. 2012. Halokinetic effects on submarine channel equilibrium profiles and implications for facies architecture: conceptual model illustrated with a case study from Magnolia Field, Gulf of Mexico. *Geological Society, London, Special Publications*. **363**, pp.289–302.

Kane, I.A., Ponten, A.S.M., Vangdal, B., Eggenhuisen, J.T., Hodgson, D.M. and Spychala, Y.T. 2017. The stratigraphic record and processes of turbidity current transformation across deep-marine lobes. *Sedimentology*. **64**(5), pp.1236-1273.

Kane, I.A., Clare, M.A., Miramontes, E., Wogelius, R., Rothwell, J.J., Garreau, P. and Pohl, F. 2020. Seafloor microplastic hotspots controlled by deep-sea circulation. *Science*. **368**(6495), pp.1140-1145.

Kao, S.J., Dai, M., Selvaraj, K., Zhai, W., Cai, P., Chen, S.N., Yang, J.Y.T., Liu, J.T., Liu, C.C., Syvitski, J.P.M. 2010. Cyclone-driven deep sea injection of freshwater and heat by hyperpycnal flow in the subtropics. *Geophysical Research Letters*. **37**(21), pp.1-5

Keevil, G.M., Peakall, J., Best, J.L. and Amos, K.J. 2006. Flow structure in sinuous submarine channels: Velocity and turbulence structure of an experimental submarine channel. *Marine Geology*. **229**(3-4), pp.241-257.

Kelly, R.W., Dorrell, R.M., Burns, A.D. and McCaffrey, W.D. 2019. The structure and entrainment characteristics of partially confined gravity currents. *Journal of Geophysical Research: Oceans*. **124**(3), pp.2110–25.

Kenyon, N.H., Amir, A. and Cramp, A. 1995. Geometry of the younger sediment bodies of the Indus Fan *In*: K. T. Pickering, R. N. Hiscott, N. H. Kenyon, F. Ricci Lucchi and R. D. A. Smith, eds. *Atlas of Deep Water Environments; Architectural Style in Turbidite systems*. London: Chapman and Hall, pp.89–93.

Kenyon, N.H., Klaucke, I., Millington, J. and Ivanov, M.K. 2002. Sandy submarine canyon-mouth lobes on the western margin of Corsica and Sardinia, Mediterranean Sea. *Marine Geology*. **184**(1–2), pp.69–84.

Khan, Z.A. and Arnott, R.W.C. 2011. Stratal attributes and evolution of asymmetric inner- and outer-bend levee deposits associated with an ancient deep-water channel-levee complex within the Isaac Formation, southern Canada. *Marine and Petroleum Geology*. **28**(3), pp.824–842.

Klaucke, I., Hesse, R. and Ryan, W.B.F. 1998. Seismic stratigraphy of the Northwest Atlantic Mid-Ocean Channel; growth pattern of a mid-ocean channel-levee complex. *Marine and Petroleum Geology*. **15**(6), pp.575–585.

Kneller, B. 1995. Beyond the turbidite paradigm: physical models for deposition of turbidites and their implications for reservoir prediction. *In*: A.J. Hartley and D.J. Prosser, eds. *Characterization of Deep Marine Clastic Systems: Geological Society of London, Special Publication*. 94, pp.31–49.

Kneller, B. 2003. The influence of flow parameters on turbidite slope channel architecture. *Marine and Petroleum Geology*. **20**(6–8), pp.901–910.

Kneller, B.C. and Branney, M.J. 1995. Sustained high-density turbidity currents and the deposition of thick massive sands. *Sedimentology*. **42**, pp.607–616.

Kneller, B. and McCaffrey, W.D. 1999. Depositional effects of flow nonuniformity and stratification within turbidity currents approaching a bounding slope: deflection, reflection, and facies variation. *Journal of Sedimentary Research*. **69**, pp.980–991.

Kneller, B.C. and Buckee, C. 2000. The structure and fluid mechanics of turbidity currents: a review of some recent studies and their geological implications. *Sedimentology*. **47**(1), pp.62–94.

Kneller, B.C. and Caffrey, W.D. 2003. The Interpretation Of Vertical Sequences In Turbidite Beds: The Influence Of Longitudinal Flow Structure. *Journal of Sedimentary Research*. **73**(5), pp.706–713.

Kneller, B.C., Edwards, D.A., McCaffrey, W.D. and Moore, R. 1991. Oblique reflection of turbidity currents. *Geology*. **19**(3), pp.250-252.

Kneller, B., Dykstra, M., Fairweather, L. and Milana, J.P. 2016. Mass-transport and slope accommodation: Implications for turbidite sandstone reservoirs. *AAPG Bulletin*. **100**(2), pp.213–235.

Kneller, B., Bozetti, G., Callow, R., Dykstra, M., Hansen, L., Kane, I., Li, P., McArthur, A., Catharina, A. S., Dos Santos, T. and Thompson, P. 2020. Architecture, process, and environmental diversity in a late Cretaceous slope channel system. *Journal of Sedimentary Research*. **90**(1), pp.1-26.

Kolla, V. 2007. A review of sinuous channel avulsion patterns in some major deep-sea fans and factors controlling them. *Marine and Petroleum Geology*. **24**(6–9), pp.450–469.

Kolla, V., Bourges, Ph., Urruty, J.-M. and Safa, P. 2001. Evolution of deep-water Tertiary sinuous channels offshore Angola (west Africa) and implications for reservoir architecture. *American Association of Petroleum Geologists Bulletin*. **85**, pp.1373– 1405.

Kolla, V., Posamentier, H.W. and Wood, L.J. 2007. Deep-water and fluvial sinuous channels-Characteristics, similarities and dissimilarities, and modes of formation. *Marine and Petroleum Geology*. **24**(6–9), pp.388–405.

Kolla, V., Bandyopadhyay, A., Gupta, P., Mukherjee, B. and Ramana, D. V. 2012. Morphology and Internal Structure of a Recent Upper Bengal Fan-Valley Complex. In: B.E. Prather, M.E. Deptuck, D. Mohrig, B. Van Hoorn and R.B. Wynn, eds. *Application of the Principles of Seismic Geomorphology to Continental-Slope and Base-of-Slope Systems: Case Studies from Seafloor and Near-Seafloor Analogues*. *SEPM Special Publication*. **99**, pp.347-369.

Komar, P.D. 1971. Hydraulic Jumps in Turbidity Currents. *Geological Society of America Bulletin*. **82**, pp.1477–1488.

Konsoer, K., Zinger, J. and Parker, G. (2013). Bankfull hydraulic geometry of submarine channels created by turbidity currents: Relations between bankfull channel characteristics and formative flow discharge. *Journal of Geophysical Research - Earth Surface*. **118**(1), pp.216-228.

Kremer, C. H., McHargue, T., Scheucher, L. and Graham, S. A. 2018. Transversely-sourced mass-transport deposits and stratigraphic evolution of a foreland submarine channel system: Deep-water tertiary strata of the Austrian Molasse Basin. *Marine and Petroleum Geology*. **92**, pp.1-19.

Kroeger, K.F., Crutchley, G.J., Kellett, R. and Barnes, P.M. 2019. A 3-D model of gas generation, migration, and gas hydrate formation at a young convergent margin (Hikurangi Margin, New Zealand). *Geochemistry, Geophysics, Geosystems*. **20**, pp.5126–5147.

Kuang, Z., Zhong, G., Wang, L. and Guo, Y. 2014. Channel-related sediment waves on the eastern slope offshore Dongsha Islands, northern South China Sea. *Journal of Asian Earth Sciences*. **79**, pp.540–551.

Kuenen, P.H. 1937. Experiments in connection with Daly's hypothesis on the formation of submarine canyons. *Leidsche Geol. Med.* **7**, pp.327–351.

Kuenen, P. H. 1957. Sole markings of graded graywacke beds. *Journal of Geology*. **65**(3), pp. 231-258.

Kuenen, P.H. and Migliorini, C.I. 1950. Turbidity Currents As A Cause Of Graded Bedding. *The Journal of Geology*. **58**(2).

Kuenen, P.H. and Sengupta, S. 1970. Experimental marine suspension currents, competency and capacity. *Geologie en mijnbouw*. **49**(2), pp.89–118.

Lamb, S. 2011. Cenozoic tectonic evolution of the New Zealand plate-boundary zone: A review. *Tectonophysics*. **509**, pp.135–164.

Lamb, M.P., Parsons, J.D., Mullenbach, B.L., Finlayson, D.P., Orange, D.L. and Nittrouer, C.A. 2008. Evidence for superelevation, channel incision, and formation of cyclic steps by turbidity currents in Eel Canyon, California. *Bulletin of the Geological Society of America*. **120**(3–4), pp.463–475.

- Lambert, A. and Giovanoli, F. 1988. Records of riverborne turbidity currents and indications of slope failures in the Rhone delta of Lake Geneva. *Limnology and Oceanography*. **33**, pp.458- 468.
- Laubach, S.E., Olson, J.E. and Gross, M.R. 2009. Mechanical and fracture stratigraphy. *AAPG Bulletin*. **93**(11), pp.1413–1426.
- Leren, B.L.S., Janbu, N.E., Nemec, W.C.H., Kirman, E., and Ilgar, A. 2007. Late Cretaceous to early Eocene sedimentation in the Sinop – Boyabat Basin, north-central Turkey: a deep-water turbiditic system evolving into littoral carbonate platform, *In: G. Nichols, E. Williams and C. Paola, eds. Sedimentary Processes, Environments and Basins: A Tribute to Peter Friend: International Association of Sedimentologists, Special Publication*. **38**, pp.401–456.
- Lewis, K. B. 1994. The 1500-km-long Hikurangi Channel: trench-axis channel that escapes its trench, crosses a plateau, and feeds a fan drift. *Geo-Marine Letters*. **14**, pp.19-28.
- Lewis, K.B. and Pettinga, J.R. 1993. The emerging, imbricate frontal wedge of the Hikurangi margin. *Sedimentary basins of the world*. **2**, pp.225–250.
- Lewis, K.B. and Barnes, P.M. 1999. Kaikoura Canyon, New Zealand: active conduit from near-shore sediment zones to trench-axis channel. *Marine Geology*. **162**, pp.39–69
- Lewis, K.B. and Pantin, H.M. 2002. Channel-axis, overbank and drift sediment waves in the southern Hikurangi Trough, New Zealand. *Marine Geology*. **192**(1-3), pp.123–151.
- Lewis, K.B., Collot, J.Y. and Lallemand, S.E. 1998. The dammed Hikurangi Trough: a channel-fed trench blocked by subducting seamounts and their wake avalanches (New Zealand-France GeodyNZ Project). *Basin Research*. **10**, pp.441–468.
- Li, P., Kneller, B., Thompson, P., Bozetti, G., and dos Santos, T. 2018. Architectural and facies organisation of slope channel fills: Upper Cretaceous Rosario Formation, Baja California, Mexico. *Marine and Petroleum Geology*. **92**, pp.632–649.
- Liang, C., Liu, C., Xie, X., Yu, X., He, Y., Chen, H., Zhou, Z., Tian, D., Lu, B., Mi, H., Li, M., Zhang, H. and Yang, Y. 2020. The role of large-scale mass wasting processes in

changing the sediment dispersal pattern in the deep-water Central Canyon of the northwestern South China Sea. *Marine and Petroleum Geology*. **122**(104693), pp.1–16.

Lindenkohl, A. 1885. Geology of the Sea-bottom in the approaches to New York Bay. *American Journal of Science*. **29**(174), pp.475–480.

Liu, Q., Kneller, B., Fallgatter, C., and Valdez Buso, V. 2018. Quantitative comparisons of depositional architectures of unconfined and confined turbidite sheet systems. *Sedimentary Geology*. **376**, pp.72–89.

Lowe, D.R. 1979. Sediment gravity flows: their classification and some problems of application to natural flows and deposits. *SEPM Special Publication, Society of Economic Paleontologists and Mineralogists*. **27**, pp.75–82.

Lowe, D.R. 1982. Sediment Gravity Flows: II. Depositional Models With Special Reference To The Deposits Of High-Density Turbidity Currents. *Journal of Sedimentary Petrology*. **52**(1), pp.279–297.

Lowe, D.R. and Guy, M. 2000. Slurry-flow deposits in the Britannia Formation (Lower Cretaceous), North Sea: a new perspective on the turbidity current and debris flow problem. *Sedimentology*. **47**, pp.31–70.

Lowe, D.R., Graham, S.A., Malkowski, M.A., and Das, B., 2019, The role of avulsion and splay development in deep-water channel systems: sedimentology, architecture, and evolution of the deep-water Pliocene Godavari “A” channel complex, India. *Marine and Petroleum Geology*. **105**, pp.81–99.

Macauley, R. V. and Hubbard, S. M. 2013. Slope channel sedimentary processes and stratigraphic stacking, Cretaceous Tres Pasos Formation slope system, Chilean Patagonia. *Marine and Petroleum Geology*. **41**, pp.146-162.

Macdonald, H.A., Peakall, J., Wignall, P.B. and Best, J. 2011. Sedimentation in deep-sea lobe-elements: implications for the origin of thickening-upward sequences. *Journal of the Geological Society*. [Online]. **168**(2), pp.319–332. Available from: <http://jgs.lyellcollection.org/cgi/doi/10.1144/0016-76492010-036>.

Maier, K.L., Fildani, A., Paull, C.K., Graham, S.A., McHargue, T.R., Caress, D.W. and McGann, M. 2011. The elusive character of discontinuous deep-water channels: new insights from Lucia Chica channel system, offshore California. *Geology*. **39**, pp.327–330.

Maier, K.L., Fildani, A., McHargue, T., Paull, C.K., Graham, S.A. and Caress, D.W. 2012. Deep-water punctuated channel migration: high-resolution subsurface data from the Lucia Channel System, offshore California. *Journal of Sedimentary Research*. **82**, pp.1–8.

Maier, K.L., Gales, J.A., Paull, C.K., Rosenberger, K., Talling, P.J., Simmons, S.M., Gwiazda, R., McGann, M., Cartigny, M.J.B., Lundsten, E., Anderson, K., Clare, M.A., Xu, J., Parsons, D., Barry, J.P., Wolfson-schwehr, M., Nieminski, N.M., and Sumner, E.J. 2019. Linking Direct Measurements of Turbidity Currents to Submarine Canyon-Floor Deposits. *Frontiers in Earth Science*. **7**(144), pp.1–18.

Manica, R. 2012. Sediment Gravity Flows : Study Based on Experimental Simulations *In: H. E. Schulz, A. L. A. Simões and R. J. Lobosco, eds. Hydrodynamics - Natural Water Bodies.*, pp.263–286.

Marsset, T., Droz, L., Dennielou, B. and Pichon, E. 2009. Cycles in the architecture of the Quaternary Zaire turbidite system: A possible link with climate *In: B. C. Kneller, O. J. Martinsen and W. D. McCaffrey, eds. SEPM Special Publication 92: External Controls on Deep-Water Depositional Systems.* SEPM Society for Sedimentary Geology, pp.89–106.

Martinsen, O. 1994. Mass movements *In: A. Maltman, ed. The geological deformation of sediments.* London, UK: Chapman & Hall, pp.127–165.

Marzo, M., Nijman, W., and Puigdefàbregas, C. 1988. Architecture of the Castissent fluvial sheet sandstones, Eocene, South Pyrenees, Spain. *Sedimentology*. **35**(5), pp.719–738.

Masalimova, L.U., Lowe, D.R., Mchargue, T., and Derksen, R. 2015. Interplay between an axial channel belt, slope gullies and overbank deposition in the Puchkirchen Formation in the Molasse Basin, Austria. *Sedimentology*. **62**(6), pp.1717–1748.

Masalimova, L.U., Lowe, D.R., Sharman, G.R., King, P.R., and Arnot, M.J. 2016. Outcrop characterization of a submarine channel-lobe complex: the lower Mount Messenger

Formation, Taranaki Basin, New Zealand. *Marine and Petroleum Geology*. **71**, pp.360–390.

Mayall, M. and Stewart, I. 2000. The Architecture of Turbidite Slope Channels *In: GCSSEPM Foundation 20th Annual Research Conference: Deep-Water Reservoirs of the World.*, pp.578–586.

Mayall, M., Jones, E. and Casey, M. 2006. Turbidite channel reservoirs — Key elements in facies prediction and effective development. *Marine and Petroleum Geology*. **23**, pp.821–841.

Mayall, M., Lonergan, L., Bowman, A., James, S., Mills, K., Primmer, T., Pope, D., Rogers, L. and Skeene, R. 2010. The response of turbidite slope channels to growth-induced seabed topography. *American Association of Petroleum Geologists Bulletin*. **94**(7), pp.1011-1030.

McArthur, A.D., and McCaffrey, W.D. 2019. Sedimentary architecture of detached deep-marine canyon heads: Examples from the East Coast Basin of New Zealand. *Sedimentology*. **66**, pp.1067-1101

McArthur, A.D. and Tek, D.E. 2021. Controls on the origin and evolution of deep-ocean trench-axial channels. *Geology*. **49**(8), pp.883-888.

McArthur, A.D., Claussmann, B., Bailleul, J., McCaffrey, W.D. and Clare, A. 2019. Variation in syn-subduction sedimentation patterns from inner to outer portions of deep-water fold and thrust belts: examples from the Hikurangi subduction margin of New Zealand. *In: J.A. Hammerstein, R. Di Cuia, M.A. Cottam, G. Zamora, R.W.H. Butler, eds. Fold and Thrust Belts: Structural Style, Evolution and Exploration Geological Society of London Special Publication*. **490**, London: The Geological Society of London; p. 490–545.

McArthur, A.D., Kane, I., Bozetti, G., Hansen, L. and Kneller, B.C. 2020. Supercritical flows overspilling from bypass-dominated submarine channels and the development of overbank bedforms. *The Depositional Record*. **6**(1), pp.21-40.

McArthur, A.D., Bailleul, J., Mahieux, G., Claussmann, B., Wunderlich, A. and McCaffrey, W.D. 2021. Deformation–sedimentation feedback and the development of anomalously

thick aggradational turbidite lobes: Outcrop and subsurface examples from the Hikurangi Margin, New Zealand. *Journal of Sedimentary Research*. **91**(4), pp.362-389.

McCaffrey, W. and Kneller, B. 2001. Process controls on the development of stratigraphic trap potential on the margins of confined turbidite systems and aids to reservoir evaluation. *AAPG Bulletin*. **85**(6), pp.971–988.

McCaffrey, W.D., Gupta, S. and Brunt, R. 2002. Repeated cycles of submarine channel incision, infill and transition to sheet sandstone development in the Alpine Foreland Basin, SE France. *Sedimentology*. **49**(3), pp.623–635.

McCave, I.N. and Carter, L. 1997. Recent sedimentation beneath the Deep Western Boundary Current off northern, New Zealand. *Deep-Sea Research Part I: Oceanographic Research Papers*. **44**, pp.1203–1237.

McHargue, T., Pycrz, M.J., Sullivan, M.D., Clark, J.D., Fildani, A., Romans, B.W., Covault, J.A., Levy, M., Posamentier, H.W. and Drinkwater, N.J. 2011. Architecture of turbidite channel systems on the continental slope: Patterns and predictions. *Marine and Petroleum Geology*. **28**(3), pp.728–743.

McHargue, T. R., Hodgson, D. M. and Shelef, E. 2021. Architectural Diversity of Submarine Lobate Deposits. *Frontiers in Earth Science*. **9**(632), pp.1-22.

Menard, H.W. 1955. Deep-sea channels, topography, and sedimentation. *American Association of Petroleum Geologists Bulletin*. **39**(2), pp.236–255.

Miall, A.D. 1985. Architectural-element analysis: A new method of facies analysis applied to fluvial deposits. *Earth-Science Reviews*. **22**, pp.261–308.

Middleton, G. V and Hampton, M.A. 1973. Part I. Sediment Gravity Flows: Mechanics of Flows and Deposition *In: G. V Middleton and A. H. Bouma, eds. Turbidites and Deep Water Sedimentation. SEPM (Society for Sedimentary Geology)*. Los Angeles, California, pp.1–38.

Middleton, G. V. and Hampton, M. A. 1976. Subaqueous sediment transport and deposition by sediment gravity flows. *In: D.J. Stanley and D.J.P. Swift, eds. Marine sediment transport and environmental management*. New York, United States: John Wiley & Sons, pp.197-218.

Migeon, S., Savoye, B. and Faugeres, J.C. 2000. Quaternary development of migrating sediment waves in the Var deep-sea fan; distribution, growth pattern, and implication for levee evolution. *Sedimentary Geology*. **133**(3-4), pp.265-293.

Migeon, S., Savoye, B., Zanella, E., Mulder, T., Faugeres, J.C. and Weber, O. 2001. Detailed seismic-reflection and sedimentary study of turbidite sediment waves on the Var sedimentary ridge (SE France); significance for sediment transport and deposition and for the mechanisms of sediment-wave construction. *Marine and Petroleum Geology*. **18**(2):179-208.

Migeon, S., Savoye, B., Babonneau, N. and Spy Andersson, F.L. 2004. Process of sediment-wave construction along the present Zaire deep-sea meandering channel: role of meanders and flow stripping. *Journal of Sedimentary Research*. **74**, pp.580–598.

Migeon, S., Mulder, T., Savoye, B. and Sage, F. 2012. Hydrodynamic processes, velocity structure and stratification in natural turbidity currents: Results inferred from field data in the Var Turbidite System. *Sedimentary Geology*. **245–246**, pp.48–62.

Miller, K.G., Kominz, M.A., Browning, J. V., Wright, J.D., Mountain, G.S., Katz, M.E., Sugarman, P.J., Cramer, B.S., Christie-Blick, N. and Pekar, S.F. 2005. The Phanerozoic record of global sea-level change. *Science*. **310**(5752), pp.1293–1298.

Millington, J., and Clark, J.D. 1995a. The Charo/Arro canyon-mouth sheet system, South-Central Pyrenees, Spain: A structurally influenced zone of sediment dispersal. *Journal of Sedimentary Research*. **B65**(4), pp.443–454.

Millington, J., and Clark, J.D. 1995b. Submarine canyon and associated base-of-slope sheet system: the Eocene Charo-Arro system, south-central Pyrenees, Spain, *In*: T.H. Nilsen, R.D. Shew, G.S. Steffens and J.R.J. Studlick, eds. *Atlas of Deep-Water Outcrops: American Association of Petroleum Geologists, Studies in Geology*. pp.150–156.

Miramontes, E., Eggenhuisen, J. T., Jacinto, R. S., Poneti, G., Pohl, F., Normandeau, A., Campbell, D. C. and Hernández-Molina, F. J. 2020. Channel-levee evolution in combined contour current–turbidity current flows from flume-tank experiments. *Geology*. **48**(4), pp.353-357.

Mitchell, N. 2004. Form of submarine erosion from confluences in Atlantic USA continental slope canyons. *American Journal of Science*. **304**, pp.590–611.

Mitchell, W.H., Whittaker, A.C., Mayall, M., Lonergan, L. and Pizzi, M. 2020. Quantifying the relationship between structural deformation and the morphology of submarine channels on the Niger Delta continental slope. *Basin Research*. **33**(1), pp.186–209.

Mohrig, D. and Marr, J.G. 2003. Constraining the efficiency of turbidity current generation from submarine debris flows and slides using laboratory experiments. *Marine and Petroleum Geology*. **20**, pp.883–899.

Mohrig, D. and Buttles, J. 2007. Deep turbidity currents in shallow channels. *Geology*. **35**(2), pp.155-158.

Mohrig, D., Ellis, C., Parker, G., Whipple, K.X., Hondzo, M. and Mohrig, D. 1998. Hydroplaning of subaqueous debris flows. *Geological Society of America Bulletin*. **110**(3), pp.387–394.

Mohrig, D., Elverhøi, A. and Parker, G. 1999. Experiments on the relative mobility of muddy subaqueous and subaerial debris flows, and their capacity to remobilize antecedent deposits. *Marine Geology*. **154**, pp.117–129.

Moore, J.C., Watkins, J.S., McMillen, K.J., Bachman, S.B., Leggett, J.K., Lundberg, N., Shipley, T.H., Stephan, J.F., Beghtel, F.W., Butt, A. and Didyk, B.M. 1982. Facies belts of the Middle America Trench and forearc region, southern Mexico: results from Leg 66 DSDP. *Geological Society, London, Special Publications*. **10**, p.77-94

Morris, E.A., Hodgson, D.M., Brunt, R.L. and Flint, S.S. 2014a. Origin, evolution and anatomy of silt-prone submarine external levees. *Sedimentology*. **61**(6), pp.1734–1763.

Morris, E.A., Hodgson, D.M., Flint, S.S., Brunt, R.L., Butterworth, P.J. and Verhaeghe, J. 2014b. Sedimentology, Stratigraphic Architecture, and Depositional Context of Submarine Frontal-Lobe Complexes. *Journal of Sedimentary Research*. **84**(9), pp.763–780.

Moscardelli, L. and Wood, L. 2008. New classification system for mass transport complexes in offshore Trinidad. *Basin Research*. **20**, pp.73–98.

Moscardelli, L., Wood, L. and Mann, P. 2006. Mass-transport complexes and associated processes in the offshore area of Trinidad and Venezuela. *AAPG Bulletin*. **90**(7), pp.1059–1088.

Mountjoy, J.J., Barnes, P.M. and Pettinga, J.R. 2009. Morphostructure and evolution of submarine canyons across an active margin: Cook Strait sector of the Hikurangi Margin, New Zealand. *Marine Geology*. **260**, pp.45–68.

Mountjoy, J.J., Howarth, J.D., Orpin, A.R., Barnes, P.M., Bowden, D.A., Rowden, A.A., Schimel, A.C.G., Holden, C., Horgan, H.J., Nodder, S.D., Patton, J.R., Lamarche, G., Gerstenberger, M., Micallef, A., Pallentin, A. and Kane, T. 2018. Earthquakes drive large-scale submarine canyon development and sediment supply to deep-ocean basins. *Science*. **4**(3), pp.1–8.

Mulder, T. and Alexander, J.A.N. 2001. The physical character of subaqueous sedimentary density flows and their deposits. *Sedimentology*. **48**, pp.269–299.

Mulder, T., Migeon, S., Savoye, B. and Faugères, J.-C. 2001. Inversely graded turbidite sequences in the deep Mediterranean: a record of deposits from flood-generated turbidity currents? *Geo-Marine Letters*. **21**, pp.86–93.

Mulder, T., Migeon, S., Savoye, B. and Faugères, J.-C. 2002. Reply to discussion by Shanmugam on Mulder et al. (2001, *Geo-Marine Letters* 21: 86 – 93) Inversely graded turbidite sequences in the deep Mediterranean. A record of deposits from flood-generated turbidity currents? *Geo-Marine Letters*. **22**, pp.112–120.

Mulder, T., Syvitski, J.P.M., Migeon, S., Faugères, J.-C., and Savoye, B. 2003. Marine hyperpycnal flows: initiation, behavior and related deposits. A review. *Marine and Petroleum Geology*. **20**, pp.861–882.

Mulder, T., Razin, P., and Faugeres, J. 2009. Hummocky cross-stratification-like structures in deep-sea turbidites: Upper Cretaceous Basque basins (Western Pyrenees, France). *Sedimentology*. **56**(4). pp.997–1015.

Muñoz, J.A. 1992. Evolution of a continental collision belt: ECORS-Pyrenees crustal balanced cross-section, *In*: K.R. McClay, ed. *Thrust Tectonics*: London, Chapman and Hall, pp.235–246.

Muñoz, J.A., McClay, K., and Poblet, J. 1994. Synchronous extension and contraction in frontal thrust sheets of the Spanish Pyrenees. *Geology*. **22**, pp.921–924.

Muñoz, J.-A., Beamud, E., Fernández, O., Arbués, P., Dinarès-Turell, J., and Poblet, J. 2013. The Ainsa Fold and thrust oblique zone of the central Pyrenees: Kinematics of a curved contractional system from paleomagnetic and structural data. *Tectonics*. **32**, pp.1142–1175.

Mutti, E. 1977. Distinctive thin-bedded turbidite facies and related depositional environments in the Eocene Hecho Group (South-central Pyrenees, Spain). *Sedimentology*. **24**, pp.107–131.

Mutti, E. 1984. The Hecho Eocene Submarine Fan System, South-Central Pyrenees, Spain. *Geo-Marine Letters*. **3**, pp.199–202.

Mutti, E. 1985. Turbidite systems and their relations to depositional sequences *In*: G. Zuffa, ed. *Provenance of Arenites*. Dordrecht, Netherlands: Reisel Publishing Company, pp.65–93.

Mutti, E. 1992. *Turbidite Sandstones*. Parma: Istituto di Geologia Università di Parma.

Mutti, E. 2019. Thin-bedded plumites: an overlooked deep-water deposit. *Journal of Mediterranean Earth Sciences*. **11**, pp.1–20.

Mutti, E. and Ricci Lucchi, F. 1972. Le torbiditi dell'Appennino settentrionale: introduzioni all'analisi di facies. *Memorie della Società Geologica Italiana*. **11**(2), pp.161–199.

Mutti, E. and Ricci Lucchi, F. 1975. Turbidite facies and facies association *In*: E. Mutti, G.C. Parea, F. Ricci Lucchi, M. Sagri, G. Zanzucchi, G. Ghibaudo, and S. Jaccarino, eds. *Examples of Turbidites Facies and Facies Association From Selected Formations of the Northern appenines. X International Congress of Sedimentology, Nice-75. Field Trip A*. pp.21-36.

Mutti, E. and Nilsen, T.H. 1981. Significance of intraformational rip-up clasts in deep-sea fan deposits *In: Proceedings of the International Association of Sedimentologists 2nd European Meeting*. Bologna, pp.117–119.

Mutti, E. and Normark, W.R. 1987. Comparing Examples of Modern and Ancient Turbidite Systems: Problems and Concepts *In*: J. K. Leggett and G. G. Zuffa, eds. *Marine Clastic Sedimentology*. London, UK: Graham and Trotman, pp.1–38.

Mutti, E. and Normark, W.R. 1991. An Integrated Approach to the Study of Turbidite Systems *In*: P. Weimer and M. H. Link, eds. *Seismic facies and sedimentary processes of submarine fans and turbidite systems*. New York: Springer-Verlag, pp.75–106.

Mutti, E., Seguret, M., and Sgavetti, M. 1988. Sedimentation and deformation in the Tertiary Sequences of the Southern Pyrenees. *American Association of Petroleum Geologists, Mediterranean Basins Conference Guidebook Field Trip*. **7**, pp.1–153.

Mutti, E., Davoli, G., Mora, S. and Papani, L. 1994. Internal stacking patterns of ancient turbidite systems from collisional basins *In*: P. Weimer, A. H. Bouma and B. F. Perkins, eds. *Submarine Fans and Turbidite Systems—Sequence Stratigraphy, Reservoir Architecture and Production Characteristics Gulf of Mexico and International.*, pp.257–268.

Mutti, E., Davoli, G., Tinterri, R., and Zavala, C. 1996. The importance of ancient fluvio-deltaic systems dominated by catastrophic flooding in tectonically active basins. *Memorie di Scienze Geologiche de Padova*. **48**. pp.233–291.

Mutti, E., Tinterri, R., Remacha, E., Mavilla, N., Angella, S., and Fava, L. 1999. An Introduction To the Analysis of Ancient Turbidite Basins From an Outcrop Perspective. *American Association of Petroleum Geologists, Continuing Education Course Notes, Series 39*: Tulsa, Oklahoma, USA, 96p.

Mutti, E., Tinterri, R., di Biase, D., Fava, L., Mavilla, N., Angella, S. and Calabrese, L. 2000. Delta-front facies associations of ancient flood-dominated fluvio-deltaic systems. *Sociedad Geológica de España, Revista*. **13**(2), pp.165–190.

Mutti, E., Tinterri, R., Benevelli, G., Biase, D. and Cavanna, G. 2003. Deltaic, mixed and turbidite sedimentation of ancient foreland basins. *Marine and Petroleum Geology*. **20**, pp.733–755.

Mutti, E., Bernoulli, D., Ricci, F. and Tinterri, R. 2009. Turbidites and turbidity currents from Alpine 'flysch' to the exploration of continental margins. *Sedimentology*. **56**, pp.267–318.

Muzzi Magalhaes, P. and Tinterri, R. 2010. Stratigraphy and depositional setting of slurry and contained (reflected) beds in the Marnoso-arenacea Formation (Langhian-Serravallian) Northern Apennines, Italy. *Sedimentology*. **57**, pp.1685–1720.

Nakajima, T. and Kneller, B.C. 2013. Quantitative analysis of the geometry of submarine external levées. *Sedimentology*. **60**(4), pp.877–910.

Nakajima, T. and Satoh, M. 2001. The formation of large mudwaves by turbidity currents on the levees of the Toyama deep-sea channel, Japan Sea. *Sedimentology*. **48**, pp.435–463.

Nakajima, T., Satoh, M. and Okamura, Y. 1998. Channel-levee complexes, terminal deep-sea fan and sediment wave fields associated with the Toyama Deep-Sea Channel system in the Japan Sea. *Marine Geology*. **147**(1-4), pp.25-41.

Nakajima, T., Peakall, J., McCaffrey, W.D., Paton, D.A. and Thompson, P.J.P. 2009. Outer-Bank Bars: A New Intra-Channel Architectural Element within Sinuous Submarine Slope Channels. *Journal of Sedimentary Research*. **79**(12), pp.872–886.

Naranjo-Vesga, J., Ortiz-Karpf, A., Wood, L., Jobe, Z., Paniagua-Arroyave, J.F., Shumaker, L., Mateus-Tarazona, D. and Galindo, P. 2020. Regional controls in the distribution and morphometry of deep-water gravitational deposits along a convergent tectonic margin. Southern Caribbean of Colombia. *Marine and Petroleum Geology*. **121**(104639), pp.1–24.

Nardin, T.R., Hein, F.J., Gorsline, D.S. and Edwards, B.D. 1979. A Review of Mass Movement Processes, Sediment and Acoustic Characteristics, and Contrasts in Slope and Base-of-slope Systems Versus Canyon-fill-basin Floor Systems. *SEPM Special Publication, Society of Economic Paleontologists and Mineralogists*. **27**, pp.61–73.

Nelson, C.H., Escutia, C., Goldfinger, C., Karabanov, E., Gutierrez-pastor, J. and DeBatist, M. 2009. External Controls On Modern Clastic Turbidite Systems : Three Case Studies. *External Controls on Deep-Water Depositional Systems. SEPM (Society for Sedimentary Geology)*. **92**, pp.57–76.

Nelson, C.H., Escutia, C., Damuth, J.E. and Twichell, D.C. 2011. Interplay Of Mass-Transport And Turbidite-System Deposits In Different Active Tectonic And Passive Continental Margin Settings: External And Local Controlling Factors. *Mass-Transport*

Deposits in Deepwater Settings. SEPM (Society for Sedimentary Geology). 96, pp.39–66.

Nemec, W. 1990. Aspects of sediment movement on steep delta slopes. *Special Publication of the International Association of Sedimentologists. 10*, pp.29–73.

Nicol, A., Mazengarb, C., Chanier, F., Rait, G., Uruski, C. and Wallace, L. 2007. Tectonic evolution of the active Hikurangi subduction margin, New Zealand, since the Oligocene. *Tectonics. 26*, pp.1–24.

Nijman, W. 1998. Cyclicity and basin axis shift in a piggyback basin: towards modelling of the Eocene Tremp-Ager Basin, South Pyrenees, Spain. In: A. Mascle, C. Puigdefàbregas, H.P. Luterbacher and M. Fernández, eds. *Cenozoic Foreland Basins of Western Europe: Geological Society of London, Special Publication. 134*, pp.135–162.

Nijman, W., and Puigdefàbregas, C. 1977. Coarse-grained point bar structure in a molasse-type fluvial system, Eocene Castisent sandstone formation, South Pyrenean Basin. *Canadian Society of Petroleum Geologists, Memoir. 5*, pp.487–510.

Normark, W.R. 1970. Growth Patterns of Deep-Sea Fans. *AAPG Bulletin. 54(11)*, pp.2170–2195.

Normark, W. R. 1978. Fan Valleys, channels, and depositional lobes on modern submarine fans; characters for recognition of sandy turbidite environments. *American Association of Petroleum Geologists Bulletin. 62(6)*, pp.912-931.

Normark, W.R., Piper, D.J.W., and Hess, G.R. 1979. Distributary channels, sand lobes, and mesotopography of Navy Submarine Fan, California Borderland, with applications to ancient fan sediments. *Sedimentology. 26(6)*, pp.749-774.

Normark, W.R., Hess, G.R., Stow, D.A.V. and Bowen, A.J. 1980. Sediment waves on the Monterey Fan levee: a preliminary physical interpretation. *Marine Geology. 37*, pp.1–18.

Normark, W.R., Posamentier, H. and Mutti, E. 1993. Turbidite systems: state of the art and future directions. *Reviews of Geophysics. 31(2)*, pp.91–116.

Normark, W.R., Piper, D.J.W., Posamentier, H., Pirmez, C. and Migeon, S. 2002. Variability in form and growth of sediment waves on turbidite channel levees. *Marine Geology*. **192**, pp.23–58.

Nugraha, H. D., Jackson, C. A. L., Johnson, H. D., Hodgson, D. M. and Reeve, M. T. 2019. Tectonic and oceanographic process interactions archived in Late Cretaceous to Present deep-marine stratigraphy on the Exmouth Plateau, offshore NW Australia. *Basin Research*. **31**(3), pp.405–430.

Nugraha, H.D., Jackson, C.A.-L., Johnson, H.D. and Hodgson, D.M. 2020. Lateral variability in strain along the toewall of a mass transport deposit: a case study from the Makassar Strait, offshore Indonesia. *Journal of the Geological Society*. **177**, pp.1261-1279.

Nwoko, J., Kane, I. and Huuse, M. 2020a. Megaclasts within mass-transport deposits: their origin, characteristics and effect on substrates and succeeding flows. *In: A. Georgiopoulou, L.A. Amy, S. Benetti, J.D. Chaytor, M.A. Clare, D. Gamboa, P.D.W. Haughton, J. Moernaut and J.J. Mountjoy, eds. Subaqueous Mass Movements and their Consequences: Advances in Process Understanding, Monitoring and Hazard Assessments, Geological Society, London, Special Publications*. **500**, pp.515-530.

Nwoko, J., Kane, I. and Huuse, M. 2020b. Mass transport deposit (MTD) relief as a control on post-MTD sedimentation: Insights from the Taranaki Basin, offshore New Zealand. *Marine and Petroleum Geology*. **120**(104489), pp.1–12.

Nyberg, B. and Howell, J.A. 2015. Is the present the key to the past? A global characterization of modern sedimentary basins. *Geology*. **43**(7), pp.643–646.

Ogata, K., Mutti, E., Andrea, G. and Tinterri, R. 2012. Tectonophysics Mass transport-related stratal disruption within sedimentary mélanges: Examples from the northern Apennines (Italy) and south-central Pyrenees (Spain). *Tectonophysics*. **568–569**, pp.185–199.

Okon, S.U., Zhong, Q. and He, Z. 2021. Experimental study on the vertical motion of colliding gravity currents. *Physics of Fluids*. **33**(016601), pp.1-11.

Oliveira, C.M.M., Hodgson, D.M., and Flint, S.S. 2011. Distribution of soft-sediment deformation structures in clinoform successions of the Permian Ecca Group, Karoo Basin, South Africa. *Sedimentary Geology*. **235**(3–4), pp.314–330.

Ortiz-karpf, A., Hodgson, D.M. and McCaffrey, W.D. 2015. The role of mass-transport complexes in controlling channel avulsion and the subsequent sediment dispersal patterns on an active margin: The Magdalena Fan, offshore Colombia. *Marine and Petroleum Geology*. **64**, pp.58–75.

Ortiz-karpf, A., Hodgson, D.M., Jackson, C.A. and McCaffrey, W.D. 2017. Influence Of Seabed Morphology And Substrate Composition On Mass-Transport Flow Processes And Pathways: Insights From The Magdalena Fan, Offshore Colombia. *Journal of Sedimentary Research*. **87**, pp.189–209.

Owen, G. 2003. Load structures: Gravity-driven sediment mobilization in the shallow subsurface. *In*: P. Van Rensbergen, R.R. Hillis, A.J. Maltman and C.K. Morley, eds. *Subsurface Sediment Mobilization: Geological Society of London, Special Publication*. **216**, pp.21–34.

Palm, F. A., Peakall, J., Hodgson, D. M., Marsset, T., Silva Jacinto, R., Dennielou, B., Babonneau, N. and Wright, T. J. 2021. Width variation around submarine channel bends: Implications for sedimentation and channel evolution. *Marine Geology*. **437**(106504), pp.1-22.

Patacci, M. 2016. A high-precision Jacob's staff with improved spatial accuracy and laser sighting capability. *Sedimentary Geology*. **335**, pp.66–69.

Patacci, M., Haughton, P.D.W. and McCaffrey, W.D. 2014. Rheological Complexity In Sediment Gravity Flows Forced To Decelerate Against A Confining Slope, Braux, SE France. *Journal of Sedimentary Research*. **84**(4), pp.270–277.

Paull, C.K., Caress, D.W., Ussler, W., Lundsten, E. and Meiner-Johnson, M. 2011. High-resolution bathymetry of the axial channels within Monterey and Soquel submarine canyons, offshore central California. *Geosphere*. **7**, pp.1077–1101.

Paull, C. K., Talling, P. J., Maier, K. L., Parsons, D., Xu, J., Caress, D. W., Gwiazda, R., Lundsten, E. M., Anderson, K., Barry, J. P., Chaffey, M., O'Reilly, T., Rosenberger, K. J., Gales, J. A., Kieft, B., McGann, M., Simmons, S. M., McCann, M., Sumner, E. J.,

Clare, M. A. and Cartigny, M. J. 2018. Powerful turbidity currents driven by dense basal layers. *Nature Communications*. **9**(4114), pp. 1-9.

Payros, A., Tosquella, J., Bernaola, G., Dinarès-turell, J., Orue-Etxebarria, X., and Pujalte, V. 2009. Filling the North European Early/Middle Eocene (Ypresian / Lutetian) boundary gap: Insights from the Pyrenean continental to deep-marine record. *Palaeogeography, Palaeoclimatology, Palaeoecology*. **280**(3–4), pp.313–332.

Peakall, J. and Sumner, E.J. 2015. Submarine channel flow processes and deposits: A process-product perspective. *Geomorphology*. **244**, pp.95–120

Peakall, J., McCaffrey, B. and Kneller, B. 2000a. A Process Model for the Evolution, Morphology, and Architecture of Sinuous Submarine Channels. *Journal of Sedimentary Research*. **70**(3), pp.434–448.

Peakall, J., Mccaffrey, W.D., Kneller, B., Stelling, C.E., Mchargue, T.R. and Schweller, W.J. 2000b. A process model for the evolution of fan submarine channels: Implications for sedimentary architecture *In: A. H. Bouma and C. Stone, eds. Fine-Grained Turbidite Systems: AAPG Memoir 72*. SEPM, pp.73–88.

Peakall, J., Amos, K. J., Keevil, G. M., Bradbury, P. W. and Gupta, S. 2007. Flow processes and sedimentation in submarine channel bends. *Marine and Petroleum Geology*. **24**, pp.470-486.

Peakall, J., Kane, I.A., Masson, D.G., Keevil, G., McCaffrey, W.D. and Corney, R. 2012. Global (latitudinal) variation in submarine channel sinuosity. *Geology*. **40**(1), pp.11–14.

Peakall, J., Best, J., Baas, J. H., Hodgson, D. M., Clare, M. A., Talling, P. J., Dorrell, R. M. and Lee, D. R. 2020. An integrated process-based model of flutes and tool marks in deep-water environments: Implications for palaeohydraulics, the Bouma sequence and hybrid event beds. *Sedimentology*. **67**(4), pp.1601-1666.

Pettinga, L., Jobe, Z., Shumaker, L. and Howes, N. 2018. Morphometric scaling relationships in submarine channel-lobe systems. *Geology*. **46**(9), pp.819-822.

Pickering, K.T., and Corregidor, J. 2000. 3D Reservoir-Scale Study of Eocene Confined Submarine Fans, South-Central Spanish Pyrenees. *Gulf Coast Section SEPM*

Foundation 20th Annual Research Conference, Deep-Water Reservoirs of the World.
pp.776–781.

Pickering, K.T. and Corregidor, J. 2005. Mass transport complexes and tectonic control on confined basin-floor submarine fans, Middle Eocene, south Spanish Pyrenees. *Geological Society, London, Special Publications.* **244**, pp.51–74.

Pickering, K.T., and Bayliss, N.J. 2009. Deconvolving tectono-climatic signals in deep-marine siliciclastics, Eocene Ainsa basin, Spanish Pyrenees: Seesaw tectonics versus eustasy. *Geology.* **37**(3), pp.203–206.

Pickering, K. T. and Cantalejo, B. 2015. Deep-marine environments of the Middle Eocene Upper Hecho Group, Spanish Pyrenees: Introduction. *Earth-Science Reviews.* **144**, pp.1-9.

Pickering, K.T., Clark, J.D., Smith, R.D.A., Hiscott, R.N., Ricci Lucchi, F. and Kenyon, N.H. 1995. Architectural element analysis of turbidite systems, and selected topical problems for sand-prone deep-water systems *In:* K. T. Pickering, R. N. Hiscott, N. H. Kenyon, F. R. Lucchi and R. D. A. Smith, eds. *Atlas of Deep Water Environments; Architectural Style in Turbidite systems.* London: Chapman and Hall, pp.1–10.

Pickering, K., Hodgson, D., Platzman, E., Clark, J. and Stephens, C. 2001. A new type of bedform produced by backfilling processes in a submarine channel, Late Miocene, Tabernas-Sorbas basin, SE Spain. *Journal of Sedimentary Research.* **71**(5), pp.692–704.

Picot, M., Droz, L., Marsset, T., Dennielou, B. and Bez, M. 2016. Controls on turbidite sedimentation: Insights from a quantitative approach of submarine channel and lobe architecture (Late Quaternary Congo Fan). *Marine and Petroleum Geology.* **72**, pp.423–446.

Piper, D.J.W. and Normark, W.R. 1983. Turbidite deposition patterns and flow characteristics, Navy Submarine Fan, Californian Borderland. *Sedimentology.* **30**(5), pp.681–694.

Piper, D.J.W. and Normark, W.R. 2001. Sandy fans - from Amazon to Hueneme and beyond. *AAPG Bulletin.* **85**(8), pp.1407–1438.

Piper, D.J.W. and Normark, W.R. 2009. Processes That Initiate Turbidity Currents and Their Influence on Turbidites: A Marine Geology Perspective. *Journal of Sedimentary Research*. **79**(6), pp.347–362.

Piper, D.J.W., Pirmez, C., Manley, P. L., Long, D., Flood, R. D., Normark, W. R. and Showers, W. (1997). Mass-transport deposits of the Amazon Fan. In: R.D. Flood, D.J.W. Piper, A. Klaus and L.C. Peterson, eds. *Proceedings of the Ocean Drilling Program, Scientific Results, Amazon Fan*. **155**, pp.109-146.

Piper, D.J.W., Cochonat, P. and Morrison, M.L. 1999a. The sequence of events around the epicentre of the 1929 Grand Banks earthquake: initiation of debris flows and turbidity current inferred from sidescan sonar. *Sedimentology*. **46**, pp.79–97.

Piper, D.J.W., Hiscott, R.N. and Normark, W.R. 1999b. Outcrop-scale acoustic facies analysis and latest Quaternary development of Hueneme and Dume submarine fans, offshore California. *Sedimentology*. **46**(1), pp.47–78.

Pirmez, C. and Flood, R.D. 1995. Morphology and structure of Amazon Channel. In: R.D. Flood, D.J.W. Piper and A. Klaus, eds. *Proceedings of the Ocean Drilling Program, Initial Reports*, **155**, pp. 23–45: College Station, TX.

Pirmez, C. and Imran, J. 2003. Reconstruction of turbidity currents in Amazon Channel. *Marine and Petroleum Geology*. **20**(6–8), pp.823–849.

Pirmez, C., Beaubouef, R.T., Friedmann, S.J. and Mohrig, D.C. 2000. Equilibrium Profile and Baselevel in Submarine Channels: Examples from Late Pleistocene Systems and Implications for the Architecture of Deepwater Reservoirs In: *GCSSEPM Foundation 20th Annual Research Conference Deep-Water Reservoirs of the World.*, pp.782–805.

Plaza-Faverola, A., Klaeschen, D., Barnes, P.M., Pecher, I., Henrys, S. and Mountjoy, J. 2012. Evolution of fluid expulsion and concentrated hydrate zones across the southern Hikurangi subduction margin, New Zealand: An analysis from depth migrated seismic data. *Geochemistry, Geophysics, Geosystems*. **13**(8), pp.1–21.

Pohl, F., Eggenhuisen, J.T., Tilston, M. and Cartigny, M.J.B. 2019. New flow relaxation mechanism explains scour fields at the end of submarine channels. *Nature Communications*. **10**(4425), pp.1-8.

Pohl, F., Eggenhuisen, J.T., Kane, I.A. and Clare, M.A. 2020a. Transport and burial of microplastics in deepmarine sediments by turbidity currents. *Environmental Science and Technology*. **54**, pp.4180–4189.

Pohl, F., Eggenhuisen, J., Cartigny, M., Tilston, M., De Leeuw, J., and Hermidas, N. 2020b. The influence of a slope break on turbidite deposits: an experimental investigation. *Marine Geology*. **424**(106160), pp.1-11.

Pope E.L., Talling P.J. and Carter L. 2016. Which earthquakes trigger damaging submarine mass movements: insights from a global record of submarine cable breaks? *Marine Geology*. **384**, pp.131-146.

Popescu, I., Lericolais, G., Panin, N., Wong, H. K. and Droz, L. 2001. Late Quaternary channel avulsions on the Danube deep-sea fan, Black Sea. *Marine Geology*. **179**(1-2): pp.25-37

Posamentier, H.W. 2003. Depositional elements associated with a basin floor channel-levee system: Case study from the Gulf of Mexico. *Marine and Petroleum Geology*. **20**(6–8), pp.677–690.

Posamentier, H.W. and Kolla, V. 2003. Seismic Geomorphology and Stratigraphy of Depositional Elements in Deep-Water Settings. *Journal of Sedimentary Research*. **73**(3), pp.367–388.

Posamentier, H.W. and Martinsen, O.J. 2011. The Character And Genesis Of Submarine Mass-Transport Deposits: Insights From Outcrop And 3d Seismic Data. *SEPM Special Publication. Mass-Transport Deposits in Deepwater Settings*. **96**, pp.7–38.

Postma, G. and Cartigny, M.J.B. 2014. Supercritical and subcritical turbidity currents and their deposits — A synthesis. *Geology*. **42**(11), pp.987–990.

Postma, G., Nemeč, W. and Kleinspehn, K.L. 1988. Large floating clasts in turbidites: a mechanism for their emplacement. *Sedimentary Geology*. **58**, pp.47–61.

Postma, G., Lang, J., Hoyal, D.C., Fedele, J.J., Demko, T., Abreu, V. and Pederson, K.H. 2021. Reconstruction of bedform dynamics controlled by supercritical flow in the channel-lobe transition zone of a deep-water delta (Sant Llorenç del Munt, north-east Spain, Eocene). *Sedimentology*. **68**, pp.1674–1697.

Poyatos-Moré, M. 2014. Physical Stratigraphy and Facies Analysis of the Castissent Tecto-Sedimentary Unit (South-Central Pyrenees, Spain) [PhD Thesis]: Universidad Autónoma de Barcelona, 282 p.

Prather, B.E. 2003. Controls on reservoir distribution, architecture and stratigraphic trapping in slope settings trapping in slope settings. *Marine and Petroleum Geology*. **20**, pp.529–545.

Prather, B.E., Booth, J.R., Steffens, G.S., and Craig, P.A. 1998. Classification, Lithologic Calibration, and Stratigraphic Succession of Seismic Facies of Intraslope Basins, Deep-Water Gulf of Mexico. *American Association of Petroleum Geologists Bulletin*. **82**(5A), pp.701–728.

Prather, B.E., O'Byrne, C., Pirmez, C. and Sylvester, Z. 2017. Sediment partitioning, continental slopes and base-of-slope systems. *Basin Research*. **29**(3), pp.394–416.

Prélat, A. and Hodgson, D.M. 2013. The full range of turbidite bed thickness patterns in submarine lobes: controls and implications. *Journal of the Geological Society*. **170**(1), pp.209–214.

Prélat, A., Hodgson, D.M. and Flint, S.S. 2009. Evolution, architecture and hierarchy of distributary deep-water deposits: a high-resolution outcrop investigation from the Permian Karoo Basin, South Africa. *Sedimentology*. **56**(7), pp.2132–2154.

Prélat, A., Covault, J.A., Hodgson, D.M., Fildani, A. and Flint, S.S. 2010. Intrinsic controls on the range of volumes, morphologies, and dimensions of submarine lobes. *Sedimentary Geology*. **232**(1–2), pp.66–76.

Prins, M.A. and Postma, G. 2000. Effects of climate, sea level, and tectonics unravelled for last deglaciation turbidite records of the Arabian sea. *Geology*. **28**, pp.375–378.

Privat, A.M.J., Hodgson, D.M., Jackson, C.A.L., Schwarz, E. and Peakall, J. 2021. Evolution from syn-rift carbonates to early post-rift deep-marine intraslope lobes: The role of rift basin physiography on sedimentation patterns. *Sedimentology*. **68**, pp.2563–2605.

Puigdefàbregas, C., and Souquet, P. 1986. Tectono-sedimentary cycles and depositional sequences of the Mesozoic and Tertiary from the Pyrenees. *Tectonophysics*. **129**, pp.173–203.

Qin, Y., Alves, T. M., Constantine, J., and Gamboa, D. 2017. The role of mass wasting in the progressive development of submarine channels (Espírito Santo Basin, SE Brazil). *Journal of Sedimentary Research*. **87**, pp.500–516.

Reading, H.G. and Richards, M. 1994. Turbidite systems in deep-water basin margins classified by grain size and feeder system. *AAPG Bulletin Bulletin*. **78**(5), pp.792–822.

Rebesco, M., Hernández-molina, F.J., Rooij, D. Van and Wåhlin, A. 2014. Contourites and associated sediments controlled by deep-water circulation processes: State-of-the-art and future considerations. *Marine Geology*. **352**, pp.111–154.

Remacha, E., and Fernández, L.P. 2003. High-resolution correlation patterns in the turbidite systems of the Hecho Group (South-Central Pyrenees, Spain). *Marine and Petroleum Geology*. **20**(6–8), pp.711–726.

Remacha, E., Fernandez, L.P., and Maestro, E. 2005. The transition between sheet-like lobe and basin-plain turbidites in the Hecho Basin (South-Central Pyrenees, Spain). *Journal of Sedimentary Research*. **75**(5), pp.798–819.

Ribó, M., Puig, P., Muñoz, A., Lo Iacono, C., Masqué, P., Palanques, A., Acosta, J., Guillén, J. and Ballesteros, M.G. 2016. Morphobathymetric analysis of the large fine-grained sediment waves over the Gulf of Valencia continental slope (NW Mediterranean). *Geomorphology*. **253**, pp.22–37.

Ricci Lucchi, F. and Valmori, E. 1980. Basin-wide turbidites in a Miocene, over-supplied deep-sea plain: a geometrical analysis. *Sedimentology*. **27**, pp.241–270.

Ridente, D., Fogliani, F., Minisini, D., Trincardi, F. and Verdicchio, G. 2007. Shelf-edge erosion, sediment failure and inception of Bari Canyon on the Southwestern Adriatic Margin (Central Mediterranean). *Marine Geology*. **246**, pp.193–207.

Romans, B.W., Castelltort, S., Covault, J.A., Fildani, A. and Walsh, J.P. 2016. Environmental signal propagation in sedimentary systems across timescales. *Earth-Science Reviews*. **153**, pp.7–29.

Ross, W.C., Halliwell, B.A., May, J.A., Watts, D.E. and Syvitski, J.P.M. 1994. Slope readjustment: a new model for the development of submarine fans and aprons. *Geology*. **22**(6), pp.511–514.

Sanders, J.E. 1965. *Primary Sedimentary Structures Formed By Turbidity Currents And Related Resedimentation Mechanisms*. Tulsa, OK, United States: Society of Economic Paleontologists and Mineralogists, SEPM (Society for Sedimentary Geology).

Savoie, B., Piper, D.J.W. and Droz, L. 1993. Plio-Pleistocene evolution of the Var deep-sea fan off the French Riviera. *Marine and Petroleum Geology*. **10**, pp.550-571.

Sawyer, D.E., Flemings, P.B., Shipp, R.C. and Winker, C.D. 2007. Seismic geomorphology, lithology, and evolution of the late Pleistocene Mars-Ursa turbidite region, Mississippi Canyon area, northern Gulf of Mexico. *AAPG Bulletin*. **91**(2), pp.215–234.

Sawyer, D., Flemings, P.B. and Nikolinakou, M. 2014. Continuous deep-seated slope failure recycles sediments and limits levee height in submarine channels. *Geology*. **42**, pp.15–18.

Schultz, M.R., Fildani, A., Cope, T.D., and Graham, S.A. 2005. Deposition and stratigraphic architecture of an outcropping ancient slope system: Tres Pasos Formation, Magallanes Basin, southern Chile. In: D.M. Hodgson and S.S. Flint, eds. *Submarine Slope Systems: Processes and Product: Geological Society of London, Special Publication*. **244**, pp.27-50.

Schwab, A., Cronin, B. and Ferreira, H. 2007. Seismic expression of channel outcrops: Offset stacked versus amalgamated channel systems. *Marine and Petroleum Geology*. **24**(6–9), pp.504–514.

Schwenk, T., Spieß, V., Breitzke, M., and Hübscher, C. 2005. The architecture and evolution of the Middle Bengal Fan in vicinity of the active channel-levee system imaged by high-resolution seismic data. *Marine and Petroleum Geology*. **22**(5), pp.637–656.

Scotchman, J.I., Bown, P., Pickering, K.T., Boudagher-fadel, M., Bayliss, N.J., and Robinson, S.A. 2015. A new age model for the middle Eocene deep-marine Ainsa Basin, Spanish Pyrenees. *Earth-Science Reviews*. **144**, pp.10–22.

Séguret, M. 1972. Étude tectonique des nappes et series décollées de la partie centrale du versant sud der Pyrénées [Ph.D. Thesis]: Publications de l'Universite de Sciences et Techniques de Languedoc, serie Geologie Structurale, **2**, Montpellier, 188 p.

Sgavetti, R., 1991, Photostratigraphy of ancient turbidite systems, *In*: P. Weimer and M.H., Link, eds. *Seismic facies and sedimentary process of submarine fans and turbidite systems*: New York, Springer, pp.107–125.

Shanmugam, G. 2000. 50 Years of the Turbidite Paradigm (1950s-1990s): Deep Water Processes and Facies Models - a Critical Perspective. *Mar. Pet. Geol.* **17**(2), pp.285–342.

Shanmugam, G. 2002. Discussion on Mulder et al . (2001, *Geo-Marine Letters* 21: 86 – 93) Inversely graded turbidite sequences in the deep Mediterranean. A record of deposits from flood-generated turbidity currents? *Geo-Marine Letters.* **22**, pp.108–111.

Shanmugam, G. 2016. Submarine fans : A critical retrospective (1950-2015). *Journal of Palaeogeography.* **5**(2), pp.110–184.

Shanmugam, G. and Muiola, R.J. 1988. Submarine Fans: Characteristics, Models, Classification, and Reservoir Potential. *Earth-Science Reviews.* **24**(6), pp.383–428.

Sharman, G. R., Graham, S. A., Masalimova, L. U., Shumaker, L. E., and King, P. R. 2015. Spatial patterns of deformation and paleoslope estimation within the marginal and central portions of a basin-floor mass-transport deposit, Taranaki Basin, New Zealand. *Geosphere.* **11**, pp.266–306

Shepard, F.P. 1963. *Submarine Geology* 2nd ed. California: Harper and Row.

Shumaker, L. E., Jobe, Z. R., Johnstone, S. A., Pettinga, L. A., Cai, D. X. and Moody, J. D. 2018. Controls on submarine channel-modifying processes identified through morphometric scaling relationships. *Geosphere.* **14**(5), pp.2171-2187.

Slotman, A. and Cartigny, M. J. B. 2020. Cyclic steps: Review and aggradation-based classification. *Earth-Science Reviews.* **201**(102949), pp.1-30.

Sohn, Y.K. 2000. Depositional Processes Of Submarine Debris Flows In The Miocene Fan Deltas, Pohang Basin, SE Korea With Special Reference To Flow Transformation. *Journal of Sedimentary Research*. **70**(3), pp.491–503.

Soler-Sampere, M., and Garrido-Megías, A. 1970. La terminación occidental del manto de Cotiella. *Pirineos*. **98**, pp.5–12.

Soutter, E.L., Kane, I.A., and Huse, M. 2018. Giant submarine landslide triggered by Paleocene mantle plume activity in the North Atlantic. *Geology*. **46**(6), pp.511–514.

Soutter, E.L., Bell, D., Cumberpatch, Z.A., Ferguson, R.A., Spychala, Y.T., Kane, I.A. and Eggenhuisen, J.T. 2021. The Influence of Confining Topography Orientation on Experimental Turbidity Currents and Geological Implications. *Frontiers in Earth Science*. **8**(620), pp.1-25.

Sømme, T.O., Helland-hansen, W., Martinsen, O.J. and Thurmond, J.B. 2009. Relationships between morphological and sedimentological parameters in source-to-sink systems: A basis for predicting semi-quantitative characteristics in subsurface systems. *Basin Research*. **21**(4), pp.361–387.

Southern, S.J., Patacci, M., Felletti, F. and McCaffrey, W.D. 2015. Influence of flow containment and substrate entrainment upon sandy hybrid event beds containing a co-genetic mud-clast-rich division. *Sedimentary Geology*. **321**, pp.105–122.

Southern, S.J., Kane, I.A., Warchoř, M.J., Porten, K.W. and Mccaffrey, W.D. 2017. Hybrid event beds dominated by transitional-flow facies: character, distribution and significance in the Maastrichtian Springar Formation, north-west Vøring Basin, Norwegian Sea. *Sedimentology*. **64**, pp.747–776.

Spencer, J.W. 1905. The submarine great canyon of the Hudson River. *American Journal of Science*. **19**(109), pp.1–15.

Sprague, A.R.G., Garfield, T.R., Goulding, F.J., Beaubouef, R.T., Sullivan, M.D., Rossen, C., Champion, K.M., Sickafoose, D.K., Abreu, V., Schellpeper, M.E., Jensen, G.N., Jennette, D.C., Pirmez, C., Dixon, B.T., Ying, D., Ardill, J., Mohrig, D.C., Porter, M.L., Farrell, M.E. and Mellere, D. 2005. Integrated slope channel depositional models: the key to successful prediction of reservoir presence and quality in offshore West Africa *In: CIPM - E-Exitep 2005, Feb 20-23, 2005, Veracruz, México.*, pp.1–13.

Spychala, Y.T., Hodgson, D.M., Elat, A.P.R., Kane, I.A., Flint, S.S. and Mountney, N.P. 2017a. Frontal and lateral submarine lobe fringes: comparing sedimentary facies, architecture and flow Processes. *Journal of Sedimentary Research*. **87**, pp.75–96.

Stevenson, C.J., Talling, P.J. and Masson, D.G. 2014. The spatial and temporal distribution of grain-size breaks in turbidites. *Sedimentology*. **61**, pp.1120–1156.

Stevenson, C.J., Talling, P.J., Wynn, R.B., Masson, D.G., Hunt, J.E., Frenz, M., Akhmetzhanov, A. and Cronin, B.T. 2013. The flows that left no trace: Very large-volume turbidity currents that bypassed sediment through submarine channels without eroding the sea floor. *Marine and Petroleum Geology*. **41**(1), pp.186–205.

Stevenson, C.J., Jackson, C.A., Hodgson, D.M., Hubbard, S.M. and Eggenhuisen, J.T. 2015. Deep-water sediment bypass. *Journal of Sedimentary Research*. **85**, pp.1058–1081.

Stevenson, C.J., Feldens, P., Georgiopolou, A., Schönke, M., Krastel, S., Piper, D.J.W., Lindhorst, K., and Mosher, D. 2018. Reconstructing the sediment concentration of a giant submarine gravity flow. *Nature Communications*. **9**(2616), pp.1–7.

Stow, D.A.V. 1986. Deep clastic seas. *In*: H.G. Reading, ed. *Sedimentary Environments and Facies*. **2**, pp.399-444. Blackwell, Oxford.

Stow, D.A. V and Shanmugam, G. 1980. Sequence of structures in fine-grained turbidites: comparison of recent deep-sea and ancient flysch sediments. *Sedimentary Geology*. **25**, pp.23–42.

Stow, D.A.V and Piper, D.J.W. 1984. Deep-water fine-grained sediments: facies models. *Geological Society, London, Special Publications*. **15**, pp.611–646.

Stow, D.A.V and Mayall, M. 2000. Deep-water sedimentary systems: New models for the 21st century. *Marine and Petroleum Geology*. **17**, pp.125–135.

Stow, D.A. V., Reading, H.G. and Collinson, J.D. 1996. Deep Seas *In*: H. G. Reading, ed. *Sedimentary environments; processes, facies and stratigraphy*. Blackwell Science, pp.395–453.

- Stow, D.A.V., Faugeres, J.-C., Viana, A. and Gonthier, E. 1998. Fossil contourites: a critical review. *Sedimentary Geology*. **115**, pp.3–31.
- Stow, D.A.V., Hunter, S., Wilkinson, D. and Hernández-Molina, F.J. 2008. The Nature of Contourite Deposition *In*: M. Rebesco and A. Camerlenghi, eds. *Developments in Sedimentology*. Elsevier B.V., pp.143–156.
- Strachan, L.J. 2002. Slump-initiated and controlled syndepositional sandstone remobilization: an example from the Namurian of County Clare, Ireland. *Sedimentology*. **49**, pp.25–41.
- Strachan, L.J. 2008. Flow transformations in slumps: a case study from the Waitemata Basin, New Zealand. *Sedimentology*. **55**, pp.1311-1332.
- Straub, K.M., Mohrig, D., McElroy, B., Buttles, J. and Pirmez, C. 2008. Interactions between turbidity currents and topography in aggrading sinuous submarine channels: A laboratory study. *Geological Society of America Bulletin*. **120**(3/4), pp.368–385.
- Straub, K.M., Mohrig, D., Buttles, J., McElroy, B. and Pirmez, C. 2011. Quantifying the influence of channel sinuosity on the depositional mechanics of channelized turbidity currents: A laboratory study. *Marine and Petroleum Geology*. **28**(3), pp.744-760.
- Sumner, E.J., Talling, P.J. and Amy, L.A. 2009. Deposits of flows transitional between turbidity current and debris flow. *Geology*. **37**(11), pp.991–994.
- Sullivan, M. D., Jensen, G. N., Goulding, F. J., Jennette, D. C., Foreman, J. L. and Stern, D. 2000. Architectural Analysis of Deep-Water Outcrops: Implications for Exploration and Development of the Diana Sub-Basin, Western Gulf of Mexico. *In*: GCSSEPM Foundation 20th Annual Research Conference, Deep-Water Reservoirs of the World. pp.1010-1031.
- Swallow, J.C. and Worthington, L. V. 1961. An observation of a deep countercurrent in the Western North Atlantic. *Deep-Sea Research*. **8**, pp.1–19.
- Sylvester, Z., Pirmez, C. and Cantelli, A. 2011. A model of submarine channel-levee evolution based on channel trajectories: Implications for stratigraphic architecture. *Marine and Petroleum Geology*. **28**(3), pp.716–727.

Symons, W.O., Sumner, E.J., Talling, P.J., Cartigny, M.J.S. and Clare, M.A. 2016. Large-scale sediment waves and scours on the modern seafloor and their implications for the prevalence of supercritical flows. *Marine Geology*. **371**, pp.130-148.

Talling, P.J. 2013. Hybrid submarine flows comprising turbidity current and cohesive debris flow: Deposits, theoretical and experimental analyses, and generalized models. *Geosphere*. **9**(3), pp.460–488.

Talling, P.J. 2014. On the triggers, resulting flow types and frequencies of subaqueous sediment density flows in different settings. *Marine Geology*. **352**, pp.155–182.

Talling, P.J., Amy, L.A., Wynn, R.B., Peakall, J. and Robinson, M. 2004. Beds comprising debrite sandwiched within co-genetic turbidite: origin and widespread occurrence in distal depositional environments. *Sedimentology*. **51**, pp.163–194.

Talling, P.J., Wynn, R.B., Masson, D.G., Frenz, M., Cronin, B.T., Schiebel, R., Akhmetzhanov, A., Dallmeier-Tiessen, S., Benetti, S., Weaver, P.P.E., Georgiopoulou, A., Zuhlsdorff, C. and Amy, L.A. 2007. Onset of submarine debris flow deposition far from original giant landslide. *Nature*. **450**, pp.541–544.

Talling, P.J., Wynn, R.B., Schmitt, D.N., Rixon, R., Sumner, E. and Amy, L. 2010. How did thin submarine debris flows carry boulder-sized intraclasts for remarkable distances across low gradients to the far reaches of the mississippi fan? *Journal of Sedimentary Research*. **80**, pp.829–851.

Talling, P.J., Masson, D.G., Sumner, E.J. and Malgesini, G. 2012. Subaqueous sediment density flows: Depositional processes and deposit types. *Sedimentology*. **59**(7), pp.1937–2003.

Talling, P.J., Allin, J., Armitage, D.A., Arnott, R.W.C., Cartigny, M.J.B., Clare, M.A., Felletti, F., Covault, J.A., Girardclos, S., Hansen, E., Hill, P.R., Hiscott, R.N., Hogg, A.J., Clarke, J.H., Jobe, Z.R., Malgesini, G., Mozzato, A., Naruse, H., Parkinson, S.A.M., Peel, F.J., Piper, D.J.W., Pope, E.D., Postma, G., Rowley, P., Sguazzini, A., Stevenson, C.J., Sumner, E.J., Sylvester, Z., Watts, C. and Xu, J. 2015. Key Future Directions For Research On Turbidity Currents And Their Deposits. *Journal of Sedimentary Research*. **85**, pp.153–169.

Tek, D.E., Poyatos-Moré, M., Patacci, M., McArthur, A.D., Colombera, L., Cullen, T.M. and McCaffrey, W.D. 2020. Syndepositional tectonics and mass-transport deposits control channelized, bathymetrically complex deep-water systems (Aínsa depocenter, Spain). *Journal of Sedimentary Research*. **90**(7), pp.729–762.

Tek, D.E., McArthur, A.D., Poyatos-Moré, M., Colombera, L., Patacci, M., Craven, B. and McCaffrey, W.D. 2021a. Relating seafloor geomorphology to subsurface architecture: how mass-transport deposits and knickpoint-zones build the stratigraphy of the deep-water Hikurangi Channel. *Sedimentology*. doi: 10.1111/sed.12890

Tek, D.E., McArthur, A.D., Poyatos-Moré, M., Colombera, L., Allen, C., Patacci, M. and McCaffrey, W.D. 2021b. Controls on the architectural evolution of deep-water channel overbank sediment wave fields: insights from the Hikurangi Channel, offshore New Zealand. *New Zealand Journal of Geology and Geophysics*. doi.org/10.1080/00288306.2021.1978509.

Timbrell, G. 1993. Sandstone architecture of the Balder Formation depositional system, UK Quadrant 9 and adjacent areas. In: J.P. Parker, ed. *Petroleum Geology of Northwest Europe: Proceedings of the 4th Conference*. *Petroleum Geology Conference series, London, United Kingdom*. **4**. London: The Geological Society of London, pp.107-121.

Tinterri, R. 2011. Combined flow sedimentary structures and the genetic link between sigmoidal- and hummocky-cross stratification. *GeoActa*. **10**, pp.1–43.

Tinterri, R., Drago, M., Consonni, A., Davoli, G. and Mutti, E. 2003. Modelling subaqueous bipartite sediment gravity flows on the basis of outcrop constraints: first results. *Marine and Petroleum Geology*. **20**, pp.911–933.

Tinterri, R. and Tagliaferri, A. 2015. The syntectonic evolution of foredeep turbidites related to basin segmentation: Facies response to the increase in tectonic confinement. *Marine and Petroleum Geology*. **67**, pp.81–110.

Tőkés, L. and Patacci, M. 2018. Quantifying tabularity of turbidite beds and its relationship to the inferred degree of basin confinement. *Marine and Petroleum Geology*. **97**, pp.659–671.

Vail, P.R., Mitchum, R.M. and Thompson, S. 1977. Seismic Stratigraphy and Global Changes of Sea Level , Part 3: Relative Changes of Sea Level from Coastal Onlap In:

C. W. Payton, ed. *Seismic Stratigraphy—Applications to Hydrocarbon Exploration: American Association of Petroleum Geologists Memoir 26.*, pp.63–81.

Van Lunsen, H. 1970. Geology of the Ara-Cinca region, Spanish Pyrenees. *Geologica Ultraiectina*. **16**, 119 p.

Van Wagoner, J.C., Posamentier, H.W., Mitchum, R.M., Vail, P.R., Sarg, J.F., Loutit, T.S. and Hardenbol, J. 1988. An overview of the fundamentals of sequence stratigraph and key definitions *In: C. K. Wilgus, H.Posamenier, C. A. Ross and C. G. St. C.Kendall, eds. SEPM (Society of Economic Paleontologists and Mineralogists) Special Publication 42: Sea-Level Changes - An Integrated Approach.*, pp.39–45.

Vendettuoli, D., Clare, M.A., Clarke, J.E.H., Vellinga, A., Hizzet, J., Hage, S., Cartigny, M.J.B., Talling, P.J., Waltham, D., Hubbard, S.M., Stacey, C. and Lintern, D.G. 2019. Daily bathymetric surveys document how stratigraphy is built and its extreme incompleteness in submarine channels. *Earth and Planetary Science Letters*. **515**, pp.231-247.

Walker, R.G. 1967. Turbidite Sedimentary Structures And Their Relationship To Proximal And Distal Depositional Environments. *Journal of Sedimentary Research*. **37**(1), pp.25–43.

Walker, R.G. 1970. Review of the geometry and facies organization of turbidites and turbidite-bearing basins. *In: Flysch sedimentology in North America*. Special Paper - Geological Association of Canada, Toronto, ON, Canada, **7**, pp.219-251.

Walker, R.G. 1978. Deep-Water Sandstone Facies and Ancient Submarine Fans: Models for Exploration for Stratigraphic Traps. *AAPG Bulletin*. **62**(6), pp.932–966.

Walker, R.G. and Mutti, E. 1973. Turbidite Facies and Facies Associations *In: Turbidites and Deep Water Sedimentation. SEPM (Society for Sedimentary Geology)*. pp.119–157.

Wallace, L. M., Beavan, J., McCaffrey, R. and Darby, D. 2004. Subduction zone coupling and tectonic block rotations in the North Island, New Zealand. *Journal of Geophysical Research*. **109**(B12406), pp.1–21.

Wallace, L. M., Barnes, P., Beavan, J., Dissen, R. Van, Litchfield, N., Mountjoy, J., Langridge, R., Lamarche, G. and Pondard, N. 2012. The kinematics of a transition from

subduction to strike-slip: An example from the central New Zealand plate boundary. *Journal of Geophysical Research*. **117**, pp.1–24.

Wang, Z., Xu, J., Talling, P.J., Cartigny, M.J., Simmons, S.M., Gwiazda, R., Paull, C.K., Maier, K.L. and Parsons, D.R. 2020. Direct evidence of a high-concentration basal layer in a submarine turbidity current. *Deep Sea Research Part I*. **161**(103300), pp.1-8.

Ward, N.I.P., Alves, T.M., and Blenkinsop, T.G. 2018. Submarine sediment routing over a blocky mass-transport deposit in the Espírito Santo Basin, SE Brazil. *Basin Research*. **30**(4), pp.816–834.

Watson, S.J., Mountjoy, J.J. and Crutchley, G.J. 2020. Tectonic and geomorphic controls on the distribution of submarine landslides across active and passive margins, eastern New Zealand. *In: A. Georgiopoulou, L.A. Amy, S. Benetti, J.D. Chaytor, M.A. Clare, D. Gamboa, P.D.W. Haughton, J. Moernaut, and J.J. Mountjoy, eds. Subaqueous Mass Movements and their Consequences: Advances in Process Understanding, Monitoring and Hazard Assessments, Geological Society, London, Special Publications*. **500**(1), pp.477-494.

Weimer, P. and Slatt, R.M. 2006. Deepwater - Reservoir Elements: Mass-Transport Deposits and Slides *In: Introduction to the Petroleum Geology of Deepwater Settings. AAPG Studies in Geology 57.*, pp.419–456.

Wells, M. and Cossu, R. 2013. The possible role of Coriolis forces in structuring large-scale sinuous patterns of submarine channel – levee systems The possible role of Coriolis forces in structuring large-scale sinuous patterns of submarine channel – levee systems. *Philosophical Transactions of the Royal Society A*. **371**(2004), pp.1–19.

Wells, M.G. and Dorrell, R.M. 2021. Turbulence Processes Within Turbidity Currents. *In: P. Moin and H.A. Stone, eds. Annual Review of Fluid Mechanics*. **53**. Palo Alto: Annual Reviews, pp.59-83.

Wood, R. and Davy, B. 1994. The Hikurangi Plateau. *Marine Geology*. **118**, pp.153–173.

Woodcock, N.H. 1979. The use of slump structures as palaeoslope orientation estimators. *Sedimentology*. **26**, pp.83–99.

Wüst, G. 1933. Thermometric measurement of depth. *Hydrographic Review*. **10**(2), pp.28-49.

Wu, N., Jackson, C.A-L., Johnson, H.D., Hodgson, D.M., Clare, M.A., Nugraha, H.D. and Li, W. 2021. The formation and implications of giant blocks and fluid escape structures in submarine lateral spreads. *Basin Research*. <https://doi.org/10.1111/bre.12532>

Wynn, R.B. and Stow, D.A.V. 2002. Classification and characterisation of deep-water sediment waves. *Marine Geology*. **192**, pp.7–22.

Wynn, R.B., Kenyon, N.H., Masson, D.G., Stow, D.A. V and Weaver, P.P.E. 2002. Channel-Lobe Transition Zones. *AAPG Bulletin*. **86**(8), pp.1441–1462.

Wynn, R.B., Cronin, B.T. and Peakall, J. 2007. Sinuous deep-water channels: Genesis, geometry and architecture. *Marine and Petroleum Geology*. **24**(6–9), pp.341–387.

Xu, J.P. 2011. Measuring currents in submarine canyons: Technological and scientific progress in the past 30 years. *Geosphere*. **7**(4), pp.868–876.

Xu, J.P., Barry, J.P. and Paull, C.K. 2013. Small-scale turbidity currents in a big submarine canyon. *Geology*. **41**(2), pp.143–146.

Zavala, C., Arcuri, M., Meglio, M. Di, Diaz, H.G. and Contreras, C. 2011. A Genetic Facies Tract for the Analysis of Sustained Hyperpycnal Flow Deposits *In*: R. M. Slatt and C. Zavala, eds. *Sediment transfer from shelf to deep water—Revisiting the delivery system: AAPG Studies in Geology.*, pp.31–52.

Zhong, G. and Peng, X. 2021. Transport and accumulation of plastic litter in submarine canyons—The role of gravity flows. *Geology*. **49**(5), pp.581-586.

9 Appendices

Appendix 1 – Table summarizing the minimum, maximum and average values of various dimensional and dip parameters exhibited by the variety of channel-related features described on the seafloor.

	Landward				Oceanward				All			
	Min.	Max.	Mean	N	Min.	Max.	Mean	N	Min.	Max.	Mean	N
Top channel wall / levee crest depth (m)	2592.2	2781.3	2674.9	28	2691	2869.7	2767.9	22	2592.2	2869.7	2715.8	50
Edge channel floor depth (m)	2809.862	3036.011	2939.1	28	2830.761	3043.455	2938.4	28	2809.862	3043.5	2938.7	56
Channel floor width (m)	N/A	N/A	N/A	N/A	N/A	N/A	N/A	N/A	773.6	4638.8	2571.2	28
Channel wall width (m)	1585.7	9438.8	5119.4	28	1000.3	7171.9	3024.1	22	1000.3	9438.8	4198.4	50
Total channel width (m)	N/A	N/A	N/A	N/A	N/A	N/A	N/A	N/A	7837.9	16556.7	11034	22
Average channel wall gradient (from profiles)	1.9	10.7	3.5	28	1.9	12.2	4.7	22	1.9	12.2	4	50
Maximum channel wall gradient (from profiles)	8	33.2	18	28	5	29.5	15	28	5	33.2	16.5	56
Terrace height (above thalweg) (m)	12.2	268.6	136	53	8	176.8	81.7	22	8	268.6	120.1	75
Normalised terrace height (between thalweg and top of chanel wall)	0.044787	0.908149	0.483518	53	0.035109	0.304348	0.38664	22	0.035109	0.908149	0.455101	75

Terrace width (all) (m)	241.6	3123.3	1082.5	53	266.3	1728.1	807.1	22	241.6	3123.3	1001.7	75
Normalised terrace height (inner bends)	0	0.9	0.5	37	0.128476	0.8565	0.43024	8	0	0.9	0.5	45
Normalised terrace height (outer bends)	0.1	0.9	0.4	16	0.035109	0.701862	0.361726	14	0	0.9	0.4	30
Terrace height (inner bends) (m)	12.24719	261.4326	149.8618	37	19.46629	149.7191	76.57303	8	12.24719	261.4326	136.8327	45
Terrace height (outer bends) (m)	12.80899	268.6236	103.9923	16	7.977528	176.8258	84.61276	14	7.977528	268.6236	94.9485	30
Terrace width (inner bends) (m)	241.573	3123.315	1182.675	37	402.5281	1178.933	755.7584	8	241.573	3123.315	1106.779	45
Terrace width (outer bends) (m)	341.8539	2663.202	850.7725	16	266.2921	1728.09	836.4767	14	266.2921	2663.202	844.1011	30
Knickpoint maximum gradient	N/A	N/A	N/A	N/A	N/A	N/A	N/A	N/A	0.6	2	1.29	7
Knickpoint height (m)	N/A	N/A	N/A	N/A	N/A	N/A	N/A	N/A	7.5	14	10	7
Knickpoint length (m)	N/A	N/A	N/A	N/A	N/A	N/A	N/A	N/A	1420	4060	2401	7
Knickpoint-zone average gradient	N/A	N/A	N/A	N/A	N/A	N/A	N/A	N/A	0.19	0.21	0.2	2
Knickpoint-zone height (m)	N/A	N/A	N/A	N/A	N/A	N/A	N/A	N/A	34	34	34	2
knickpoint-zone length (m)	N/A	N/A	N/A	N/A	N/A	N/A	N/A	N/A	9198	10234	9716	2

Appendix 2 – Table containing dimension and dip measurements from the variety of channel-related features (excluding terraces; see S3) seen on the seafloor, measured from profiles 1 to 28 (Fig. 2B, 4.3). See Fig. 4.4A for reference; data displayed in Fig. 4.4C, D, E and F.

Profile #	Channel floor width (km)	Difference between levee heights (km)	Landward levee height (km)	Landward channel wall width (km)	Landward channel wall average dip	Landward maximum dip	Oceanward levee height (km)	Oceanward channel wall width (km)	Oceanward channel wall average dip	Oceanward maximum dip	Thalweg depth (m)	Thalweg depth (km)	Landward levee depth (m)	Oceanward levee depth (m)	Total channel width (km)	Landward height difference between thalweg and channel-walls base (km)	Oceanward height difference between thalweg and channel wall base (km)	Landward depth of base channel walls (m)	Oceanward depth of base channel walls (m)
1	4.397	0.085	0.237	4.15	3.27	16.81	0.152	3.667	2.37	13.84	2842.81	2.84	2606	2691	12.213	0.033	0.012	2810	2831
2	4.162	0.107	0.251	3.642	3.94	12.53	0.144	4.051	2.04	4.96	2842.81	2.84	2592	2699	11.854	0.023	0.013	2819	2830
3	3.18	0.086	0.252	4.472	3.23	16.84	0.166	4.051	2.35	5.25	2857.08	2.86	2605	2691	11.703	0.026	0.031	2831	2826
4	4.441	0.087	0.243	3.004	4.63	14.6	0.156	1.109	8.01	9.44	2871.46	2.87	2628	2715	8.553	0.014	0.036	2857	2835
5	4.639	0.086	0.25	4.329	3.3	9.4	0.164	2.583	3.63	15.2	2871.46	2.87	2622	2708	11.551	0.011	0.022	2860	2850
6	4.376		0.266	5.007	3.04	11.9				8.72	2878.54	2.88	2613			0.022	0.039	2857	2840
7	3.447		0.269	5.044	3.05	27.66				6.6	2885.73	2.89	2617			0.009	0.019	2877	2867
8	0.774		0.283	4.481	3.61	32.36				6.18	2900	2.9	2617			0.008	0.006	2892	2894
9	1.032		0.304	3.437	5.06	33.2				6.56	2921.46	2.92	2617			0.012	0.006	2910	2915
10	1.771		0.298	1.586	10.64	21.2				8.78	2921.46	2.92	2624			0.006	0.004	2915	2917
11	2.326	0.077	0.304	5.837	2.98	29.9	0.227			16.23	2928.54	2.93	2624			0.008	0.006	2921	2923
12	2.585	0.054	0.297	6.8	2.5	19.8	0.243	7.172	1.94	29.48	2935.73	2.94	2639	2693	16.557	0.006	0.006	2930	2929
13	2.799	0.089	0.31	9.439	1.88	7.95	0.22	3.307	3.81	12.83	2942.81	2.94	2633	2722	15.546	0.013	0.005	2929	2937
14	2.873	0.111	0.316	7.931	2.28	31.84	0.204	3.654	3.2	5.55	2950	2.95	2634	2746	14.459	0.007	0.013	2943	2937
15	2.868	0.133	0.302	4.979	3.47	30.21	0.169	2.422	3.99	8.37	2957.08	2.96	2655	2788	10.269	0.004	0.007	2953	2950
16	2.595	0.118	0.309	6.324	2.8	12.22	0.191	4.509	2.43	14.77	2964.27	2.96	2655	2773	13.428	0.01	0.013	2954	2951
17	1.994	0.094	0.268	4.323	3.55	11.67	0.174	3.543	2.81	17.66	2971.35	2.97	2703	2797	9.86	0.014	0.011	2957	2961
18	2.415	0.057	0.259	4.763	3.11	18.03	0.202	2.05	5.63	28.13	2978.54	2.98	2719	2776	9.228	0	0.019	2978	2960
19	2.279	0.055	0.235	2.96	4.53	13.56	0.179	2.713	3.78	26.79	2985.73	2.99	2751	2806	7.952	0.008	0.014	2978	2971
20	2.744	0.066	0.241	4.348	3.17	10.86	0.175	2.031	4.92	26.65	2993	2.99	2752	2818	9.123	0.008	0.013	2985	2980
21	2.273	0.055	0.264	5.128	2.95	8.92	0.209	1.214	9.76	23.61	3007.08	3.01	2743	2798	8.615	0.026	0.005	2981	3002
22	1.83	0.057	0.273	5.908	2.65	10.37	0.217	1	12.23	28.07	3014.27	3.01	2741	2798	8.739	0.007	0.008	3007	3006
23	2.007	0.043	0.275	6.085	2.59	8.13	0.232	1.294	10.17	15.14	3021.46	3.02	2746	2789	9.386	0.014	0.017	3007	3004
24	1.276	0.028	0.28	7.401	2.17	11.12	0.252	2.36	6.09	26.77	3021.46	3.02	2742	2770	11.037	0.012	0.01	3010	3011
25	1.604	0.046	0.3	7.339	2.34	21.77	0.254	3.252	4.47	18.78	3035.73	3.04	2735	2782	12.195	0.008	0.006	3028	3030
26	1.536	0.073	0.301	7.723	2.23	26.38	0.228	4.274	3.05	11.46	3042.81	3.04	2742	2815	13.533	0.008	0.005	3035	3037
27	2.093	0.088	0.283	3.481	4.64	22.99	0.195	3.537	3.15	10.65	3042.81	3.04	2760	2848	9.11	0.01	0.006	3033	3037

28	1.675	0.088	0.269	3.422	4.49	11.82	0.18	2.741	3.76	13.51	3050	3.05	2781	2870	7.838	0.014	0.007	3036	3043
Mean	2.571	0.078	0.276	5.119	3.5	18	0.197	3.024	4.71	15	2951.27	2.95	2675	2768	11.034	0.012	0.013	2939	2938

Appendix 3 – Table containing dimension measurements of all terraces observed in the modern channel-walls, measured from profiles 1 to 28 (Fig. 4.2B, 4.3); see Fig. 4.4A for reference; data displayed in Fig. 4.4B.

Terrace	Profile	Landward (L) or	Inner or	Terrace	Terrace	Normalised
1	1	L	Outer	0.460112	0.044129	0.186204
2	1	O	Inner	1.139607	0.019466	0.128476
3	2	O	Inner	1.178933	0.039522	0.274322
4	2	L	Outer	0.743258	0.012809	0.05111
5	2	L	Outer	0.914607	0.065843	0.262721
6	3	L	Outer	0.898034	0.083511	0.331217
7	4	L	Outer	1.442978	0.140084	0.575401
8	5	L	Inner	0.637921	0.157107	0.628568
9	6	L	Inner	1.170506	0.083399	0.313483
10	7	L	Inner	2.73764	0.1325	0.493462
11	7	L	Inner	0.823876	0.243848	0.908149
12	8	L	Inner	2.923315	0.152781	0.540334
13	9	L	Inner	2.445506	0.214803	0.705638
14	10	L	Inner	0.389045	0.115421	0.387459
15	12	O	Outer	1.72809	0.168371	0.693188
16	12	O	Outer	0.486236	0.144242	0.593848
17	12	L	Inner	0.613202	0.017191	0.0579
18	13	O	Outer	0.380899	0.040899	0.185525
19	14	O	Outer	0.266292	0.120758	0.591009
20	14	L	Inner	2.669382	0.189298	0.599395
21	14	L	Inner	0.926966	0.253876	0.803878
22	15	L	Inner	0.34691	0.058146	0.192308
23	15	L	Inner	1.610393	0.145787	0.482163
24	15	L	Inner	0.34073	0.215787	0.713675
25	16	O	Inner	0.941292	0.029017	0.151912
26	16	L	Outer	2.663202	0.225871	0.73027
27	16	L	Outer	0.922753	0.268624	0.868495
28	17	O	Inner	0.619382	0.08059	0.46319
29	17	L	Outer	0.692978	0.039663	0.147745
30	17	L	Outer	0.728652	0.08927	0.332531
31	18	O	Inner	0.408708	0.114213	0.564801
32	18	L	Outer	0.66264	0.066264	0.255663
33	18	L	Outer	0.341854	0.118764	0.45822
34	19	O	Inner	0.402528	0.125197	0.69837
35	20	O	Inner	0.844663	0.149719	0.8565

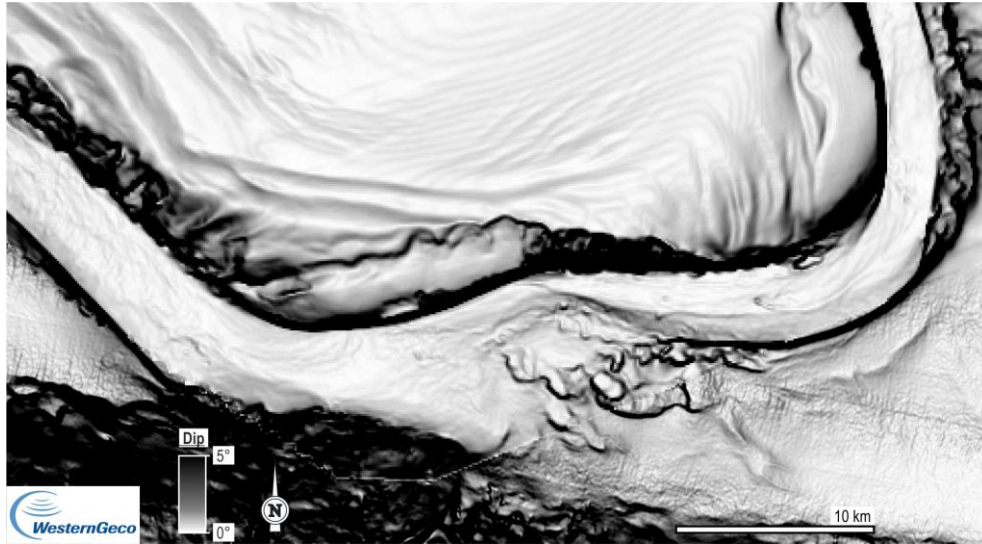
36	20	L	Outer	0.463483	0.019972	0.083022
37	20	L	Outer	0.641011	0.157781	0.655885
38	21	L	Inner	0.480056	0.042163	0.159732
39	21	L	Inner	0.244663	0.085758	0.324891
40	21	L	Inner	0.916573	0.196629	0.744919
41	21	L	Inner	1.320225	0.224185	0.849314
42	22	L	Inner	0.298596	0.012247	0.044787
43	22	L	Inner	0.243539	0.043062	0.157473
44	22	L	Inner	0.31264	0.0725	0.265126
45	22	L	Inner	0.693539	0.122219	0.446944
46	22	L	Inner	0.532584	0.16691	0.610375
47	22	L	Inner	3.112921	0.211489	0.773395
48	23	O	Outer	0.377809	0.158989	0.684981
49	23	L	Inner	0.383989	0.04691	0.170304
50	23	L	Inner	1.040449	0.14059	0.510402
51	23	L	Inner	2.310112	0.218315	0.792576
52	24	O	Outer	0.707022	0.176826	0.701862
53	24	O	Outer	0.517135	0.030056	0.1193
54	24	L	Inner	0.241573	0.054073	0.193254
55	24	L	Inner	0.402247	0.192893	0.689389
56	24	L	Inner	1.850281	0.232669	0.831543
57	25	O	Outer	0.566573	0.079213	0.311947
58	25	O	Outer	0.767978	0.039607	0.155973
59	25	L	Inner	1.142697	0.127472	0.42439
60	25	L	Inner	1.591854	0.214607	0.714486
61	25	L	Inner	3.123315	0.257528	0.857383
62	26	O	Outer	1.233708	0.100337	0.440824
63	26	O	Outer	1.292416	0.057051	0.250648
64	26	L	Inner	0.351124	0.135028	0.449252
65	26	L	Inner	1.467135	0.201966	0.671963
66	26	L	Inner	2.059831	0.261433	0.869813
67	27	O	Outer	1.033989	0.051011	0.261898
68	27	L	Inner	0.69691	0.069635	0.246421
69	27	L	Inner	1.306742	0.234663	0.830417
70	28	O	Inner	0.510955	0.05486	0.304348
71	28	L	Outer	0.854775	0.050815	0.189127
72	28	L	Outer	0.366854	0.07559	0.281338
73	28	L	Outer	0.815169	0.204888	0.762572
74	11	O	Outer	1.257303	0.007978	0.035109
75	12	O	Outer	1.095225	0.009242	0.038048
Mean	N/A	N/A	N/A	1.001708	0.120079	0.455101

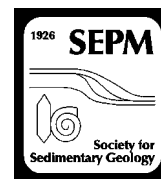
Appendix 4 – Table containing dimension and dip measurements from the seven knickpoints and two knickpoint-zones identified on the modern channel-floor. Data displayed on Figs 4.2C and 4.5D.

Knickpoint	Maximum gradient	Height (m)	Length (km)	Length (m)
1	1.6	14	2.6	2600
2	1.1	7.5	1.42	1420
3	1.4	7.5	1.79	1790
4	0.6	8	2.02	2020
5	2	13	2.6	2600
6	0.7	9	2.32	2320
7	1.6	12.5	4.06	4060
Mean	1.285714	10.21429	2.401429	2401.429

Knickpoint-zone	Maximum gradient	Height (m)	Length (km)	Length (m)
1	0.212	0.034043	9.198218	9198.218
2	0.191	0.034043	10.2346	10234.6
Mean	0.2015	0.034043	9.716407	9716.407

Appendix 5 – Uninterpreted dip map of the seafloor shown in Fig. 4.5A.





SYNDEPOSITIONAL TECTONICS AND MASS-TRANSPORT DEPOSITS CONTROL CHANNELIZED, BATHYMETRICALLY COMPLEX DEEP-WATER SYSTEMS (AÍNSA DEPOCENTER, SPAIN)

DANIEL E. TEK,¹ MIQUEL POYATOS-MORÉ,² MARCO PATACCI,¹ ADAM D. McARTHUR,¹ LUCA COLOMBERA,¹ TIMOTHY M. CULLEN,¹
AND WILLIAM D. McCAFFREY¹

¹*School of Earth and Environment, University of Leeds, Leeds LS2 9JT, U.K.*

²*Department of Geosciences, University of Oslo, Oslo 0371, Norway*
e-mail: ee11dt@leeds.ac.uk

ABSTRACT: The inception and evolution of channels in deep-water systems is controlled by the axial gradient and lateral confinement experienced by their formative flows. These parameters are often shaped by the action of tectonic structures and/or the emplacement of mass-transport deposits (MTDs). The Arro turbidite system (Aínsa depocenter, Spanish Pyrenees) is an ancient example of a deep-water channelized system from a bathymetrically complex basin, deposited in an active tectonic setting. Sedimentologic fieldwork and geologic mapping of the Arro system has been undertaken to provide context for a detailed study of three of the best-exposed outcrops: Sierra de Soto Gully, Barranco de la Caxigosa, and Muro de Bellos. These locations exemplify the role of confinement in controlling the facies and architecture in the system. Sedimentologic characterization of the deposits has allowed the identification of fifteen facies and eight facies associations; these form a continuum and are non-unique to any depositional environment. However, architectural characterization allowed the grouping of facies associations into four depositional elements: i) weakly confined, increasing-to-decreasing energy deposits; ii) progradational, weakly confined to overbank deposits; iii) alternations of MTDs and turbidites; iv) channel fills. Different styles of channel architecture are observed. In Barranco de la Caxigosa, a master surface which was cut and subsequently filled hosts three channel stories with erosional bases; channelization was enhanced by quasi-instantaneous imposition of lateral confinement by the emplacement of MTDs. In Muro de Bellos, the inception of partially levee-confined channel stories was enhanced by progressive narrowing of the depositional fairway by tectonic structures, which also controlled their migration. Results of this study suggest that deep-water channelization in active tectonic settings may be enhanced or hindered due to: 1) flow interaction with MTD-margin topography or; 2) MTD-top topography; 3) differential compaction of MTDs and/or sediment being loaded into MTDs; 4) formation of megascours by erosive MTDs; 5) basin-floor topography being reset by MTDs. Therefore, the Arro system can be used as an analog for ancient subsurface or outcrop of channelized deposits in bathymetrically complex basins, or as an ancient record of deposits left by flow types observed in modern confined systems.

INTRODUCTION

Deep-water depositional elements are the product of flows that erode, bypass, and deposit along the constituent parts of a deep-water sedimentary system (Kneller 2003; Stevenson et al. 2013). The architecture (geometry, distribution, and size) of these elements can be captured in seismic data (e.g., Mayall and Stewart 2000; Posamentier 2003; Posamentier and Kolla 2003; Prather 2003; Schwenk et al. 2005; Mayall et al. 2006; Wynn et al. 2007; Deptuck et al. 2003, 2007, 2008; Marsset et al. 2009); however, a flow-scale understanding of their constructional mechanisms is essential to inform generic models of their evolution (Peakall and Sumner 2015). Despite recent advancements in experimental (De Leeuw et al. 2016) and numerical (Dorrell et al. 2018) modeling, direct flow monitoring (Xu et al. 2013; Clare et al. 2016; Hughes Clarke 2016; Azpiroz-Zabala et al. 2017; Paull et al. 2018; Maier et al. 2019), flow reconstruction (Talling et al. 2007; Stevenson et al. 2013, 2018; Mountjoy et al. 2018), and repeat bathymetry surveying (Hizzett et al. 2018; Vendettuoli et al. 2019),

process-informed outcrop studies still provide the most detailed account of system evolution over geologic timescales.

A central parameter of the erosion-deposition threshold of suspended sediment in turbidity currents is velocity (Kuenen and Sengupta 1970; Kneller 2003; Stevenson et al. 2015; Dorrell et al. 2013, 2018). Substrate morphology is among the most significant factors which control flow velocity. Kneller (1995) provided a summary overview of topographic effects on flow velocity (Fig. 1A), whereby a flow may change its velocity along a downstream transect due to a change in its down-flow gradient or lateral flow constriction (Fig. 1). However, the complexity of turbidity current “run-up” (Kneller and McCaffrey 1999) and interaction with asymmetrical (Bell et al. 2018a) and oblique (McCaffrey and Kneller 2001) obstacles must be acknowledged.

Frontal confinement is defined as a reversal in the dip direction of the down-flow gradient along a longitudinal transect of a basin or flow pathway (Fig. 1A). Flow-scale frontal confinement can cause sufficient velocity reduction to initiate deposition and promote channel backfilling

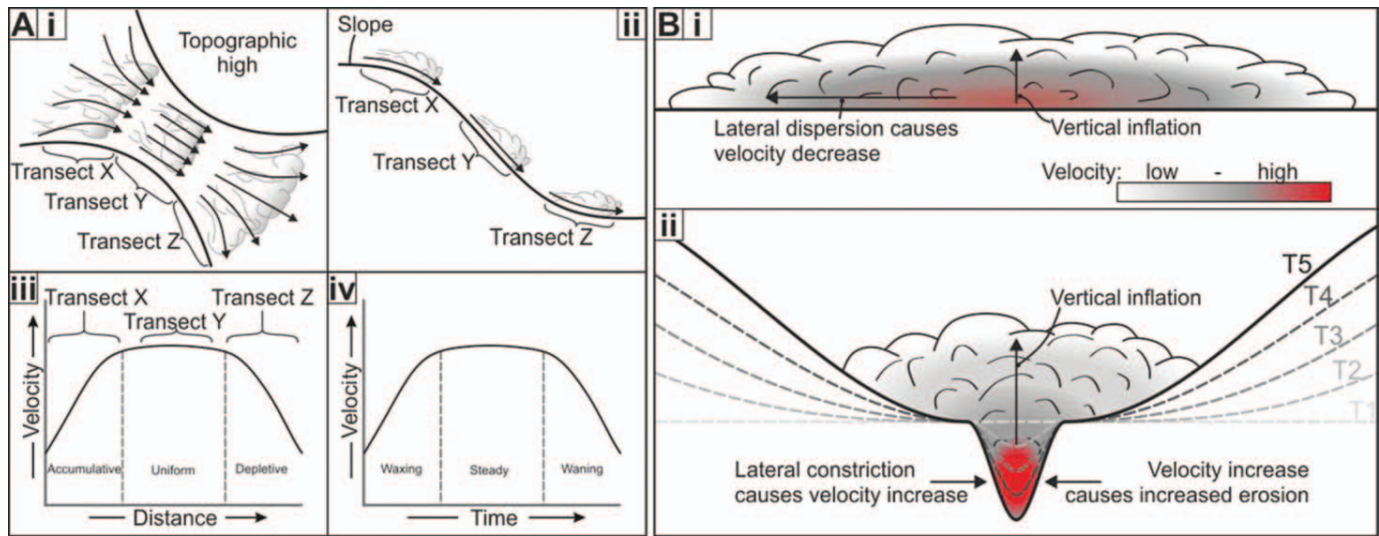


FIG. 1.—Schematic diagrams showing the effect of axial gradient and lateral confinement on flow velocity. A)(i) Lateral constriction and release of a flow, or (ii) increasing and decreasing the axial flow gradient can (iii) increase or decrease flow velocity over a longitudinal transect of a flow, or (iv) temporally at the base of a passing flow (modified from Kneller 1995). B) Velocity response of an unconfined flow (i) as it undergoes progressive lateral confinement (ii).

(Pickering et al. 2001). Where deceleration is rapid, it may generate hydraulic jumps (commonly at the ends of channels; Mutti and Normark 1987, 1991; Hofstra et al. 2018) or cause the formation of hybrid event beds (Haughton et al. 2009). At larger (architectural) scales, down-flow gradient is considered a primary variable in studies of slope grading (Prather et al. 1998, 2017) and submarine channel equilibrium profiles (Kneller 2003; McHargue et al. 2011; Georgiopoulou and Cartwright 2013). Lateral confinement occurs due to the presence of two elongate surfaces situated at both lateral edges of a basin or flow pathway, each orientated quasi-parallel to input flow or regional paleocurrent (Fig. 1B). The architectural effect of lateral confinement is manifested at multiple scales. A flow may be partially or fully confined by prominent basin-floor topography, or by a channel wall composed of incised substrate or overspill deposits. These overspill deposits (commonly referred to as terraces or internal levees; Hansen et al. 2015) may themselves be confined within larger external levees (Kane and Hodgson 2011), a canyon wall (Kane et al. 2009a), or by confining structures (Casciano et al. 2019). At flow scale, substrate erosion (Eggenhuisen et al. 2011), construction of depositional topography (e.g., levees) from preceding flows (De Leeuw et al. 2016), or both (Hodgson et al. 2016), can progressively generate lateral confinement, increasing the velocity, and hence bypass potential of subsequent flows (Fig. 1B). Continued flow input may trigger a positive feedback mechanism (a “channelization feedback” *sensu* Eggenhuisen et al. 2011; De Leeuw et al. 2016), whereby elevated flow velocities lead to increased basal erosion and lateral overspill, hence imposing greater lateral confinement leading to channelization. The onset of this feedback mechanism occurs as a “channelization threshold” is crossed (*sensu* Eggenhuisen et al. 2011; De Leeuw et al. 2016). Understanding what controls this threshold, when it is crossed, and whether imposition of externally derived lateral confinement may influence this, is crucial to understanding deep-water channel inception.

The processes of deep-water channel initiation and infill have a varied architectural expression (Clark and Pickering 1996; Deptuck et al. 2003; Macauley and Hubbard 2013), and a large range of potential autogenic and allogenic controlling factors (Pickering and Corregidor 2005; Clark and Cartwright 2011; Flint et al. 2011; Jobe et al. 2015; Gong et al. 2016). In structurally active settings, the influence of protruding structures and mass-transport deposits (hereinafter MTDs) is particularly prevalent.

Channels can be blocked or diverted by a growing structure, or incise through it, depending on: i) rate of relative sedimentation to structural growth, ii) timing of structuration, and iii) geometry and interaction of different structures (Gee and Gawthorpe 2006; Mayall et al. 2010; Clark and Cartwright 2011; Jolly et al. 2016). The growth of synsedimentary fault-derived folds may also result in paleoflow directions to be oriented parallel to the structures; in such cases, progressive lateral confinement may be generated by the development of these structures (Clark and Cartwright 2011).

Herein, MTD is used as a term to describe any of the products of *en masse* transport and deposition (Nelson et al. 2011; Kneller et al. 2016). The term encompasses a continuum of deposits, distinguished by the degree of internal deformation or disaggregation (Moscardelli and Wood 2008; Bull et al. 2009; Ogata et al. 2012), and named in accordance with their deformational processes: slides (least internal deformation), slumps, and debris flows (most internal deformation). In tectonically active basins, longitudinally emplaced MTDs (see Kremer et al. 2018 for definition) may be sourced from the headwall or sidewalls of a feeding canyon (Nelson et al. 2011) or from a proximal shelf or slope failure (Ortiz-Karpp et al. 2017); transversely emplaced MTDs may be sourced from the local collapse of channel walls (Hansen et al. 2015) or from a laterally confining slope (Arbués et al. 2007a). MTDs can have a profound influence on the evolution and architecture of submarine channels through: i) quasi-instantaneous imposition of lateral confinement by MTD-top or -margin topography (Schultz et al. 2005; Hansen et al. 2013; Kneller et al. 2016; Masalimova et al. 2016; Kremer et al. 2018; Ward et al. 2018) and/or the development of evacuation scars (Dakin et al. 2013; Hodgson et al. 2016; Qin et al. 2017) leading to channelization; ii) the perturbation of flows leading to backfilling (Posamentier and Kolla 2003; Nelson et al. 2009; Bernhardt et al. 2012; Corella et al. 2016); iii) thalweg plugging, facilitating lateral channel migration (Kremer et al. 2018), diversion (Nelson et al. 2011; Kneller et al. 2016), or avulsion (Ortiz-Karpp et al. 2015); iv) affecting the development of channel sinuosity (Deptuck et al. 2007).

To help bridge the resolution gap between event-bed and seismic scale, outcrops from ancient structurally complex basins are commonly used as analogs (e.g., McCaffrey et al. 2002; Brunt et al. 2007; Leren et al. 2007; Janbu et al. 2007; Hubbard et al. 2008; Bernhardt et al. 2011, 2012; Casciano et al. 2019; McArthur and McCaffrey 2019). One such

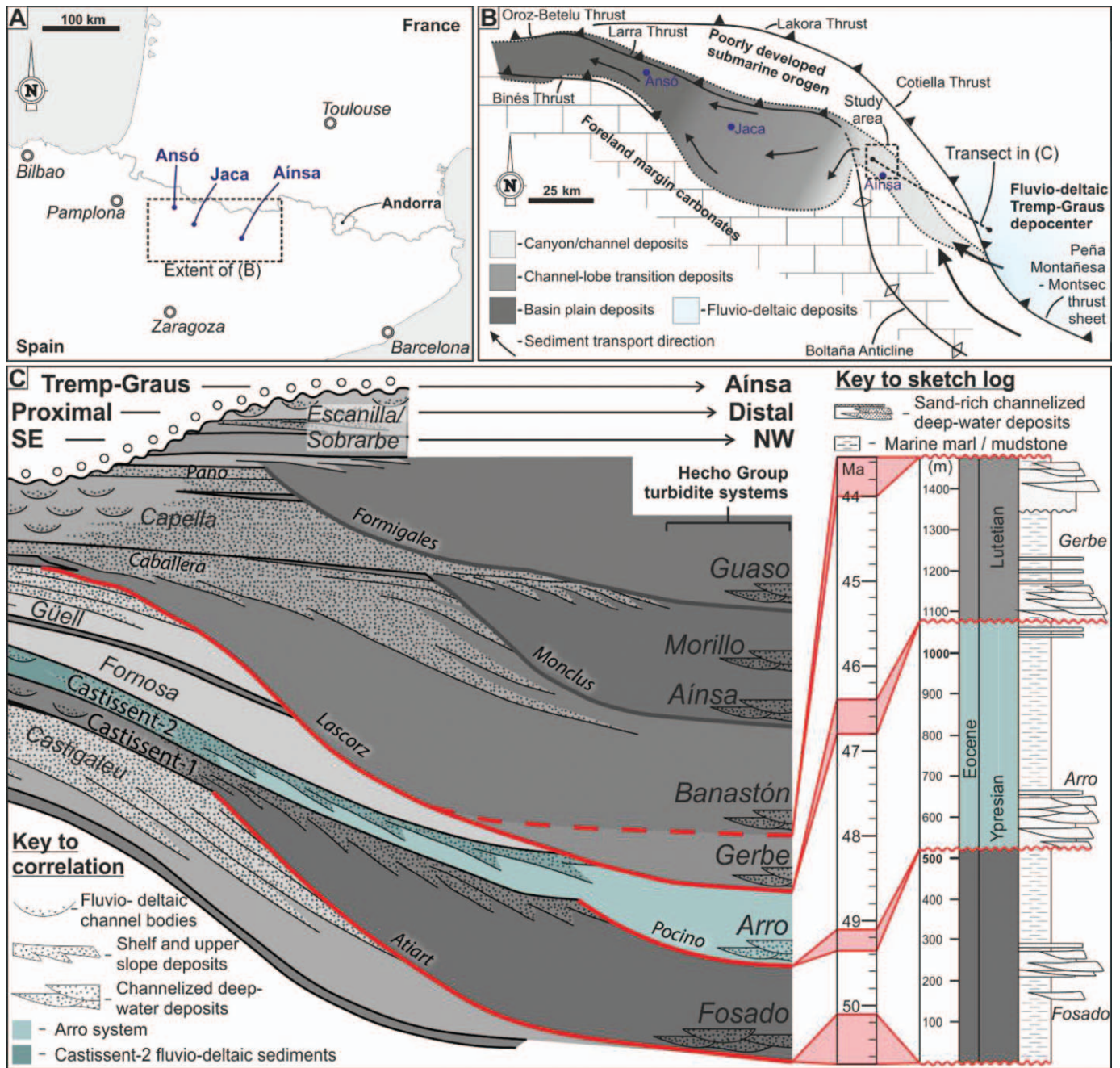


FIG. 2.—**A**) Map showing broad location of the South Pyrenean Foreland Basin in northern Spain. **B**) Schematic map showing the sediment routing system from Tremp-Graus (east) to Jaca depocenter (west) in the Eocene, modified from Remacha and Fernández (2003) and Caja et al. (2010). **C**) Depositional dip section showing the correlation of fluvio-deltaic units in the distal part of the Tremp-Graus depocenter to their contemporaneous deep-water units in the Aínsa depocenter, with inset showing the chronostratigraphy of the Fosado, Arro, and Gerbe systems (modified from Clark et al. 2017).

“natural laboratory” is the Eocene Hecho Group, in the Aínsa depocenter (South Pyrenean Foreland Basin, Spain), where the effect of structures and mass-transport deposits on deep-water channels has been well documented (Pickering and Corregidor 2005; Arbués et al. 2007a, 2007b; Pickering and Bayliss 2009; Dakin et al. 2013; Bayliss and Pickering 2015). This study provides a sedimentologic and architectural characterization of the Arro turbidite system, in the Hecho Group (see Scotchman et al. 2015 for definitions; Fig 2), describing, for the first time, its distal expression in the Aínsa depocenter. The study is used to investigate the extent to which mass-transport- and thrust-related

structures influence the establishment, evolution, and infill of axial submarine channels, and the scales at which this control is exerted. A particular line of enquiry is whether the channelization process may be enhanced or hindered by the imposition of frontal or lateral confinement during the emplacement or growth of these features. Investigating the sedimentologic and architectural response to evolving basin-floor topography in channelized deep-water systems is important for elucidating how channels are initiated and what controls their presence and distribution. The findings herein may therefore be used to inform studies in other ancient and modern confined basins.

GEOLOGIC SETTING

The lower Eocene stratigraphy of the Ainsa depocenter is part of the fill of the South Pyrenean Foreland Basin, formed on the southern margin of the doubly verging Pyrenean Orogen (Fig. 2; Séguret 1972; Cámara and Klimowitz 1985; Puigdefàbregas and Souquet 1986; Muñoz 1992; Bentham and Burbank 1996; Barnolas and Gil-Peña 2001; Fernández et al. 2004; Arbués et al. 2011). The South Pyrenean Foreland Basin comprises three parts: the terrestrial-to-shallow-marine “Trempe–Graus depocenter”; the channelized deep-water “Ainsa depocenter”; the unconfined, deep-water “Jaca depocenter.” The Ainsa depocenter is located in an oblique transfer zone between the Montsec–Peña Montañesa and Cotiella thrust units (Fernández et al. 2004, 2012; Muñoz et al. 2013). This “relay” forms a wider zone of smaller-wavelength thrust-related SE–NW structures propagating through Cretaceous–Neogene carbonate and clastic sedimentary rocks from a Triassic decollement (Séguret 1972; Cámara and Klimowitz 1985; Choukroune 1992; Muñoz 1992; Clark et al. 2017).

During the Ypresian, channelized deep-water deposits in the Ainsa depocenter were connected to unconfined deposits in the downstream Jaca depocenter (Fig. 2), hence their collective name: the Hecho Group (Mutti 1984). Here, the scheme presented by Clark et al. (2017) is followed, wherein the Hecho Group is divided into seven turbidite systems (Fig. 2C). However, nomenclatural inconsistency is common in the description of the deep-water Ainsa depocenter fill (cf. Mutti 1985; Fernández et al. 2004; Pickering and Corregidor 2005; Arbués et al. 2007a; Das Gupta and Pickering 2008; Heard and Pickering 2008; Pickering and Bayliss 2009; Muñoz et al. 2013; Heard et al. 2014; Pickering and Cantalejo 2015; Scotchman et al. 2015; Cornard and Pickering 2019).

Sediment in the turbidite systems of the Hecho Group was derived predominantly from the fluvio-deltaic environments in the Trempe–Graus depocenter to the east, entering the Ainsa depocenter through a series of submarine canyon systems to the southeast (Fig. 2B). Shelfal deposits of the Castigaleu Group are incised by the Atiart surface, a large submarine unconformity, which is filled by deep-water sediments of the Castissent Group (time equivalent to the Fosado and Arro systems) (Soler-Sampere and Garrido-Megías 1970; Puigdefàbregas and Souquet 1986; Mutti et al. 1988; Muñoz et al. 1994; Scotchman et al. 2015; Chanvry et al. 2018). The Arro system, which was active during the Ypresian (Fig. 2C), was fed through the Pocino surface, a subtle canyon first recognized by Mutti et al. (1988, see also Sgavetti 1991; Millington and Clark 1995a, 1995b) which was in turn incised by the Lascorz surface (the feeder of the overlying Gerbe system) (Muñoz et al. 1994; Payros et al. 2009; Poyatos-Moré 2014; Castellort et al. 2017).

To date, detailed sedimentologic and stratigraphic analysis has been conducted only on the most proximal Arro outcrops, i.e., those of Charo (exposing part of the Arro’s feeder canyon fill), Río de la Nata, Los Molinos Road, and Santa Catalina (Millington and Clark 1995a, 1995b; Arbués et al. 2007a, 2007b) (Fig. 3). The Los Molinos Road has commonly been used as the “type locality” for the Arro system (Das Gupta and Pickering 2008; Caja et al. 2010). Van Lunsen (1970) and Castellort et al. (2017) present data from more distal outcrops, but the sedimentology and stratigraphy remain undescribed. This study is focused on the sedimentologic characterization of the more distal parts of the Arro system in the Ainsa depocenter (Fig. 3).

DATA AND METHODS

The field area, located N–NE of the town of Ainsa, covers approximately 40 km² (Fig. 3) along an ~ 13-km-long transect oriented SE–NW (parallel to regional paleocurrent). A revised version of a geologic map by Clark et al. (2017) is used; structural amendments are informed by 448 strike and dip measurements of bedding (Fig. 4C) and the tracing of

some of the larger, depocenter-scale structures (Fig. 3). Detailed sedimentologic analysis of twenty-two outcrops was undertaken using traditional field methods, augmented by study of aerial photographs acquired using an unmanned aerial vehicle. A total of 230 paleocurrent measurements were taken from flute casts, and ripple and cross-bed foresets (Fig. 4). Fifty-six logs totaling 1,088 m of stratigraphy were measured with centimeter resolution and drawn at 1:10 to 1:50 scale to capture vertical facies and grain-size variations at multiple scales; a high-precision Jacob’s staff (Patacci 2016) was used. As the Charo area and the most proximal outcrops (1, 3, and 4 in Fig. 3) have been studied in detail previously (Millington and Clark 1995a, 1995b; Arbués et al. 2007a, 2007b), this study is focused primarily on three outcrops in the more distal part of the Arro system in the Ainsa depocenter: Sierra de Soto Gully, Barranco de la Caxigosa, and Muro de Bellos (Fig. 3; outcrops 10, 14, and 22 respectively). At these locations, multiple laterally offset logs, field sketches, and interpreted photomosaics (from ground and aerial photographs) have been used to generate architectural panels.

Large-Scale Trends

The trend of paleocurrents for the Arro system is dominantly to the NW (Fig. 4), which is consistent with the findings of Millington and Clark (1995a, 1995b) and Arbués et al. (2007a, 2007b), who present data from the proximal localities and feeder system. The regional trend of strike orientation of thrusts and related folding within the area is also NW–SE, which is consistent with the trend of the larger, depocenter-bounding structures, such as the Mediano, Anisclo, and Boltaña anticlines (Millington and Clark 1995a, 1995b; Arbués et al. 2007a; Muñoz et al. 2013). It is possible that these structures have undergone clockwise rotation along with the regional structures (Muñoz et al. 2013). Regardless, the correspondence of the regional paleocurrents (from flutes, ripples, and cross beds; Fig. 4B) and the structural trend (Fig. 4C) allow the Arro system to be classified as an axial deep-water system.

FACIES ANALYSIS

The fifteen facies and sub-facies defined in the Arro turbidite system are described in Table 1, with photographs presented in Figure 5. These facies and sub-facies are defined according to lithology, grain size, and composition, the presence and type of sedimentary structures, and grading.

The facies are grouped together to form eight facies associations (FA1–8) that can be widely recognized in the Arro system (Fig. 6). These facies associations are not unique to a single depositional environment and often exhibit gradational transitions between one another; the observed continuum prevented any meaningful quantitative facies-association definition based upon facies proportions. The logs displayed in Figure 6 are from representative sections. The interpretation of depositional elements (DE1–4) was therefore based on the combination of facies association occurrence and the presence of key bounding surfaces (see “Depositional Elements” section).

Turbidite and MTD character is a record of the velocity, concentration, magnitude, and grain size (and modality thereof) of flows traversing the depocenter. As the specific role of each of these parameters is generally indiscernible, the term “energy” will be used such that high-energy flows are those of high velocity, concentration, and magnitude, and coarse grain size (and vice versa for low-energy flows).

Facies Association 1 (FA1): Background Thin Beds

Description.—Constituting most of the depocenter fill, this facies association contains very thin (typically < 3 cm, average thickness ~ 1 cm) very fine- to medium-grained beds of lenticular (Lf3), rippled (Lf4a), and ungraded, structureless (Lf6b) sandstone, which alternate with finer-

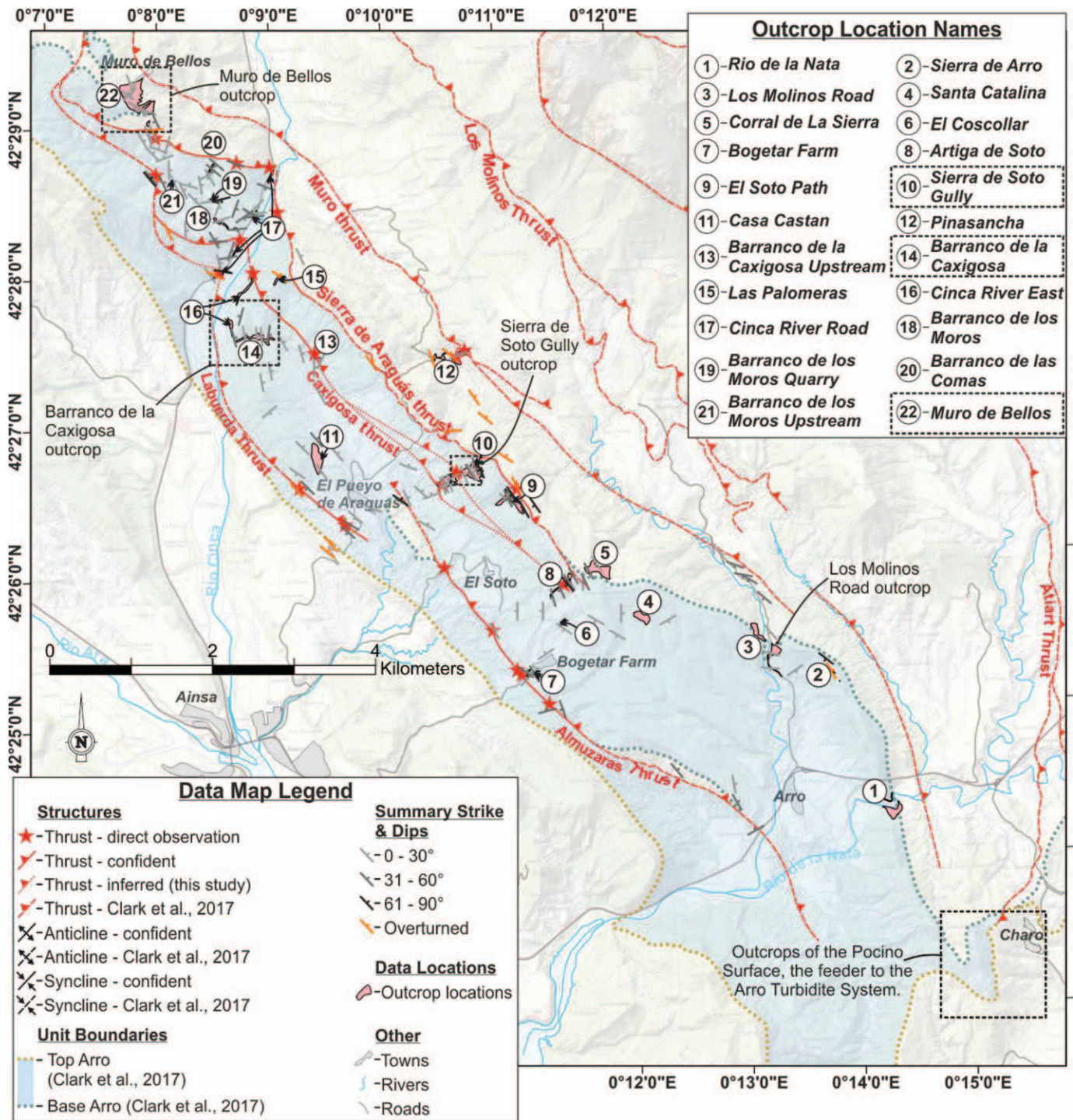


Fig. 3.—Map of the Arro turbidite system modified from Clark et al. (2017) with data from this study, showing locations and names of major tectonic structures, the top and base of the Arro turbidite system, some summary structural data, and the twenty-two locations used to inform this study with Sierra de Soto Gully, Barranco de la Caxigosa, and Muro de Bellos highlighted. Grid is in degrees, minutes, and seconds, georeferenced in European Datum 1950 UTM zone 30N. Basemap at 1:25,000 scale courtesy of Instituto Geográfico Nacional, available from: http://centrodedescargas.cnig.es/CentroDescargas/locale?request_locale=en.

grained siltstone and mudstone facies of structureless mudstone (Lf1) and graded siltstone (Lf2) (Table 1); Lf2 is dominant. The thickness of mudstone and siltstone layers in FA1 varies from 3 to 25 cm (average: 7 cm), with variable proportions of clay and silt (Fig. 6A). Bedding-concordant packages (a few decimeters to ten meters thick) of alternating grain size can be traced for tens to hundreds of meters. In some outcrops,

such as Muro de Bellos (Fig. 7), wedging geometries in these packages are observed. Bioturbation on sandstone bed tops and bases is seldom observed (possibly due to outcrop limitations), but sand-filled burrows are found in finer-grained layers. Distinct beds of fully disaggregated debrites (Lf8a) are rare, but FA1 is often highly deformed because of syndimentary remobilization or due to later tectonic activity; subtle

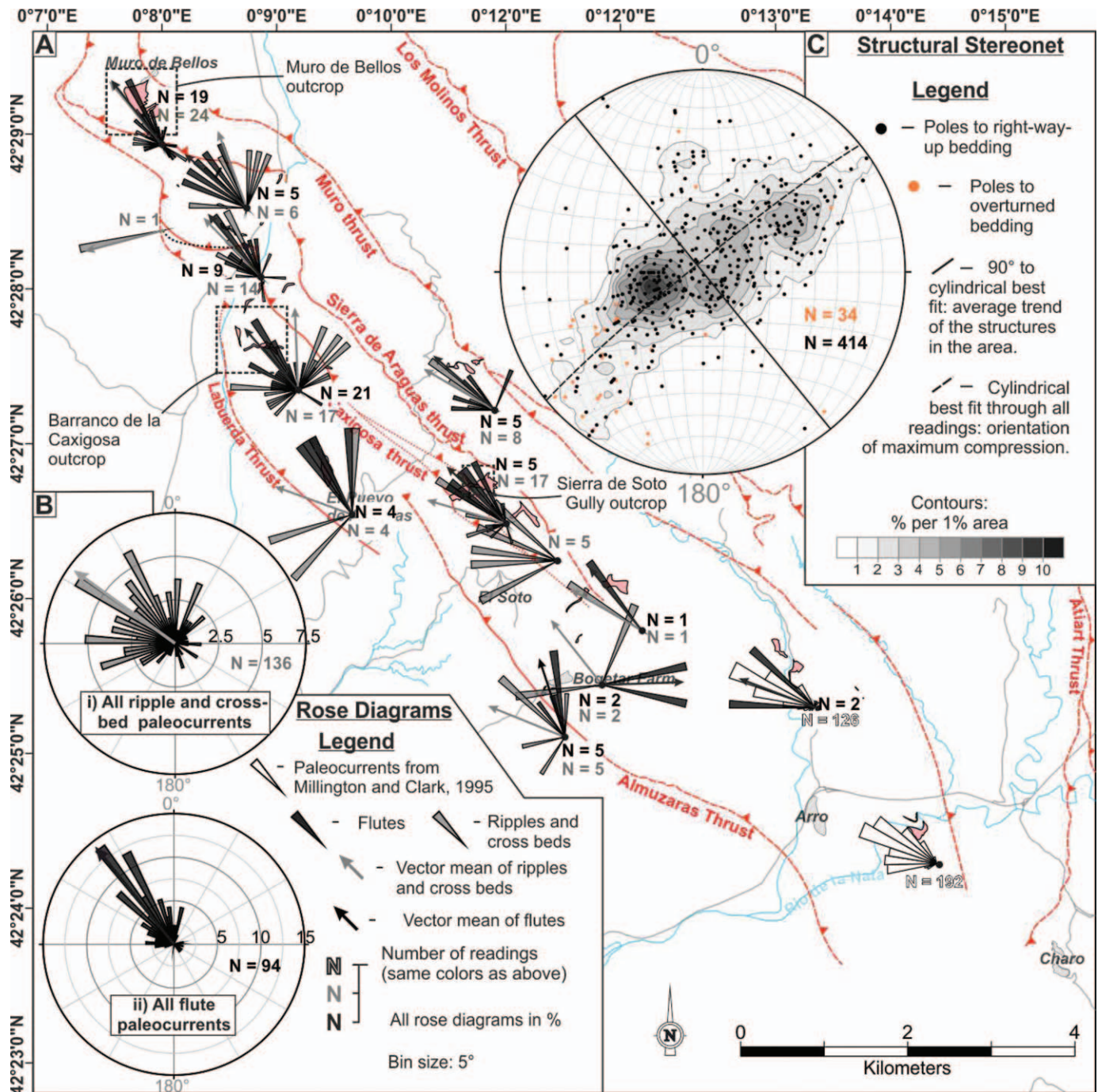


FIG. 4.—A) Map presenting paleocurrent data from fourteen of the visited locations illustrating their relationship with the basinal structures. B) Regional paleocurrent data measured from i) ripples and cross beds, and ii) flute casts. C) All strike and dip measurements of bedding, indicating the average structural trend.

deformation can be hard to detect at outcrop scale. The two causes are distinguished by the presence of calcite veining along shear horizons (or faults), which are taken as an indicator of tectonic deformation. FA1 can be found as heterolithic packages between incisional and non-incisional sandstone beds of FA4 and FA5. Lateral and vertical transitions into laterally variable (FA2) and laterally continuous (FA3) thin beds are observed; a continuum exists between these three facies associations.

Interpretation.—FA1 comprises the deposits of dilute, low-density flows (Mutti 1977), which experienced periodic variations in silt and sand

content, together with hemipelagites. The vertical distribution of FA1 between and within other facies associations (FA4 and FA5) suggests that it represents the dominant background sedimentation, but not necessarily from hemipelagic settling alone, as has also been recognized in the deep-water strata of the Tanqua depocenter, Karoo Basin (Boulestex et al. 2019). The formative flows may have been derived from: i) small sediment failures on the shelf, on the upper slope, or in the feeder canyon (Clare et al. 2016); ii) hyperpycnal flows associated with direct sediment input from a canyon-connected river mouth, whereby variations in grain size may reflect variations in the flux of the feeding river (Mulder et al. 2003; Mutti

TABLE 1.—Descriptions of the fifteen facies and sub-facies recognized in the stratigraphy of the Arro system, including their lithologies, typical thicknesses, and interpretations of their depositional processes.

LITHOFACIES	LITHOLOGY	DESCRIPTION	THICKNESS	PROCESS INTERPRETATION	PHOTO
Lf1: Structureless mudstone	Carbonate mudstone containing silt.	No obvious grading or structure, weathers with a texture comprising loose spheroids < 10 cm long. Concretionary horizons occur with variable spacing (0.5–10 m).	No clear bedding or lamination	Hemipelagic suspension fallout.	Fig. 5A
Lf2: Graded siltstone	Sometimes graded from very fine-grained sand to mud, typically silt to mud.	Usually structureless, however parallel lamination and starved ripples are sometimes present.	0.1–4 cm	Fine-grained, dilute-gravity-current deposits, equivalent to a coarse T _e division of Bouma (1962) or a T ₆ division of Stow and Shanmugam (1980).	Fig. 5B
Lf3: Lenticular sandstone	Very fine- to medium-grained sandstone, occasionally coarse silt or coarse sandstone.	Lenses of sandstone typically 3–7 cm wide, separated laterally by 0.1–10 cm. Lenses are aligned along bedding-conformable horizons which can usually be traced laterally for over 10 m and often over 20 m.	0.1–1.5 cm	Deposition from a dilute, dominantly bypassing turbidity current.	Fig. 5C
Lf4a: Rippled sandstone	Very fine- to coarse-grained sandstone.	Unless they are eroded, rippled bed tops are usually preserved, commonly with internal ripple cross lamination observed, both of which may be disturbed by dewatering effects. Where Lf4a occurs as isolated beds, bases are usually flat but some exhibit basal scouring, making the beds pinch and swell. Ripple heights (crest to trough) typically range from 1.5–5 cm. Ripple lengths (trough to trough) typically range from 7 to 30 cm. In the thinnest intervals the facies nears a lenticular geometry.	1.5–10 cm	Deposition and tractional reworking by dilute, low-density gravity current (Allen 1973, 1982).	Fig. 5D
Lf4b: Hummocky-cross-stratified sandstone	Very fine- to medium-grained sandstone.	Characterized by undulating laminae with wavelengths ranging from 5 to 25 cm and amplitudes ranging from 0.5 to 5 cm, comprising internal lamination truncations and dip changes. Bed tops display 3D bedforms with no dominant inferred paleocurrent direction. Always located at the tops of sandstone beds, sometimes overlying ungraded, cross-stratified (< 7-cm-thick foresets, typically pervasive through an event bed or scour fill), cross-laminated (> 7-cm-thick foresets) or parallel-laminated sandstones.	2–6 cm	Deposition and reworking from reflected or deflected dilute flows, typically in the bypassing part of a bipartite flow (Mutti 1992; Mulder et al. 2009; Muzzi Magalhaes and Tinetti 2011; Bell et al. 2018a).	Fig. 5E
Lf4c: Planar-cross-stratified sandstone	Fine- to medium-grained sandstone.	Foreset heights range from 7 to 50 cm, commonly infilling concave-convex scoured surfaces, sometimes exhibiting positive depositional relief, and sometimes both. Foreset angles vary significantly from ~ 10° to ~ 40°. Fluted bases and rippled tops are also seen. Cross stratification can be pervasive throughout isolated beds or occur above ungraded structureless sandstones.	7–50 cm	1) Dunes or mega ripples formed by traction and fallout from a dilute flow (Tinetti, 2011); 2) "pseudo dunes" formed from scour derived instabilities in a unidirectional flow (Arnott and Al-Mufti 2017).	Fig. 5F
Lf5: Parallel-laminated sandstone	Very fine- to coarse-grained sandstone.	Parallel laminae spaced 0.1–1 cm apart which may underlie or overlie any other sandstone-rich facies. Can be disturbed or convoluted in parts due to bioturbation and dewatering.	5–50 cm	Traction carpets from upper-stage plane beds or lower-stage plane beds (Talling et al. 2012).	Fig. 5G
Lf6a: Graded, structureless sandstone	Large grain-size range with some beds fining from granules to very fine sand. Typically coarse or medium or medium or fine sand.	Bedded, internally structureless sandstone except for dish structures. Some beds are capped with siltstone, whereas others are bounded by amalgamation surfaces. At amalgamation surfaces and bedding boundaries, load balls and flame structures are seen; flutes, some of which loaded, are common on bed bases, but grooves are rare.	0.1–2.75 m	Bouma (1962) sequence T _{3a} division deposited from a depositional, and potentially erosional, high-density turbidity current (Lowe 1982), often with subsequent dewatering.	Fig. 5H
Lf6b: Ungraded, structureless sandstone	Fine to coarse-grained sandstone.	Lack of grading characterizes this facies. Flames, load balls, and flutes are found on many bed bases. Amalgamation surfaces and intense internal deformation relating to dewatering are common.	0.04–1.25 m	Bouma (1962) sequence T _{3a} division deposited from a depositional, and potentially erosional, high-density turbidity current (Lowe 1982).	Fig. 5I

TABLE 1.—Continued.

LITHOFACIES	LITHOLOGY	DESCRIPTION	THICKNESS	PROCESS INTERPRETATION	PHOTO
Lf6c: Sandstone with mudclasts	Fine to coarse sandstone.	Bedded sandstone similar to Lf6a and Lf6b, but containing up to 40% rounded to subangular mudclasts, sometimes armored with sand and granules. Mudclasts may be concentrated at bed bases, tops, or distributed throughout. Amalgamation surfaces exhibiting scouring geometries are sometimes lined with mudclasts. In some cases mudclasts are concentrated on distinct planar, inclined horizons within beds, potentially highlighting cross strata.	0.2–4 m (upper limit possibly a series of amalgamated beds)	Erosional and depositional high-density turbidity current (Lowe 1982) carrying “rip-up clasts” (Mutti and Nilsen 1981; Mutti 1992).	Fig. 5J
Lf7a: Extraclast conglomerate	Granule- to cobble-size extraclasts and bioclasts supported by very poorly sorted, polymictic, argillaceous usually coarse-grained sandstone.	Characterized by the presence, and dominance, of rounded to subangular extrabasinal lithic fragments composed of limestone, quartzite, or other mineral aggregates. The silt and clay content of the matrix varies significantly between and within (laterally and vertically) individual beds. Mudclasts, rounded clasts of sandstone and local heterolithics, and bioclasts such as <i>Nummulites</i> and shell fragments (of oysters, other bivalves, and brachiopods) are common yet not in dominant quantities. Extraclasts are almost always matrix supported but may be locally clast supported.	8–70 cm	Deposition from the traction carpet of dominantly bypassing flow(s) (Mayall et al. 2006; Stevenson et al. 2015) due to frictional freezing (Mutti et al. 2000).	Fig. 5K
Lf7b: Mudclast conglomerate	Pebble-size mudclasts supported by sandy matrix of varying texture and grain size.	Size (0.5–20 cm long axis), rounding (rounded to subangular), and proportion (typically > 75% of clasts) of mudclasts varies between and within (laterally and vertically) beds; some mudclasts are armored with coarse sand. Extraclasts and bioclasts are often present. The matrix composition ranges from well-sorted medium and coarse sandstone to poorly sorted, clay- and silt-rich sandstone.	5–30 cm	A high-energy erosional and dominantly bypassing flow containing abundant “rip-up clasts” (Mutti and Nilsen 1981; Mutti 1992) deposited as a lag (Mayall et al. 2006; Stevenson et al. 2015); type A1 and B1 of Johanssen and Stow (1995).	Fig. 5L
Lf8a: Chaotic mudstone	Chaotic mud-rich deposit supporting rafts of heterolithic stratigraphy, blocks of sandstone, extraclasts, and bioclasts	A clay-rich matrix with variable silt and sand content contain: deformed, disaggregated blocks (up to 5 m long axis) of fine-grained heterolithic sediment which exhibit internal structure similar to stratigraphy found elsewhere in the basin; bioclasts such as <i>Nummulites</i> and shell fragments; 5–20 cm rounded to subrounded blocks of coarse sandstone, sometimes nummulite and shell rich, similar to that seen in the proximal (shelfal) Castissent Formation; 3–40 cm rounded to subrounded clasts of well-sorted fine to coarse sandstone resembling Lf4–6; and granule- to pebble-size extrabasinal lithic fragments (see Lf7a). The presence and relative proportions of these components is highly variable between deposits.	0.2–20 m	<i>En masse</i> deposition from debris flows and highly disaggregated slumps (termed “blocky beds” by Ogata et al. 2012). The formative material was sourced from: local stratigraphy, possibly due to a growing basin-floor structure (Arbués et al. 2007a, 2007b) or channel-bank collapse (Barton et al. 2010); or from the proximal fluvio-deltaic and shelf deposits of the Castissent Formation (Nijman and Puigdefabregas 1977; Mutti et al. 1996, 2000; Nijman 1998).	Fig. 5M
Lf8b: Deformed heterolithics	Deformed, not disaggregated local heterolithic stratigraphy.	Folded heterolithic packages with wavelengths between 0.1 and 3 m, sometimes overlying a heavily deformed basal surface. The constituent stratigraphy can be easily matched to the adjacent or underlying stratigraphy and is therefore generally devoid of shelf material.	0.5–6 m	Slumped local stratigraphy. A continuum exists between these and Lf8a distinguished by the degree of disaggregation (Posamentier and Martinsen 2011; Ogata et al. 2012).	Fig. 5N
Lf9: Polymictic, bioclastic sandstone	Ranging from very poorly sorted polymictic coarse- to very coarse-grained (average) sandstone with abundant bioclasts.	This bedded facies can exhibit normal grading and scouring bases, sometimes with flutes and sometimes overlying amalgamation surfaces. <i>Nummulites</i> (0.2–2.5 cm diameter) are the dominant bioclast with fragmented oyster shells (0.2–4 cm long axis) also abundant; gastropods are rarely found. Relative and absolute bioclast proportions vary between beds and (vertically and laterally) within beds, sometimes over < 5 cm. In some cases bioclasts occur in such abundance that this facies can be classed as a carbonate packstone.	0.03–1m	Sandstones and bioclasts introduced by density currents, sourced from the Castissent shelf (Marzo et al. 1988; Nijman 1998).	Fig. 5O

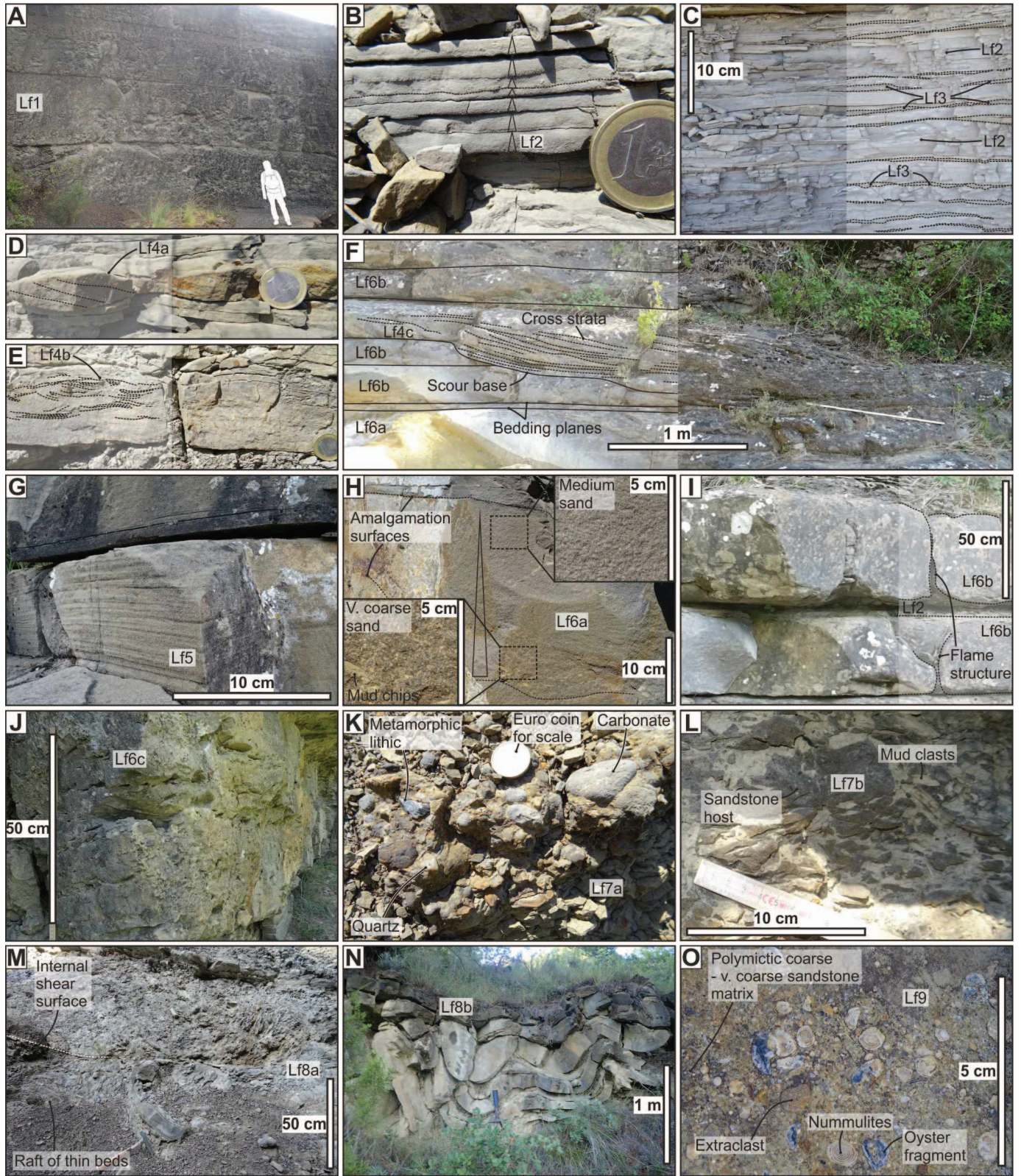


Fig. 5.—Photographs of all fifteen facies and sub-facies which constitute the stratigraphy of the Arro system; descriptions are provided in Table 1. **A)** Lf1, structureless mudstone; **B)** Lf2, graded siltstone; **C)** Lf3, lenticular siltstone; **D)** Lf4a, rippled sandstone; **E)** Lf4b, hummocky-cross-stratified sandstone; **F)** Lf4c, planar-cross-stratified sandstone; **G)** Lf5, parallel-laminated sandstone; **H)** Lf6a, graded, structureless sandstone; **I)** Lf6b, ungraded, structureless sandstone; **J)** Lf6c, sandstone with mudclasts; **K)** Lf7a, extraclast conglomerate; **L)** Lf7b, mudclast conglomerate; **M)** Lf8a, chaotic mudstone; **N)** Lf8b, deformed heterolithics; **O)** Lf9, polymictic, bioclastic sandstone.

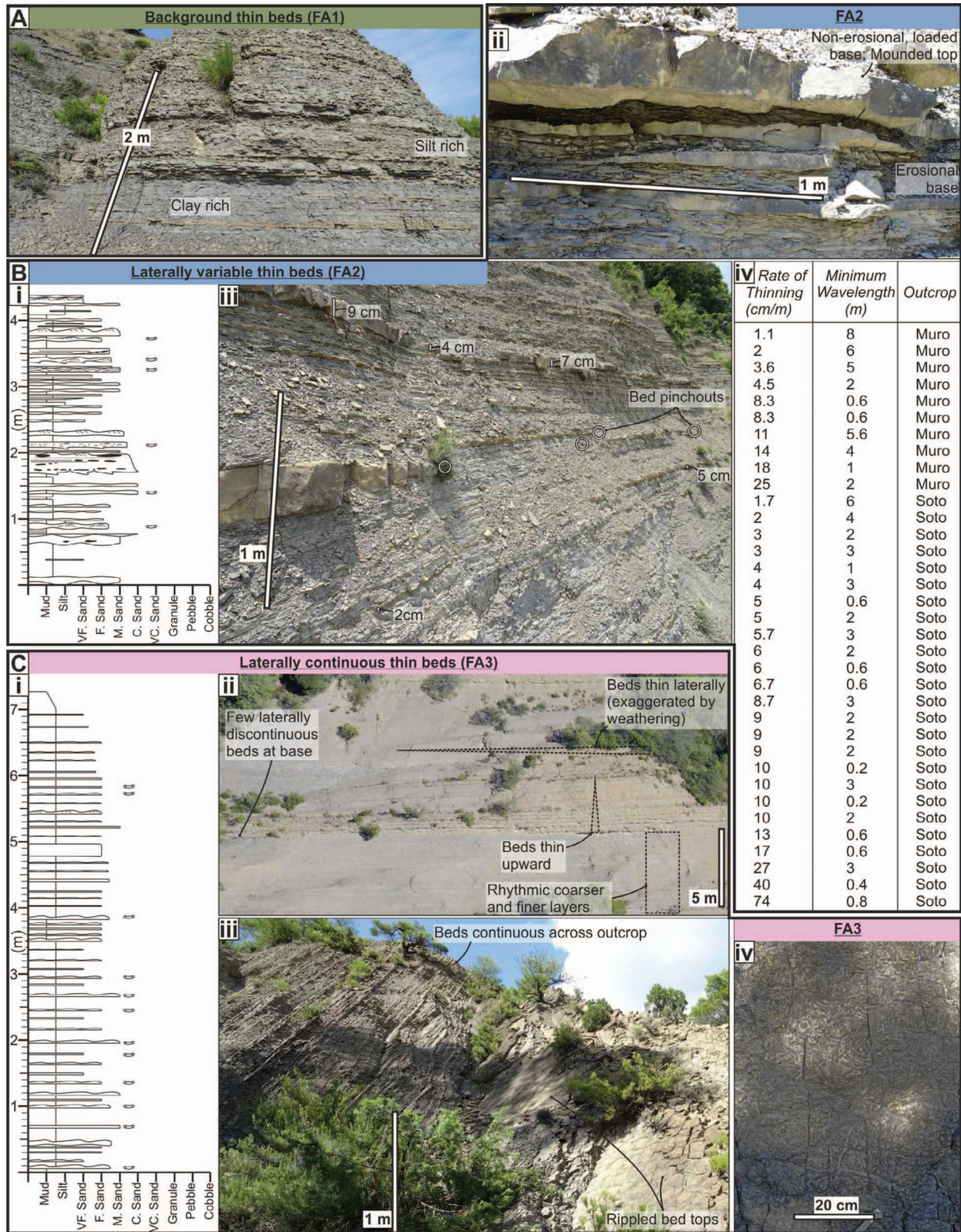


FIG. 6.—A–H) Typical nature of facies associations 1 to 8 (FA1–FA8) respectively. A, Bii–iii, Cii–iii, Dii–iii, Eii, Fii–iii, Gii, and Hi) Representative photographs of all eight facies associations; Bi, Ci, Di, Ei, Fi, and Gi) representative logs through idealized sections of FA2–FA7 respectively; Biv) thinning rates and wavelengths of pinching and swelling beds in FA2; Ci) bed top in FA3 covered by *Scolicia*; Hi) debris mass-transport deposit of FA7 forming a steep-walled scour surface into an underlying sandstone bed.

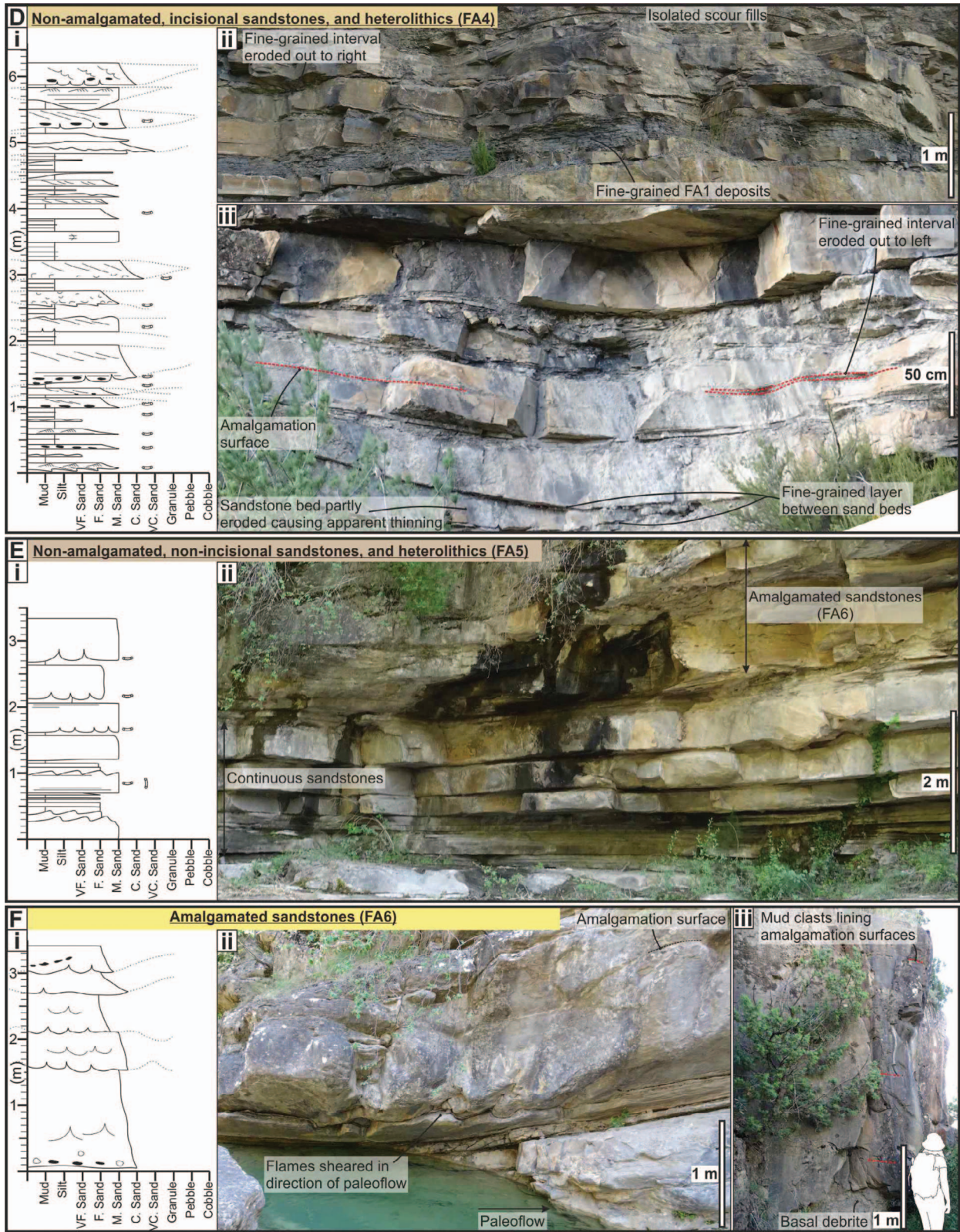


FIG. 6.—Continued.

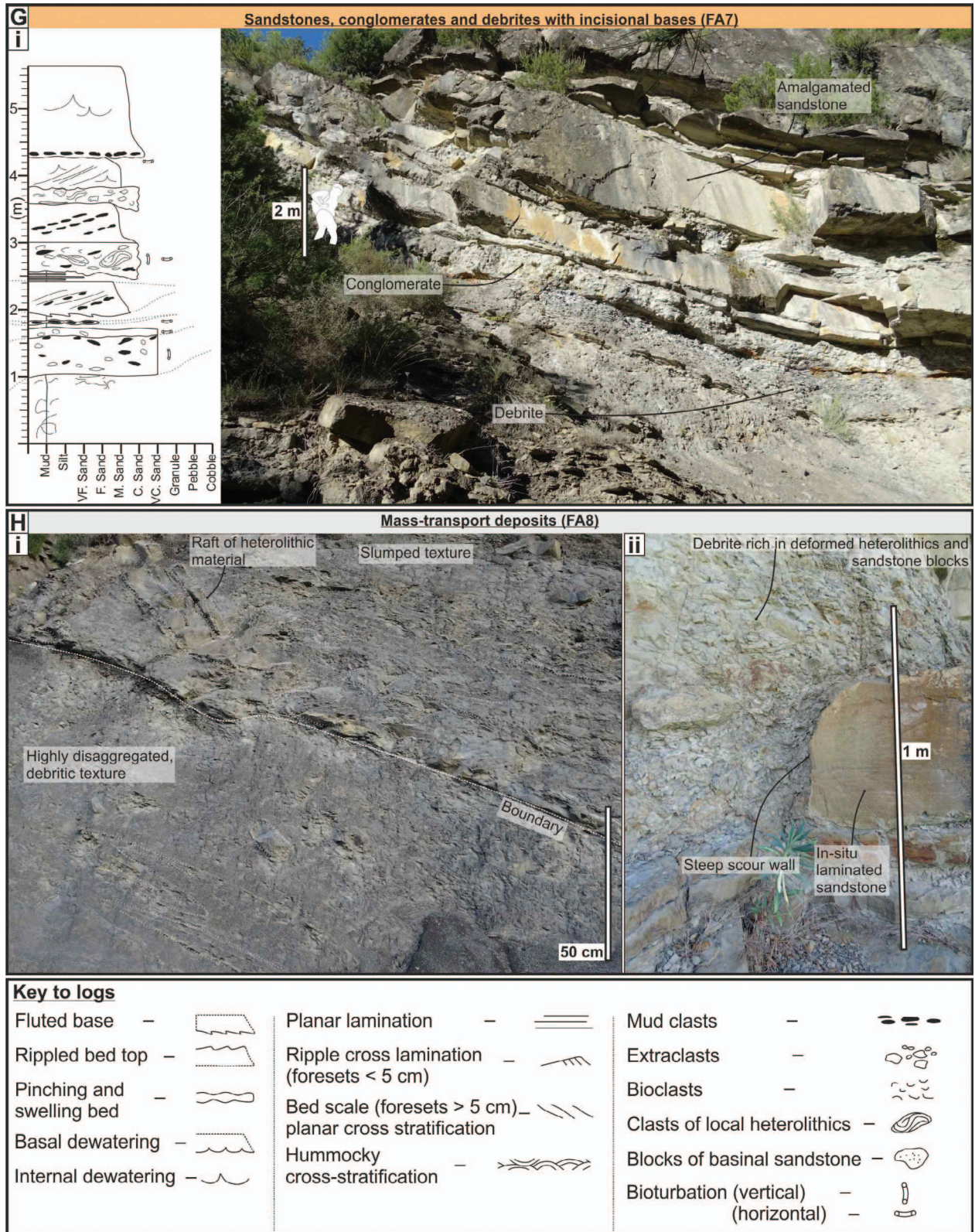


FIG. 6.—Continued.

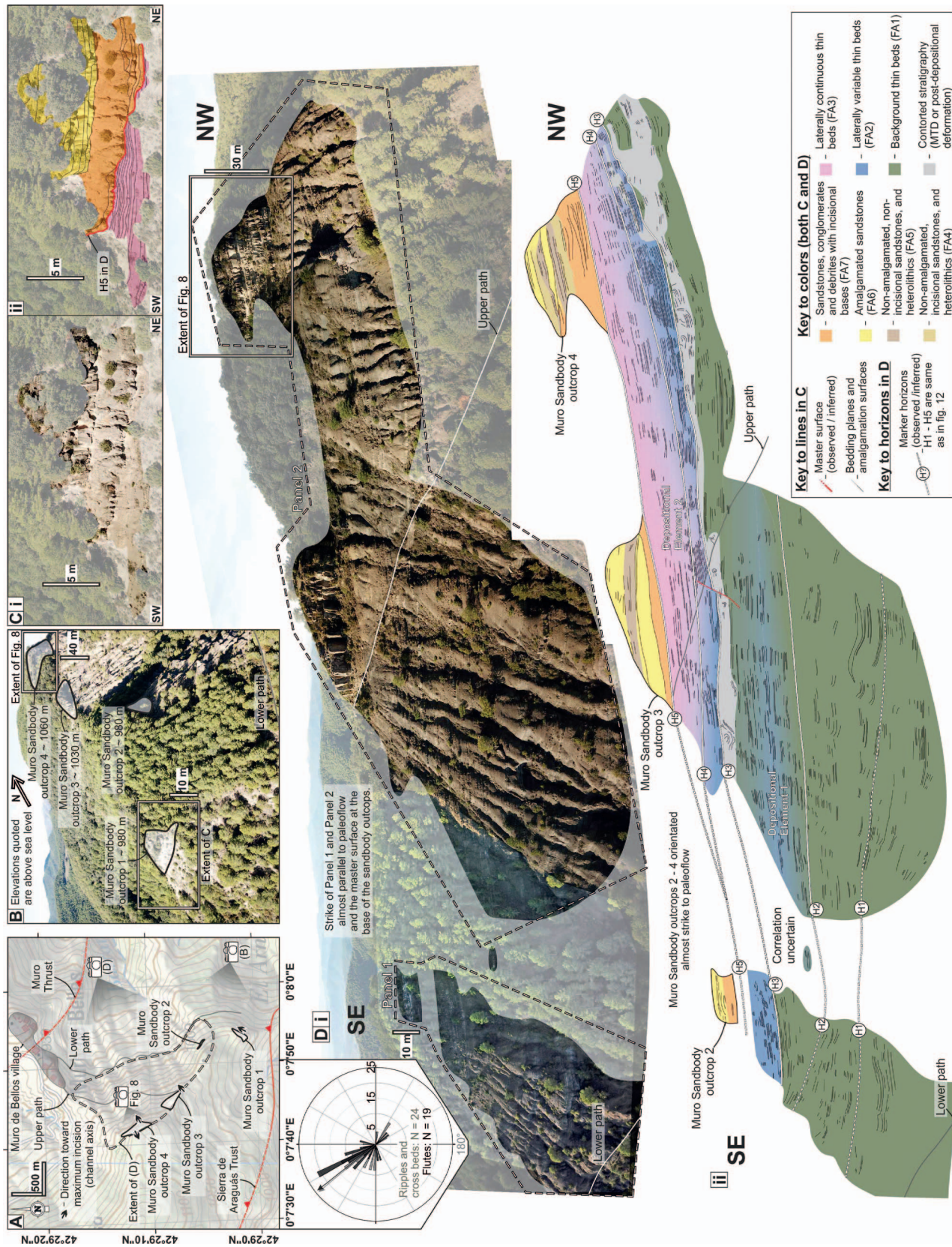


Fig. 7.—Architecture of the Muro de Bellos outcrop. **A**) Locations of the Muro Sandbody outcrops 1–4 and the inferred direction towards their axes, the Muro and Sierra de Aragüas thrusts, panels 1 and 2 in Part D, and a rose diagram showing all paleocurrents collected from the outcrop (channelized and non-channelized stratigraphy combined). **B**) Drone photograph from the east showing the relationship between sandbody outcrops 1–4 and their respective elevations; **C**) Raw (i) and interpreted (ii) photograph of Muro Sandbody outcrop 1. **D**) Photomosaic showing the location of outcrop 1. **D**(i) Interpretation of the photomosaic shown above (panel numbers and marker horizons are the same as in Fig. 12).

et al. 2003; Zavala et al. 2011); iii) the down-slope flow of sediment plumes that build at the mouth of a feeding river and collapse upon attainment of a critical density (Hizzett et al. 2018; Mutti 2019). The presence of FA1 lateral to, and gradational with, FA2 and FA3 suggests that FA1 may also represent distal-most or lateral-most fan or levee deposits. In periods of contemporaneous fan or levee deposition, laterally or upstream, this facies association may therefore have experienced increased rates of aggradation.

Facies Association 2 (FA2): Laterally Variable Thin Beds

Description.—FA2 is highly variable with respect to its constituent facies, bed thickness, and bed nature. It is composed of mainly fine-grained packages (3–50 cm thick) of Lf1, Lf2, and Lf3, interbedded with sandstone beds (> 1 cm, < 50 cm, typically 3–25 cm thick) comprising: rippled (Lf4a), hummocky (Lf4b), and planar cross-stratified (Lf4c), parallel-laminated (Lf5), graded, structureless, and mudclast-bearing (Lf6a–c) and polymictic, bioclastic sandstone (Lf9) (Table 1). Lf4a and Lf6b (Fig. 5) are the dominant sandstone facies (Fig. 6B); Lf4b is particularly prevalent in Sierra de Soto Gully. Bioclasts in beds of Lf9 are fragmented and do not display organization; *Nummulites* typically exhibit a lower degree of fragmentation than bivalve and gastropod bioclasts. Chaotic mudstone (Lf8a) is very rarely observed and, where present, occurs as < 50 cm beds. *Ophiomorpha*, *Nereites*, and *Scolicia* traces are found on some sandstone bed tops, *Thalassinoides* burrows are found on some sandstone bed tops and bases, and other undifferentiated sand-filled burrows are found in some of the fine-grained intervals; no single trace is dominant.

The characteristic feature of this facies association is the geometry of its constituent sandstone beds. Some beds form isolated lenses, some form lenses that pinch out along distinct horizons, and others subtly pinch and swell without forming lenses (Fig. 6B). Bed thinning rates and minimum pinch-and-swell wavelengths (constrained by bed exposures) have been calculated from thirty-five measured beds (average thinning rate: 11.3 cm/m; average minimum wavelength: 235 cm) from the Muro de Bellos (average thinning rate: 9.6 cm/m; average minimum wavelength: 348 cm; N = 10) and Sierra de Soto Gully (average thinning rate: 12 cm/m; average minimum wavelength 190 cm; N = 25) outcrops. Ripple-scale bed thickness variations (7–30 cm wavelength) are sometimes superimposed onto the aforementioned, larger-wavelength, pinching and swelling trends (see Fig. 6B (iv)); the two are usually distinguishable. Bed bases can be flat, lightly incisional (< 10 cm), or exhibit a concave-up geometry which is non-erosional and concordant with bedding below; bed tops can be mounded or flat.

FA2 occurs in all locations and is observed in every depositional element (DE1–4; see “Depositional Elements”), forming lateral transitions with non-amalgamated, incisional sandstones, and heterolithics (FA4) and background thin beds (FA1), and a vertical transition with laterally continuous thin beds (FA3). In some locations, gradational lateral transitions from a package of FA2 in the center to FA1 are observed in both directions. The nature of the bed tops and bases may change dependent on the depositional element in which they are found.

Interpretation.—The presence and fragmented nature of bioclasts in Lf9 suggests that some of the original sediment was derived from a shallow-marine domain. Hummocky cross stratification (Lf4b), interpreted as the product of combined flow, could indicate current reflection or deflection by the interaction with syndepositional basin-floor topography (Tinterri 2011). Beds with erosional bases could represent either the tail deposits of a bypassing turbidity current that deposited coarser-grained material downstream, or the deposit of a lower-energy flow that infilled an erosional surface left by a preceding, higher-energy flow (Kane et al. 2009b). Bedding-concordant (non-erosional) bed bases, still concave-up,

are interpreted to have filled some substrate topography formed by local tectonic deformation or slumping. Mounded bed tops suggest a bedform-related origin, particularly in beds containing planar or hummocky cross stratification (Lf4b–c). In beds with concave-up bases these bedforms may have formed in relation to the infilling of depressions (*sensu* Arnott and Al-Mufti 2017); however, this process does not account for those with flat-bed bases. Another possible formative mechanism is deposition and tractional reworking of sediment forming dunes (Mutti 1977) or megaripples (Tinterri 2011). Postdepositional loading and deformation may also cause or enhance the lateral thickness variability observed in these beds (e.g., Owen 2003; Oliveira et al. 2011).

FA2 exhibits multiple modes of occurrence. Lateral and vertical transitions into a range of other associations means a number of formative scenarios are possible; these are presented in the “Depositional Elements” section.

Facies Association 3 (FA3): Laterally Continuous Thin Beds

Description.—FA3 comprises fine-grained intervals (2–30 cm thick) of structureless mudstone (Lf1), graded siltstone (Lf2), and lenticular sandstone (Lf3) punctuated by beds (typically 2–8 cm thick, average thickness ~ 3 cm) of rippled sandstone (Lf4) which tend to weather proud. Hummocky and planar cross stratified (Lf4b–c), and ungraded, structureless (Lf6b) sandstone beds are also common. Graded (Lf6a) and mudclast-bearing (Lf6c) sandstones are rare. Chaotic mudstone (Lf8a) beds are rare (but more common than in the laterally variable thin beds; FA2) and, where present are < 75 cm thick. Packages of deformed heterolithics (Lf8b), up to 2 m thick, can be found in FA3. Sand-filled burrows are found in the finer-grained intervals, and *Thalassinoides* is occasionally present on sandstone bed bases (< 10% of beds); however *Scolicia* is the dominant trace in FA3. Where bed tops are exposed, they are commonly (> 50% of beds) pervasively bioturbated with *Scolicia* (Fig. 6C).

While the facies assemblage may resemble that of FA2, sandstone beds of FA3 do not pinch and swell, aside from undulations related to their rippled tops (7–30 cm wavelength). Thin (< 8 cm) sandstone beds are largely observed to maintain their thickness laterally over ~ 20 m (Fig. 6C). However, in outcrops with exposures greater than tens of meters, a systematic lateral thinning of these beds is observed. Concomitant with this lateral thinning, FA3 transitions gradationally into background thin beds (FA1; Fig. 6C). FA3 also grades upwards into FA1.

Interpretation.—The regular, thin-bedded nature and systematic thinning of the rippled and structureless sandstone beds is consistent with overbank deposition from dilute turbidity currents which overspill a contemporaneous lateral conduit (Mutti 1977; Mutti et al. 1988; Millington and Clark 1995a, 1995b; Bayliss and Pickering 2015). Susceptibility to slumping and remobilization is common in overbank deposits (Kane and Hodgson 2011; Hansen et al. 2015), and the intensity of *Scolicia* bioturbation also supports this interpretation (Heard et al. 2014).

Facies Association 4 (FA4): Non-Amalgamated, Incisional Sandstones, and Heterolithics

Description.—In this facies association, heterolithic packages of graded siltstone (Lf2) and thin (< 5 cm) beds of lenticular (Lf3) and rippled (Lf4a) sandstone are interbedded predominantly with thin to thick beds (highly variable from 5 to 100 cm thick, typically 20–50 cm) of: planar-cross-stratified (Lf4c), parallel-laminated (Lf5), structureless (Lf6a–b), mudclast-bearing (Lf6c) and bioclastic (Lf9) sandstone. Beds (< 50 cm) of extraclast (Lf7a) and mudclast (Lf7b) conglomerates, and debrites (Lf8a) are observed less commonly. The relative proportions of sandstone beds and fine-grained intervals vary between outcrops (Fig. 6D).

Lateral variability in sandstone bed thickness is related to the presence of erosional surfaces that incise the tops of underlying sandstone beds and into the fine-grained intervals, and that host thicker sediment accumulations in the loci of maximum incision (Fig. 6D). These surfaces are almost always filled mainly by sandstone beds (Lf4c, Lf5, and Lf6a–c) or debrites (Lf8a), and they are often draped by finer-grained deposits (Lf2, Lf3 and < 5 cm beds of Lf4a and Lf6b) that also thicken towards the locus of maximum incision. On rare occasions, the fine-grained deposits are observed to heal the erosional surface completely. FA4 forms a continuum between laterally variable thin beds (FA2) and amalgamated sandstones (FA6). The tendency for the erosional surfaces to cut one another (and lateral transitions into FA2 and FA6) makes measurements of their width and relief problematic, but bed thinning rates (which can be used as proxies) range from ~ 4 to 20 cm/m. Sand-filled burrows are observed in the finer-grained intervals, and *Ophiomorpha* traces are observed.

Interpretation.—The diversity of sandstone facies (similar to that of FA2) and presence of Lf7a, Lf7b, and Lf8a suggests deposition from flows of various concentrations, magnitudes, grain sizes, and velocities. Fine-grained drapes on scoured surfaces likely represent combined accumulation from the fine-grained remnants of bypassing flows (which formed the scour) and possibly subsequent ones (e.g., Mutti and Normark 1987; Mutti 1992; Kane et al. 2009b; Stevenson et al. 2015; Bell et al. 2018a), and a temporary return to background sedimentation (respectively the “bypass” and “abandonment” drape of Barton et al. 2010; Alpak et al. 2013). The erosional nature of FA4 was attained either by unconfined to weakly confined scouring flows which were not fully contained by their lateral confinement but were still able to scour and bypass coarse sediment fractions, and/or as the lateral expression of higher-energy channelized deposits.

Facies Association 5 (FA5): Non-Amalgamated, Non-Incisional Sandstones, and Heterolithics

Description.—This facies association consists of medium-bedded (10–100 cm) rippled (Lf4a), parallel-laminated (Lf5), and structureless (graded and ungraded; Lf6a–b) sandstones interbedded with finer-grained heterolithic packages. These packages (typically < 20 cm thick) comprise graded siltstone (Lf2) and thin (< 5 cm) beds of lenticular (Lf3), rippled (Lf4a) and graded, structureless (Lf6a) sandstone. Sandstone beds usually exhibit a sharp basal boundary followed by a thickening-upward and sometimes a coarsening-upward trend (Fig. 6E). Both sandstone beds and fine-grained packages maintain their thickness for up to 40 m laterally, unless incised by an erosional surface underlying another facies association (Fig. 8). FA5 is observed solely in outcrops containing channelized deposits (locations 3, 18, and 22; Fig. 2), wherein it may both overlie and underlie non-amalgamated, incisional sandstones, and heterolithics (FA4) or amalgamated sandstones (FA6) (Figs. 6E, 8).

Interpretation.—Laterally continuous, non-erosional sandstone beds associated with channel deposits may form when a channel has filled its confining surface (the “spill” phase; Gardner et al. 2003), or from the deposition of sand “sheets” from flows which were fully laterally confined but possessed insufficient energy to erode (McCaffrey et al. 2002). The latter interpretation is favored due to the sharp base and upward thickening. The presence of a sharp basal contact with underlying FA4 and FA6 (Fig. 8) deposits which, internally, contain more evidence of erosion, is interpreted to be due to a rapid drop in local sedimentation rate, likely due to an upstream blockage, or avulsion causing an abrupt lateral shift in the channel axis. Vertical transitions into overlying FA4 and FA6 deposits represent a return to high-energy flow conditions, potentially accompanying an increase in local sedimentation rate (McCaffrey et al. 2002).

Facies Association 6 (FA6): Amalgamated Sandstones

Description.—FA6 is composed solely of sandstone facies, comprising rippled (Lf4a), planar-cross-stratified (Lf4c), parallel-laminated (Lf5), structureless (graded and ungraded; Lf6a–b) and mudclast-bearing (Lf6c) sandstones. Among these, Lf6a–c appear dominant, but its common pervasive dewatering may obscure the identification of sedimentary structures (Fig. 6F). Sandstone packages of FA6 can be > 5 m thick, but internal amalgamation surfaces picked out by grain-size breaks or horizons of aligned mudclasts are ubiquitous (Fig. 6F); these erode into and are filled by sandstone beds. Amalgamation surfaces are concave-up and typically exhibit dips of up to 40° (corrected for local bedding). In outcrops oriented quasi-perpendicular (60–90°) to local paleoflow (e.g., locations 3 and 14; Fig. 2), the wavelength of scouring varies from ~ 1.5 m to > 25 m. In such outcrops, the locus of maximum incision of successive scours switches laterally in both directions; however, scour walls dipping towards higher-energy sandstones, conglomerates, and debrites with incisional bases (FA7) are preferentially preserved. In outcrops orientated subparallel (0–30°) to local paleoflow (e.g., locations 18 and 19; Fig. 2), scour walls exist in the same dip range, but do not have a preferential orientation of preservation. In FA6, packages of Lf6b can be up to 4 m thick without development of any obvious amalgamation surfaces, although dewatering might obscure them. Where dewatering is not present, maximum bed thickness (between amalgamation surfaces) is rarely > 1.2 m, and is never greater than 2 m, in keeping with typical channel bed thicknesses quoted in Fryer and Jobe (2019). This facies association lies in a continuum between non-amalgamated, incisional sandstones, and heterolithics (FA4) and (FA7).

Interpretation.—FA6 is the result of deposition from recurrent, sand-rich turbidity currents that locally eroded, bypassed, and deposited. Common amalgamation surfaces may have been filled by their formative flows or represent periods of sustained bypass (e.g., Kane et al. 2009b; Bell et al. 2018a). Surface-lining mudclasts likely represent residual lag deposits (Stevenson et al. 2015), possibly derived externally (from a proximal source), or locally, from the erosion of a fine-grained drape (Mutti 1992; Kane et al. 2017). The frequency and/or magnitude of events increased towards a depositional low (i.e., channel axis), causing the preferred preservation of axis-dipping scour walls in cross section, but not longitudinal, paleoflow-parallel sections.

Facies Association 7 (FA7): Sandstones, Conglomerates, and Debrites with Incisional Bases

Description.—FA7 comprises rippled (Lf4a), cross-stratified (Lf4c), parallel-laminated (Lf5), structureless (graded and ungraded; Lf6a–b), mudclast-bearing (Lf6c) and bioclastic (Lf9) sandstones, extraclast and mudclast conglomerates (Lf7a–b), and MTDs (Lf8a–b) (Fig. 6G). MTDs in FA7 are sometimes stacked (Fig. 8). They mostly occur as < 1-m-thick debrites of variable composition, with a silt- and clay-rich matrix containing a combination of: i) sandstone (< 40 cm long axis) and local heterolithic (< 1 m long axis) blocks; ii) bioclasts (< 1.5 cm long axis); iii) extraclasts (< 3 cm long axis, typically comprising lithic fragments and clasts of rounded carbonate). In distinguishing debrites within FA7 from those comprising FA8, their architectural context is used: debrites in package-bounding confining surfaces (such as channel walls; cf. DE3 and DE4; see “Depositional Elements”) are classified as FA7 deposits (Fig. 9).

FA7 displays internal erosion, with bed bases of each lithofacies incising into one another. Bed thicknesses increase towards the maximum depth of the bounding erosional surface (Fig. 9). In longitudinal, paleoflow-parallel sections, some erosional bed bases are asymmetric, steeper upflow (maximum dip ~ 40°) than downflow (maximum dip ~ 20°). These surfaces can contain a higher concentration of imbricated mudclasts

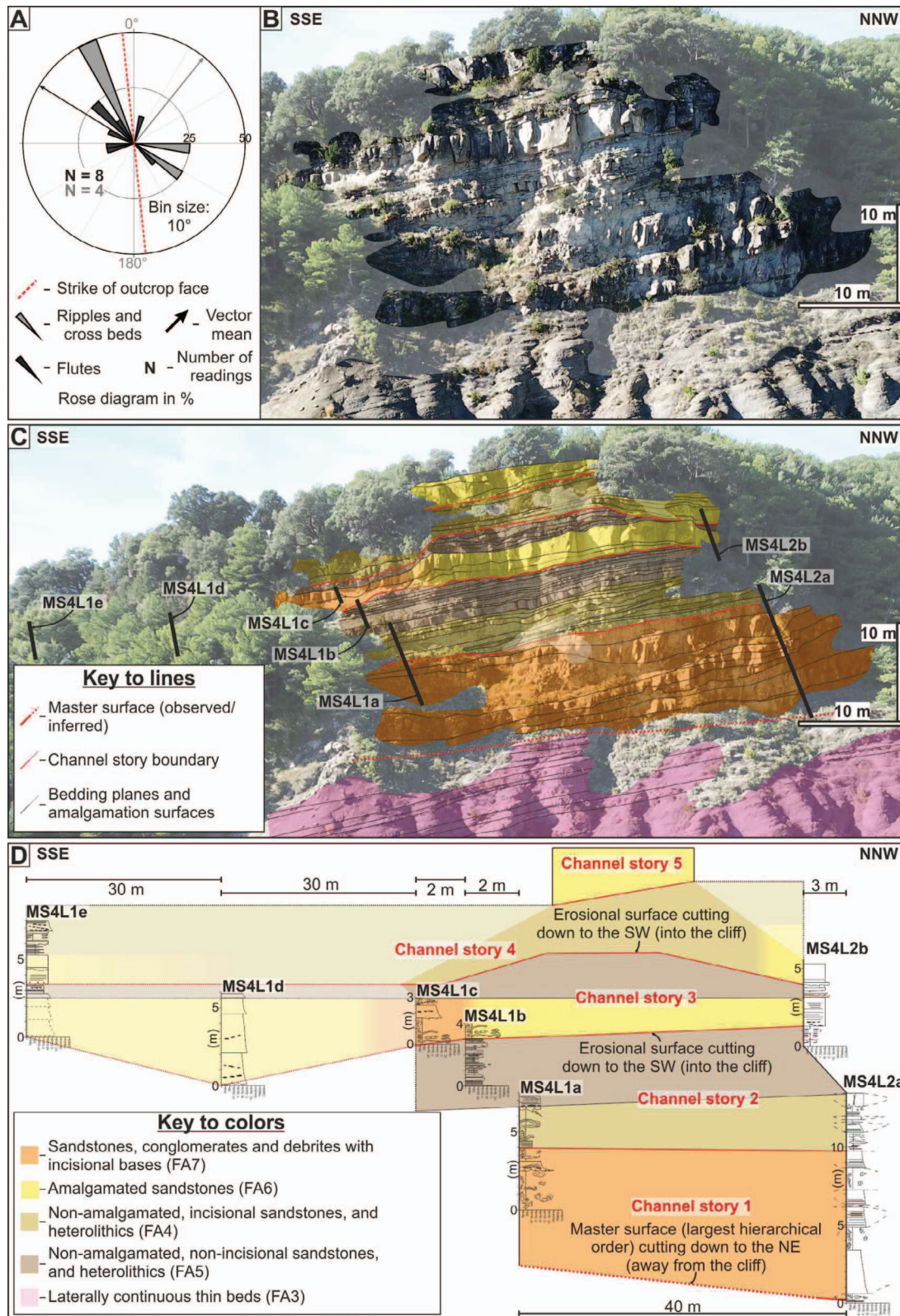


FIG. 8.—A) Rose diagram showing local paleoflow and its relationship with the strike of the outcrop face. B) Drone photograph of the Muro Sandbody outcrop 4. C) Interpretation of photograph in Part B, showing bedding planes, facies associations, and log locations. D) Correlation panel built from the logs in Part C.

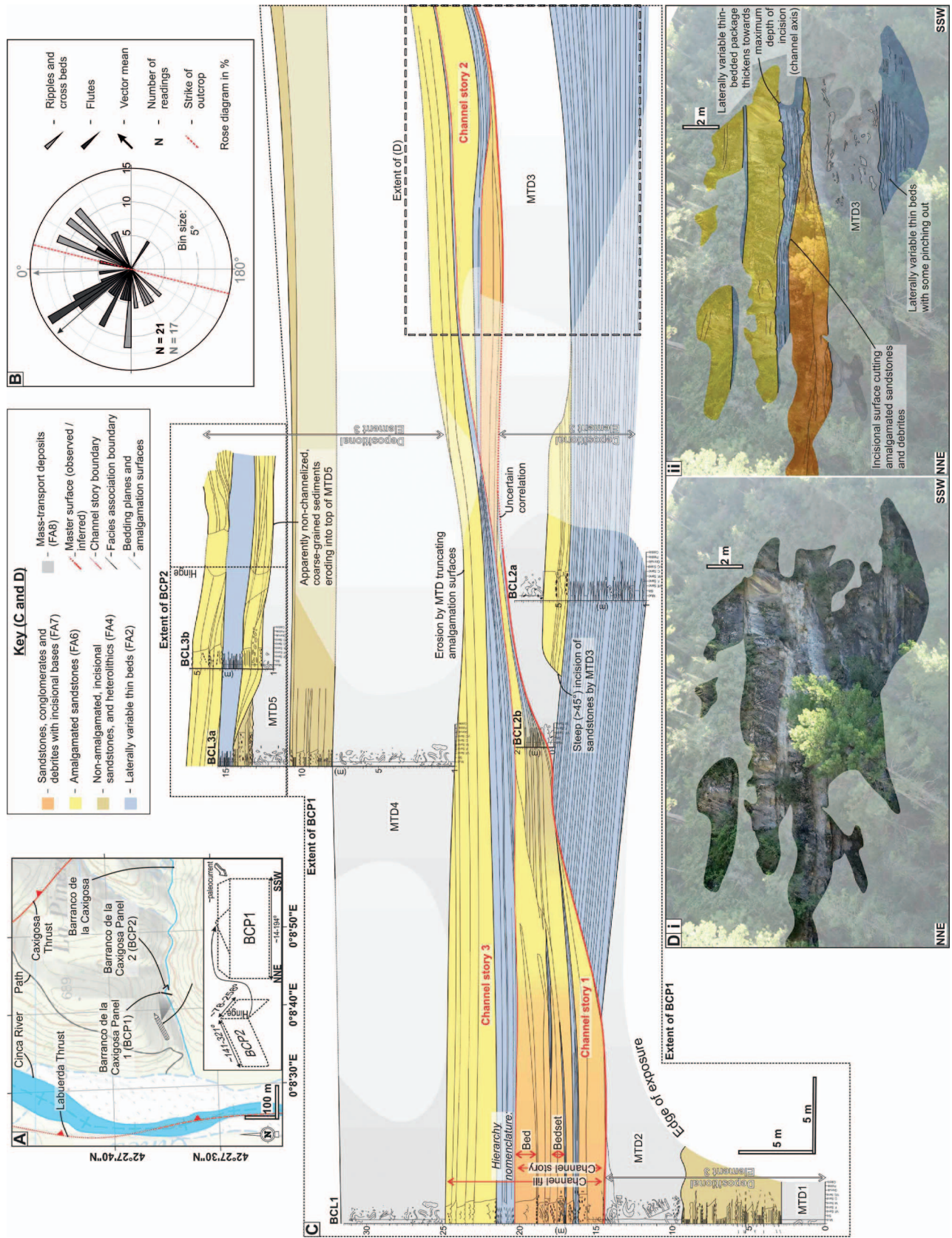


Fig. 9.—Architecture of the Barranco de la Caxigosa outcrop: **A)** Summary map showing the locations and orientations of the panels in Part C, and the Labuerda and Caxigosa thrusts. **B)** Rose diagram showing local paleoflow and its relationship with the strike of panel BCP1. **C)** Correlation panel built from logs and interpreted photographs, such as in Part D, showing bedding planes, facies associations, and channel stories. **D)** Raw (i) and interpreted (ii) photographs forming the basis for the correlation in the WSW of panel BCP1.

against the steep side, dipping down-flow; they are interpreted as megafutes (Elliott 2000; Kane et al. 2009b). FA7 forms a continuum with amalgamated sandstones (FA6).

Interpretation.—Erosional, generally coarse-grained lags and debrites are commonly observed in channel thalwegs (Mayall et al. 2006; Hubbard et al. 2009; Kane et al. 2009a; Bell et al. 2018b). These build incrementally through repeated scouring, bypassing, and deposition from passing, possibly supercritical flows (Froude number > 1 , Komar 1971).

Facies Association 8 (FA8): Mass-Transport Deposits (MTDs)

Description.—FA8 is composed solely of MTDs exhibiting debritic (Lf8a) and slumped (Lf8b) textures, found outside of confining surfaces that bound packages (see FA7 for distinction); they are typically > 1 m thick and sometimes stack up to > 22 m thick (Fig. 6H). The composition of the debrites (Lf8a) is highly variable, with blocks or clasts derived from any of the other lithofacies in the system (see Table 1) hosted within a heterolithic matrix. Blocks of conglomerate (Lf7) and bioclastic, polymict sandstone (Lf9) are observed amongst isolated extraclasts and bioclasts. Deformed, isolated blocks (a few decimeters to meters) of background (FA1), laterally variable (FA2) and laterally continuous (FA3) thin beds are common in FA8. The composition of Lf8b is almost exclusively fine-grained heterolithic, thin-bedded deposits.

Basal contacts of FA8 packages can incise up to 3 m into underlying deposits, and are sometimes manifested as broad erosional surfaces (Fig. 9) with the MTD thickening towards the maximum incision depth, or as steep (up to 90° in some cases) walled scours (Fig. 6H). The tops of FA8 packages are commonly eroded and filled by FA2, FA4, FA6, and FA7 (Fig. 9).

Interpretation.—The formative flow type and the resultant depositional character of an MTD depends mainly on the composition (mainly its clay content) and degree of disaggregation (controlled principally by its transport history; Moscardelli and Wood 2008; Bull et al. 2009; Ogata et al. 2012). Because the MTDs of FA8 are highly variable in their texture and composition, determining transport distance is problematic. Furthermore, compositional indicators often used to determine source, such as dispersed bioclasts and extraclasts, might all be derived from their feeding lithologies or have been incorporated through basal substrate erosion. Isolated extraclasts and bioclasts may have been incorporated from the disaggregation of blocks of Lf7 and Lf8 during transportation.

Arbués et al. (2007a, 2007b) attributed the < 20 m thick, stacked MTDs at Los Molinos Road to failures on a structurally controlled, laterally confining slope. Mutti (1985) and Dakin et al. (2013), however, recognize longitudinally emplaced MTDs in the Aínsa channel systems. The data presented herein do not allow conclusive determination of whether the thick (> 1 m) MTDs of FA8 (Fig. 9) were derived dominantly from transverse sources, such as growing structures (Arbués et al. 2007a) or the collapse of a confining surface (Hansen et al. 2015), or from more proximal sources such as the head or wall of a feeding canyon (Nelson et al. 2011), the shelf or upper slope (Ortiz-Karpf et al. 2017). Furthermore, an MTD that may appear (based on composition and/or degree of disaggregation) to have been emplaced longitudinally may have been derived from a transverse source in a more proximal location, potentially kilometers upstream. Based on the (slumped) character and composition (all apparently derived from local stratigraphy) of the deposits, a transverse source is favored for the emplacement of the MTDs in FA8.

DEPOSITIONAL ELEMENTS

Classification of depositional elements is useful in systems where facies associations are not unique to a single depositional environment. The following depositional elements are derived from groups of facies

associations on the basis of systematically recurring vertical or lateral interrelationships, or of relationships with key bounding surfaces.

Depositional Element 1 (DE1): Weakly Confined, Increasing-to-Decreasing-Energy Deposits

Observations.—The base, top, and lateral edges of DE1 (best observed in Sierra de Soto Gully; between H4 and H5 in Fig. 10) are transitional. Within its basal transition, background thin beds (FA1) grade into laterally variable thin beds (FA2) over 1–4 m. At its top, FA2 grades into FA1 over 2–6 m. Laterally, FA2 transitions into FA1 over tens of meters away from the depositional locus (the location of maximum net sandstone thickness and average sandstone bed thickness). Lateral transitions show a gradual upward increase, followed by a subsequent decrease, in the extent of sandstone beds. While in some outcrops both lateral margins are observed, in most well exposed locations only one margin is preserved. The longitudinal expression of DE1 is poorly constrained, but it is assumed to be elongate in a down-flow orientation. Constituent sandstone beds exhibit all bed geometries recognized in FA2: flat, lightly incisional, or concave-up but non-erosional bases; flat or mounded tops. No common lateral thickening trend is recognized in the sandstone beds, but their average thickness increases towards the depositional locus. From tracing FA2 packages laterally, aggradation in the depositional locus appears to be comparable to that of the margins and surrounding FA1 deposits. Non-amalgamated, incisional sandstones, and heterolithic (FA4) are sometimes present within the depositional locus, transitioning laterally and vertically into FA2.

In Sierra de Soto Gully (Fig. 10), the lateral transition from FA2 to FA1 migrates towards the WSW, away from the Sierra de Araguás thrust; paleoflow directions based on the ripples and cross beds therein also show a western deflection, relative to the flute casts (Fig. 10B). At Muro de Bellos, the same lateral facies transition occurs towards the Muro and Sierra de Araguás Thrusts, which laterally bound the stratigraphy (Fig. 7).

Interpretation.—No master confining surface bounds DE1 at the outcrop scale, so the velocity maxima of the formative flows of constituent FA2 deposits were effectively unconfined. However, the constituent sandstones are thinner, laterally more variable, and less amalgamated than those typical of unconfined, sand-rich deposits (cf. Remacha et al. 2005; Liu et al. 2018; Fryer and Jobe 2019); evidence for compensation is also lacking. The pinching and swelling geometries and bypassing nature of constituent sandstone beds, and the lack of amalgamation and compensation, suggests these are unlike classical “lobes” (Mutti et al. 1994; Prélat et al. 2010). Facies and bed geometries in FA2 deposits show evidence for tractional reworking and scouring (Fig. 6B). However, coarse-grained lag deposits and mud-draped scours indicative of bypassing, high-concentration flows (Barton et al. 2010; Alpak et al. 2013; Stevenson et al. 2015) are largely absent. Therefore, FA2 deposits in DE1 represent low-concentration, generally fine-grained but dominantly bypassing flow deposits.

Observed vertical transitions within DE1 represent increasing and subsequently decreasing flow energy. This motif arises in response to variations in local sediment delivery (Fig. 11), due either to an upstream levee crevasse (formed from a failed avulsion), or driven by basinal supply (Lowe et al. 2019). The relationship with structures suggests that the depositional axes of DE1 coincided with the deepest part of elongate topographic lows, which also controlled the location of lateral facies transitions. Movement (dominantly forward propagation) of fairway-bounding structures is inferred to be responsible for the lateral shifts in the depositional axis and subtle lateral facies association transitions as seen in Sierra de Soto Gully (Fig. 10). Lateral facies transitions are associated with increasing local sand input, as the high-velocity sand-rich part of flows was able to spread over a wider area, whilst still contained within the fairway (Fig. 11B).

Increases in velocity on steep axial gradients may allow a weak flow to exceed its bypass threshold, causing it to erode or bypass, and leaving a thin

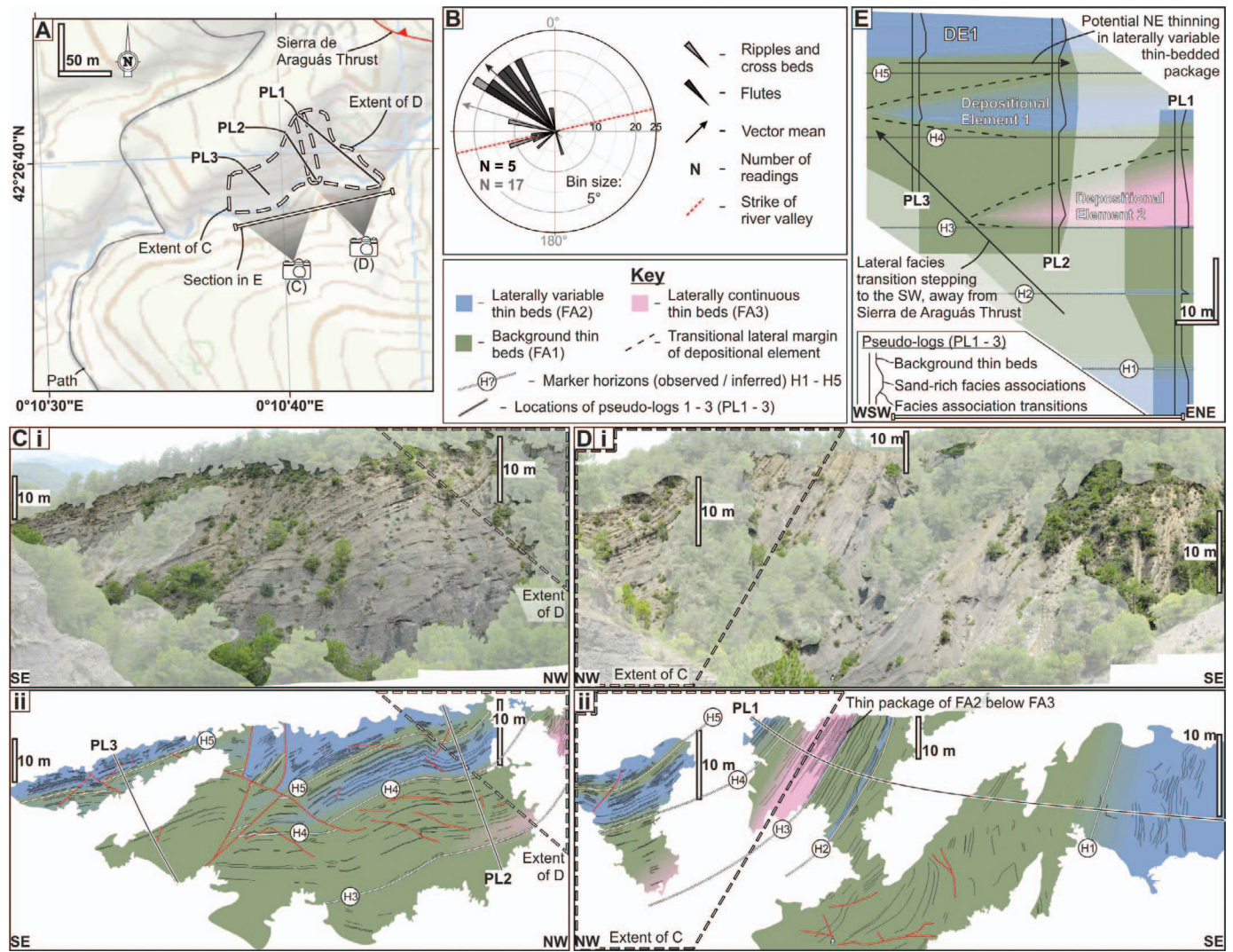


FIG. 10.—Architecture of the Sierra de Soto Gully outcrop: **A)** summary map showing the extent of the panels in Parts C and D, and the locations of the pseudo-logs in Part E and Sierra de Araguás Thrust. **B)** Rose diagram showing local paleoflow and its relationship with the strike of the gully. **C)** Photomosaic (i) and interpreted line drawing (ii) of the western outcrop panel. **D)** Photomosaic (i) and interpreted line drawing (ii) of the eastern outcrop panel. **E)** Correlation panel showing DE1 and DE2, and their constituent vertical and lateral facies association transitions, built from pseudo-logs created using outcrop panel interpretations supported by measured log data.

deposit or no deposit (Stevenson et al. 2015; Dorrell et al. 2018). Elongate sediment pathways provide subtle lateral confinement, which may also cause flow velocity to increase (Fig. 1). At the bases of these weakly confined flows, substrate topography (meters to tens of meters in wavelength) generated by previous flows, sediment loading, or small structures cause localized velocity variability (Eggenhuisen et al. 2010; Dorrell et al. 2019), which leads to the formation of tractional bedforms and scours (Fig. 11). Modern canyons (Paull et al. 2018) and fjord-head delta slopes (Hughes Clarke 2016) also experience broad lateral confinement (a few kilometers across). Turbidity currents monitored in such settings commonly die out only kilometers from the source (e.g., Paull et al. 2018). DE1 may provide an ancient analog for these weak flows.

Depositional Element 2 (DE2): Progradational, Weakly Confined to Overbank Deposits

Observations.—DE2 is observed in Muro de Bellos (Fig. 7) and Sierra de Soto Gully (Fig. 10). Similarly to the increasing-to-decreasing-energy

deposits of DE1, there is a basal vertical transition from background thin beds (FA1) into laterally variable thin beds (FA2) over 1–4 m; the same lateral transition as in DE1 (from FA2 to FA1 over tens of meters away from the depositional locus) is also observed (Fig. 11). Above this, another transition is observed, with a gradual upward decrease in pinching and swelling of beds (of FA2), and a proportional increase in laterally continuous thin beds (FA3). The boundary between the two is arbitrary; however, the FA3 part tends to be thicker (> 20 m) than the FA2 part (> 10 m). FA3 deposits grade vertically into FA1 at the top of DE2. Constituent FA3 deposits can span a wider depositional area than the underlying FA2, leading to some vertical sections showing FA3 grading to FA1 above and below, with an apparently sharp base (see PL1 and PL2, Fig. 10). In Muro de Bellos panel 2 (Fig. 7), DE2 is mostly underlain by a zone of contorted stratigraphy containing folds of meters to tens of meters in wavelength, faults with up to 2 m displacement, and blocks measuring up to several meters. This deformed stratigraphy appears to be composed of, and contained within, FA1 deposits, but locally ramps up and down through the stratigraphy.

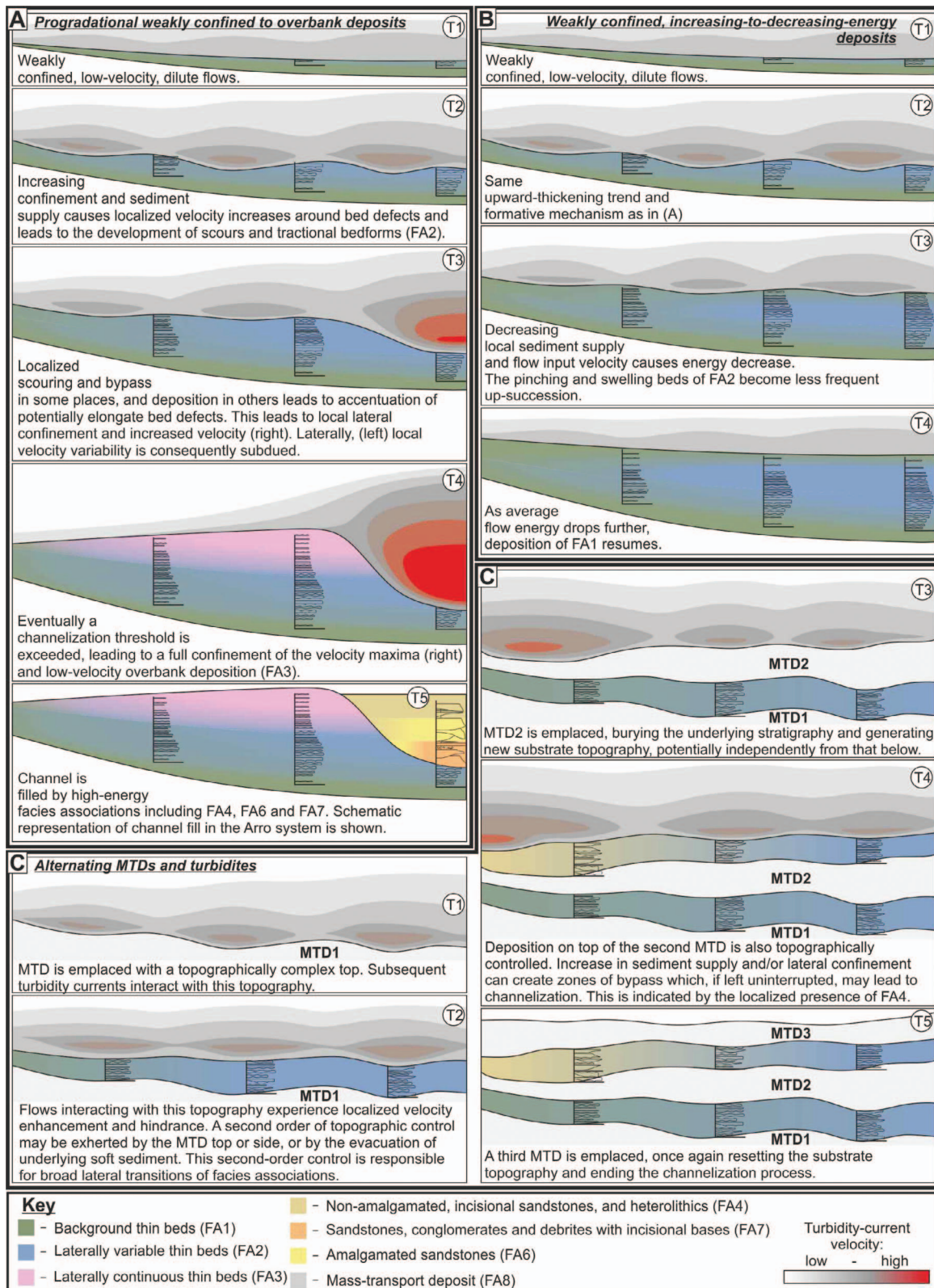


Fig. 11.—Schematic diagrams showing the interpreted formation and evolution of depositional elements 1–4: A) DE2 and DE4, B) DE1, C) DE3.

Interpretation.—DE2 is interpreted to represent the transition from weakly confined deposits (FA2), into overbank deposits (FA3), possibly lateral to the position where a nearby channel was forming (Fig. 11); this is comparable to the transition zone from levee to lobe fringe (Normark et al. 1979; Kane and Hodgson 2011). With locally increasing sediment delivery, weakly confined deposits will prograde; once flow magnitude in the depositional axis crosses the erosional threshold, a channelization feedback may be initiated (Eggenhuisen et al. 2011; De Leeuw et al. 2016) (Fig. 1B). Accordingly, greater proportions of successive flows will become laterally confined, meaning that progressively lower-energy, finer-grained, and better-sorted flows will deposit on the margins (Fig. 11). The progressive nature of this process is reflected in the transitional nature of the contact between FA2 and FA3. DE1 and DE2 represent end members of a continuum controlled by channel development. It is unclear whether the disturbed interval beneath DE2 in Muro de Bellos was emplaced as a large MTD, or is a postdepositional product of tectonically or gravitationally driven deformation (Fig. 12). If the former is true, the contorted zone may have influenced progradation and channel inception. However, due to the fact that this contorted zone is not constrained to a stratigraphic interval and ramps into overlying stratigraphy, the deformation is likely postdepositional.

Depositional Element 3 (DE3): Alternating MTDs and Turbidites

Observations.—DE3 comprises packages (1–8 m thick) of turbidite facies associations (background (FA1) or laterally variable (FA2) thin beds, or non-amalgamated, incisional sandstones, and heterolithics (FA4) between stacked or single MTDs (FA8) (< 20 m)). It is best observed in Barranco de la Caxigosa, where five MTDs (MTD1–MTD5; Fig. 9) are interbedded with ~ 3–10-m-thick, dominantly turbiditic, packages, one of which (between MTD3 and MTD4) is obviously channelized and is not included within DE3 (see DE4). Any of the turbidite packages (FA1, FA2, or FA4), which exist in a continuum with each other, can overlie and underlie sharp basal and top contacts with MTDs of FA8. Lateral transitions exist between FA1 and FA2, and between FA2 and FA4. Where lateral transitions are visible, the higher-energy facies associations overlie the deepest part of the basal contact (MTD top), transitioning laterally into thinner, lower-energy packages. The contacts with the overlying MTDs are commonly erosional. Exposure of MTDs in the Arro system is insufficient to trace their full extent. Millington and Clark (1995a, 1995b) and Arbués et al. (2007a, 2007b) describe DE3 at Los Molinos Road, where the turbidite-prone intervals dominantly thin towards the NE, with one notable exception thinning to the SW.

Interpretation.—The nature of DE3 is interpreted to be controlled by the interplay between an underlying MTD and the magnitude, concentration, and grain size of overpassing turbidity currents. The response of turbidity currents to this MTD-top topography is recorded in the overlying turbidite deposits. Depositional lows present on the top of MTDs, or left behind by erosive MTDs, can either generate partial ponding or provide lateral confinement which may enhance channelization (Fig. 11; Schultz et al. 2005; Bull et al. 2009; Hansen et al. 2013; Kneller et al. 2016; Ward et al. 2018). The reason turbidite packages in DE3 may not have crossed a channelization threshold and formed DE4 may be that the lateral confinement or axial gradient provided by the underlying MTD were insufficient, or the emplacement of a subsequent MTD may have interrupted the process and reset the basin-floor topography (Fig. 11). The interplay of the aforementioned factors means that DE3 can form a continuum with increasing-to-decreasing-energy deposits (DE1), progradational-to-overbank deposits (DE2) and channels (DE4).

Arbués et al. (2007a, 2007b) interpreted deposits of this type at Los Molinos Road as the lateral expression of non-exposed channel bodies to the SW of the outcrop. Therein, FA2 deposits (their “TS” facies

association) are interpreted as marginal deposits associated with channel bodies, which are formed in response to the emplacement of MTDs. Definitive distinction of the aforementioned interpretations is not possible based on field data due to limited outcrop exposure in both Los Molinos Road and Barranco de la Caxigosa. However, it is likely that a continuum exists between DE3 and DE4, whereby the early stages of channelization in locations prone to MTD emplacement are similar to those responsible for the deposition of the turbiditic intervals in DE3.

Depositional Element 4 (DE4): Channels

DE4 comprises sandbodies which are characterized by nested erosional surfaces (see below) and that contain non-amalgamated, incisional sandstones, and heterolithics (FA4), non-amalgamated, non-incisional sandstones, and heterolithics (FA5), amalgamated sandstones (FA6), and sandstones, conglomerates, and debrites with incisional bases (FA7).

Four sandbody exposures crop out at the Muro de Bellos location (Muro Sandbody outcrops 1–4; Fig. 7) above a thick (> 150 m) succession of predominantly background thin beds (FA1), but with laterally variable (FA2) and laterally continuous (FA3) thin beds in the upper ~ 30 m (Fig. 7D). While all four outcrops contain DE4 elements, sandbody outcrop 4 exhibits the greatest exposure, therefore allowing the most detailed analysis (Fig. 8). In the Barranco de la Caxigosa outcrop (described above), one of the five turbidite packages (up to 11 m thick) contains FA2, FA4, FA6, and FA7 (Fig. 9) and multiple nested erosional surfaces; this package is therefore classed as DE4.

Because of their characteristic nested erosional surfaces and sandy fill, DE4 deposits are interpreted as the fill of submarine channels. Further description and discussion of these deposits is presented below.

Key Surfaces and Hierarchy.—Channelized deposits are hosted within concave-up surfaces which may be generated by erosion and/or co-genetic thin-bedded turbidites formed from overspill (Hodgson et al. 2011; Brunt et al. 2013). At least three hierarchical orders of confining surface are observed, which are named according to the hierarchical nomenclature scheme of Sprague et al. (2005; Fig. 9). These orders are distinguished based on scale and the recognition of nested surfaces starting at the smallest: bed bases. While key surfaces are used to define each hierarchical order, in areas where bed truncation is not apparent, these surfaces are picked out by major changes in facies associations:

1. Bed or bedset surfaces (< 3 m deep) with scour-like geometries are observed in paleoflow-parallel and -perpendicular sections (Figs. 8, 9); in sections subparallel to flow (SE–NW; e.g., location 18, Fig. 2) megafutes can be observed. Scours were cut by the erosive part of an unsteady flow (Kneller 1995), or by wholly erosive or bypassing flows. They were filled by the depositional part of the scour-forming flow, or by a subsequent depositional flow (e.g., Kane et al. 2009b; Stevenson et al. 2015; Bell et al. 2018a). The process of cut and fill builds stratigraphy incrementally in deep-water channels.
2. Channel story surfaces (3–10 m deep at axis) are concave-up and elongate (in the direction of local paleoflow), and are best observed at Barranco de la Caxigosa (Fig. 9). These cut through bed and/or bedset fills and exist within larger channel fill surfaces (below). Ranges for the typical depth of incision of bedsets and channel stories overlap, such that these two scales can be difficult to distinguish (Sprague et al. 2005; Cullis et al. 2018). However, at least three channel stories are identified at Barranco de la Caxigosa (Fig. 9), and at least five in Muro Sandbody outcrop 4 (Fig. 8). Sprague et al. (2005) quote typical channel story thicknesses of 3–5 m, meaning that scale overlap with channel fills (10–30 m) is unlikely. However, the basal 10 m of Muro Sandbody outcrop 4 is interpreted to belong to a single channel story. In axial sections, distinguishing bed- or

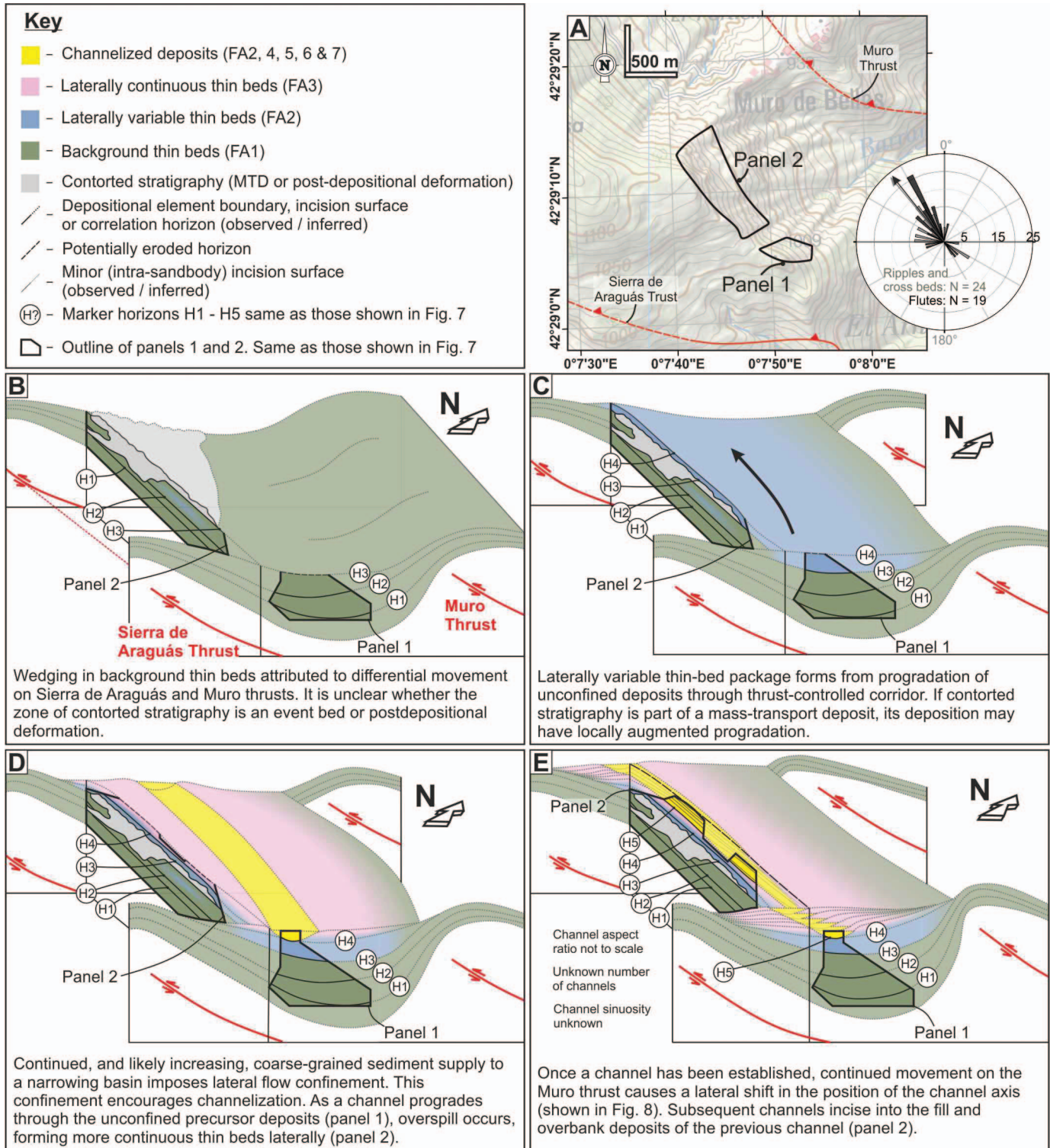


Fig. 12.—A) Map showing the locations of panels 1 and 2, the Sierra de Araguás and Muro thrusts, and local paleocurrent (rose diagram same as in Fig. 7A); B–E) sketch diagrams showing the evolution of the channels in Muro de Bellos through four time steps. Interpreted panels 1 and 2 presented in Figure 7 have been used to inform the interpretation and are displayed herein.

bedset-scale amalgamation within a story from a story bounding surface is difficult. Therefore, it is possible that, within this package, more stories are hidden due to the cliff striking at a low angle to local paleoflow, or that an overlap may exist between the channel story scale and the channel fill scale.

3. Channel-fill surfaces (10–50 m deep at axis) are compound surfaces that bound channel fill deposits in Barranco de la Caxigosa and Muro de Bellos. They result from amalgamation of the bases of laterally and vertically stacked channel stories, such that they also act as the confining surface to channel stories (Figs. 12, 13).

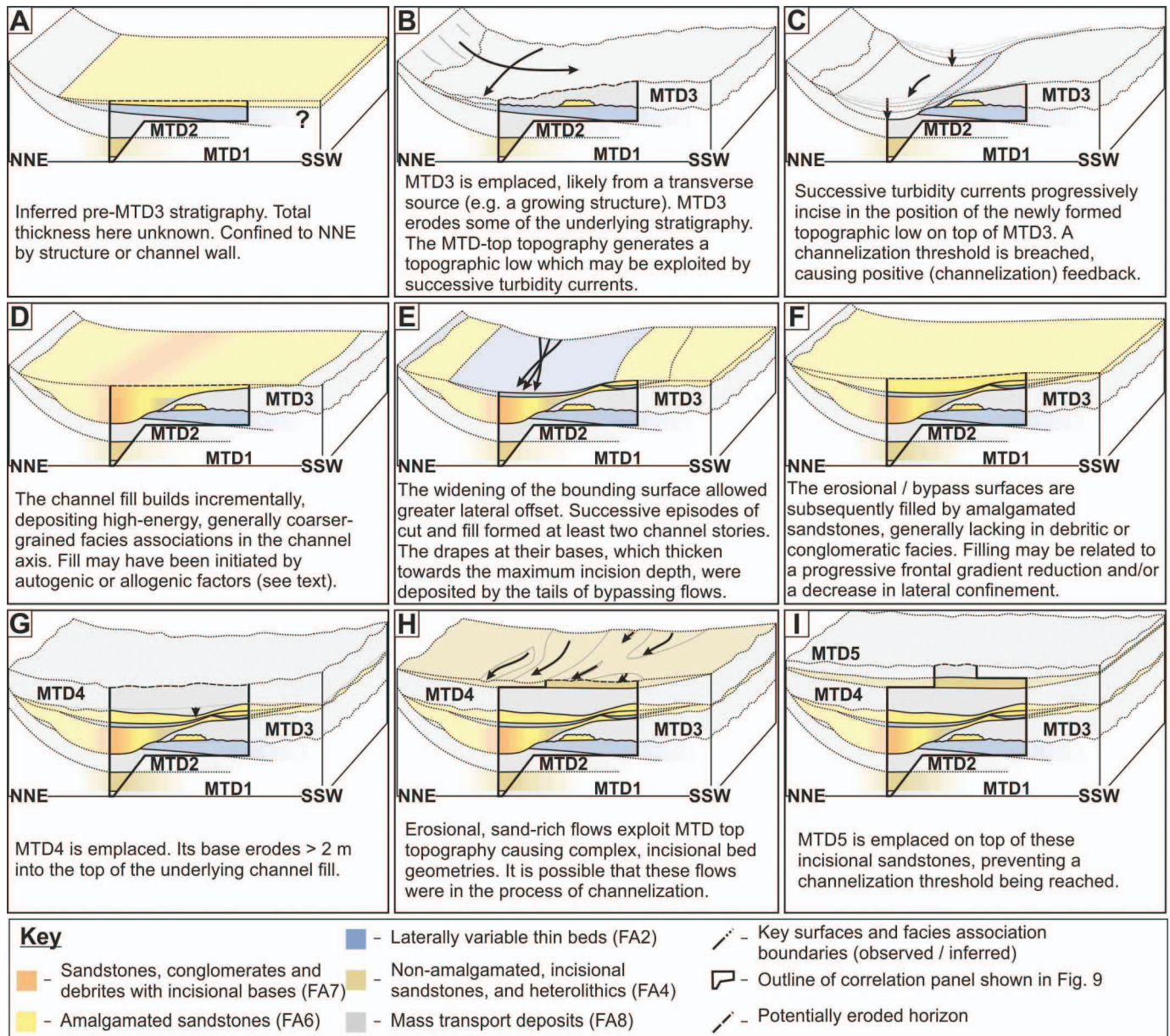


FIG. 13.—A–I) Sketch block models showing the evolution of Barranco de la Caxigosa through nine time steps. Interpretation is informed by panels presented in Figure 9 and displayed herein.

Vertical and Lateral Facies Variability.—Channel story 1 in Barranco de la Caxigosa (Fig. 9) exhibits a lateral facies transition from high-energy deposits of FA7 towards the “axis,” through lower-energy “off-axis” deposits of FA4 and FA6, to fine-grained, laterally variable thin-bedded FA2 deposits at its “margin” (*sensu* McHargue et al. 2011; Hubbard et al. 2014). Sandstone beds of marginal FA2 deposits thin towards (and sometimes onlap onto) their confining surface; towards the axis they thicken or are truncated by the incisional bases of overlying beds. The channel margin thin beds in Barranco de la Caxigosa represent the interplay between i) marginal deposits of dominantly bypassing flows that did not deposit along the paleo-thalweg, ii) the marginal expression of fully depositional flows which thickened towards the channel axis, where some were subsequently eroded, iii) deposits left by the tails of bypassing flows, and hosted within scours, and iv) fine-grained drapes which formed during quiescent periods. Lenses of FA2, independent of the aforementioned

margin deposits, exist within the axial fill. These overlie bedset- and channel-story-scale surfaces; they are thickest in the deepest point of the surface and pinch out towards the margin (Fig. 9). Constituent sandstone beds thicken towards the axis of the lens, with thickness variations due to incision at their base. These lenses may represent bypass drapes (Barton et al. 2010; Alpak et al. 2013; Stevenson et al. 2015), whereby sediment from the tail of a dominantly bypassing flow filled topography generated by the flow itself or by a precursor flow. At the base of channel story 1, a single rippled sandstone likely represents reworking during a relatively short bypassing stage, after channel incision (Fig. 9). The bases of channel stories 2 and 3 are overlain by thick (> 1.5 m) bypass drapes that thicken towards the maximum depth of the confining surfaces, partially healing them. These are overlain by amalgamated sandstones (FA6), which are thickest in the axis of the confining surface and gradually thin away from it. Unlike in channel story 1, lateral transitions into marginal FA2 or axial

FA7 deposits are not observed; transitions between axis and margin are accommodated by thinning of FA6 deposits and bypass drapes (Fig. 9). The infill of all stories in Barranco de la Caxigosa exhibit vertical trends associated with an upward decrease of energy. In story 1 this is represented by an upward decrease in debritic and conglomeratic facies. In stories 2 and 3 it is marked by the basal bypass drape and gradual fining-up of the overlying amalgamated sandstones (Fig. 9). In the margin of story 1, however, coarsening- and thickening-up is observed as beds and bedsets become progressively wider up-succession (Fig. 9; Hubbard et al. 2014). An apparent upward increase in the interpreted energy of facies at channel story margins may not be reflective of the nature of the flows that filled it. As a concave-up surface is filled, widening of the conduit causes the margin pinch-out of coarse-grained beds to step away from the channel axis, leading to the superposition of thicker beds onto thinner beds.

In Muro Sandbody outcrop 4 (Fig. 8) FA4, FA6, and FA7 are seen transitioning laterally into one another, and are thought to exhibit a similar axial-to-marginal trend as in Barranco de la Caxigosa, except without laterally variable thin beds (FA2). Fining-up patterns of individual channel stories are also more subtle in Muro de Bellos. At their tops, channel stories 2 and 3 contain > 5 m packages of non-amalgamated sandstones (FA5) which are tabular across the outcrop. These overlie a sharp basal transition and are commonly incised by overlying, higher-energy facies associations (FA4, FA6, and FA7). In Muro Sandbody outcrop 4, the presence of FA5 in channel stories 2 and 3 marks a decrease in average flow energy, possibly due to autogenic processes, in response to a partial upstream blockage (potentially from an MTD) or to an upstream avulsion.

At channel-fill scale, an overall upward decrease in energy is inferred in Muro Sandbody outcrop 4. However, in Barranco de la Caxigosa, vertical facies trends are complex, as they are influenced by the stacking of the constituent channel stories.

Architecture and Migration Patterns.—The exposures at Muro de Bellos all strike at a low angle to local paleoflow, making the architecture of the constituent channel stories difficult to ascertain. Therefore, extrapolation of architectures in the Muro de Bellos outcrop has been attempted using geometric relationships between confining surfaces and underlying stratigraphy, and assuming that channel stories exhibit similar axis-to-margin facies-association transitions as in Barranco de la Caxigosa (Fig. 9). Muro Sandbody outcrops 1 and 2 are along strike, at similar elevations (~ 980 m) and can be connected along paleoflow. The master confining surfaces beneath outcrop 1 (Fig. 7C), outcrop 3, and outcrop 4 (Fig. 8) truncate progressively older underlying thin beds towards the NE (Fig. 7A). Muro Sandbody outcrop 3, which comprises dominantly axial FA7 and off-axis FA6 deposits, is laterally (perpendicularly to paleoflow) offset ~ 200 m and vertically offset ~ 50 m (not restored for local tilt of ~ 11–16°) from outcrop 2, which contains axial FA7 deposits. Muro Sandbody outcrop 4 is ~ 50 m laterally (perpendicular to paleoflow) and ~ 30 m vertically offset from sandbody outcrop 3. In sandbody outcrop 4, four incision surfaces are observed, two of which cut progressively older underlying beds to the SW (into the cliff), the direction opposite to the incision at the base of the outcrop (NE); the cutting direction of the other two surfaces is not obvious (Fig. 8). While a general vertical decrease in the energy of the facies associations in Muro Sandbody outcrop 4 (Fig. 8) is interpreted, the base of channel stories 3 and 5 comprise dominantly off-axis FA6 deposits, interpreted as higher energy than the FA4 deposits that constitute the basal part of their underlying channel stories (2 and 4 respectively). This variability may reflect changes in the overall energy of the fill of successive channel stories, or variability of channel story stacking, superimposing more axial onto more marginal facies associations.

McHargue et al. (2011) define two contrasting styles of stacking observed (in plan view) at channel-fill scale (therein “channel elements”): i) disorganized, whereby successive channels do not resemble each other;

ii) organized, where successive channels modify the course of the previous element. Herein, we apply this terminology to describe the stacking of channel stories. We interpret that the channel stories in Muro Sandbody outcrops 1–4 stacked vertically and laterally to the southwest, generally in an organized manner (Fig. 12), based principally on the vertical and lateral offset of axial FA7 deposits between outcrops 2, 3, and 4, and the vertical change from the NE truncation of older underlying stratigraphy to SW truncation in outcrop 4. However, the superposition of channel stories containing high-energy FA6 deposits (stories 3 and 5) onto those containing lower-energy FA4 deposits (stories 2 and 5; Fig. 8) suggests that local variability may exist.

Compounded erosion of these channel stories may create a through-going surface on their southwestern side (represented by H5; Fig. 7); the architecture on the northeastern margin cannot be constrained (Fig. 12).

In Barranco de la Caxigosa, channel stories 1 and 2 are offset at least 70 m laterally and 6 m stratigraphically. Stories 2 and 3 are laterally offset by ~ 50 m, and the maximum depth of the confining surface of story 3 is ~ 50 cm stratigraphically lower than that of story 2. Although none of the stories is fully exposed, story 1 appears to have a lower aspect ratio than story 3. The master bounding surface, containing the channel fill, displays a concave-up geometry which then abruptly flattens to the SSW; the concave-up part is ~ 6 m thick. The increase in lateral offset (relative to vertical) of channel story axes, and vertical increase in aspect ratio is concomitant with the widening and flattening of the master bounding surface (Fig. 9).

The channel fill at Barranco de la Caxigosa is situated within an erosional bounding surface (Figs. 9, 13), in which the channel stories are stacked in a disorganized or compensational manner. Changes in lateral stacking and aspect ratio were potentially controlled by a widening of the master confining surface: stories 2 and 3, situated above the wider and shallower part of the master confining surface, experienced greater offset and formed channel deposits of higher aspect ratios, likely because their confinement was not dictated by the presence of a steep channel wall.

DISCUSSION

Timing of Structures in the Arro System

The western deflection of ripples and cross beds (relative to flutes) and westward stepping of the lateral facies transitions in Sierra de Soto Gully (Figs. 4, 10) suggest that the formative flows interacted with growing seafloor topography to the east, likely caused by growth of the Sierra de Araguás thrust. Wedging geometries of the background thin beds (Fig. 7) and the onset of channelization in Muro de Bellos are attributed to movement on the Muro and Sierra de Araguás thrusts (Fig. 12). Previous works suggest that structures in the most proximal outcrops were active at the time of deposition, with the growth of the Los Molinos Thrust as the cause of MTD emplacement at Los Molinos Road (Millington and Clark 1995a, 1995b; Arbués et al. 2007a, 2007b). It is therefore also possible that the origin of the MTDs in Barranco de la Caxigosa was linked to the activity of the nearby Caxigosa thrust. Furthermore, cross sections through the Ainsa depocenter fill (e.g., Muñoz et al. 2013; Clark et al. 2017) commonly show a thinning of Arro stratigraphy towards the depocenter-bounding thrust-cored anticlines, suggesting that these structures were growing during deposition.

Controls on Variability in Channel-Deposit Architecture

Multiple autogenic and allogenic controls dictate the architecture and facies distribution of deep-water deposits (Clark and Cartwright 2011). For example, sequence stratigraphy is built on various scales of external forcing (Vail et al. 1977; Gardner et al. 2003; Flint et al. 2011), whereas other studies focus on the stratigraphic response of autogenic processes (Pirmez et al. 2000; McHargue et al. 2011). Furthermore, studies from

modern deep-water channel systems (e.g., Vendettuoli et al. 2019) are beginning to reveal the true complexity of seabed deposition. However, although it can be challenging to discern the extent to which individual factors control the nature of ancient sedimentary successions, it is possible to assess the relative importance of a suite of controls at various hierarchical scales.

At bed to bedset scale, local scouring and filling builds stratigraphy incrementally in a channel. Scours may be filled by their formative flow or by successive flows (Kane et al. 2009b). The preserved deposit of a flow may be present only in the axis or margin of a channel, or across its entirety (Hubbard et al. 2014). Variations in scour depth and fill between individual beds is likely due to random variations in the type and magnitude of individual flows.

Because there may be scale overlap between bedset and channel story surfaces, the relative likelihood of different factors controlling their inception may also vary, rather than being fixed for each level. Both Muro de Bellos and Barranco de la Caxigosa display incision at the bases of their constituent channel stories, and a general upward decrease in the inferred energy of their constituent facies associations (Figs. 8, 9). Therefore, they are interpreted to result from repeated incision and filling of the surfaces that confine them. Repeated “cut and fill” can be attributed to:

- Increases (cut) and subsequent decreases (fill) in average flow magnitude and erosive potential arising from variations in sediment delivery rate and/or caliber enhanced by relative sea-level changes and/or climatic variations (Gardner et al. 2003; Flint et al. 2011).
- Surfaces being generated by erosive flows trying to maintain equilibrium, potentially after an upstream avulsion (Pirmez et al. 2000). In this case fill is initiated by backfilling due to a downstream blockage (Pickering et al. 2001) or a decrease in flow efficiency (Mutti et al. 1999; Hodgson et al. 2011, 2016), or by aggradation of a below-grade channel, seeking its equilibrium profile (Pirmez et al. 2000; Kneller 2003; Prather 2003).
- The upstream migration of knickpoints (Heiniö and Davies 2007; Gales et al. 2019) or other bedforms, as seen in modern submarine channels (Hage et al. 2018; Vendettuoli et al. 2019), may produce an erosional surface. Immediately downstream of knickpoints (commonly the location of hydraulic jumps) flow efficiency is reduced, resulting in deposition of higher-energy sediments from flows which would previously have bypassed (Postma and Cartigny 2014). As channel-floor topography is healed and the knickpoint or bedform migrates farther upstream, flow efficiency is reattained. This may cause a general upwards decrease in inferred flow energy as the higher-energy parts of flows bypass with increasing efficiency.
- Quasi-instantaneous erosion by a bypassing MTD (Dakin et al. 2013) or an oversized turbidity current may generate the confining surface. The infill is progressive: as the narrowest and deepest part of a concave-up surface (axis) is filled with high-energy facies, the effective conduit size widens. Lateral confinement is relieved, leading to a decrease in efficiency of the next flow, which may form a feedback mechanism, depositing progressively lower-energy facies.

The relative likelihood of these formative mechanisms can be determined based on the architecture of the channel fill more generally. The architectural interpretation of Muro de Bellos is that of partially overbank-confined channel stories, whose southwestern migration is accommodated by small-scale avulsions (Fig. 12). Therefore, their architectural expression is likely due to (structurally derived) changes in lateral confinement and axial gradient. In contrast, the internal architecture of the channel fill at Barranco de la Caxigosa is less well organized; the bounding surface likely resulted from cut and fill. In this scenario, any of the aforementioned mechanisms may have formed its channel stories. However, the Barranco de la Caxigosa outcrop contains multiple MTDs with incisional bases, interbedded with channelized and non-obviously

channelized turbidite deposits. Due to the MTD-prone nature of the deposits, it is possible that the confining surfaces of channel stories 2 and 3 were excavated partially or fully by large, erosive MTDs. The surface originally generated by this large flow may have been partially filled by the deposit of the formative MTD, and is likely to have been modified, progressively, by successive flows that shaped its preserved geometry (Fig. 9). Progressive incision alone, however, cannot be ruled out.

The master confining surface of the channel fill at Muro de Bellos is interpreted to represent a compound surface. This did not exist as a basin-floor feature in its entirety at any point, but instead formed by the lateral and vertical migration (stacking) of its channel stories in response to movement on the Muro thrust (Fig. 12). The basal incision at Barranco de la Caxigosa is interpreted to have formed from the cut and fill of a steep-sided conduit, at channel-story hierarchical order. Once this basal story was filled, channel stories formed within a much larger conduit, potentially derived from structural confinement or a lower order channel surface. The evolution away from flow-scale lateral confinement was responsible for the increase in the ratio of horizontal to vertical stacking and lower-energy facies in stories 2 and 3 (Fig. 13). At the lowest order, an overall increase then decrease in the rate of delivery of coarse-grained sediment to each location is necessary for the inception, fill, and occlusion of these channels.

Observations from outcrops of deep-water channel systems such as those in the Laingsburg (Di Celma et al. 2011), Capistrano (Campion et al. 2005) and Tres Pasos (Macauley and Hubbard 2013) formations has led to the development of predictive models, wherein laterally offset stacking is observed at channel-fill scale, whereas channel stories are assumed to stack vertically with little or no lateral offset (McHargue et al. 2011). In both Muro de Bellos and Barranco de la Caxigosa, and in other systems of the Ainsa depocenter (Pickering and Cantalejo 2015), lateral stacking of channel stories is observed. In Barranco de la Caxigosa, disorganized lateral channel-story stacking was driven by the interplay between MTDs and turbidites (Fig. 13); in Muro de Bellos, organized lateral channel-story stacking was driven by thrust-derived shifting of the depositional fairway (Fig. 12). It is possible that, in exceptionally tectonically active and MTD-prone areas like the Ainsa depocenter, the processes which typically affect the lateral stacking of channel fills, such as avulsion, MTDs and tectonic structure, may act at smaller temporal scales. This may result in less predictable channel-story stacking patterns, and may obscure the distinction between channel stories and channel fills, making hierarchy-based comparisons with other systems difficult.

Despite their differences in architecture, vertical sections through the channel fill in Barranco de la Caxigosa and Muro de Bellos (Muro Sandbody outcrop 4) show a similar facies trend: high-energy facies at the base, which gradually decrease upwards, with channel stories providing nested higher-order trends. In Muro de Bellos, this trend arises from the progressive superposition of off-axial deposits on top of axial facies associations. The presence of debritic and conglomeratic material at the base of both Muro Sandbody outcrops 1 and 4 (Fig. 7) suggests that the fill of the successive channel stories was similar. Therefore, observed vertical facies transitions are more likely to reflect the progressive migration of the channel-story axes, than a decrease in input flow energy between successive channel stories (Fig. 12). In Barranco de la Caxigosa, the trend in channel fill is interpreted to be partly due to a marked widening of the master confining surface, leading to a decrease in flow efficiency in the axis. However, this widening allowed subsequent channel stories to stack with greater lateral offset (Fig. 13; Li et al. 2018). Axial deposits of channel stories 2 and 3 were superimposed onto the margin of channel story 1, leading to a local upward increase in inferred flow energy (Figs. 9, 13). The fill of channel story 1 exhibits the same pattern. While a section through the axis of channel story 1 (BCL1 in Fig. 9C) records an upward decrease in inferred flow energy, a section through the margin (in the position of BCL2b in Fig. 9C) records upward bed thickening (Fig. 9).

This marginal trend is interpreted to be due to the widening of the depositional fairway as the channel was progressively filled, meaning that the sand-rich part of the flows could deposit over more of the channel floor (Hubbard et al. 2014). The decrease in flow-scale lateral confinement accompanying conduit widening may also have inhibited the bypass potential at the axis of the channel, causing an autogenic decrease in the inferred energy of channel-axis facies. Therefore, at this scale, vertical facies trends may be more influenced by filling of sea-floor topography rather than records of energy changes. At channel-fill scale (see Fig. 9), one-dimensional facies trends recording an upward decrease in inferred energy may be generated by the vertical and lateral migration of constituent channel stories (Muro de Bellos) (Figs. 7, 8, 12) or by the widening of the master confining surface (Barranco de la Caxigosa) (Figs. 9, 13). Therefore, stacking-pattern analysis is best undertaken at the channel-story scale. However, at channel-story scale, axial facies trends recording upward decreasing flow energies may be associated with marginal facies which record the opposite. Architectural information is therefore required when imposing environmental interpretations onto non-unique facies associations.

Influence of MTDs on Channelization and Channel-Deposit Architecture

Previous studies have focused mainly on the effect of MTDs on established channel forms (e.g., Masalimova et al. 2015; Kremer et al. 2018). Mass-transport deposits can form blockages which may lead to backfilling (Posamentier and Kolla 2003; Nelson et al. 2009; Bernhardt et al. 2012; Corella et al. 2016) or avulsion (Ortiz-Karpf et al. 2015). Less attention has been given to how MTDs may lead to, or prevent, the formation of channelized flow pathways. In the Arro system, the interplay between sediment supply, axial gradient and lateral confinement may be the principal drivers of channelization at the channel-fill hierarchical scale, whereas MTDs may have a profound influence on the channelization process at the channel-story scale. Five processes are proposed below, to describe the ways MTDs can enhance or hinder channelization (Fig. 14) in elongate confined settings (bounded by a large-scale erosional surface or tectonic structures). Although the origin of the MTDs in the Arro system is unknown, it should be noted that each mechanism can be associated with either longitudinally or transversely emplaced mass-transport deposits. These processes may co-occur.

MTD-Margin Topography.—Arbués et al. (2007a) propose a model in which relief on the margin of transversely emplaced MTDs provides lateral confinement that is responsible for the formation of channels. A similar model may be invoked in Barranco de la Caxigosa: channel initiation, and formation of the bounding surface for channel story 1 (Fig. 13), likely formed in response to MTD-margin topography (Fig. 14A). In the case of transversely emplaced MTDs, either the margin farthest from the source (e.g., Arbués et al. 2007a) or the near-source margin (e.g., Kremer et al. 2018) can provide this confinement (Fig. 14A). Other studies from the Austrian Molasse Basin (Bernhardt et al. 2012; Masalimova et al. 2015) show how the lateral edges of longitudinally emplaced MTDs can have the same effect (Fig. 14A). Pickering and Corregidor (2000, 2005) show how the upstream margin of an MTD can frontally confine or reduce the axial gradient of subsequent turbidites, causing a loss of efficiency which may hinder channel development (Fig. 14B).

MTD-Top Topography.—The effects of MTD-top and -margin topography are similar. MTDs, particularly large slumps and slides, often exhibit very complex topography on their tops (Armitage et al. 2009; Kneller et al. 2016; Brooks et al. 2018; Ward et al. 2018; Bull et al. 2020). Depressions elongate in the direction of paleoflow provide lateral confinement and are likely to encourage channelization (Fig. 14C).

Thickness variations and localized scouring in turbidite deposits that overlie MTDs in Barranco de la Caxigosa (comprising DE3 deposits) are interpreted as the result of interaction with such depressions (Figs. 11, 13). Depressions which have no elongation or are elongate in a paleoflow-perpendicular orientation may provide frontal confinement and therefore hinder channelization (Fig. 14D).

Accentuation or hindrance of channelization can be achieved by either transversely or longitudinally emplaced MTDs. However, the typical distribution and orientation of structures on large MTDs, with secondary ridges striking at a high angle to the emplacement direction (Sharman et al. 2015), means that transversely emplaced MTDs are more likely to encourage channelization, whereas longitudinally emplaced MTDs are likely to hinder it.

Syn depositional Substrate Deformation and/or Differential Compaction.—The complexity of the composition of MTDs dictates the spatial distribution of mechanically strong and weak areas. Lithological zones of varying competence and the presence of large mostly undeformed blocks may allow higher compaction rates on top of weak zones (Alves 2010; Dykstra et al. 2011; Ward et al. 2018). Furthermore, the depositional weakness of mud-rich MTDs may be sufficient for evacuation of substrate material below subsequently deposited turbidites (Kneller et al. 2016). If the initial MTD-top deposits are elongate and aligned with local paleoflow, differential compaction may cause lateral confinement and hence encourage channelization (Fig. 14E). If the deposits and the depression formed by their presence are elongated in a paleoflow-perpendicular orientation or are not elongated, frontal confinement and ponding may arise, inhibiting channel formation (Fig. 14F). Substrate deformation and/or differential compaction is likely responsible for the lateral facies transitions observed in the turbidite packages which are underlain and overlain by MTDs (DE3) and may have augmented channelization in Barranco de la Caxigosa.

Megascour Evacuation by Erosive MTDs.—Dakin et al. (2013) show how longitudinally sourced, erosive-mass-transport deposits in the Upper Hecho Group can create “megascours,” which may show cross-sectional profiles similar to submarine channels (see also Moscardelli and Wood 2008; Brooks et al. 2018; Soutter et al. 2018). The proximal–distal longitudinal section of Dakin et al. (2013) through the Ainsa II fan passes from a fully evacuated elongate megascour on the slope, through a zone filled with chaotic deposits at the base of slope, ending distally in turbidite deposition. These quasi-instantaneously generated pathways can provide sufficient lateral confinement to subsequent turbidity currents for a channelization threshold to be exceeded (Fig. 14G). A similar process has been documented at larger scales, where lateral confinement and a local increase in the axial gradient can be provided by the proximal headwall scar of a large MTD (Qin et al. 2017). The stratigraphic and architectural context of channel stories 2 and 3 in Barranco de la Caxigosa (below erosive MTD4; Fig. 9) suggest that their confining surfaces may have been formed or initiated by mass-transport-derived megascours. These megascours may have been exploited and possibly significantly modified by subsequent bypassing, and potentially erosive, flows, which formed channel-base drapes, and were eventually filled by amalgamated sandstones (Fig. 13E, F). If the axial orientation of the erosional surface is perpendicular to local paleoflow, the downstream wall of the erosional surface may cause a decrease in axial gradient and block, or deviate, successive turbidity currents (Fig. 14H). Commonly, the erosional basal surfaces of MTDs on the lower slope and basin-floor are partially or fully filled by the remnant deposit of their formative flow (e.g., MTD4, Fig. 9; Dakin et al. 2013). The lack of remnant MTD at the base of channel stories 2 and 3 may be because: i) Barranco de la Caxigosa was sufficiently proximal, or possessed a sufficient axial gradient, for MTDs to have fully evacuated their basal surface (Gomis-Cartesio et al. 2018), ii) the flows that

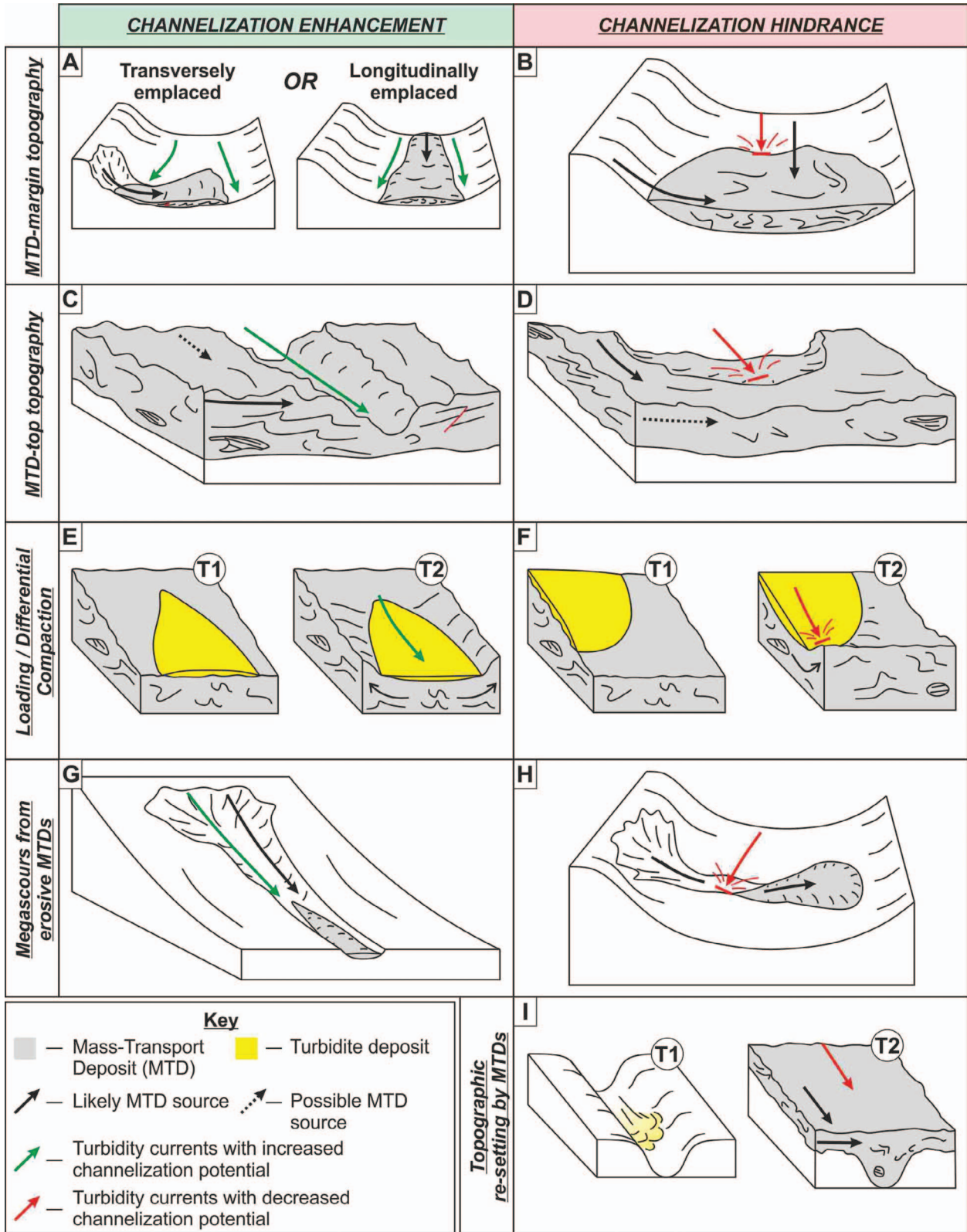


FIG. 14.—Conceptual diagram showing the mechanisms by which MTD emplacement can help (A, C, E, G) or hinder (B, D, F, H, I) channelization: **A, B**) interaction with MTD-margin topography; **C, D**) interaction with MTD-top topography; **E, F**) syndepositional substrate deformation and/or differential compaction; **G, H**) megascours excavated by erosive MTDs; **I**) MTDs filling a fully or partially channelized pathway and resetting basin-floor topography.

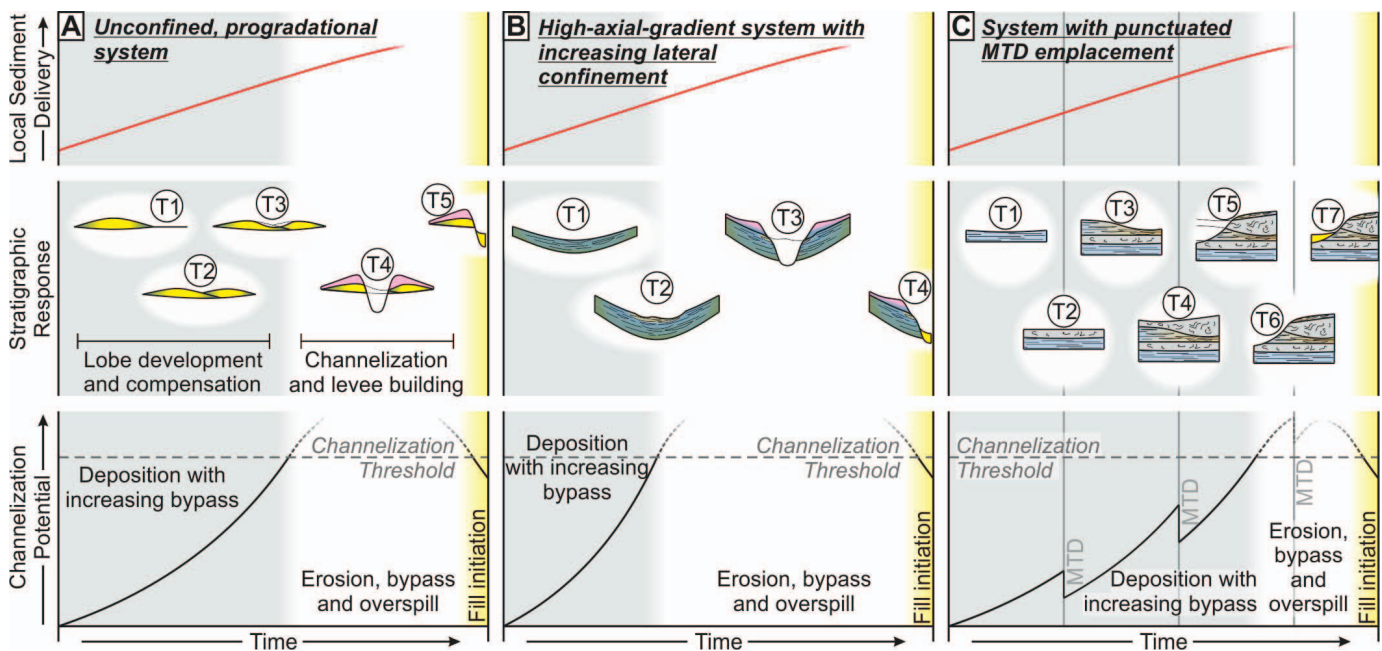


Fig. 15.—Conceptual diagrams showing how progressive, structurally derived lateral confinement, and the punctuated emplacement of MTDs can affect channel inception and resultant sedimentary architecture: **A**) in an unconfined, progradational system experiencing increasing local coarse-grained sediment delivery, a channel will incise through unconfined precursor deposits after a channelization threshold is crossed (sketches based on Hodgson et al. 2016); **B**) imposed lateral confinement from growing tectonic structures allows the channelization threshold to be crossed earlier and at lower rates of delivery of coarse-grained sediment, inhibiting the development of sand-rich unconfined precursor deposits (example from Muro de Bellos); **C**) regular input of MTDs can interrupt the channelization process by periodically removing the previously formed lateral confinement, which leads to delayed crossing of the channelization threshold and the formation of DE3 deposits in replacement of sand-rich unconfined precursor deposits (example from Barranco de la Caxigosa).

formed the basal surfaces of channel stories 2 and 3 were abnormally large and were therefore able to erode and bypass for longer distances downstream, or iii) the remnant MTD has been eroded and replaced by subsequent turbidity currents and their deposits (e.g., Qin et al. 2017).

Topographic Resetting by MTDs.—Of the five turbidite packages that separate the MTDs in Barranco de la Caxigosa, only one is obviously channelized. The mechanism invoked to explain the hindrance of channelization in these nonchannelized intervals (which, together with their associated MTDs, form DE3) is burial by subsequent MTDs. A large depositional MTD may fill the elongate flow pathway, suppressing and effectively resetting the basin-floor topography (Figs. 11C, 14I); the channelization process is thereby halted and must then start again (McArthur and McCaffrey 2019).

Precursor Deposits and Channel Initiation

Examples of lobate, unconfined deposits cut by a channel that progrades over them are well documented (e.g., Gardner et al. 2003; Macdonald et al. 2011; Hodgson et al. 2011, 2016). Deposits from the Laingsburg depocenter, Karoo Basin, South Africa, record evidence of channel progradation cutting into unconfined deposits (Hodgson et al. 2011, 2016), and are herein compared with examples from the Arro system (Fig. 15). For fine-grained background deposits (FA1) to be overlain or incised by coarse-grained channelized deposits requires an increase in local delivery of coarse-grained sediment to the particular outcrop location (not necessarily to the whole basin). Channelization in an unconfined, progradational system will typically be preceded by deposition of lobes (deposited by unconfined flows) followed by progressive channelization, caused by incision and levee construction (Burgreen and Graham 2014; Hodgson et al. 2016). If assuming time-transgressive flow confinement in

submarine channels is the norm, the absence of precursor lobate deposits is enigmatic. Such cases may arise when: i) a master erosional surface has completely eroded through the axis or the thinner marginal parts of a precursor lobe (more likely where lateral architectural control is limited), ii) the conduit was formed (and filled) quasi-instantaneously, negating the requisite for frontal lobe development and channel progradation, or iii) precursor unconfined deposits are absent or are not in the form of classical lobes, potentially because the axial gradient or externally imposed lateral confinement was sufficient to promote bypass.

Muro de Bellos is an example of where lobate precursor deposits are apparently absent. Progradation and channelization are interpreted to have arisen from steadily increasing local delivery of coarse-grained sediment through a corridor confined by the Muro and Sierra de Araguás thrusts, both of which were active at the time of deposition (Fig. 12B). The assumed high axial gradient of the depositional fairway and broad lateral confinement imposed by these structures is thought to be partially responsible for the bypass-prone nature of the laterally variable thin-bed deposits (FA2) that form part of both increasing-to-decreasing-energy deposits (DE1), and progradational-to-overbank (DE2) deposits. Enhanced velocities related to high axial gradients and lateral confinement likely prevent the formation of thick and continuous lobate deposits (Fig. 12C). Contemporaneous narrowing of this (high gradient) corridor and increasing local delivery of coarse-grained sediment is then thought to have initiated a channelization feedback mechanism and the formation of Muro Sandbody outcrops 1 and 2 (Fig. 12D). Subsequent migration of partially levee-confined channels to the SW arose due to movement of the inboard Muro Thrust (located to the NE) predominating over movement on the outboard Sierra de Arguas thrust (located to the SW) (Fig. 12D). In this example, the lack of well-developed, sand-rich, unconfined precursor deposits is therefore likely due to the elevated bypass potential experienced by the formative flows of turbidites of FA2. By extension, thrust-derived,

progressive lateral confinement may have augmented the effects of a high axial gradient in lowering the channelization threshold, allowing channelization to occur earlier, and at lower coarse-grained sediment delivery rates, than in an unconfined setting (Fig. 15). Therefore, less sand is sequestered in the pre-channelization stratigraphy, and more is transported down dip.

A delay in crossing the channelization threshold can be caused by the regular deposition of MTDs that reset topography (Fig. 14I), because of their effect of removing the lateral confinement developed by preceding flows (Fig. 15). The result of this process is the development of pre-channelization interbedded packages of MTDs and turbidites (DE3), such as those seen in Barranco de la Caxigosa (Fig. 9). These might represent the equivalent deposits in an MTD-prone setting to the pre-channelization precursor lobes deposited in the absence of MTDs (cf. those shown by Hodgson et al. 2016). In areas where MTD and turbidite deposition occur concurrently, decreasing the frequency of MTD input or increasing the frequency or magnitude of turbidity-current input may lead to conditions favorable for channelization.

The Arro System as an Analog

Much of the research on the younger channelized systems in the Aínsa depocenter, principally the Banastón, Aínsa, and Morillo systems, is centered around the role of syndepositional structures (Pickering and Bayliss 2009; Bayliss and Pickering 2015) or MTDs (Pickering and Corregidor 2005; Dakin et al. 2013) in controlling the sedimentology and architecture of turbidite deposits; deposition in the Arro system was influenced by, and records the effects of, both. The processes discussed in this article can be exported to other exhumed topographically complex basins traversed by axial sediment routing systems such as the Magallanes foreland basin (Hubbard et al. 2008; Bernhardt et al. 2011, 2012), the Sinop basin (Leren et al. 2007; Janbu et al. 2007), the Grès du Champsaur (McCaffrey et al. 2002; Brunt et al. 2007), and the Gorgoglione Flysch (Casciano et al. 2019). Studies concerning interplay between structures, MTDs, and turbidite deposition in the Austrian Molasse basin (Bernhardt et al. 2012; Masalimova et al. 2015; Kremer et al. 2018) may provide a subsurface analog.

The Arro system formed in an elongate corridor with high axial gradients bound by structures or canyon walls, similar to that of the younger Aínsa systems (Cornard and Pickering 2019). The deposits therein can therefore be compared with those deposited in modern high-gradient confined systems such as large canyons (e.g., the Monterey Canyon; Paull et al. 2018) or fjord-head delta slopes (e.g., the Bute Inlet, British Columbia; Hughes Clark 2016). Comparing the results of this study to these modern systems allows i) evaluation of the possible depositional signature of modern seafloor processes, and ii) postulation of new mechanisms for the formation of recognized deep-water facies associations that have not hitherto been interpreted or have been attributed to other processes. For example, the dilute flows which form the background thin beds (FA1) of the Arro system have three possible origins, all of which have been monitored directly in fjord-head systems: a) hyperpycnal flows, b) small sediment failures on the shelf, upper slope, or in the feeder canyon (Clare et al. 2016), and c) plume related density currents, which generate so-called "plumites" (Hizzett et al. 2018; Mutti 2019). Weak, partially bypassing flows are inferred to have created the bedforms in laterally variable thin beds (FA2), specifically in increasing-to-decreasing-energy (DE1) and progradational-to-overbank (DE2) deposits. These may be analogous to some of the short-run-out flows observed by Hughes Clark (2016) and Paull et al. (2018), which do not reach the terminal deposits of the system. Traditionally, models accounting for the formation of channel stories invoke episodic variations in sediment supply and/or equilibrium gradients. Upstream-migrating knickpoints and crescentic bedforms are commonly recognized in modern submarine channels (Heiniö and Davies

2007; Hughes Clark 2016; Gales et al. 2019), indicating that more spatio-temporally complex patterns of incision and deposition may be involved in building submarine-channel stratigraphy (Hage et al. 2018; Vendettuoli et al. 2019). In the channelized units (DE4) of the Arro system, cut and fill at channel-story scale may result from the passing of upstream-migrating knickpoints or other bedforms; other causes however, cannot be discounted.

No interpretation is given for the source or triggers of flows that formed the Arro turbidite system because its constituent facies associations (from background thin beds, FA1, to sandstones, conglomerates, and debrites with incisional bases, FA7) exist as part of a continuum with non-unique representations. If the formative flows were initiated by a single process (e.g., hyperpycnal flows or instability-driven sediment failures) that acted at a large range of magnitudes, a natural lack of distinction between different facies assemblages and bed types might be expected. Alternatively, if flows of overlapping magnitude were initiated by different trigger mechanisms, a range of processes may result in deposits with similar sedimentologic character. Flow genesis cannot, therefore, be differentiated using the methodologies employed here and in the current state of knowledge.

CONCLUSIONS

The Arro turbidite system is confirmed as a channelized, axial sedimentary system that traversed the SE–NW-oriented Aínsa depocenter during the Eocene (Ypresian). It records a complex interplay between tectonic structuration, emplacement of mass-transport deposits (MTDs), and routing of turbidity currents. The principal findings from this field-based study are that:

- The locations of sandy turbidite and muddy debrite pathways were controlled by the development of tectonic structures that were active at the time of deposition.
- The deposits of the Arro system can be grouped into eight facies associations. These form a continuum of constituent facies and bed geometries attributed principally to variations in the velocity, magnitude, and grain size of their formative flows. In the Arro system, facies associations are non-unique to single depositional elements. Four depositional elements are recognized by the combined observation of groupings of facies associations, their lateral and vertical transitions, and the presence or absence of key surfaces: i) weakly confined, increasing-to-decreasing-energy deposits (DE1), ii) progradational, weakly confined to overbank deposits (DE2), iii) alternating MTDs and turbidites (DE3), and iv) submarine-channel deposits (DE4). The different styles of observed channel architecture contain at least three orders of hierarchical organization.
- Tectonic structuration and emplacement of MTDs can affect the timing and nature of channel inception, and may inhibit the formation of precursor sand-rich, lobe deposits of the type typically observed in unconfined, progradational systems. Thus 1) high axial gradients and lateral confinement (e.g., due to thrust-related fairway narrowing) can promote higher flow velocities, allowing the onset of channelization earlier (and at lower rates of local delivery of coarse-grained sediment) than would be expected in an unconfined system, resulting in the development of discontinuous, thin-bedded deposits below the channelized deposits (as seen in the Muro de Bellos outcrop). 2) Extra-channel MTD emplacement may act to delay the onset of channelization due to the punctuated healing of substrate topography and eradication of lateral confinement. The stratigraphic response to this is the presence of alternating MTDs and packages of non-channelized turbidites, below the channelized deposits (as observed in the Barranco de la Caxigosa outcrop).

• Five mechanisms describe how the emplacement of extra-channel MTDs can affect seafloor topography and therefore channelization: i) flow interaction with MTD-margin topography or; ii) MTD-top topography; iii) differential compaction of MTDs and/or synsedimentary loading into them; iv) formation of megascours by erosive MTDs; or v) resetting of basin-floor topography by MTDs that occlude fully or partially channelized pathways. Apart from the last, which may only impede it, any of these mechanisms may accelerate or hinder the channelization process.

In this study confinement imposed by tectonic structures and by MTDs is seen to exert significant control on the inception, evolution, and fill of deep-water channels. The controlling processes are likely analogous to those observed or inferred in both modern and ancient confined systems. Therefore, in basins traversed by axial channel systems, the bathymetric expression of tectonic structures and MTDs may dictate the presence, distribution, architecture, and internal sedimentologic character of channelized units and their precursor deposits.

ACKNOWLEDGMENTS

This work was funded by Turbidites Research Group sponsors: AkerBP, BP, ConocoPhillips, Equinor, Eni, HESS, Murphy, OMV, OXY, and Shell. We thank reviewers Suzanne Bull and Julian Clark for their constructive comments which helped improve the manuscript. We would also like to thank Adriana Crisostomo Figueroa, Alex Burton-Johnson, Ashley Ayckbourne, and Laura Bührig for their assistance in the field. Cai Puigdefàbregas is thanked for discussions which helped improve the manuscript.

REFERENCES

- ALLEN, J.R.L., 1973, A classification of climbing-ripple cross-lamination: *Geological Society of London, Journal*, v. 129, p. 537–541.
- ALLEN, J.R.L., 1982, *Sedimentary Structures: Their Character and Physical Basis*: Amsterdam, Elsevier, 592 p.
- ALPAK, F.O., BARTON, M.D., AND NARUK, S.J., 2013, The impact of fine-scale turbidite channel architecture on deep-water reservoir performance: *American Association of Petroleum Geologists, Bulletin*, v. 97, p. 251–284.
- ALVES, T.M., 2010, 3D Seismic examples of differential compaction in mass-transport deposits and their effect on post-failure strata: *Marine Geology*, v. 271, p. 212–224.
- ARBUÉS, P., MELLERE, D., PUIG, M., AND MARZO, M., 2007a, Los Molinos Road, Spain: the effect of slumping on sandstone distribution in the Arro turbidites, *in* Nilsen, T.H., Shew, R.D., Steffens, G.S., and Studlick, J.R.J., eds., *Atlas of Deep-Water Outcrops*: American Association of Petroleum Geologists, *Studies in Geology*, p. 1–17.
- ARBUÉS, P., MELLERE, D., PUIG, M., AND MARZO, M., 2007b, The Effect of Slumping on Sandstone Distribution in the Arro Turbidites, Los Molinos Road, Spain, *in* Nilsen T.H., Shew, R.D., Steffens, G.S., and Studlick, J.R.J., eds., *Atlas of Deep-Water Outcrops*: American Association of Petroleum Geologists, *Studies in Geology*, p. 333–335.
- ARBUÉS, P., BUTILLÉ, M., LÓPEZ-BLANCO, M., MARZO, M., MONLEÓN, O., MUÑOZ, J.A., AND SERRA-KIEL, J., 2011, Exploring the relationships between deepwater and shallow-marine deposits in the Ainsa piggy-back basin fill (Eocene, South-Pyrenean Foreland Basin), *in* Arenas, C., Pomar, L., and Colombo, F., eds., *Post-Meeting Field Trip Guidebook, 28th International Association of Sedimentologists Meeting*, Zaragoza, p. 199–240.
- ARMITAGE, D.A., ROMANS, B.W., COVALLI, J.A., AND GRAHAM, S.A., 2009, The influence of mass-transport-deposit surface topography on the evolution of turbidite architecture: the Sierra Contreras, Tres Pasos Formation (Cretaceous), southern Chile: *Journal of Sedimentary Research*, v. 79, p. 287–301.
- ARNOTT, R.W.C., AND AL-MUFTI, O., 2017, Deep-marine pseudo dune cross-stratification: similar, but completely different: *Journal of Sedimentary Research*, v. 87, p. 312–323.
- AZPIROZ-ZABALA, M., CARTIGNY, M.J.B., TALLING, P.J., PARSONS, D.R., SUMNER, E.J., CLARE, M.A., SIMMONS, S.M., COOPER, C., AND POPE, E.L., 2017, Newly recognized turbidity current structure can explain prolonged flushing of submarine canyons: *Science Advances*, v. 3, p. 1–12.
- BARNOLAS, A., AND GIL-PEÑA, I., 2001, Ejemplos de relleno sedimentario multipisódico en una cuenca de antepais fragmentada: la Cuenca Surpirenaica: *Boletín Geológico y Minero*, v. 112, p. 17–38.
- BARTON, M., BYRNE, C.O., PIRMEZ, C., PRATHER, B., VAN DER VLUGT, F., ALPAK, F.O., AND SYLVESTER, Z., 2010, Turbidite channel architecture: recognizing and quantifying the distribution of channel-base drapes using core and dipmeter data, *in* Pöppelreiter, M., García-Carballido, C., and Kraaijveld, M., eds., *Dipmeter and Borehole Image Log Technology*: American Association of Petroleum Geologists, *Memoir* 92, p. 195–210.
- BAYLISS, N., AND PICKERING, K.T., 2015, Transition from deep marine lower slope erosional channels to proximal basin floor stacked channel-levee-overbank deposits, and synsedimentary growth structures, middle Eocene Banastón System, Ainsa Basin, Spanish Pyrenees: *Earth-Science Reviews*, v. 144, p. 23–46.
- BELL, D., STEVENSON, C.J., KANE, I.A., HODGSON, D.M., AND POYATOS-MORÉ, M., 2018a, Topographic controls on the development of contemporaneous but contrasting basin-floor depositional architectures: *Journal of Sedimentary Research*, v. 88, p. 1166–1189.
- BELL, D., KANE, I.A., PONTÉN, A.S.M., FLINT, S.S., HODGSON, D.M., AND BARRETT, B.J., 2018b, Spatial variability in depositional reservoir quality of deep-water channel-fill and lobe deposits: *Marine and Petroleum Geology*, v. 98, p. 97–115.
- BENTHAM, P.A., AND BURBANK, D.W., 1996, Chronology of Eocene foreland basin evolution along the western oblique margin of the south-central Pyrenees, *in* Friend, P.F., and Dabrio, C.J., eds., *Tertiary Basins of Spain*: New York, Cambridge University Press, p. 144–152.
- BERNHARDT, A., JOBE, Z.R., AND LOWE, D.R., 2011, Stratigraphic evolution of a submarine channel-lobe complex system in a narrow fairway within the Magallanes foreland basin, Cerro Toro Formation, southern Chile: *Marine and Petroleum Geology*, v. 28, p. 785–806.
- BERNHARDT, A., JOBE, Z.R., GROVE, M., AND LOWE, D.R., 2012, Palaeogeography and diachronous infill of an ancient deep-marine foreland basin, Upper Cretaceous Cerro Toro Formation, Magallanes Basin: *Basin Research*, v. 24, p. 269–294.
- BOULESTEIX, K., POYATOS-MORÉ, M., FLINT, S.S., TAYLOR, K.G., HODGSON, D.M., AND HASIOTIS, S.T., 2019, Transport and deposition of mud in deep-water environments: processes and stratigraphic implications: *Sedimentology*, v. 66, p. 1–32.
- BOUMA, A.H., 1962, *Sedimentology of Some Flysch Deposits: A Graphic Approach to Facies Interpretation*: New York, Elsevier, 168 p.
- BROOKS, H.L., HODGSON, D.M., BRUNT, R.L., PEAKALL, J., AND FLINT, S.S., 2018, Exhumed lateral margins and increasing flow confinement of a submarine landslide complex: *Sedimentology*, v. 65, p. 1067–1096.
- BRUNT, R.L., MCCAFFREY, W.D., AND BUTLER, R.W.H., 2007, Architectural Elements of the Grès du Champsaur: Chaillol Area, Haute Alpes, southeast France, *in* Nilsen, T.H., Shew, R.D., Steffens, G.S., and Studlick, J.R.J., eds., *Atlas of Deep-Water Outcrops*: American Association of Petroleum Geologists, *Studies in Geology*, p. 1–17.
- BRUNT, R.L., DI CELMA, C.N., HODGSON, D.M., FLINT, S.S., KAVANAGH, J.P., AND VAN DER MERWE, W.C., 2013, Driving a channel through a levee when the levee is high: an outcrop example of submarine down-dip entrenchment: *Marine and Petroleum Geology*, v. 41, p. 134–145.
- BULL, S., CARTWRIGHT, J., AND HUISE, M., 2009, A review of kinematic indicators from mass-transport complexes using 3D seismic data: *Marine and Petroleum Geology*, v. 26, p. 1132–1151.
- BULL, S., BROWNE, G.H., ARNOT, M.J., AND STRACHAN, L.J., 2020, Influence of Mass Transport Deposit (MTD) surface topography on deep-water deposition: an example from a predominantly fine-grained continental margin, New Zealand, *in* Wagreich, M., Hart, B.M., Sames, B., and Yilmaz, I.O., eds., *Cretaceous Climate Events and Short-Term Sea-Level Changes*: Geological Society of London, *Special Publication* 500, p. 147–171.
- BURGESS, B., AND GRAHAM, S., 2014, Evolution of a deep-water lobe system in the Neogene trench-slope setting of the East Coast Basin, New Zealand: lobe stratigraphy and architecture in a weakly confined basin configuration: *Marine and Petroleum Geology*, v. 54, p. 1–22.
- CAJA, M.A., MARFIL, R., GARCIA, D., REMACHA, E., MORAD, S., MANSURBEG, H., AMOROSI, A., MARTÍNEZ-CALVO, C., AND LAHOZ-BELTRÁ, R., 2010, Provenance of siliciclastic and hybrid turbidite arenites of the Eocene Hecho Group, Spanish Pyrenees: implications for the tectonic evolution of a foreland basin: *Basin Research*, v. 22, p. 157–180.
- CÁMARA, P., AND KILMOWITZ, J., 1985, Interpretación geodinámica de la vertiente centro-occidental surpirenaica (cuencas de Jaca–Trempe): *Estudios Geológicos*, v. 41, p. 391–404.
- CAMPION, K.M., SPRAGUE, A.R.G., AND SULLIVAN, M.D., 2005, *Architecture and lithofacies of the Capistrano Formation (Miocene–Pliocene), San Clemente, California*: SEPM, Pacific Section, Fieldtrip Guidebook, 42 p.
- CASCIANO, C.I., PATACCI, M., LONGHITANO, S.G., TROPEANO, M., MCCAFFREY, W.D., AND DI CELMA, C., 2019, Multi-scale analysis of a migrating submarine channel system in a tectonically-confined basin: the Miocene Gorgoglione Flysch Formation, southern Italy: *Sedimentology*, v. 66, p. 205–240.
- CASTELLORT, S., HONEGGER, L., ADATTE, T., CLARK, J.D., PUIGDEFÀBREGAS, C., SPANGENBERG, J.E., DYKSTRA, M.L., AND FILDANI, A., 2017, Detecting eustatic and tectonic signals with carbon isotopes in deep-marine strata, Eocene Ainsa Basin, Spanish Pyrenees: *Geology*, v. 45, p. 707–710.
- CHANVRY, E., DESCHAMPS, R., JOSEPH, P., PUIGDEFÀBREGAS, C., POYATOS-MORÉ, M., SERRA-KIEL, J., GARCIA, D., AND TEINTURIER, S., 2018, Impact of intrabasinal tectonics in the stratigraphic evolution of piggyback basin fills: an example from the Eocene South-Pyrenean Foreland Basin (Spain): *Sedimentary Geology*, v. 377, p. 34–62.
- CHOUKROUNE, P., 1992, Tectonic evolution of the Pyrenees: *Annual Review of Earth and Planetary Sciences*, v. 20, p. 143–158.
- CLARE, M.A., HUGHES CLARKE, J.E., TALLING, P.J., CARTIGNY, M.J.B., AND PRATOMO, D.G., 2016, Preconditioning and triggering of offshore slope failures and turbidity currents revealed by most detailed monitoring yet at a fjord-head delta: *Earth and Planetary Science Letters*, v. 450, p. 208–220.
- CLARK, I.R., AND CARTWRIGHT, J.A., 2011, Key controls on submarine channel development in structurally active settings: *Marine and Petroleum Geology*, v. 28, p. 1333–1349.

- CLARK, J.D., AND PICKERING, K.T., 1996, Architectural elements and growth patterns of submarine channels: applications to hydrocarbon exploration: *American Association of Petroleum Geologists, Bulletin*, v. 80, p. 194–222.
- CLARK, J., PUIGDEFÀBREGAS, C., CASTELLTORT, S., AND FILDANI, A., 2017, Propagation of Environmental Signals within Source-to-Sink Stratigraphy: SEPM, Field Trip Guidebook 13, 63 p.
- CORELLA, J.P., LOIZEAU, J.L., KREMER, K., HILBE, M., GERARD, J., LE DANTEC, N., STARK, N., GONZÁLEZ-QUIJANO, M., AND GIRARDLOS, S., 2016, The role of mass-transport deposits and turbidites in shaping modern lacustrine deepwater channels: *Marine and Petroleum Geology*, v. 77, p. 515–525.
- CORNARD, P.H., AND PICKERING, K.T., 2019, Supercritical-flow deposits and their distribution in a submarine channel system, middle Eocene, Ainsa Basin, Spanish Pyrenees: *Journal of Sedimentary Research*, v. 89, p. 576–597.
- CULLIS, S., COLOMERA, L., PATACCI, M., AND MCCAFFREY, W.D., 2018, Hierarchical classifications of the sedimentary architecture of deep-marine depositional systems: *Earth-Science Reviews*, v. 179, p. 38–71.
- DAKIN, N., PICKERING, K.T., MOHRIG, D., AND BAYLISS, N.J., 2013, Channel-like features created by erosive submarine debris flows: field evidence from the Middle Eocene Ainsa Basin, Spanish Pyrenees: *Marine and Petroleum Geology*, v. 41, p. 62–71.
- DAS GUPTA, K., AND PICKERING, K.T., 2008, Petrography and temporal changes in petrofacies of deep-marine Ainsa–Jaca basin sandstone systems, Early and Middle Eocene, Spanish Pyrenees: *Sedimentology*, v. 55, p. 1083–1114.
- DE LEEUW, J., EGGENHUISEN, J.T., AND CARTIGNY, M.J.B., 2016, Morphodynamics of submarine channel inception revealed by new experimental approach: *Nature Communications*, v. 7, p. 1–7.
- DEPTUCK, M.E., STEFFENS, G.S., BARTON, M., AND PIRMEZ, C., 2003, Architecture and evolution of upper fan channel-belts on the Niger Delta slope and in the Arabian Sea: *Marine and Petroleum Geology*, v. 20, p. 649–676.
- DEPTUCK, M.E., SYLVESTER, Z., PIRMEZ, C., AND O'BYRNE, C., 2007, Migration-aggradation history and 3-D seismic geomorphology of submarine channels in the Pleistocene Benin–Major Canyon, western Niger Delta slope: *Marine and Petroleum Geology*, v. 24, p. 406–433.
- DEPTUCK, M.E., PIPER, D.J.W., SAVOYE, B., AND GERVAIS, A., 2008, Dimensions and architecture of late Pleistocene submarine lobes off the northern margin of East Corsica: *Sedimentology*, v. 55, p. 869–898.
- DI CELMA, C.N., BRUNT, R.L., HODGSON, D.M., FLINT, S.S., AND KAVANAGH, J.P., 2011, Spatial and temporal evolution of a Permian submarine slope channel–levee system, Karoo Basin, South Africa: *Journal of Sedimentary Research*, v. 81, p. 579–599.
- DORRELL, R.M., HOGG, A.J., AND PRITCHARD, D., 2013, Polydisperse suspensions: erosion, deposition, and flow capacity: *Journal of Geophysical Research: Earth Surface*, v. 118, p. 1–17.
- DORRELL, R.M., AMY, L.A., PEAKALL, J., AND MCCAFFREY, W.D., 2018, Particle size distribution controls the threshold between net sediment erosion and deposition in suspended load dominated flow: *Geophysical Research Letters*, v. 45, p. 1443–1452.
- DORRELL, R.M., PEAKALL, J., DARBY, S.E., PARSONS, D.R., JOHNSON, J., SUMNER, E.J., WYNN, R.B., ÖZSOY, E., AND TEZCAN, D., 2019, Self-sharpening induces jet-like structure in seafloor gravity currents: *Nature Communications*, v. 10, p. 1–10.
- DYKSTRA, M., GARYFALOU, K., KERTZUS, V., KNELLER, B.C., MILANA, J.P., MOLINARO, M., SZUMAN, M., AND THOMPSON, P., 2011, Mass transport deposits: combining outcrop studies and seismic forward modeling to understand lithofacies distributions, deformation, and their seismic stratigraphic expression, *in* Shipp, R.C., Weimer, P., and Posamentier, H.W., eds., *Mass-Transport Deposits in Deepwater Settings*: SEPM, Special Publication 96, p. 293–310.
- EGGENHUISEN, J.T., MCCAFFREY, W.D., HAUGHTON, P.D.W., AND BUTLER, R.W.H., 2010, Small-scale spatial variability in turbidity-current flow controlled by roughness resulting from substrate erosion: field evidence for a feedback mechanism: *Journal of Sedimentary Research*, v. 80, p. 129–136.
- EGGENHUISEN, J.T., MCCAFFREY, W.D., HAUGHTON, P.D.W., AND BUTLER, R.W.H., 2011, Shallow erosion beneath turbidity currents and its impact on the architectural development of turbidite sheet systems: *Sedimentology*, v. 58, p. 936–959.
- ELLIOTT, T., 2000, Depositional architecture of a sand-rich, channelised turbidite system: the Upper Carboniferous Ross Sandstone Formation, western Ireland, *in* Weimer, P., ed., *SEPM, Gulf Coast Section, Deep-Water Reservoirs of the World*, p. 342–373.
- FERNÁNDEZ, O., MUÑOZ, J.A., ARBUÉS, P., FALIVENE, O., AND MARZO, M., 2004, Three-dimensional reconstruction of geological surfaces: an example of growth strata and turbidite systems from the Ainsa basin (Pyrenees, Spain): *American Association of Petroleum Geologists, Bulletin*, v. 88, p. 1049–1068.
- FERNÁNDEZ, O., MUÑOZ, J.A., ARBUÉS, P., AND FALIVENE, O., 2012, 3D structure and evolution of an oblique system of relaying folds: the Ainsa basin (Spanish Pyrenees): *Geological Society of London, Journal*, v. 169, p. 545–559.
- FLINT, S.S., HODGSON, D.M., SPRAGUE, A.R., BRUNT, R.L., VAN DER MERWE, W.C., FIGUEROA, J., PRÉLAT, A., BOX, D., DI CELMA, C., AND KAVANAGH, J.P., 2011, Depositional architecture and sequence stratigraphy of the Karoo basin floor to shelf edge succession, Laingsburg depocentre, South Africa: *Marine and Petroleum Geology*, v. 28, p. 658–674.
- FRYER, R.C., AND JOBE, Z.R., 2019, Quantification of the bed-scale architecture of submarine depositional environments: SEPM, *The Depositional Record*, v. 5, p. 192–211.
- GARDNER, M.H., BORER, J.M., MELICK, J.J., MAVILLA, N., DECHESNE, M., AND WAGERLE, R.N., 2003, Stratigraphic process–response model for submarine channels and related features from studies of Permian Brushy Canyon outcrops, West Texas: *Marine and Petroleum Geology*, v. 20, p. 757–787.
- GALES, J.A., TALLING, P.J., CARTIGNY, M.J.B., HUGHES CLARKE, J., LINTERN, G., STACEY, C., AND CLARE, M.A., 2019, What controls submarine channel development and the morphology of deltas entering deep-water fjords?: *Earth Surface Processes and Landforms*, v. 44, p. 535–551.
- GEE, M.J.R., AND GAWTHORPE, R.L., 2006, Submarine channels controlled by salt tectonics: examples from 3D seismic data offshore Angola: *Marine and Petroleum Geology*, v. 23, p. 443–458.
- GEORGIPOULOU, A., AND CARTWRIGHT, J.A., 2013, A critical test of the concept of submarine equilibrium profile: *Marine and Petroleum Geology*, v. 41, p. 35–47.
- GOMIS-CARTESEO, L.E., POYATOS-MORÉ, M., HODGSON, D.M., AND FLINT, S.S., 2018, Shelf-margin clinothem progradation, degradation and readjustment: Tanqua depocentre, Karoo Basin (South Africa): *Sedimentology*, v. 65, p. 809–841.
- GONG, C., STEEL, R.J., WANG, Y., LIN, C., AND OLARIU, C., 2016, Grain size and transport regime at shelf edge as fundamental controls on delivery of shelf-edge sands to deepwater: *Earth-Science Reviews*, v. 157, p. 32–60.
- HAGE, S., CARTIGNY, M.J.B., CLARE, M.A., SUMNER, E.J., VENDETTUOLI, D., CLARKE, J.E.H., HUBBARD, S.M., TALLING, P.J., LINTERN, D.G., STACEY, C.D., ENGLERT, R.G., VARDY, M.E., HUNT, J.E., YOKOKAWA, M., PARSONS, D.R., HIZZETT, J.L., AZPIROZ-ZABALA, M., AND VELLINGA, A.J., 2018, How to recognize crescentic bedforms formed by supercritical turbidity currents in the geologic record: insights from active submarine channels: *Geology*, v. 46, p. 563–566.
- HANSEN, L., L'HEUREUX, J.S., SAUVIN, G., POLOM, G., LECOMTE, I., VANESTE, M., LONGVA, O., AND KRAWCZYK, C., 2013, The effect of mass-wasting on the stratigraphic architecture of a fjord-valley fill: correlation of onshore, shear wave seismics and marine seismic data at Trondheim, Norway: *Sedimentary Geology*, v. 289, p. 1–18.
- HANSEN, L.A.S., CALLOW, R.H.T., KANE, I.A., GAMBERI, F., ROVERE, M., CRONIN, B.T., AND KNELLER, B.C., 2015, Genesis and character of thin-bedded turbidites associated with submarine channels: *Marine and Petroleum Geology*, v. 67, p. 852–879.
- HAUGHTON, P., DAVIS, C., MCCAFFREY, W., AND BARKER, S., 2009, Hybrid sediment gravity flow deposits: classification, origin and significance: *Marine and Petroleum Geology*, v. 26, p. 1900–1918.
- HEARD, T.G., AND PICKERING, K.T., 2008, Trace fossils as diagnostic indicators of deep-marine environments, Middle Eocene Ainsa–Jaca basin, Spanish Pyrenees: *Sedimentology*, v. 55, p. 809–844.
- HEARD, T.G., PICKERING, K.T., AND CLARK, J.D., 2014, Ichnofabric characterization of a deep-marine clastic system: a subsurface study of the Middle Eocene Ainsa System, Spanish Pyrenees: *Sedimentology*, v. 61, p. 1298–1331.
- HEINIÖ, P., AND DAVIES, R.J., 2007, Knickpoint migration in submarine channels in response to fold growth, western Niger Delta: *Marine and Petroleum Geology*, v. 24, p. 434–449.
- HIZZETT, J.L., HUGHES CLARKE, J.E., SUMNER, E.J., TALLING, P.J., AND CLARE, M.A., 2018, Which triggers produce the most erosive, frequent, and longest runout turbidity currents on deltas?: *Geophysical Research Letters*, v. 45, p. 855–863.
- HODGSON, D.M., DI CELMA, C.N., BRUNT, R.L., AND FLINT, S.S., 2011, Submarine slope degradation and aggradation and the stratigraphic evolution of channel–levee systems: *Geological Society of London, Journal*, v. 168, p. 625–628.
- HODGSON, D.M., KANE, I.A., FLINT, S.S., BRUNT, R.L., AND ORTIZ-KARPE, A., 2016, Time-transgressive confinement on the slope and the progradation of basin-floor fans: implications for the sequence stratigraphy of deep-water deposits: *Journal of Sedimentary Research*, v. 86, p. 73–86.
- HOFSTRA, M., PEAKALL, J., HODGSON, D.M., AND STEVENSON, C.J., 2018, Architecture and morphodynamics of subcritical sediment waves in an ancient channel–lobe transition zone: *Sedimentology*, v. 65, p. 2339–2367.
- HUBBARD, S.M., ROMANS, B.W., AND GRAHAM, S.A., 2008, Deep-water foreland basin deposits of the Cerro Toro Formation, Magallanes basin, Chile: architectural elements of a sinuous basin axial channel belt: *Sedimentology*, v. 55, p. 1333–1359.
- HUBBARD, S.M., DE RUIG, M.J., AND GRAHAM, S.A., 2009, Confined channel–levee complex development in an elongate depo-center: deep-water Tertiary strata of the Austrian Molasse basin: *Marine and Petroleum Geology*, v. 26, p. 85–112.
- HUBBARD, S.M., COVAULT, J.A., FILDANI, A., AND ROMANS, B.W., 2014, Sediment transfer and deposition in slope channels: deciphering the record of enigmatic deep-sea processes from outcrop: *Geological Society of America, Bulletin*, v. 126, p. 857–871.
- HUGHES CLARKE, J.E., 2016, First wide-angle view of channelized turbidity currents links migrating cyclic steps to flow characteristics: *Nature Communications*, v. 7, p. 1–13.
- JANBU, N.E., NEMEC, W., KIRMAN, E., AND ÖZAKSOY, V., 2007, Facies anatomy of a sand-rich channelized turbidite system: the Eocene Kusuri Formation in the Sinop Basin, north-central Turkey, *in* Nichols, G., Williams, E., and Paola, C., eds., *Sedimentary Processes, Environments and Basins: A Tribute to Peter Friend*: International Association of Sedimentologists, Special Publication 38, p. 457–517.
- JOBE, Z.R., SYLVESTER, Z., PARKER, A.O., HOWES, N., SLOWEY, N., AND PIRMEZ, C., 2015, Rapid adjustment of submarine channel architecture to changes in sediment supply: *Journal of Sedimentary Research*, v. 85, p. 729–753.
- JOHANSSON, M., AND STOW, D.A.V., 1995, A classification scheme for shale clasts in deep water sandstones, *in* Hartley, A.J., and Prosser, D.J., eds., *Characterization of Deep Marine Clastic Systems*: Geological Society of London, Special Publication 94, p. 221–241.

- JOLLY, B.A., LONERGAN, L., AND WHITTAKER, A.C., 2016, Growth history of fault-related folds and interaction with seabed channels in the toe-thrust region of the deep-water Niger delta: *Marine and Petroleum Geology*, v. 70, p. 58–76.
- KANE, I.A., AND HODGSON, D.M., 2011, Sedimentological criteria to differentiate submarine channel-levee subenvironments: exhumed examples from the Rosario Fm. (Upper Cretaceous) of Baja California, Mexico, and the Fort Brown Fm. (Permian), Karoo Basin, S. Africa: *Marine and Petroleum Geology*, v. 28, p. 807–823.
- KANE, I.A., DYKSTRA, M.L., KNELLER, B.C., TREMBLAY, S., AND MCCAFFREY, W.D., 2009a, Architecture of a coarse-grained channel-levee system: the Rosario Formation, Baja California, Mexico: *Sedimentology*, v. 56, p. 2207–2234.
- KANE, I.A., MCCAFFREY, W.D., AND MARTINSEN, O.J., 2009b, Allogenic vs. autogenic controls on megafault formation: *Journal of Sedimentary Research*, v. 79, p. 643–651.
- KANE, I.A., PONTEN, A.S.M., VANGDAL, B., EGGENHUISEN, J.T., HODGSON, D.M., AND SPYCHALA, Y.T., 2017, The stratigraphic record and processes of turbidity current transformation across deep-marine lobes: *Sedimentology*, v. 64, p. 1236–1273.
- KNELLER, B., 1995, Beyond the turbidite paradigm: physical models for deposition of turbidites and their implications for reservoir prediction, *in* Hartley, A.J., and Prosser, D.J., eds., *Characterization of Deep Marine Clastic Systems*: Geological Society of London, Special Publication 94, p. 31–49.
- KNELLER, B., 2003, The influence of flow parameters on turbidite slope channel architecture: *Marine and Petroleum Geology*, v. 20, p. 901–910.
- KNELLER, B., AND MCCAFFREY, W.D., 1999, Depositional effects of flow nonuniformity and stratification within turbidity currents approaching a bounding slope: deflection, reflection, and facies variation: *Journal of Sedimentary Research*, v. 69, p. 980–991.
- KNELLER, B., DYKSTRA, M., FAIRWEATHER, L., AND MILANA, J.P., 2016, Mass-transport and slope accommodation: implications for turbidite sandstone reservoirs: *American Association of Petroleum Geologists, Bulletin*, v. 100, p. 213–235.
- KOMAR, P.D., 1971, Hydraulic Jumps in Turbidity Currents: *Geological Society of America, Bulletin*, v. 82, p. 1477–1488.
- KREMER, C.H., MCHARGUE, T., SCHEUCHER, L., AND GRAHAM, S.A., 2018, Transversely-sourced mass-transport deposits and stratigraphic evolution of a foreland submarine channel system: deep-water tertiary strata of the Austrian Molasse Basin: *Marine and Petroleum Geology*, v. 92, p. 1–19.
- KUENEN, P.H., AND SENGUPTA, S., 1970, Experimental marine suspension currents, competency and capacity: *Geologie en Mijnbouw*, v. 49, p. 89–118.
- LEREN, B.L.S., JANBU, N.E., NEMEC, W.C.H., KIRMAN, E., AND ILGAR, A., 2007, Late Cretaceous to early Eocene sedimentation in the Sinop–Boyabat Basin, north-central Turkey: a deep-water turbiditic system evolving into littoral carbonate platform, *in* Nichols, G., Williams, E., and Paola, C., eds., *Sedimentary Processes, Environments and Basins: A Tribute to Peter Friend*: International Association of Sedimentologists, Special Publication 38, p. 401–456.
- LI, P., KNELLER, B., THOMPSON, P., BOZETTI, G., AND DOS SANTOS, T., 2018, Architectural and facies organisation of slope channel fills: Upper Cretaceous Rosario Formation, Baja California, Mexico: *Marine and Petroleum Geology*, v. 92, p. 632–649.
- LIU, Q., KNELLER, B., FALLGATTER, C., AND VALDEZ BUSO, V., 2018, Quantitative comparisons of depositional architectures of unconfined and confined turbidite sheet systems: *Sedimentary Geology*, v. 376, p. 72–89.
- LOWE, D.R., 1982, Sediment gravity flows: II. Depositional models with special reference to the deposits of high-density turbidity currents: *Journal of Sedimentary Petrology*, v. 52, p. 279–297.
- LOWE, D.R., GRAHAM, S.A., MALKOWSKI, M.A., AND DAS, B., 2019, The role of avulsion and splay development in deep-water channel systems: sedimentology, architecture, and evolution of the deep-water Pliocene Godavari “A” channel complex, India: *Marine and Petroleum Geology*, v. 105, p. 81–99.
- MACAULEY, R.V., AND HUBBARD, S.M., 2013, Slope channel sedimentary processes and stratigraphic stacking, Cretaceous Tres Pasos Formation slope system, Chilean Patagonia: *Marine and Petroleum Geology*, v. 41, p. 146–162.
- MACDONALD, H.A., PEAKALL, J., WIGNALL, P.B., AND BEST, J.L., 2011, Sedimentation in deep-sea lobe-elements: implications for the origin of thickening-upward sequences: *Geological Society of London, Journal*, v. 168, p. 319–332.
- MAIER, K.L., GALES, J.A., PAULL, C.K., ROSENBERGER, K., TALLING, P.J., SIMMONS, S.M., GWIAZDA, R., MCGANN, M., CARTIGNY, M.J.B., LUNDSTEN, E., ANDERSON, K., CLARE, M.A., XU, J., PARSONS, D., BARRY, J.P., WOLFSON-SCHWEHR, M., NIEMINSKI, N.M., AND SUMNER, E.J., 2019, Linking Direct Measurements of Turbidity Currents to Submarine Canyon-Floor Deposits: *Frontiers in Earth Science*, v. 7, p. 1–18.
- MARSETT, T., DROZ, L., DENNIELOU, B., AND PICHON, E., 2009, Cycles in the architecture of the Quaternary Zaire turbidite system: a possible link with climate, *in* Kneller, B.C., Martinsen, O.J., and McCaffrey, W.D., eds., *External Controls on Deep-Water Depositional Systems*: SEPM, Special Publication 92, p. 89–106.
- MARZO, M., NIJMAN, W., AND PUIGDEFABREGAS, C., 1988, Architecture of the Castissent fluvial sheet sandstones, Eocene, South Pyrenees, Spain: *Sedimentology*, v. 35, p. 719–738.
- MASALIMOVA, L.U., LOWE, D.R., MCHARGUE, T., AND DERKSEN, R., 2015, Interplay between an axial channel belt, slope gullies and overbank deposition in the Puchkirchen Formation in the Molasse Basin, Austria: *Sedimentology*, v. 62, p. 1717–1748.
- MASALIMOVA, L.U., LOWE, D.R., SHARMAN, G.R., KING, P.R., AND ARNOT, M.J., 2016, Outcrop characterization of a submarine channel-lobe complex: the lower Mount Messenger Formation, Taranaki Basin, New Zealand: *Marine and Petroleum Geology*, v. 71, p. 360–390.
- MAYALL, M., AND STEWART, I., 2000, The Architecture of Turbidite Slope Channels, *in* Weimer, P., Slatt, R.M., Coleman, J.L., Rosen, N., Nelson, C.H., Bouma, A.H., Styzen, M., and Lawrence, D.T., eds., *Deep-Water Reservoirs of the World*: SEPM, Gulf Coast Section, 20th Annual Research Conference, p. 578–586.
- MAYALL, M., JONES, E., AND CASEY, M., 2006, Turbidite channel reservoirs: key elements in facies prediction and effective development: *Marine and Petroleum Geology*, v. 23, p. 821–841.
- MAYALL, M., LONERGAN, L., BOWMAN, A., JAMES, S., MILLS, K., PRIMMER, T., POPE, D., ROGERS, L., AND SKEENE, R., 2010, The response of turbidite slope channels to growth-induced seabed topography: *American Association of Petroleum Geologists, Bulletin*, v. 94, p. 1011–1030.
- MCCARTHUR, A.D., AND MCCAFFREY, W.D., 2019, Sedimentary architecture of detached deep-marine canyon heads: examples from the East Coast Basin of New Zealand: *Sedimentology*, v. 66, p. 1067–1101.
- MCCAFFREY, W.D., AND KNELLER, B., 2001, Process controls on the development of stratigraphic trap potential on the margins of confined turbidite systems and aids to reservoir evaluation: *American Association of Petroleum Geologists, Bulletin*, v. 85, p. 971–988.
- MCCAFFREY, W.D., GUPTA, S., AND BRUNT, R., 2002, Repeated cycles of submarine channel incision, infill and transition to sheet sandstone development in the Alpine Foreland Basin, SE France: *Sedimentology*, v. 49, p. 623–635.
- MCHARGUE, T., PYRCZ, M.J., SULLIVAN, M.D., CLARK, J.D., FILDANI, A., ROMANS, B.W., COVAULT, J.A., LEVY, M., POSAMENTIER, H.W., AND DRINKWATER, N.J., 2011, Architecture of turbidite channel systems on the continental slope: patterns and predictions: *Marine and Petroleum Geology*, v. 28, p. 728–743.
- MILLINGTON, J., AND CLARK, J.D., 1995a, The Charo–Arro canyon-mouth sheet system, south-central Pyrenees, Spain: a structurally influenced zone of sediment dispersal: *Journal of Sedimentary Research*, v. 65, p. 443–454.
- MILLINGTON, J., AND CLARK, J.D., 1995b, Submarine canyon and associated base-of-slope sheet system: the Eocene Charo–Arro system, south-central Pyrenees, Spain, *in* Nilsen, T.H., Shew, R.D., Steffens G.S., and Studlick, J.R.J., eds., *Atlas of Deep-Water Outcrops*: American Association of Petroleum Geologists, Studies in Geology, p. 150–156.
- MOSCARDELLI, L., AND WOOD, L., 2008, New classification system for mass transport complexes in offshore Trinidad: *Basin Research*, v. 20, p. 73–98.
- MOUNTJOY, J.J., HOWARTH, J.D., ORPIN, A.R., BARNES, P.M., BOWDEN, D.A., ROWDEN, A.A., SCHIMEL, A.C.G., HOLDEN, C., HORGAN, H.J., NODDER, S.D., PATTON, J.R., LAMARCHE, G., GERSTENBERGER, M., MICALLEE, A., PALLENTIN, A., AND KANE, T., 2018, Earthquakes drive large-scale submarine canyon development and sediment supply to deep-ocean basins: *Science Advances*, v. 4, p. 1–8.
- MULDER, T., SVVITSKI, J.P.M., MIGEON, S., FAUGÈRES, J.-C., AND SAVOYE, B., 2003, Marine hyperpycnal flows: initiation, behavior and related deposits. A review: *Marine and Petroleum Geology*, v. 20, p. 861–882.
- MULDER, T., RAZIN, P., AND FAUGÈRES, J., 2009, Hummocky cross-stratification-like structures in deep-sea turbidites: Upper Cretaceous Basque basins (Western Pyrenees, France): *Sedimentology*, v. 56, p. 997–1015.
- MUÑOZ, J.A., 1992, Evolution of a continental collision belt: ECORS–Pyrenees crustal balanced cross-section, *in* McClay, K.R., ed., *Thrust Tectonics*: London, Chapman and Hall, p. 235–246.
- MUÑOZ, J.A., MCCLAY, K., AND POBLET, J., 1994, Synchronous extension and contraction in frontal thrust sheets of the Spanish Pyrenees: *Geology*, v. 22, p. 921–924.
- MUÑOZ, J.-A., BEAMUD, E., FERNÁNDEZ, O., ARBUÉS, P., DINARÉS-TURELL, J., AND POBLET, J., 2013, The Ainsa Fold and thrust oblique zone of the central Pyrenees: kinematics of a curved contractional system from paleomagnetic and structural data: *Tectonics*, v. 32, p. 1142–1175.
- MUTTI, E., 1977, Distinctive thin-bedded turbidite facies and related depositional environments in the Eocene Hecho Group (south-central Pyrenees, Spain): *Sedimentology*, v. 24, p. 107–131.
- MUTTI, E., 1984, The Hecho Eocene Submarine Fan System, South-Central Pyrenees, Spain: *Geo-Marine Letters*, v. 3, p. 199–202.
- MUTTI, E., 1985, Turbidite systems and their relations to depositional sequences, *in* Zuffa, G.G., ed., *Provenance of Arenites*: Dordrecht, Reidel Publishing Company, p. 65–93.
- MUTTI, E., 1992, Turbidite Sandstones, San Donato Milanese: Istituto di Geologia, Università di Parma, 275 p.
- MUTTI, E., 2019, Thin-bedded plumites: an overlooked deep-water deposit: *Journal of Mediterranean Earth Sciences*, v. 11, p. 1–20.
- MUTTI, E., AND NILSEN, T.H., 1981, Significance of intraformational rip-up clasts in deep-sea fan deposits: *International Association of Sedimentologists, 2nd European Meeting, Bologna, Proceedings*, p. 117–119.
- MUTTI, E., AND NORMARK, W.R., 1987, Comparing examples of modern and ancient turbidite systems: problems and concepts, *in* Leggett, J.K., and Zuffa, G.G., eds., *Marine Clastic Sedimentology: Concepts and Case Studies*: London, Graham and Trotman, p. 1–38.
- MUTTI, E., AND NORMARK, W.R., 1991, An integrated approach to the study of turbidite systems, *in* Weimer, P., and Link, M.H., eds., *Seismic Facies and Sedimentary Processes of Submarine Fans and Turbidite Systems*: New York, Springer-Verlag, p. 75–106.
- MUTTI, E., SEGURET, M., AND SGAVETTI, M., 1988, Sedimentation and deformation in the Tertiary Sequences of the Southern Pyrenees: *American Association of Petroleum Geologists, Mediterranean Basins Conference Guidebook, Field Trip No. 7*, p. 1–153.

- MUTTI, E., DAVOLI, G., MORA, S., AND PAPANI, L., 1994, Internal stacking patterns of ancient turbidite systems from collisional basins, *in* Weimer, P., Bouma, A.H., and Perkins, B.F., eds., *Submarine Fans and Turbidite Systems: Sequence Stratigraphy, Reservoir Architecture and Production Characteristics*, Gulf of Mexico and International: SEPM, Gulf Coast Section, 15th Annual Research Conference, p. 257–268.
- MUTTI, E., DAVOLI, G., TINTERRI, R., AND ZAVALA, C., 1996, The importance of ancient fluvio-deltaic systems dominated by catastrophic flooding in tectonically active basins: *Memorie di Scienze Geologiche de Padova*, v. 48, p. 233–291.
- MUTTI, E., TINTERRI, R., REMACHA, E., MAVILLA, N., ANGELLA, S., AND FAVA, L., 1999, An Introduction to the Analysis of Ancient Turbidite Basins from an Outcrop Perspective: *American Association of Petroleum Geologists, Continuing Education Course Notes, Series 39*, 96 p.
- MUTTI, E., TINTERRI, R., DI BIASE, D., FAVA, L., MAVILLA, N., ANGELLA, S., AND CALABRESE, L., 2000, Delta-front facies associations of ancient flood-dominated fluvio-deltaic systems: *Sociedad Geológica de España, Revista*, v. 13, p. 165–190.
- MUTTI, E., TINTERRI, R., BENEVELLI, G., DI BIASE, D., AND CAVANNA, G., 2003, Deltaic, mixed and turbidite sedimentation of ancient foreland basins: *Marine and Petroleum Geology*, v. 20, p. 733–755.
- MUZZI MAGALHAES, P., AND TINTERRI, R., 2010, Stratigraphy and depositional setting of slurry and contained (reflected) beds in the Marnoso-arenacea Formation (Langhian–Serravallian) Northern Apennines, Italy: *Sedimentology*, v. 57, p. 1685–1720.
- NELSON, C.H., ESCUTIA, C., GOLDFINGER, C., KARABANOV, E., GUTIERREZ-PASTOR, J., AND DEBATIST, M., 2009, External controls on modern clastic turbidite systems: three case studies, *in* Kneller, B.C., Martinsen, O.J., and McCaffrey, W.D., eds., *External Controls on Deep-Water Depositional Systems*: SEPM, Special Publication 96, p. 57–76.
- NELSON, C.H., ESCUTIA, C., DAMUTH, J.E., AND TWICHELL, D.C., 2011, Interplay of mass-transport and turbidite-system deposits in different active tectonic and passive continental margin settings: external and local controlling factors, *in* Shipp, R.C., Weimer, P., and Posamentier, H.W., eds., *Mass-Transport Deposits in Deepwater Settings*: SEPM, Special Publication 96, p. 39–66.
- NIMAN, W., 1998, Cyclicity and basin axis shift in a piggyback basin: towards modelling of the Eocene Tremp–Ager Basin, South Pyrenees, Spain, *in* Mascle, A., Puigdefàbregas, C., Luterbacher, H.P., and Fernández, M., eds., *Cenozoic Foreland Basins of Western Europe*: Geological Society of London, Special Publication 134, p. 135–162.
- NIMAN, W., AND PUIGDEFÀBREGAS, C., 1977, Coarse-grained point bar structure in a molasse-type fluvial system, Eocene Castisent sandstone formation, South Pyrenean Basin: *Canadian Journal of Petroleum Geologists, Memoir 5*, p. 487–510.
- NORMARK, W.R., PIPER, D.J.W., AND HESS, G.R., 1979, Distributary channels, sand lobes, and mesotopography of Navy Submarine Fan, California Borderland, with applications to ancient fan sediments: *Sedimentology*, v. 26, p. 749–774.
- OGATA, K., MUTTI, E., ANDREA, G., AND TINTERRI, R., 2012, Mass transport-related stratal disruption within sedimentary mélanges: examples from the northern Apennines (Italy) and south-central Pyrenees (Spain): *Tectonophysics*, v. 568–569, p. 185–199.
- OLIVEIRA, C.M.M., HODGSON, D.M., AND FLINT, S.S., 2011, Distribution of soft-sediment deformation structures in clinoform successions of the Permian Eccla Group, Karoo Basin, South Africa: *Sedimentary Geology*, v. 235, p. 314–330.
- ORTIZ-KARPE, A., HODGSON, D.M., AND MCCAFFREY, W.D., 2015, The role of mass-transport complexes in controlling channel avulsion and the subsequent sediment dispersal patterns on an active margin: the Magdalena Fan, offshore Colombia: *Marine and Petroleum Geology*, v. 64, p. 58–75.
- ORTIZ-KARPE, A., HODGSON, D.M., JACKSON, C.A., AND MCCAFFREY, W.D., 2017, Influence of seabed morphology and substrate composition on mass-transport flow processes and pathways: insights from the Magdalena Fan, offshore Colombia: *Journal of Sedimentary Research*, v. 87, p. 189–209.
- OWEN, G., 2003, Load structures: gravity-driven sediment mobilization in the shallow subsurface, *in* Van Rensbergen, P., Hillis, R.R., Maltman, A.J., and Morley, C.K., eds., *Subsurface Sediment Mobilization*: Geological Society of London, Special Publication 216, p. 21–34.
- PATACCI, M., 2016, A high-precision Jacob's staff with improved spatial accuracy and laser sighting capability: *Sedimentary Geology*, v. 335, p. 66–69.
- PAULL, C.K., TALLING, P.J., MAIER, K.L., PARSONS, D., XU, J., CARESS, D.W., GWIAZDA, R., LUNDSTEN, E.M., ANDERSON, K., BARRY, J.P., CHAFFEY, M., REILLY, T.O., ROSENBERGER, K.J., GALES, J.A., KIEFT, B., MCGANN, M., SIMMONS, S.M., MCCANN, M., SUMNER, E.J., CLARE, M.A., AND CARTIGNY, M.J., 2018, Powerful turbidity currents driven by dense basal layers: *Nature Communications*, v. 9, p. 1–9.
- PAYROS, A., TOSQUELLA, J., BERNAOLA, G., DINARES-TURELL, J., ORUE-ETXEBARRIA, X., AND PUJALTE, V., 2009, Filling the North European Early/Middle Eocene (Ypresian/Lutetian) boundary gap: insights from the Pyrenean continental to deep-marine record: *Palaeogeography, Palaeoclimatology, Palaeoecology*, v. 280, p. 313–332.
- PEAKALL, J., AND SUMNER, E.J., 2015, Submarine channel flow processes and deposits: a process–product perspective: *Geomorphology*, v. 244, p. 95–120.
- PICKERING, K.T., AND BAYLISS, N.J., 2009, Deconvolving tectono-climatic signals in deep-marine siliciclastics, Eocene Ainsa basin, Spanish Pyrenees: seesaw tectonics versus eustasy: *Geology*, v. 37, p. 203–206.
- PICKERING, K.T., AND CANTALEJO, B., 2015, Deep-marine environments of the middle Eocene upper Hecho Group, Spanish Pyrenees: Introduction: *Earth-Science Reviews*, v. 144, p. 1–9.
- PICKERING, K.T., AND CORREGIDOR, J., 2000, 3D Reservoir-scale study of Eocene confined submarine fans, south-central Spanish Pyrenees, *in* Weimer, P., Slatt, R.M., Coleman, J.L., Rosen, N., Nelson, C.H., Bouma, A.H., Styzen, M., and Lawrence, D.T., eds., *Deep-Water Reservoirs of the World*: SEPM, Gulf Coast Section, 20th Annual Research Conference, p. 776–781.
- PICKERING, K.T., AND CORREGIDOR, J., 2005, Mass transport complexes and tectonic control on confined basin-floor submarine fans, Middle Eocene, south Spanish Pyrenees, *in* Hodgson, D.M., and Flint, S.S., eds., *Submarine Slope Systems: Processes and Product*: Geological Society of London, Special Publication 244, p. 51–74.
- PICKERING, K.T., HODGSON, D.M., PLATZMAN, E., CLARK, J.D., AND STEPHENS, C., 2001, A new type of bedform produced by backfilling processes in a submarine channel, late Miocene, Tabernas–Sorbas basin, SE Spain: *Journal of Sedimentary Research*, v. 71, p. 692–704.
- PIRMEZ, C., BEAUBOUËF, R.T., FRIEDMANN, S.J., AND MOHRIG, D.C., 2000, Equilibrium profile and baselevel in submarine channels: examples from late Pleistocene systems and implications for the architecture of deepwater reservoirs, *in* Weimer, P., Slatt, R.M., Coleman, J.L., Rosen, N., Nelson, C.H., Bouma, A.H., Styzen, M., and Lawrence, D.T., eds., *Deep-Water Reservoirs of the World*: SEPM, Gulf Coast Section, 20th Annual Research Conference, p. 782–805.
- POSAMENTIER, H.W., 2003, Depositional elements associated with a basin floor channel–levee system: case study from the Gulf of Mexico: *Marine and Petroleum Geology*, v. 20, p. 677–690.
- POSAMENTIER, H.W., AND KOLLA, V., 2003, Seismic geomorphology and stratigraphy of depositional elements in deep-water settings: *Journal of Sedimentary Research*, v. 73, p. 367–388.
- POSAMENTIER, H.W., AND MARTINSEN, O.J., 2011, The character and genesis of submarine mass-transport deposits: insights from outcrop and 3D seismic data, *in* Shipp, R.C., Weimer, P., and Posamentier, H.W., eds., *Mass-Transport Deposits in Deepwater Settings*: SEPM, Special Publication 96, p. 39–66.
- POSTMA, G., AND CARTIGNY, M.J.B., 2014, Supercritical and subcritical turbidity currents and their deposits: a synthesis: *Geology*, v. 42, p. 987–990.
- POYATOS-MORE, M., 2014, Physical Stratigraphy and Facies Analysis of the Castisent Tecto-Sedimentary Unit (South-Central Pyrenees, Spain) [Ph.D. Thesis]: Universidad Autónoma de Barcelona, 282 p.
- PRATHER, B.E., 2003, Controls on reservoir distribution, architecture and stratigraphic trapping in slope settings: *Marine and Petroleum Geology*, v. 20, p. 529–545.
- PRATHER, B.E., BOOTH, J.R., STEFFENS, G.S., AND CRAIG, P.A., 1998, Classification, lithologic calibration, and stratigraphic succession of seismic facies of intraslope basins, deep-water Gulf of Mexico: *American Association of Petroleum Geologists, Bulletin*, v. 82, p. 701–728.
- PRATHER, B.E., O'BYRNE, C., PIRMEZ, C., AND SYLVESTER, Z., 2017, Sediment partitioning, continental slopes and base-of-slope systems: *Basin Research*, v. 29, p. 394–416.
- PRÉLAT, A., COVAULT, J.A., HODGSON, D.M., FILDANI, A., AND FLINT, S.S., 2010, Intrinsic controls on the range of volumes, morphologies, and dimensions of submarine lobes: *Sedimentary Geology*, v. 232, p. 66–76.
- PUIGDEFÀBREGAS, C., AND SOUQUET, P., 1986, Tectono-sedimentary cycles and depositional sequences of the Mesozoic and Tertiary from the Pyrenees: *Tectonophysics*, v. 129, p. 173–203.
- QIN, Y., ALVES, T.M., CONSTANTINE, J., AND GAMBOA, D., 2017, The role of mass wasting in the progressive development of submarine channels (Espírito Santo Basin, SE Brazil): *Journal of Sedimentary Research*, v. 87, p. 500–516.
- REMACHA, E., AND FERNÁNDEZ, L.P., 2003, High-resolution correlation patterns in the turbidite systems of the Hecho Group (south-central Pyrenees, Spain): *Marine and Petroleum Geology*, v. 20, p. 711–726.
- REMACHA, E., FERNÁNDEZ, L.P., AND MAESTRO, E., 2005, The transition between sheet-like lobe and basin-plain turbidites in the Hecho Basin (south-central Pyrenees, Spain): *Journal of Sedimentary Research*, v. 75, p. 798–819.
- SCHULTZ, M.R., FILDANI, A., COPE, T.D., AND GRAHAM, S.A., 2005, Deposition and stratigraphic architecture of an outcropping ancient slope system: Tres Pasos Formation, Magallanes Basin, southern Chile, *in* Hodgson, D.M., and Flint, S.S., eds., *Submarine Slope Systems: Processes and Product*: Geological Society of London, Special Publication 244, p. 27–50.
- SCHWENK, T., SPIEB, V., BREITZKE, M., AND HÜBSCHER, C., 2005, The architecture and evolution of the Middle Bengal Fan in vicinity of the active channel–levee system imaged by high-resolution seismic data: *Marine and Petroleum Geology*, v. 22, p. 637–656.
- SCOTCHMAN, J.I., BOWN, P., PICKERING, K.T., BOUDAGHER-FADEL, M., BAYLISS, N.J., AND ROBINSON, S.A., 2015, A new age model for the middle Eocene deep-marine Ainsa Basin, Spanish Pyrenees: *Earth-Science Reviews*, v. 144, p. 10–22.
- SÉGURET, M., 1972, Étude tectonique des nappes et series décollées de la partie centrale du versant sud der Pyrénées [Ph.D. Thesis]: Publications de l'Université de Sciences et Techniques de Languedoc, Serie Geologie Structurale, 188 p.
- SGAVETTI, R., 1991, Photostratigraphy of ancient turbidite systems, *in* Weimer, P., and M.H., Link, eds., *Seismic Facies and Sedimentary Process of Submarine Fans and Turbidite Systems*: New York, Springer, p. 107–125.
- SHARMAN, G.R., GRAHAM, S.A., MASALIMOVA, L.U., SHUMAKER, L.E., AND KING, P.R., 2015, Spatial patterns of deformation and paleoslope estimation within the marginal and central portions of a basin-floor mass-transport deposit, Taranaki Basin, New Zealand: *Geosphere*, v. 11, p. 266–306.
- SOLER-SAMPERE, M., AND GARRIDO-MEGÍAS, A., 1970, La terminación occidental del manto de Cotiella: *Pirineos*, v. 98, p. 5–12.

- SOUTTER, E.L., KANE, I.A., AND HUUSE, M., 2018, Giant submarine landslide triggered by Paleocene mantle plume activity in the North Atlantic: *Geology*, v. 46, p. 511–514.
- SPRAGUE, A.R.G., GARFIELD, T.R., GOULDING, F.J., BEAUBOUËF, R.T., SULLIVAN, M.D., ROSSEN, C., CAMPION, K.M., SICKAFOOSE, D.K., ABREU, V., SCHELLPEPER, M.E., JENSEN, G.N., JENNETTE, D.C., PIRMEZ, C., DIXON, B.T., YING, D., ARDILL, J., MOHRIG, D.C., PORTER, M.L., FARRELL, M.E., AND MELLERE, D., 2005, Integrated slope channel depositional models: the key to successful prediction of reservoir presence and quality in offshore West Africa, in *Colegio de Ingenieros Petroleros de México, E-Exitep 2005*, Veracruz, México, p. 1–13.
- STEVENSON, C.J., TALLING, P.J., WYNN, R.B., MASSON, D.G., HUNT, J.E., FRENZ, M., AKHMETZHANOV, A., AND CRONIN, B.T., 2013, The flows that left no trace: Very large-volume turbidity currents that bypassed sediment through submarine channels without eroding the sea floor: *Marine and Petroleum Geology*, v. 41, p. 186–205.
- STEVENSON, C.J., JACKSON, C.A., HODGSON, D.M., HUBBARD, S.M., AND EGGENHUISEN, J.T., 2015, Deep-water sediment bypass: *Journal of Sedimentary Research*, v. 85, p. 1058–1081.
- STEVENSON, C.J., FELDENS, P., GEORGIOPOULOU, A., SCHÖNKE, M., KRÄSTEL, S., PIPER, D.J.W., LINDHORST, K., AND MOSHER, D., 2018, Reconstructing the sediment concentration of a giant submarine gravity flow: *Nature Communications*, v. 9, p. 1–7.
- STOW, D.A.V. AND SHANMUGAM, G., 1980, Sequence of structures in fine-grained turbidites: comparison of recent deep-sea and ancient flysch sediments: *Sedimentary Geology*, v. 25, p. 23–42.
- TALLING, P.J., WYNN, R.B., MASSON, D.G., FRENZ, M., CRONIN, B.T., SCHIEBEL, R., AKHMETZHANOV, A.M., DALLMEIER-TIESSEN, S., BENETTI, S., WEAVER, P.P.E., GEORGIOPOULOU, A., ZÜHLSDORFF, C., AND AMY, L.A., 2007, Onset of submarine debris flow deposition far from original giant landslide: *Nature*, v. 450, p. 541–544.
- TALLING, P.J., MASSON, D.G., SUMNER, E.J., AND MALGESINI, G., 2012, Subaqueous sediment density flows: depositional processes and deposit types: *Sedimentology*, v. 59, p. 1937–2003.
- TINTERRI, R., 2011, Combined flow sedimentary structures and the genetic link between sigmoidal- and hummocky-cross stratification: *GeoActa*, v. 10, p. 1–43.
- VAIL, P.R., MITCHUM, R.M., AND THOMPSON, S., 1977, seismic stratigraphy and global changes of sea level, part 3: relative changes of sea level from coastal onlap, in Payton, C.E., ed., *Seismic Stratigraphy: Applications to Hydrocarbon Exploration*: American Association of Petroleum Geologists, Memoir 26, p. 63–81.
- VAN LUNSEN, H., 1970, Geology of the Ara–Cinca region, Spanish Pyrenees: *Geologica Ultraiectina*, v. 16, 119 p.
- VENDETTUOLI, D., CLARE, M.A., HUGHES CLARKE, J.E., VELLINGA, A., HIZZET, J., HAGE, S., CARTIGNY, M.J.B., TALLING, P.J., WALTHAM, D., HUBBARD, S.M., STACEY, C., AND LINTERN, D.G., 2019, Daily bathymetric surveys document how stratigraphy is built and its extreme incompleteness in submarine channels: *Earth and Planetary Science Letters*, v. 515, p. 231–247.
- WARD, N.I.P., ALVES, T.M., AND BLENKINSOP, T.G., 2018, Submarine sediment routing over a blocky mass-transport deposit in the Espírito Santo Basin, SE Brazil: *Basin Research*, v. 30, p. 816–834.
- WYNN, R.B., CRONIN, B.T., AND PEAKALL, J., 2007, Sinuous deep-water channels: Genesis, geometry and architecture: *Marine and Petroleum Geology*, v. 24, p. 341–387.
- XU, J.P., BARRY, J.P., AND PAULL, C.K., 2013, Small-scale turbidity currents in a big submarine canyon: *Geology*, v. 41, p. 143–146.
- ZAVALA, C., ARCURI, M., DI MEGLIO, M., GAMERO DIAZ, H., AND CONTRERAS, C., 2011, A Genetic Facies Tract for the Analysis of Sustained Hyperpycnal Flow Deposits, in Slatt, R.M., and Zavala, C., eds., *Sediment Transfer from Shelf to Deep Water: Revisiting the Delivery System*: American Association of Petroleum Geologists, Studies in Geology, p. 31–52.

Received 19 November 2019; accepted 26 February 2020.

Relating seafloor geomorphology to subsurface architecture: How mass-transport deposits and knickpoint-zones build the stratigraphy of the deep-water Hikurangi Channel

DANIEL E. TEK* , ADAM D. MCARTHUR* , MIQUEL POYATOS-MORÉ†, LUCA COLOMBERA* , MARCO PATACCI* , BENJAMIN CRAVEN* and WILLIAM D. MCCAFFREY*

*School of Earth and Environment, University of Leeds, Leeds, LS2 9JT, UK
(E-mail: ee11dt@leeds.ac.uk)

†Department of Geosciences, University of Oslo, Oslo, 0371, Norway

Associate Editor – Anna Pontén

ABSTRACT

Monitoring of modern deep-water channels has revealed how migrating channel-floor features generate and remove stratigraphy, improving understanding of how channel morphologies relate to their deposits. Here, seafloor and subsurface data are reconciled through an integrated study of high-resolution bathymetry and three-dimensional seismic data imaging a *ca* 150 km stretch of the trench-axial Hikurangi Channel, offshore New Zealand. On the seafloor, terraced channel-walls bound a flat, wide, channel-floor, ornamented with three scales of features that increase then decrease in longitudinal gradient downstream, and widen downstream: cyclic-steps, knickpoints and knickpoint-zones (in increasing size). Mass-transport deposits derived from channel-wall collapse, are bordered by wide and flat reaches of channel-floor upstream and by knickpoint-zones (reaches containing multiple knickpoints) downstream. In the subsurface, recognition of ten seismofacies and five types of surface enables identification of four depositional elements: channel-fill, sheet or terrace, levée, and mass-transport deposits. Integration of subsurface and seafloor interpretations reveals that knickpoint-zones initiate on the downstream margins of channel-damming mass-transport deposits; they migrate and incise through the mass-transport deposits and weakly-confined deposits formed upstream, as the channel tends towards equilibrium. Downstream of a knickpoint-zone, a flat channel-floor is bounded by newly-formed terraces. Knickpoints migrate by eroding upstream and depositing downstream, generating filled concave-up (cross-sectional) surfaces in their wake. Within knickpoint-zones, knickpoint-generated surfaces are re-incised by subsequently-passing knickpoints to produce a composite bounding surface; this surface does not delineate the morphology of any palaeo-conduit. The Hikurangi Channel's subsurface architecture records the localized erosional response to mass-transport deposit emplacement via knickpoint-zone migration, showcasing how transient seafloor features can build channelized stratigraphy. This model provides an additional mechanism to conventional models of channel deposit formation through 'cut-and-fill' over long stretches of channel. These findings may aid subsurface interpretation in systems lacking a contemporary self-analogue or with poor data coverage.

Keywords Bathymetry, channel fill, mass-transport deposit, New Zealand, seismic, submarine channel, trench-axial channel.

INTRODUCTION

Deep-water channels are conduits formed by erosion, bypass and deposition from turbidity currents and other sediment-laden flows (Peakall & Sumner, 2015). Alongside terrigenous sediment deep-water channels also transport, and potentially sequester, pollutants (Zhong & Peng, 2021), organic carbon (Hage *et al.*, 2020) and nutrients (Heezen *et al.*, 1955). Their deposits can provide archives of environmental change (e.g. Prins & Postma, 2000; Castelltort *et al.*, 2017) and catastrophic events such as earthquakes (e.g. Goldfinger, 2011; Mountjoy *et al.*, 2018). Deep-water channels on the seafloor can reach thousands of kilometres in length (Covault *et al.*, 2012; Shumaker *et al.*, 2018). Their scales and morphologies vary along an individual channel and between channels; channel heights range from metres to hundreds of metres, and widths range from tens of metres to kilometres (Shumaker *et al.*, 2018; Jobe *et al.*, 2020). Deep-water channel deposits are hosted within elongate (longitudinally), concave-up (in cross-section) surfaces that can be identified in outcrop or seismic data and exhibit a broad range of cross-sectional architectures (Clark & Pickering, 1996; Deptuck *et al.*, 2003; Macauley & Hubbard, 2013). Multiple, stacked concave-up surfaces may be hosted within larger surfaces (Clark & Pickering, 1996; McHargue *et al.*, 2011). The common observation of multiple nested scales of surfaces has led to the categorization of the hierarchical organization of the deposits of many channel systems (Cullis *et al.*, 2018). Resolution constraints of conventional seismic data make it difficult to distinguish filled palaeo-conduits from composite, diachronous surfaces formed by amalgamation of multiple smaller surfaces (Hodgson *et al.*, 2016; Hubbard *et al.*, 2020). Reconstructing palaeo-conduit morphologies from deep-water channel deposits is therefore problematic.

Bathymetry and shallow subsurface data reveal how features such as sediment waves and cyclic-steps (Hughes Clark, 2016; Hage *et al.*, 2018; Mountjoy *et al.*, 2018; Vendettuoli *et al.*, 2019; Englert *et al.*, 2020), knickpoints (Heiniö & Davies, 2007; Guiastrennec-Faugas *et al.*, 2020, 2021; Heijnen *et al.*, 2020), terraces (Babonneau *et al.*, 2002, 2004, 2010; Hansen *et al.*, 2015, 2017a) and mass-transport deposits (MTDs) (Hansen *et al.*, 2015, 2017a; Watson *et al.*, 2020), generate longitudinal variability in channel

morphology. Repeat seafloor surveying has shown how migrating cyclic-steps and knick-points are instrumental in constructing channelized stratigraphy. Cyclic-steps are crescent-shaped (widening downstream) in plan-view, and in long section possess a short, steep, downstream-dipping upstream side, and a longer, flat or upstream-dipping downstream side (Cartigny *et al.*, 2011, 2014). Cyclic-steps in deep-water channels are typically regularly-spaced, exhibit wavelengths of tens of metres, metre-scale relief, and generate packages of stratigraphy at bed-scale to bedset-scale (up to a few metres thick; Hage *et al.*, 2018; Vendettuoli *et al.*, 2019; Englert *et al.*, 2020). Knickpoints are crescent-shaped or V-shaped (widening downstream) features that exhibit steep upstream sides, and shallower, downstream-dipping downstream sides. They are larger than cyclic-steps, are typically spaced hundreds of metres to a few kilometres apart, exhibit metres to tens of metres of relief, and generate larger-scale stratigraphic packages (tens of metres; Heijnen *et al.*, 2020). Knickpoints migrate upstream by headward incision and downstream deposition. They can either exist as solitary channel-floor features, or as part of knickpoint-zones (*sensu* Heijnen *et al.*, 2020; Guiastrennec-Faugas *et al.*, 2020, 2021) within which, multiple, closely-spaced knickpoints collectively form longer reaches of elevated average longitudinal gradient. The formation of knickpoints and knickpoint-zones may allow deep-water channels to attain or maintain an idealized 'equilibrium profile' (Pirmez *et al.*, 2000; Kneller, 2003; Guiastrennec-Faugas *et al.*, 2020). However, their subsurface manifestation and preservation potential at larger architectural scales are less well understood.

Seismic studies of channel deposits on convergent margins (e.g. Ortiz-Karppf *et al.*, 2015; McArthur & McCaffrey, 2019) are rarer than on passive margins (Deptuck *et al.*, 2003, 2007; Jegou *et al.*, 2008; Janocko *et al.*, 2013; Jobe *et al.*, 2015; Hansen *et al.*, 2017a), with the three-dimensional architecture of axial channel-fills in deep-ocean trenches even less studied (McArthur & Tek, 2021). Here, high-resolution bathymetry and 3D seismic data from the trench-axial Hikurangi Channel, offshore New Zealand (Fig. 1) are integrated. This study aims to: (i) investigate how common seafloor surfaces and transient features (for example, MTDs, terraces and knickpoints) are manifested in channelized stratigraphy, how they interact with one another, and at what scales; (ii)

compare the mechanisms of knickpoint formation and migration with those in other subaqueous channel systems; (iii) identify the barriers to, and ways to reduce uncertainty in, reconstructing the palaeo-seafloor from subsurface channel deposits. The objectives of this study are to: (i) provide the most detailed description, to date, of the three-dimensional subsurface architecture of a trench-axial channel system; (ii) use the modern Hikurangi Channel as a self-analogue to reconcile observations from the seafloor and subsurface, and link seafloor features (and inferred processes) to their deposits; (iii) generate three-dimensional palaeo-seafloor reconstructions through the formation of subsurface channel architecture, accounting for longitudinal variability. Bridging the disconnect between seafloor morphology and preserved stratigraphy is important for understanding how deep-water channels evolve, how they transport and sequester sediment, and how accurately their deposits may record palaeoenvironmental signals. The interpretations, models and principles presented herein challenge existing concepts of how channelized strata is built and may be exported to aid interpretation in other deep-water channel systems.

GEOLOGICAL SETTING

The *ca* 1800 km long Hikurangi Channel (Lewis & Pantin, 2002; Mountjoy *et al.*, 2009, 2018) is located at the Hikurangi subduction margin, offshore New Zealand. The subduction of the Pacific Plate beneath the Australian Plate (Fig. 1) began at *ca* 27 Ma (Ballance, 1975; Nicol *et al.*, 2007; Barnes *et al.*, 2010; Lamb, 2011; Jiao *et al.*, 2015), generating a north-east/south-west orientated trench (the 'Hikurangi Trench') and an adjacent subduction complex (Davey *et al.*, 1986; Lewis & Pettinga, 1993; Nicol *et al.*, 2007; McArthur *et al.*, 2019). Towards its southern end, the deformation becomes increasingly oblique, eventually transitioning into the transpressive Marlborough and Alpine Fault systems (Wallace *et al.*, 2004, 2012). Most of the fill of the trench and construction of the accretionary prism has occurred in the last *ca* 3.5 Ma (Barnes & Mercier de Lepinay, 1997; Barnes *et al.*, 2010; Ghisetti *et al.*, 2016). The trench fill decreases in thickness from *ca* 6 km in the south-west to *ca* 1 km in the north-east (Lewis *et al.*, 1998; Barnes *et al.*, 2010; Plaza-Faverola *et al.*, 2012). The fill dominantly comprises turbidites resulting from overbank deposition from the Hikurangi

Channel, and transverse drainage networks that traversed the bounding slope (Lewis, 1994; Lewis *et al.*, 1998; Mountjoy *et al.*, 2009; McArthur *et al.*, 2021).

The Hikurangi Channel is fed by a network of canyons, which incise the continental shelf and capture sediment from the North and South Islands (Fig. 1; Carter, 1992; Lewis, 1994; Lewis *et al.*, 1998; Lewis & Barnes, 1999; Mountjoy *et al.*, 2009, 2018). The channel is dominantly fed by the flushing of canyons during earthquake-triggered failure events (Carter *et al.*, 1982; Carter, 1992; Lewis, 1994; Lewis *et al.*, 1998; Lewis & Barnes, 1999; Mountjoy *et al.*, 2009, 2018). Downstream of the confluence of its feeder canyons, the channel flows east for *ca* 130 km along the northern margin of the Chatham Rise (Fig. 1; Wood & Davy, 1994; Davy *et al.*, 2008). The channel then runs north-east for *ca* 500 km through the trench before abruptly changing direction offshore of Hawke Bay (*ca* 110° in <10 km), due to subducting seamounts and submarine landslides blocking the trench (Fig. 1; Lewis *et al.*, 1998; Collot *et al.*, 2001; Lewis & Pantin, 2002). Downstream of its departure from the trench, the channel continues for *ca* 550 km east across the Hikurangi Plateau before continuing for a further *ca* 600 km across the Pacific abyssal plain to its terminus (Fig. 1; Lewis & Pantin, 2002). Leftward flow deflection by the Coriolis force and the presence of deep-ocean currents (particularly a shallow branch of the Deep Western Boundary Current) have been interpreted to impact overbank flow processes and sedimentation within the trench (McCave & Carter, 1997; Lewis *et al.*, 1998; Lewis & Pantin, 2002; Bailey *et al.*, 2020). Submarine landslides at the Hikurangi Margin range in scale from large margin collapses (Lewis *et al.*, 1998; Collot *et al.*, 2001; Couvin *et al.*, 2020) to smaller collapses of the walls of the Hikurangi Channel (Lewis & Pantin, 2002; Watson *et al.*, 2020).

DATA

This study primarily utilises 2600 km² of pre-stack Kirchhoff depth migrated (broadband) 3D seismic data, acquired in 2017 by WesternGeco. This dataset images a *ca* 150 km long stretch of the Hikurangi Channel (Figs 1 and 2). Full stack data are displayed such that a downward increase in acoustic impedance is shown as a trough (white reflection). The horizontal resolution of the survey is *ca* 25 m and the vertical resolution

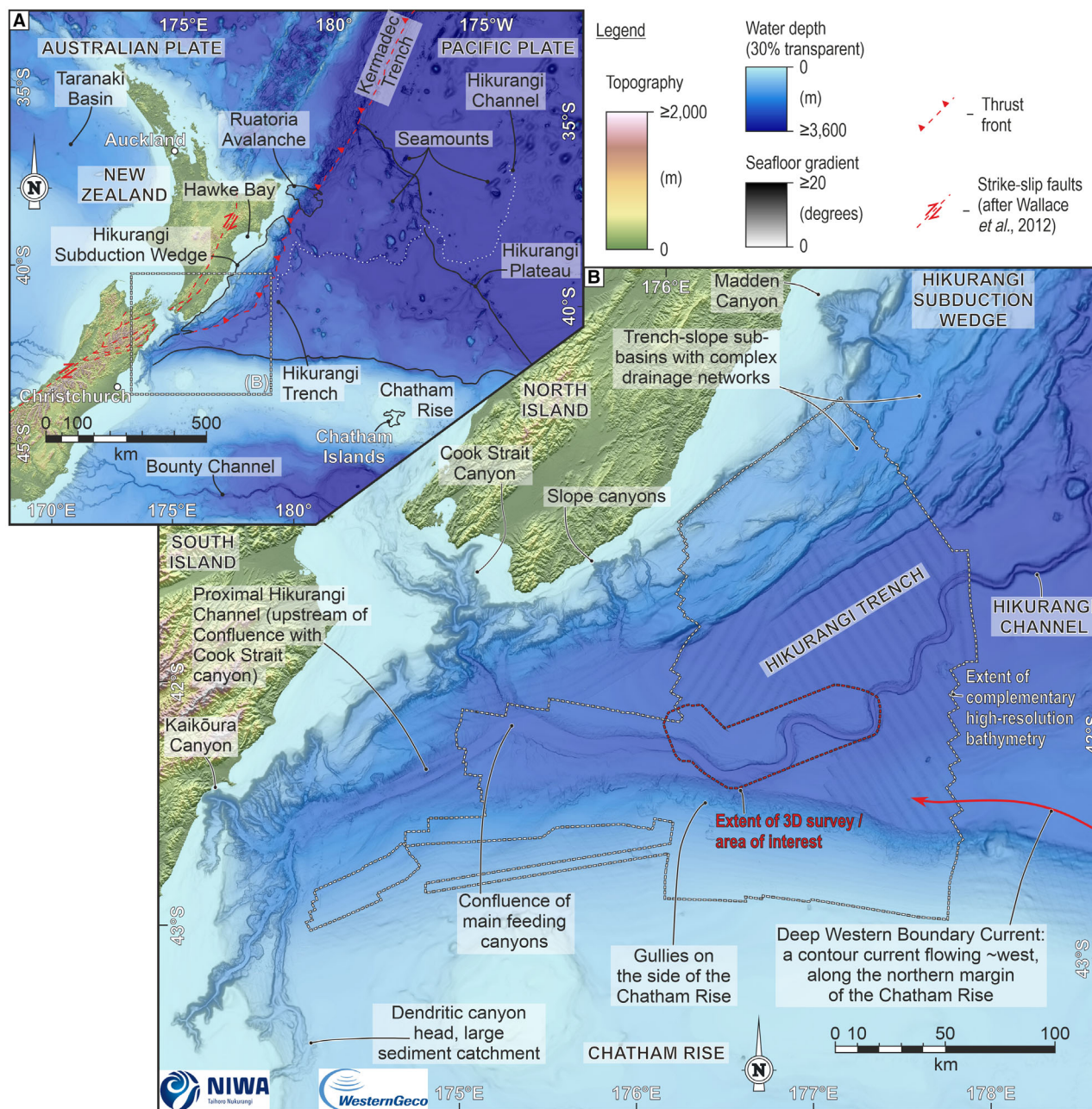


Fig. 1. Location maps showing: (A) the location of the Hikurangi Margin, and plate-scale features and structures; (B) the most proximal reach of the Hikurangi Channel, showing its relationship with its feeder canyons, slope-traversing trench-perpendicular systems, the Chatham Rise, Hikurangi Trench and the Hikurangi Subduction Wedge. Bathymetry were provided by the New Zealand National Institute for Water and Atmosphere (NIWA), and bathymetry is displayed as slope gradient maps with transparent water depth overlays.

is *ca* 7 m (values accurate at seafloor; Crisóstomo-Figueroa *et al.*, 2020). High-resolution bathymetry rendered from the 3D seismic data is augmented with 25 m grid bathymetry data, provided by New Zealand Petroleum and Minerals (NZPM). This bathymetry data was collected by the

National Institute of Water and Atmospheric Research (NIWA) using an EM302 multibeam echosounder (Kongsberg Maritime AS, Norway) at a frequency of 30 kHz, in 2012 and 2013 (see Bland *et al.*, 2014). Collectively, these surveys cover *ca* 32 000 km² and contain a *ca* 320 km long

stretch of the Hikurangi Channel (Fig. 1). The study focuses on the shallowest *ca* 500 m of the trench fill, which contains several large (kilometres across) channelforms, each of which follows a similar path to their predecessor.

METHODS

Seismic interpretation, horizon mapping, surface extraction and attribute analysis [Root Mean Squared (RMS) amplitude, variance, spectral decomposition] were conducted in Petrel© and Palaeoscan™. Seafloor maps and profiles were prepared using ArcGIS™ and Python. Most of the bathymetric analysis, including the extraction of all seafloor profiles, was conducted using a seafloor horizon generated from the seismic survey; outside the area covered by the seismic survey, complementary bathymetry data were used.

The interpretation herein is based on the identification of seismofacies and related surfaces, whose interrelations allow the classification of depositional elements. Descriptions of the seafloor, and subsurface seismofacies and surfaces are permitted by high-resolution imaging of the channel. Where reflector terminations hinder correlation, relationships between concave-up surfaces and packages of deformed reflectors interpreted as MTDs were used to determine a relative age framework and infer correlation.

RESULTS

Seafloor expression

Description. Within the study area, twenty-eight thalweg-perpendicular cross-sections (Figs 2B, 3 and 4), a longitudinal profile (Fig. 2C), and bathymetric and gradient maps (Figs 2 and 5) are used to quantify the seafloor expression of the Hikurangi Channel. The channel is concave-up in cross-section, with a relatively flat channel-floor and steep channel-walls (Fig. 3). The channel exhibits a moderate sinuosity (calculated as channel thalweg length divided by the straight line separation of the channel endpoints; see Friend & Sinha, 1993) of 1.3 (cf. Peakall *et al.*, 2012; Figs 1 and 2). Landward channel-walls, on the inside and outside of meander bends, are consistently higher than oceanward walls (Figs 3, 4D and 4F). Landward channel-walls shallow upward before reaching a levée crest, where the gradient reverses to form

a wider (tens to 100 km) outer levée surface that dips away from the channel at $<2^\circ$ (Fig. 3). On the oceanward walls, levée crests and concomitant gradient reversals are largely absent, with the overbank dipping gently ($<0.5^\circ$) towards the channel, before steepening at the edge of the Chatham Rise or subducting plate (Fig. 3); in profiles 6 to 8 the Chatham Rise forms the oceanward channel-wall (Figs 2B and 5B). Channel-walls dip between 2° and 12° (mean 4°) towards the thalweg (Fig. 4). Both walls are stepped, with steeper parts (up to 33°) connecting gentler parts ($<4^\circ$) that form terraces (*sensu* Babonneau *et al.*, 2004) (Figs 2 and 4). The oceanward channel-wall is narrower (mean 3024 m) and steeper (mean 4.7° ; measured from the top of the channel-wall to the thalweg) than the landward one (mean 5119 m and 3.5° , respectively); the landward wall exhibits steeper maximum gradients than the oceanward one (mean 18° and 15° , respectively) (Fig. 4C). Terraces occur from <10 m to 269 m above the thalweg, and range in width from 242 m to 3123 m (mean 1002 m). Terraces are: (i) wider towards the top of their host wall; (ii) more commonly located towards the base of the channel-wall and become more abundant distally; and (iii) wider and more abundant on the landward side and inner meander bends (Figs 4B, 4F and 5). At any given location a channel-wall may contain multiple terraces that may coalesce, upstream or downstream, with adjacent terraces (forming a larger terrace), the channel-floor, or overbanks (Figs 2, 3, 4 and 5F). A variety of overbank features, such as two large fields of sediment waves that are concentric around bends 1 and 4, shallow fanning gullies inside of bend 4, and an area containing 'scallop-shaped' features (Figs 2 and 5) may obscure the identification of terraces and levée crests.

The widths of the channel-floor (mean 2571 m) and the wider channel (including channel-walls; mean 11 034 m) generally decrease from *ca* 4650 m and *ca* 16 600 m (respectively) in proximal parts, to *ca* 1700 m and *ca* 7800 m (respectively) at the distal end of the survey (Figs 2 and 4). Within the broader area of bathymetric coverage (Fig. 1), the channel thalweg exhibits an asymptotic longitudinal profile, with an average longitudinal gradient (measured from the mouth of the Kaikōura Canyon; Fig. 1B) of 0.23° ; the longitudinal gradient within the study area (averaged over 140 km) is much shallower: 0.09° (Fig. 2C). Locally, both channel-floor width and longitudinal gradient vary substantially over kilometre scales (Figs 2C, 4E and 5).

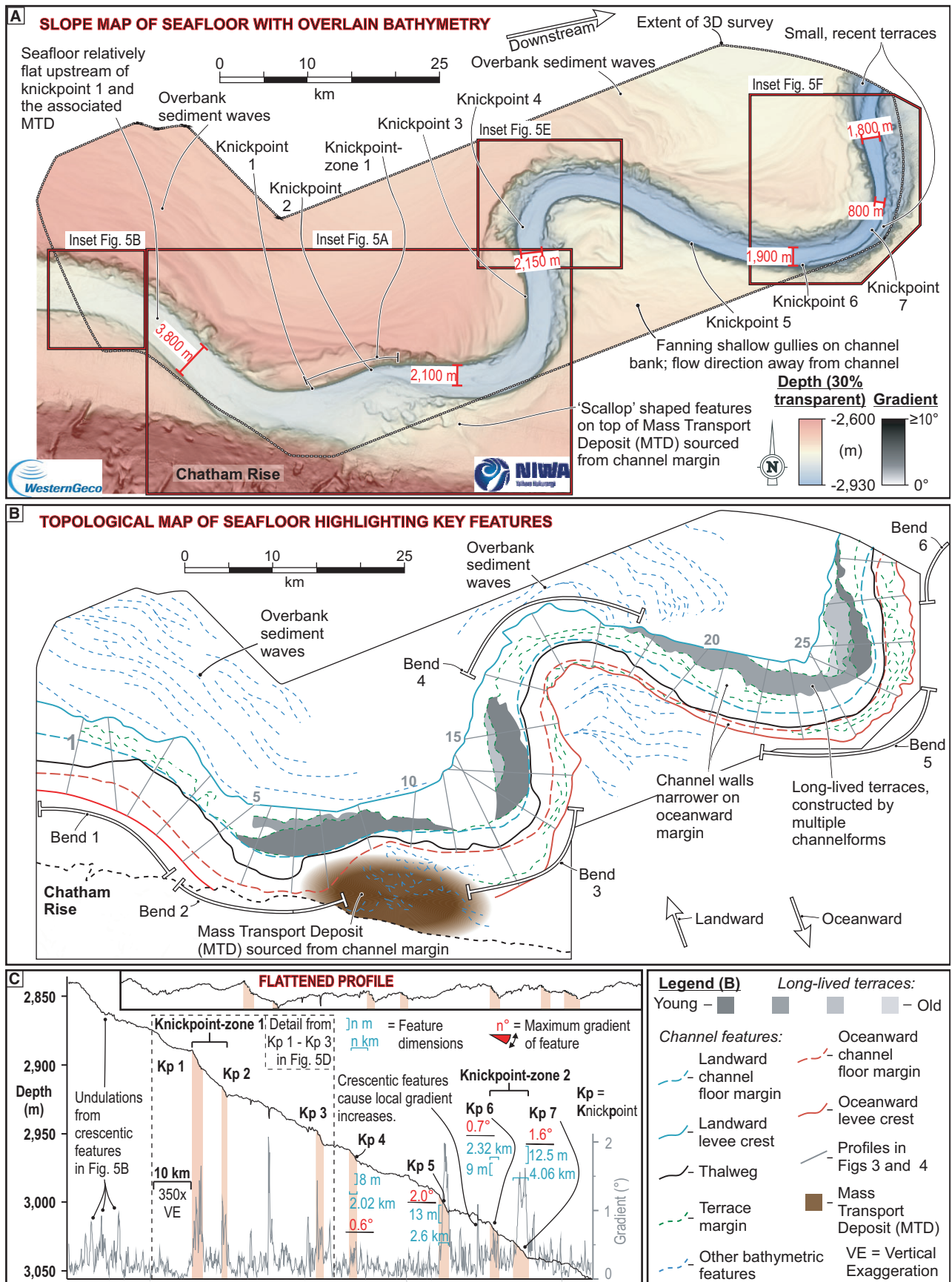


Fig. 2. (A) Gradient map with bathymetric overlay of the modern Hikurangi Channel within the study area. (B) Interpreted topological line drawing highlighting the location of bends 1 to 6 referenced in the text, main overbank and channel-wall features, and the locations of the profiles and morphometric features shown in Figs 3 and 4. (C) Detailed longitudinal depth and gradient profile along the thalweg of the channel showing the locations of the two knickpoint-zones, seven knickpoints, and other channel-floor features detailed in Fig. 5.

The largest scale longitudinal gradient variations occur in two steep knickpoint-zones (1 and 2, Fig. 2C), which are *ca* 10 000 m long and *ca* 35 m tall with downstream gradients of *ca* 0.2° (Fig. 2C); knickpoint-zone 1 is slightly steeper (0.212°) than knickpoint-zone 2 (0.191°). Seven smaller-scale steep areas, knickpoints 1 to 7, are also observed within the studied channel section (knickpoints 1 to 7 in Fig. 2C). Knickpoint-zones 1 and 2 contain two knickpoints each (knickpoints 1 and 2, and knickpoints 6 and 7, respectively; Fig. 2C), that superimpose higher magnitude gradient increases onto their host knickpoint-zone (Figs 2, 5 and 6). Three solitary knickpoints (knickpoints 3 to 5; Fig. 2C), that exist independently of knickpoint-zones, are spaced at *ca* 5 to 25 km intervals between knickpoint-zones 1 and 2 (Figs 2, 5 and 6). Knickpoints are 1420 to 4060 m long (mean 2401 m), 7.5 to 14 m tall (mean 10 m), with maximum gradients of 0.6° to 2.0° (mean 1.3°). In plan-view knickpoints and knickpoint-zones are narrowest upstream, at the point of maximum gradient increase. Knickpoint-zone 1 marks an abrupt change in channel morphology over <10 km longitudinally (Figs 5A and 6). Upstream of knickpoint-zone 1 (and hence knickpoint 1) the channel-floor is 3500 to 4000 m wide and relatively flat; immediately downstream of the head of knickpoint-zone 1, the channel is effectively V-shaped with a very narrow (<200 m) channel-floor; *ca* 10 km downstream of the head of knickpoint-zone 1, *ca* 5 km of knickpoint 2, the channel-floor widens to *ca* 2000 m and is adjacent to a flat, <1000 m wide, terrace elevated 5 to 30 m above the thalweg that gets progressively shorter, and eventually disappears distally over *ca* 15 km (Figs 5A and 6).

Knickpoint-zone 1 is north of and adjacent to the aforementioned area of ‘scallop-shaped’ depressions. These *ca* 1 to 5 km wide (long axis), <25 m deep features dip steeply (<10°) north on their southern side, and are shallower (<5°) to flat on their northern side (Figs 5A and 6). Into the subsurface, the scallop-shaped features can be traced to lineaments against which reflectors abruptly terminate and/or change in dip, all hosted within a chaotic <120 m thick package with a sharp basal contact with

undisturbed underlying reflectors (Fig. 5A). Knickpoint-zone 2 (which hosts knickpoints 6 and 7) is *ca* 5 km upstream of a locally narrow (800 m) stretch of channel-floor bordering a flat, <500 m wide terrace elevated 30 to 50 m above the channel-floor upstream of the narrowest point; downstream it borders a highly rugose, <2500 m wide terrace (Fig. 5F).

Subtle features are common on the channel-floor. The most common are crescentic features that are steep (<2°) and narrow upstream but widen and shallow downstream (Fig. 5B and C). They most commonly occur as thalweg-aligned trains of <500 m long, <5 m deep features, spaced <1 km apart, often near the head of knickpoints (Fig. 5B and C). Where crescentic features are isolated (spaced <5 km apart), they are longer (<1 km) and deeper (<7.5 m) (Fig. 5F). Thalweg-perpendicular ridges with straight <1 km long crests, steep and long (<750 m) upstream sides, and short (<300 m), shallowly-dipping or upstream-dipping sides are also present on parts of the channel-floor (Fig. 5B).

Interpretations. Terraces may have initiated through: (i) the establishment of a new conduit that is laterally offset from the axial fill of a precursor conduit (punctuated channel migration; e.g. Maier *et al.*, 2012); (ii) the formation of lateral accretion deposits in a migrating conduit (progressive channel migration; e.g. Abreu *et al.*, 2003; Deptuck *et al.*, 2007); or (iii) the local emplacement of an MTD from the collapse of a channel-wall (Hansen *et al.*, 2017a,b). They subsequently aggraded by the marginal deposition of finer grained sediment from the overspilling upper parts of flows that traversed the newly formed conduit (Kane & Hodgson, 2011; Hansen *et al.*, 2015). Narrow terraces with low elevations above the channel-floor formed recently on top of MTDs derived from the local collapse of a channel-wall, or the incision of a narrow conduit into the fill of a precursor, likely at the edge (Maier *et al.*, 2012; Hansen *et al.*, 2015, 2017a,b; Figs 5A, 5E, 5F and 6). These processes likely co-occur, causing the abundance of small terraces near the channel-floor. Larger terraces near the top of the channel-walls (Fig. 5F) are longer-lived features that likely formed during the

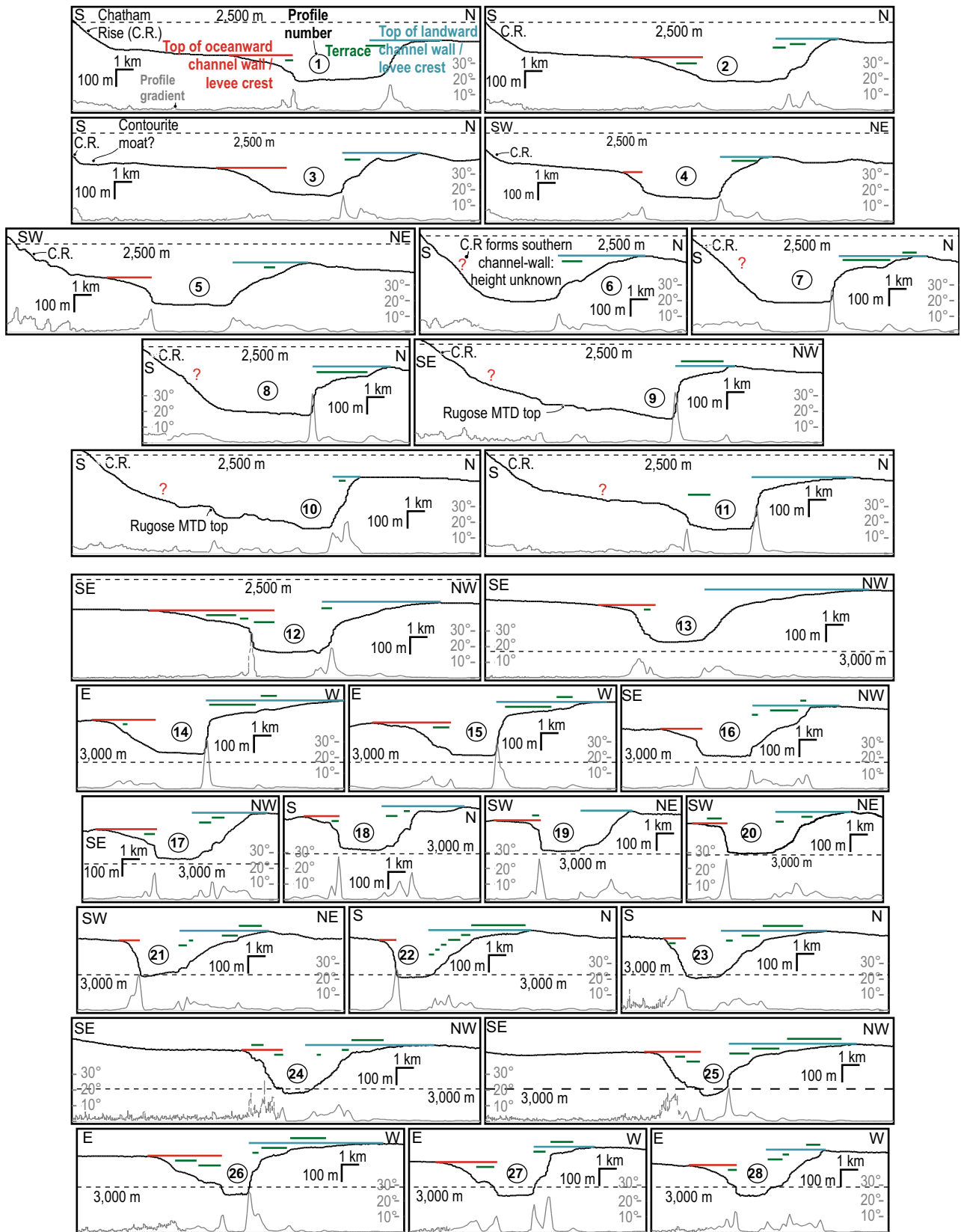


Fig. 3. Cross-sectional seafloor profiles 1 to 28 (see Fig. 2 for locations), highlighting the features shown in Fig. 4.

establishment and infill of palaeo-conduits. Long-lived terraces can receive sediment from multiple sequentially-active palaeo-conduits (Fig. 2B), and are preferentially preserved on inner bends and destroyed on outer bends, as meanders expand (Fig. 5A and F).

Scallop-shaped features on the oceanward channel bank are interpreted as fault scarps on top of a quasi-instantaneously emplaced MTD that formed through channel-wall collapse (Figs 2 and 5; see also Lewis & Pantin, 2002; Watson *et al.*, 2020). It partially filled and dammed the channel, likely causing a reduction in flow velocity and deposition upstream (Pickering & Corregidor, 2000, 2005; Tek *et al.*, 2020; Soutter *et al.*, 2021), to form the wide, flat channel-floor upstream of knickpoint-zone 1 (Figs 2, 5D and 6). Knickpoint-zone 1 formed because of increased flow velocities and erosive power in response to an increase in longitudinal gradient (Kneller, 1995) on the downstream side of the MTD. Upstream migration of knickpoints is interpreted as the primary erosive mechanism in the studied reach of the Hikurangi Channel, and operates at a smaller hierarchical scale than that of knickpoint-zones. The migration of knickpoint-zones (and their constituent knickpoints) allows the channel to re-attain its equilibrium after alteration (Heiniö & Davies, 2007; Guiastrenec-Faugas *et al.*, 2020). A narrow channel-floor and adjacent terrace may be formed downstream of a migrating knickpoint-zone (Deptuck *et al.*, 2007; Heiniö & Davies, 2007; Guiastrenec-Faugas *et al.*, 2020, 2021; Heijnen *et al.*, 2020), as is observed downstream of knickpoint-zone 1 (Fig. 5A). As knickpoint-zones migrate, they may shallow and lengthen until the conduit attains equilibrium. While knickpoint-zone 2 is also interpreted to have formed after the quasi-instantaneous emplacement of a channel-wall-derived MTD (Fig. 5F), it is shallower and longer than knickpoint-zone 1 (Figs 2, 5A and 5F). Having migrated farther upstream, knickpoint-zone 2 has formed a long terrace where it has successively incised through the MTD (forming the rugose part of the terrace on the oceanward channel-wall in Fig. 5F), and the wide, partially ponded deposits that formed upstream of it (forming the flat part of the terrace on the oceanward channel-wall in Fig. 5F). Once a knickpoint-zone has passed, the newly-formed terrace will then aggrade as finer parts of flows are deposited on it. Knickpoints may initiate in response to a localized modification of a longitudinal profile

(e.g. Heiniö & Davies, 2007), potentially by small MTDs derived from channel-wall collapse, effectively making them small knickpoint-zones. Alternatively, knickpoints may occur naturally through the exploitation of channel-floor relief or by longitudinal variations in flow velocity (Heijnen *et al.*, 2020).

At the smallest scale, crescentic features interpreted as cyclic-steps (Cartigny *et al.*, 2011, 2014) and ridge-like features interpreted as sediment waves (Mountjoy *et al.*, 2018) are observed in discrete areas of the channel-floor (Fig. 5C); they may be more widespread but undetectable at the resolution of the dataset.

Seismofacies, surfaces and depositional elements

Ten seismofacies, categorized on the properties of their reflectors and/or their terminations, are described in Table 1. Five seismic surface types distinguished by abrupt changes in seismofacies, or reflector character, dip or thickness, are described in Table 2. Surfaces can be concave-up, or unidirectionally dipping (from sub-horizontal to vertical). For concave-up surfaces, reflectors above or inside the surface will be described hereafter as 'inboard'; reflectors outside will be described as 'outboard'. For unidirectionally dipping surfaces, reflectors on the down-dip side will be described as 'inboard' and on the up-dip side as 'outboard'. Interrelationships between seismofacies and surfaces have allowed the establishment of four types of depositional elements:

Depositional Element 1 – Channel-fill

Observations. Channel-fill comprises: (i) High-Amplitude Reflectors (HARs) and HAR Packages (HARPs) that can be narrow (<1 km wide) and lens shaped (SF1; Fig. 7A and E) or wide (1 to 3 km) and flat (SF3; Fig. 7B and C); (ii) laterally stacked, unidirectionally inclined reflector packages (SF2; Fig. 7B and D); and (iii) chaotic/transparent packages (SF8; Fig. 7A and E). Channel-fill deposits sit within channelform surfaces (Table 2; Fig. 7B). At smaller scales, one or more packages of SF1, SF2, SF3 and SF8, themselves bounded by HARP-bounding surfaces, constitute the broader channel-fill (for example, Fig. 7C). A channelform surface can be truncated by a younger channelform surface or MTD-base (Fig. 7B, C and G). If the thalweg of a subsequent channelform is sufficiently deep, older channel-fills may be juxtaposed against the sheet

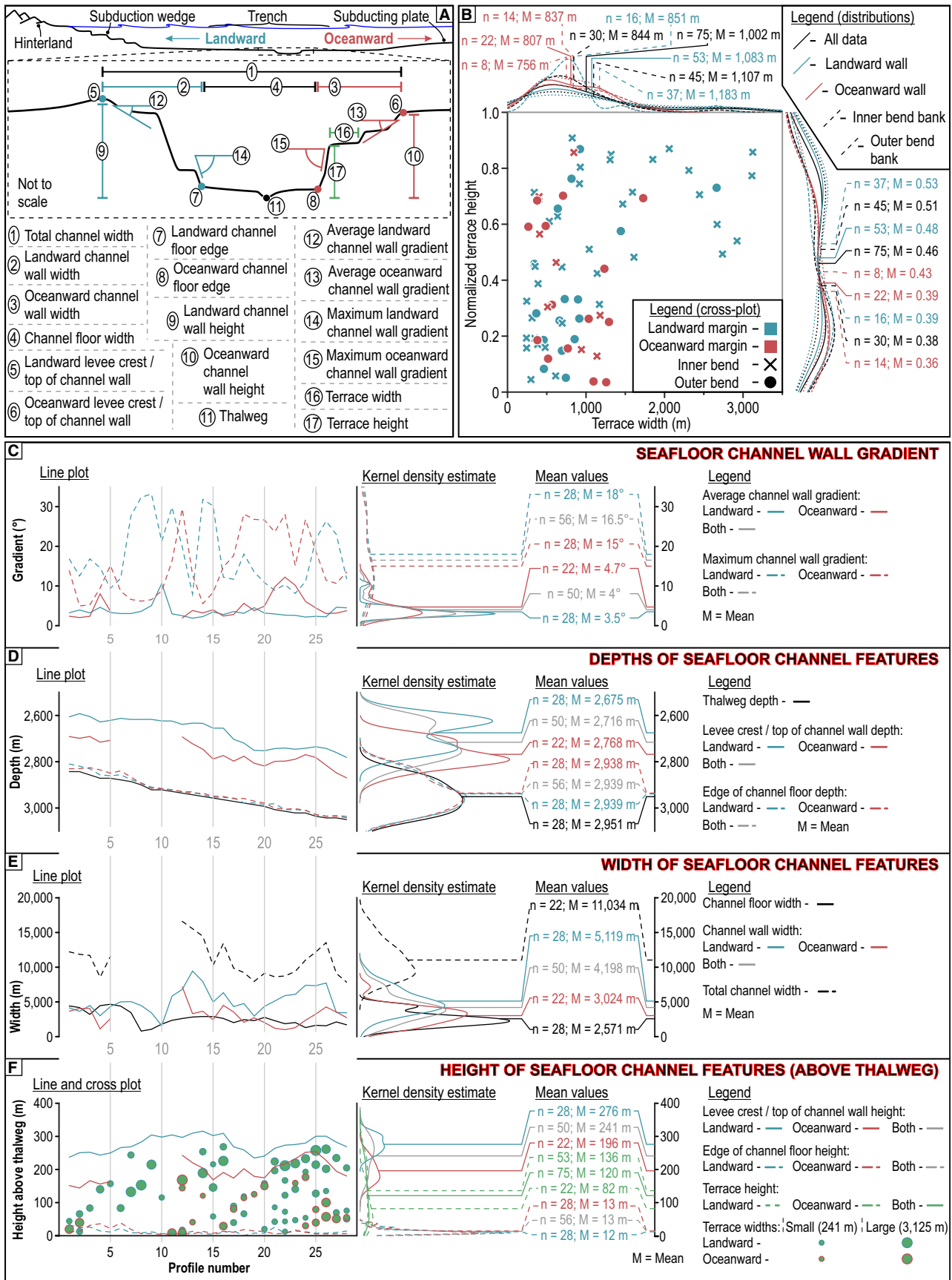


Fig. 4. (A) Summary sketch of the nomenclature used in the text and the parameters presented in parts (B) to (F). (B) Plot of terrace width versus normalized terrace height (its vertical position between the base and top of the host channel-wall), and the kernel density estimations thereof, derived from profiles 1 to 28 (Fig. 3). (C) Average and maximum channel-wall gradients against profile (a proxy for along-channel distance, which totals 140 km), and distributions and means thereof. (D) Depth versus distance (profile number) plot of the thalweg, channel-floor edges and tops of the channel-walls, and the distributions thereof. (E) Width versus distance (profile number) plot showing the width of the channel-floor, channel-walls, and total channel width, and distributions thereof. (F) Plot showing the height of the channel-floor edges, channel-wall tops and the height, width and abundance of terraces above the thalweg, and distributions thereof. Note that a section (profiles 6 to 11 inclusive) of the oceanward channel-wall top is outside of the survey extent, measurements in this section are therefore missing in (C) to (F). Data are provided as Supplementary Material.

or terrace-bounding surface formed by a younger channelform. Channel-fills can be overlain by a relatively flat MTD-base that spans the width of the underlying fill (Fig. 7B and C), or be gradationally overlain by tabular reflectors (Fig. 7G).

Interpretations. The presence of SF1 and SF2 (sand-rich channel-floor deposits), SF3 (laterally stacked marginal deposits of SF1) and SF4 (mega-clasts or debrites sourced from palaeo-conduit walls) (Table 1), and the occurrence of HARP-bounding surfaces within channel-fills suggests that at least two orders of hierarchy are present. Incision and infill at HARP-bounding surface scale may have formed in response to: (i) erosion and deposition in palaeo-conduits (Janocko *et al.*, 2013; Hansen *et al.*, 2017), possibly in response to increases and decreases in input flow energy (Gardner *et al.*, 2003; Flint *et al.*, 2011); or (ii) may represent the stratigraphic manifestation of the passage of channel-floor features such as knickpoints (Guiastrennec-Faugas *et al.*, 2020, 2021; Heijnen *et al.*, 2020). Local blockages or diversions caused by the emplacement of mega-clasts (SF8) (Deptuck *et al.*, 2003, 2007) may also have caused incision and infill by either of the aforementioned mechanisms.

A channelform surface is a composite surface of a larger hierarchical order than a HARP-bounding surface (Table 2). Degradation and infill at channelform surface scale is caused by the system adjusting to its idealized equilibrium profile (Pirmez *et al.*, 2000; Kneller, 2003). Channelform surfaces likely start off as smaller, narrower surfaces (HARP-bounding surface scale), that are filled and modified during successive iterations of formation and infill of HARP-bounding surfaces (Hubbard *et al.*, 2020). Time-transgressive modification by widening and deepening of the bounding channelform surface is achieved by the erosion and/or collapse of one or both walls of a palaeo-conduit.

Depositional Element 2 – Sheet or terrace

Description. Sheet or terrace deposits comprise two seismofacies constituting tabular reflectors, distinguished based on whether they are (SF5) or are not (SF4) truncated by a younger surface (Fig. 7E, F and G; Table 1). On the outboard side, sheet or terrace deposits are bounded laterally by a sheet or terrace-bounding surface or an MTD-top (Fig. 7E, F and G). On the inboard side, reflectors in SF5 terminate against younger channelform surfaces, sheet or terrace-bounding surfaces, or MTD-bases (Fig. 7F and G). At their base, sheet or terrace deposits may grade from channel-fill deposits or overlie an MTD-top. Adjacent packages of truncated tabular reflectors can converge upward to form a larger, through-going reflector package, and eventually either transition upward into overlying levée deposits, or be overlain by an MTD-base (Fig. 7F and G).

Interpretations. Reflectors that are continuous across their bounding surfaces (SF4; Fig. 7C, E and F) represent sheet deposits formed from passive fill or weakly confined, depositional flows in response to a decrease in or reversal of the downstream gradient and/or lateral confinement (Table 1). Where reflectors are truncated by a younger surface (SF5; Fig. 7F and G), they may represent incised sheet deposits or terrace deposits formed by overspill from a younger palaeo-conduit (Table 1). Sheet or terrace-bounding surfaces may have formed during both the fill of a palaeo-conduit and subsequent incision forming a HARP-bounding surface or channelform surface, or by contemporaneous aggradation of two terraces, or a terrace and a levée; as such, they cannot be tied to any one channelform. A vertical transition likely exists between incised sheet and terrace deposits (from sheet deposits at the base to terrace deposits towards the top), making their definitive distinction difficult based on seismic character alone (Deptuck *et al.*, 2003). The

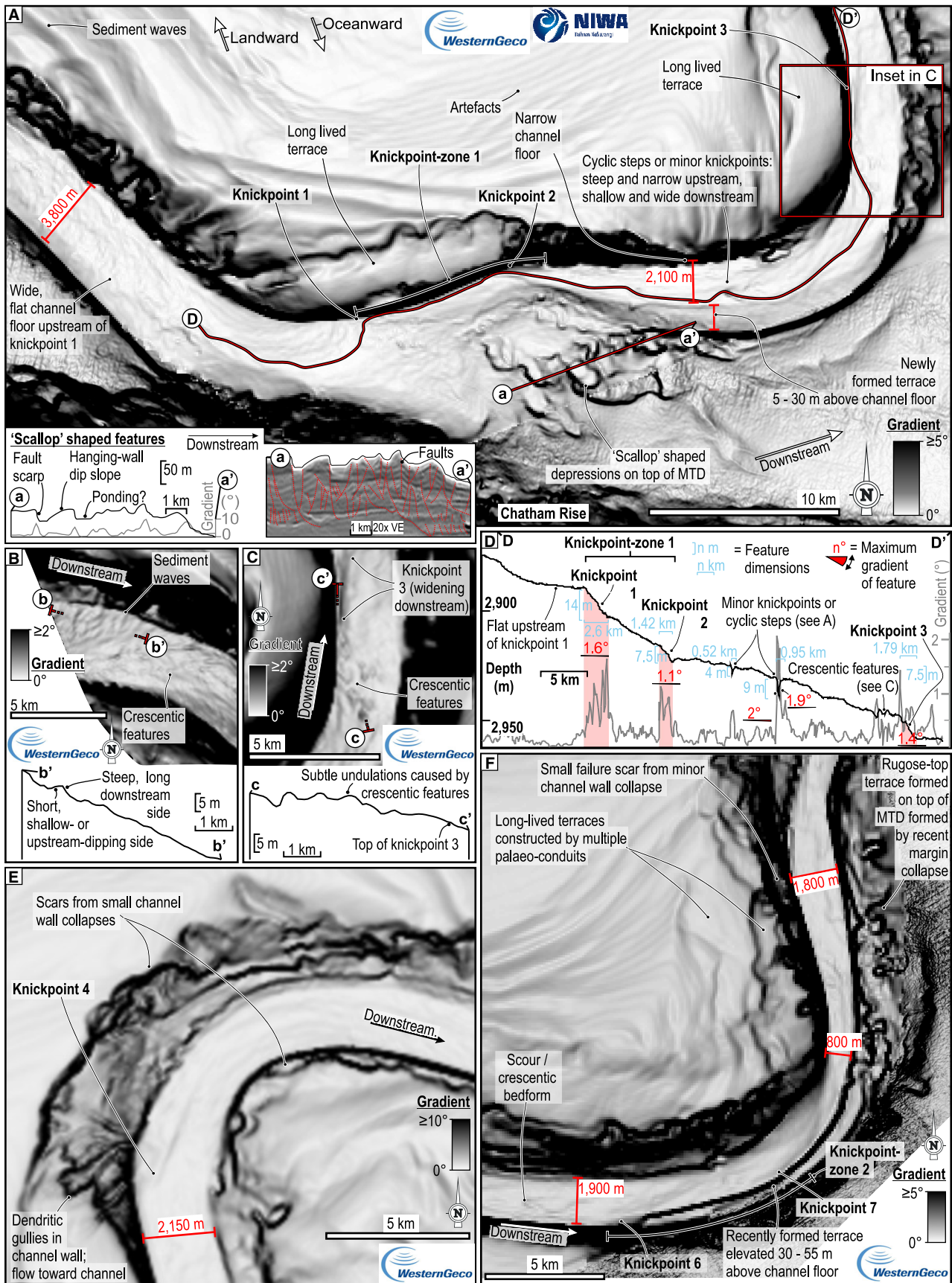


Fig. 5. Seafloor gradient maps and profiles from various features in the channel-floor, walls and banks. (A) Map showing the downstream-narrowing channel-floor containing knickpoints 1 to 3 and knickpoint-zone 1, bound by steep channel-walls with terraces of varied widths, adjacent to an area of overbank (to the south) containing scallop-shaped depressions; a seafloor and interpreted seismic profile are provided as insets to aid interpretation of the scallop-shaped features (uninterpreted dip map in supplementary). (B) Map and longitudinal profile showing thalweg-perpendicular ridges interpreted as sediment waves and a train of crescentic features on the channel-floor. (C) Map and longitudinal profile through a train of crescentic features upstream of knickpoint 3. (D) Longitudinal profile through section in (A), showing: a low gradient upstream of knickpoint-zone 1; the sizes and gradients of knickpoint-zone 1; knickpoints 1 to 3; and crescentic features. (E) Map of bend 4 showing knickpoint 4 present on the outer bend, a number of small terraces on the inner bank and one larger terrace with dendritic gullies on the outer bank. (F) Map of bend 5 showing: the channel-floor narrowing as it passes knickpoint 6 and 7, where it is bound by a newly formed terrace, and widening further downstream; numerous large terraces situated near the top of the inner bend channel-wall.

upward convergence of two terraces to form a larger one, and gradational vertical transition into overlying levée deposits suggests that terraces closer to the thalweg aggrade faster and may heal terrace-top topography; this concept is supported by an observed upward increase in terrace width

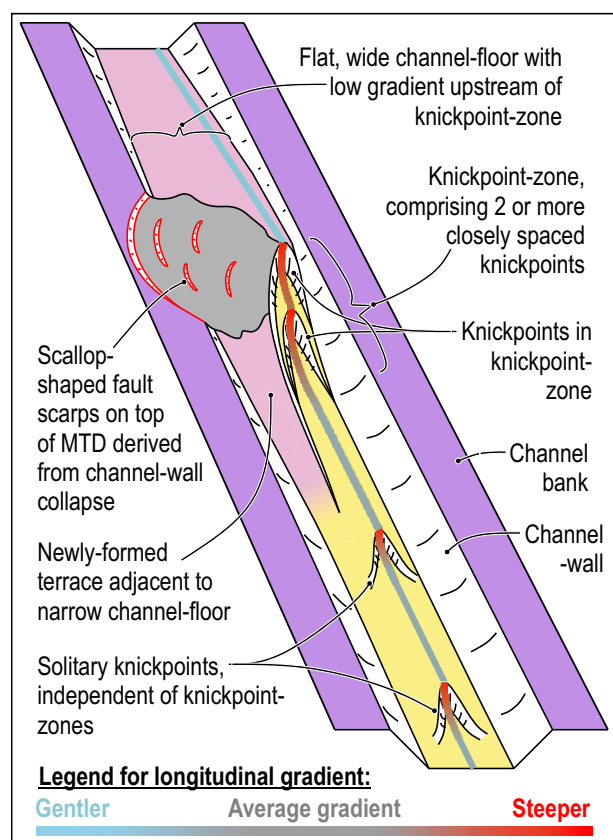


Fig. 6. Schematic 3D diagram showing the relationships between the various described seafloor features. The diagram is modelled on the area in Fig. 5A but the channel is displayed as straight, rather than sinuous as in reality, and the positions of solitary knickpoints are further upstream than in reality.

and decrease in terrace frequency on the modern channel-walls (Fig. 4B).

Depositional Element 3 – Levées

Description. Levée deposits comprise laterally continuous packages of reflectors which may be devoid of (SF6; Fig. 7F, G and I) or contain (SF7; Fig. 7H) sediment waves. Towards the channel, reflectors terminate against channel-form surfaces, sheet or terrace-bounding surfaces or MTD-bases (Fig. 7F, G and I). Away from the channel, on the landward side, they interfinger with wedging reflector packages that thicken towards the subduction margin (McArthur *et al.*, 2019). On the oceanward side, reflectors terminate against the Chatham Rise or Hikurangi Plateau (Fig. 1).

Interpretations. Where reflectors decrease in amplitude and thickness away from the channel, they are interpreted as unconfined external levées (Pirmez & Flood, 1995; Deptuck *et al.*, 2003; Posamentier & Kolla, 2003; Nakajima & Kneller, 2013). Where reflectors terminate against the Chatham Rise or Hikurangi Plateau, they are interpreted as confined external levées (Clark & Cartwright, 2011). Reflector tapering, however, does not necessarily correspond to depositional relief (Fig. 3), as transversely sourced trench filling sediment may enhance aggradation near the subduction front, therefore leading to relatively even aggradation across the trench-floor, and the suppression of wedge shaped levée development.

Depositional Element 4 – Mass-transport deposits from channel-wall collapse

Description. MTDs comprise a variety of reflector styles: chaotic/transparent intervals (SF8), folded and faulted reflectors (SF9) and steep-sided blocks of coherent reflectors (SF10)

Table 1. Descriptions and interpretations of the ten seismofacies observed within the studied stratigraphy.

Facies	Seismic properties	Description, distribution and variability	Interpretation
Lens-like HARs/HARPs (SF1): <ul style="list-style-type: none"> • Fig. 7A • Sand-rich channel-floor deposits 	<p>One to five variably stacked reflectors. High to very high amplitude (positive or negative). Reflectors <20 m, in packages <80 m thick. 100 m–1 km wide. Laterally variable package thickness. Reflectors lens-like in cross-section and decrease in thickness and amplitude towards the margins; elongate downstream.</p>	<p>Each HAR (High Amplitude Reflector) or HARP (High Amplitude Reflector Package) sits within a HARP-bounding surface or a channelform surface, but may also be cut by another HARP-bounding surface or channelform surface. HARs or HARPs may be juxtaposed against chaotic/transparent zones (SF8) stratigraphically higher or lower. These reflectors form a continuum with flat, wide, HARs/HARPs (SF3). Distinct HARs/HARPs may converge upstream or downstream to form a through-going package of SF1 or SF3 (Fig. 7A).</p>	<p>Coarse-grained sediments, likely sand-rich with high porosity (and therefore fluid content) that elicits a strong amplitude response (Flood & Piper, 1997; Mayall & Stewart, 2000; Deptuck et al., 2003, 2007; Posamentier & Kolla, 2003; Posamentier, 2003). Reflector geometries are interpreted as deposits infilling incised surfaces at a smaller scale than their host channelform surface (Mayall et al., 2006; Deptuck et al., 2007). Incision and infill may be due to: (a) time-transgressive seafloor degradation (Hodgson et al., 2011, 2016) creating HARP-bounding surface-scale palaeo-conduits, that were subsequently filled (Janocko et al., 2013; Hansen et al., 2017a) in response to a drop in input flow energy or a downstream blockage; (b) knickpoints that incised and infilled locally (longitudinally) as they migrated upstream (Heijnen et al., 2020).</p>
Inclined reflector packages (SF2): <ul style="list-style-type: none"> • Fig. 7B, D • Unilaterally stacked margins of sand-rich channel-floor deposits 	<p>One to ten, inclined reflectors, stacked laterally and vertically. Low to high amplitude. Reflectors <15 m, in packages <50 m thick. Reflectors and packages <1.5 km wide. In cross-section reflectors increase in thickness and amplitude in direction of inclination; elongate downstream.</p>	<p>Reflectors consistently dip (at 2–7°) towards one margin of the confining channelform surface (Fig. 7B). At their base, these reflectors coalesce to form a through-going, flat based, generally laterally continuous HAR (SF3). In some sections, the stacking of inclined reflectors is less consistent and two are observed, dipping in opposing directions forming a lens-like HAR (SF1). In plan-view (Fig. 7D) they form linear features that generally follow the path of the channelform but become progressively more arcuate and eventually mirror the form of the youngest stacked reflector. The youngest reflector is usually most sinuous and has a lens shape in cross-section.</p>	<p>These deposits either represent: (a) point bars formed by lateral accretion (Abreu et al., 2003; Armott., 2007; Alpak et al., 2013); (b) the unidirectional, lateral migration of palaeo-conduits at HARP-bounding surface scale that formed and were infilled sequentially, preferentially destroying one margin of its precursor and preserving the other (Peakall et al., 2000; Kolla et al., 2001; McHargue et al., 2011); (c) the product of sequentially migrating knickpoints (see SF1) that preferentially hugged one side of a wider palaeo-conduit, thus preferentially preserving one margin (Heijnen et al., 2020). Definitive distinction is impossible, but due to their scale, presence on outer bends and occasional inconsistencies in stacking direction, (a) is unfavourable. Through-going basal HARs likely contain similar coarse-grained sediments as in SF1.</p>

Table 1. (continued)

Facies	Seismic properties	Description, distribution and variability	Interpretation
<p>Flat, wide, HARPs/ HARPs (SF3):</p> <ul style="list-style-type: none"> • Fig. 7A, C • Laterally stacked sand-rich channel-floor deposits below seismic resolution 	<p>One to four vertically stacked reflectors. High to very high amplitude. Reflectors <20 m, in packages <40 m thick. Typically 1–3 km wide. Laterally continuous package thickness. Reflectors tabular (thickness maintained across ca 80% of width) in cross-section, elongate downstream.</p>	<p>Reflectors terminate abruptly at both margins against their confining surface; SF3 is virtually always confined by a channelform surface, and/or cut by a subsequent channelform surface (Fig. 7C). SF3 deposits form a continuum with SF1. A narrow HAR or HARP may widen, or multiples may converge to form an apparently through-going reflector (Fig. 7A). A narrow (<500 m wide), elongate, lens-shape (in cross-section) pathway is commonly preserved beneath the otherwise flat base of SF3 deposits.</p>	<p>Same coarse-grained sediments as in SF1. Relationships with SF1, SF2 and SF8 suggest that these may represent amalgamated ‘sandbodies’ (Millington & Clark, 1995; Pickering <i>et al.</i>, 1995) with internal variability below seismic resolution (Schwab <i>et al.</i>, 2007). Unresolvable HARP-bounding surfaces, each hosting lithologically similar deposits, stacked laterally in an ‘organized’ or ‘disorganized’ manner (<i>sensu</i> McHargue <i>et al.</i>, 2011) and underwent little vertical aggradation. Stacking and migration may have occurred in response to sequential palaeo-conduit formation and infill or the passage of upstream-migrating knickpoints (see SF1 and SF2).</p>
<p>Non-truncated tabular reflector packages (SF4):</p> <ul style="list-style-type: none"> • Fig. 7E, F • Sheet deposits 	<p>One to seven vertically stacked reflectors. Typically low to medium (rarely high) amplitude. Reflectors <10–20 m, in packages <50 m thick. 1–4 km wide. Packages taper towards edge of their bounding surface (constituent reflectors widen upward). Reflectors tabular (thickness maintained across ca 80% of width) in cross-section, elongate downstream.</p>	<p>Continuous (SF4) and truncated (SF5) tabular reflector packages are distinguished based on their relationships with their lateral bounding surfaces. Reflectors of SF4 terminate abruptly, at both margins, against sheet or terrace-bounding surfaces or an MTD-top that dips in opposing directions. SF4 deposits commonly gradationally overlie SF1 deposits (Fig. 7E, F).</p>	<p>Sheet deposits (Pickering <i>et al.</i>, 1995; Tóké & Patacci, 2018; Liang <i>et al.</i>, 2020) from flows that deposited across the entirety of their host palaeo-conduit. Sheet deposits may be a product of: (a) passive palaeo-conduit fill, probably representing a systematic decrease in input flow energy accompanying abandonment (Haughton, 2000; Deptuck <i>et al.</i>, 2003); or (b) confined flows that were dominantly depositional (McCaifrey <i>et al.</i>, 2002) because of a shallow longitudinal gradient, or a release of lateral confinement, potentially in response to partial ponding upstream of an MTD (Kneller <i>et al.</i>, 2016; Liang <i>et al.</i>, 2020), or downstream of a knickpoint (Heijnen <i>et al.</i>, 2020). Sediments within these reflector packages may be sand-rich (Posamentier & Kolla, 2003), mud-rich (Mayall <i>et al.</i>, 2006) or heterolithic (Janocko <i>et al.</i>, 2013). The apparent gradation from underlying SF1 deposits suggests an overall upward fining (McHargue <i>et al.</i>, 2011).</p>

Table 1. (continued)

Facies	Seismic properties	Description, distribution and variability	Interpretation
Truncated, tabular reflector packages (SF5): <ul style="list-style-type: none"> • Fig. 7F, G • Incised sheets or terrace deposits 	One to tens of vertically stacked reflectors. Typically low (rarely very low) to medium (rarely high) amplitude. Reflectors <10 m–20 m thick, in packages <300 m thick. 1–5 km wide (widening-up). Packages (and reflectors therein) subtly widen upward. Reflectors tabular or taper slightly away from channel-fills in cross-section, elongate downstream.	SF5 comprises the same reflector styles as SF4 but terminate, on their outboard side, against a sheet or terrace-bounding surface or an MTD-top. However, on their inboard side, reflectors in SF5 terminate against a subsequently formed channelform surface, an MTD-base or a sheet or terrace-bounding surface, which can lead to their juxtaposition against younger SF1, SF3 or SF4 deposits. SF5 deposits commonly gradationally overlie SF1 or SF4 deposits, and underlie (also gradationally) SF2 deposits (Fig. 7F, G).	These deposits may represent: (a) sheet deposits (SF4) that have been incised; (b) terrace deposits, formed during the formation and fill of a subsequent channelform, by overspill onto a high confined by a sheet or terrace-bounding surface (Deptuck <i>et al.</i> , 2003, 2007; Babonneau <i>et al.</i> , 2004; Hansen <i>et al.</i> , 2015, 2017a,b). A descriptive distinction between SF4 and SF5 is provided, based on the relationship with subsequently formed surfaces: continuous reflectors that terminate, at both margins, against sheet or terrace-bounding surfaces or MTD-tops that dip in opposing directions are classified as SF4; reflectors that terminate on one side against a sheet or terrace-bounding surface or MTD-top, but are truncated on the other side by a surface that dips in the same direction are classed as SF5.
Continuous reflectors without undulation (SF6): <ul style="list-style-type: none"> • Fig. 7F, G, I • Levées without sediment waves 	Vertically stacked reflectors. Very low to medium amplitude. Reflectors <10–25 m, in packages hundreds of metres thick. Packages traceable for <50 km away from the channel. Laterally continuous package thickness or slight tapering away from channel. Reflectors tabular in all directions or tapering away from channel.	On the landward channel margin they thin away from the channel. On the oceanward margin the reflectors typically maintain their thickness. Packages of SF6 are continuous for <45 km on the landward margin, and on the oceanward margin they widen upward from <i>ca</i> 20–50 km.	Interpreted as external levée deposits (Pirmez & Flood, 1995; Deptuck <i>et al.</i> , 2003; Posamentier & Kolla, 2003; Kane & Hodgson, 2011; Nakajima & Kneller, 2013).

Table 1. (continued)

Facies	Seismic properties	Description, distribution and variability	Interpretation
<p>Continuous reflectors with undulation (SF7):</p> <ul style="list-style-type: none"> • Fig. 7H • Levées with sediment waves 	<p>Vertically stacked reflectors. Very low to medium amplitude. Reflectors <10–25 m, in packages hundreds of metres thick. Packages traceable for <40 km away from the channel. Slight tapering away from channel. Sigmoidal reflector geometries.</p>	<p>Reflectors systematically pinch and swell to form sigmoidal, wave like geometries (Fig. 7H) with sediment wave wavelengths varying from ca 300 m to 4 km and amplitudes from <10 m to ca 75 m. These deposits are mainly observed on the landward channel margin where the thick limbs of the sigmoidal waves dip towards the channel. In plan-view, the waves are concentric around outer meander bends.</p>	<p>External levée deposits with sediment waves (Normark <i>et al.</i>, 1980, 2002; Flood, 1988; Nakajima & Satoh, 2001; Wynn & Stow, 2002; Posamentier & Kolla, 2003; Posamentier, 2003; Migeon <i>et al.</i>, 2004). Based on their dimensions they are interpreted to be formed by fine-grained turbidity currents overspilling from a channel or palaeo-conduit (Normark <i>et al.</i>, 1980; Wynn & Stow, 2002). Fine-grained sediment waves aggrade and migrate towards the channel by accretion on their upstream side (Flood, 1988; Nakajima & Satoh, 2001).</p>
<p>Chaotic/translucent zones (SF8):</p> <ul style="list-style-type: none"> • Fig. 7A, E, J, K • Slump and/or debris-flow deposits, or megaclasts 	<p>Low amplitude zones with no coherent internal reflectivity. Three modes of occurrence: (1) Within depositional element 1 deposits:</p> <ul style="list-style-type: none"> • Zones less than 10 m (below data resolution) to ca 50 m thick. • Zones up to 2 km across. • Usually no preferred elongation.(2) Distinct from and overlying depositional element 1 deposits: • Typically between 30 m and 100 m thick. • 1–4 km wide. • Elongate and mounded downstream.(3) Distinct from depositional element 1 deposits, lateral to and between zones of SF9 and SF10: • Typically between 50 m to 150 m thick. 	<p>(1) SF8 may exist adjacent to any SF1, SF2 or SF3 deposit (Fig. 7A, E). These may sit within, or be cut by, HARP-bounding surfaces or channelform surfaces. In plan-view these zones sometimes form relatively undefined patches, but they commonly form defined polygons that usually have no preferred orientation and are typically <100 m across, but can reach 1 km. (2) SF8 overlying SF1 deposits that are underlain by a pre-existing channelform surface. They thicken to the deepest part of the channelform surface and pinch out to the edges (Fig. 7C). (3) SF8 may form part of much larger, areally-extensive MTDs and therefore exhibit a complex planform distribution (Fig. 7); see depositional element 4). A continuum exists between the three modes of occurrence.</p>	<p>Chaotic zones that form discrete polygons [mode of occurrence (1)] are interpreted as megaclasts (Posamentier & Martinsen, 2011; Ortiz-Karpf <i>et al.</i>, 2017; Casson <i>et al.</i>, 2020; Naranjo-Vesga <i>et al.</i>, 2020). Those without a defined polygonal planform are interpreted as debris-flow or slump deposits (see Moscardelli & Wood, 2008; Bull <i>et al.</i>, 2009; Ogata <i>et al.</i>, 2012, for definition). Either may have been proximally sourced from the shelf or feeder canyon (Nelson <i>et al.</i>, 2011; Bernhardt <i>et al.</i>, 2012; Masalimova <i>et al.</i>, 2015; Ortiz Karpf <i>et al.</i>, 2017) or locally sourced from the palaeo-conduit walls and adjacent overbank (Clark & Pickering, 1996; Deptuck <i>et al.</i>, 2007; Hansen <i>et al.</i>, 2017; Kremer <i>et al.</i>, 2018); the latter is favoured for both due to the abundance of failure scars observed in the channel-walls.</p>

Table 1. (continued)

Facies	Seismic properties	Description, distribution and variability	Interpretation
Folded and faulted reflectors (SF9):	Vertically stacked reflectors. Very low to medium amplitude. Reflectors <10–20 m, packages <200 m thick.	SF9 comprises: (a) folded reflectors, with fold wavelengths from 100 m to 1 km, amplitudes tens of metres to 100 m; (b) straight reflectors of varying dips that terminate against sub-vertical normal and reverse faults (Fig. 7I). The strike of kinematic indicators (folds and faults) is typically sub-parallel to the trend of adjacent channelforms.	Interpreted as the product of slumping and sliding (Mosccardelli & Wood, 2008; Bull <i>et al.</i> , 2009; Ogata <i>et al.</i> , 2012) during the collapse of terrace (SF5) or levée deposits (SF6 and SF7).
• Fig. 7I	Highly variable lateral extent and complex planform distribution.		
• Slump and/or slide deposits	Packages may or may not be elongate downstream. Reflectors highly variable in their continuity and dip.		
Steep-sided blocks of coherent reflectors (SF10):	Vertically stacked reflectors. Very low to medium amplitude. Reflectors <10–20 m, packages <200 m thick.	Steep-sided blocks of reflectors resembling those of SF4, SF5 and SF6. Dip and strike of reflectors is concordant with underlying stratigraphy. Blocks are sometimes underlain and/or overlain by chaotic zones (SF8), but not always (Fig. 7I). Blocks are typically elongate in the orientation of adjacent channelforms (Fig. 7J). Steep block sides usually separate SF10 from SF8 and SF9 deposit.	Interpreted as megaclasts (Jackson, 2011; Posamentier & Martinsen, 2011; Ortiz-Karpf <i>et al.</i> , 2017; Hodgson <i>et al.</i> , 2018; Nugraha <i>et al.</i> , 2020) formed during channel-wall collapse composed of intact terrace or levée stratigraphy, some of which moved on a sub-seismic scale decollement horizon. These megaclasts differ from those of chaotic/transparent zones as they possess internal reflectivity.
• Fig. 7I, J	Reflectors tabular but terminate abruptly against steep sides.		
• Megaclasts	Polygonal in plan-view, up to 6 km wide.		

Table 2. Descriptions and interpretations of the five seismic surfaces observed within the studied stratigraphy.

Seismic surface	Description	Bounded by/bounding:	Interpretation
HARP-bounding surface: Fig. 7A, B, D, E	<ul style="list-style-type: none"> • Concave-up in cross-section except when truncated by a younger surface. • Surfaces truncate <60 m of stratigraphy, and are always <2 km wide, typically <500 m. • Elongate downstream, traceable for hundreds of metres to tens of kilometres until they are truncated, or disappear because they are unresolvable in the data or they become part of another surface. • HARP-bounding surfaces form the lens like geometry of lens like HARs/HARPs (SF1) and separate reflectors in inclined reflector packages (SF2). Parts of a HARP-bounding surfaces form sections of channelform surfaces that bound channel-fill deposits. 	<p>Inboard – Channel-fill deposits of any type (SF1, SF2, SF3, SF8).</p> <p>Outboard – Reflectors of older channel-fill deposits are truncated. HARP-bounding surfaces within a given channelform surface incise to similar maximum depths (<50 m of each other).</p> <p>Top – Can be overlain by flat reflectors of sheet or terrace deposits.</p> <p>Truncation – Can be truncated by a younger HARP-bounding surface, channelform surface or MTD-base.</p> <p>Nomenclature – Where a HARP-bounding surface also forms part of (or all of) a channelform surface, it is classified as a channelform surface (Fig. 7A, B, E).</p>	<p>The smallest resolvable elongate, concave-up surface ('channel-forms' of Deptuck <i>et al.</i>, 2003, 2007). They are formed by incision and infill caused by local blockages and/or diversions, or variations in the nature of the formative flows. Avulsions and confluences form the cross-cutting relationships between surfaces and deposits of different ages and the longitudinally discontinuous nature of these surfaces (Fig. 7A). They may represent buried palaeo-conduits (Janocko <i>et al.</i>, 2013), or the passage of upstream-migrating channel-floor features such as knickpoints (Guiastrennec-Faugas <i>et al.</i>, 2020; Heijnen <i>et al.</i>, 2020).</p>
Channelform surface: Fig. 7A, B, C, D, E	<ul style="list-style-type: none"> • Concave-up except when truncated by a younger surface. Surface typically shallows in both directions from a thalweg, before abruptly steepening at both sides. • Surfaces truncate <80 m of stratigraphy, and are typically <3 km wide. • Elongate downstream, most continuous surfaces in the dataset, traceable for tens of kilometres to >100 km. • Two or more HARP-bounding surfaces commonly coalesce to form a through-going channelform surface. 	<p>Inboard – Channel-fill deposits (SF1).</p> <p>Outboard – reflectors of channel-fill, sheet or terrace, MTDs, or, less commonly, levée deposits can be truncated.</p> <p>Top – Transitions into a sheet or terrace-bounding surface.</p> <p>Truncation – Can be truncated by a subsequent channelform surface, sheet or terrace-bounding surface, or MTD-base.</p> <p>Nomenclature – Where a channelform surface is also an MTD-top, the surface is classed as a channelform surface (Fig. 7E, G, D).</p>	<p>Records the compound result of the diachronous modification of the base and sides of a longer lived palaeo-conduit through the formation and infill of one or more HARP-bounding surface (Sylvester <i>et al.</i>, 2011; Hodgson <i>et al.</i>, 2016).</p> <p>Channelform surface bases are interpreted to incise into underlying MTDs or sheet or terrace deposits. However, in some cases aggradation of the palaeo-channel-floor may juxtapose channel-fill deposits against terrace deposits that formed earlier in the history of the same palaeo-conduit (Hodgson <i>et al.</i>, 2011; Brunt <i>et al.</i>, 2013).</p>
Sheet or terrace-bounding surface: Fig. 7C, F, G	<ul style="list-style-type: none"> • Straight or slightly curved dipping surface. A sheet or terrace-bounding surface can only be unequivocally identified where it is inclined, as the base and top of the surface either transitions into: another surface, a channelform surface or MTD-top, or into through-going, sub-horizontal reflectors with concordant dips. 	<p>Inboard – Reflectors of sheet or terrace deposits terminate against a sheet or terrace-bounding surface.</p> <p>Outboard – Reflectors of channel-fill, sheet or terrace or levée deposits can terminate against a sheet or terrace-bounding surface.</p> <p>Base – A sheet or terrace-bounding surface can: (a) terminate against or transition into an MTD-top; (b) transition into a</p>	<p>Formed by: (a) erosion of pre-existing sheet or mass-transport deposits by a channelform, followed by aggradation, and resultant juxtaposition, of sheet and/or terrace deposits from a subsequent channel against an originally erosional surface (Hodgson <i>et al.</i>, 2011); (b) the construction of a depositional terrace that created a bathymetric surface which was then filled by</p>

Table 2. (continued)

Seismic surface	Description	Bounded by/bounding:	Interpretation
	<ul style="list-style-type: none"> • Surfaces are <200 m thick, typically 100 m to 2 km wide (one inclined surface, not concave-up). • Elongate downstream, traceable hundreds of metres to tens of kilometres (traceable until incised by a subsequent channelform or MTD). • As a sheet or terrace-bounding surface is defined based on the presence of sheet or terrace deposits on its inboard side, vertical transitions from channel-fill to sheet or terrace deposits are accompanied by a transitional boundary between a channelform surface and overlying sheet or terrace-bounding surface. 	<p>channelform surface; or (c) transition into throughgoing sheet or terrace deposits.</p> <p>Top – Sheet or terrace-bounding surfaces gradually flatten as the inboard sheet or terrace deposits grade into overlying sheet or terrace or levée deposits.</p> <p>Truncation – Can be truncated by a younger channelform surface, sheet or terrace-bounding surface, or MTD-base.</p> <p>Nomenclature – Reflectors of sheet or terrace deposits may also terminate against an MTD-top. Where a sheet or terrace-bounding surface is also an MTD-top (see below), the surface is classed as an MTD-top (Fig. 7G).</p>	<p>sheet deposits of that channel, and/or by terrace deposits from a subsequent channel (Hansen <i>et al.</i>, 2015); (c) aggradation of terrace or levée deposits on both sides of a pre-existing sheet or terrace-bounding surface. As the deposits outboard and inboard of the surface aggrade independently, eventually the inboard deposits will be juxtaposed against a surface generated solely by deposition.</p>
MTD-base: Fig. 7C, F, G, I, J, K	<ul style="list-style-type: none"> • If the overlying MTD fills a concave-up surface (Fig. 7C, J), the MTD-base usually overlies channel-fill or sheet (SF4) deposits at the base and truncates reflectors of sheet or terrace (SF4) and/or levée deposits at the sides. MTD-bases below large, areally extensive MTDs are usually: much wider (higher aspect ratio) than those overlying channel-fills or confined to the overbank; have flat bases and steep, stepped sides; are asymmetrical about the surface they fill; are overlain by thick deposits of folded or faulted reflectors (SF8), or megaclasts (SF10; Fig. 7I). If the overlying MTD is confined to the overbank (Fig. 7F, K), the MTD-base exists as an isolated, inclined surface. 	<p>Inboard (above) – Always an MTD; any of the 'zones' recognized may be present.</p> <p>Outboard (below) – Reflectors of any seismic facies or any other seismic surface can be truncated or terminate.</p> <p>Top – An MTD-base merges with the MTD-top surface as the MTD between them pinches out or is eroded.</p> <p>Truncation – An MTD-base can be truncated by a channelform surface, sheet or terrace-bounding surface or another MTD-base.</p> <p>Nomenclature – Where an MTD-base apparently forms the continuation of a channelform surface, the surface is classed as an MTD-base (Fig. 7C).</p>	<p>The stepped nature of an MTD-base is produced by deformation localization along sub-vertical faults or 'scars' at the sides and sub-horizontal decollements at the base of the failing stratigraphy (Nugraha <i>et al.</i>, 2019, 2020; Nwoko <i>et al.</i>, 2020a,b). Where an MTD-base overlies channel-fill deposits and follows the shape of the channelform surface underlying the channel-fill deposits, the overlying MTD is interpreted to be filling a pre-existing surface. Where evidence of erosion at the base of an MTD is absent, the MTD-base may record the instantaneous morphology (predominantly the width) of a palaeo-conduit it filled.</p>

Table 2. (continued)

Seismic surface	Description	Bounded by/bounding:	Interpretation
	<ul style="list-style-type: none"> • Surfaces are variable in scale: <300 m thick, <7 km wide. • Elongate downstream, traceable for two to tens of kilometres (albeit with variable depths). • MTD-bases are commonly 'stepped' in cross-section, with abrupt changes in dip (up to 90°) occurring over <100 m laterally. • Where reflectors below and above the MTD-bases are concordant (e.g. below a megaclast) the 3D context is used to differentiate. 		
MTD-top: Fig. 7C, F, G, H, I	<ul style="list-style-type: none"> • If the underlying MTD fills a channelform surface (Fig. 7C, I), the MTD-top is usually concave-up in cross-section; if it is confined to the overbank (Fig. 7F, K), it occurs as an isolated, inclined surface. MTD-tops can be irregular, and packages of concordant (usually flat) reflectors of sheet or terrace, or levée deposits thicken into lows on both sides. • Surfaces are variable in scale: <200 m thick, <7 km wide. • MTD-top surfaces are topographically complex, but are generally elongate and mounded in longitudinal section. Traceable downstream for two to tens of kilometres (variable depths). • Because the MTD between a MTD-top and MTD-base usually thickens towards the lowest part of a MTD-base, MTD-tops show a similar but subdued concave-up profile relative to their associated MTD-base. MTD-tops generally show less abrupt changes in dip than their associated MTD-base. Where reflectors below and above the MTD-top are concordant (e.g. above a megaclast) the 3D context is used to differentiate. 	<p>Inboard (above) – Reflectors of any seismic facies.</p> <p>Outboard (below) – Always an MTD; any of the 'zones' recognized may be present.</p> <p>Top – An MTD-top can: (a) terminate abruptly against overlying, throughgoing reflectors of sheet or terrace or levée deposits; or (b) transition abruptly into a sheet or terrace-bounding surface.</p> <p>Truncation – An MTD-top can be truncated by a younger channelform surface, sheet or terrace-bounding surface, or MTD-base.</p> <p>MTD-tops on top of large, areally extensive MTDs are more commonly truncated by a channelform surface (Fig. 7I).</p>	<p>MTDs heal the topography at their base making depth and dip changes on MTD-tops smaller and less abrupt. Small-scale local rugosity, larger, deposit scale topography (concave-up cross-section and mounded longitudinal profile), and/or post-depositional loading may cause: (a) ponding on an MTD-top; and/or (b) the focusing of subsequent flows leading to erosion and the truncation of an MTD-top (Armitage <i>et al.</i>, 2009; Alves, 2010; Dykstra <i>et al.</i>, 2011; Kneller <i>et al.</i>, 2016; Brooks <i>et al.</i>, 2018; Ward <i>et al.</i>, 2018; Bull <i>et al.</i>, 2020; Tek <i>et al.</i>, 2020). The presence of analogous channel-blocking MTDs on the seafloor, and their sharp tops and lack of associated rotated, fanning reflectors on their tops in the subsurface, suggests that the underlying MTDs were formed quasi-instantaneously; non-eroded MTD-tops are therefore reliable chronostratigraphic markers.</p>

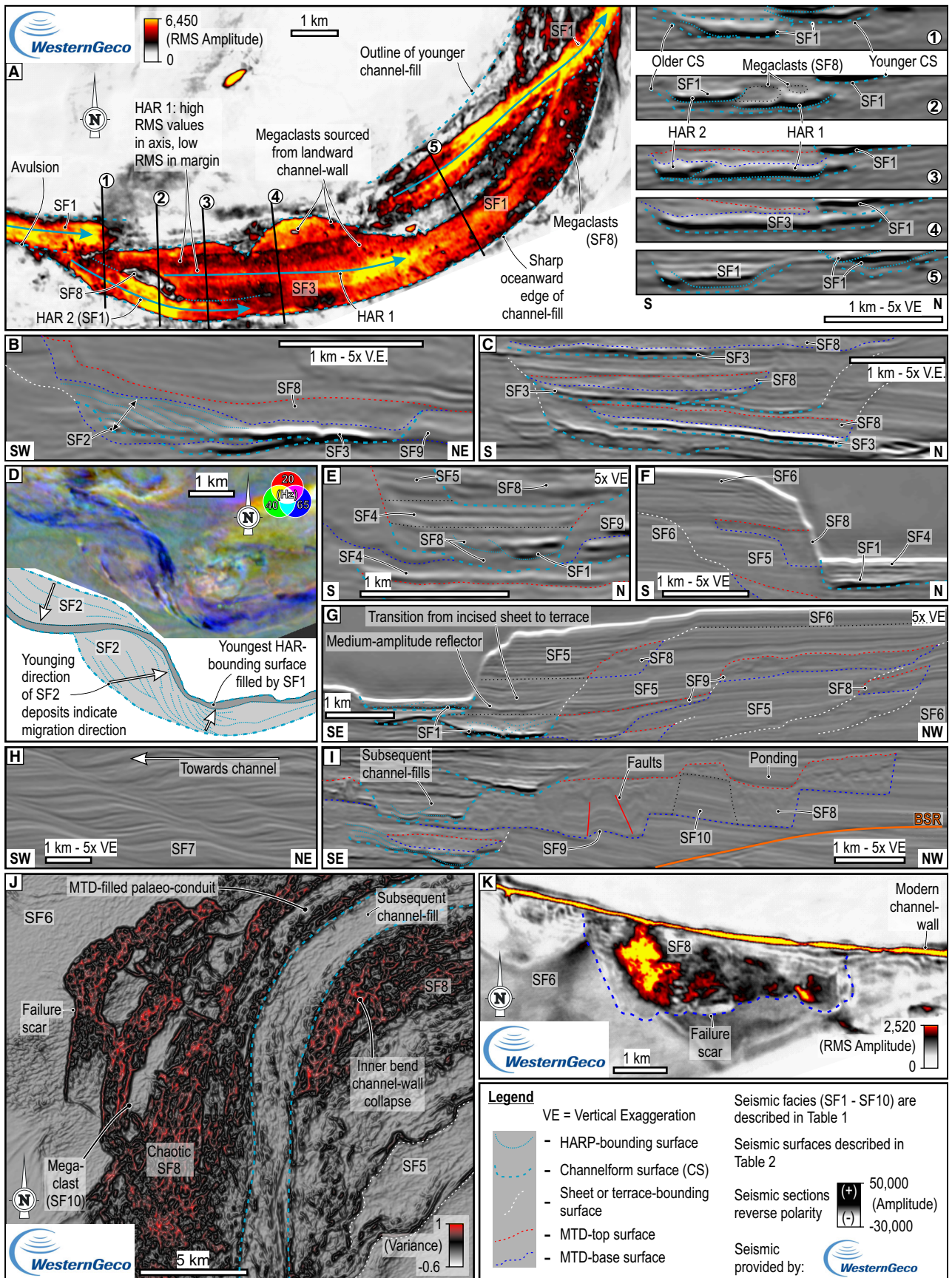


Fig. 7. Seismic sections and z-slices displaying the ten seismofacies and five seismic surfaces observed in the area, containing: (A) RMS amplitude z-slice, from 3000 m depth, and seismic sections showing dominantly SF1, SF2, SF8, HAR-bounding surfaces and channelform surfaces; (B) section showing SF2, SF3, SF8, HAR-bounding surfaces, channelform surfaces, MTD-bases and MTD-tops; (C) section showing SF2, SF8, channelform surfaces, sheet or terrace-bounding surfaces, MTD-bases and MTD-tops; (D) spectral decomposition and interpreted line drawing showing SF3, SF1, HAR-bounding surfaces, channelform surfaces; (E) section showing SF1, SF4, SF5, SF8, HAR-bounding surfaces, channelform surfaces, MTD-bases and MTD-tops; (F) section showing SF1, SF5, SF4, SF5, SF6, SF8, channelform surfaces, sheet or terrace-bounding surfaces, MTD-bases and MTD-tops; (G) section showing SF1, SF5, SF6, SF8, SF9, HAR-bounding surfaces, channelform surfaces, sheet or terrace-bounding surfaces, MTD-bases and MTD-tops; (H) section showing SF7; (I) section showing areally extensive SF8, SF9 and SF10 deposits, HAR-bounding surfaces, channelform surfaces, MTD-bases and MTD-tops (BSR: Bottom Simulating Reflector); (J) variance attribute z-slice showing areally extensive SF8 and SF10 deposits and their context with SF5, SF6, MTD-bases, sheet or terrace-bounding surfaces, channelform surfaces; (K) RMS amplitude z-slice showing an areally non-extensive SF8 deposit and bounding MTD-base, and SF6.

(Table 1). Chaotic/transparent intervals that sit among channel-fill deposits (Fig. 7A) are classified as channel-fill (Depositional Element 1, see above). Deformed reflectors within MTDs were originally sheet or terrace and/or levée deposits. They usually overlie and thicken towards the fill of a pre-existing channelform, and thin into adjacent sheet or terrace and/or levée deposits. Transitions between seismofacies and thickness changes can be very abrupt (Fig. 7I).

Mass-transport deposits are bound below (and/or laterally) by an MTD-base (Fig. 7B, C, F, G and I; Table 2). Above (and/or laterally), they are bound by an MTD-top (Fig. 7B, C, F, G and I), by the base of a younger MTD (Fig. 7G), or are incised by a channelform surface (Fig. 7G, I and J; Table 2). They are commonly cut by a younger channelform surface, often to or through their underlying MTD-base, but rarely more than 20 m below (Fig. 7E, G and I). MTDs may be present on both sides of an incising channelform surface (Fig. 7G), or on just one side (Fig. 7I). If the depth of incising channelform is sufficient, a sheet or terrace-bounding surface may be juxtaposed against an MTD-top (Table 2).

Mass-transport deposits have three modes of occurrence: (a) Areally extensive (Fig. 7I and J), containing a part overlying pre-existing channel-fill deposits, and a part preserved within in adjacent terrace or levée deposits; these parts may be spatially separated by a sheet or terrace-bounding surface (Fig. 7G; Table 2). These MTDs can span over 300 km² and be up to 200 m thick; they are usually thicker and more laterally extensive on one side of the channel-fill they overlie (Fig. 7J). (b) Deposits that overlie pre-existing channel-fill

but have no expression in the adjacent overbank. SF8 and heavily folded SF9 reflectors dominate (Fig. 7C). (c) Deposits that are confined to terrace or levée stratigraphy; they are less areally extensive (typically <50 km²) than those described in 'a' (Fig. 7F and K). MTDs confined to overbank (c) or above channel-fill (b) may transition up or downstream into areally extensive MTDs (a). A marked scale gap is apparent between large, areally extensive MTDs ('a' above), with maximum thicknesses >100 m and areal extent >100 km², and smaller, typically localized MTDs ('b' and 'c' above) with maximum thicknesses typically <100 m and areal extent <50 km². At least five very large MTDs, are observed in the studied stratigraphy. These deposits can be sourced from either channel-wall and there appears to be no preferred location for their source.

Interpretations. The MTDs formed by the remobilization of sheet, terrace or levée deposits (Deptuck *et al.*, 2003, 2007; Hansen *et al.*, 2017). Deposits comprise the product of *en masse* transport and deposition via a continuum of processes (Moscardelli & Wood, 2008; Bull *et al.*, 2009; Ogata *et al.*, 2012; Wu *et al.*, 2021) distinguished based on the degree of internal deformation or disaggregation. MTDs here record the product of debris flow (SF8), slumping (SF8 and SF9), and sliding and spreading (SF9); blocks of coherent reflectors are megaclasts (SF10). The diversity of processes interpreted from these deposits is greater than typically observed from channel-wall collapse (cf. Sawyer *et al.*, 2007, 2014; Hansen *et al.*, 2017). A lack of fanning reflectors within or above the deposits (Tables 1 and 2) suggests that these failures were not progressive like in some other systems (e.g. Sawyer *et al.*, 2014). They are

akin to the large MTD seen partially filling the modern Hikurangi Channel (Figs 2 and 5; Lewis & Pantin, 2002; Watson *et al.*, 2020), which was emplaced quasi-instantaneously.

Where MTDs are confined to the channelform they fill, they may have been sourced from the collapse of a confining terrace or levée where the source has been fully ‘evacuated’ (Kremer *et al.*, 2018; Nugraha *et al.*, 2020) or transported from more proximal locations (Bernhardt *et al.*, 2012; Masalimova *et al.*, 2015). Due to the presence of small, fully evacuated scars on the modern channel-wall (Fig. 7E and F), the former is favoured. MTDs confined to the overbank may have initially had a counterpart filling the adjacent channelform that has since been eroded by channel-traversing flows; remnants of these deposits may form local debrites or slumps within the channel-fills.

Stratigraphic relationships and three-dimensional correlation

The classifications of seismic facies, surfaces and depositional elements allow the lithological interpretation of the studied stratigraphy, and the lateral and vertical transitions between them can be used to establish the relative ages of the deposits (Fig. 8). The two sequence types presented below describe the cross-sectional evolution through the fill and abandonment of a primary channelform surface (hereunder ‘channelform surface A’) and the establishment of a second channelform surface (hereunder ‘channelform surface B’), the result of which formed two distinct channel-fills (‘channelform A’ and ‘channelform B’).

Sequence-type 1

Description (Fig. 9A and B). Channelform surface A, partially filled by channel-fill deposits, is overlain by an areally extensive MTD. The top, and sometimes the base, of the MTD are incised by channelform surface B, which is also filled by channel-fill deposits. Tabular reflectors overlie the MTD outboard of channelform surface B. On their inboard side they are usually truncated by channelform surface B, and/or a sheet or terrace-bounding surface that channelform surface B has transitioned into. On their outboard side, they terminate against the MTD-top and, if present, a sheet or terrace-bounding surface. Rarely, non-truncated, tabular reflectors that onlap an MTD-top at both sides are preserved below incised sheet or terrace

deposits. Sequence-type 1 can occur upstream or downstream of the thickest part of the MTD.

Interpretations (Fig. 9C, D and E). A palaeo-conduit existed on the seafloor. Conduit-traversing flows were laterally confined by steep channel-walls that consisted of terrace, levée and/or incised sheet deposits formed by erosion and overspill of flows that formed channelform A. They flowed over a wide, flat channel-floor formed by channel-fill deposits that partially filled channelform surface A. The channel-walls then collapsed (collapses of one or both channel-walls are observed in different parts of the stratigraphy), forming an MTD with an irregular top, which partially dammed the conduit. Partial ponding may have occurred in depressions formed by rugose MTD-top topography (Armitage *et al.*, 2009; Kneller *et al.*, 2016; Ward *et al.*, 2018; Tek *et al.*, 2020). Following MTD emplacement, sheet deposits formed upstream and downstream of the thickest part of the MTD due to changes in longitudinal gradient and lateral confinement, and downstream flow perturbation related to upstream ponding. Subsequently, channelform surface B was formed through the repeated formation and infill of small HARP-bounding surfaces, which progressively widened and deepened channelform surface B; the initial location of incision was determined by the MTD-top topography. Through the time-transgressive formation and infill of channelform surface B, overspilling parts of palaeo-conduit-traversing flows deposited laterally to and outside of the conduit, forming terrace deposits on top of the MTD and/or precursor incised sheet deposits. Definitive distinction between incised sheets on top of the MTD and terrace deposits formed by flows that generated channelform surface B is not usually possible.

Sequence-type 2

Description (Fig. 10A and B). The fill of channelform A is overlain by, and transitions into, tabular reflectors. These terminate, on their outboard side, against a sheet or terrace-bounding surface that channelform surface A transitions into vertically, or an MTD-top. The inboard side of these tabular reflectors, and sometimes the underlying channel-fill and parts of channelform surface A, are truncated by channelform surface B, a sheet or terrace-bounding surface that it transitions into, or a subsequently formed MTD-base. Rarely, non-truncated, tabular deposits that terminate at both sides against a sheet or

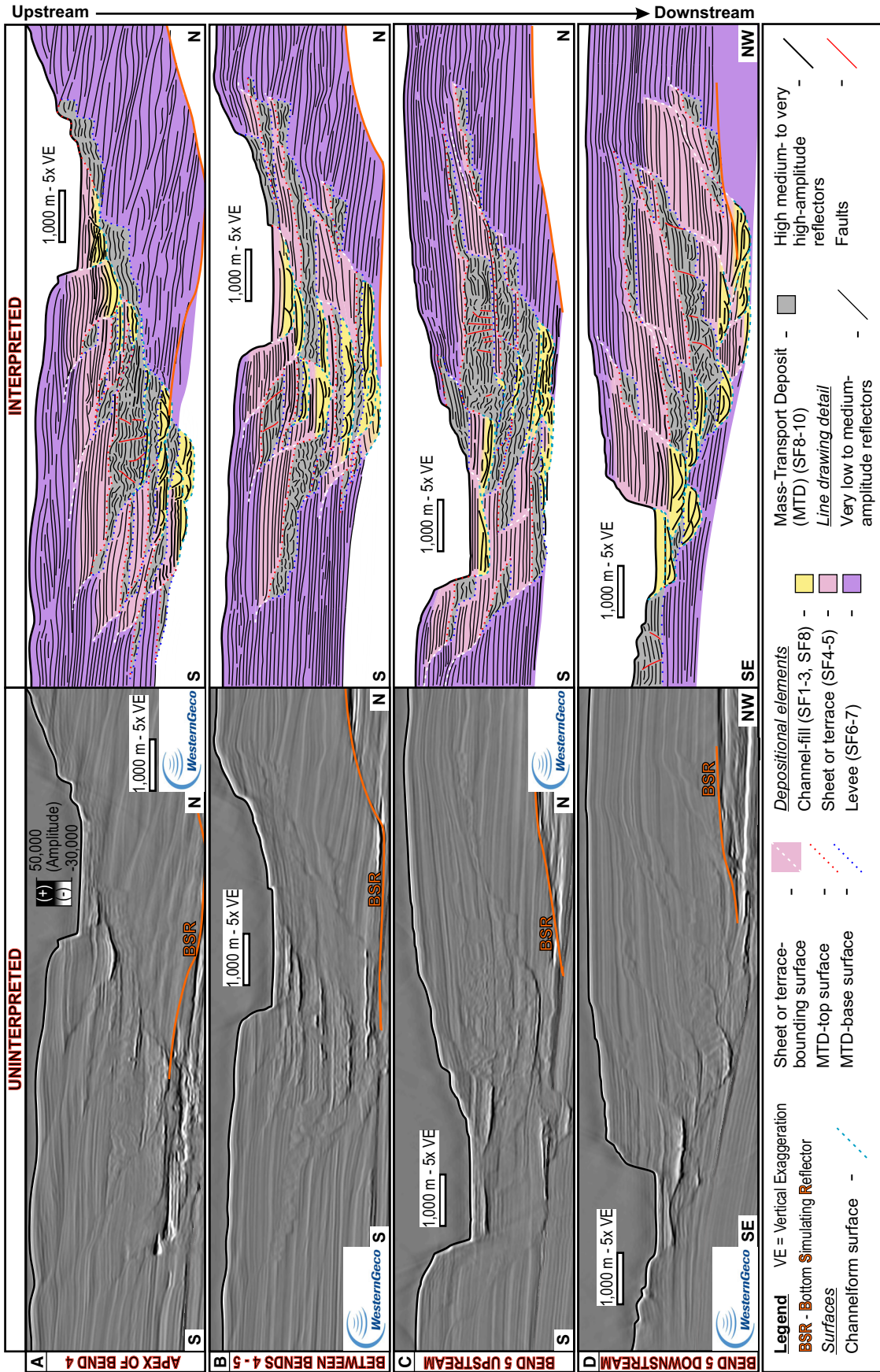


Fig. 8. Uninterpreted images (left) and interpreted line drawings (right) of seismic sections from: (A) the apex of bend 4; (B) the straight section between bends 4 and 5; (C) upstream of the apex of bend 5; (D) downstream of the apex of bend 5. Note: all sections displayed looking upstream.

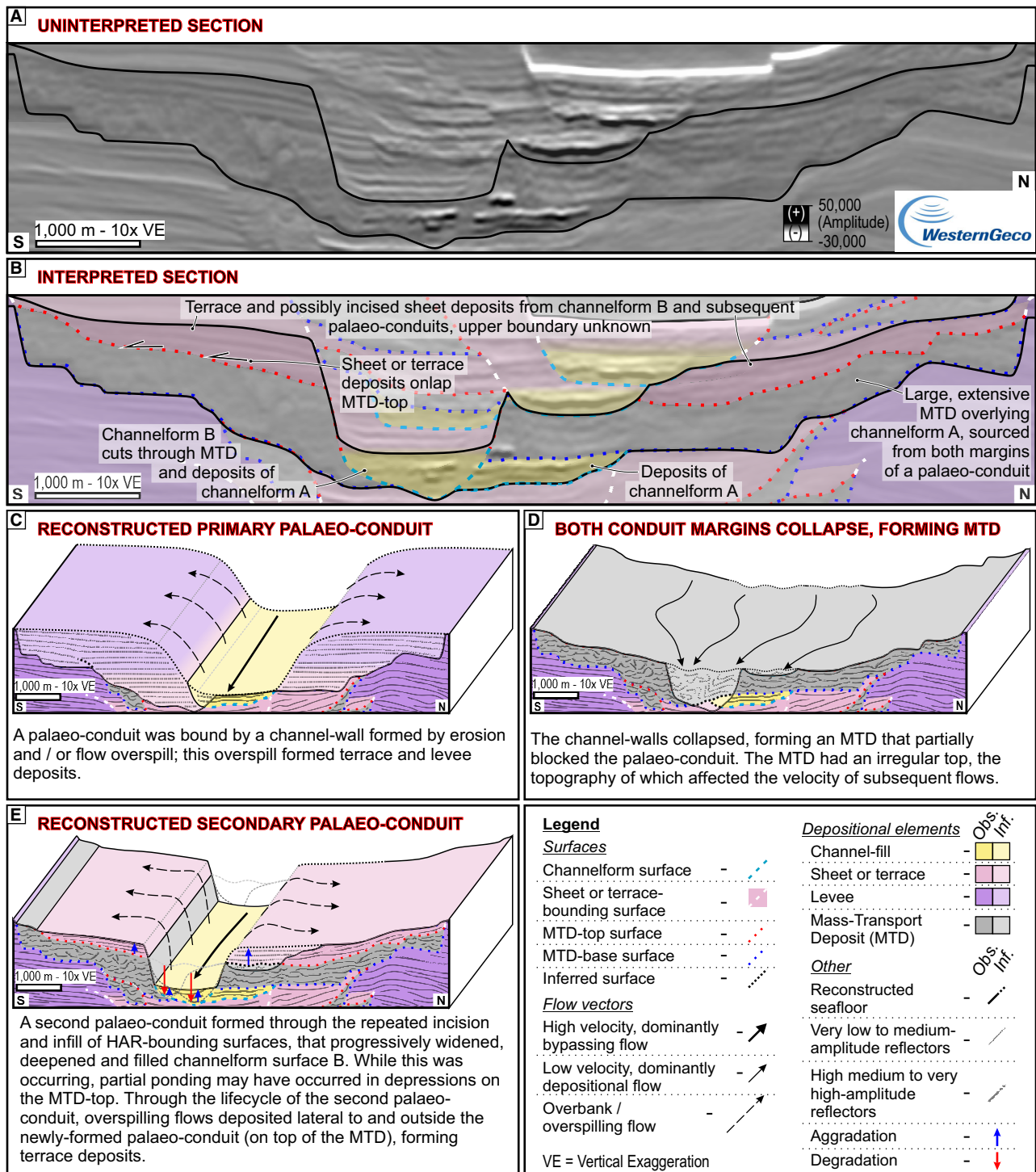


Fig. 9. (A) Minimally interpreted and (B) interpreted sections showing ‘sequence-type 1’ (described in the text). (C), (D) and (E) Evolutionary block diagrams showing the formation of ‘sequence-type 1’.

terrace-bounding surface are preserved above the channelform A fill and below the axis of channelform surface B.

Interpretations (Fig. 10C, D and E). An existing palaeo-conduit was filled by sheet deposits formed on top of pre-existing channel-fill

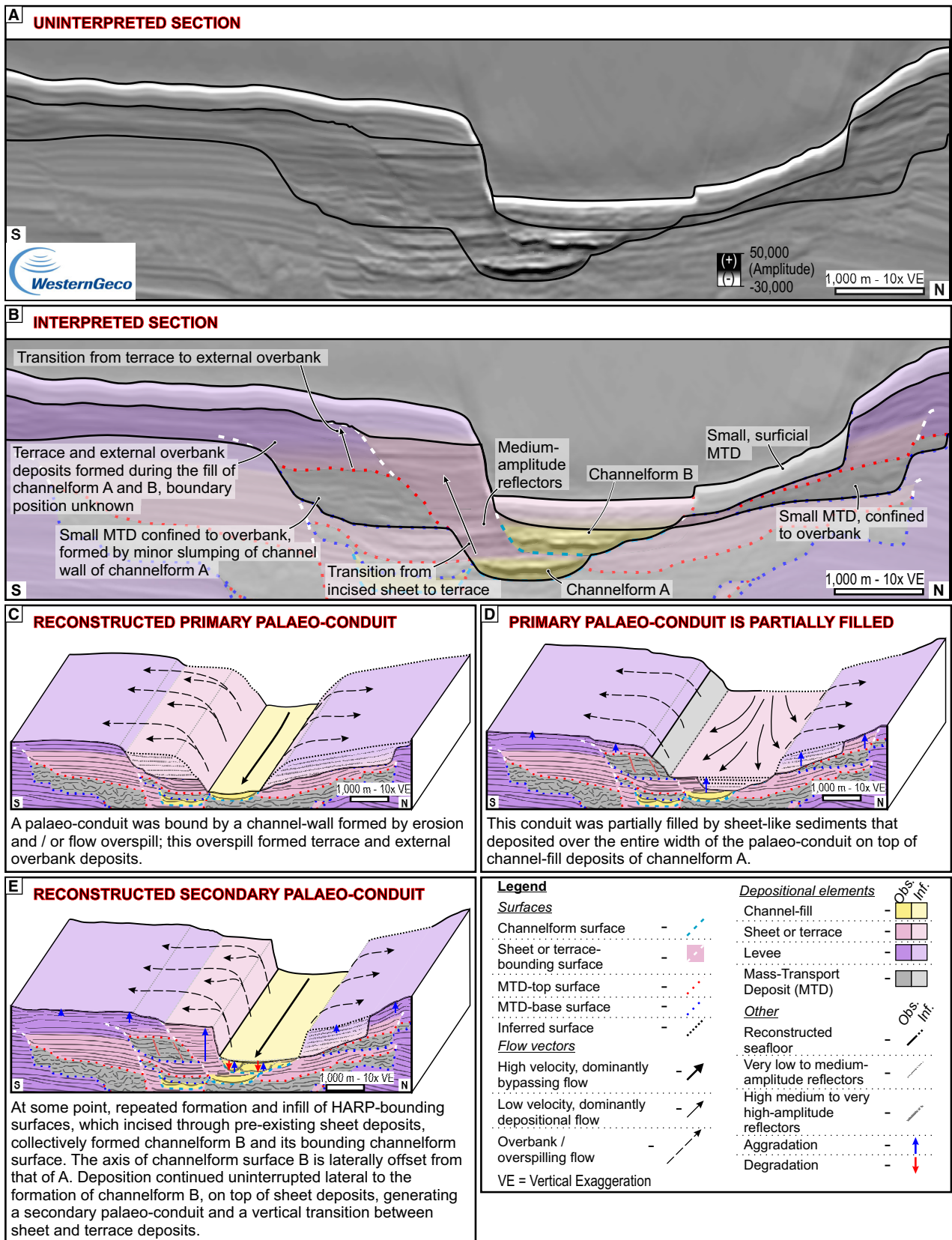


Fig. 10. (A) Minimally interpreted and (B) interpreted sections showing 'sequence-type 2' (described in the text). (C), (D) and (E) Evolutionary block diagrams showing the formation of 'sequence-type 2'.

deposits. Some of these sheets were incised during the establishment of channelform surface B, that formed by the repeated formation and infill of multiple HARP-bounding surfaces. During the formation of channelform surface B, overspilling flows deposited terrace deposits on top of incised sheet deposits, generating a (likely complex) vertical transition between channel-fill, incised sheet and terrace deposits (Deptuck *et al.*, 2003; Hubbard *et al.*, 2020). These overspilling flows deposited sediment on two adjacent, vertically offset terraces.

Three-dimensional stratigraphic correlation

The interpretations of the depositional sequence-types allow distinction of the relative ages of depositional elements in cross-section, which have been traced upstream and downstream. Where this was not possible, MTDs, which are interpreted to have been emplaced quasi-instantaneously, are used as chronostratigraphic markers. Non-eroded MTD-tops are useful stratigraphic markers as MTDs mobilized after deposition of their constituent stratigraphy and before their onlapping strata. Where younger concave-up surfaces truncate the MTD-tops, the surfaces and their fill must be younger than the underlying MTD. Where a concave-up surface is filled by an MTD, or the reflectors hosted within that surface are incorporated into an overlying or adjacent MTD, the MTD must be younger. These relationships have allowed 3D stratigraphic correlation (Fig. 11) through areas where channel-fills are discontinuous, incised by subsequent channel-fills, or obscured by the presence of MTDs. Through the piecemeal linking of segments of channel-fills and their surrounding deposits, and using MTDs as chronostratigraphic markers, ten channelform surfaces containing channel-fills (hereafter termed 'channelforms 1 to 10') were traced across the entire study area (Fig. 12).

Architectural variability and integration with seafloor observations

While the categorization of depositional elements and interpretation of sequence-types 1 and 2 provide a framework for subsurface interpretation, integration with seafloor observations can inform models of architectural genesis. In this section, the seismic character of recent deposits is linked to geomorphological features. Subtle variability in the seismic character of

depositional elements, and the nature of transitions between them and their seismofacies, are then linked to observations from the shallow subsurface immediately below prominent seafloor features.

Description. The seismic character within the transition from channel-fill to terrace and sheet deposits is variable. In this transition, tabular reflectors commonly vary in amplitude and thickness, and contain transparent patches (Fig. 7E). Sometimes, <50 m above the transition, one to three medium to high-amplitude reflectors are observed. These exhibit insufficient amplitudes to be classified as another seismofacies, but are anomalously higher than most sheet or terrace deposits (Figs 7E, 7G and 10B). These reflectors are only present upstream of large MTDs. Upstream of the large, recently emplaced MTD observed on the modern seafloor (Fig. 5A), a *ca* 50 m thick succession of tabular reflectors with highly variable thicknesses and amplitudes and containing distinct transparent patches overlies channelform 10 (Fig. 13B). These are topped by a *ca* 20 m thick medium to high-amplitude reflector that is present immediately below the seabed and spans the entire 3800 m wide, flat channel-floor (Figs 5 and 13B).

At the head of knickpoint 2 (Figs 2 and 5), within knickpoint-zone 1, the aforementioned MTD has a maximum thickness of *ca* 90 m (Fig. 13C). It systematically thins away from the oceanward channel-wall, and pinches out on top of channelforms 9 and 10, which are amalgamated at that point. On top of the MTD and channelforms 9 and 10, a *ca* 55 m thick package of tabular reflectors with variable amplitudes is incised by a *ca* 40 m deep, *ca* 500 m wide, HARP-bounding surface cutting down from the landward edge of the channel-floor (Fig. 13C); the high-amplitude deposits within this surface are exposed on the seafloor, exhibiting high RMS amplitude values (Fig. 13A). This surface shallows and disappears *ca* 500 m upstream of the head of knickpoint 2. At the head of knickpoint 2, the channel-floor contains a *ca* 300 m wide U-shaped depression that is also confined to the north by the oceanward channel-wall (Fig. 13C). This depression sits within a 1300 m wide, subtler depression, below which tabular reflectors are exposed. Laterally adjacent to the southern margin of this depression, a 6 km wide mound of medium to high-amplitude reflectors is present between the MTD-top and the seabed.

When the HARs exposed just upstream of knickpoint 2, and their associated HARP-

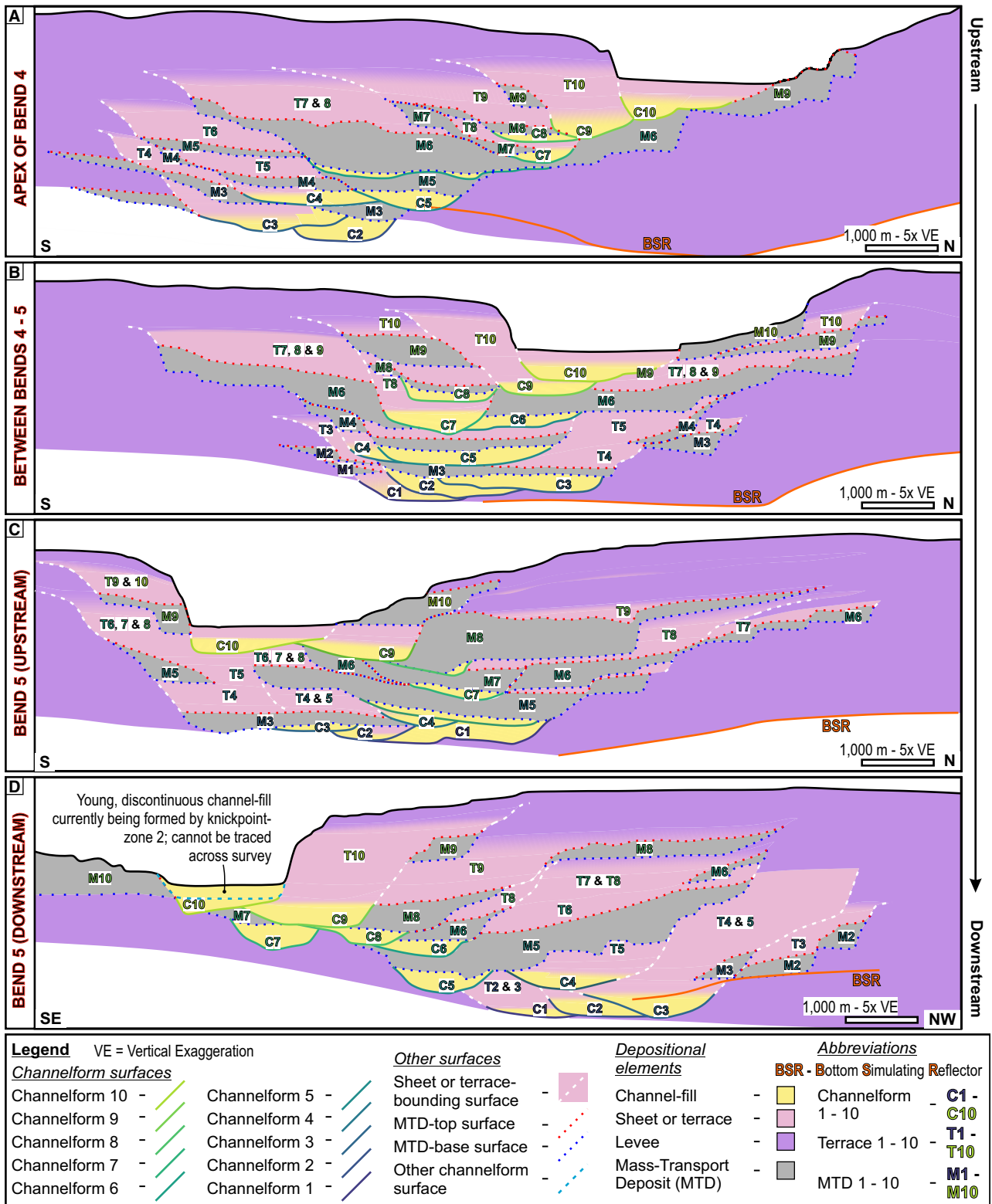


Fig. 11. Interpretations of sections in Fig. 8 showing the relative ages of the different depositional elements, and their longitudinal correlations.

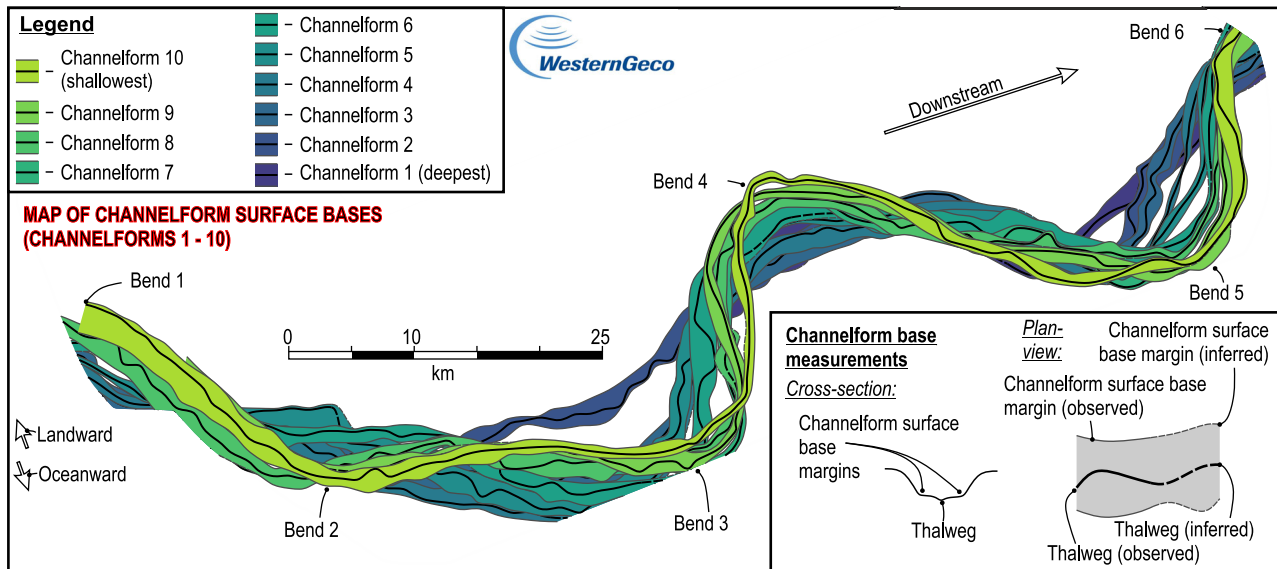


Fig. 12. Map of the thalwegs and edges of the flat bases of channelform surfaces 1 to 10 that have been traced across the area.

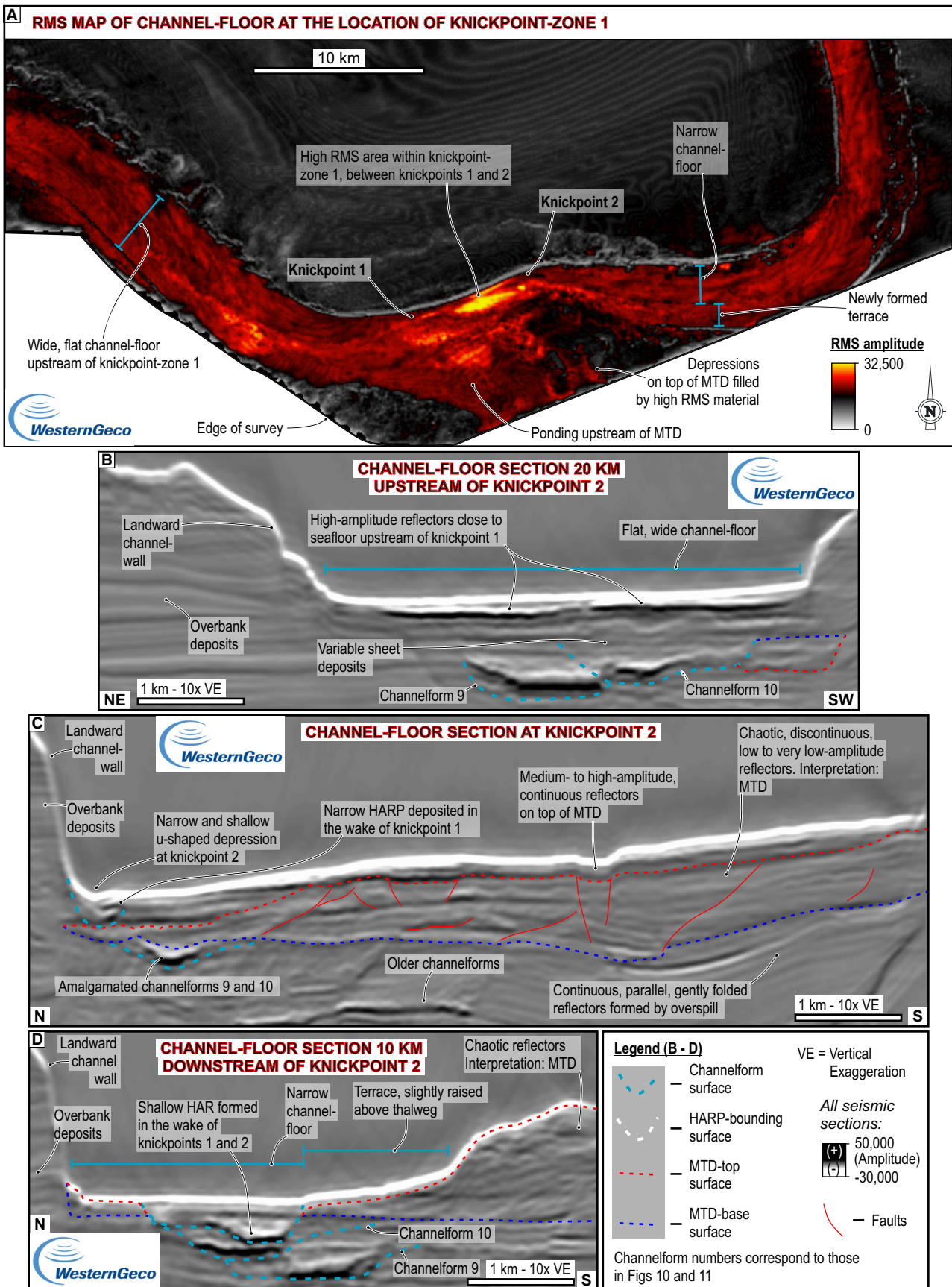
bounding surface, are traced *ca* 7.5 km downstream, the surface becomes *ca* 55 m deep and 1500 m wide, and partially truncates channelform 10 (Fig. 13D). At this location the MTD has a maximum thickness of 150 m, but thins dramatically northward before the top flattens out to form a *ca* 1300 m wide terrace (Fig. 13D). The location of knickpoint formation on the seafloor is on the landward side, opposite the source of the formative MTD.

Interpretations. Amplitude variability and transparent intervals in sheet deposits upstream of a conduit-damming MTD may result from initial partial ponding as flows rapidly decelerate upon encountering the MTD (Liang *et al.*, 2020). Deceleration may lead to the formation of more chaotic, yet still weakly-confined, flow deposits. Anomalously high-amplitude reflectors observed above sheet deposits with variable amplitudes may reflect sand-rich deposits from weakly-confined flows (McArthur *et al.*, 2021) after initial MTD-margin topography was healed, leaving a less severe reduction in longitudinal gradient.

These deposits formed immediately prior to, and during, re-incision and may mark the transition from incised sheet to terrace deposits.

As little remnant MTD is preserved on the landward side of the channel, it is unclear whether the modern MTD was deposited across the full channel-floor width; it is inferred that it did due to its relationship with deposits upstream. Knickpoints 1 and 2 (constituting knickpoint-zone 1) are in the process of upstream migration. They have incised through the thickest part (longitudinally) of the MTD, and any initial downstream deposits, and are currently incising weakly-confined deposits upstream (Fig. 13). If MTDs are sourced from one channel-wall, the locus of incision into MTD-tops in the subsurface is typically on the side opposite its source. Both knickpoints create concave-up depressions in cross-section that widen downstream. At its head, knickpoint 1 is dominantly erosional. In its downstream wake (upstream of knickpoint 2) knickpoint 1 generated a HARP-bounding surface containing

Fig. 13. (A) Root Mean Square (RMS) amplitude map of the seafloor showing the location of knickpoint-zone 1 (delineated by an area of high RMS amplitude), the flat, wide channel-floor upstream of knickpoint-zone 1, and the narrow channel-floor bound by a newly formed terrace downstream of knickpoint-zone 1. (B), (C) and (D) Seismic sections from the shallow subsurface (B) in the area with a wide, flat channel-floor, *ca* 15 km upstream of knickpoint-zone 1, (C) immediately (*ca* 300 m) downstream of knickpoint 2 and (D) *ca* 7.5 km downstream of knickpoint 2.



channel-fill deposits that exhibit high RMS amplitude values where exposed at the seafloor. Knickpoint 2 is interpreted to be presently incising into the deposits formed downstream of knickpoint 1.

DISCUSSION

An alternative model for the stratigraphic evolution of deep-water channels

The currently active state of the channel (Moun-tjoy *et al.*, 2018) together with the young age (<2 Ma) of the studied stratigraphy (Ghisetti *et al.*, 2016), and the correspondence of features identified on the seafloor with seismic surfaces and seismofacies in the subsurface validate the use of the modern Hikurangi Channel as a 'self-analogue' for its deposits (Fig. 14). This article presents a new model for the stratigraphic evolution of deep-water channels that may help to explain complexities in observed channel-fills and complement existing models of channel cut-and-fill.

Upstream of the emplacement of a wall-derived MTD, flow deceleration accompanying a reduction in longitudinal gradient and lateral confinement caused deposition (Corella *et al.*, 2016; Liang *et al.*, 2020; Tek *et al.*, 2020), filling the palaeo-conduit and widening the palaeo-channel-floor (Figs 14B, 14C and 15B). Potentially sand-rich 'sheet-like' deposits in this area are preserved as medium to high-amplitude, tabular reflectors (Figs 7E, 7G, 10B and 13B). Downstream of MTDs, sheet deposition may have occurred initially due to flow disequilibrium related to increased overspill (Peakall *et al.*, 2000) resulting from the shallowing of the partially-filled palaeo-conduit, and/or flow perturbation by their interaction with rugose MTD-top topography (e.g. Kneller *et al.*, 2016; Ward *et al.*, 2018; Bull *et al.*, 2020). As partial ponding started healing short-wavelength MTD-top topography and upstream aggradation partially healed longer-wavelength topography, flow velocities increased downstream (Fig. 14C). Further velocity increase due to an increased longitudinal gradient led to the formation of a knickpoint-zone (Figs 14C, 14D, 15C and 15D).

The knickpoint-zone, that comprised multiple, closely-spaced knickpoints, migrated upstream, sequentially incising first sheet-like deposits downstream of the MTD, then the MTD, and finally the sheet-like deposits upstream of the

MTD (Figs 14 and 15). The 'frontal' (furthest upstream; *sensu* Heijnen *et al.*, 2020) knickpoint marks the highest and most upstream point of a knickpoint-zone. The elevation of the head of the frontal knickpoint of the knickpoint-zone was dictated by the longitudinal profile of the channel immediately upstream of it. The elevation of the most downstream knickpoint in the knickpoint-zone was likely situated at or near the channel's equilibrium profile (Guiastrenne-Faugas *et al.*, 2020). As the knickpoint-zone migrated upstream, and the difference between the actual longitudinal profile upstream of the knickpoint-zone and its equilibrium profile decreased, so did the overall height of the knickpoint-zone (Fig. 16A). Eventually, as equilibrium was re-attained, the knickpoint-zone may have disappeared, or formed a solitary knickpoint.

Downstream of the knickpoint-zone, a channel-form surface was buried beneath a new, flat channel-floor that likely hosted a series of relatively regularly-spaced solitary knickpoints as seen on the seafloor, bound by a newly-formed terrace (Figs 2C and 14E). The position of knickpoint-zone 2 (comprising knickpoints 6 and 7 on the seafloor; Figs 2C and 5F), over 20 km upstream of its causative blockage, suggests that knickpoint-zones are non-static. However, due to the uncertainties in knickpoint migration rates and lack of constraint of the timing of MTD emplacement, a detailed explanation of the migratory mechanism of knickpoint-zones is not possible. Studies have shown how large, composite concave-up surfaces (herein 'channel-form surfaces') can form in response to widespread aggradation and degradation of the channel thalweg in response to variations in the nature (type, magnitude, velocity and grain size) of channel-traversing flows (Gardner *et al.*, 2003; Kneller, 2003; Flint *et al.*, 2011; Sylvester *et al.*, 2011; Hodgson *et al.*, 2016; Kneller *et al.*, 2020). In such situations (commonly cyclical) periodic changes in flow nature alter the equilibrium gradient to which a channel tends to adjust, generating repeated periods of net erosion and deposition over long channel reaches (Kneller, 2003; Fig. 16B). Conversely, in the Hikurangi Channel, localized channel damming by MTDs induced modification of the actual channel profile, promoting deposition upstream and forcing the channel out of equilibrium. Through knickpoint-zone formation and migration, the longitudinal channel profile then tended towards re-attaining its equilibrium profile

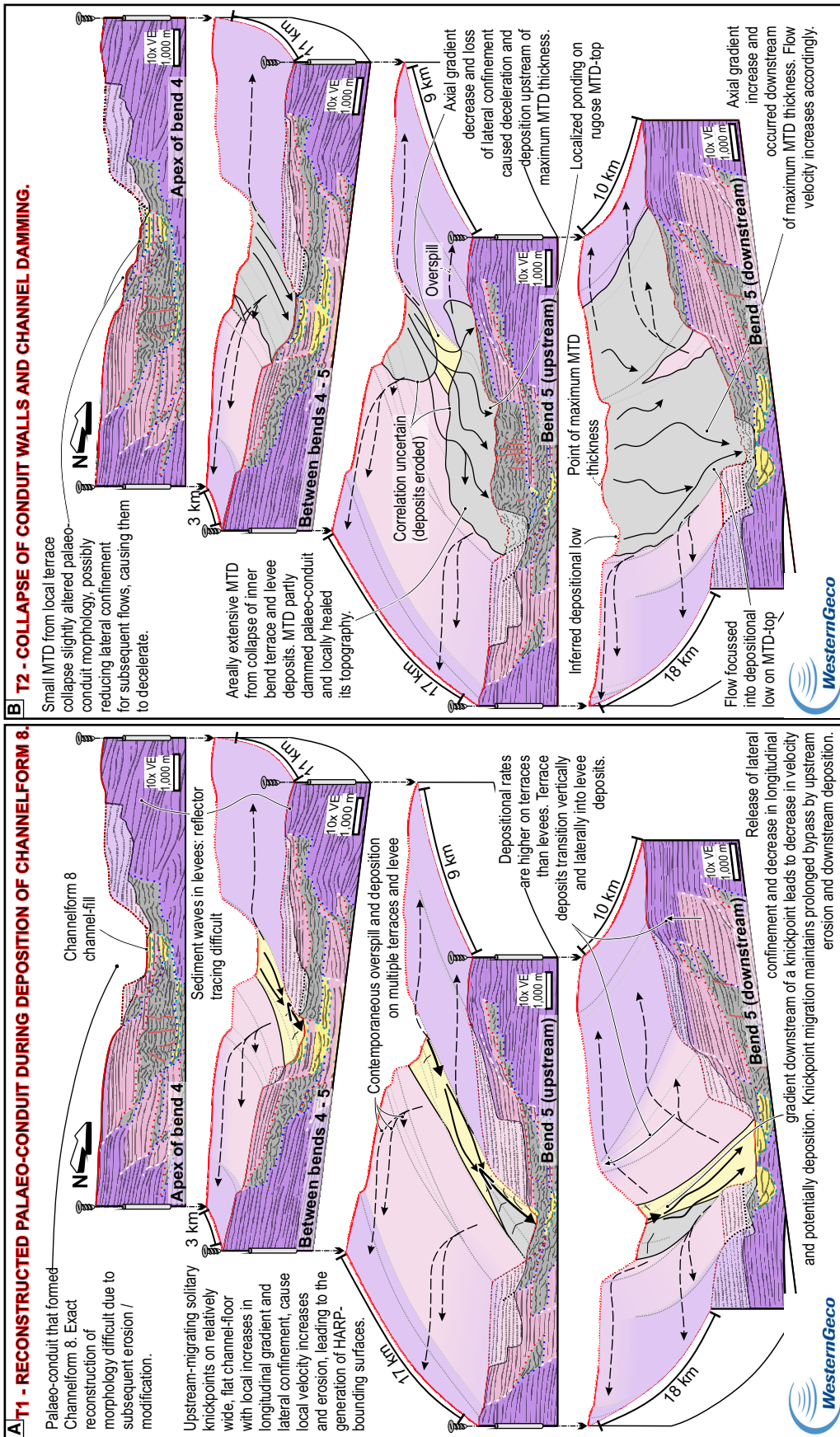


Fig. 14. Interpreted seafloor reconstructions detailing the processes by which one palaeo-conduit is infilled and a subsequent one is created through five time-steps: (A) T1 – palaeo-conduit overlying channelform 8 has a wide channel-floor containing regularly spaced knickpoints; (B) T2 – collapse of the channel-wall forms an MTD that partially dams the channel, eliciting a decrease in longitudinal gradient upstream, and an increase downstream; (C) T3 – a knickpoint-zone forms and begins to migrate upstream, incising through, and leaving terrace deposits on top of, the MTD; (D) T4 – the knickpoint-zone migrates further upstream, incising through, and leaving terrace deposits on top of, sheet deposits that formed upstream of the blockage but were contemporaneous to initial knickpoint-zone incision; (E) a new palaeo-conduit is formed in the downstream wake of the knickpoint-zone.

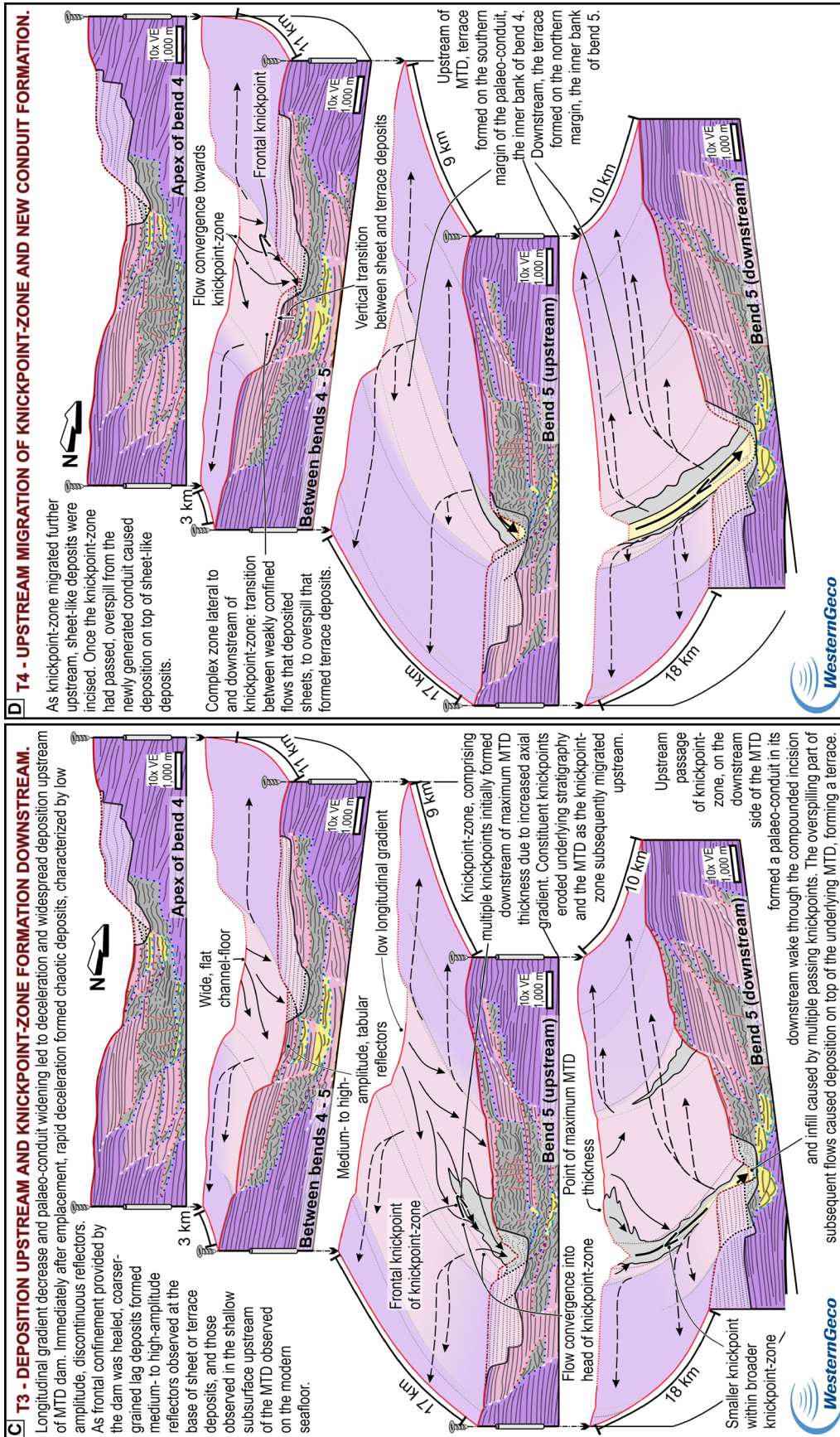


Fig. 14. Continued

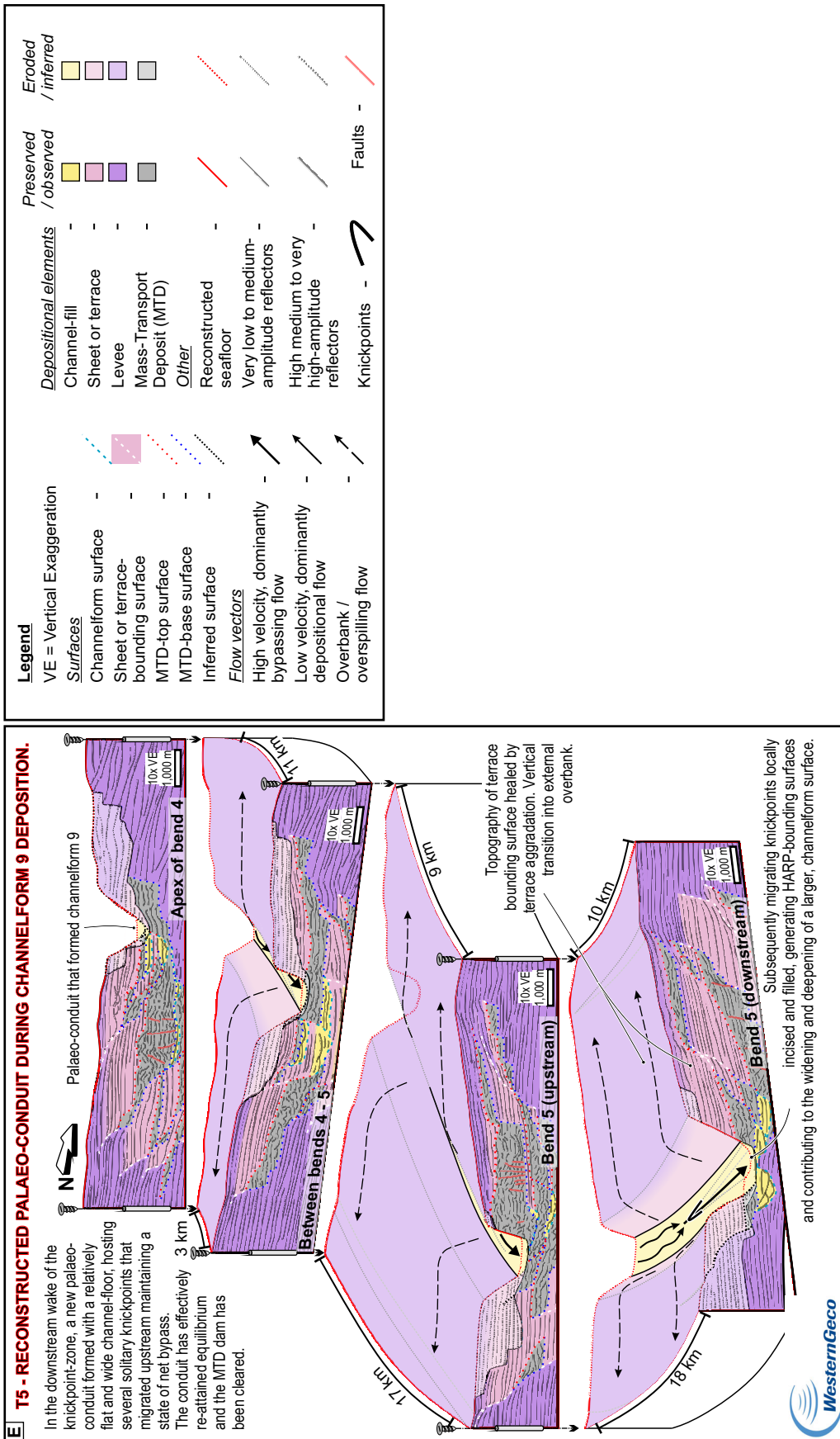


Fig. 14. Continued

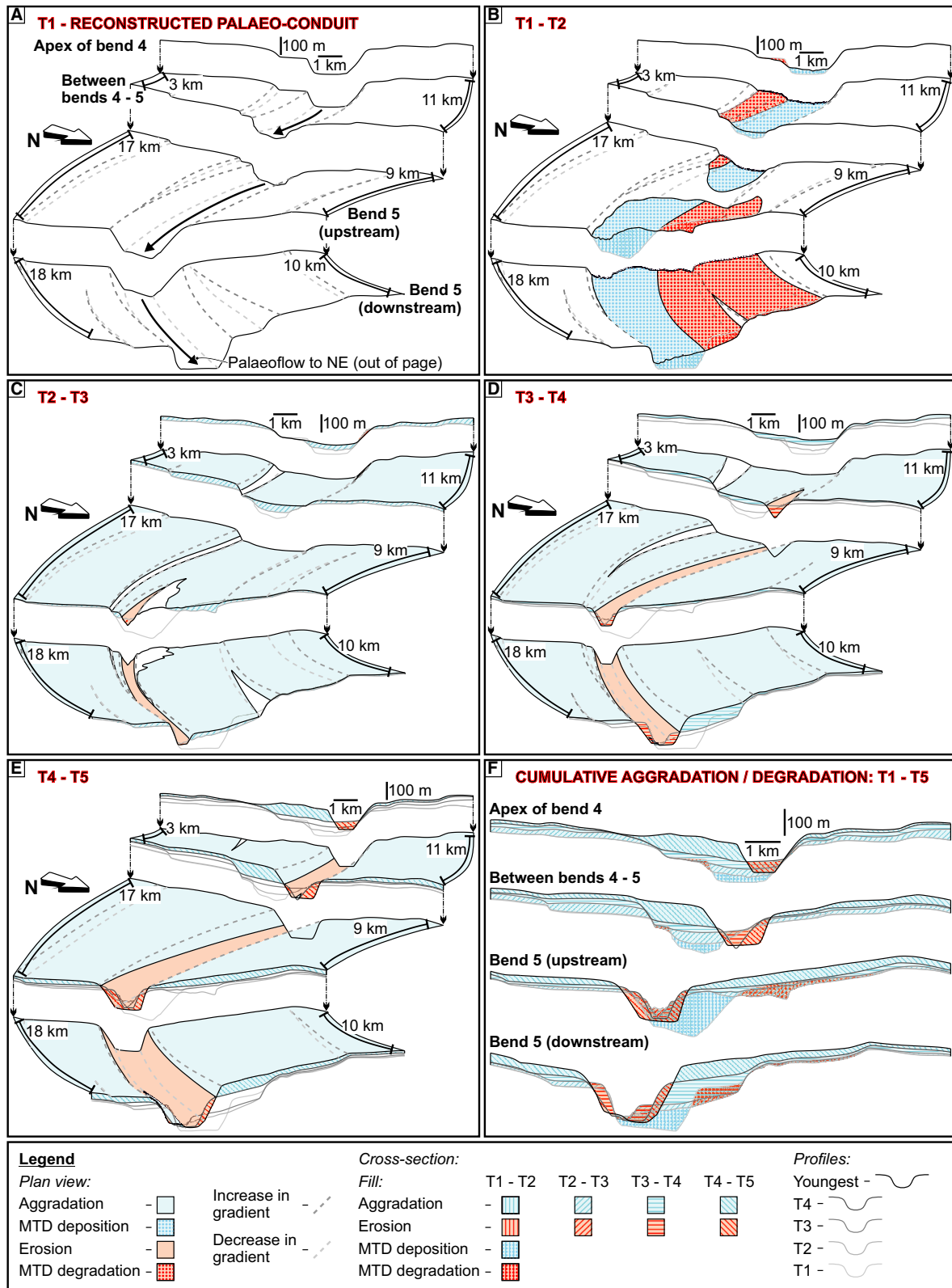


Fig. 15. Relative change diagrams showing the location of interpreted seafloor aggradation and degradation between the five time steps shown in Fig. 14: (A) T1, the initial surface; (B) T1 – T2; (C) T2 – T3; (D) T3 – T4; (E) T4 – T5; (F) cumulative product of T1 – T5.

(Fig. 16A). Other mechanisms that can modify longitudinal channel profiles and induce similar, localized architectural motifs include structural growth (Heiniö & Davies, 2007; Georgiopoulou & Cartwright, 2013), halokinesis (Gee & Gawthorpe, 2006) and meander bend cut-off (Deptuck *et al.*, 2007). However, none of these mechanisms affected the studied reach of the Hikurangi Channel.

While damming may be local at the scale of an entire channel, the low average longitudinal gradient of the channel (assumed similar throughout deposition), means that a 100 m thick blockage would, when restored to flat using simple trigonometry (a minimum estimate), cause aggradation up to *ca* 64 km upstream. However, if sporadic episodes of localized channel-wall collapse, dam formation by MTDs, and clearance by knickpoint-zones (Fig. 16A) had been the only process responsible for the generation and infill of channelform surfaces, their subsurface distribution would have been complex and chaotic. Therefore, the fact that ten discrete channelform surfaces can be traced across the study area, suggests the existence of larger-scale cyclicity. Sediment supply to the canyons that feed the Hikurangi Channel is estimated to have been two to three times higher in glacial periods, when sediment was not trapped in glacial lakes (Lewis, 1994). Sediment supply-driven cyclicity may have resulted from periodic variations in the nature of flows that traversed the channel, causing repeated episodes of net aggradation followed by net erosion over long reaches of the channel, resembling a conventional 'cut-and-fill' model (Fig. 16B). More localized effects of channel damming (Fig. 16A) may be superimposed onto the effects of this broader cyclicity, generating the architecture observed in the Hikurangi Channel. Alternatively, apparent cyclicity could arise from repeated periods where the channel is particularly prone to channel-wall collapse, and periods of relative channel-wall stability. The aforementioned models likely interact. However, additional data are required to discern the relative importance of factors such as sediment supply, seismicity, seafloor stability, and potential temporal variations in knickpoint and knickpoint-zone dynamics in controlling the evolution of the Hikurangi Channel.

Channel-wall collapse is common in submarine channels. However, the architecture of channel-wall derived MTDs in passive margin systems is commonly that of rotated blocks of

coherent overbank stratigraphy (e.g. Sawyer *et al.*, 2007, 2014), or relatively small slumps or debrites that comprise part of the channel-fill but are not preserved in adjacent overbank stratigraphy (e.g. Deptuck *et al.*, 2003; Hansen *et al.*, 2015). MTDs of similar scales and architectures to those in the Hikurangi Channel are observed in the axial channel deposits in the Northern Alpine Foreland Basin (Kremer *et al.*, 2018). Furthermore, contrasting passive and active areas of the eastern continental margin of New Zealand, Watson *et al.* (2020) demonstrated that submarine landslides (including channel-wall collapses) are more prevalent and larger in active areas. Therefore, channels on seismically quiescent margins may experience less influence of MTDs on their architecture, when compared with channels on seismically active margins. However, a paucity of studies focused on the influence of channel-wall derived MTDs in channelized deep-water stratigraphy means that data from more systems is needed to validate this relationship.

The subsurface expression of knickpoints and knickpoint-zones

Two nested scales of concave-up surfaces are observed in the subsurface of the Hikurangi Channel: small scale 'HARP-bounding surfaces' and larger 'channelform surfaces' (Table 2).

HARP-bounding surfaces truncate <60 m of stratigraphy, are <1 km wide (Fig. 7A and B) and are the smallest hierarchical order of surface preserved in the seismic data. They are interpreted to form from the passage of upstream-migrating knickpoints that incise upstream over short lengths (herein *ca* 2.5 km) and deposit immediately downstream (Table 2; Fig. 17A).

Channelform surfaces truncate <80 m of stratigraphy, are <3 km wide, and represent composite surfaces that contain one or more HARP-bounding surfaces (Fig. 7A and B). Channelform surfaces initiate by the passage of knickpoint-zones (containing multiple knickpoints) that form in response to local damming by MTDs (Figs 14 and 15). Channelform surfaces and their formative knickpoint-zones operate at a larger hierarchical order than HARP-bounding surfaces and their formative knickpoints (Fig. 17A).

In the Hikurangi Channel, as the frontal knickpoint in a knickpoint-zone migrated upstream, it generated an initial HARP-bounding surface

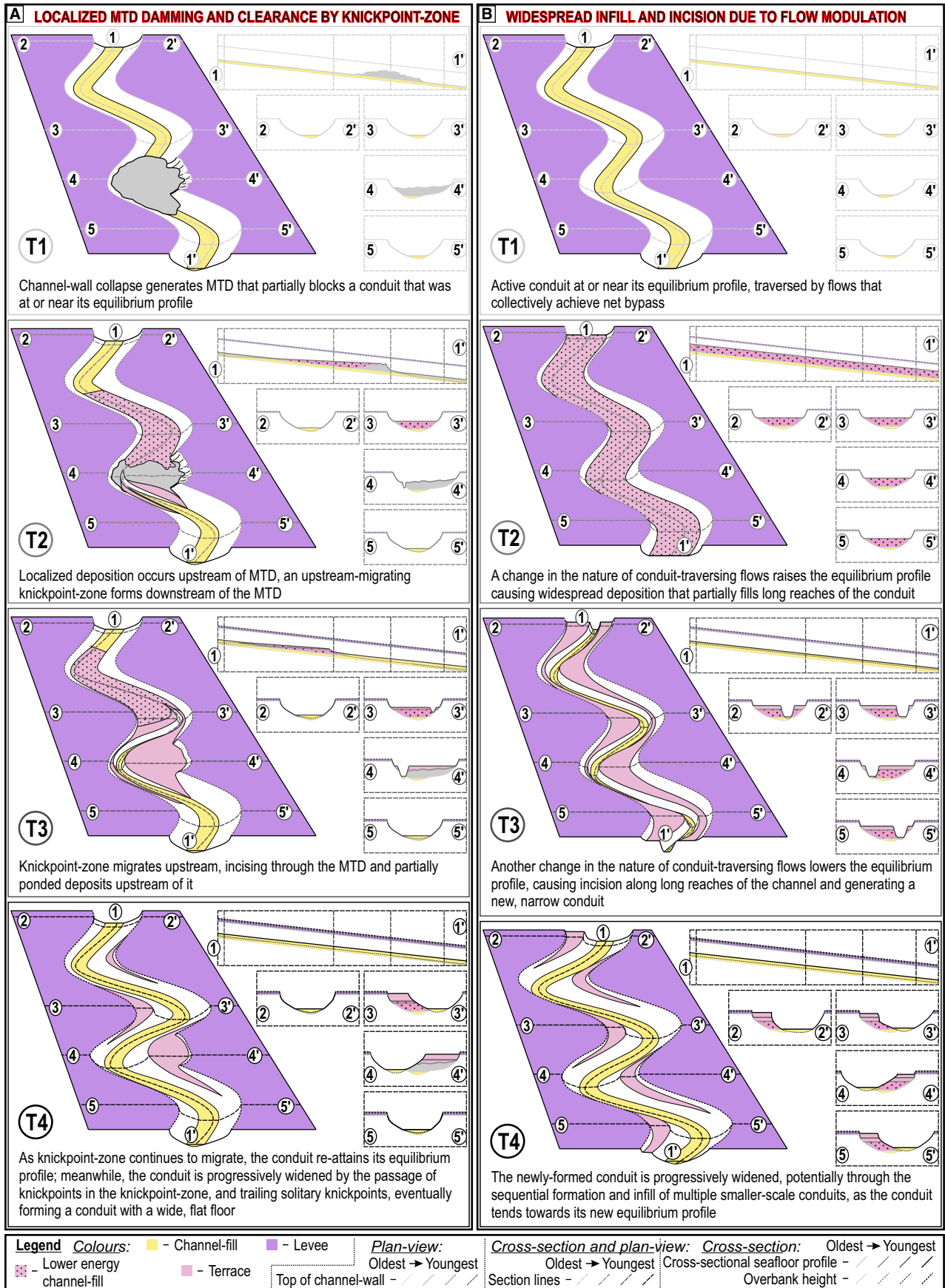


Fig. 16. Two schematic models of channel evolution, explaining the potential processes responsible for the infill of a composite channelform surface, and the establishment of another. (A) Channel damming by an MTD, then clearance by an upstream-migrating knickpoint-zone causing a localized morphodynamic response. (B) Variations in the nature of the channel-traversing flows causing widespread deposition then incision along the entire channel reach (roughly the same as the studied reach of the Hikurangi Channel). ‘Lower energy channel-fill’ encompasses a range of possible architectures, from weakly confined sheet deposits (this study) to isolated, meandering channels (e.g. Kneller *et al.*, 2020).

(Fig. 17A). The initial surface was progressively deepened and widened by punctuated episodes of incision and infill by subsequent, passing knickpoints (Fig. 14C, D and E) forming a composite channelform surface (Fig. 17A). Channelform surfaces therefore record the protracted evolution of the channel system (Sylvester *et al.*, 2011; Hubbard *et al.*, 2014, 2020; Hodgson *et al.*, 2016) attempting to re-attain equilibrium after modification (Kneller, 2003; Georgiopolou & Cartwright, 2013; Guiastrenec-Faugas *et al.*, 2020), whereas HARP-bounding surfaces record the remnant signature of a localized downstream transition from erosion to deposition in response to transient, upstream-migrating knickpoints. Because they both formed by longitudinally localized erosion and deposition by geologically transient features, neither scale of surface existed, in its entirety, as a geomorphic feature and neither delineates the instantaneous form of a palaeo-conduit at any one time. The generation of apparent stratigraphic hierarchy by the localized action of different scales of transient seafloor features (the ‘knickpoint migration’ model presented herein; Fig. 17A; see also Guiastrenec-Faugas *et al.*, 2021) departs from conventional ‘cut-and-fill’ models (Gardner *et al.*, 2003; Maier *et al.*, 2012; Fig. 17B). Both models can generate two nested scales of concave-up (in cross-section) surfaces like those observed in the Hikurangi Channel (Fig. 17C). To form the smaller-scale surfaces (equivalent to HARP-bounding surfaces in the Hikurangi Channel), cut-and-fill models invoke the repeated excavation and infill of conduits in response to cyclical variations in the nature of channel-traversing flows (Hansen *et al.*, 2017b; Bell *et al.*, 2020; Fig. 17B). In such models, larger-scale surfaces (equivalent to channelform surfaces in the Hikurangi Channel) are generated by progressive widening and deepening, then infilling through the action of the smaller-scale conduits, in response to higher order variations in the nature of channel-traversing flows (Hodgson *et al.*, 2011, 2016; Fig. 17B). While the formative mechanism of large-scale composite surfaces is

comparable between the knickpoint-based and cut-and-fill models, the formative mechanisms of small-scale surfaces are very different.

At the smallest scale, the migration of features interpreted as cyclic-steps and sediment waves, observed on the floor of the modern Hikurangi Channel, may build and erase stratigraphy at the scale of a few metres (Vendettuoli *et al.*, 2019; Englert *et al.*, 2020). However, data with finer resolution are required to determine how pervasive these features may be in the studied reach of the Hikurangi Channel, as well as in other channels, and the impact these features may have on the preserved stratigraphy.

Comparison with knickpoints and knickpoint-zones in other systems

Knickpoints and knickpoint-zones in deep-water channels can form in response to avulsions (Pirmez & Flood, 1995; Dennielou *et al.*, 2017), structural growth (Heiniö & Davies, 2007; Mitchell *et al.*, 2020), halokinesis (Gee & Gawthorpe, 2006), bend cut-off (Deptuck *et al.*, 2007), longitudinal variations in substrate composition (Mitchell, 2004), MTD emplacement (Corella *et al.*, 2016) or longitudinal variations in flow parameters (Heijnen *et al.*, 2020). Ponding upstream and knickpoint generation downstream of MTDs has been observed in submarine canyon deposits (Paull *et al.*, 2011; Corella *et al.*, 2016). Repeat bathymetry surveys on the Rhone Delta Canyon (Girardclos *et al.*, 2012; Corella *et al.*, 2016) show that in the 12 to 14 years after MTD emplacement widespread deposition (>6 m) occurred upstream, generating a flat, wide channel-floor, whilst a knickpoint formed downstream eroded >6 m into the substrate, forming a new conduit offset from the original one (Fig. 18A and B). In contrast, MTDs in the Hikurangi Channel cannot be thicker than the height of their source channel-wall, meaning that they cannot fully occlude the channel, thereby allowing flows downstream to continue along the same path. Repeat surveying on the Fraser River Delta slope (Hill, 2012) shows how

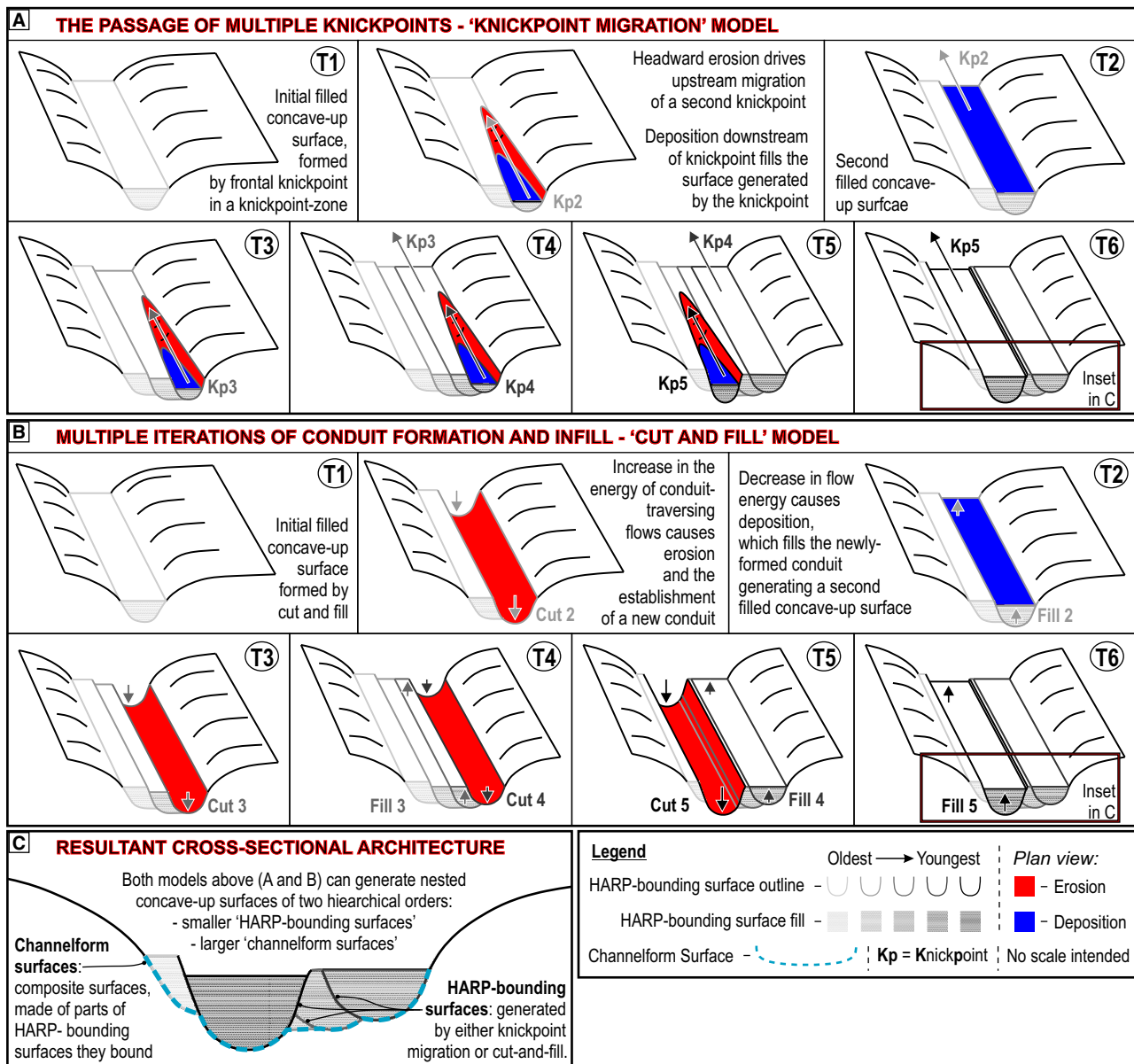


Fig. 17. Schematic diagrams showing two contrasting models for the generation of two nested scales of filled, concave-up surfaces in cross-section. (A) Multiple knickpoints, likely organized into a knickpoint-zone, migrate upstream by headward erosion and deposition immediately downstream, leaving a series of concave-up surfaces (equivalent to HARP-bounding surfaces in the Hikurangi Channel), the edges of which constitute a larger-scale, composite surface (equivalent to a channelform surface in the Hikurangi Channel). (B) The formation and infill of multiple small-scale, incisional conduits generate a series of concave-up surfaces (HARP-bounding surface equivalent), the edges of which also constitute a larger, composite surface (channelform surface equivalent). (C) Schematic cross-section showing how both models could generate the same cross-sectional architecture.

continual deposition on levées and terraces can occur during knickpoint migration, with deposition also occurring immediately upstream and downstream of knickpoints (Fig. 18C). Similar behaviours are interpreted to have contributed to the development of the Hikurangi Channel (cf. Figs 14 and 15). Spatially localized erosion

at the head of migrating knickpoints (and knickpoint-zones) may therefore contribute significantly to erosion in deep-water canyon and channel systems.

Knickpoints observed in the Hikurangi Channel appear shallower than those studied in systems with steep longitudinal gradients, where

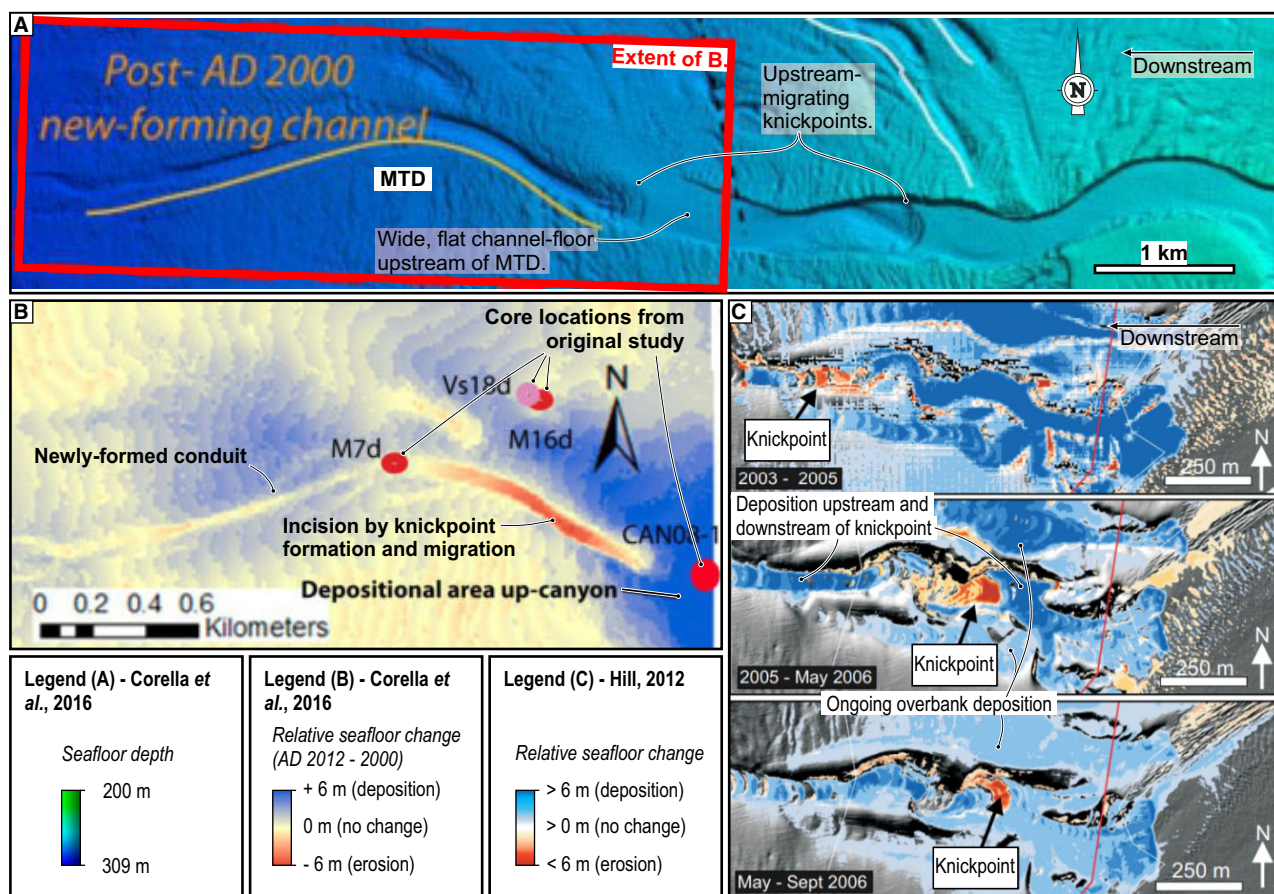


Fig. 18. (A) Bathymetry map from the Rhone Delta in Lake Geneva, modified from Corella *et al.* (2016; original bathymetry from Girardclos *et al.*, 2012), showing a channel with a wide, flat channel-floor upstream of an MTD that is being incised by a knickpoint and a newly-formed conduit; reproduced with permission from Elsevier. (B) Map of seafloor change between AD 2000 and 2012 of the inset shown in (A), again modified from Corella *et al.* (2016), showing deposition upstream and erosion downstream of knickpoint; reproduced with permission from Elsevier. (C) Map of seafloor change between AD 2003 and 2006 on the Fraser River delta, modified from Hill (2012), showing ongoing deposition on the overbanks, and upstream and downstream of a migrating knickpoint, with erosion localized to the knickpoint head; reproduced with permission from the International Association of Sedimentologists (IAS).

knickpoints may exceed 30° (e.g. Heijnen *et al.*, 2020) and are similar to those observed in systems with shallow longitudinal gradients, which are all less than 5° (e.g. Babonneau *et al.*, 2002). This may however be due to differences in data resolution, as gradients in datasets with finer horizontal resolution are more likely to be accurate. Knickpoints in the Hikurangi Channel may initiate in response to: (i) small-scale channel-wall collapse (a similar mechanism to knickpoint-zones); (ii) exploitation of smaller-scale bedforms; or (iii) longitudinal variability in flow parameters. Heijnen *et al.* (2020) present three mechanisms for knickpoint migration: (i) enhanced erosion by supercritical flow upstream

of a hydraulic jump; (ii) mass failure in response to loading or shaking by a passing flow; and (iii) mass failure due to oversteepening by basal erosion. Knickpoint migration rates measured from repeat bathymetric surveys in canyon or channel systems in relatively shallow-water (up to *ca* 500 m), namely on the Fraser River Delta (British Columbia, Canada; Hill, 2012), Rhone Delta (Lake Geneva, Switzerland; Corella *et al.*, 2016), Capbreton Canyon (Bay of Biscay, France; Guaiastrennec-Faugas *et al.*, 2020, 2021), and Bute Inlet (British Columbia, Canada; Heijnen *et al.*, 2020), range between 50 and 600 m year⁻¹. Channels in these highly active systems are traversed by one (Capbreton Canyon; Brocheray *et al.*,

2014) to over thirty (Rhone Delta Canyon; Lambert & Giovanoli, 1988) flows per year. In contrast, earthquake-driven canyon flushing in the Kaikōura Canyon, generating turbidity currents large enough to reach the trench, is calculated to occur every *ca* 140 years (Mountjoy *et al.*, 2018). Furthermore, in a direct monitoring study from the Monterey Canyon, Paull *et al.* (2018) recorded fewer events at distal moorings than proximal ones per time period, suggesting that distal parts of channel systems receive fewer events than their feeding canyons. Therefore, knickpoints in shallow-water, high-gradient reaches of channels and canyons may be expected to migrate faster than distal, shallow-gradient reaches. However, because multiple canyons feed the Hikurangi Channel, knickpoint migration rates in distal, shallow-gradient parts of the channel may be accelerated. Furthermore, channel-traversing turbidity currents can accelerate as they entrain sediment from the substrate (Heerema *et al.*, 2020), meaning the few flows that reach distal parts of the channel may exhibit larger average magnitudes, leading to knickpoints migrating further during each event.

Reconstructing the palaeo-seafloor from seismic data

Channels on the modern seafloor provide only a snapshot of the evolution of a channel system. In the absence of detailed chronostratigraphic control or thick hemipelagic drapes (e.g. Maier *et al.*, 2011, 2012; Jobe *et al.*, 2015), instantaneous reconstruction of the palaeo-seafloor from seismic data can be problematic because:

1 Surfaces elongate in the direction of palaeoflow with concave-up cross-sections may be generated by the passage of transient features such as knickpoints and knickpoint-zones (Heijnen *et al.*, 2020; Tek *et al.*, 2020; this study). These surfaces are diachronous, did not exist in their entirety at any one time (Sylvester *et al.*, 2011; Hodgson *et al.*, 2016), and may represent the compound product of one or more upstream-migrating knickpoints (Guiastrennec-Faugas *et al.*, 2020, 2021).

2 Synchronous deposition upstream, and erosion downstream, of an MTD dam hinders chronostratigraphic correlation, especially when upstream deposits are subsequently eroded and terrace deposits coalesce to form a single depositional element (Figs 14D and 15). As a result, concave-up surfaces may be progressively older

downstream, making them less reliable as chronostratigraphic markers.

3 An upward transition can occur between the late-stage fill of a palaeo-conduit, and overlying terrace deposits formed by overspill from a secondary palaeo-conduit. In this case, a single surface does not provide a chronostratigraphic marker of the boundary between two successive palaeo-conduits (Deptuck *et al.*, 2003; Figs 7G, 10 and 14D).

4 Deposits on any one terrace may have formed through the lifecycle of multiple adjacent palaeo-conduits (Figs 11, 14 and 15). Likewise, the overspill of a single palaeo-conduit may be manifested in multiple terraces (Droz *et al.*, 2003; Babonneau *et al.*, 2010; Kolla *et al.*, 2012; Li *et al.*, 2018; Figs 2, 5, 11, 14A and 15). Furthermore, two adjacent terraces may merge, in time, through differential aggradation (Fig. 14). Attributing terrace deposits to a single formative palaeo-conduit can therefore be difficult.

5 Terrace bounding surfaces may be constructed by sustained, contemporaneous deposition on an inboard (towards the coeval palaeo-conduit) terrace and an adjacent, outboard terrace or levée (Table 1), thus obscuring estimates of terrace and levée height and width.

6 Failure of channel-walls and subsequent MTDs may significantly alter the morphology of a palaeo-conduit (Figs 14B and 15B).

Therefore, deposits and surfaces in outcrop and subsurface provide the most reliable record of protracted channel evolution, and channel-margin and overbank deposits are the most complete as they are less prone to extended periods of erosion or non-deposition (Hubbard *et al.*, 2020). In large, well imaged, long-lived channel systems prone to collapses of their channel-walls, such as the Hikurangi Channel, uncertainty related to some of the aforementioned factors can be mitigated by utilising:

1 Quasi-instantaneously emplaced MTDs as reliable chronostratigraphic markers. Five approaches to aid seismic interpretation and seafloor reconstruction from seismic sections containing MTDs are presented in Fig. 19A.

2 Subtle changes in reflector character akin to those observed in the shallow subsurface, which can be related to geomorphological features. Three seismic-stratigraphic relationships that can reduce uncertainty in evolutionary interpretations in sections upstream of MTD dams are presented in Fig. 19B.

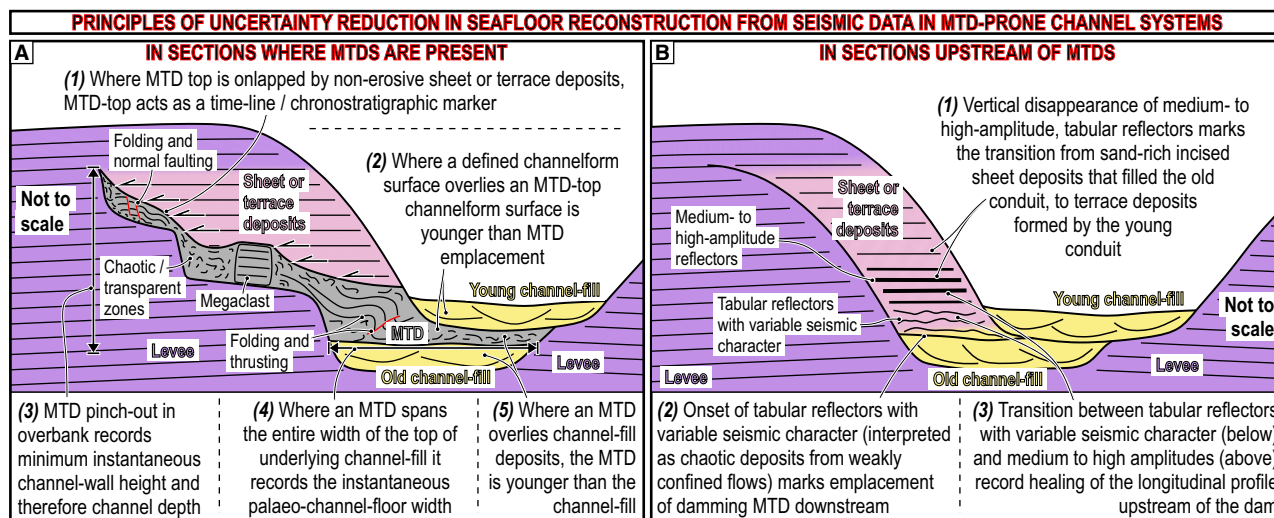


Fig. 19. Schematic cross-sections showing the principles by which uncertainty in seafloor reconstruction may be reduced in the presence of channel-damming MTDs. Sections either: (A) where MTDs are present; or (B) upstream of channel-damming MTDs, can be used to inform seafloor reconstruction.

Regardless, the cross-sectional morphology of the infill of ancient deep-water channels ultimately reflects the compound effect of various local, time-transgressive processes which have affected an area of a specific channel, not necessarily the boundary conditions under which the channels formed. Care must be taken when extrapolating the dimensions of palaeo-seafloor features, specifically palaeo-conduits, from the dimensions of the depositional elements they generate in these inherently complex sedimentary systems.

CONCLUSIONS

This study uses high-resolution bathymetry and 3D seismic data to provide the most detailed description to date of the seafloor geomorphology and three-dimensional subsurface architecture of a trench-axial deep-water channel: the Hikurangi Channel. The identification of ten seismofacies and five surface types allowed categorization of the stratigraphy into four depositional elements: channel-fill, sheet or terrace, levée, and mass-transport deposits (MTDs). Relationships between depositional elements, their constituent seismofacies and bounding surfaces, allowed three-dimensional correlation and interpretation of several depositional sequences. The modern Hikurangi Channel can be used as a self-analogue for its palaeo-incarnations;

integration of seafloor and subsurface data enabled the role of seafloor features in deposit formation to be elucidated, facilitating the reconstruction of the palaeo-seafloor through time and development of a new model for the genesis of submarine channel deposits.

The subsurface architecture of the Hikurangi Channel is principally controlled by the response to the quasi-instantaneous emplacement of local MTD dams derived from channel-wall collapses. Following MTD emplacement, sheet-like deposits formed upstream due to reduced longitudinal gradients and lateral confinement. Downstream a knickpoint-zone, comprising multiple smaller-scale, closely-spaced knickpoints formed due to increased longitudinal gradients. Knickpoint-zones and knickpoints are areas of steepened longitudinal gradient, that are concave-up in cross-section and widen downstream. The knickpoint-zone migrated upstream and eventually diminished as the channel approached equilibrium. Accompanying migration, the knickpoint-zone incised sequentially through the MTD and sheet-like deposits upstream, leaving a new, flat channel-floor bound by newly-formed terraces in its wake. These results are consistent with findings from studies of active channel systems.

At least two nested scales of elongate, concave-up surfaces are preserved, interpreted to be formed by two distinct scales of migrating channel-floor features: (i) High-Amplitude

Reflector Package (HARP)-bounding surfaces truncate <60 m of stratigraphy and are typically *ca* 500 m wide. They are formed by upstream-migrating knickpoints that leave a filled, or partially-filled, surface in their wake as they erode upstream and deposit immediately downstream. (ii) Channelform surfaces truncate <80 m of stratigraphy and are <3 km wide, formed by knickpoint-zones. One or more HARP-bounding surfaces are contained within, and constitute the edges of a channelform surface. Channelform surfaces are diachronous, composite surfaces that are initiated and modified by the passage of knickpoints within their formative knickpoint-zone; thus, they represent a larger hierarchical order than HARP-bounding surfaces. Both scales of surface form through the migration of transient features and were therefore never present as bathymetric features in their entirety at any time.

Reconstruction of palaeo-seafloor morphology from seismic data is problematic due to the time-transgressive and transitional nature of surface and deposit formation. However, the presence of quasi-instantaneously emplaced MTDs that can act as stratigraphic markers, and an active modern channel acting as a self-analogue for its subsurface deposits, mitigate uncertainty in this study.

By integrating sedimentary architecture and seafloor geomorphology, the data presented here permit a new model for the construction of channelized deep-water stratigraphy. This model complements existing models describing the formation and infill of deep-water channels, accounting for architectural complexity, and it is consistent with observations from the seafloor. Insights from this study may be used to aid interpretation in other channel systems where a direct seafloor analogue is lacking or data coverage is sparse.

ACKNOWLEDGEMENTS

This work was funded by Turbidites Research Group sponsors: AkerBP, CNOOC, ConocoPhillips, Murphy, OMV and OXY. Schlumberger WesternGeco are thanked for access to the seismic data used in this study. Multibeam bathymetry data displayed are made available for download by NIWA, and can be obtained from NZPM. We thank Richard Wild and Maarten Heijnen for their detailed and constructive reviews that vastly improved this manuscript,

and Associate Editor Anna Pontén and Editor Ian Kane for their handling of this manuscript.

DATA AVAILABILITY STATEMENT

Seismic data are available upon application to Schlumberger WesternGeco. Bathymetry data are available from New Zealand Petroleum and Minerals. Statistical data are available as supplementary material.

REFERENCES

- Abreu, V., Sullivan, M., Pirmez, C. and Mohrig, D. (2003) Lateral accretion packages (LAPs): an important reservoir element in deep water sinuous channels. *Mar. Pet. Geol.*, **20**, 631–648.
- Alpak, F.O., Barton, M.D. and Naruk, S.J. (2013) The impact of fine-scale turbidite channel architecture on deep-water reservoir performance. *Am. Asso. Petrol. Geol. Bull.*, **97**, 251–284.
- Alves, T.M. (2010) 3D Seismic examples of differential compaction in mass-transport deposits and their effect on post-failure strata. *Mar. Geol.*, **271**, 212–224.
- Armitage, D.A., Romans, B.W., Covault, J.A. and Graham, S.A. (2009) The influence of mass-transport-deposit surface topography on the evolution of turbidite architecture: the Sierra Contreras, Tres Pasos Formation (Cretaceous), Southern Chile. *J. Sed. Res.*, **79**, 287–301.
- Arnott, R.W.C. (2007) Stratal architecture and origin of lateral accretion deposits (LADs) and conterminous inner-bank levee deposits in a base-of-slope sinuous channel, lower Isaac Formation (Neoproterozoic), East-Central British Columbia, Canada. *Mar. Pet. Geol.*, **24**, 515–528.
- Babonneau, N., Savoye, B., Cremer, M. and Klein, B. (2002) Morphology and architecture of the present canyon and channel system of the Zaire deep-sea fan. *Mar. Pet. Geol.*, **19**, 445–467.
- Babonneau, N., Savoye, B., Cremer, M. and Bez, M. (2004) Multiple terraces within the deep incised Zaire Valley (Zaiango Project): are they confined levees? In: *Confined Turbidite Systems* (Eds Lomas, S.A. and Joseph, P.), *Journal of the Geological Society of London Special Publication*, **222**, 91–114.
- Babonneau, N., Savoye, B., Cremer, M. and Bez, M. (2010) Sedimentary architecture in meanders of a submarine channel: detailed study of the present Congo turbidite channel (Zaiango Project). *J. Sed. Res.*, **80**, 852–866.
- Bailey, W.S., McArthur, A.D. and McCaffrey, W.D. (2020) Distribution of contourite drifts on convergent margins: examples from the Hikurangi subduction margin of New Zealand. *Sedimentology*, **68**(1), 294–323.
- Ballance, P.F. (1975) Evolution of the India-Pacific plate boundary in North Island, New Zealand. *Bull. Aust. Soc. Explor. Geophys.*, **6**, 58–59.
- Barnes, P.M., Lamarche, G., Bialas, J., Henrys, S., Pecher, I., Netzeband, G.L., Greinert, J., Mountjoy, J.J., Pedley, K. and Crutchley, G. (2010) Tectonic and geological framework for gas hydrates and cold seeps on the

- Hikurangi subduction margin, New Zealand. *Mar. Geol.*, **272**, 26–48.
- Barnes, P.M. and Mercier de Lepinay, B.** (1997) Rates and mechanics of rapid frontal accretion along the very obliquely convergent southern Hikurangi margin, New Zealand. *J. Geophys. Res.*, **102**, 24931–24952.
- Bell, D., Hodgson, D.M., Pontén, A.S.M., Hansen, L.A.S., Flint, S.S. and Kane, I.A.** (2020) Stratigraphic hierarchy and three-dimensional evolution of an exhumed submarine slope channel system. *Sedimentology*, **67**, 3259–3289.
- Bernhardt, A., Jobe, Z.R., Grove, M. and Lowe, D.R.** (2012) Palaeogeography and diachronous infill of an ancient deep-marine foreland basin, Upper Cretaceous Cerro Toro Formation, Magallanes Basin. *Basin Res.*, **24**(3), 269–294.
- Bland, K.J., Lamarche, G., Anderson, O., Barnes, P.M., Black, J., Bowden, D., Chiswell, S., Crutchley, G., Gorman, R., Mountjoy, J., Niel, H., Notman, P., Pallentin, A., Rowden, A., Stagpoole, V.M. and Strogon, D.P.** (2014) Pegasus Basin Petroleum Prospectivity Screening Report. *GNS Science Consultancy Report 2014/103, NZP&M, Ministry of Business, Innovation & Employment (MBIE), New Zealand Unpublished Report PR(CR2014-103)*, 139 pp.
- Brocheray, S., Cremer, M., Zaragosi, S., Schmidt, S., Eynaud, F., Rossignol, L. and Gillet, H.** (2014) 2000 years of frequent turbidite activity in the Capbreton Canyon (Bay of Biscay). *Mar. Geol.*, **347**, 136–152.
- Brooks, H.L., Hodgson, D.M., Brunt, R.L., Peakall, J. and Flint, S.S.** (2018) Exhumed lateral margins and increasing flow confinement of a submarine landslide complex. *Sedimentology*, **65**, 1067–1096.
- Brunt, R.L., Di Celma, C.N., Hodgson, D.M., Flint, S.S., Kavanagh, J.P. and van der Merwe, W.C.** (2013) Driving a channel through a levee when the levee is high: an outcrop example of submarine down-dip entrenchment. *Mar. Pet. Geol.*, **41**, 134–145.
- Bull, S., Browne, G.H., Arnot, M.J. and Strachan, L.J.** (2020) Influence of Mass Transport Deposit (MTD) surface topography on deep-water deposition: an example from a predominantly fine-grained continental margin, New Zealand. In: *Subaqueous mass movements and their consequences: advances in process understanding, monitoring and Hazard assessments* (Eds Georgiopoulou, A., Amy, L.A., Benetti, S., Chaytor, J.D., Clare, M.A., Gamboa, D., Haughton, P.D.W., Moernaut, J. and Mountjoy, J.J.), *Geological Society, London, Special Publications*, **500**, 147–171.
- Bull, S., Cartwright, J. and Huuse, M.** (2009) A review of kinematic indicators from mass-transport complexes using 3D seismic data. *Mar. Pet. Geol.*, **26**(7), 1132–1151.
- Carter, L.** (1992) Acoustical characterisation of seafloor sediments and its relationship to active sedimentary processes in Cook Strait, New Zealand. *NZ J. Geol. Geophys.*, **35**, 289–300.
- Carter, R.M., Carter, L. and Griggs, G.B.** (1982) Sedimentation in the Conway Trough, a deep near-shore marine basin at the junction of the Alpine transform and Hikurangi subduction plate boundary, New Zealand. *Sedimentology*, **29**, 475–497.
- Cartigny, M.J.B., Postma, G., Van den Berg, J.H. and Mastbergen, D.R.** (2011) A comparative study of sediment waves and cyclic steps based on geometries, internal structures and numerical modelling. *Mar. Geol.*, **280**, 40–56.
- Cartigny, M.J.B., Ventra, D., Postma, G. and Van den Berg, J.H.** (2014) Morphodynamics and internal structures of bedforms under supercritical-flow conditions. *Sedimentology*, **61**, 712–748.
- Casson, M., Calvès, G., Huuse, M., Sayers, B. and Redfern, J.** (2020) Cretaceous continental margin evolution revealed using quantitative seismic geomorphology, offshore northwest Africa. *Basin Res.*, **33**(1), 66–90.
- Castelltort, S., Honegger, L., Adatte, T., Clark, J.D., Puigdefàbregas, C., Spangenberg, J.E., Dykstra, M.L. and Fildani, A.** (2017) Detecting eustatic and tectonic signals with carbon isotopes in deep-marine strata, Eocene Ainsa Basin, Spanish Pyrenees. *Geology*, **45**(8), 707–710.
- Clark, I.R. and Cartwright, J.A.** (2011) Key controls on submarine channel development in structurally active settings. *Mar. Pet. Geol.*, **28**(7), 1333–1349.
- Clark, J.D. and Pickering, K.T.** (1996) Architectural elements and growth patterns of submarine channels: Applications to hydrocarbon exploration. *Am. Asso. Petrol. Geol. Bull.*, **80**(2), 194–222.
- Collot, J.-Y., Lewis, K.B., Lamarche, G. and Lallemand, S.** (2001) The giant Ruatoria debris avalanche on the northern Hikurangi margin, New Zealand: result of oblique seamount subduction. *J. Geophys. Res.*, **106**, 271–297.
- Corella, J.P., Loizeau, J.L., Kremer, K., Hilbe, M., Gerard, J., le Dantec, N., Stark, N., González-Quijano, M. and Girardclos, S.** (2016) The role of mass-transport deposits and turbidites in shaping modern lacustrine deepwater channels. *Mar. Petrol. Geol.*, **77**, 515–525.
- Couvin, B., Georgiopoulou, A., Mountjoy, J.J., Amy, L., Crutchley, G.J., Brunet, M., Cardona, S., Gross, F., Böttner, C., Krastel, S. and Pecher, I.** (2020) A new depositional model for the Tuaheni Landslide Complex, Hikurangi Margin, New Zealand. In: *Subaqueous Mass Movements and their Consequences: Advances in Process Understanding, Monitoring and Hazard Assessments* (Eds Georgiopoulou, A., Amy, L.A., Benetti, S., Chaytor, J.D., Clare, M.A., Gamboa, D., Haughton, P.D.W., Moernaut, J. and Mountjoy, J.J.), *Geological Society, London, Special Publications*, **500**, 551–566.
- Covault, J.A., Shelef, E., Traer, M., Hubbard, S.M., Romans, B.W. and Fildani, A.** (2012) Deep-water channel run-out length: insights from seafloor geomorphology. *J. Sed. Res.*, **82**, 25–40.
- Crisóstomo-Figueroa, A., McArthur, A.D., Dorrell, R.M., Amy, L. and McCaffrey, W.D.** (2020) *A New Modelling Approach to Sediment Bypass Prediction Applied to the East Coast Basin, New Zealand*. GSA Bull., <https://doi.org/10.1130/B35687.1>.
- Cullis, S., Colombera, L., Patacci, M. and McCaffrey, W.D.** (2018) Hierarchical classifications of the sedimentary architecture of deep-marine depositional systems. *Earth Sci. Rev.*, **179**, 38–71.
- Davey, F.J., Hamfton, M.A., Childs, J., Fisher, M.A., Lewis, K.B. and Pettinga, J.R.** (1986) Structure of a growing accretionary prism, Hikurangi margin, New Zealand. *Geology*, **14**, 663–666.
- Davy, B., Hoernle, K. and Werner, R.** (2008) Hikurangi Plateau: crustal structure, rifted formation, and Gondwana subduction history. *Geochem. Geophys. Geosyst.*, **9**, 1–31.
- Dennielou, B., Droz, L., Babonneau, N., Jacq, C., Bonnel, C., Picot, M., Le Saout, M., Saout, Y., Bez, M., Savoye, B. and Olu, K.** (2017) Morphology, structure, composition and build-up processes of the active channel-mouth lobe

- complex of the Congo deep-sea fan with inputs from remotely operated underwater vehicle (ROV) multibeam and video surveys. *Deep-Sea Res. Part II: Topical Stud. Oceanogr.*, **142**, 25–49.
- Deptuck, M.E., Steffens, G.S., Barton, M. and Pirmez, C.** (2003) Architecture and evolution of upper fan channel-belts on the Niger Delta slope and in the Arabian Sea. *Mar. Pet. Geol.*, **20**(6–8), 649–676.
- Deptuck, M.E., Sylvester, Z., Pirmez, C. and O'Byrne, C.** (2007) Migration-aggradation history and 3-D seismic geomorphology of submarine channels in the Pleistocene Benin-major Canyon, western Niger Delta slope. *Mar. Pet. Geol.*, **24**(6–9), 406–433.
- Droz, L., Marsset, T., Ondreas, H., Lopez, M., Savoye, B. and Spy-Anderson, F.-L.** (2003) Architecture of an active mud-rich turbidite system: the Zaire Fan (Congo-Angola margin southeast Atlantic). Results from Zaiango 1 and 2 cruises. *Am. Asso. Petrol. Geol. Bull.*, **87**(7), 1145–1168.
- Dykstra, M., Garyfalou, K., Kertznus, V., Kneller, B., Milana, J.P., Molinaro, M., Szuman, M. and Thompson, P.** (2011) Mass-transport deposits: combining outcrop studies and seismic forward modeling to understand lithofacies distributions, deformation, and their seismic stratigraphic expression. In: *Mass Transport Deposits in Deepwater Settings* (Eds Shipp, C., Weimer, P. and Posamentier, H.), *SEPM Special Publications*, **96**, 293–310.
- Englert, R.G., Hubbard, S.M., Cartigny, M.J.B., Clare, M.A., Coutts, D.S., Hage, S., Hughes Clarke, J., Jobe, Z., Lintern, D.G., Stacey, C. and Vendettuoli, D.** (2020) Quantifying the three-dimensional stratigraphic expression of cyclic steps by integrating seafloor and deep-water outcrop observations. *Sedimentology*, **68**, 1465–1501.
- Flint, S.S., Hodgson, D.M., Sprague, A.R., Brunt, R.L., Van der Merwe, W.C., Figueiredo, J., Pr el at, A., Box, D., Di Celma, C. and Kavanagh, J.P.** (2011) Depositional architecture and sequence stratigraphy of the Karoo basin floor to shelf edge succession, Laingsburg depocentre, South Africa. *Mar. Petrol. Geol.*, **28**(3), 658–674.
- Flood, R.D.** (1988) A lee wave model for deep-sea mudwave activity. *Deep-Sea Res. Part I: Oceanogr. Res. Pap.*, **35**, 973–983.
- Flood, R.D. and Piper, D.J.** (1997) Amazon Fan sedimentation: the relationship to equatorial climate change, continental denudation, and sea-level fluctuations. In: *Proceedings-Ocean Drilling Program, Scientific Results, Amazon Fan* (Eds Flood, R.D., Piper, D.J., Klaus, A. and Peterson, L.C.), *National Science Foundation*, **155**, 653–675.
- Friend, P.F. and Sinha, R.** (1993) Braiding and meandering parameters. In: *Braided Rivers* (Eds Best, J.L. and Bristow, C.S.), *Geological Society, London, Special Publications*, **75**, 105–111.
- Gardner, M.H., Borer, J.M., Melick, J.J., Mavilla, N., Dechesne, M. and Wagerle, R.N.** (2003) Stratigraphic process-response model for submarine channels and related features from studies of Permian Brushy Canyon outcrops, West Texas. *Mar. Petrol. Geol.*, **20**(6–8), 757–787.
- Gee, M.J.R. and Gawthorpe, R.L.** (2006) Submarine channels controlled by salt tectonics: examples from 3D seismic data offshore Angola. *Mar. Pet. Geol.*, **23**, 443–458.
- Georgiopolou, A. and Cartwright, J.A.** (2013) A critical test of the concept of submarine equilibrium profile. *Mar. Pet. Geol.*, **41**, 35–47.
- Ghisetti, F.C., Barnes, P.M., Ellis, S., Plaza-Faverola, A. and Barker, D.H.N.** (2016) The last 2 Myr of accretionary wedge construction in the central Hikurangi margin (North Island, New Zealand): Insights from structural modelling. *Geochem. Geophys. Geosyst.*, **17**, 2661–2686.
- Girardoc, S., Hilbe, M., Corella, J.P., Loizeau, J.-L., Kremer, K., DelSontro, T., Arantegui, A., Moscarriello, A., Arlaud, F., Akhtman, Y., Anselmetti, F.S. and Lemmin, U.** (2012) Searching the Rhone delta channel in Lake Geneva since Fran ois-Alphonse Forel. *Arch. Sci.*, **65**(1–2), 103–118.
- Goldfinger, C.** (2011) Submarine paleoseismology based on turbidite records. *Ann. Rev. Mar. Sci.*, **3**, 35–66.
- Guiastrennec-Faugas, L., Gillet, H., Jacinto, R.S., Dennielou, B., Hanquiez, V., Schmidt, S., Simplet, L. and Rousset, A.** (2020) Upstream migrating knickpoints and related sedimentary processes in a submarine canyon from a rare 20-year morphobathymetric time-lapse (Capbreton submarine canyon, Bay of Biscay, France). *Mar. Geol.*, **423** (106143), 1–18.
- Guiastrennec-Faugas, L., Gillet, H., Peakall, J., Dennielou, B., Galliot, A. and Jacinto, R.S.** (2021) Initiation and evolution of knickpoints and their role in cut-and-fill processes in active submarine channels. *Geology*, **49**(3), 314–319.
- Hage, S., Cartigny, M.J.B., Clare, M.A., Sumner, E.J., Vendettuoli, D., Clarke, J.E.H., Hubbard, S.M., Talling, P.J., Lintern, D.G., Stacey, C.D., Englert, R.G., Vardy, M.E., Hunt, J.E., Yokokawa, M., Parsons, D.R., Hizzett, J.L., Azpiroz-zabala, M. and Vellinga, A.J.** (2018) How to recognize crescentic bedforms formed by supercritical turbidity currents in the geologic record: Insights from active submarine channels. *Geology*, **46**(6), 563–566.
- Hage, S., Galy, V.V., Cartigny, M.J.B., Acikalin, S., Clare, M.A., Gr ocke, D.R., Hilton, R.G., Hunt, J.E., Lintern, D.G., McGhee, C.A., Parsons, D.R., Stacey, C.D., Sumner, E.J. and Talling, P.J.** (2020) Efficient preservation of young terrestrial organic carbon in sandy turbidity-current deposits. *Geology*, **48**(9), 882–887.
- Hansen, L.A.S., Callow, R.H.T., Kane, I.A., Gamberi, F., Rovere, M., Cronin, B.T. and Kneller, B.C.** (2015) Genesis and character of thin-bedded turbidites associated with submarine channels. *Mar. Pet. Geol.*, **67**, 852–879.
- Hansen, L.A.S., Callow, R., Kane, I.A. and Kneller, B.C.** (2017b) Differentiating submarine channel related thin-bedded turbidite facies: outcrop example from the Rosario Formation, Mexico. *Sed. Geol.*, **358**, 19–34.
- Hansen, L., Janocko, M., Kane, I.A. and Kneller, B.** (2017a) Submarine channel evolution, terrace development, and preservation of intra-channel thin-bedded turbidites: Mahin and Avon channels, offshore Nigeria. *Mar. Geol.*, **383**, 146–167.
- Houghton, P.D.** (2000) Evolving turbidite systems on a deforming basin floor, Tabernas, SE Spain. *Sedimentology*, **47**, 497–518.
- Heerema, C.J., Talling, P.J., Cartigny, M.J., Paull, C.K., Bailey, L., Simmons, S.M., Parsons, D.R., Clare, M.A., Gwiazda, R., Lundsten, E., Anderson, K., Maier, K.L., Xu, J.P., Sumner, E.J., Rosenberger, K., Gales, J., McGann, M., Carter, L., Pope, E. and Monterey Coordinated Canyon Experiment (CEE) Team.** (2020) What determines the downstream evolution of turbidity currents? *Earth Planet. Sci. Lett.*, **532**, 116023.
- Heezen, B.C., Ewing, M. and Menzies, R.J.** (1955) The influence of submarine turbidity currents on abyssal productivity. *Oikos*, **6**(2), 170–182.
- Heijnen, M.S., Clare, M.A., Cartigny, M.J.B., Talling, P.J., Hage, S., Lintern, D.G., Stacey, C., Parsons, D.R.,**

- Simmons, S.M., Chen, Y., Sumner, E.J., Dix, J.K. and Hughes Clarke, J.E. (2020) Rapidly-migrating and internally-generated knickpoints can control submarine channel evolution. *Nat. Commun.*, **11**(3129), 1–15.
- Heiniö, P. and Davies, R.J. (2007) Knickpoint migration in submarine channels in response to fold growth, western Niger Delta. *Mar. Pet. Geol.*, **24**(6–9), 434–449.
- Hill, P.R. (2012) Changes in submarine channel morphology and slope sedimentation patterns from repeat multibeam surveys in the Fraser River delta, western Canada. In: *Sediments, Morphology and Sedimentary Processes on Continental Shelves: Advances in Technologies, Research and Applications* (Eds Li, M.Z., Sherwood, C.R. and Hill, P.R.), *International Association of Sedimentologists Special Publications*, **44**, 47–70.
- Hodgson, D.M., Browning, J.V., Miller, K.G., Hesselbo, S., Poyatos-More, M., Mountain, G.S. and Proust, J.-N. (2018) Sedimentology, stratigraphic context, and implications of Miocene bottomset deposits, offshore New Jersey. *Geosphere*, **14**, 95–114.
- Hodgson, D.M., Di Celma, C., Brunt, R.L. and Flint, S.S. (2011) Submarine slope degradation and aggradation and the stratigraphic evolution of channel-levee systems. *J. Geol. Soc. London*, **168**, 625–628.
- Hodgson, D.M., Kane, I.A., Flint, S.S., Brunt, R.L. and Ortiz-Karppf, A. (2016) Time-transgressive confinement on the slope and the progradation of basin-floor fans: implications for the sequence stratigraphy of deep-water deposits. *J. Sed. Res.*, **86**(2), 73–86.
- Hubbard, S.M., Covault, J.A., Fildani, A. and Romans, B.W. (2014) Sediment transfer and deposition in slope channels: deciphering the record of enigmatic deep-sea processes from outcrop. *Geol. Soc. Am. Bull.*, **126**, 857–871.
- Hubbard, S.M., Jobe, Z.R., Romans, B.W., Covault, J.A., Sylvester, Z. and Fildani, A. (2020) The stratigraphic evolution of a submarine channel: linking seafloor dynamics to depositional products. *J. Sed. Res.*, **90**(7), 673–686.
- Hughes Clarke, J.E. (2016) First wide-angle view of channelized turbidity currents links migrating cyclic steps to flow characteristics. *Nat. Commun.*, **7**(11896), 1–13.
- Jackson, C.-A.-L. (2011) Three-dimensional seismic analysis of megaclast deformation within a mass transport deposit; implications for debris flow kinematics. *Geology*, **39**, 203–206.
- Janocko, M., Nemec, W., Henriksen, S. and Warchoł, M. (2013) The diversity of deep-water sinuous channel belts and slope valley-fill complexes. *Mar. Pet. Geol.*, **41**, 7–34.
- Jegou, I., Savoye, B., Pirmez, C. and Droz, L. (2008) Channel-mouth lobe complex of the recent Amazon Fan: the missing piece. *Mar. Geol.*, **252**, 62–77.
- Jiao, R., Seward, D., Little, T.A. and Kohn, B.P. (2015) Unroofing of fore-arc ranges along the Hikurangi Margin, New Zealand: constraints from low-temperature thermochronology. *Tectonophysics*, **656**, 39–51.
- Jobe, Z.R., Howes, N.C., Straub, K.M., Cai, D., Deng, H., Laugier, F.J., Pettinga, L.A. and Shumaker, L.E. (2020) Comparing aggradation, superelevation, and avulsion frequency of submarine and fluvial channels. *Front. Earth Sci.*, **8**(53), 1–22.
- Jobe, Z.R., Sylvester, Z., Parker, A.O., Howes, N., Slowey, N. and Pirmez, C. (2015) Rapid adjustment of submarine channel architecture to changes in sediment supply. *J. Sed. Res.*, **85**(6), 729–753.
- Kane, I.A. and Hodgson, D.M. (2011) Sedimentological criteria to differentiate submarine channel levee subenvironments: Exhumed examples from the Rosario Fm. (Upper Cretaceous) of Baja California, Mexico, and the Fort Brown Fm. (Permian), Karoo Basin, S. Africa. *Mar. Pet. Geol.*, **28**(3), 807–823.
- Kneller, B. (1995) Beyond the turbidite paradigm: physical models for deposition of turbidites and their implications for reservoir prediction. In: *Characterization of Deep Marine Clastic Systems* (Eds Hartley, A.J. and Prosser, D.J.), *Geological Society, London, Special Publications*, **94**, 31–49.
- Kneller, B. (2003) The influence of flow parameters on turbidite slope channel architecture. *Mar. Pet. Geol.*, **20**(6–8), 901–910.
- Kneller, B., Bozetti, G., Callow, R., Dykstra, M., Hansen, L., Kane, I., Li, P., McArthur, A., Catharina, A.S., Dos Santos, T. and Thompson, P. (2020) Architecture, process, and environmental diversity in a late Cretaceous slope channel system. *J. Sediment. Res.*, **90**(1), 1–26.
- Kneller, B., Dykstra, M., Fairweather, L. and Milana, J.P. (2016) Mass-transport and slope accommodation: implications for turbidite sandstone reservoirs. *Am. Assoc. Petrol. Geol. Bull.*, **100**(2), 213–235.
- Kolla, V., Bandyopadhyay, A., Gupta, P., Mukherjee, B. and Ramana, D.V. (2012) Morphology and internal structure of a recent upper Bengal Fan–valley complex. In: *Application of the Principles of Seismic Geomorphology to Continental-Slope and Base-of-Slope Systems: Case Studies from Seafloor and Near-Seafloor Analogues*. (Eds Prather, B.E., Deptuck, M.E., Mohrig, D., Van Hoorn, B. and Wynn, R.B.), *SEPM Special Publications*, **99**, 347–369.
- Kolla, V., Bourges, P.h., Urruty, J.-M. and Safa, P. (2001) Evolution of deep-water Tertiary sinuous channels offshore Angola (west Africa) and implications for reservoir architecture. *Am. Assoc. Petrol. Geol. Bull.*, **85**, 1373–1405.
- Kremer, C.H., Mchargue, T., Scheucher, L. and Graham, S.A. (2018) Transversely-sourced mass-transport deposits and stratigraphic evolution of a foreland submarine channel system: deep-water tertiary strata of the Austrian Molasse Basin. *Mar. Pet. Geol.*, **92**, 1–19.
- Lamb, S. (2011) Cenozoic tectonic evolution of the New Zealand plate-boundary zone: a review. *Tectonophysics*, **509**, 135–164.
- Lambert, A. and Giovanoli, F. (1988) Records of riverborne turbidity currents and indications of slope failures in the Rhone delta of Lake Geneva. *Limnol. Oceanogr.*, **33**, 458–468.
- Lewis, K.B. (1994) The 1500-km-long Hikurangi Channel: trench-axis channel that escapes its trench, crosses a plateau, and feeds a fan drift. *Geo.-Mar. Lett.*, **14**, 19–28.
- Lewis, K.B. and Barnes, P.M. (1999) Kaikoura Canyon, New Zealand: active conduit from near-shore sediment zones to trench-axis channel. *Mar. Geol.*, **162**, 39–69.
- Lewis, K.B., Collot, J.Y. and Lallemand, S.E. (1998) The dammed Hikurangi Trough: a channel-fed trench blocked by subducting seamounts and their wake avalanches (New Zealand-France GeodyNZ Project). *Basin Res.*, **10**, 441–468.
- Lewis, K.B. and Pantin, H.M. (2002) Channel-axis, overbank and drift sediment waves in the southern Hikurangi Trough, New Zealand. *Mar. Geol.*, **192**, 123–151.
- Lewis, K.B. and Pettinga, J.R. (1993) The emerging, imbricate frontal wedge of the Hikurangi margin. *Sed. Basins World*, **2**, 225–250.

- Li, P., Kneller, B., Thompson, P., Bozetti, G. and dos Santos, T. (2018) Architectural and facies organisation of slope channel fills: Upper Cretaceous Rosario Formation, Baja California, Mexico. *Mar. Pet. Geol.*, **92**, 632–649.
- Liang, C., Liu, C., Xie, X., Yu, X., He, Y., Chen, H., Zhou, Z., Tian, D., Lu, B., Mi, H., Li, M., Zhang, H. and Yang, Y. (2020) The role of large-scale mass wasting processes in changing the sediment dispersal pattern in the deep-water Central Canyon of the northwestern South China Sea. *Mar. Pet. Geol.*, **122**(104693), 1–16.
- Macauley, R.V. and Hubbard, S.M. (2013) Slope channel sedimentary processes and stratigraphic stacking, Cretaceous Tres Pasos Formation slope system, Chilean Patagonia. *Mar. Pet. Geol.*, **41**, 146–162.
- Maier, K.L., Fildani, A., Paull, C.K., Graham, S.A., McHargue, T.R., Caress, D.W. and McGann, M. (2011) The elusive character of discontinuous deep-water channels: new insights from Lucia Chica channel system, offshore California. *Geology*, **39**, 327–330.
- Maier, K.L., Fildani, A., McHargue, T., Paull, C.K., Graham, S.A. and Caress, D.W. (2012) Deep-water punctuated channel migration: high-resolution subsurface data from the Lucia Channel System, offshore California. *J. Sed. Res.*, **82**, 1–8.
- Masalimova, L.U., Lowe, D.R., Mchargue, T. and Derksen, R. (2015) Interplay between an axial channel belt, slope gullies and overbank deposition in the Puchkirchen Formation in the Molasse Basin, Austria. *Sedimentology*, **62**(6), 1717–1748.
- Mayall, M., Jones, E. and Casey, M. (2006) Turbidite channel reservoirs—key elements in facies prediction and effective development. *Mar. Pet. Geol.*, **23**, 821–841.
- Mayall, M. and Stewart, I. (2000) The architecture of turbidite slope channels. In: *Deep-Water Reservoirs of the World* (Eds Weimer, P., Slatt, R.M., Coleman, J., Rosen, N.C., Nelson, H., Bouma, A.H., Styzen, M.J. and Lawrence, D.T.), *Gulf Coast Section SEPM, 20th Annual Research Conference*, 578–586.
- McArthur, A.D., Bailleul, J., Mahieux, G., Claussmann, B., Wunderlich, A. and McCaffrey, W.D. (2021) Deformation-sedimentation feedback and the development of anomalously thick aggradational turbidite lobes: outcrop and subsurface examples from the Hikurangi Margin, New Zealand. *J. Sed. Res.*, **91**(4), 362–389.
- McArthur, A.D., Claussmann, B., Bailleul, J., McCaffrey, W.D. and Clare, A. (2019) Variation in syn-subduction sedimentation patterns from inner to outer portions of deep-water fold and thrust belts: examples from the Hikurangi subduction margin of New Zealand. In: *Fold and Thrust Belts: Structural Style, Evolution and Exploration* (Eds Hammerstein, J.A., Di Cuia, R., Cottam, M.A., Zamora, G. and Butler, R.W.H.), *Geological Society, London, Special Publications*, **490**, 490–545.
- McArthur, A.D. and McCaffrey, W.D. (2019) Sedimentary architecture of detached deep-marine canyon heads: Examples from the East Coast Basin of New Zealand. *Sedimentology*, **66**, 1067–1101.
- McArthur, A.D. and Tek, D.E. (2021) Controls on the origin and evolution of deep-ocean trench-axial channels. *Geology*, <https://doi.org/10.1130/G48612.1>.
- McCaffrey, W.D., Gupta, S. and Brunt, R. (2002) Repeated cycles of submarine channel incision, infill and transition to sheet sandstone development in the Alpine Foreland Basin, SE France. *Sedimentology*, **49**, 623–635.
- McCave, I.N. and Carter, L. (1997) Recent sedimentation beneath the Deep Western Boundary Current off northern, New Zealand. *Deep-Sea Res. Part I: Oceanogr. Res. Pap.*, **44**, 1203–1237.
- McHargue, T., Pyrcz, M.J., Sullivan, M.D., Clark, J.D., Fildani, A., Romans, B.W., Covault, J.A., Levy, M., Posamentier, H.W. and Drinkwater, N.J. (2011) Architecture of turbidite channel systems on the continental slope: patterns and predictions. *Mar. Pet. Geol.*, **28**(3), 728–743.
- Migeon, S., Savoye, B., Babonneau, N. and Spy Andersson, F.L. (2004) Process of sediment-wave construction along the present Zaire deep-sea meandering channel: role of meanders and flow stripping. *J. Sed. Res.*, **74**, 580–598.
- Millington, J.J. and Clark, J.D. (1995) The Charo/Arro canyon-mouth sheet system, south-central Pyrenees, Spain: a structurally influenced zone of sediment dispersal. *J. Sed. Res.*, **B65**, 443–454.
- Mitchell, N. (2004) Form of submarine erosion from confluences in Atlantic USA continental slope canyons. *Am. J. Sci.*, **304**, 590–611.
- Mitchell, W.H., Whittaker, A.C., Mayall, M., Lonergan, L. and Pizzi, M. (2020) Quantifying the relationship between structural deformation and the morphology of submarine channels on the Niger Delta continental slope. *Basin Res.*, **33**(1), 1–24.
- Moscaredelli, L. and Wood, L. (2008) New classification system for mass transport complexes in offshore Trinidad. *Basin Res.*, **20**(1), 73–98.
- Mountjoy, J.J., Barnes, P.M. and Pettinga, J.R. (2009) Morphostructure and evolution of submarine canyons across an active margin: Cook Strait sector of the Hikurangi Margin, New Zealand. *Mar. Geol.*, **260**, 45–68.
- Mountjoy, J.J., Howarth, J.D., Orpin, A.R., Barnes, P.M., Bowden, D.A., Rowden, A.A., Schimel, A.C.G., Holden, C., Horgan, H.J., Nodder, S.D., Patton, J.R., Lamarche, G., Gerstenberger, M., Micallef, A., Pallentin, A. and Kane, T. (2018) Earthquakes drive large-scale submarine canyon development and sediment supply to deep-ocean basins. *Sci. Adv.*, **4**(3), 1–8.
- Nakajima, T. and Kneller, B.C. (2013) Quantitative analysis of the geometry of submarine levees. *Sedimentology*, **60**, 877–910.
- Nakajima, T. and Satoh, M. (2001) The formation of large mudwaves by turbidity currents on the levees of the Toyama deep-sea channel, Japan Sea. *Sedimentology*, **48**, 435–463.
- Naranjo-Vesga, J., Ortiz-Karppf, A., Wood, L., Jobe, Z., Paniagua-Arroyave, J.F., Shumaker, L., Mateus-Tarazona, D. and Galindo, P. (2020) Regional controls in the distribution and morphometry of deep-water gravitational deposits along a convergent tectonic margin. Southern Caribbean of Colombia. *Mar. Pet. Geol.*, **121**(104639), 1–24.
- Nelson, C.H., Damuth, J.E. and Twichell, D.C. (2011) Interplay of mass-transport and turbidite-system deposits in different active tectonic and passive continental margin settings: external and local controlling factors. In: *Mass-Transport Deposits in Deepwater Settings* (Eds Shipp, C.R., Weimer, P. and Posamentier, H.W.), *SEPM Special Publications*, **96**, 39–66.
- Nicol, A., Mazengarb, C., Chanier, F., Rait, G., Uruski, C. and Wallace, L. (2007) Tectonic evolution of the active Hikurangi subduction margin, New Zealand, since the Oligocene. *Tectonics*, **26**, 1–24.
- Normark, W.R., Hess, G.R., Stow, D.A.V. and Bowen, A.J. (1980) Sediment waves on the Monterey Fan levee: a preliminary physical interpretation. *Mar. Geol.*, **37**, 1–18.

- Normark, W.R., Piper, D.J., Posamentier, H., Pirmez, C. and Migeon, S. (2002) Variability in form and growth of sediment waves on turbidite channel levees. *Mar. Geol.*, **192**, 23–58.
- Nugraha, H.D., Jackson, C.A.L., Johnson, H.D., Hodgson, D.M. and Reeve, M.T. (2019) Tectonic and oceanographic process interactions archived in Late Cretaceous to Present deep-marine stratigraphy on the Exmouth Plateau, offshore NW Australia. *Basin Res.*, **31**(3), 405–430.
- Nugraha, H.D., Jackson, C.-A.-L., Johnson, H.D. and Hodgson, D.M. (2020) Lateral variability in strain along the toewall of a mass transport deposit: a case study from the Makassar Strait, offshore Indonesia. *J. Geol. Soc.*, **177** (6), 1261–1279.
- Nwoko, J., Kane, I. and Huuse, M. (2020b) Mass transport deposit (MTD) relief as a control on post-MTD sedimentation: Insights from the Taranaki Basin, offshore New Zealand. *Mar. Pet. Geol.*, **120**(104489), 1–12.
- Nwoko, J., Kane, I. and Huuse, M. (2020a) Megaclasts within mass-transport deposits: their origin, characteristics and effect on substrates and succeeding flows. In: *Subaqueous Mass Movements and their Consequences: Advances in Process Understanding, Monitoring and Hazard Assessments* (Eds Georgiopoulou, A., Amy, L.A., Benetti, S., Chaytor, J.D., Clare, M.A., Gamboa, D., Haughton, P.D.W., Moernaut, J. and Mountjoy, J.J.), *Geological Society, London, Special Publications*, **500**, 515–530.
- Ogata, K., Mutti, E., Andrea, G. and Tinterri, R. (2012) Tectonophysics Mass transport-related stratal disruption within sedimentary mélanges: Examples from the northern Apennines (Italy) and south-central Pyrenees (Spain). *Tectonophysics*, **568–569**, 185–199.
- Ortiz-Karppf, A., Hodgson, D.M. and McCaffrey, W.D. (2015) The role of mass-transport complexes in controlling channel avulsion and the subsequent sediment dispersal patterns on an active margin: The Magdalena Fan, offshore Colombia. *Mar. Pet. Geol.*, **64**, 58–75.
- Ortiz-Karppf, A., Hodgson, D.M., Jackson, C.A.L. and McCaffrey, W.D. (2017) Influence of seabed morphology and substrate composition on mass-transport flow processes and pathways: insights from the Magdalena fan, offshore Colombia. *J. Sed. Res.*, **87**, 1–21.
- Paul, C.K., Caress, D.W., Ussler, W., Lundsten, E. and Meiner-Johnson, M. (2011) High-resolution bathymetry of the axial channels within Monterey and Soquel submarine canyons, offshore central California. *Geosphere*, **7**, 1077–1101.
- Paul, C.K., Talling, P.J., Maier, K.L., Parsons, D., Xu, J., Caress, D.W., Gwiazda, R., Lundsten, E.M., Anderson, K., Barry, J.P., Chaffey, M., Reilly, T.O., Rosenberger, K.J., Gales, J.A., Kieft, B., McGann, M., Simmons, S.M., McCann, M., Sumner, E.J., Clare, M.A. and Cartigny, M.J. (2018) Powerful turbidity currents driven by dense basal layers. *Nat. Commun.*, **9**(4114), 1–9.
- Peakall, J., Kane, I.A., Masson, D.G., Keevil, G., McCaffrey, W. and Corney, R. (2012) Global (latitudinal) variation in submarine channel sinuosity. *Geology*, **40**, 11–14.
- Peakall, J., McCaffrey, W.D. and Kneller, B.C. (2000) A process model for the evolution, morphology, and architecture of sinuous submarine channels. *J. Sed. Res.*, **70**, 434–448.
- Peakall, J. and Sumner, E.J. (2015) Submarine channel flow processes and deposits: a process-product perspective. *Geomorphology*, **244**, 95–120.
- Pickering, K.T., Clark, J.D., Smith, R.D.A., Hiscott, R.N., Ricci Lucchi, F. and Kenyon, N.H. (1995) Architectural element analysis of turbidite systems, and selected topical problems for sand-prone deep-water systems. In: *Atlas of Deep Water Environments: Architectural Style in Turbidite Systems* (Eds Pickering, K.T., Hiscott, R.N., Kenyon, N.H., Ricci Lucchi, F. and Smith, R.D.A.), 1–10.
- Pickering, K.T. and Corregidor, J. (2000) 3D Reservoir-Scale Study of Eocene Confined Submarine Fans, South-Central Spanish Pyrenees. In: *Deep-Water Reservoirs of the World*. (Eds Weimer, P., Slatt, R.M., Coleman, J., Rosen, N.C., Nelson, H., Bouma, A.H., Styzen, M.J. and Lawrence, D.T.), *Gulf Coast Section SEPM, 20th Annual Research Conference*, 776–781.
- Pickering, K.T. and Corregidor, J. (2005) Mass transport complexes and tectonic control on confined basin-floor submarine fans, Middle Eocene, south Spanish Pyrenees. In: *Submarine Slope Systems: Processes and Product* (Eds Hodgson, D.M. and Flint, S.S.), *Geological Society, London, Special Publications*, **244**, 51–74.
- Pirmez, C., Beaubouef, R.T., Friedmann, S.J. and Mohrig, D.C. (2000) Equilibrium Profile and Baselevel in Submarine Channels: Examples from Late Pleistocene Systems and Implications for the Architecture of Deepwater Reservoirs. In: *Deep-Water Reservoirs of the World* (Eds Weimer, P., Slatt, R.M., Coleman, J., Rosen, N.C., Nelson, H., Bouma, A.H., Styzen, M.J. and Lawrence, D.T.), *Gulf Coast Section SEPM, 20th Annual Research Conference*, 782–805.
- Pirmez, C. and Flood, R.D. (1995) Morphology and structure of Amazon Channel. In: *Proceedings of the Ocean Drilling Program, Initial Reports* (Eds Flood, R.D., Piper, D.J.W. and Klaus, A.), **155**, pp. 23–45. College Station, TX.
- Plaza-Faverola, A., Klaeschen, D., Barnes, P.M., Pecher, I., Henrys, S. and Mountjoy, J. (2012) Evolution of fluid expulsion and concentrated hydrate zones across the southern Hikurangi subduction margin, New Zealand: An analysis from depth migrated seismic data. *Geochem. Geophys. Geosyst.*, **13**(8), 1–21.
- Posamentier, H.W. (2003) Depositional elements associated with a basin floor channel-levee system: case study from the Gulf of Mexico. *Mar. Pet. Geol.*, **20**, 677–690.
- Posamentier, H.W. and Kolla, V. (2003) Seismic geomorphology and stratigraphy of depositional elements in deep-water settings. *J. Sed. Res.*, **73**(3), 367–388.
- Posamentier, H.W. and Martinsen, O.J. (2011) The character and genesis of submarine mass-transport deposits: insights from outcrop and 3D seismic data. In: *Mass-Transport Deposits in Deepwater Settings* (Eds Shipp, R.G., Weimer, P. and Posamentier, H.W.), *SEPM Special Publications*, **96**, 7–38.
- Prins, M.A. and Postma, G. (2000) Effects of climate, sea level, and tectonics unravelled for last deglaciation turbidite records of the Arabian sea. *Geology*, **28**, 375–378.
- Sawyer, D., Flemings, P.B., Shipp, R. and Winker, C. (2007) Seismic geomorphology, lithology, and evolution of the late Pleistocene Mars-Ursa turbidite region, Mississippi Canyon area, northern Gulf of Mexico. *Am. Asso. Petrol. Geol. Bull.*, **91**, 215–234.
- Sawyer, D., Flemings, P.B. and Nikolinakou, M. (2014) Continuous deep-seated slope failure recycles sediments and limits levee height in submarine channels. *Geology*, **42**, 15–18.
- Schwab, A., Cronin, B. and Ferreira, H. (2007) Seismic expression of channel outcrops: offset stacked versus amalgamated channel systems. *Mar. Pet. Geol.*, **24**(6–9), 504–514.

- Shumaker, L.E., Jobe, Z.R., Johnstone, S.A., Pettinga, L.A., Cai, D. and Moody, J.D.** (2018) Controls on submarine channel-modifying processes identified through morphometric scaling relationships. *Geosphere*, **14**, 2171–2187.
- Soutter, E.L., Bell, D., Cumberpatch, Z.A., Ferguson, R.A., Spychala, Y.T., Kane, I.A. and Eggenhuisen, J.T.** (2021) The influence of confining topography orientation on experimental turbidity currents and geological implications. *Front. Earth Sci.*, **8**(540633), 1–25.
- Sylvester, Z., Pirmez, C. and Cantelli, A.** (2011) A model of submarine channel-levee evolution based on channel trajectories: implications for stratigraphic architecture. *Mar. Pet. Geol.*, **28**, 716–727.
- Tek, D.E., Poyatos-Moré, M., Patacci, M., McArthur, A.D., Colombera, L., Cullen, T.M. and McCaffrey, W.D.** (2020) Syndepositional tectonics and mass-transport deposits control channelized, bathymetrically complex deep-water systems (Ainsa depocenter, Spain). *J. Sed. Res.*, **90**(7), 729–762.
- Tökés, L. and Patacci, M.** (2018) Quantifying tabularity of turbidite beds and its relationship to the inferred degree of basin confinement. *Mar. Pet. Geol.*, **97**, 659–671.
- Vendettuoli, D., Clare, M.A., Hughes Clarke, J.E., Vellinga, A., Hizzet, J., Hage, S., Cartigny, M.J.B., Talling, P.J., Waltham, D., Hubbard, S.M., Stacey, C. and Lintern, D.G.** (2019) Daily bathymetric surveys document how stratigraphy is built and its extreme incompleteness in submarine channels. *Earth Planet. Sci. Lett.*, **515**, 231–247.
- Wallace, L.M., Barnes, P., Beavan, J., Dissen, R.V., Litchfield, N., Mountjoy, J., Langridge, R., Lamarche, G. and Pondard, N.** (2012) The kinematics of a transition from subduction to strike-slip: an example from the central New Zealand plate boundary. *J. Geophys. Res.*, **117**, 1–24.
- Wallace, L.M., Beavan, J., McCaffrey, R. and Darby, D.** (2004) Subduction zone coupling and tectonic block rotations in the North Island, New Zealand. *J. Geophys. Res.*, **109**(B12406), 1–21.
- Ward, N.I.P., Alves, T.M. and Blenkinsop, T.G.** (2018) Submarine sediment routing over a blocky mass-transport deposit in the Espírito Santo Basin, SE Brazil. *Basin Res.*, **30**(4), 816–834.
- Watson, S.J., Mountjoy, J.J. and Crutchley, G.J.** (2020) Tectonic and geomorphic controls on the distribution of submarine landslides across active and passive margins, eastern New Zealand. In: *Subaqueous Mass Movements and their Consequences: Advances in Process Understanding, Monitoring and Hazard Assessments* (Eds Georgiopolou, A., Amy, L.A., Benetti, S., Chaytor, J.D., Clare, M.A., Gamboa, D., Haughton, P.D.W., Moernaut, J. and Mountjoy, J.J.), *Geological Society, London, Special Publications*, **500**(1), 477–494.
- Wood, R. and Davy, B.** (1994) The Hikurangi Plateau. *Mar. Geol.*, **118**, 153–173.
- Wu, N., Jackson, C.-A.-L., Johnson, H.D., Hodgson, D.M., Clare, M.A., Nugraha, H.D. and Li, W.** (2021) The formation and implications of giant blocks and fluid escape structures in submarine lateral spreads. *Basin Res.*, <https://doi.org/10.1111/bre.12532>.
- Wynn, R.B. and Stow, D.A.V.** (2002) Classification and characterisation of deep-water sediment waves. *Mar. Geol.*, **192**, 7–22.
- Zhong, G. and Peng, X.** (2021) Transport and accumulation of plastic litter in submarine canyons—the role of gravity flows. *Geology*, **49**(5), 581–586.

Manuscript received 21 October 2020; revision accepted 20 April 2021

Supporting Information

Additional information may be found in the online version of this article:

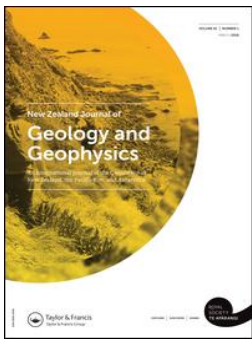
Appendix S1. Table summarizing the minimum, maximum and average values of various dimensional and dip parameters exhibited by the variety of channel-related features described on the seafloor.

Appendix S2. Table containing dimension and dip measurements from the variety of channel-related features (excluding terraces; see S3) seen on the seafloor, measured from profiles 1 to 28 (Figs 2B, 3). See Fig. 4A for reference; data displayed in Fig. 4C, D, E and F.

Appendix S3. Table containing dimension measurements of all terraces observed in the modern channel-walls, measured from profiles 1 to 28 (Figs 2B, 3); see Fig. 4A for reference; data displayed in Fig. 4B.

Appendix S4. Table containing dimension and dip measurements from the seven knickpoints and two knickpoint-zones identified on the modern channel-floor. Data displayed on Figs 2C and 5D.

Appendix S5. Uninterpreted dip map of the seafloor shown in Fig. 5A.



Controls on the architectural evolution of deep-water channel overbank sediment wave fields: insights from the Hikurangi Channel, offshore New Zealand

Daniel E. Tek, Adam D. McArthur, Miquel Poyatos-Moré, Luca Colombera, Charlotte Allen, Marco Patacci & William D. McCaffrey

To cite this article: Daniel E. Tek, Adam D. McArthur, Miquel Poyatos-Moré, Luca Colombera, Charlotte Allen, Marco Patacci & William D. McCaffrey (2021): Controls on the architectural evolution of deep-water channel overbank sediment wave fields: insights from the Hikurangi Channel, offshore New Zealand, New Zealand Journal of Geology and Geophysics, DOI: [10.1080/00288306.2021.1978509](https://doi.org/10.1080/00288306.2021.1978509)

To link to this article: <https://doi.org/10.1080/00288306.2021.1978509>



© 2021 The Author(s). Published by Informa UK Limited, trading as Taylor & Francis Group



[View supplementary material](#)



Published online: 04 Oct 2021.



[Submit your article to this journal](#)



[View related articles](#)



[View Crossmark data](#)

Controls on the architectural evolution of deep-water channel overbank sediment wave fields: insights from the Hikurangi Channel, offshore New Zealand

Daniel E. Tek^a, Adam D. McArthur^a, Miquel Poyatos-Moré^b, Luca Colombera^a, Charlotte Allen^c, Marco Patacci^a and William D. McCaffrey^a

^aSchool of Earth and Environment, University of Leeds, Leeds, UK; ^bDepartament de Geologia, Universitat Autònoma de Barcelona, Cerdanyola del Vallés, Spain; ^cShell International Ltd., London, UK

ABSTRACT

Deep-water channels can be bound by overbank deposits, resulting from overspilling flows, which are often ornamented with sediment waves. Here, high-resolution bathymetry, backscatter, and 2D and 3D seismic data are integrated to discern the controls on flow processes on the overbank areas of the Hikurangi Channel. Qualitative seismic interpretation and quantitative analyses of sediment wave morphologies and distributions are conducted through the shallowest 600 m of stratigraphy up to the seafloor. Four outer-bend wave fields are present throughout the studied stratigraphy on the landward margin (left margin looking down-channel) only. Originally closely spaced or combined, these fields evolved to become spatially separated; two of the separate wave fields became further subdivided into distinct outer- and inner-bend fields, whose constituent waves developed distinct differences in morphology and distribution. Sediment wave character is used to interpret the direction and strength of overbank flow. Nine controls on such flow and associated deposition are identified: flow versus conduit size, overbank gradient, flow tuning, Coriolis forcing, contour current activity, flow reflection, centrifugal forcing, interaction with externally derived flows, and interaction of overspill from different locations. Their relative importance may vary across parts of overbank areas, both spatially and temporally, controlling wave field development such that: (1) outer-bend wave fields only develop on the landward margin; (2) the influence of centrifugal force on outer-bend overbanks has increased through time, accompanying a general increase in channel sinuosity; (3) inner-bend wave fields on the landward margin form by the interaction of Coriolis-enhanced inner-bend overbank flow, and outer-bank flow from up-channel bends; (4) inner-bend fields on the oceanward margin form by the interaction of axial flow through wave troughs, and a transverse, toward-channel flow component. This work has implications for interpreting overbank flow from seafloor and seismic data, and for palaeogeographic reconstructions from outcrop data.

ARTICLE HISTORY

Received 17 July 2021
Accepted 6 September 2021

HANDLING EDITOR

Lorna Strachan

KEYWORDS

Overspill; levee; submarine channel; seismic; bathymetry; seafloor; quantitative; sediment waves

Introduction

Deep-water channels are subaqueous conduits through which turbidity currents and other sediment-laden flows transport sediment (Normark 1970), which can contain pollutants (Kane et al. 2020; Zhong and Peng 2021), organic carbon (Hage et al. 2020), fresh water (Kao et al. 2010), and nutrients (Heezen et al. 1955), to the deep seas. Turbidity currents thicker than the depth of the channel they traverse spill onto their overbank areas, depositing fine-grained ‘overbank’ sediments from dilute flows (Piper and Normark 1983). Overbank deposits are accumulations of sediments that can reach almost one thousand metres in thickness and tens of kilometres in width (Pirmez and Flood 1995; Nakajima and Kneller 2013). These deposits can provide a more complete depositional record of channel

evolution than deposits formed on the floors of palaeo-channels, which are susceptible to being excavated by repeated episodes of incision (Morris et al. 2014). Previous studies have led to the development of models of overbank flow and architecture evolution in which progressive trends of diminishing grain size (typically from fine sand to mud) and deposit thickness are seen in transects away from the levee crest (Kane et al. 2007; Morris et al. 2014). However, these simple trends may be complicated by the influence of factors such as: variations in the size of turbidity currents relative to their host conduit (Dennielou et al. 2006), flow ‘tuning’ (Mohrig and Buttles 2007; Kelly et al. 2019), variations in overbank slope gradient (Kane et al. 2010; Nakajima and Kneller 2013), sinuosity (Timbrell 1993; Kane et al. 2008), structural confinement (Clark and Cartwright 2011), the Coriolis

CONTACT Daniel E. Tek  ee11dt@leeds.ac.uk

 Supplemental data for this article can be accessed <https://doi.org/10.1080/00288306.2021.1978509>.

© 2021 The Author(s). Published by Informa UK Limited, trading as Taylor & Francis Group
This is an Open Access article distributed under the terms of the Creative Commons Attribution-NonCommercial-NoDerivatives License (<http://creativecommons.org/licenses/by-nc-nd/4.0/>), which permits non-commercial re-use, distribution, and reproduction in any medium, provided the original work is properly cited, and is not altered, transformed, or built upon in any way.

force (Klaucke et al. 1998; Cossu et al. 2015), and contour currents (Fuhrmann et al. 2020; Miramontes et al. 2020).

Channel overbank areas are often ornamented with sediment waves. Sediment waves are undulating bedforms that are commonly observed on the modern seafloor in a range of sedimentary environments (see Wynn and Stow 2002; Symons et al. 2016). The crests of sediment waves on channel overbanks are typically orientated parallel to the slope contours (Wynn and Stow 2002), meaning they can range in orientation from parallel (e.g. Nakajima and Satoh 2001) to perpendicular to their adjacent channel (e.g. Kuang et al. 2014). In crest-perpendicular transects overbank sediment waves have distinct stoss (upstream) sides that typically dip toward the channel and lee (downstream) sides that dip away from the channel, and typically exhibit wavelengths up to 7 km and heights up to 80 m (Wynn and Stow 2002). They are found adjacent to reaches of channels that may extend hundreds of kilometres (e.g. Damuth 1979; Migeon et al. 2004), and form fields that can extend for tens of kilometres (laterally) away from their formative channel (e.g. Normark et al. 1980; Carter et al. 1990). The upstream migration of sediment waves generates quasi-sinusoidal geometries commonly observed in seismic data imaging sediments beneath sediment wave fields. These depositional geometries can be present through hundreds of metres of stratigraphy (e.g. Migeon et al. 2000, 2001; Nakajima and Satoh 2001). Two models have been proposed to explain the generation of such geometries: (a) flows with uniformly low Froude numbers, wherein increases in near-bed shear stresses on the lee sides inhibits deposition (the 'lee wave model'; Flood 1988; Figure 1A); or (b) flows with variable Froude numbers, wherein supercritical flow on the lee sides of the waves inhibits deposition, and a transition to subcritical flow occurs on the stoss side, essentially making the waves 'cyclic-steps' (Slootman and Cartigny 2020; Figure 1B).

It is commonly inferred that the crests of overbank sediment waves are orientated subperpendicular to the dominant local flow direction (Nakajima et al. 1998; Migeon et al. 2000), and their wavelengths and heights scale with the thickness, and velocity, of the

overspilling flows that formed them (Normark et al. 2002). Therefore, the morphology of sediment waves can be valuable in inferring the dynamics of overspilling flow from modern deep-water channels (Normark et al. 1980, 2002). However, a lack of high-resolution, 3D seismic data imaging deep-water overbank deposits has hitherto inhibited analysis of their architectures and morphological analysis of buried sediment waves. This has hindered the capacity to infer the nature of, and controls upon, ancient overbank flow dynamics, and how the importance of different controls may change through time.

Here, high-resolution bathymetry, and 2D and 3D seismic data, that image the seafloor geomorphology and subsurface architecture of the Hikurangi Channel and its overbanks, offshore New Zealand, are integrated to address this knowledge gap. This contribution complements Tek et al. (2021), which detailed the channel evolution; the focus here is on the overbank areas. Lewis and Pantin (2002) described the seafloor expression of the Hikurangi Channel and its overbanks, using swath bathymetry and backscatter data. They interpreted centrifugal force, the Coriolis force, and the action of bottom currents as controls on flow dynamics on the overbanks. They also performed a subsurface interpretation, based on 2D seismic data and shallow (<5 m) cores, but did not possess 3D constraint to speculate on the evolution of the wave fields. This study aims to: (a) determine the controls on overbank flow processes, deposition, and resultant depositional architectures, through ~600 m of overbank stratigraphy, and compare these controls with those invoked by Lewis and Pantin (2002); (b) determine how these controls interact with one another, constraining the spatial variability of their influence, and how their relative importance has changed through the depositional period; (c) discern the origin of enigmatic wave-like features on inner-overbanks of channel bends. The objectives of this study are to: (a) characterise the seafloor geomorphology and subsurface architecture of the overbank stratigraphy; (b) identify, and categorise different overbank feature types, and interpret their genesis; (c) perform a quantitative analysis of sediment wave morphologies on the seafloor and subsurface stratigraphy. The

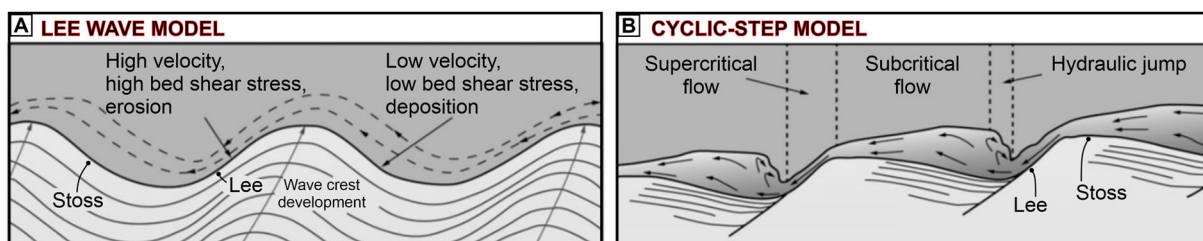


Figure 1. Schematic diagrams showing how sediment waves migrate via **A**, the lee wave model (from Symons et al. 2016; after Flood 1988), and **B**, the cyclic-step model (from Symons et al. 2016; after Cartigny et al. 2011); flow direction is from right to left on both diagrams.

results of this study have fundamental implications for determining controls on the evolution of deep-water channel-levee systems and can facilitate the development of understanding of channel-levee evolution in other modern and ancient systems.

Geological setting

The study area covers $\sim 21,000$ km² of the trench-floor, adjacent to the junction between the Chatham Rise and the subducting Pacific plate, containing a ~ 250 km stretch of the Hikurangi Channel (Figure 2B). This study focuses on the upper ~ 600 m of trench-fill (upper trench fill in Figures 3 and 4), wherein ten channel-forms can be traced for the ~ 140 km length of the 3D seismic survey described in the 'data' section (Tek et al. 2021; Figure 4).

The NE flowing ~ 1800 km long Hikurangi Channel (Figure 2; Lewis and Pantin 2002; Mountjoy et al. 2009, 2018; Tek et al. 2021) sits within the NE-SW oriented Hikurangi Trench, which has developed over the last ~ 27 Ma due to the subduction of the Pacific plate beneath the Australian plate (Ballance 1975; Nicol et al. 2007; Barnes et al. 2010; Lamb 2011; Jiao et al. 2015). Most of the trench-fill has accumulated during the last 3.5 Ma (Figure 3A; Ghisetti et al. 2016; Kroeger et al. 2019), and is interpreted to consist predominantly of turbidites associated with the Hikurangi Channel (Lewis 1994; Lewis et al. 1998; McArthur and Tek 2021) and with transverse drainage networks that traversed the slope and subduction wedge (Figure 2B; Mountjoy et al. 2009; McArthur et al. 2021). In the SW of the trench, where this study is focused, the trench-fill is ~ 6 km thick; the top ~ 600 m of stratigraphy, studied herein (Figure 3), is dominated by overbank deposits from the Hikurangi Channel (McArthur and Tek 2021). To the NE, the trench-fill thins to ~ 1 km (Lewis et al. 1998; Barnes et al. 2010; Plaza-Faverola et al. 2012).

The Hikurangi Channel is fed by a network of shelf-incising canyons that capture sediment from the North and South Islands of New Zealand (Carter 1992; Lewis 1994; Lewis et al. 1998; Lewis and Barnes 1999; Mountjoy et al. 2009), and are flushed by earthquake-triggered failure events (Mountjoy et al. 2018; Howarth et al. 2021). Downstream of the confluence with the Cook Strait Canyon, the Hikurangi Channel flows east along the northern margin of the Chatham Rise (Wood and Davy 1994; Davy et al. 2008) for ~ 130 km (Figure 2). It then runs through the trench for ~ 500 km before abruptly changing direction and continuing a further ~ 1150 km across the Hikurangi Plateau and the Pacific abyssal plain (Figure 2; Lewis et al. 1998; Collot et al. 2001; Lewis and Pantin 2002). In the study area, in the proximal part of the trench, where the channel departs from the Chatham

Rise, the overbank areas of the channel are ornamented by the scars from numerous channel-wall failures (Watson et al. 2020; Tek et al. 2021) and by sediment waves (Lewis et al. 1998; Lewis and Pantin 2002).

A change in the nature of the trench-fill (Figure 3) is observed between ~ 600 and ~ 800 m depth (above R4 in Figure 3), from deeper isolated channel-forms that exhibit significant lateral offsets, to shallower aggradational channel-forms that each follows a similar course to their predecessor (Figure 3A; McArthur and Tek 2021). The stratigraphy of interest is located above this transition, where the trench-fill comprises thick, compound overbank deposits that bound the aforementioned aggradational channel-forms.

Contour currents have been identified in the Hikurangi Trench but their locations and orientations are poorly constrained, and their effects have likely changed through time (Carter et al. 2002; Lewis and Pantin 2002; Fernandez et al. 2018; Bailey et al. 2020). For example, based on seafloor geomorphology and seismic architecture, Lewis and Pantin (2002) inferred that a shallow branch of the Deep Western Boundary Current (DWBC) flowed WNW along the northern edge of the Chatham Rise (Figure 2A). The DWBC is interpreted to generate waves on the oceanward channel margin, and to have been active during glacial periods (Lewis and Pantin 2002). However, modern oceanographic data show that the East Cape Current (ECC) is currently the dominant contour current in the study area (Carter et al., 2002; Fernandez et al. 2018). The ECC flows SW following the subduction front before turning anti-clockwise and crossing the channel near or within the study area (Figure 2A); the exact location of its crossing with the channel is unclear.

Data

Analysis of the seafloor was conducted using high-resolution multibeam bathymetry and backscatter data covering $\sim 47,000$ km² (Figure 2A), collected by the National Institute of Water and Atmospheric Research (NIWA) between 2001 and 2013; the data are provided by New Zealand Petroleum and Minerals (NZPAM) as part of their 2017 datapack. Within the study area (Figure 2B), data from two cruises (TAN1207 and TAN1307 respectively) acquired in 2012 and 2013 using an EM302 multibeam echosounder at 30 kHz with a 25 m grid size, are primarily used (Bland et al. 2014; Figure 2B).

Subsurface analysis was conducted using three seismic datasets acquired by Westerngeco: (a) 2600 km² of pre-stack Kirchhoff depth migrated (broadband) 3D seismic data (acquired in 2017) with a horizontal resolution of ~ 25 m and a vertical resolution of ~ 7 m (values accurate at seafloor; Crisóstomo-Figueroa et al. 2020); (b) depth converted 2D seismic data

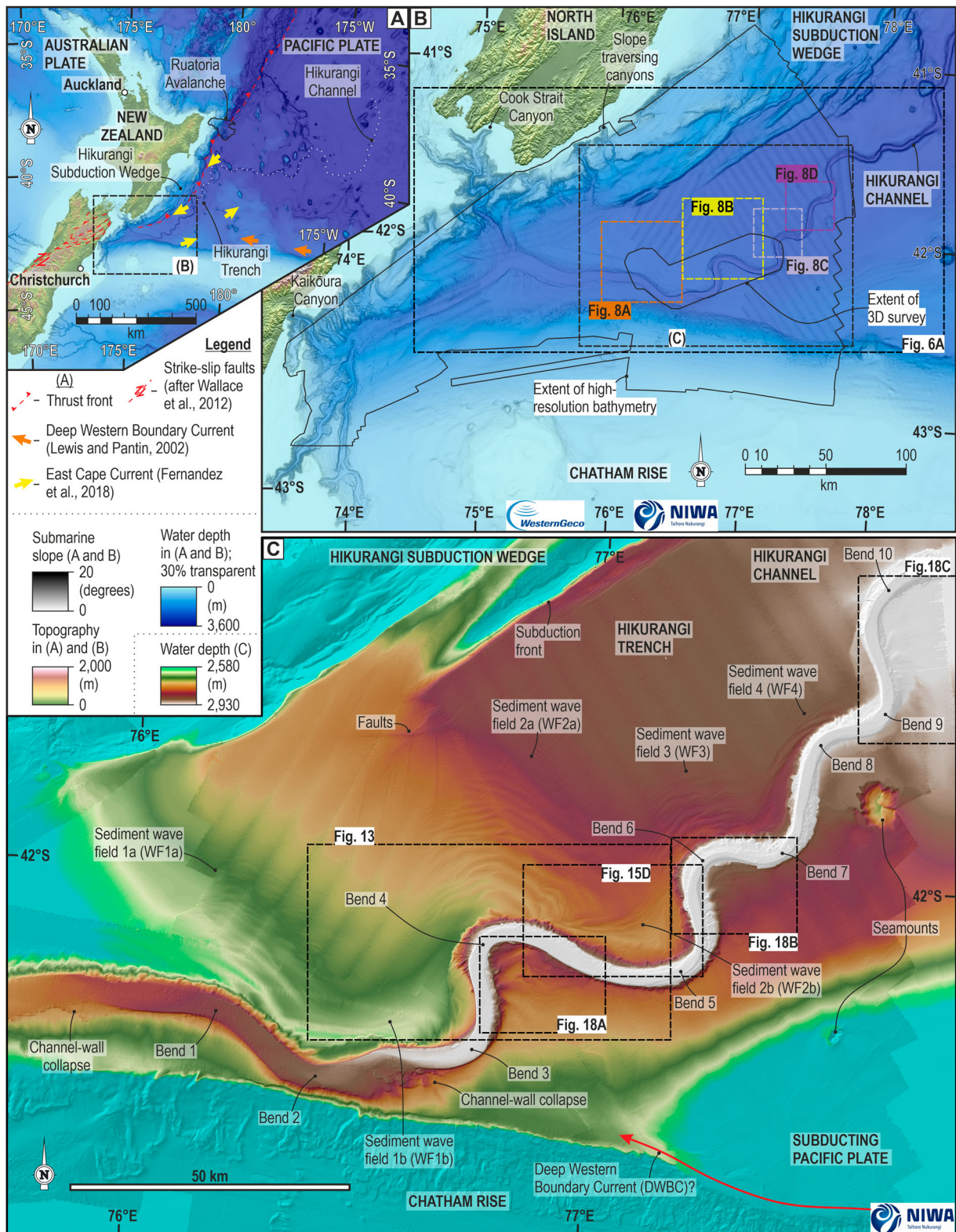


Figure 2. Location maps showing: **A**, the location of the Hikurangi Margin; **B**, the proximal reach of the Hikurangi Channel, showing its relationship with its feeder canyons, the location of the study area slope-traversing trench-perpendicular systems, the location of the study area (see **C**) and the extent of the bathymetry and 3D seismic data used herein; **C**, seafloor morphology in the study area, highlighting the ten channel bends referenced throughout the text, the sediment wave fields on the channel overbanks, and the channels' relationships with the Hikurangi subduction wedge, the Chatham Rise, and the Pacific Plate. Bathymetry data were provided by the New Zealand National Institute for Water and Atmosphere (NIWA) and WesternGeco.

(3–200 Hz frequency), acquired in 2014; (c) time-domain 2D seismic data (30–40 Hz frequency), acquired in 2009. Full-stack data are displayed SEG

positive; a downward decrease in acoustic impedance is shown as a trough (white reflection). All presented seismic sections are shown in depth.

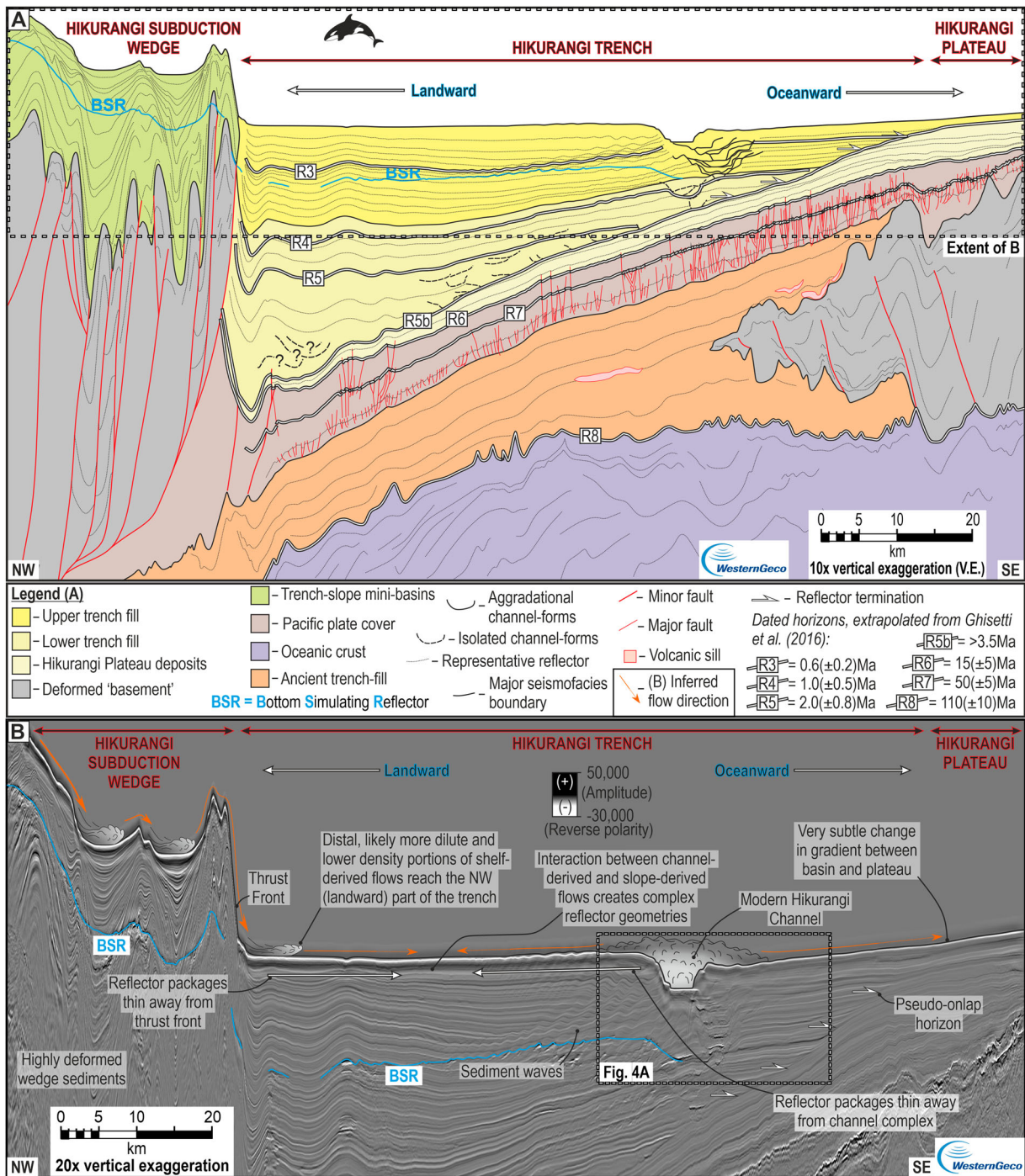


Figure 3. A, Interpreted seismic section through the Hikurangi Trench and its fill modified from McArthur and Tek (2021). **B**, Annotated part of seismic section in A, showing the key geomorphic and seismic features present in and bounding the trench-fill and the potential sources of trench sedimentation.

Methods

Bathymetry analysis and seismic interpretation

Analysis of the bathymetry and backscatter data, including the generation of depth, slope and hillshade maps, digitisation and segmentation of sediment wave crests and the channel trendline, and the generation of seafloor profiles, were conducted using ArcGISTM.

Three regionally traceable horizons (Overbank Horizons 1–3) form the basis for the subsurface interpretation. Seismic interpretation, including the

tracing of reflectors, surface generation, the mapping of sediment wave fields, and the generation of three-dimensional images was conducted in Schlumberger Petrel©. Reflectors were first traced throughout the 3D seismic volume, then extrapolated along the 2D seismic lines for the purpose of mapping the extents of the wave fields; ties between the time- and depth-domain data were conducted by identifying marker horizons present in both surveys and interpreting the position of the reflector of interest between those marker horizons. Analysis of sediment waves, which

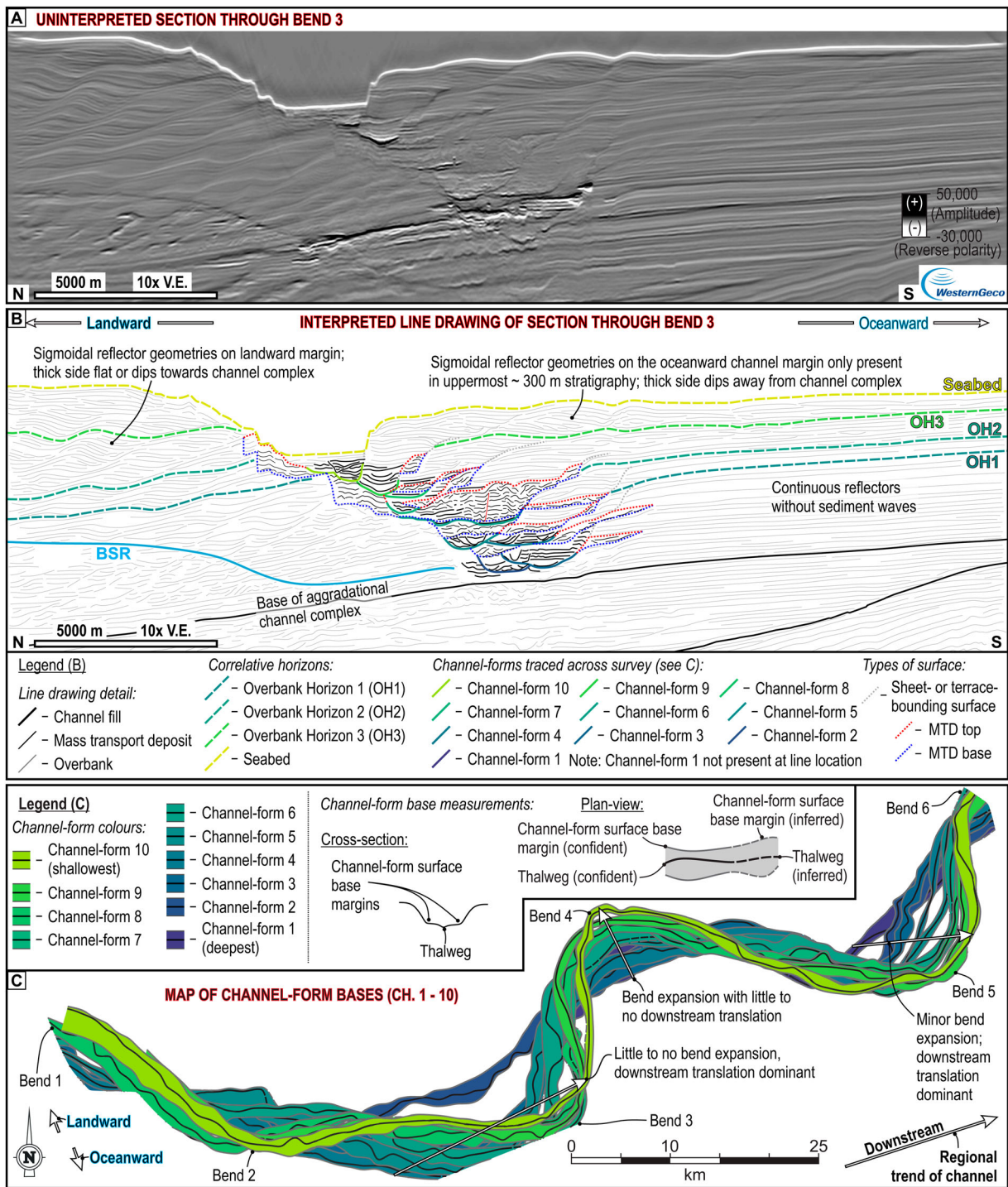


Figure 4. A, Uninterpreted seismic section (location on Figure 3B) and B, interpreted line drawing through the Hikurangi Channel and its landward and oceanward overbanks, highlighting the three subsurface horizons referenced in the text and nine of the ten channel-forms that have been traced across the study area. C, Map of the thalwegs and edges of the flat bases of the ten traced channel-forms modified from Tek et al. (2021).

was only conducted within the boundaries of the 3D survey, was achieved by importing the subsurface horizons into ArcGIS™, where they were analysed in the same way as the bathymetry data: generation of depth and slope maps, and digitisation and segmentation of wave crests.

To ensure consistency in the resolution and spatial extent of the data, and to negate the potential effect of the migration of overbank features related to the 2016

Kaikōura canyon flushing event and its associated turbidity current (Mountjoy et al. 2018), a seafloor horizon generated from the 3D seismic data is used when comparing the orientations and morphologies of overbank features in the subsurface, to those on the seafloor.

When referring to the position of waves or profiles along a channel, those in more proximal channel reaches are referred to as ‘up-channel’ when compared

to more distal, ‘down-channel’ reaches. Within a wave field, along an overbank transect normal to the channel, features located close to the channel are referred to as ‘upstream’, whereas features that are further away from a channel are referred to as ‘downstream’.

Sediment wave orientations and flow analysis

The plan-view morphology of outer-bend sediment waves was used to infer modern overbank flow and palaeocurrent directions, and investigate how the orientational spread of a sediment wave field relates to the morphology of the adjacent channel (Figure 5A–C). On the seafloor, this analysis was performed on four sediment wave fields present on the landward overbank (WF1a, WF2a, WF3 and WF4; Figure 2). However, as WF2a is the only field that is imaged along its entire (up-channel to down-channel) width within the 3D seismic survey, subsurface analysis was limited to waves beneath WF2a; it should also be noted that only the upstream part of WF2a is imaged by the 3D survey.

Sediment wave crests and the trend of the adjacent channel bend were digitised and divided into 1 kilometre long segments using ArcGIS™ (Figure 5A, B); the extent of each bend is defined as the along-channel connection from the midpoint between the apex of the

relevant bend and the adjacent up-channel bend, to the midpoint between the apex of the relevant bend and the adjacent down-channel bend (Figure 5A). Channel trend segments were vectorised via connection to their down-channel neighbour, their directions were then extracted using Python programming and plotted as rose diagrams in Stereonet 10 (Cardozo and Allmendinger 2013; Figure 5B, C). The spread of segment directions is inversely proportional to the mean vector length of the orientations (Fig. 5C); hence, the inverse of mean vector length is used hereafter as a direct measure of channel bend curvature. The local overbank flow direction is assumed to be perpendicular to the local orientation of the sediment wave crests (Migeon et al. 2000; Normark et al. 2002); vectors approximating local flow direction were therefore generated at 90° to each sediment wave crest segment (directed away from the channel; Figure 5B) using Python. When local overbank flow directions are plotted on rose diagrams, the mean vector orientation indicates the mean flow direction, and the mean vector length provides an inverse measure of the bulk curvature of the sediment wave crests (Figure 5C). The relationship between channel bend, and sediment wave curvature on the seafloor and in the subsurface is examined in the ‘outer-bend sediment waves’ sections.

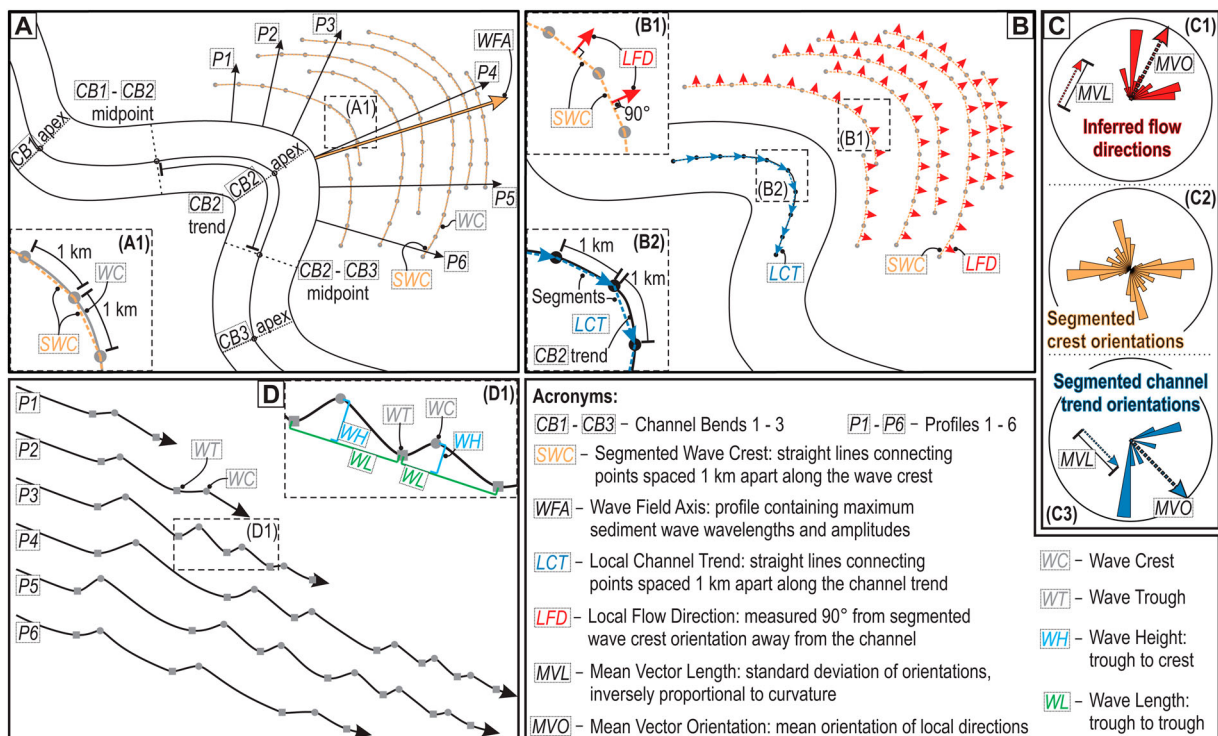


Figure 5. Schematic, fictitious example showing the methodologies applied on the seafloor and subsurface horizons for sediment wave orientations and flow analysis, and morphological analysis of the sediment waves. **A**, Shows the segmentation of the wave crests shown in **B** and **C**, the distributions of the representative longitudinal profiles used to extract wave measurements in **D**, and how channel bends are defined. **B**, Shows the segmentation of the channel bend and how inferred palaeocurrents are extracted from the segmented wave crests. **C**, Rose diagrams illustrating analysis of the orientations of overbank flow directions, of wave crests and of channel trend (data from segments in **B**). **D**, Shows how sediment wave wavelengths and wave heights are calculated in the profiles shown in **A**.

Morphological analysis of sediment waves

To analyse the size distribution of sediment waves within each outer-bend wave field and on each subsurface horizon, six longitudinal profiles, distributed incrementally along the up- to down-channel width of the field, were digitised perpendicular to the dominant wave crest orientation (Figure 5A). Along each profile, wave crests and troughs were interpreted (Figure 5D), with the interpretations validated against the plan-view expression of the identified waves. Sediment wave wavelengths are calculated as the distance between two consecutive troughs. Wave heights are calculated as the distance from a wave crest to a straight line connecting two consecutive troughs, measured normal to the trough-connecting line (Figure 5D; Ribó et al. 2016). Sediment wave dimensions and their position in their host wave field were extracted using PythonTM from profiles digitised in CorelDRAW[®]. Wave lengths and heights are assumed to scale with increasing flow thickness (Normark et al.

2002), and hence with (unidirectional) flow velocity, meaning they can provide insight into modern flow and palaeoflow dynamics across the wave fields. A longitudinal profile through the ‘axis’ of each wave field, defined as the profile containing the largest overall wavelengths and wave heights, was also digitised but was not used in the morphometric analysis.

Results

Large-scale seafloor morphology and seismic stratigraphy

Observations

The ~250 km reach of the Hikurangi Channel in the study area exhibits steep (up to 35°) channel walls and a relatively flat channel-floor that progressively narrows from ~6.5 km in the most proximal parts, to ~1 km distally (Figures 2B and 6). In the most proximal region of the study area (Figure 2B) the channel is situated near (e.g. Bend 1; profiles 1–3, Figure 6) or at

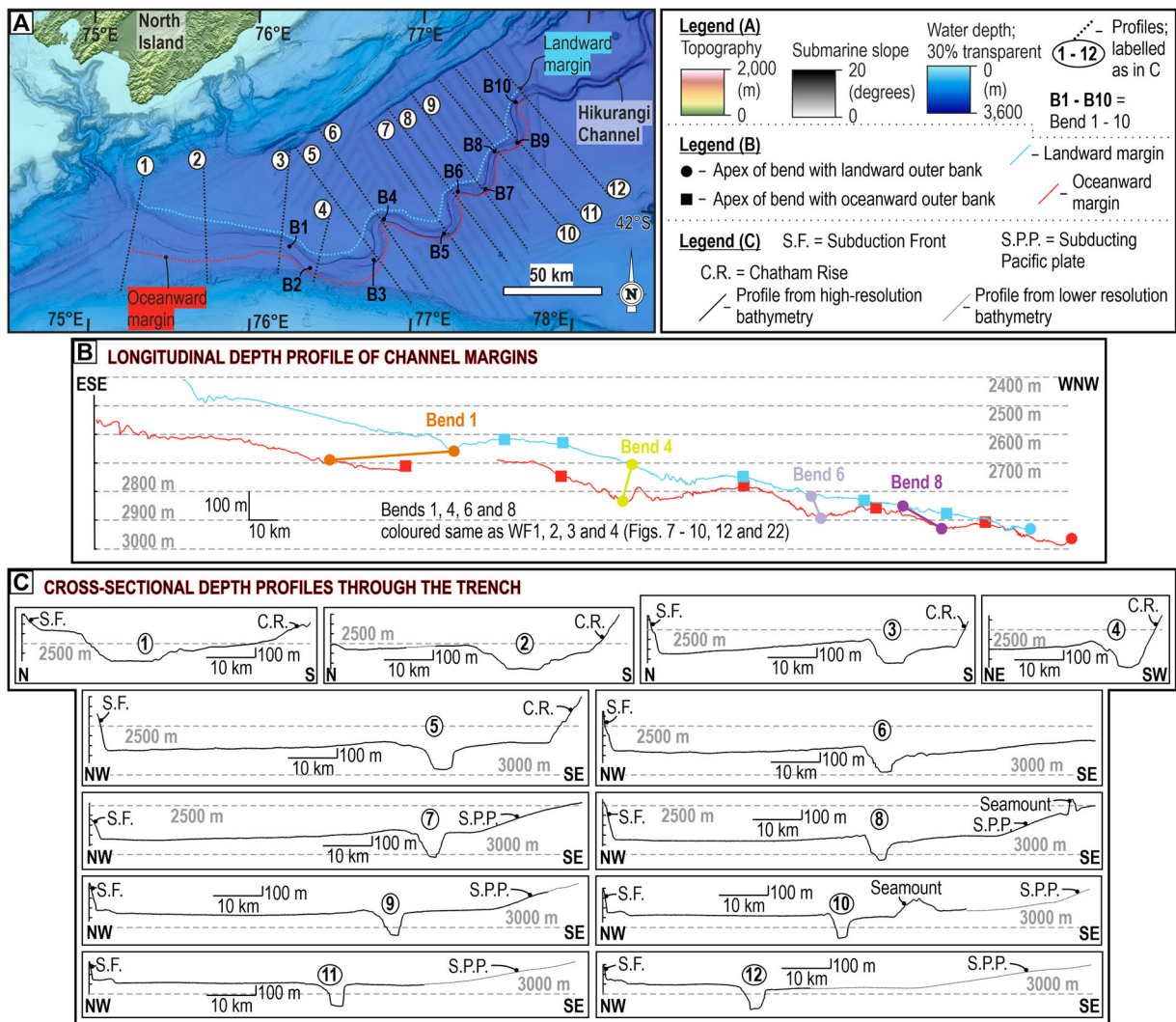


Figure 6. A, Map (location shown in Figure 2B) showing locations of the trench profiles shown in B and C. B–C, Longitudinal profiles through the trench showing the seafloor morphology of: (B) the tops of the channel walls, highlighting the depth difference between the two channel margins along the channel; (C) trench-perpendicular profiles, each through the apex of successive bends, showing the channel-perpendicular seafloor expression of the channel overbanks on both margins.

(e.g. Bend 2; profile 4, Figure 6) the northern margin of the Chatham Rise. Further down-channel, the channel is located close to the margin of the subducting Pacific plate but becomes gradually more central within the trench distally (profiles 7–12, Figure 6).

The landward (northern) channel overbank is consistently higher than the oceanward (southern) one, except where the channel is pinned against the Chatham Rise (Figure 6); the height differential is greater on bends with landward outer-bend overbanks (profiles 3, 6, 8, 10 and 12, Figure 6). The trench-floor on the landward overbank either: (a) dips gently (up to 0.8°), from a poorly defined levee crest away from the channel (NW) and toward the subduction front (e.g. profile 3, Figure 6); (b) dips gently away from the channel for tens of kilometres before becoming subhorizontal (e.g. profile 9, Figure 6); or (c) is subhorizontal across its entire width (e.g. profile 11, Figure 6). In all cases, an abrupt contact at the subduction front sees the seafloor dipping steeply (up to 35°) to the SE. The oceanward overbank either dips gently (up to 0.6°) toward the channel (NW) (e.g. profile 8, Figure 6) or is subhorizontal (e.g. profile 7, Figure 6). Where the trench-floor is bounded by the Chatham Rise, an abrupt steepening occurs at its boundary (e.g. profile 5, Figure 6); where it is bound by the subducting Pacific plate, a subtle steepening occurs (e.g. profile 9, Figure 6). In any trench-perpendicular transect in the study area, the thalweg of the channel is the deepest point of the trench (Figure 6).

At its landward edge, the trench-fill is bound by deformed subduction wedge deposits (Table 1); the contact between the two is typically marked by a frontal thrust; however, minor folding is sometimes observed in the adjacent trench-fill (Figure 3). At its oceanward edge, the trench-fill is bound proximally by the faulted strata that comprise the Chatham Rise (Table 1), and distally by strata imaged as low amplitude reflectors that top the subducting plate (Table 1). The trench-fill comprises deposits of the Hikurangi Channel, made up of channel-fill, sheet and terrace, and mass-transport deposits (Table 1; see Tek et al. 2021), and the overbank deposits studied here (Tables 1 and 2). The overbank deposits comprise most of the studied trench-fill, and can be categorised into three types (Table 2): overbank sediments with sediment waves; overbank sediments without sediment waves that terminate against the Chatham Rise or subducting plate; overbank sediments without sediment waves that terminate against the subduction front, and that display compensational wedging patterns and terminate against the subduction front.

Interpretations

The observed channel-bank asymmetry is consistent with previous studies focused on the Hikurangi Channel (Lewis et al. 1998; Lewis and Pantin 2002; Tek et al.

2021) and is interpreted to be dominantly due to leftward flow deflection by the Coriolis force. Local enhancement of overspill and aggradation on the landward margin and concomitant hindrance on the oceanward margin may be caused by flow reflection off the Chatham Rise and possibly the subducting plate, in addition to an overbank gradient that slopes towards the channel on the oceanward margin, and away from the channel on the landward margin. Elevated channel overbank heights on outer channel bends with landward outer-overbanks suggest that the centrifugal force of the flow field also enhances overspill and aggradation at these locations (Straub et al. 2008; Kane et al. 2010).

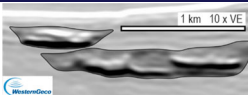
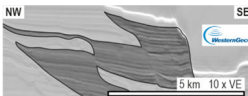
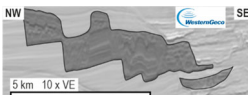
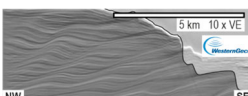
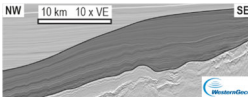
Despite the lack of well-defined levees on the seafloor, the fact that the channel-forms throughout the studied stratigraphy are bounded laterally by compound overbank deposits, with no master incision surface hosting them (Figures 3 and 4; Table 2) allows their classification as ‘aggradational’ channel deposits. The lack of a ‘wing-shaped’, tapering cross-sectional profile (a common feature of levees adjacent to aggradational channels) is due to aggradation rates being similar across the entire trench-floor. On the narrow oceanward overbank, overspilling flows can reach the edge of the trench-floor (the Chatham Rise or subducting plate) and deposit over the entire overbank area (Figure 3B). It is also possible that overbank flows may also deposit over the entirety of the wider landward overbank. Aggradation near the subduction front may be accelerated by deposition from fine-grained distal parts of flows that traversed drainage networks on the bounding slope (Figure 3B; Mountjoy et al. 2009; McArthur et al. 2019). Alternatively, overspill on the landward overbank may not reach the subduction front, with the interaction of overspilling flows and slope-traversing flows occurring somewhere in the trench.

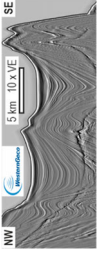
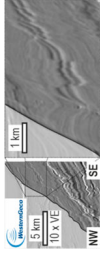
Outer-bend sediment waves on the seafloor

Observations

The four prominent sediment wave fields (WF1a, WF2a, WF3 and WF4, Figures 2B, 7 and 8) present on the landward channel overbank collectively cover 3300 km^2 of the channel overbank. Individual fields range from 130 to 1400 km^2 and extend up to 28 km away from the channel. The size (area, length and width; Figure 7) of the wave fields decreases down-channel (Figures 7D, E and 8). Waves in WF1a, WF2a, WF3 and WF4 are concentric around the outer-overbanks of bends 1, 4, 6, and 8 respectively (Figure 2C). On the seafloor, WF1a and WF2a are distinct from the wave fields present on the inner-overbanks of bends 3 and 5 (WF1b and WF2b respectively; Figure 2C). Each wave field is separate from its neighbours.

Table 1. Descriptions and interpretations of the seven seismofacies observed within and adjacent to the studied trench-fill.

Seismofacies name	Description	Amplitude	Geometry	Trench-parallel continuity	Trench-perpendicular continuity	Bound by: toward channel	Bound by: away from channel	Dip/inclination	Internal structure	Interpretation	Example
Channel-fill	Lens-shaped High-Amplitude Reflector Packages (HARPs)	High	Lens-shaped, pinch and swell over 100s – m to kms laterally, reaching < 60 m thick	10–100 s of km	<3 km	N/A; lens-shaped	Older channel-fill, sheet or terrace, MTD or overbank	Concave-up cross section; very shallow (<1°), trench-parallel dip to NE	Concave-up surfaces within packages; unilaterally migrating reflectors; transparent areas	Coarse-grained channel-fill deposits (Flood et al. 1995)	
Sheet or terrace deposits	Narrow, tabular reflector packages adjacent to channel-fills	Low – medium	Tabular	Kms – 10 s of km	Kms – 10 s of km	Channel-fill, sheet or terrace, or MTD	Sheet or terrace, MTD, or overbank	Horizontal or very gently dipping (<1°) in any direction	Sometimes gullies toward their margin away from the channel	Weakly confined, sand-rich sheet-like deposits (Pickering et al. 1995) or heterolithic terrace deposits (Babonneau et al. 2004; Hansen et al. 2015)	
Mass-Transport Deposits (MTDs)	Deformed and chaotic reflector packages	Typically low to very low; can locally contain medium or high	Highly variable: contorted reflectors or transparent	Kms – 10 s of km	Kms – ~10 km	Channel-fill, sheet or terrace, or MTD	Sheet or terrace, MTD, or overbank	Internal dips; overall dip toward channel	Folds; normal and thrust faults; and transparent zones	Mass-Transport Deposits, the product of debris flow, slumping, and sliding, comprising remobilised overbank and terrace deposits (Tek et al. 2021)	
Overbank	Laterally continuous, tabular or undulating reflector packages	Low to medium	Tabular or very subtle reflector thickening/thinning (ms over kms laterally)	10–100 s of km	10 s of km – ~100 km	Channel-fill, sheet or terrace, or MTD	Subduction front, subducting slab or Chatham Rise	Horizontal or gentle (<1°) landward (NW) dip	Sediment waves; gullies; sometimes faults	Fine grained (silt and clay), heterolithic external overbank deposits formed by overspill from channel-traversing turbidity currents (Normark et al. 1980; Pirmez and Flood 1995; Migeon et al. 2004)	
Plate-top sediments	Low amplitude, very continuous reflector packages with subtle wedging	Low	Tabular or subtle wedging in all directions (ms vertically over kms laterally)	10–100 s of km	10–100 s of km	Reflectors that terminate against trench-fill are bound by overbank; reflectors that continue under the trench, terminate against the subduction front; SE termination not imaged		Consistent landward dip < 3°, sub-parallel to dip of subducting slab	Subtle wedging; sometimes faults	Muddy hemi-pelagites and contourites deposited on the Pacific plate during subduction (Barnes et al. 2020)	

Subduction wedge deposits	Heavily folded reflector packages with variable thicknesses	Low to high; increases toward seabed	Highly variable in reflector thickness (ms vertically over kms laterally) and amplitude over metres to kms	Kms – 10 s of km	Kms – 10 s of km	Overbank	N/A; outside of study area	Highly variable dips due to structure; flat to sub-vertical and locally overturned reflectors	Thrust-cored anticlines, fanning reflectors, axis-thickening synforms	Coarse-grained deposits of trench slope mini-basins and the structures that bound them (McArthur et al. 2019)	
Chatham Rise deposits	Heavily faulted reflector packages with internal truncations	Low to high	Packages and reflectors traceable over 10s to 100s of km, subtly thinning toward subduction front; reflector displacement/abrupt dip changes common	10–100 s of km	10–100 s of km	Trench-fill of any type: channel-fill, sheet or terrace, or MTD, or overbank	N/A; outside of study area	Packages follow dip of subducting plate, < 3° NW; dips of reflectors vary abruptly at faults	Pervasive normal faults (10s to 100s of m offset), spaced 100 m – 5 km apart	Sedimentary rocks that comprise the upper part of the Chatham Rise (Davy et al. 2008)	

Bend 4 exhibits the greatest curvature (lowest mean vector length), followed by bends 6 and 8; bend 1 is the straightest (Figure 8). The down-channel limit of WF2a and WF3 is further down-channel of the apex of their associated bends than the up-channel limits of the wave fields; WF1a and WF3 are more symmetric about the apex of their associated bends (Figures 7 and 8). The orientations of the segmented wave crests, and therefore the inferred local flow directions, exhibit the greatest spread (inversely proportional to mean vector length) in WF2a, and the least in WF1a (Figures 8, 9A and C). Except on WF4, the ‘axis’ of the wave field (the channel-perpendicular transect containing the largest waves; Figure 5) is consistently orientated down-channel of the mean flow direction (mean vector orientation; Figures 8 and 9A).

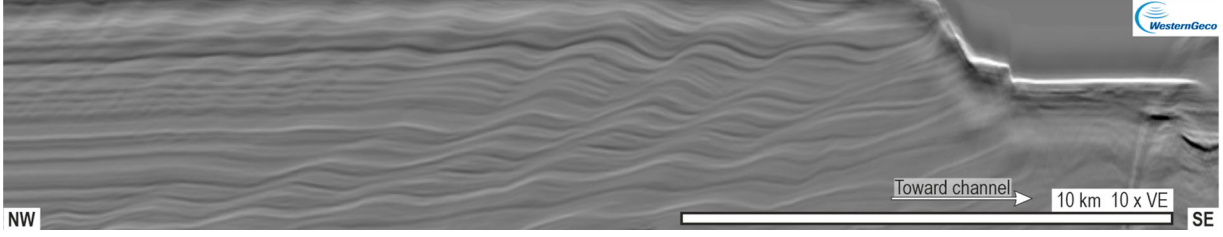
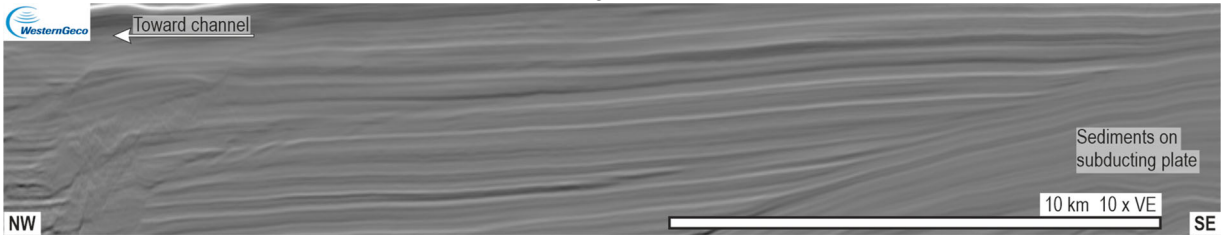
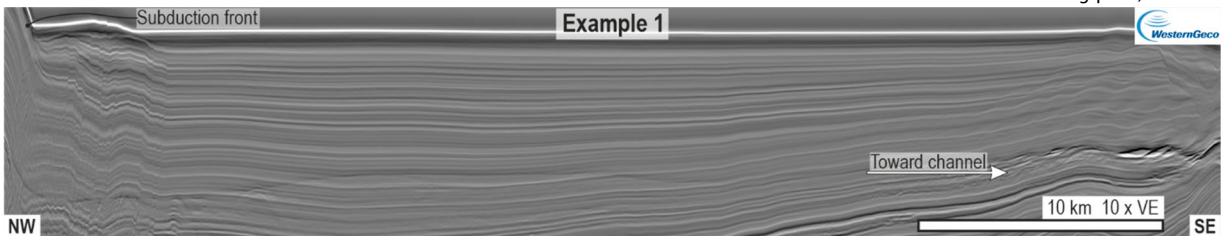
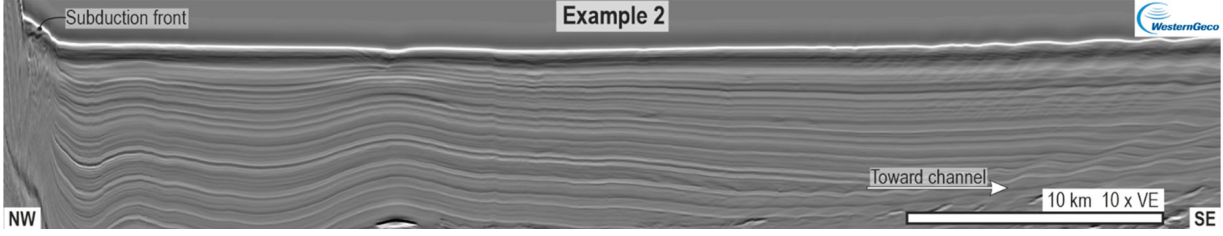
In crest-perpendicular transects (see profiles 1–6; Figure 8), sediment waves typically have narrow stoss sides that can be horizontal, or dip gently toward the channel, and wider lee sides that dip more steeply away from the channel (Figure 10). Stoss sides exhibit higher backscatter reflectivity and Root Mean Squared (RMS) amplitude values than lee sides (Figure 11A, B).

Waves on the seafloor exhibit wavelengths that range from 6639 to 439 m with a mean wavelength of 1734 m (Figure 12; Tables 3 and 4). Wave heights range from 48 m to below the data resolution (<1.5 m) with a mean height of 9 m (Figure 12; Tables 3 and 4); smaller waves are likely present but undetectable at the resolution of the available data (Figures 10 and 12A). No systematic wavelength or wave height trends are observed between successive bends moving down-channel (Figure 12A); however, the maximum wavelength and height in each wave field does decrease down-channel (Table 3). Most profiles (Figure 8) display a systematic downstream decrease in wave height (Figures 10 and 12B). In some profiles individual wavelengths and the overall range of wavelengths also decrease downstream (e.g. WF1a axis; Figures 10 and 12B); however, a systematic downstream variation in wavelength is not apparent (Figure 12B). Wavelengths and wave heights decrease toward the up-channel and down-channel margins of each wave field, and therefore away from the bend apex (Figures 8, 10 and 12C). The decrease in wavelength and height is more abrupt at the down-channel margin of the field. The profiles containing the highest maximum and average wavelengths and heights (profiles 3, 4 or 5) are located toward the middle of each sediment wave field (Figure 12C).

Interpretations

The exclusive presence of outer-bend wave fields on only the landward margin suggests that the velocity and/or magnitude of the overspilling flow was enhanced on the landward and hindered on the oceanward overbank. This may have occurred due to: (a) the

Table 2. Descriptions, interpretations, and seismic cross-sections of the three types of overbank geometry observed within the studied trench-fill.

Overbank type	Description	Occurrence/context	Interpretation
			
Overbank sediments with sediment waves	Laterally continuous low to medium amplitude reflectors that systematically thicken and thin to form sigmoidal sediment waves. While some individual reflectors may disappear in the thin limb of the sediment waves, most reflectors can be traced across the length of the wave field.	Present through shallowest ~700 m of stratigraphy. Dominantly observed on the landward channel margin. Toward the channel, reflectors terminate abruptly against channel-fill, terrace deposits, or MTDs (Table 1). Away from the channel, reflectors transition into overbank sediments without sediment waves that terminate against the subduction front.	Fine grained overbank sediment waves formed by unidirectional overspilling flow from turbidity currents that traversed the Hikurangi Channel and its palaeo-incarnations. Aggradation occurs faster on their upstream (toward the channel) limb and they migrate toward the channel.
			
Overbank sediments without sediment waves that terminate against Chatham Rise/subducting plate	Reflectors are tabular or subtly thin away from channel. On the side away from the channel, reflectors thin and either terminate or steepen abruptly against subducting plate-top sediments.	This overbank type is only observed on the oceanward (SE) channel margin. The contact between overbank reflectors and plate-top sediments (Table 1) migrates vertically and oceanward through the stratigraphy.	'Confined external levee' <i>sensu</i> Clark and Cartwright (2011) deposited by overspilling flow from turbidity currents that deposited over the entire area between the channel and the oceanward trench margin (bound by the Chatham Rise or top of the subducting plate).
			
			
Overbank sediments without sediment waves that terminate against the subduction front	Reflectors are generally laterally continuous and usually thicken away from the channel (example 1 above). However, reflectors and reflector packages thin and occasionally pinch out onto highs and thicken into lows exhibited by deeper reflectors (example 2 above). In both cases, reflectors are deformed near to, and abruptly terminate against, the subduction front.	This overbank type is only observed on the landward (NW) channel margin. The expression of deep structures, typically thrust-cored anticlines, is muted toward the seafloor, which is generally subhorizontal. Structures are more common nearer the subduction front, sometimes causing packages of overbank reflectors to thin away from the channel.	These deposits likely represent a combination of fine-grained deposition from overspilling flow from the Hikurangi Channel, and the fine-grained, dilute, distal expression of flows that traverse the trench-slope basins of the Hikurangi Subduction wedge. Sediments from both sources collectively act to heal the expression of growing structures and maintain a relatively flat seafloor.

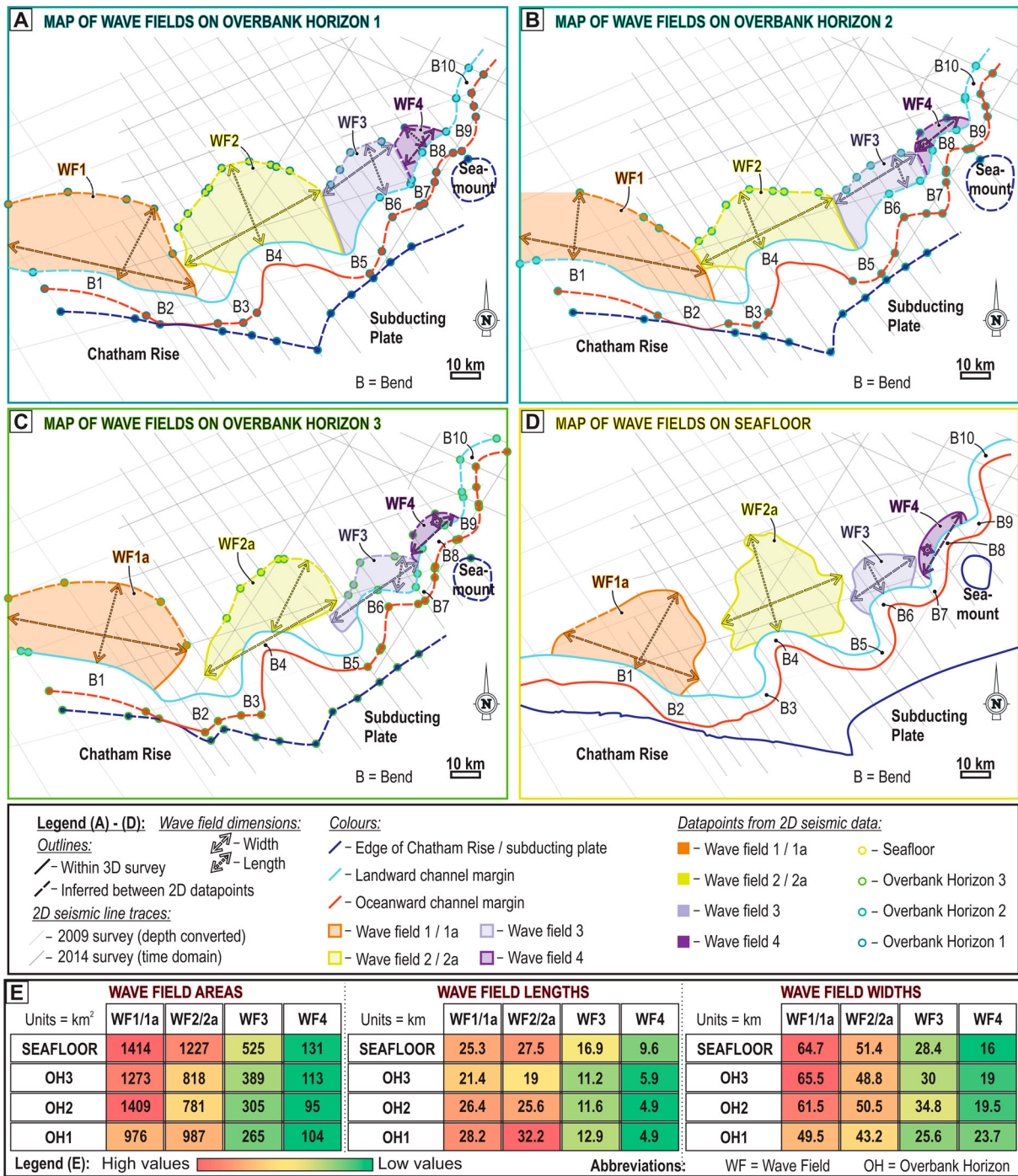


Figure 7. A–D, Topological maps of the four outer-bend wave fields on the landward channel margin, highlighting their stratigraphic evolution from Overbank Horizon 1 (A), through Overbank Horizons 2 (B) and 3 (C), to the seafloor (D). **E,** Dimensions of the wave fields in A–D, showing area, length (measured away from the channel), and width (measured along the channel).

influence of the Coriolis force (Wells and Cossu 2013), or (b) overspilling flow reflecting (Kneller et al. 1991; Bell et al. 2018) off the Chatham Rise and/or the subducting plate generating a transverse (landward; to the northwest) component of flow that likely counteracts overspill on the oceanward margin, and potentially aids overspill on the landward margin. scenario (a) likely affects the whole channel, whereas the effects of (b) are likely to be spatially variable. The observed down-channel decrease in wave field size is potentially a result of flow tuning, whereby the portion of a flow

capable of overspilling systematically decreases down-channel as the flow thins due to material being lost from the upper part of the flow as it traversed successive up-channel bends (Mohrig and Buttles 2007; Kelly et al. 2019). However, the East Cape Current, a contour current that flows SW along the subduction front before turning anti-clockwise and crossing the channel in the location of the study area (Fernandez et al. 2018), may counteract overbank flow on the landward margin in the distal parts of the study area, further inhibiting sediment wave development in WF3 and WF4.

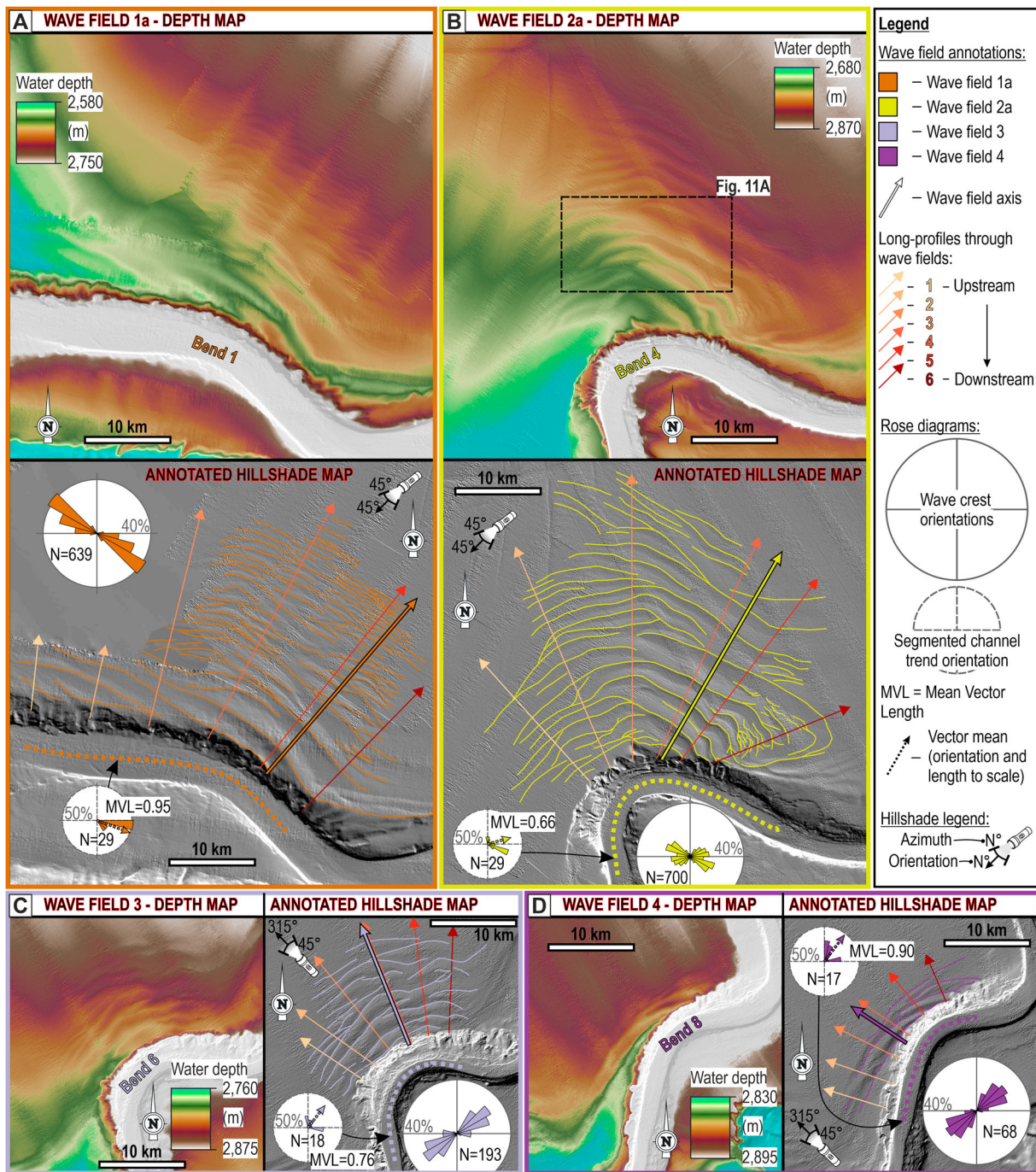


Figure 8. Maps showing **A**, the seafloor expression of wave field 1a, **B**, wave field 2a, **C**, wave field 3, and **D**, wave field 4. For each wave field, an uninterpreted depth map and an interpreted hillshade map are displayed. On the interpreted map, the wave crests, the trend of the related channel bend, the locations of the longitudinal profiles shown in Figure 10, including the wave field axis, and two inset rose diagrams showing the (bi-directional) orientations of the wave crest segments and the vector directions of the segmented channel bend trend are highlighted.

The observed pattern of diminishing wave heights up- and down-channel from the wave field axis is interpreted as the result of overbank flow travelling sub-perpendicular to the wall of the channel bend it originates from, which typically occurs along most of the length of that bend. Thus, bulk wave curvature in a wave field generally scales proportionally with the curvature of its formative bend (Figure 9C). However, the action of centrifugal force leads to increased overspill, and consequently the generation of larger

waves, downstream of the bend apex, with overspill diminishing up- and down-channel from the wave field axis (Straub et al. 2008).

The wavelengths and heights of the outer-bend waves observed here are consistent with the ranges quoted by Wynn and Stow (2002) for those on levees (<7 km and <80 m respectively). Cores from the overbanks of the Hikurangi Channel examined by Lewis and Pantin (2002) and Mountjoy et al. (2018) contain thin-bedded turbidites that grade from fine sand or silt

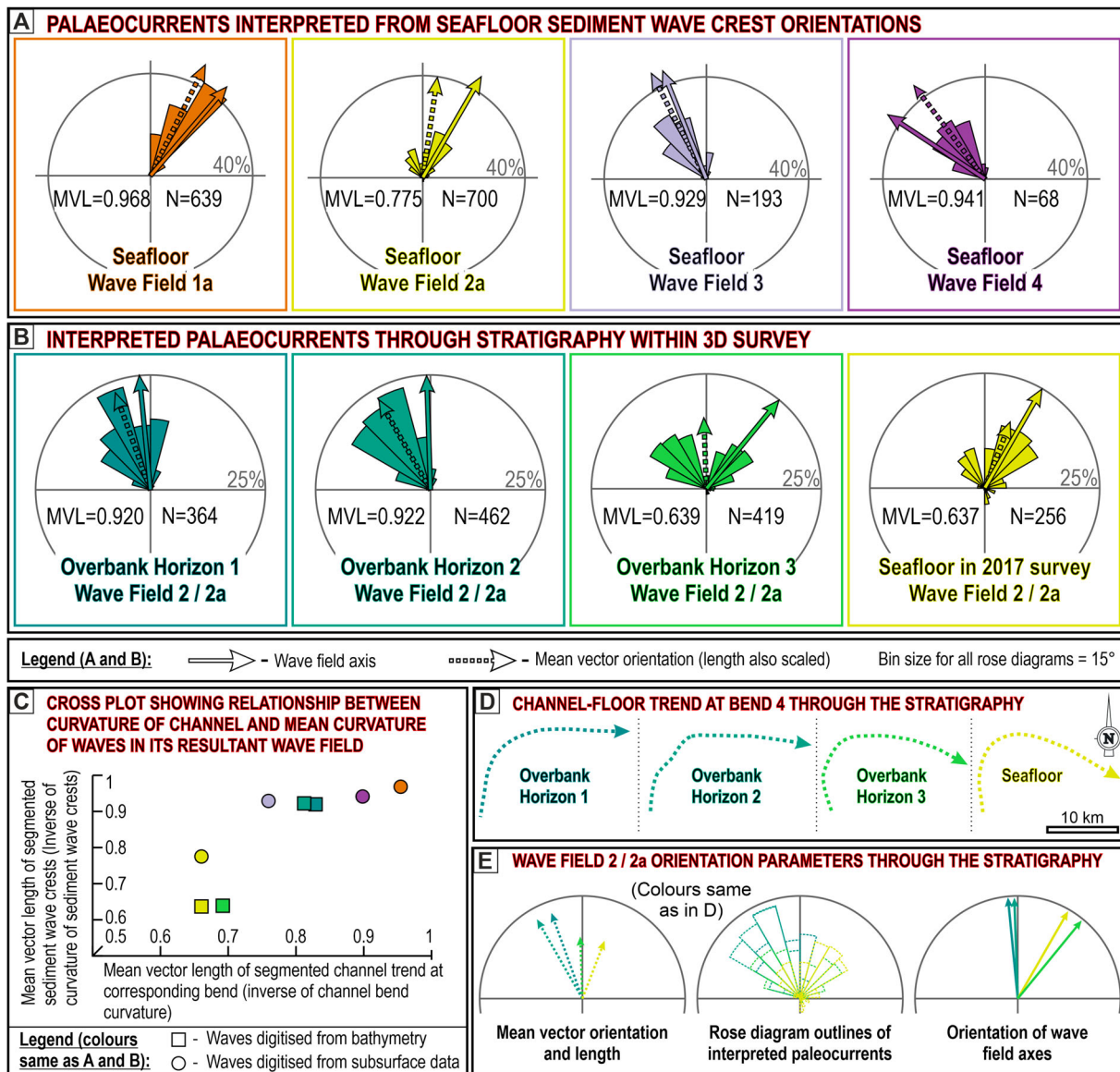


Figure 9. **A**, Rose diagrams showing the orientations of interpreted palaeocurrents from wave fields 1a, 2a, 3 and 4 on the seafloor, calculated from the segmented wave crests. **B**, Rose diagrams showing the orientations of interpreted palaeocurrents from wave field 2/2a in the 3D seismic survey Overbank Horizon 1, 2, 3 and the seafloor. **C**, Graph showing the relationship between the bend curvature, and the bulk curvature of the wave crests in their associated wave fields, calculated using the mean vector lengths of the segmented channel trend and the interpreted palaeocurrents from the segmented wave crests. **D**, Plan-view of the trend of bend 4 through the stratigraphy, showing an overall increase in bend curvature from Overbank Horizon 1 to the seafloor. **E**, Hemispheric rose diagrams showing the mean vector orientation and length, interpreted palaeocurrents, and orientation of wave field axis through the stratigraphy, showing an overall clockwise rotation from the deep stratigraphy (Overbank Horizons 1 and 2), to the shallow stratigraphy (Overbank Horizon 3) and the seafloor.

to mud (a mixture of silt and clay), which is also consistent with typical grain-sizes observed on submarine channel overbanks (Wynn and Stow 2002). High backscatter and RMS amplitude values observed on the stoss sides of the waves (Figure 11A and B) suggest that the stoss sides of the sediment waves contain coarser sediment than the lee sides; this finding is consistent with observations made by Lewis and Pantin (2002). These patterns may arise due to coarse-grained sediment being preferentially bypassed on the lee sides where finer-grained deposits form from the tails of overspilling flows. Meanwhile, on the upstream-

dipping stoss sides deposition of a wider grain-size range is permitted.

Outer-bend sediment waves in the subsurface

Observations

In the subsurface, waves are present through the shallowest 800 m of stratigraphy, although only the upper 600 m of stratigraphy is the focus of this study. In crest-perpendicular cross-sections, they exhibit sigmoidal geometries with thicker reflectors on their stoss sides, and their troughs and crests consistently

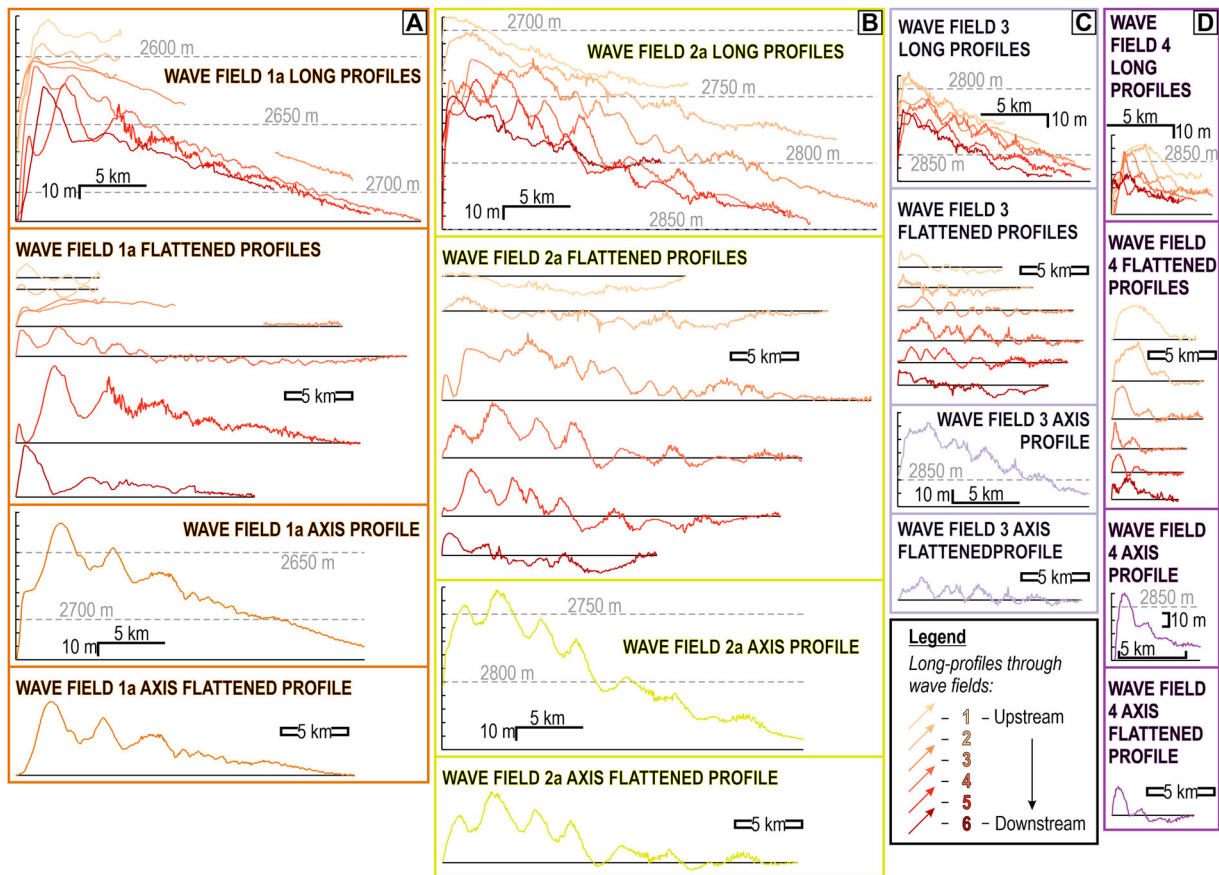


Figure 10. Crest-perpendicular seafloor profiles (locations shown in Figure 8) through wave fields 1a (A), wave field 2a (B), wave field 3 (C), and wave field 4 (D). For each wave field, the six profiles used for the extraction of wave dimensions in Figure 12 are shown in depth and flattened to their upstream and downstream ends, and the wave field axis (profile containing the largest overall wavelength and wave heights), which is also shown in depth and flattened.

stack toward the channel (Figure 11C). Reflectors also exhibit higher RMS amplitudes on their stoss sides than their lee sides (Figure 11B). The same four outer-bend wave fields observed on the seafloor have been mapped in the subsurface (WF1/1a, WF2/2a, WF3 and WF4; Figure 7) on three subsurface horizons (Overbank Horizons 1–3; shallowing respectively; Figures 4 and 7). A down-channel decrease in wave field size is observed on all subsurface horizons (Figure 7). The fields appear to show a general upward increase in area through the stratigraphy (Figure 7E), but this may be due to diminished data resolution at depth impeding detection of smaller waves at the extremities of the field. The wave fields also change shape through the stratigraphy, from being relatively wide (along-channel) and short (distance away from the channel) fields that interfinger with their up-channel and down-channel neighbours in the deeper stratigraphy (Figure 7A, B), to being narrow and long seafloor wave fields that are distinct from their neighbours (Figure 7D).

Analysing the 3D distributions and morphologies of waves through the stratigraphy beneath WF2a permits an examination of the evolution of the wave field. The curvature of bend 4 (the formative bend of WF2a) increases through progressively shallower stratigraphy

(Figures 9D and 13), accompanied by: (a) an increase in the spread of the wave crest segment orientations and inferred palaeoflow (Figures 9B, C and 13), (b) a down-channel shift and rotation of the up-channel and down-channel extent of the wave field, the mean palaeoflow orientation (mean vector orientation of palaeocurrents), and the wave field axis (Figures 9B, E and 13). The axis of WF2/2a is consistently positioned down-channel of the mean palaeocurrent orientation and the apex of bend 4 (Figure 9B).

The wave heights and wavelengths (Tables 3 and 4) in WF2/2a become larger through progressively shallower stratigraphy but appear to be smaller on the seafloor than in Overbank Horizon 3 (Figures 12A, 13 and 14). Similar trends of wave morphology to those observed on the seafloor are observed throughout the subsurface: crest-perpendicular transects typically display a downstream decrease in wave height (Figures 12B, 13 and 14), and wave heights and wavelengths generally increase toward the centre of the wave field (Figures 12C, 13 and 14).

Interpretations

The cross-sectional geometries of the waves are consistent with upstream-migrating sediment waves observed on the overbanks of many other submarine

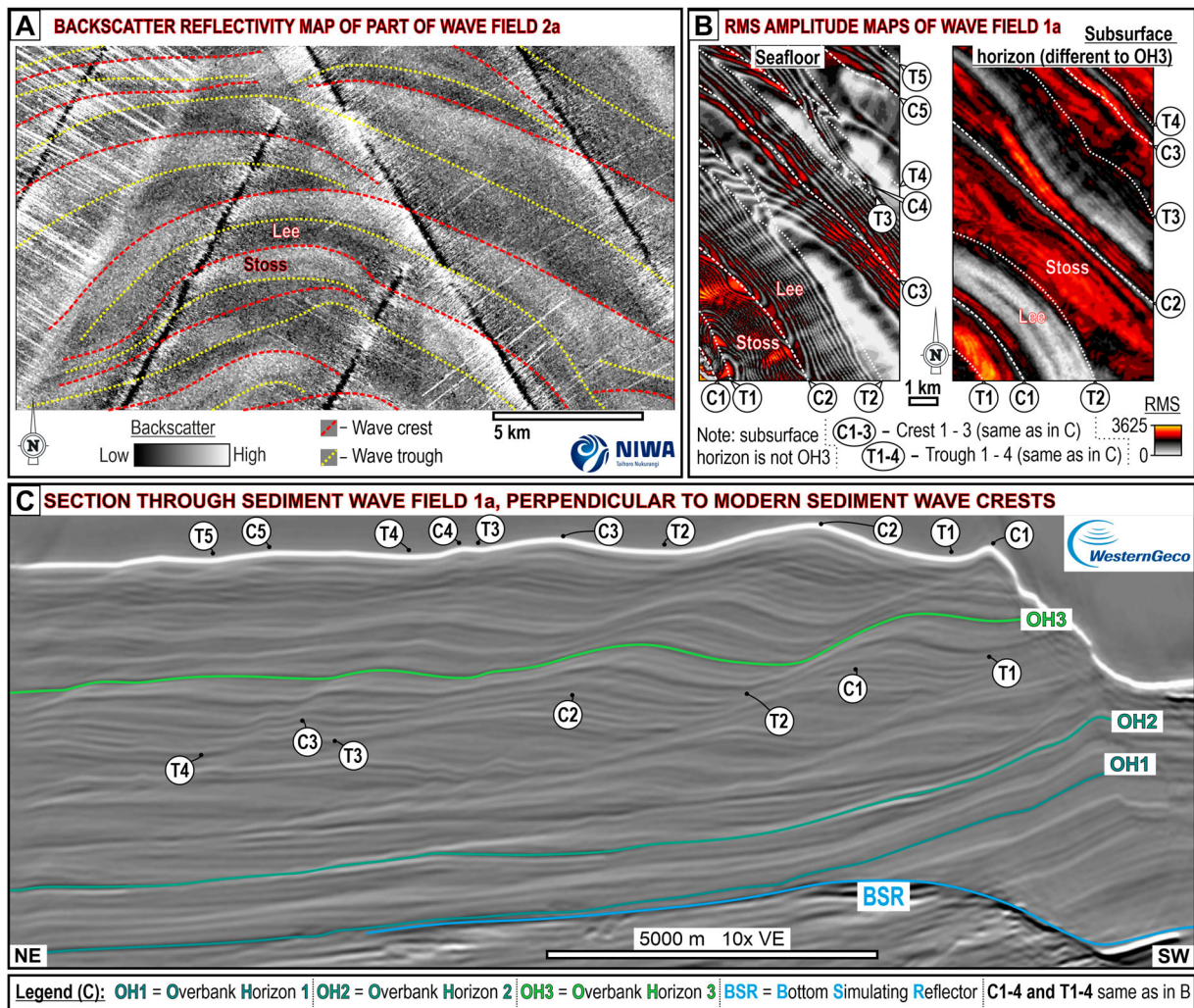


Figure 11. **A**, Seafloor backscatter map imaging part of wave field 2a, showing that higher backscatter values occur on the upstream stoss sides of waves than on their lee sides. **B**, Root Mean Squared (RMS) amplitude maps from the seafloor and the subsurface (depth shown in C) showing that, in general, RMS values are higher on the stoss (SW) sides of the waves in wave field 1. **C**, Crest-perpendicular seismic section through wave field 1a, showing the locations of the three subsurface horizons and the locations of the horizons in **B**.

channel systems, wherein deposition on the shallow or upstream-dipping stoss sides occurs faster than on the lee sides, where bypass prevails (e.g. Migeon et al. 2000, 2001; Nakajima and Satoh 2001; Normark et al. 2002). Observed reflector thickness trends (thicker stoss sides) and RMS amplitude trends (higher on the stoss sides) can be generated by either the 'lee wave' (Flood 1988; Lewis and Pantin 2002) or 'cyclic-step' (Slootman and Cartigny 2020) models (Figure 1).

At the time of Overbank Horizons 1 and 2, the channel was straighter compared to the modern channel and likely had steeper outer-levee gradients, allowing almost continuous overspill on the landward overbank, with a slight superimposed increase in overspill toward bend apices. Coriolis forcing likely enhanced overspill on the landward overbank. Through time, as the channel became more sinuous, centrifugal force became more dominant causing a

focusing of thicker, faster overbank flow just downstream of the bend apices (Hay 1987; Straub et al. 2011), leading to: (a) a separation of the wave fields from their up-channel and down-channel neighbours, (b) an increase in wave crest curvature, and (c) a down-channel shift in the wave field axis, the mean inferred flow orientation, and the up-channel, and down-channel limits of the wave fields. Effects of bend expansion may have been enhanced by diminishing outer levee gradients as trench sedimentation from transverse drainage networks became more voluminous and suppressed levee growth (see 'large scale trends' section above).

Up-stratigraphy increases in average wave heights and wavelengths (Figure 12A) may reflect an enhancement in maximum overspilling flow velocities within each wave field due to increasing centrifugal influence, or combination of compactional effects and limits in data resolution; however, temporal variability in the

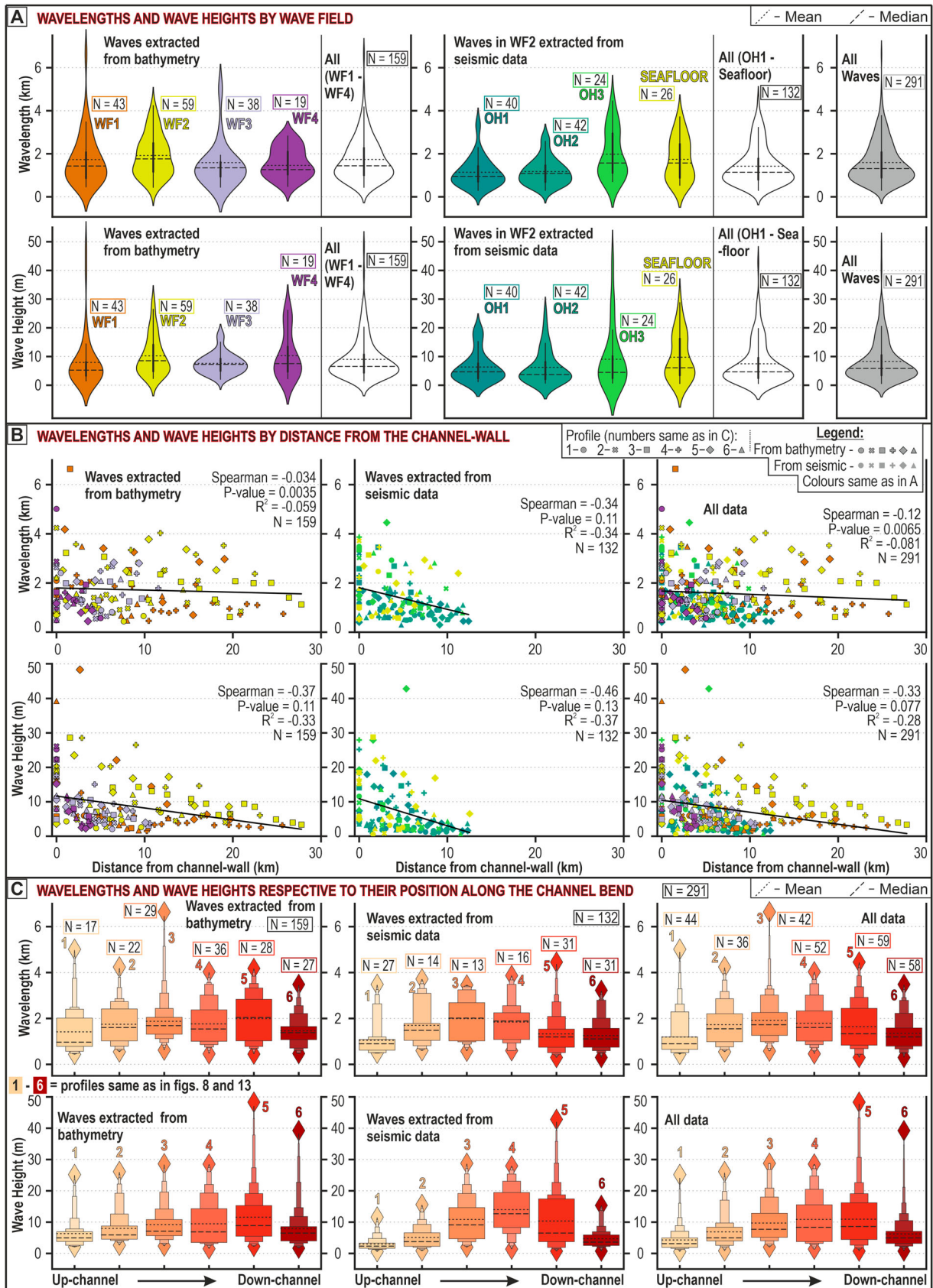


Figure 12. A, Violin plots showing the distributions of sediment wave wavelengths and wave heights displayed by wave field on the seafloor and by measured Overbank Horizon in the subsurface for waves in wave field 2. B, Scatterplots showing wavelengths and wave heights extracted from bathymetry data (coloured by wave field), seismic data from wave field 2 (coloured by the horizon they were extracted from), and all data. Separate plots of wave height versus distance from channel wall for each wave field and profile are provided as supplementary material. C, Letter-value plots (Hofmann et al. 2017) showing wavelengths and wave heights displayed by profile number (profiles 1–6 in Figures 8 and 10) highlighting up- to down-channel variability in the morphology of waves extracted from bathymetry, seismic, and all data; diamonds represent the minimum (resolvable) and maximum values, and boxes are scaled proportionally to number of datapoints.

Table 3. Minimum (resolvable), maximum and average wavelengths and heights of the sediment waves in each wave field.

	Name	Wavelength (m)				Wave Height (m)				No. of readings (N)
		Minimum	Maximum	Mean	Median	Minimum	Maximum	Mean	Median	
Measured From Bathymetry	Wave Field 1	460	6639	1730	1430	1.5	48.3	8.0	5.2	43
	Wave Field 2	439	4240	1919	1763	2.3	28.6	10.3	8.5	59
	Wave Field 3	484	2829	1589	1352	2.1	17.7	7.6	7.3	38
	Wave Field 4	447	5013	1461	1266	2.3	26.1	10.3	7.5	19
Measured From Seismic	All From Bathymetry	439	6639	1734	1439	1.5	48.3	9.0	6.6	159
	Overbank Horizon 1, Wave Field 2	299	3454	1142	949	1.2	19.8	6.3	4.7	40
	Overbank Horizon 2, Wave Field 2	299	2793	1172	1088	0.7	25.2	6.2	3.7	42
	Overbank Horizon 3, Wave Field 2	705	4455	1981	1571	0.7	42.8	9.0	4.5	24
	Seafloor, Wave Field 2	534	3718	1739	1571	0.6	28.8	9.8	6.1	26
	All From Seismic	299	4455	1422	1142	0.6	42.8	7.5	4.7	132
All Data		299	6639	1592	1314	0.6	48.3	8.3	5.9	291

Table 4. Minimum (resolvable), maximum and average wavelengths and heights of sediment waves across all fields, displayed by profile (shown in Figures 8 and 13); profile 1 is furthest up-channel and profile 6 is furthest down-channel.

	Name	Wavelength				Wave Height				No. of readings (N)
		Minimum	Maximum	Mean	Median	Minimum	Maximum	Mean	Median	
Measured From Bathymetry	Profile 1	439	5013	1416	968	2.1	25.2	6.3	5.0	17
	Profile 2	546	4240	1747	1604	2.6	26.1	8.0	5.9	22
	Profile 3	622	6639	1878	1687	2.4	28.6	9.2	7.1	29
	Profile 4	460	4033	1764	1540	1.5	28.5	9.5	6.9	36
	Profile 5	447	4179	1993	2044	2.3	48.3	11.6	8.9	28
	Profile 6	473	3483	1462	1383	1.7	39.2	8.0	6.5	27
Measured From Seismic	Profile 1	490	3483	1049	896	0.6	11.6	3.0	2.3	27
	Profile 2	598	3718	1700	1482	0.8	15.6	5.1	3.8	14
	Profile 3	577	3454	1995	2016	2.0	28.8	10.9	9.1	13
	Profile 4	597	3868	1844	1887	1.4	28.0	14.0	12.7	16
	Profile 5	299	4455	1328	1194	0.7	42.8	10.4	6.5	31
	Profile 6	299	3227	1255	1109	0.7	15.3	4.7	3.6	31
All Waves	Profile 1	439	5013	1191	896	0.6	25.2	4.3	3.1	44
	Profile 2	546	4240	1729	1550	0.8	26.1	6.9	5.0	36
	Profile 3	577	6639	1914	1725	2.0	28.8	9.7	7.7	42
	Profile 4	460	4033	1789	1606	1.4	28.5	10.9	8.4	52
	Profile 5	299	4455	1644	1337	0.7	48.3	10.9	8.6	59
	Profile 6	299	3483	1351	1196	0.7	39.2	6.2	5.0	58

average thickness of channel-traversing flows related to changes in sediment supply entering the system from the feeder canyons cannot be discounted.

Inner-bend overbank waves on landward channel margin

Observations

On the seafloor discrete wave fields are observed on the inner-overbanks of bends 3 and 5 (WF1b and WF2b; Figure 2C); these are smaller (~105 and ~115 km² respectively) than adjacent outer-bend fields and are not present in the deepest studied stratigraphy (Overbank Horizons 1 and 2). On Overbank Horizons 1 and 2, the down-channel ends of waves in WF2 interfinger with the up-channel ends of waves in WF3. Between Overbank Horizon 2 and 3, WF2 divides into two distinct fields (Figure 15): 'WF2a', within which waves are arcuate and broadly concentric around the outside of bend 4 (Figure 13), and 'WF2b', where waves are relatively straight and orientated at a high angle to the channel-wall (WSW-ENE) (Figure 15D). WF1 shows

a similar division into WF1a and WF1b. Wave crests at the down-channel end of WF2a are orientated sub-perpendicular to the crests of waves in WF2b, and terminate abruptly along a boundary that follows the crests of the waves in WF2b. In Overbank Horizon 3, waves in WF2b interfinger with waves in WF3, but on the seafloor WF2b and WF3 are distinct (Figures 13 and 15).

Waves in WF2b (visible on Overbank Horizon 3 and the seafloor) exhibit wavelengths of < 1500 m (mean 1250) and heights of < 20 m (mean 10) at their up-channel (WSW) end. Wavelengths and heights decrease downstream and down-channel (Figure 15), where they branch into multiple smaller waves that interfinger with waves in WF3 (e.g. on Overbank Horizon 3; Figure 15C) or diminish to heights below data resolution (e.g. on the seafloor; Figure 15D). On the seafloor, immediately NE of WF2a, is a broad, flat area devoid of sediment waves (Figure 15D) that sits stratigraphically above buried waves. This area constituted the upstream part of WF3 in Overbank Horizon 3 (Figure 15C).

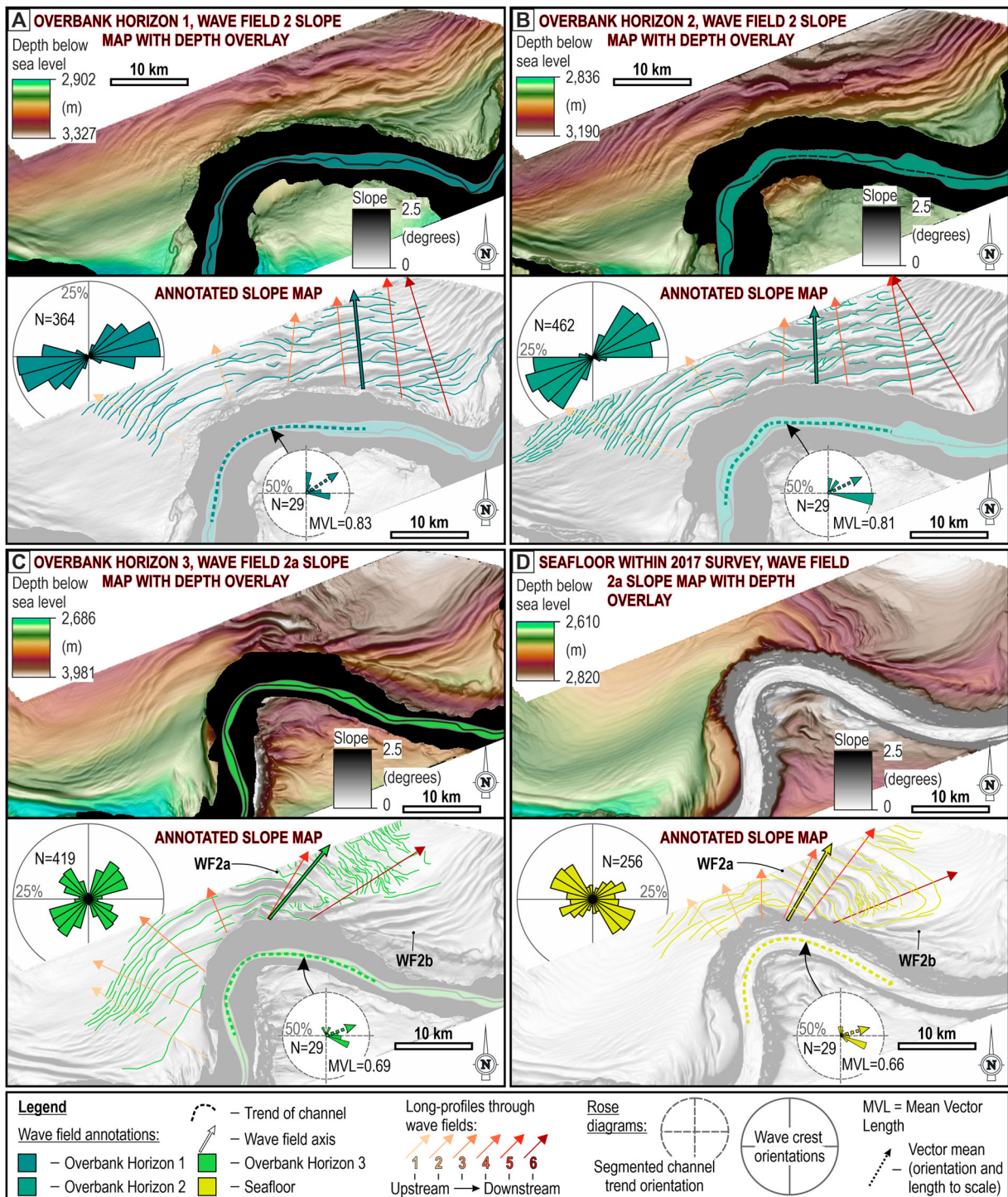


Figure 13. Maps showing the seafloor expression of wave field 2/2a within the extent of the 3D seismic survey on Overbank Horizon 1 (A), Overbank Horizon 2 (B), Overbank Horizon 3 (C), and the seafloor (D). For each horizon, an uninterpreted slope map with depth overlay and an interpreted slope gradient map are displayed. On the interpreted map, the wave crests, the trend of the related channel bend, the locations of the longitudinal profiles shown in Figure 14, including the wave field axis, and two inset rose diagrams showing the (bi-directional) orientations of the wave crest segments and the vector directions of the segmented channel bend trend are highlighted.

In crest-perpendicular cross-section, waves in WF2b exhibit the same sigmoidal reflector geometries with upstream-stacking troughs and crests, similar to outer-bank wave fields (cf. Figures 11C and 16). The crest and trough trajectories of waves in WF2b continue uninterrupted through ~500 m of stratigraphy, and the orientations of their peaks and troughs are concordant through the separation of WF2 into

WF2a and WF2b (Figure 16), suggesting the waves in WF2b have remained relatively static, while waves in WF2a have rotated clockwise. In cross-sections orientated obliquely to wave crests in WF2a and WF2b, the waves from the two fields appear concordant (Figure 16A). However, in sections orientated at higher angles to wave crests in WF2b, there is an abrupt lateral transition between sigmoidal

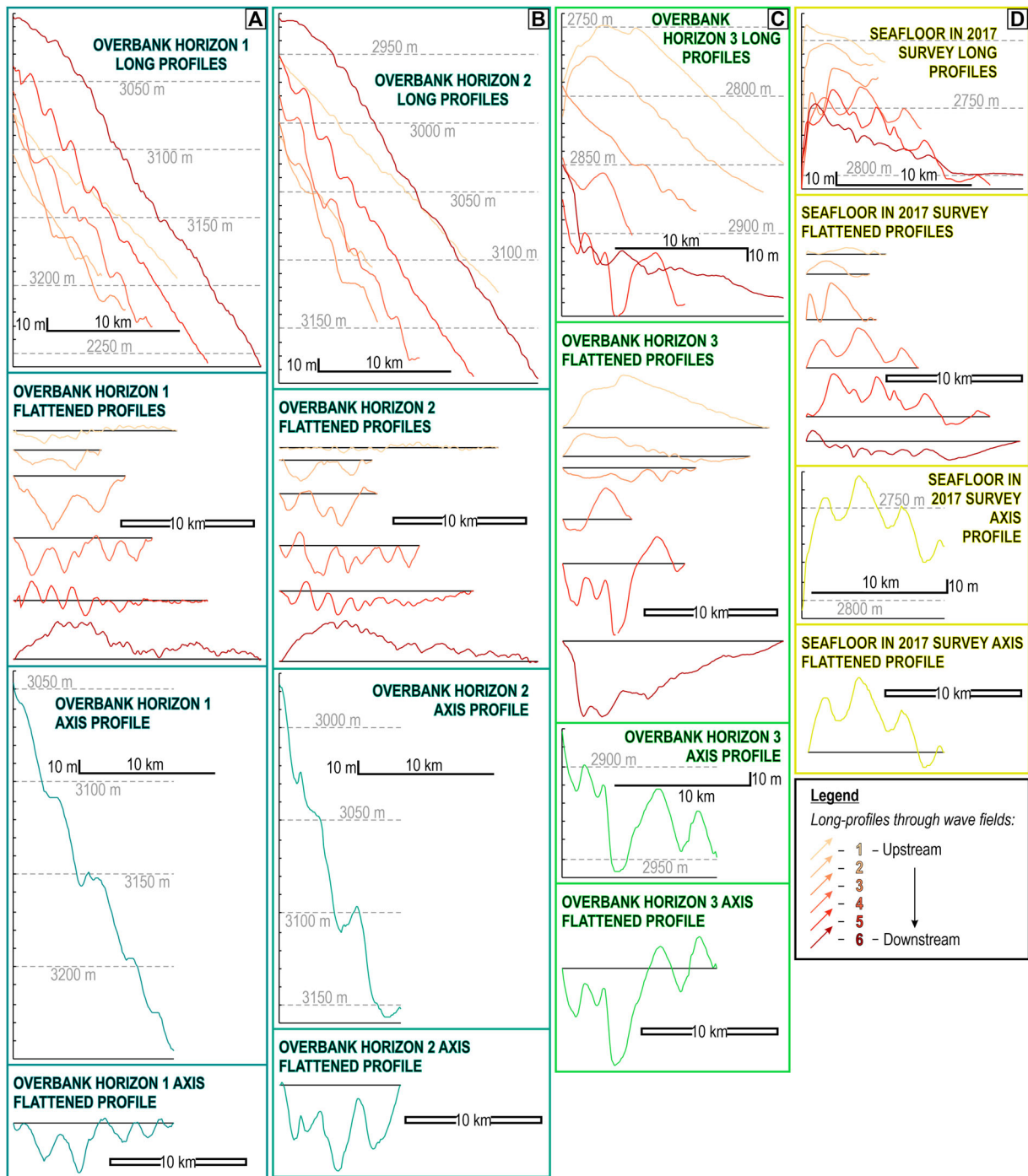


Figure 14. Crest-perpendicular profiles (locations shown in Figure 13) through wave field 2/2a, within the extent of the 3D seismic survey, measured on Overbank Horizon 1 (A), Overbank Horizon 2 (B), Overbank Horizon 3 (C), and the seafloor (D). For each wave field, the six profiles used for the extraction of wave dimensions in Figure 12 are shown in depth and flattened to their upstream and downstream ends, and the wave field axis (profile containing the largest overall wavelength and wave heights), which is also shown in depth and flattened.

wave-bearing reflectors of WF2b that dip away from the channel, to apparently flatter, mounded or tabular reflectors that represent the crest-parallel expression of waves in WF2a (Figure 16B, C). Reflectors (and packages thereof) in WF2a are thicker than contemporaneous reflectors in WF2b, causing the transition between the wave fields to step channelward through progressively shallower stratigraphy, coinciding with the areal growth of WF2a and shrinkage of WF2b (cf. Figure 15C and D). This transition is marked by

a subtle trough (Figure 15D), at which reflectors associated with both wave fields terminate, although the onlap of reflectors in WF2a onto those in WF2b may be mis-interpreted (Figure 15B, C).

Interpretations

Accompanying the expansion of bend 4, WF2 divided into distinct outer-bend (WF2a) and inner-bend (WF2b) fields as overspill on the outer-bank of bend

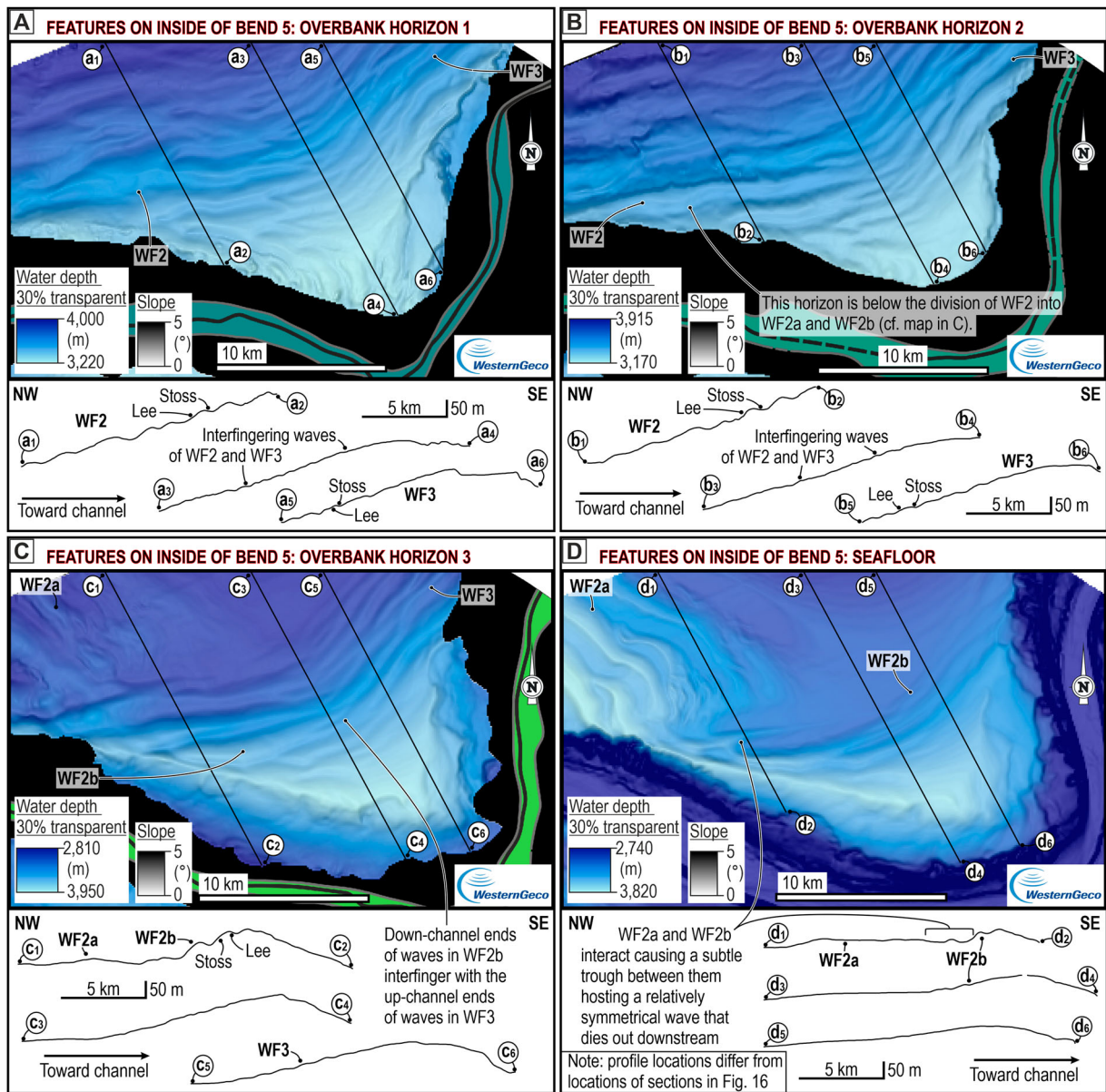


Figure 15. A–D, Slope maps with depth overlays centred on wave field 2/2b showing its relationship with field 2a and field 3, and three ~ crest-perpendicular profiles extracted from: Overbank Horizon 1 (A), Overbank Horizon 2 (B), Overbank Horizon 3 (C), and the seafloor (D).

4 became focused downstream of the bend apex due to an increase in the influence of centrifugal force.

Wave crest-perpendicular overbank flow at the location of WF2b is interpreted to have occurred consistently since sediment wave initiation (deeper than Overbank Horizon 1). The waves in WF2b formed and migrated upstream (SSE) through crest-perpendicular, NNW directed overspill on the inside of bend 5, in a similar manner to the outer-bank sediment waves described above. Overspill on inner-bend overbanks flowing away from the apex of bend 5 can only occur on the landward overbank, due to flow enhancement by the Coriolis force. As WF2a separated from WF2b and rotated, an area of flow interaction was generated between the two fields (Figure 17). Thick overspilling flows that traversed WF2a likely spread out due to flow relaxation (Pohl et al. 2019), generating

an ESE directed component of flow at the down-channel end of the wave field. This ESE-directed flow component interacted with NNW-directed flow traversing WF2b, hindering the development of sediment waves, and forming a trough in which flow originating from both wave fields travelled ~NE (Figure 17A, B, D). Such troughs may represent areas of higher velocity, and potentially contain deposits of coarser grain size.

Based on the thicknesses of contemporaneous reflector packages (Figure 17B), sedimentation rates in WF2a are interpreted to be higher than in WF2b. As WF2a expanded, the outer-levee gradient on the landward channel margin was progressively healed. The disappearance of the up-channel part of WF3 and establishment of a large, waveless area likely occurred as combined overbank flow from WF2a and WF2b became dominant, inhibiting channel-

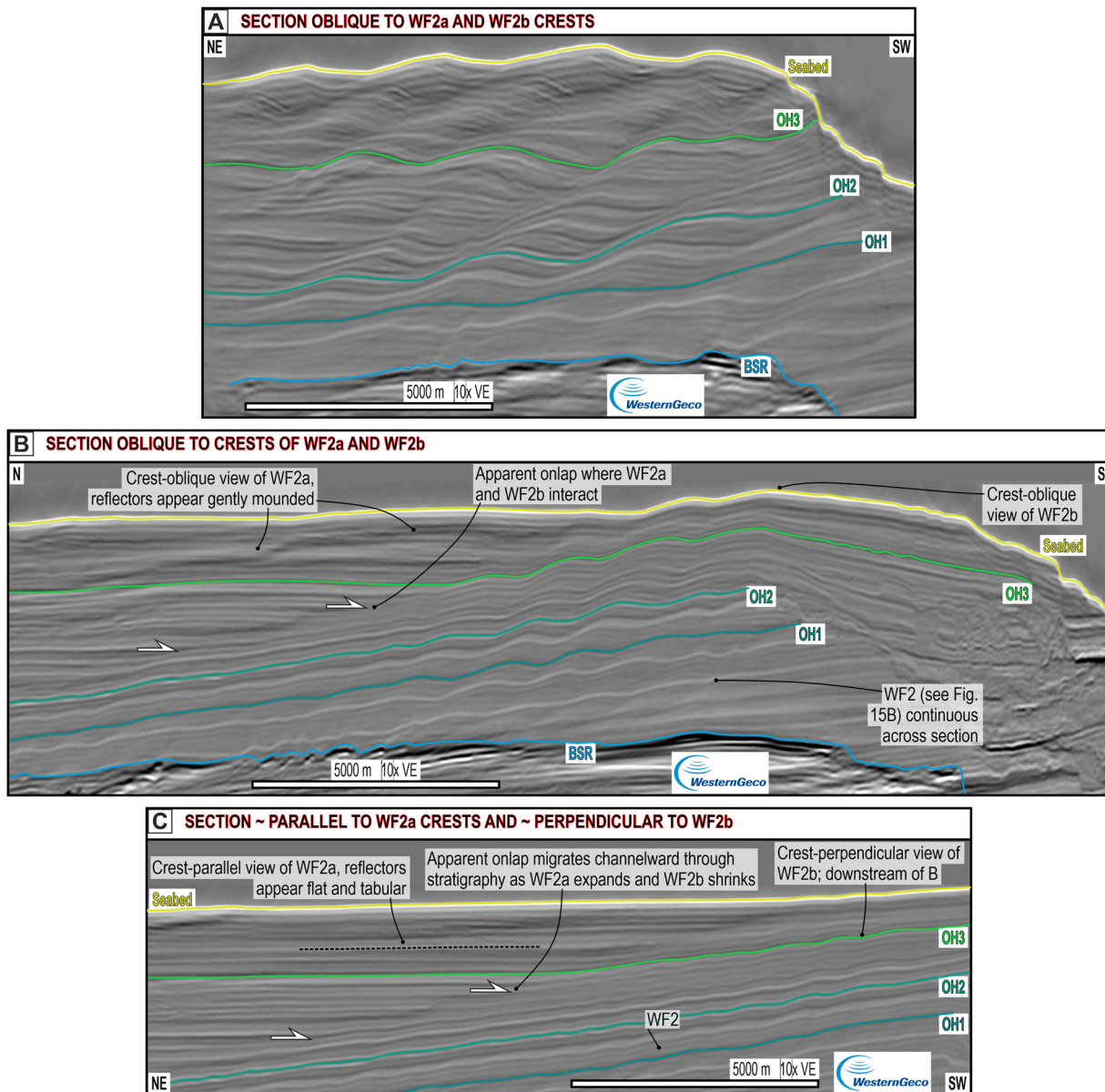


Figure 16. Annotated seismic sections at different angles to the wave crests in wave field 2a and 2b: **A**, is orientated oblique ($\sim 45^\circ$) to crests in both fields, **B**, is orientated oblique to crests in both fields, but at a higher angle ($\sim 70^\circ$) to crests in field 2b, and a lower angle to those in field 2a, **C**, is orientated \sim perpendicular to crests in field 2b and \sim parallel to those in field 2a. Differences in sediment wave height and wavelength are related to the profile locations at different positions along the channel. Note that these sections do not correspond to the profile locations in Figure 15.

perpendicular unidirectional flow on the up-channel outer-overbank of bend 6 (the formative bend of WF3) (Figure 17A, B); down-channel focusing of overspill accompanying the expansion of bend 6 likely augmented this process. Some flow from WF2a and WF2b likely re-enters the channel at the down-channel end of WF2b; much of the sediment is, however, interpreted to be deposited in the flat areas on the up-channel outer-overbank of bend 6 (Figure 17A, B, C).

Inner-bend waves on oceanward channel margin

Observations

Sediment waves are also present on the oceanward margin, on the inner-overbanks of bends 4, 6 and 10

(Figure 18A, B, C). Oceanward inner-bend waves are observed on the seafloor (Figure 18A) and within Overbank Horizon 3 (Figure 18D); they are likely present in deeper stratigraphy (to depths below Overbank Horizon 1) but their 3D geometries are uncertain. The crests of these waves are typically oriented SW-NE to NW-SE at the up-channel end of the field, where they are aligned at orientations sub-perpendicular to oblique to the channel. They curve down-channel and are typically oriented E-W to NW-SE at the down-channel end of the field, where they are aligned subparallel to oblique to the channel (Figure 18). On the inner-overbank of bend 4, at their up-channel end, the troughs of these waves form depressions in the oceanward channel-wall on the straight reach between the apices of bends 3 and 4, reaching over 50 m deep where they intersect the

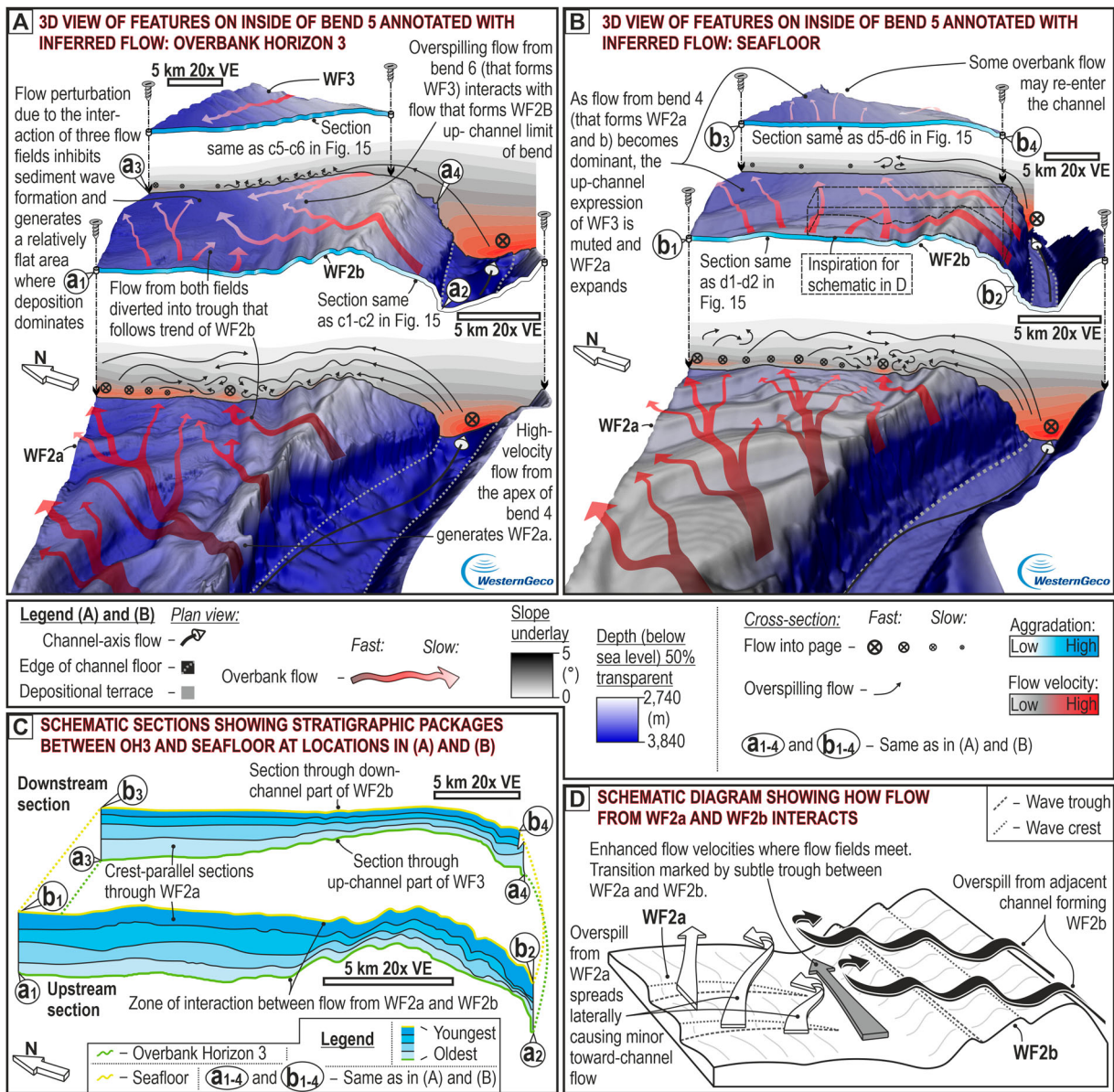


Figure 17. A, Part of Overbank Horizon 3 (same as shown in Figure 15C) displayed in 3D looking down-channel over the inner-overbank of bend 5, annotated with interpreted overbank flow orientations and velocities, and locations of aggradation. **B**, Part of the seafloor (same as shown in Figure 15D) displayed and annotated in the same way as **A**. **C**, Interpreted seismic sections through the locations displayed in A and B, showing the thickness of depositional packages between Overbank Horizon 1 and the seafloor, highlighting an overall down-channel decrease in package thickness and that reflector packages associated with wave field 2a are thicker than those of equivalent age in field 2b. **D**, Schematic section showing the interpreted nature of overbank flow interaction between wave fields 2a and 2b.

channel-wall (Figure 19A, B). The wavelengths and heights of these waves decrease down-channel, and waves branch to form multiple, smaller waves (Figures 18A, B, C, and 19A, B).

In wave crest-perpendicular cross-sections, at their up-channel end, the waves exhibit sigmoidal geometries similar to those observed in waves on the landward margin (cf. Figures 11C and 16 with Figures 18E and 19C). However, on the oceanward margin the wave troughs and crests stack vertically and away from the channel (S to SE), with thicker reflectors on their lee sides, which dip away from the channel (Figure 18E, F).

At the top of packages of terrace deposits, relatively tabular reflectors that form the main body of the terrace transition vertically into lenticular packages of reflectors that are thickest (up to 20 m) immediately channelward of the adjacent terrace-bounding surface (Figure 18E, F). These reflectors thin abruptly (over tens to a couple of hundred metres) away from the channel and terminate against their adjacent terrace-bounding surface, and gradually thin and pinch out (over hundreds of metres to two kilometres) toward the channel. The thickest part of these lens-like reflectors stacks vertically and away from the channel (southward) (Figures 18E, F and 19C). Through

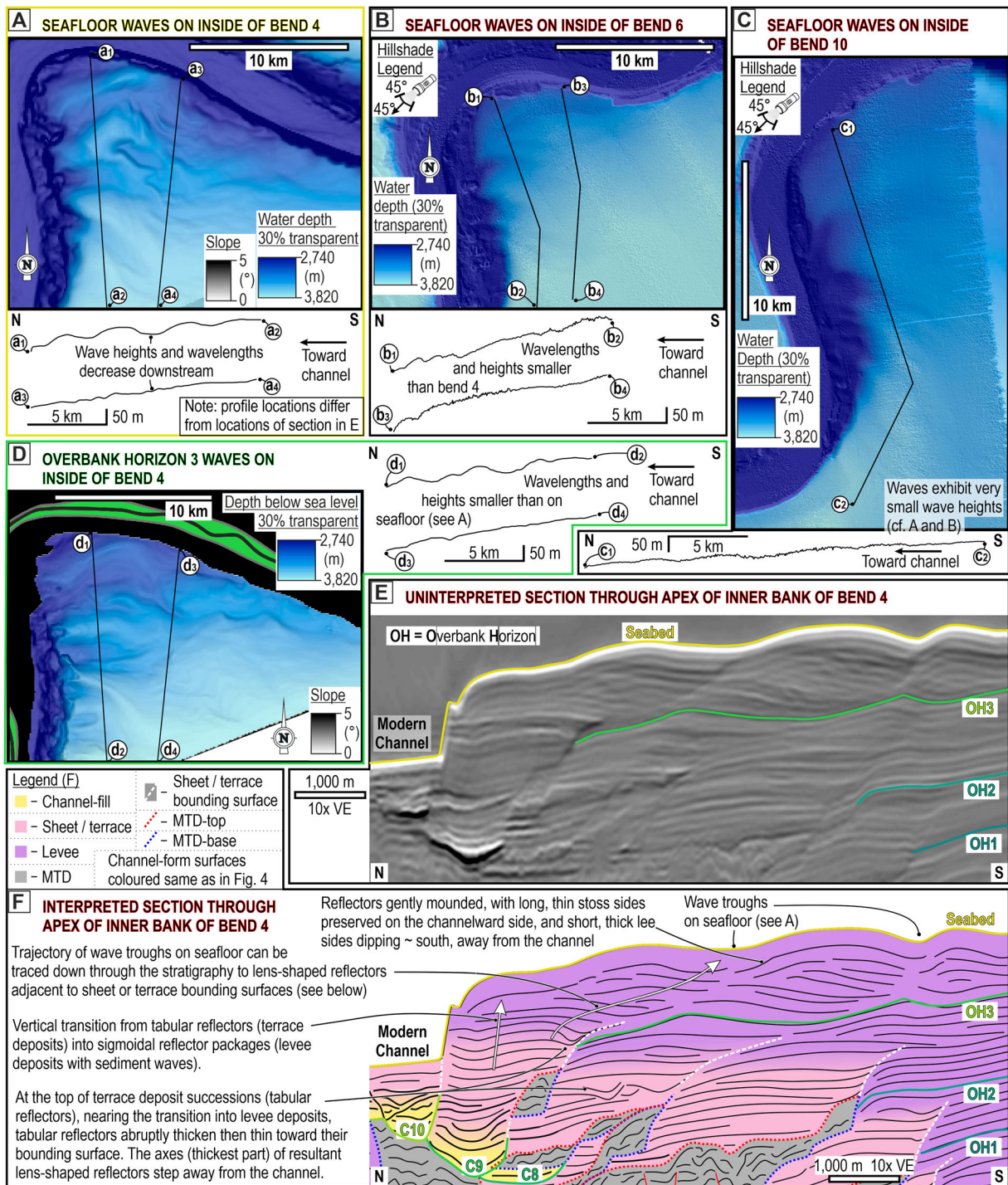


Figure 18. A–C, Seafloor maps displayed as slope (A), or hillshade (B and C) maps with depth overlays, showing inner-bend waves on the oceanward margin, on the insides of bends 4, 6 and 10; crest-perpendicular profiles are also included. D, Slope map with depth overlay showing the waves on the inner-overbank of bend 4 on Overbank Horizon 3; two ~ crest perpendicular profiles included. E, Annotated seismic section and F, interpreted line drawing thereof, showing the seismic expression of the waves on the inner-overbank of bend 4 orientated perpendicular to the wave crests.

progressively shallower stratigraphy, the deepest part of these lens-like reflectors transition into the troughs of the waves observed on the seafloor and Overbank Horizon 3; the reflectors themselves transition into the thick lee sides of the waves near the seafloor (Figure 18E, F). The terrace-bounding surfaces, the deepest parts of lens-like reflectors, and the wave troughs follow a common trajectory that exhibits a

progressively gentler inclination up-stratigraphy and away from the channel (Figure 18E, F). Small waves in the down-channel parts of the field are relatively symmetrical, and do not appear to exhibit distinct differences in reflector geometries on their lee and stoss sides (Figure 19C), although this could be due to geometric variability being below the resolution of the data.

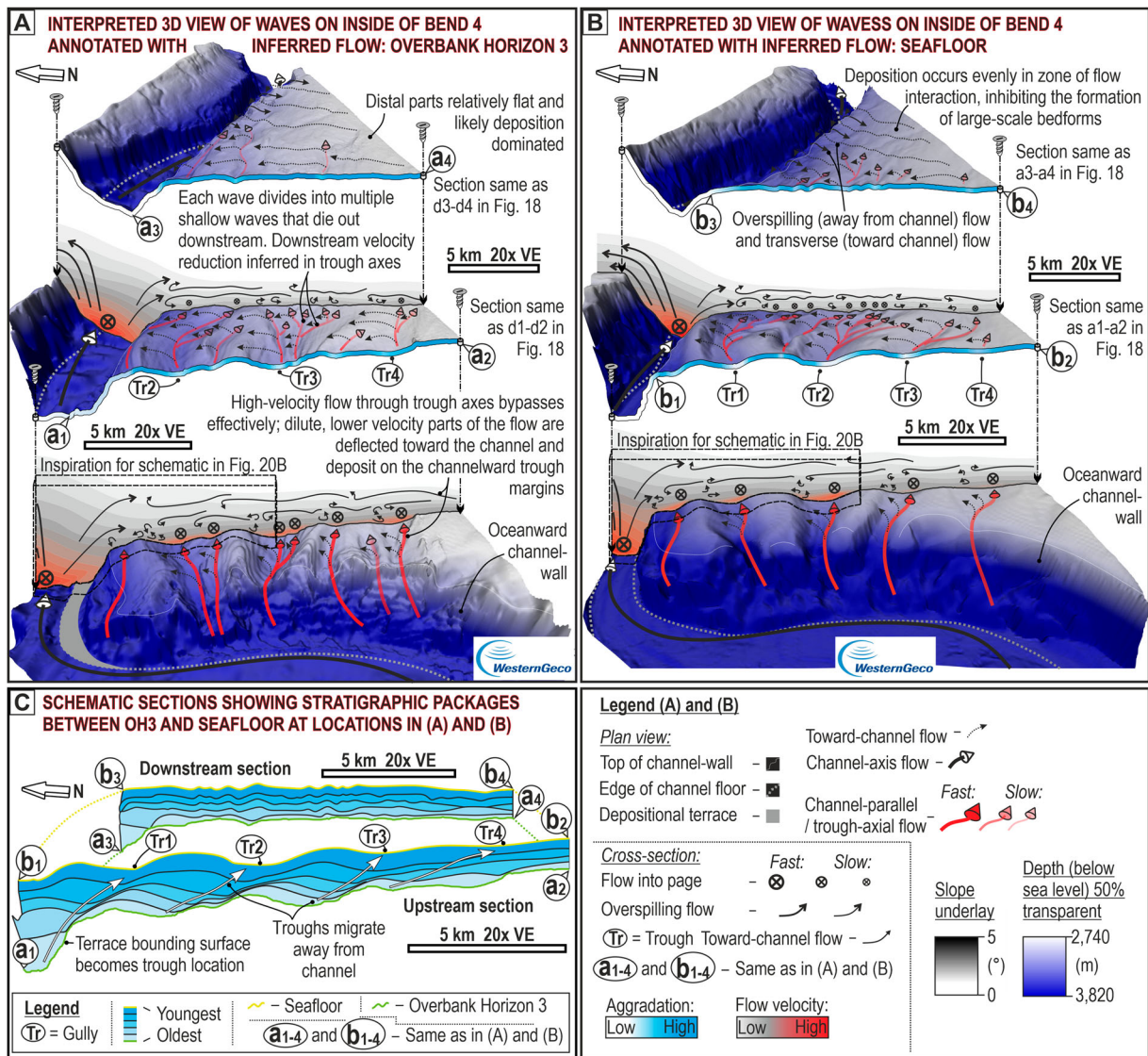


Figure 19. A, Interpreted part of Overbank Horizon 3 (same as shown in Figure 18D) displayed in 3D looking down-channel over the inner-overbank of bend 4, annotated with interpreted overbank flow orientations and velocities, and locations of aggradation. **B**, Interpreted part of the seafloor (same as shown in Figure 18A) displayed and annotated in the same way as **A**. **C**, Interpreted seismic sections through the locations displayed in **A** and **B**, showing the thickness of depositional packages between Overbank Horizon 1 and the seafloor, highlighting an overall down-channel decrease in the sediment wave wavelengths and heights.

Interpretations

Overspill on the oceanward margin is enhanced in the straight channel section between bends 3 and 4 by the influence of centrifugal force downstream of the apex of bend 3. The point of maximum overspill may have also been shifted further down-channel by the influence of the Coriolis force, shifting the point of maximum shear stress on the outside of bend 3 further down-channel. Higher velocity and potentially coarser-grained parts of the overbank flow on the inner-overbank of bend 4 were funnelled through the wave troughs that form depressions in the channel wall (Figures 19A, B and 20A, B). On the channel overbank, higher concentration, higher velocity, dominantly bypassing parts of the overbank flow (McArthur et al. 2020) travel through the axis of the wave troughs. However, a more dilute component of flow, generated dominantly by deflection due to the

Coriolis force and, potentially aided by flow reflected off the Chatham Rise and the subducting plate, and the influence of the DWBC, flows toward the channel (Figure 20A). This transverse component of flow leads to faster deposition on the lee sides of the waves (away from channel), than on the stoss sides; deposition in the axis of troughs is suppressed by the axial flow component (Figures 19A, B and 20B). Through time, these processes build the sigmoidal reflector geometries and troughs that stack away from the channel that are observed in the subsurface (Figure 19C); this migration pattern differs from the interpreted toward-channel migration of waves on the oceanward overbank (Figure 16).

The aforementioned waves evolve from terraces. Terraces aggrade faster than levees in the Hikurangi Channel, as evidenced by observed vertical transitions from terrace to overbank deposits (Figure 18E, F; Tek

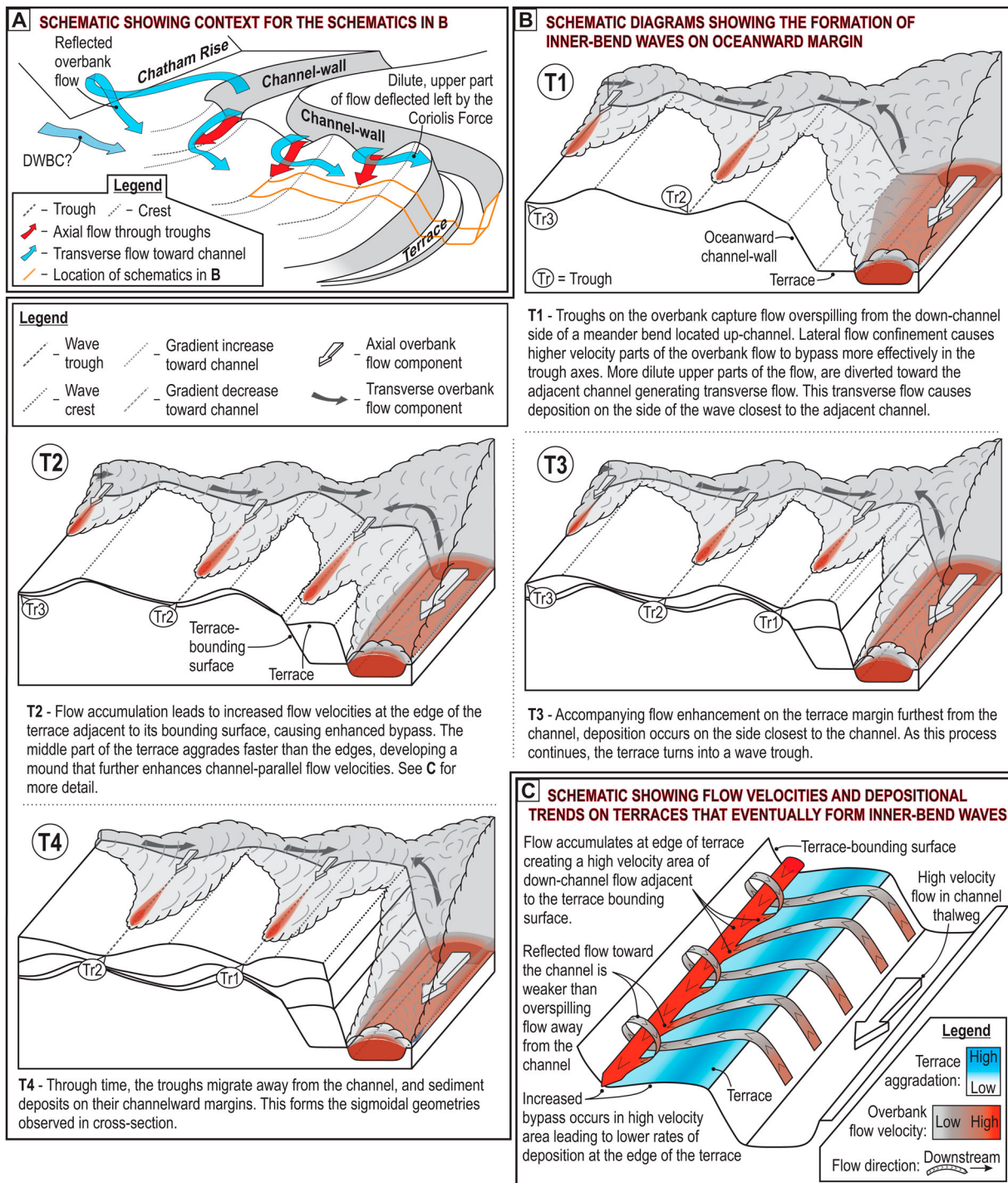


Figure 20. Diagrams showing the formation and evolution of inner-bend waves on the oceanward overbank, specifically on the inside of bend 4. **A**, Three-dimensional schematic showing the context of the inner-bend waves detailed in **B**, and the cause of transverse flow toward the channel and its relationship with trough-axial flow. **B**, Detailed schematic diagrams (location on Figure 19A and B; stratigraphic evolution based on upstream section in Figure 19C; note perspective change from Figure 19 to looking up-channel) demonstrating how the sediment waves evolve from terraces, and how the interaction between axial flow through the wave troughs and transverse flow toward the channel causes sediment wave migration away from the channel. **C**, Schematic showing how flow accumulation against the terrace-bounding surface generates a high-velocity component of down-channel flow leading to bypass at the terrace edge and mounding in the centre.

et al. 2021). Flow on terraces is complex, commonly comprising a primary component that flows down-channel and away from the channel, and a secondary component that flows down-channel and toward the channel after being reflected off the terrace-bounding surface (Figure 20C; Hansen et al. 2015). When a terrace has aggraded to near the height of its adjacent

levee, the primary flow component dominates the reflected flow component, causing flow convergence (*sensu* Kneller 1995) adjacent to the terrace-bounding surface. Accumulative flow leads to a high-velocity component of flow that travels down-channel, parallel to the confining terrace-bounding surface (Kneller and McCaffrey 1999), where erosion and/or bypass is

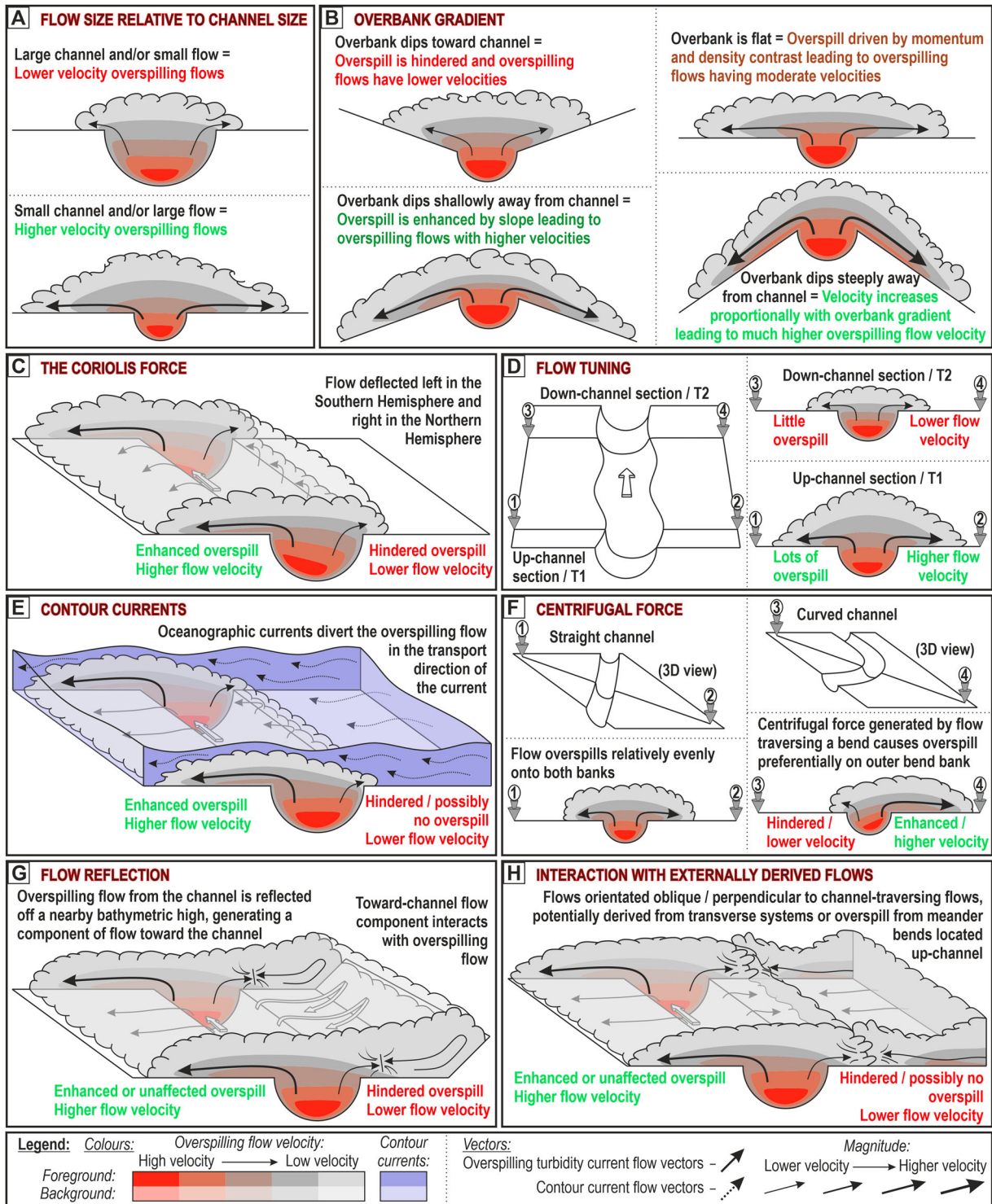


Figure 21. Schematic diagrams showing eight of the nine processes interpreted to control overspill from the Hikurangi Channel: **A**, flow size relative to conduit size, **B**, overbank gradient, **C**, flow tuning, **D**, the Coriolis force, **E**, contour current, **F**, centrifugal force, **G**, flow reflection, **H**, interaction with externally derived flows. The interaction of flows originating from different parts of the channel is demonstrated in [Figure 23](#).

enhanced, and deposition is hindered ([Figure 20C](#)). This process generates mounded reflectors on the terraces and concave-up surfaces adjacent to terrace-bounding surfaces, which are filled with lens-like reflectors (T2 in [Figure 20B](#)). High-velocity down-channel flow is also sheltered from a Coriolis-induced transverse component of overbank flow (potentially influenced by other processes) that travels toward the

channel (responsible for deposition on the lee sides of the waves; see above) by the terrace-bounding surface. As the terrace aggrades further, the influence of this transverse flow component becomes greater. As such, the mounded, middle part of the terrace becomes an inner-overbank wave crest, and the area of enhanced bypass adjacent to the terrace-bounding surface becomes a trough (T3 and T4 in [Figure 20B](#)).

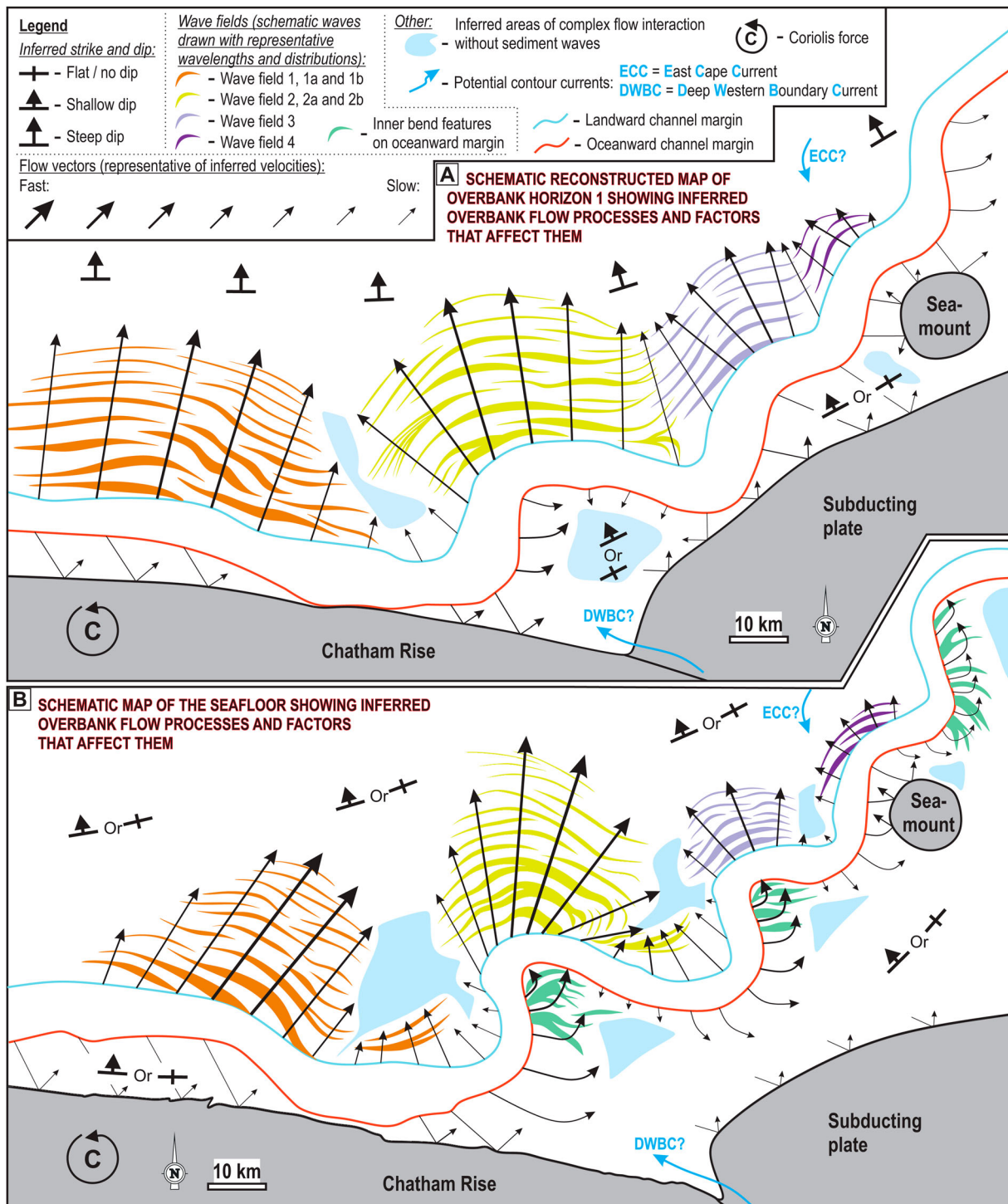


Figure 22. Schematic diagrams showing the distribution of sediment waves and interpreted overbank flow in the deep stratigraphy, on Overbank Horizon 1 (A), and on the seafloor (B).

Further down-channel, the influence of flow through the axis of the troughs is interpreted to diminish progressively, causing fanning of the waves and rotation of the wave crests to be oriented subparallel to the reach of channel downstream of the bend apex. The less well-pronounced waves in down-channel parts of the field are interpreted to have formed dominantly by the transverse, toward-channel component of flow (Figure 19). The more symmetrical shape of these waves suggests that overbank flow away from the channel on the up-channel outer-

overbank of bend 5 may have generated a competing component of flow, impeding strong unidirectional flow and leading to more even deposition (Figure 19).

Discussion

Controls on overspill processes on the overbanks of the Hikurangi Channel

Nine factors that control the nature of overbank flow and the resultant overbank depositional architecture

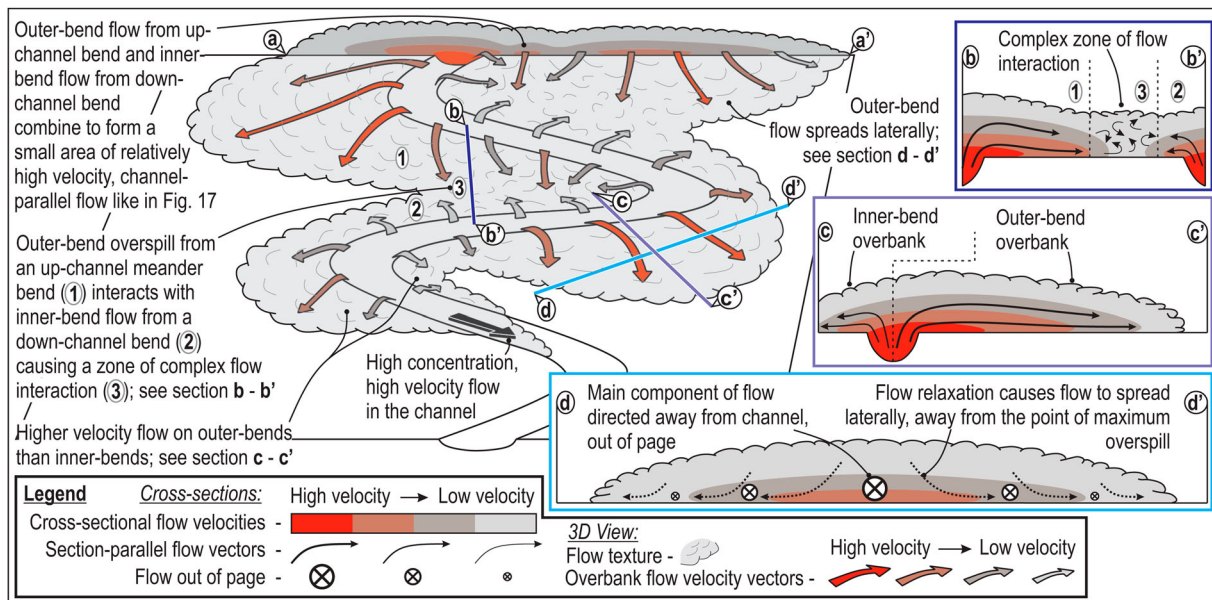


Figure 23. Schematic diagram showing how overbank flow originating from different parts of a channel interacts on the overbanks.

of the Hikurangi Channel have been identified (Figure 21).

Flow size versus conduit size

The thickness of a turbidity current relative to the depth of its host conduit is a fundamental control on the magnitude and velocity of overbank flow. Larger flows generate thicker and likely higher velocity overbank flow, meaning coarser parts of stratified flows can escape the conduit (Figure 21A; Dennielou et al. 2006).

Overbank gradient

Flow velocity may be enhanced on channel overbanks with steep outer-levee gradients that slope away from their conduit and hindered on overbanks that slope toward the channel (Figure 21B; Kane et al. 2010; Nakajima and Kneller 2013). In the studied reach of the Hikurangi Channel, the oceanward overbank is horizontal, or slopes toward the channel throughout the studied stratigraphy. This appears to have hindered overbank flow and inhibited the formation of sediment waves on the oceanward overbank (Figure 22). On the landward margin, the outer-levee gradient is interpreted to have shallowed progressively as slope-traversing drainage networks were established, and overbank flow downstream of the apex of expanding bends acted to redistribute sediment in the trench, leading to a largely flat trench-floor and gently-sloping to flat outer-levees (Table 2, Figures 3B and 22).

Flow 'tuning'

A systematic down-channel decrease in the magnitude and velocity of overspill from the Hikurangi Channel is attributed to the process of flow 'tuning'. This arises from the loss of material from the dilute, upper parts

of flows in up-channel locations, causing the range of flow heights to decrease down-channel as flows progressively lose material, with thicker flows losing more than thinner-ones (Figure 21C; Mohrig and Buttles 2007; Kelly et al. 2019). Flow tuning has generated a down-channel decrease in the size of the outer-bend wave fields (Figure 22).

The Coriolis force

The leftward deflection of overbank (and potentially in-channel) flow characteristic of the Coriolis force in the southern hemisphere (Figure 21D; Klauke et al. 1998; Cossu et al. 2015) has exerted a significant control on overbank architecture throughout the depositional period along the studied channel reach (Figure 22); this control was also recognised by Lewis and Pantin (2002). This flow deflection contributed to the generation of large, outer-bend wave fields solely on the landward overbank. It was also instrumental in the generation of transverse flow toward the channel that forms inner-bend waves on the oceanward channel margin (Figures 19 and 22), and in maintaining continual flow away from the channel on inner-bend overbanks on the landward margin (Figures 17 and 22).

Contour currents

Contour currents may locally hinder overspill that flows counter to them and augment overspill in the same direction (Figure 21E; Miramontes et al. 2020). While the locations and orientations of contour currents in the studied part of the Hikurangi Trench are poorly constrained, two currents have potentially affected the study area at different times. Lewis and Pantin (2002) inferred that a shallow branch of the

DWBC flowed W along the northern edge of the Chatham Rise, which controlled the formation of inner-bend sediment waves on the oceanward margin (Figures 2 and 22). The detailed observations made herein allow for the interpretation that the DWBC helped generate a toward-channel component of overbank flow that contributes to the formation of inner-overbank waves (Figure 20). However, the presence of similar waves on the inside of bends 6 and 10, where the DWBC would be unlikely to act, suggests that its effect may have been relatively minor. Furthermore, the DWBC is not observed to be presently active in the study area (Fernandez et al. 2018), meaning its potential effect would vary temporally. The ECC, in contrast, is currently active and likely flows SE across the channel in the study area, but the location of the crossing is unclear (Figure 2). If the ECC crosses the down-channel parts of the studied channel reach, it may be partially responsible for the down-channel decrease in wave field size on the landward overbank (Figure 22). If the ECC crosses the channel in a location further up-channel, its effects are likely negligible and are not recorded by the sediment wave distributions. Bailey et al. (2020) tentatively interpreted that a bottom current crossed the Hikurangi Channel at bend 4, which they inferred locally modified the channel and overbank wave field. However, analysis of the morphology and distribution of these sediment waves herein suggests they are more likely related to overbank flow, meaning that if the ECC crosses the channel at bend 4 it is unlikely to significantly affect overbank sediment wave development. Definitively determining the influence of contour currents on overbank sedimentation in the Hikurangi Trench requires additional oceanographic data.

Centrifugal force

Accompanying a channel bend's expansion, centrifugal force causes a focusing of overspill downstream of bend apices (Figure 21F; Timbrell 1993; Kane et al. 2008). Through time, as the channel became more sinuous, the wave fields on the landward channel overbank became spatially separated from one another, and some divided into distinct outer-bend and inner-bend fields (Figure 22). The plan-view morphologies and distributions of wavelengths and wave heights in each field also changed concomitantly with increased channel sinuosity (Figure 22). The effect of centrifugal force on sediment wave geometries on the seafloor in the study area was originally noted by Lewis and Pantin (2002).

Flow reflection

The Chatham Rise and the less prominent subducting Pacific plate generate seafloor topography that runs along the oceanward margin of the channel. Overbank flow reflects off this topography, generating

(potentially in conjunction with other factors) a component of flow toward the channel (Figures 21G and 22). This toward-channel component of flow may inhibit the formation of outer-bend sediment waves on the oceanward overbank, and contribute to the formation of inner-bend waves on the oceanward overbank (Figure 20). The thickness of contemporaneously formed reflector packages (Table 2 and Figure 3) suggest deposition rates are generally higher on the flat trench floor than on the steep Chatham Rise and subducting plate. Therefore, largely tabular reflectors were generated, allowing the classification of the oceanward overbank deposits as 'confined external levees' (Table 2; Clark and Cartwright 2011).

Interaction with externally derived flows

The interaction with turbidity currents of different origins (Figure 21H; Okon et al. 2021) may exert a control on overbank flow in the Hikurangi Channel. The dilute, distal parts of SE flowing, slope-traversing turbidity currents may interact with distal, NW flowing overbank flow near the subduction front (Figure 2). Interaction of these turbidity currents may reduce the velocity of unidirectional overbank flow and restrict the size of outer-bend wave fields (Figure 22). Alternatively, flow of these different origins may not interact, but their deposits may stack compensationally; more data are needed to determine which process is dominant in the Hikurangi Trench. Regardless of whether the individual flows interact, combined deposition from slope-traversing and overbank flows may occur over the entire trench floor (outside of the channel), suppressing the development of steep outer-levee gradients and leading to a relatively flat trench floor (Table 2, Figures 3 and 6). In systems where two contemporaneously active channels run parallel to one another, overspill derived from the two channels may also interact on their mutual overbank, causing flow complexity.

Interaction of overspill from different locations

Overbank flows originating from different locations along the channel may generate areas of complex flow interaction, inhibiting the development of sediment waves. In the Hikurangi Channel, overspill down-channel of a landward facing bend may interact with lower velocity up-channel overspill from the next down-channel (landward facing) bend (Figures 22 and 23). This interaction could initially occur due to bend expansion causing a separation of the wave fields and focusing flow on the downstream sides of bends, generating a complex zone of flow interaction (Figure 23). Consistent unidirectional flow does not occur in these zones and consequently they are devoid of sediment waves (Figure 22). Interaction of flow from different bends is likely to be more common in channel systems with relatively flat, laterally-confined overbanks like

the Hikurangi Channel, where the gradient of the outer-levee does not cause overspill to flow consistently away from the channel.

Spatio-temporal variability and interaction of controls

The subsurface architecture and seafloor expression of the studied overbank deposits are a product of the complex interaction between the controls listed above. The effect of most controls will also differ between individual flows as the flow height fundamentally dictates the volume of overspill (Figure 21A); tuning effects may eventually suppress such differences. The influence of some controls, such as the Coriolis force, is also partially dependent on the nature of channel-traversing flows (Cossu et al. 2015; Davarpanah Jazi et al. 2020). Variations in flow thickness and nature can also occur cyclically, in response to sea-level fluctuations and climatic changes (Romans et al. 2016). The effect of some controls, such as contour currents, may also vary over a range of distinct timescales. For example, the ECC is highly variable on interannual and decadal timescales (Fernandez et al. 2018), and the shallow branch of the DWBC invoked by Lewis and Pantin (2002) may only be active during glacial periods. However, the analysis of sediment waves and seismic-scale architecture herein has allowed the spatio-temporal variability of the influence of different controls on net overbank flow and sedimentation over longer timescales to be determined. This helps to mitigate uncertainty related to variability at timescales between individual flows.

Spatial variability in the magnitude at which controls operate is inferred on the seafloor and in the subsurface. Coriolis forcing (Figure 21D) is the only control that is not spatially restricted at the scale of observation, and consistently affects overbank flow across the entire area. The effect of some controls changes up- or down-channel. For example, by definition, flow tuning (Figure 21C) generates a down-channel decrease in the magnitude of overspill. However, some controls, such as centrifugal force (Figure 21F), overbank gradient (Figure 21B) and interaction of overspill from different locations (Figure 23), are inherently linked to the morphology of the channel and its overbanks. As such, they can produce more localised effects and are subject to feedback effects. For example, the influence of centrifugal force is dependent on bend curvature, meaning its effect will vary between adjacent bends (tens of km) (Figure 22). Other controls that present localised effects but are not directly related to channel morphology include contour currents (Figure 21E) and flow reflection (Figure 21A). For example, in this setting flow reflection is likely to influence flow dominantly on the oceanward overbank (Figure 22).

Additionally, as topography generated by the Chatham Rise is steeper, taller, and closer to the channel than the Pacific plate, the strength of reflected flow likely also decreases downstream.

Changes in sediment wave morphology are observed through the studied stratigraphy. These changes are caused by long-term temporal variations in the relative influence of some controls; other controls have affected overbank flow and sedimentation consistently throughout the depositional period. For example, the Coriolis force (Figure 21D) has consistently affected overbank flow and sedimentation throughout deposition (Figure 22). However, the influence of centrifugal force has increased with increasing channel sinuosity. The effect of other controls may have been constant throughout deposition in some areas, but variable in other areas. For example, the effect of toward-channel overbank gradients on the oceanward margin has been constant, whereas the away-from-channel gradient on the landward overbank is interpreted to have progressively shallowed through time, changing its influence on overbank flow (Figure 22).

Multiple controls that influence overbank flow in a given location can either augment or act against one another. For example, on the oceanward overbank the effects of the Coriolis force (Figure 21D), an overbank gradient that sloped toward the channel (Figure 21B), and flow reflecting off the Chatham Rise and the Pacific plate (Figure 21G), combine to generate a component of flow that travels toward the channel (Figures 20 and 22). These three factors counteract the effect of centrifugal force on the oceanward margin, inhibiting the formation of outer-bend sediment waves on the oceanward margin (Figure 22). In addition to separate controls competing for dominance in a given area, the effect of some controls is directly dependent on the presence of others. For example, the interaction of overspill originating from different bends (Figure 23) is effectively dependent on channel sinuosity and the effect of centrifugal force; an increase in sinuosity, and therefore centrifugal force, will consequently increase the interaction of down-channel overbank flow from up-channel bends, and up-channel flow from down-channel bends, leading to a progressive loss of sediment waves in the location of interaction.

Overall, the complex interaction between controls that have affected overspill on different parts of the overbank area consistently through time, vs. those that are temporally variable has led to the complex sediment wave distributions and depositional architectures described herein. It is therefore difficult to rank the importance of all controls. However, granted that overspill is occurring, evidence for leftward flow deflection is observed across the entire overbank area meaning that, while the effects of other controls locally augmented its effects, the Coriolis force is

dominantly responsible for enhanced landward overbank flow and hindered oceanward overbank flow. Through progressively shallower stratigraphy, accompanying an increase in channel sinuosity, the morphologies of the waves on the landward margin have changed accordingly. Therefore, the interaction between Coriolis and centrifugal forcing are interpreted to have produced the most significant effect on overbank sediment wave distribution and overbank architecture, particularly on the landward overbank. These interpretations are generally in accordance with those of Lewis and Pantin (2002).

Inner-bend sediment wave fields

Identification of inner-bend wave fields on both sides of the channel was permitted by using high-resolution bathymetry and 3D seismic data. Inner-bend wave fields on each side of the channel are interpreted to have different mechanisms of formation, but both form as a result of multiple components of overbank flow originating in different locations and travelling in various orientations (Figures 17, 19 and 20). As such, they record more complex patterns of overbank flow and sedimentation than outer-bend waves and the morphologies of their constituent waves do not show simple relationships with the orientations of their formative flows.

Lewis and Pantin (2002) interpreted that waves that migrate away from the channel on the oceanward margin on the inside of bend 4 (this study), were produced solely by westward flowing contour currents (a shallow branch of the DWBC). However, in-depth analysis of these waves and their 3D subsurface architecture suggests that these waves are the product of the complex interaction between two different overbank flow components: some overspilling flow generates an axial flow component that is funnelled through the wave troughs; some is deflected by the Coriolis force, reflected off the Chatham Rise or subducting plate, and possibly influenced by the DWBC, generating a transverse flow component toward the channel (Figures 19 and 20).

On the landward margin, inner-bend sediment wave fields have formed and become separated from wave fields on the outer-overbanks as the shape and distributions of outer-bend wave fields have progressively rotated and migrated down-channel (Figures 7, 9, 13, and 22). The inner-bend waves are formed and maintained by overspill on the inner-overbank of bends, the velocity of which in the study area is augmented by the Coriolis force. However, a subtle trough marks the contact between the outer- and inner-bend wave fields, which is interpreted to funnel relatively high-velocity parts of the flow (Figures 17 and 23); the crests of waves in the outer-bend fields are oriented normal to those in the inner-bend fields.

The separation of outer bend fields and the complexity of inferred flow within them and at their boundary is due to the interaction of flow components originating from different parts of the channel (Figure 23).

Sedimentological implications

The many controls listed above act to control flow processes and the development of sediment waves on the overbank areas of the Hikurangi Channel. The effect each control exerted on the overbank deposit architecture varied along the channel and through time, generating overbank deposits with a complex three-dimensional architecture. These deposits, their trends, and their sedimentary structures, may differ from those portrayed in conventional models derived from studies using outcrop, seafloor, or 2D seismic data.

On the seafloor, the Hikurangi Channel apparently lacks well-defined levees along much of its length. However, this bears no reflection on how effectively channel-traversing flows overspill, nor the nature of the channel and overbank deposits in the subsurface. It is merely a result of deposition by slope-traversing flows derived from the subduction margin and overspilling from the Hikurangi Channel occurring across the floor of a laterally-confined trench, and effectively filling the lateral accommodation space therein (Figure 3); the Hikurangi Channel is highly aggradational (cf. Casciano et al. 2019). The fact that highly aggradational channels such as the Hikurangi Channel can be bordered by effectively flat overbank areas on the seafloor means the seafloor profile of submarine channel overbanks can be an unreliable predictor of subsurface channel and overbank architecture.

The orientation of overbank flow from the Hikurangi Channel is interpreted to vary substantially. On the oceanward and landward overbanks, the interaction of flows from different bends, flow reflection, and the Coriolis force generate areas with complex multidirectional flow. Deposits in these areas may exhibit highly variable palaeocurrents and may contain 'combined flow' bedforms such as hummocky cross-stratification (Muzzi Magalhaes and Tinterri 2010). In outcrop, palaeocurrent variability has been used to distinguish 'internal levees' or 'terraces', which typically exhibit highly variable palaeocurrents, from 'external levees', which exhibit less variability (Kane and Hodgson 2011). However, in outcropping confined channel systems with low overbank gradients, that are analogous to the Hikurangi Channel, this criterion may not be reliable.

In high latitude systems, the dominance of Coriolis forcing upon cross channel flow results in preferential deposition along one channel overbank (Cossu et al. 2015) and hinders sinuosity development (Peakall et al. 2012). In low latitude settings, Coriolis forces

are negligible, and flow dynamics are dominated by centrifugal forces, leading to preferential overspill at bend apices on opposing sides of the channel, in successive bends (Keevil et al. 2006; Cossu and Wells 2010). The overbank architecture of the mid-latitude (*sensu* Menard 1955; Savoye et al. 1993) Hikurangi Channel displays evidence of the effect of both Coriolis and centrifugal forces on overbank architecture. The relative influence of these competing controls varied through time as a result of changing channel morphology, generating a more complex architecture than can be predicted by either of the aforementioned end member controls.

On the seafloor and in the subsurface of the Hikurangi Channel, evidence for the interaction of overbank flow and deposition from different locations along the channel are observed (Figure 23). Interacting packages of overbank deposits can thin toward, and interfinger with, each other (Table 2 and Figure 16). In 2D seismic sections or in outcropping sections, these depositional architectures may be interpreted to be derived from an extra-channel source. Evidence for the interaction of contemporaneous overspill from different parts of the channel (Figure 23) is also observed. In outcrop or core, these areas of interaction may exhibit complex paleocurrent variability and contain complex combinations of sedimentary structures and architectures that appear uncharacteristic of classic levee deposits.

Therefore, in the Hikurangi Channel, and probably in channels in other confined basins in mid-latitudes, simple models explaining bed thicknesses and sandstone distribution, palaeocurrent orientations, and sedimentary structures cannot be applied universally. This has implications for the interpretation of overbank deposits and therefore palaeogeographic reconstructions in outcropping ancient channel systems, but also for categorising channel types and inferring flow processes in channels and on their overbanks from bathymetric data alone.

Conclusions

Integration of high-resolution bathymetry, 2D, and 3D seismic data is used to investigate the controls on overbank flow processes and depositional architecture on the overbank areas of the Hikurangi Channel. Novel techniques for the quantitative analysis of sediment wave orientations and morphologies are conducted on the seafloor and on three, regionally-traceable subsurface horizons, and are used to interpret the three-dimensional subsurface architecture, and infer overbank flow processes.

Nine factors are interpreted to have controlled overbank flow processes on the overbanks of the Hikurangi Channel: flow size versus conduit size, overbank gradient (magnitude and orientation), flow tuning, the Coriolis force, contour currents, flow reflection,

centrifugal force, interaction with externally derived flows, and interaction of overspill from different locations along the channel. These controls mutually interact, and their relative importance has varied significantly throughout the depositional period, and in different parts of the studied overbanks, generating complex patterns of overbank flow and sedimentation.

In deeper stratigraphy the Hikurangi Channel was straighter and was bordered on the landward margin by four sediment wave fields, with no wave fields preserved on the oceanward margin. Overspill that formed sediment waves on the landward margin occurred along the whole studied channel reach, and flowed away from the channel over relatively steep external levees; overbank flow velocities decreased down-channel and increased toward the apices of the then poorly-developed bends. Sediment wave formation was inhibited on the oceanward and enhanced on the landward margin by the combined effects of the oceanward channel overbank sloping toward the channel, flow reflection off the Chatham Rise and the subducting plate, and leftward flow deflection by the Coriolis force.

Through progressively shallower stratigraphy, focusing of overbank flow downstream of bend apices led to the spatial separation of the four wave fields on the landward margin, the division of the most up-channel two wave fields into distinct inner-and outer-bend fields, and the development of inner-bend waves on the oceanward margin. These morphological trends chiefly arose due to an increase in channel sinuosity, augmented by a reduction in gradient on the landward margin as the trench-floor became flat; other controls such as the interaction of overbanks flow with slope-traversing turbidity currents near the subduction margin, and two contour currents (the East Cape Current and the Deep Western Boundary Current) may also have exerted some control.

This study builds on work by Lewis and Pantin (2002). However, detailed observations from high-resolution data have permitted new quantitative analysis of wave morphologies and distributions, and interpretation of how the influence of each control has varied through time. It has also allowed the novel identification of distinct inner-bend wave fields. The nature of inner-bend fields on the landward margin is controlled by the interaction of Coriolis-enhanced overspill on wave-hosting inner-bends, and flow from the down-channel outer-bend overbank of the adjacent, up-channel bend. Inner-bend wave fields on the oceanward margin originate as terraces then evolve and migrate through the combined effects of axial flow funnelled through the wave troughs, and transverse flow toward the channel created by dilute overspill reflected off the Chatham Rise or subducting slab, and deflected by the Coriolis force.

Some or all of the controls on overbank flow and overbank deposit architectures identified in the Hikurangi Channel are common to most modern and ancient channel systems, and particularly those in mid-latitude and/or confined basins. This work has implications for the interpretation of overbank flow processes from seafloor data, and palaeoenvironmental reconstructions from ancient, outcropping overbank deposits.

Acknowledgements

This work was funded by Turbidites Research Group; we thank sponsors AkerBP, CNOOC, ConocoPhillips, Murphy, OMV, and OXY. Schlumberger WesternGeco are thanked for access to the seismic data used in this study. Multibeam bathymetry and backscatter data displayed are made available for download by NIWA, and can be obtained from NZPM. Marta Ribó is thanked for insightful discussions that helped improve the methodologies used herein. We thank Emma Morris and an anonymous reviewer for their thorough reviews that have improved the quality of the manuscript, and Editor Lorna Strachan for handling the manuscript.

Disclosure statement

No potential conflict of interest was reported by the author(s).

Funding

This work was supported by China National Offshore Oil Corporation; ConocoPhillips; Murphy; Oxy; Aker BP; OMV.

Data availability statement

The data that support the findings of this study are available upon application to Schlumberger WesternGeco (<https://www.slb.com/companies/westerngeco>). Restrictions apply to the availability of these data, which were used under license for this study. Bathymetry data available from New Zealand Petroleum and Minerals as part of their 2016 datapack (<https://www.nzpam.govt.nz/maps-geoscience/petroleum-datapack/>).

References

- Babonneau N, Savoye B, Cremer M, Bez M. 2004. Multiple terraces within the deep incised Zaire Valley (ZaiAngo Project): are they confined levees? In: Lomas SA, Joseph P, editor. Confined turbidite systems. Geological Society of London Special Publication, Vol. 222. London: The Geological Society of London; p. 91–114.
- Bailey WS, McArthur AD, McCaffrey WD. 2020. Distribution of contourite drifts on convergent margins: examples from the Hikurangi subduction margin of New Zealand. *Sedimentology*. 68(1):296–323.
- Ballance PF. 1975. Evolution of the India-Pacific plate boundary in North Island, New Zealand. *Bulletin of the Australian Society of Exploration Geophysicists*. 6:58–59.
- Barnes PM, Lamarche G, Bialas J, Henrys S, Pecher I, Netzeband GL, Greinert J, Mountjoy JJ, Pedley K, Crutchley G. 2010. Tectonic and geological framework for gas hydrates and cold seeps on the Hikurangi subduction margin, New Zealand. *Marine Geology*. 272:26–48.
- Barnes PM, Wallace LM, Saffer DM, Bell RE, Underwood MB, Fagereng A, Meneghini F, Savage HM, Rabinowitz HS, Morgan JK, et al. 2020. Slow slip source characterized by lithological and geometric heterogeneity. *Science Advances*. 6(13):eaay3314:1–10.
- Bell D, Stevenson CJ, Kane IA, Hodgson DM, Poyatos-Moré M. 2018. Topographic controls on the development of contemporaneous but contrasting basin-floor depositional architectures. *Journal of Sedimentary Research*. 88(10):1166–1189.
- Bland KJ, Lamarche G, Anderson O, Barnes PM, Black J, Bowden D, Chiswell S, Crutchley G, Gorman R, Mountjoy J, et al. 2014. Pegasus basin petroleum prospectivity screening report. GNS Science Consultancy Report 2014/103, NZP&M, Ministry of Business, Innovation & Employment (MBIE), New Zealand Unpublished Report PR(CR2014-103). p. 1–139.
- Cardozo N, Allmendinger RW. 2013. Spherical projections with OSXStereonet. *Computers and Geosciences*. 51:193–205.
- Carter L. 1992. Acoustical characterisation of seafloor sediments and its relationship to active sedimentary processes in Cook Strait, New Zealand. *New Zealand Journal of Geology and Geophysics*. 35:289–300.
- Carter L, Carter RM, Nelson CS, Fulthorpe CS, Neil HL. 1990. Evolution of Pliocene to recent abyssal sediment waves on bounty channel levees, New Zealand. *Marine Geology*. 95(2):97–109.
- Carter L, Manighetti B, Elliot M, Trustrum N, Gomez B. 2002. Source, sea level and circulation effects on the sediment flux to the deep ocean over the past 15 ka off eastern New Zealand. *Global and Planetary Change*. 33(3–4):339–355.
- Cartigny MJB, Postma G, van den Berg JH, Mastbergen DR. 2011. A comparative study of sediment waves and cyclic steps based on geometries, internal structures and numerical modeling. *Marine Geology*. 280(1–4):40–56.
- Casciano CI, Patacci M, Longhitano SG, Tropeano M, McCaffrey WD, Di Celma C. 2019. Multi-scale analysis of a migrating submarine channel system in a tectonically-confined basin: The miocene gorgoglione flysch formation, southern Italy. *Sedimentology*. 66(1):205–240.
- Clark IR, Cartwright JA. 2011. Key controls on submarine channel development in structurally active settings. *Marine And Petroleum Geology*. 28(7):1333–1349.
- Collot J-Y, Lewis KB, Lamarche G, Lallemand S. 2001. The giant Ruatoria debris avalanche on the northern Hikurangi margin, New Zealand: result of oblique seamount subduction. *Journal of Geophysical Research*. 106:271–297.
- Cossu C, Wells GW. 2010. Coriolis forces influence the secondary circulation of gravity currents flowing in large-scale sinuous submarine channel systems. *Geophysical Research Letters*. 37(7):1–6.
- Cossu R, Wells MG, Peakall J. 2015. Latitudinal variations in submarine channel sedimentation patterns: the role of Coriolis forces. *Journal of the Geological Society*. 172(2):161–174.
- Crisóstomo-Figueroa A, McArthur AD, Dorrell RM, Amy L, McCaffrey WD. 2020. A new modelling approach to sediment bypass prediction applied to the East Coast Basin, New Zealand. *Geological Society of America Bulletin*. doi:10.1130/B35687.1.
- Damuth JE. 1979. Migrating sediment waves created by turbidity currents in the northern South China Basin. *Geology*. 7(11):520–523.

- Daarpanah Jazi S, Wells MG, Peakall J, Dorrell RM, Thomas RE, Keevil GM, Darby SE, Sommeria J, Viboud S, Valran T. 2020. Influence of coriolis force upon bottom boundary layers in a large-scale gravity current experiment: implications for evolution of sinuous deep-water channel systems. *Journal of Geophysical Research – Oceans*. 125(e2019JC015284):1–30.
- Davy B, Hoernle K, Werner R. 2008. Hikurangi Plateau: crustal structure, rifted formation, and Gondwana subduction history. *Geochemistry, Geophysics, Geosystems*. 9:1–31.
- Denniellou B, Huchon A, Beaudouin C, Berne S. 2006. Vertical grain-size variability within a turbidite levee: autocyclicity or allocyclicity? A case study from the Rhone neofan, Gulf of Lions, Western Mediterranean. *Marine Geology*. 234(1-4):191–213.
- Fernandez D, Bowen MM, Sutton PJH. 2018. Variability, coherence and forcing mechanisms in the New Zealand ocean boundary currents. *Progress in Oceanography*. 165:168–188.
- Flood RD. 1988. A lee wave model for deep-sea mudwave activity. *Deep-Sea Research*. 35:973–983.
- Flood RD, Piper DJW, Klaus A, Burns SJ, Busch WH, Cisowski S, Cramp A, Damuth JE, Goni MA, Haberle SG, et al. 1995. Leg 155 introduction; Amazon Fan. In: Marin JA, editor. *Proceedings of the Ocean Drilling Program, part A: Initial Reports*. Vol. 155. College Station: Texas A & M University, Ocean Drilling Program; p. 5–16.
- Fuhrmann A, Kane IA, Clare MA, Ferguson RA, Schomacker E, Bonamini E, Contreras FA. 2020. Hybrid turbidite-drift channel complexes: An integrated multiscale model. *Geology*. 48(6):562–568.
- Ghissetti FC, Barnes PM, Ellis S, Plaza-Faverola A, Barker DHN. 2016. The last 2 Myr of accretionary wedge construction in the central Hikurangi margin (North Island, New Zealand): insights from structural modelling. *Geochemistry, Geophysics, Geosystems*. 17:2661–2686.
- Hage S, Galy VV, Cartigny MJB, Acikalin S, Clare MA, Gröcke DR, Hilton RG, Hunt JE, Lintern DG, McGhee CA, et al. 2020. Efficient preservation of young terrestrial organic carbon in sandy turbidity-current deposits. *Geology*. 48(9):882–887.
- Hansen LAS, Callow RHT, Kane IA, Gamberi F, Rovere M, Cronin BT, Kneller BC. 2015. Genesis and character of thin-bedded turbidites associated with submarine channels. *Marine and Petroleum Geology*. 67:852–879.
- Hay AE. 1987. Turbidity currents and submarine channel formation in Rupert Inlet, British Columbia; 2, The roles of continuous and surge-type flow. *Journal of Geophysical Research–Oceans*. 92(3):2883–2900.
- Heezen BC, Ewing M, Menzies RJ. 1955. The influence of submarine turbidity currents on abyssal productivity. *Oikos*. 6(2):170–182.
- Hofmann H, Wickham H, Kafadar K. 2017. Letter-value plots: boxplots for large data. *Journal of Computational and Graphical Statistics*. 26(3):469–477.
- Howarth JD, Orpin AR, Kaneko Y, Strachan LJ, Nodder SD, Mountjoy JJ, Barnes PM, Bostock HC, Holden C, Jones K, Cağatay MN. 2021. Calibrating the marine turbidite palaeoseismometer using the 2016 Kaikōura earthquake. *Nature Geoscience*. 14:161–167.
- Jiao R, Seward D, Little TA, Kohn BP. 2015. Unroofing of fore-arc ranges along the Hikurangi Margin, New Zealand: constraints from low-temperature thermochronology. *Tectonophysics*. 656:39–51.
- Kane IA, Clare MA, Miramontes E, Wogelius R, Rothwell JJ, Garreau P, Pohl F. 2020. Seafloor microplastic hotspots controlled by deep-sea circulation. *Science*. 368(6495):1140–1145.
- Kane IA, Hodgson DM. 2011. Sedimentological criteria to differentiate submarine channel levee subenvironments: exhumed examples from the Rosario Fm. (Upper Cretaceous) of Baja California, Mexico, and the Fort Brown Fm. (Permian), Karoo Basin, S. Africa. *Marine and Petroleum Geology*. 28(3):807–823.
- Kane IA, Kneller BC, Dykstra M, Kassem A, McCaffrey WD. 2007. Anatomy of a submarine channel-levee: An example from Upper Cretaceous slope sediments, Rosario formation, Baja California, Mexico. *Marine and Petroleum Geology*. 24:540–563.
- Kane IA, McCaffrey WD, Peakall J. 2008. Controls on sinuosity evolution within submarine channels. *Geology*. 36(4):287–290.
- Kane IA, McCaffrey WD, Peakall J, Kneller BC. 2010. Submarine channel levee shape and sediment waves from physical experiments. *Sedimentary Geology*. 223(1-2):75–85.
- Kao SJ, Dai M, Selvaraj K, Zhai W, Cai P, Chen SN, Yang JYT, Liu JT, Liu CC, Syvitski JPM. 2010. Cyclone-driven deep sea injection of freshwater and heat by hyperpycnal flow in the subtropics. *Geophysical Research Letters*. 37(21):1–5.
- Keevil GM, Peakall J, Best JL, Amos KJ. 2006. Flow structure in sinuous submarine channels: velocity and turbulence structure of an experimental submarine channel. *Marine Geology*. 229(3-4):241–257.
- Kelly RW, Dorrell RM, Burns AD, McCaffrey WD. 2019. The structure and entrainment characteristics of partially confined gravity currents. *Journal of Geophysical Research: Oceans*. 124(3):2110–2125.
- Klaucke I, Hesse R, Ryan WBF. 1998. Seismic stratigraphy of the Northwest Atlantic Mid-Ocean Channel; growth pattern of a mid-ocean channel-levee complex. *Marine and Petroleum Geology*. 15(6):575–585.
- Kneller BC. 1995. Beyond the turbidite paradigm: physical models for deposition of turbidites and their implications for reservoir prediction. In: Hartley AJ, Prosser DJ, editor. *Characterization of deep marine clastic systems*. Geological Society of London Special Publication, Vol. 94. London: The Geological Society of London; p. 31–49.
- Kneller BC, Edwards DA, McCaffrey WD, Moore R. 1991. Oblique reflection of turbidity currents. *Geology*. 19(3):250–252.
- Kneller BC, McCaffrey WD. 1999. Depositional effects of flow nonuniformity and stratification within turbidity currents approaching a bounding slope; deflection, reflection, and facies variation. *Journal of Sedimentary Research*. 69(5):980–991.
- Kroeger KF, Crutchley GJ, Kellett R, Barnes PM. 2019. A 3-D model of gas generation, migration, and gas hydrate formation at a young convergent margin (Hikurangi Margin, New Zealand). *Geochemistry, Geophysics, Geosystems*. 20:5126–5147.
- Kuang Z, Zhong G, Wang L, Guo Y. 2014. Channel-related sediment waves on the eastern slope offshore Dongsha Islands, northern South China Sea. *Journal of Asian Earth Sciences*. 79:540–551.
- Lamb S. 2011. Cenozoic tectonic evolution of the New Zealand plate-boundary zone: A review. *Tectonophysics*. 509:135–164.
- Lewis KB. 1994. The 1500-km-long Hikurangi Channel: trench-axis channel that escapes its trench, crosses a plateau, and feeds a fan drift. *Geo-Marine Letters*. 14:19–28.
- Lewis KB, Barnes PM. 1999. Kaikōura Canyon, New Zealand: active conduit from near-shore sediment zones to trench-axis channel. *Marine Geology*. 162:39–69.

- Lewis KB, Collot JY, Lallemand SE. 1998. The dammed Hikurangi Trough: a channel-fed trench blocked by subducting seamounts and their wake avalanches (New Zealand-France GeodyNZ Project). *Basin Research*. 10:441–468.
- Lewis KB, Pantin HM. 2002. Channel-axis, overbank and drift sediment waves in the southern Hikurangi Trough, New Zealand. *Marine Geology*. 192(1-3):123–151.
- McArthur AD, Tek DE. 2021. Controls on the origin and evolution of deep-ocean trench-axial channels. *Geology*. doi:10.1130/G48612.1.
- McArthur AD, Claussmann B, Bailleul J, McCaffrey WD, Clare A. 2019. Variation in syn-subduction sedimentation patterns from inner to outer portions of deep-water fold and thrust belts: examples from the Hikurangi subduction margin of New Zealand. In: Hammerstein JA, Di Cuija R, Cottam MA, Zamora G, Butler RWH, editor. *Fold and thrust belts: structural style, evolution and exploration* Geological Society of London Special publication, Vol. 490. London: The Geological Society of London; p. 490–545.
- McArthur AD, Bailleul J, Mahieux G, Claussmann B, Wunderlich A, McCaffrey WD. 2021. Deformation-sedimentation feedback and the development of anomalously thick aggradational turbidite lobes: outcrop and subsurface examples from the Hikurangi Margin, New Zealand. *Journal of Sedimentary Research*. 91(4):362–389.
- McArthur AD, Kane I, Bozetti G, Hansen L, Kneller BC. 2020. Supercritical flows overspilling from bypass-dominated submarine channels and the development of overbank bedforms. *The Depositional Record*. 6(1):21–40.
- Menard HW. 1955. Deep-sea channels, topography, and sedimentation. *American Association of Petroleum Geologists Bulletin*. 39(2):236–255.
- Migeon S, Savoye B, Faugeres JC. 2000. Quaternary development of migrating sediment waves in the Var deep-sea fan; distribution, growth pattern, and implication for levee evolution. *Sedimentary Geology*. 133(3-4):265–293.
- Migeon S, Savoye B, Babonneau N, Andersson FLS. 2004. Processes of sediment-wave construction along the present Zaire deep-sea meandering channel: role of meanders and flow stripping. *Journal of Sedimentary Research*. 74(4):580–598.
- Migeon S, Savoye B, Zanella E, Mulder T, Faugeres JC, Weber O. 2001. Detailed seismic-reflection and sedimentary study of turbidite sediment waves on the Var sedimentary ridge (SE France); significance for sediment transport and deposition and for the mechanisms of sediment-wave construction. *Marine and Petroleum Geology*. 18(2):179–208.
- Miramontes E, Eggenhuisen JT, Jacinto RS, Poneti G, Pohl F, Normandeau A, Campbell DC, Hernández-Molina FJ. 2020. Channel-levee evolution in combined contour current–turbidity current flows from flume-tank experiments. *Geology*. 48(4):353–357.
- Mohrig D, Buttles J. 2007. Deep turbidity currents in shallow channels. *Geology*. 35(2):155–158.
- Mountjoy JJ, Barnes PM, Pettinga JR. 2009. Morphostructure and evolution of submarine canyons across an active margin: Cook Strait sector of the Hikurangi Margin, New Zealand. *Marine Geology*. 260(1-4):45–68.
- Mountjoy JJ, Howarth JD, Orpin AR, Barnes PM, Bowden DA, Rowden AA, Schimel AC, Holden C, Horgan HJ, Nodder SD. 2018. Earthquakes drive large-scale submarine canyon development and sediment supply to deep-ocean basins. *Science Advances*. 4(3):eaar3748.
- Morris EA, Hodgson DM, Brunt RL, Flint SS. 2014. Origin, evolution and anatomy of silt-prone submarine external levees. *Sedimentology*. 61(6):1734–1763.
- Muzzi Magalhaes P, Tinterri R. 2010. Stratigraphy and depositional setting of slurry and contained (reflected) beds in the Marnoso-arenacea formation (Langhian-Serravallian) Northern Apennines, Italy. *Sedimentology*. 57(7):1685–1720.
- Nakajima T, Kneller BC. 2013. Quantitative analysis of the geometry of submarine external levees. *Sedimentology*. 60(4):877–910.
- Nakajima T, Satoh M. 2001. The formation of large mudwaves by turbidity currents on the levees of the Toyama deep-sea channel, Japan Sea. *Sedimentology*. 48(2):435–463.
- Nakajima T, Satoh M, Okamura Y. 1998. Channel-levee complexes, terminal deep-sea fan and sediment wave fields associated with the Toyama deep-sea channel system in the Japan Sea. *Marine Geology*. 147(1-4):25–41.
- Nicol A, Mazengarb C, Chanier F, Rait G, Uruski C, Wallace L. 2007. Tectonic evolution of the active Hikurangi subduction margin, New Zealand, since the Oligocene. *TectonicS*. 26:1–24.
- Normark WR. 1970. Growth patterns of deep-sea fans. *AAPG Bulletin*. 54(11):2170–2195.
- Normark WR, Hess GR, Stow DAV, Bowen AJ. 1980. Sediment waves on the Monterey Fan levee; a preliminary physical interpretation. *Marine Geology*. 37(1-2):1–18.
- Normark WR, Piper DJW, Posamentier H, Pirmez C, Migeon S. 2002. Variability in form and growth of sediment waves on turbidite channel levees. *Marine Geology*. 192(1-3):23–58.
- Okon SU, Zhong Q, He Z. 2021. Experimental study on the vertical motion of colliding gravity currents. *Physics of Fluids*. 33(016601):1–11.
- Peakall J, Kane IA, Masson DG, Keevil GM, McCaffrey WD, Corney R. 2012. Global (latitudinal) variation in submarine channel sinuosity. *Geology*. 40(1):11–14.
- Pickering KT, Clark JD, Smith RDA, Hiscott RN, Ricci Lucchi F, Kenyon NH. 1995. Architectural element analysis of turbidite systems, and selected topical problems for sand-prone deep-water systems. In: Pickering KT, Hiscott RN, Kenyon NH, Lucchi FR, Smith RDA, editor. *Atlas of deep water environments; Architectural style in turbidite systems*. London: Chapman and Hall; p. 1–10.
- Piper DJW, Normark WR. 1983. Turbidite depositional patterns and flow characteristics, Navy submarine fan, California Borderland. *Sedimentology*. 30(5):681–694.
- Pirmez C, Flood RD. 1995. Morphology and structure of the Amazon channel. In: Marin JA, editor. *Proceedings of the ocean drilling program, part A: initial reports*. Vol. 155. College Station: Texas A & M University, Ocean Drilling Program; p. 23–45.
- Plaza-Faverola A, Klaeschen D, Barnes PM, Pecher I, Henrys S, Mountjoy J. 2012. Evolution of fluid expulsion and concentrated hydrate zones across the southern Hikurangi subduction margin, New Zealand: An analysis from depth migrated seismic data. *Geochemistry, Geophysics, Geosystems*. 13(8):1–21.
- Pohl F, Eggenhuisen JT, Tilston M, Cartigny MJB. 2019. New flow relaxation mechanism explains scour fields at the end of submarine channels. *Nature Communications*. 10(4425):1–8.
- Ribó M, Puig P, Muñoz A, Lo Iacono C, Masqué P, Palanques A, Acosta J, Guillén J, Ballesteros MG. 2016. Morphobathymetric analysis of the large fine-grained

- sediment waves over the Gulf of Valencia continental slope (NW Mediterranean). *Geomorphology*. 253:22–37.
- Romans BW, Castellort S, Covault JA, Fildani A, Walsh JP. 2016. Environmental signal propagation in sedimentary systems across timescales. *Earth Science Reviews*. 153:7–29.
- Savoie B, Piper DJW, Droz L. 1993. Plio-Pleistocene evolution of the Var deep-sea fan off the French Riviera. *Marine and Petroleum Geology*. 10:550–571.
- Sloutman A, Cartigny MJB. 2020. Cyclic steps: review and aggradation-based classification. *Earth-Science Reviews*. 201(102949):1–30.
- Straub KM, Mohrig D, Buttles J, McElroy B, Pirmez C. 2011. Quantifying the influence of channel sinuosity on the depositional mechanics of channelized turbidity currents: A laboratory study. *Marine and Petroleum Geology*. 28(3):744–760.
- Straub KM, Mohrig D, McElroy B, Buttles J, Pirmez C. 2008. Interactions between turbidity currents and topography in aggrading sinuous submarine channels; a laboratory study. *Geological Society of America Bulletin*. 120(3-4):368–385.
- Symons WO, Sumner EJ, Talling PJ, Cartigny MJS, Clare MA. 2016. Large-scale sediment waves and scours on the modern seafloor and their implications for the prevalence of supercritical flows. *Marine Geology*. 371:130–148.
- Tek DE, McArthur AD, Poyatos-Moré M, Colombera L, Patacci M, Craven B, McCaffrey WD. 2021. Relating seafloor geomorphology to subsurface architecture: how mass-transport deposits and knickpoint-zones build the stratigraphy of the deep-water Hikurangi channel. *Sedimentology*. Accepted.
- Timbrell G. 1993. Sandstone architecture of the balder formation depositional system, UK Quadrant 9 and adjacent areas. In: Parker JP, editor. *Petroleum Geology of Northwest Europe: Proceedings of the 4th Conference*. Petroleum Geology Conference series, London, United Kingdom, Vol. 4. London: The Geological Society of London; p. 107–121.
- Watson SJ, Mountjoy JJ, Crutchley GJ. 2020. Tectonic and geomorphic controls on the distribution of submarine landslides across active and passive margins, eastern New Zealand. In: Georgiopoulou A, Amy LA, Benetti S, Chaytor JD, Clare MA, Gamboa D, Houghton PDW, Moernaut J, Mountjoy JJ, editor. *Subaqueous mass movements and their consequences: advances in process understanding, monitoring and hazard assessments*, Geological Society, London, Special publications, Vol. 500. London: The Geological Society of London; p. 477–494.
- Wells M, Cossu R. 2013. The possible role of Coriolis forces in structuring large-scale sinuous patterns of submarine channel-levee systems. *Philosophical Transactions of the Royal Society A – Mathematical Physical and Engineering Sciences*. 371(2004):1–19.
- Wood R, Davy B. 1994. The Hikurangi Plateau. *Marine Geology*. 118:153–173.
- Wynn RB, Stow DAV. 2002. Classification and characterisation of deep-water sediment waves. *Marine Geology*. 192(1-3):7–22.
- Zhong G, Peng X. 2021. Transport and accumulation of plastic litter in submarine canyons—The role of gravity flows. *Geology*. 49(5):581–586.